TIME-DEPENDENT RELIABILITY OF FRP STRENGTHENED REINFORCED CONCRETE BEAMS UNDER COUPLED CORROSION AND CHANGING LOADING EFFECTS

Osama Ali

FIABILITE DANS LE TEMPS DE POUTRES EN BETON ARME RENFORCEES PAR DES PRF ET SOUMISES AUX EFFETS COUPLES DE LA CORROSION ET DE CHARGEMENTS EVOLUTIFS

TIME-DEPENDENT RELIABILITY OF FRP STRENGTHENED REINFORCED CONCRETE BEAMS UNDER COUPLED CORROSION AND CHANGING LOADING EFFECTS

THESE DE DOCTORAT

Spécialité : Sciences de l'Ingénieur
ECOLE DOCTORALE SCIENCES ET TECHNOLOGIES DE L'INFORMATION ET MATHEMATIQUES

Présentée et soutenue publiquement

le : 10 octobre 2012

à : l'Institut des Sciences et Techniques de l'Ingénieur d'Angers

par : Osama Mahmoud Mohamed ALI

Devant le jury ci-dessous :

Frédéric DUPRAT	Rapporteur	Maître de conférences, HDR à l'INSA de Toulouse
Emmanuel FERRIER	Rapporteur	Professeur à l'Université Claude Bernard Lyon 1
Brahim BENMOKRANE	Examinateur	Professeur à l'Université de Sherbrooke, Québec, Canada
Sofiane AMZIANE	Examinateur	Professeur à Polytech'Clermont
Abdessamad KOBI	Examinateur	Professeur à l'Université d'Angers

Directeur de thèse : **David BIGAUD**

Laboratoire : **LAboratoire en Sûreté de fonctionnement, QUalité et Organisation
Institut des Sciences et Techniques de l'Ingénieur d'Angers
62, avenue Notre Dame du Lac
49000 ANGERS**

To my family

ACKNOWLEDGEMENTS

There are many people whose help and contributions I would like to acknowledge. First of all, I am deeply indebted to my advisor Prof. *David BIGAUD*. Beyond having provided critical evaluation of my work and exceptional professional and personal support, he has consistently provided me with opportunities and encouragement that has allowed me to be self sufficient in carrying out my research

I would like to extend special gratitude to Prof. *Abdessamad KOBI* for accepting me within the research group of LASQUO laboratory.

I would further like to express my gratitude to the examining committee members, Prof. *Emmanuel FERRIER* and Dr. *Frédéric DUPRAT* for their helpful and valuable comments on this study. A special thanks for Prof. *Brahim BEN-MOKRANE* and Prof. *Sofiane AMZIANE* for accepting to be members of the examining committee.

I would also like to thank the fellow doctoral candidates in LASQUO laboratory, Angers University, Their fruitful discussions helped me to better understand research problems, and without their friendship, it would have been difficult to carry out this study.

I am forever grateful for the unconditional love and support of my family. In particular, I would like to extend my heartfelt gratitude to my parents. They consistently backed all my projects and taught me to forge ahead and accomplish my dreams.

RESUME

La durabilité des ponts en béton armé placés dans un environnement non-agressif est particulièrement satisfaisante. Toutefois, dans certaines conditions environnementales, leur durée de vie peut être significativement réduite sous l'influence de facteurs externes. Si l'on se réfère aujourd'hui aux codes de dimensionnement existants, les méthodes de contrôle des durées de vie se concentrent sur les effets pris séparément des principaux processus de dégradation (la corrosion, l'augmentation des chargements,…etc.). Il apparait toutefois essentiel d'étudier le couplage des effets de ces différents processus car leurs interactions peuvent conduire à la rapide perte d'intégrité des structures. A partir d'un certain niveau de dégradation le renforcement devient nécessaire afin de compenser les pertes de résistances et/ou de supporter des chargements complémentaires. Le collage extérieur de polymères renforcés de fibres (PRF) constitue une solution technologique de plus en plus privilégiée pour la réhabilitation des structures béton existantes. En vue de continuer à promouvoir l'utilisation de ces matériaux, une analyse de la fiabilité fonction du temps prenant en compte les incertitudes inhérentes aux (1) propriétés des matériaux constitutifs, (2) modèles et leurs paramètres, (3) facteurs environnementaux et (4) chargements induits par le trafic, est requise.

La contribution du présent travail de recherche est de proposer une analyse de la fiabilité en fonction du temps des poutres en béton armé réparées à l'aide de matériaux composites à base de PRF. Deux facteurs de dégradation seront considérés principalement : la corrosion des aciers d'armature et l'augmentation de la charge d'exploitation au cours du temps. Les modèles permettant de décrire les variations des propriétés des matériaux constitutifs, des dimensions et des chargements appliqués sur la structure sont extraits de la littérature. Plusieurs techniques d'analyse fiabiliste sont comparées ; la méthode d'approximation de fiabilité de premier ordre (ou First Order Reliability Method, FORM sous sons acronyme anglais), la simulation Monte Carlo et une méthode développée dans le cadre la thèse : une simulation type Monte Carlo exploitant les Réseaux de Neurones Artificiels. En parallèle, un bilan des travaux de recherche existants sur les composites à base de PRF collés extérieurement a conduit à l'identification des états limites, des modes de défaillance et les formules analytiques de dimensionnement correspondantes, qui devront être intégrés dans l'analyse de la fiabilité dans le temps.

Trois principaux objectifs sont considérés dans la présente étude. Le premier est de proposer des modèles probabilistes dépendant du temps pour les aciers d'armature (lois de distribution des sections) et des chargements d'exploitation. Le second objectif exprimé est de

conduire une analyse en termes de probabilité de défaillance ou d'indice de fiabilité variant dans le temps. L'analyse fiabiliste est fondée sur la méthode de dimensionnement des facteurs de charges et résistances (ou Load and Resistance Factor Design – LRFD en anglais) qui fournit un cadre idéal pour de telles analyses. Les modes de défaillance des poutres en béton armé réparées par composites à base de PRF, retenus dans la littérature, seront simulés en termes probabilistes par le biais de la méthode de fiabilité de premier ordre (on parlera de « probabilisation » de modèle) ; on parle ici des modes de défaillance par écrasement du béton, du décollement des composites, de leur rupture,… Le troisième objectif de la recherche a été de développer, afin de vérifier les résultats de la méthode de fiabilité de premier ordre en termes de temps calculés de réparation, une simulation de type Monte Carlo basée sur l'exploitation de Réseaux de Neurones et couplée avec la méthode des éléments finis (l'outil MOC-RENA-MEF). L'approche bâtie sur la base de cet outil permet au final de conduire des analyses fiabilistes et structurales plus pertinentes que celles réalisées en s'appuyant sur la méthode de fiabilité de premier ordre et les formules analytiques simplifiées de dimensionnement.

Les résultats des simulations révèlent que le couplage de la corrosion et de l'augmentation des chargements d'exploitation dans le temps affectent considérablement la fiabilité des poutres en béton armé, conduisant ainsi à une réduction importante de la durée de vie visée. En outre, les résultats montrent que l'efficacité de la réparation par composites à base de PRF sur le profil de fiabilité dans le temps des poutres en béton armé dépend, à l'état limite ultime, du mode de défaillance atteint : écrasement du béton ou décollement du PRF…On peut aussi conclure que le niveau de dégradation avant réparation n'affecte pas l'augmentation de la fiabilité induite par le renforcement à l'aide de PRF. Enfin, contrairement à l'état limite ultime, l'état limite de service en déplacement est affecté de manière significative, en termes de fiabilité, par la croissance des chargements quelque soit la dégradation induite par la corrosion.

Les résultats de ce travail permettent d'identifier plus clairement les nombreuses variables influençant la fiabilité des éléments de structures renforcés et d'affirmer le besoin de recherches complémentaires en vue de saisir plus précisément ces influences. Les deux variables significatives sur ce point sont : l'état de la structure existante au moment de la réparation et la complexité des chargements appliqués sur la structure.

Mots-clefs **:** pénétration des ions chlorures, corrosion, poutres béton armé renforcées par PRF, fiabilité, réseaux de neurones, méthode des éléments finis.

ABSTRACT

Durability of reinforced concrete bridges placed in non-aggressive environments is notably satisfactory. However, under certain environmental conditions, there are external factors that significantly reduce their lifetime. Referring to existing design codes, lifetime assessment of deteriorating structures nowadays focuses on the isolated effects of the main deterioration processes (corrosion, growth of loads…etc). However, it is paramount to study the coupled effects of various deterioration processes because such interactions could reduce structural integrity. At a certain level of deterioration, strengthening is an essential tool to compensate strength losses and/or to support additional loads. Externally bonded fiber reinforced polymer (FRP) composites are an increasingly adopted technology for the renewal of existing concrete structures. In order to encourage the further use of these materials, a time-dependent reliability analysis that considers the uncertainty inherent in (1) material properties, (2) models and their parameters, (3) environmental factors and (4) traffic loading, is needed.

The scope of the present study is to propose a time dependent reliability analysis of FRP strengthened RC beams. Two deterioration factors were considered: corrosion of steel reinforcement and growth of live load over time. Models to describe variations in the constitutive materials properties, dimensions and the structural loadings are drawn from the literature. Techniques for reliability analysis are compared; First Order Reliability Method FORM, Monte-Carlo MC simulation and, a method developed within the present research work: Monte-Carlo simulation based on Neural Network MC-NN. In parallel, existing works of externally bonded FRP are surveyed. This leads to identify the limit states, failure modes and their corresponding analytical design formulas to integrate in the time-dependent reliability analysis.

Three main objectives were considered in the present study. First one is to propose time-dependent probabilistic models of steel reinforcement and live load. Second objective is to perform probabilistic analysis in term of time dependent failure probability or reliability index. The reliability analysis is based on the Load and Resistance Factor Design (LRFD) that provides an ideal framework for reliability consideration. Failure modes of FRP strengthened RC beam included in the survey were probabilistically simulated (e.g. concrete crushing, FRP debonding, FRP rupture …etc) using FORM method. These failure modes are based on analytical expressions and simplified formulas reported in previous studies. The third objective is to develop a Monte-Carlo simulation based on Neural Networks and Finite Element Method MC-NN-FEM which aims at verifying the results of reliability analysis

using FORM method in terms of calculated time to strengthening. Simulation results show that MC-NN-FEM method provides eventually more accurate reliability and structural analyses than that obtained using FORM and simplified analytical design formulas.

Simulations results reveal that the combined effects of corrosion and growth of live loads over time strongly influence the reliability of RC beam, leading to large reduction in expected lifetime. Furthermore, the effectiveness of FRP strengthening on the reliability profile of RC beam depends on failure mode included in considered ultimate limit state ULS: concrete crushing or FRP debonding...etc. It is also concluded that the level of deterioration before strengthening does not affect the increase in the reliability due to strengthening. Unlike the ULS, serviceability limit state – deflection – is significantly affected, in terms of reliability, by the growth of live load regardless deterioration due to corrosion.

The results of this work bring to light the many variables affecting the reliability of strengthened members and the need for continuing research to better describe these variables. Two variables of particular significance, requiring extensive further study, are the state of the existing structure when strengthening is applied and the complexity of loads acting on the structure.

Key-words: chloride ingress, corrosion, FRP strengthened RC beams, reliability, neural network, finite element analysis.

TABLE OF CONTENTS

INTRODUCTION (EN FRANÇAIS)

INTRODUCTION

PART I: LITERATURE REVIEW

Chapter I.1: Deterioration of RC structures

Chapter I.2: Strengthening of RC beams using FRP composites

PART II: STRUCTURAL RELIABILITY OF FRP STRENGTHENED RC BEAM

Chapter II.1: Modeling of FRP strengthened RC beam

Chapter II.2: Structural analysis using neural networks applications

Chapter II.3: Structural reliability aspects

PART III: NUMERICAL APPLICATION AND RESULTS

Chapter III.1: Probabilistic model of design variables

Chapter III.2: Results of Reliability analysis

GENERAL CONCLUSIONS

CONCLUSIONS GENERALES

REFERENCES

APPENDICES

Appendix A: Experimental datasets

Appendix B: Statistical distributions

Appendix C: Results of reliability analysis

Appendix D: Abaqus input files

NOTATIONS

Latin letters

A_s	Area of reinforcement in tension zone;
A_{sc}	Area of reinforcement in compression zone;
ac	Aggregate-cement ratio
c_{comp}	Depth of compression zone in concrete section;
c	Thickness of concrete cover;
B	Shear span of the beam.
b_c	Width of concrete beam;
b_{FRP}	Width of FRP plate;
C_{nO_2}	Oxygen concentration at the steel surface;
C_{O_2}	Oxygen concentration on the concrete surface;
CoV_X	Coefficient of variation of a variable X;
C_s	Chloride surface concentration;
C_{th}	Critical threshold chloride concentration;
$D_{cl}(t)$	Chloride diffusion coefficient as function of time;
$D_{cl,ref}$	Reference chloride diffusion coefficient ;
D_{H_2O}	Diffusion coefficient in an infinite solution;
D	Diameter of corroded bar;
D_o	Diameter of non-corroded bar;
D_{O_2}	Oxygen diffusion coefficient;
D_{nO_2}	Oxygen diffusion coefficient at time t_n;
d_{FRP}	Distance between the top of the beam to the center of the plate;
$d_{FRP,v}$	Effective depth of shear FRP; = d_s for rectangular section, =d_s-slab thickness for T section);
d_s	Distance between the top of the beam to the center of tensile rebars;
d_{sc}	Distance between the top of the beam to the center of compressive rebars;
E_a	Modulus of adhesive layer;
E_c	Elastic modulus of concrete;
E_{FRP}	Elastic modulus of FRP composites;
$E_{FRP,v}$	Young's modulus of the FRP used for shear strengthening.
E_s	Elastic modulus of steel reinforcements;
F	Faraday's constant
f_{ct}	Tensile strength of the concrete;
$f_{FRP,u}$	Strength of FRP composites;
f_y	Yield stress of the reinforcement;
$f_{y,v}$	Yield strength of the steel stirrups
f_{yk}	Characteristic yield stress of the reinforcement;
f'_c	Compressive strength of the concrete;
f'_{ck}	Characteristic compressive strength of the concrete;
f'_{cu}	Concrete compressive strength over concrete cube;

Notations

G_a	Shear modulus of the adhesive layer
$g_i(X)$	Limit state i function of a vector of random variables X in physical x-space;
$H_i(U)$	Limit state i of function of a vector of random variables U is standard normal u-space ;
h_c	Over all depth of the concrete section;
i_{corr}	Corrosion current;
M_u	Ultimate moment capacity;
m_{age}	Aging coefficient of chloride diffusion process;
n_s	Homogenization coefficient of the flexural steel reinforcement;
n_{FRP}	Homogenization coefficient of the flexural FRP composites;
$n_{FRP,v}$	Homogenization coefficient of the shear FRP composites;
n_{O2}	Electric number of oxygen molecules participating in chemical reaction;
n_{sv}	Homogenization coefficient of the shear steel reinforcement;
$I_{FRP,v}$	Moment of inertia of the FRP plate used for shear strengthening;
$h_{FRP,v}$	Total height of FRP strip used for shear strengthening;
$f_{FRP,uv}$	Ultimate strength of FRP composite used for shear strengthening;
$f_{FRP,u}$	Ultimate strength of FRP composite used for flexural strengthening;
P_f	Probability of failure;
R	Resistance of the structural element;
R_c	Coefficient of correlation;
RH	Relative humidity;
RH_c	critical relative humidity $=0.75$;
s_{FRP}	Spacing between FRP strips for shear strengthening;
S_i	Applied bending moment or shearing force due to load case i; dead, Live, impact …etc;
s_s	Spacing between steel stirrups;
t	Time;
t_a	Thickness of adhesive layer;
T	Temperature;
$t_{FRP,v}$	Thickness of the FRP flexural strip;
$t_{FRP,v}$	Thickness of the FRP shear strips;
t_n	Time at which Oxygen concentration at steel level is closer to Oxygen concentration on concrete surface (assumed equals to 500 years);
t_{ini}	Time to corrosion initiation;
t_{sp}	Time to severe cracking of concrete cover;
U_c	Activation energy of diffusion process;
U_{O_2}	Activation energy of the coefficient of oxygen diffusion;
V	Ultimate shear capacity;
V_c	Contribution of concrete of the shearing force;
V_{FRP}	FRP of concrete of the shearing force;
V_s	Steel of concrete of the shearing force;
W_c	Amount of corrosion product;
W_{cr}	Critical mass of corrosion products;
w_c	Surface crack width of concrete cover due to corrosion;
wc	Water-to-cement ratio;
w_{FRP}	Width of the FRP strips for shear strengthening;
X_n	Nominal value of a variable X;
z	Flexural lever arm of RC section;

Greek letters

β	Reliability index;
β_{min}	Minimum required reliability index;
β_T	Target reliability index;
γ_i	Partial safety factor of an applied loads corresponds to a loading case i; dead, Live, impact …etc;
ε_c	Concrete strain;
$\varepsilon_{c,max}$	Maximum concrete strain;
ε_{cs}	Compressive steel strain;
ε_{co}	Concrete strain at stress equals to concrete compressive strength;
ε_{FRP}	FRP plate strain;
$\varepsilon_{FRP,exist}$	Tensile strain in concrete at the interface between concrete and FRP material due to dead loads only;
$\varepsilon_{FRP,uv}$	Ultimate strain of FRP composite used for shear strengthening;
ε_s	Strain in tensile steel;
ε_{cu}	Ultimate crushing concrete strain;
ε_y	Yield strain of steel rebars;
θ	Angle between the critical shear crack and the longitudinal axis of the beam;
λ_m	Structural model error of the limit state m
λ_X	Bias ratio of a variable X;
μ_X	Mean value of a variable X;
v_c	Poisson's ratio of the concrete;
ρ_a	Density of aggregate;
ρ_c	Density of cement;
ρ_{rust}	Density of corrosion product;
ρ_s	Density of steel;
σ_X	Standard variation of a variable X;
Φ	Normal standard function;
ϕ	General safety factor of the structural resistance;
ψ_{FRP}	Specific FRP contribution partial safety factor;

LIST OF TABLES

LIST OF FIGURES

****

****

****

****

****

****

<u>INTRODUCTION</u>

<u>(en Français)</u>

INTRODUCTION

ASPECTS GENERAUX

Les ouvrages en béton armé constituent une part importante des infrastructures mondiales. Ces ouvrages moulés présentent une variété de formes et de finitions. Ils sont considérés comme stables, durables et performants tout au long de leur cycle de vie en service. Toutefois, les ouvrages en béton armé ne présentent pas un comportement satisfaisant dans le temps lorsqu'ils sont placés dans des environnements agressifs ou extrêmes (par exemple, c'est le cas de structures en environnements marins ou soumis à un trafic intense). Dans de tels environnements, les ouvrages BA peuvent être sévèrement endommagés et voir leur fiabilité réduites au fur et à mesure de leur exploitation

L'attaque des ions chlorures initiant la corrosion des barres d'armature constitue un problème majeur pour les ouvrages du génie civil. Un effort de recherche considérable a été consenti afin d'évaluer les effets de la corrosion résultant de l'attaque des ions chlorure. Les conclusions des études réalisées mettent en évidence le fait que la corrosion provoque une dégradation des propriétés mécaniques dans la mesure où les sections, contraintes élastiques et déformations ultimes des bars d'armature sont réduites. [Cairns *et al* 2005; Almusallam 2001]. Ces pertes de propriétés des barres d'armature, qui constituent l'impact principal de la corrosion, contribuent au vieillissement prématuré des structures en béton armé. Palsson et Mizra en (2002) rapportent le cas au Canada d'un pont d'une quarantaine d'années ayant perdu jusqu'à 80% de ses sections d'armatures au moment de sa démolition en 1999. Mais l'accumulation de produits de la corrosion à l'interface entre le béton et les barres en acier à d'autres effets : la perte d'adhérence entre béton et acier, l'apparition de fissures et l'éclatement de l'enrobage de béton. [Lui and Weyers 1998; Li *et al* 2006]. La Figure 1.1 ci-dessous illustre ces cas d'endommagement après corrosion. La défaillance de l'interface entre barres d'acier corrodé et le béton a bien plus d'impact vis-à-vis de l'état limite de service que de l'état limite ultime. Des observations effectuées par Stewart et Mullard en (2007) ont permis de montrer que même pour des cas de fissurations sévères des ponts en béton armé, la perte de résistance enregistrée n'était que de 10 à 20 pourcents. L'impact en termes de sécurité est donc peu significatif.
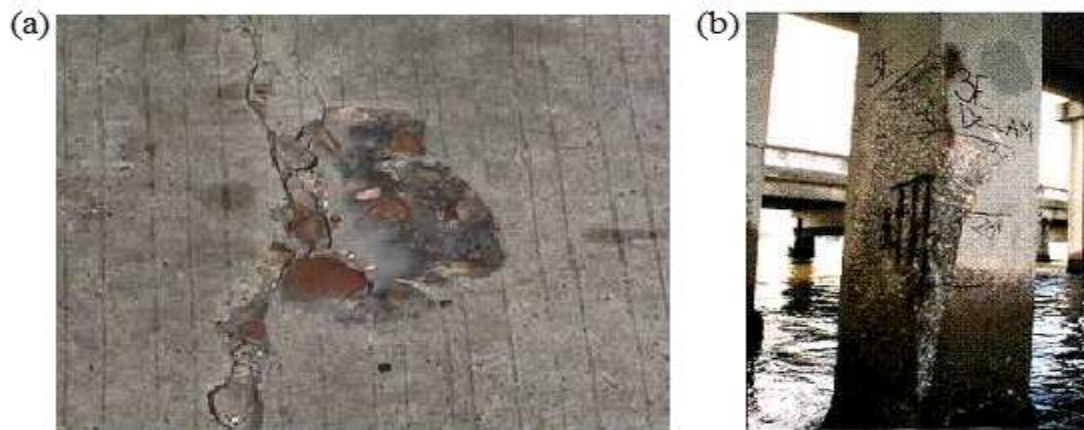
Figure 1.1 : Dégradation après corrosion des barres d'armatures en acier (a) fissuration du béton (b) éclatement du béton.

En termes de coûts, une étude conduite par le laboratoire CC Technologies Laboratories Inc en 2001 a permis de chiffrer l'impact économique de la corrosion dans les secteurs de l'industrie aux Etats-Unis. Il ressort de cette étude que le coût direct total de la corrosion est proche de 137,9 milliards de dollars par an, considérant l'ensemble des domaines industriels (infrastructure, équipements, transports, fabrication,…) – cf Figure 1.2(a). Pour le seul domaine des infrastructures, la part du coût direct induit par les problèmes de corrosion a été estimée à 16,4% (soit 22,6 milliards de dollar par an). La Figure 1.2(b) présente le détail de la contribution de chaque secteur au domaine des infrastructures.

(a) Coûts annuels induits par les problèmes de corrosion dans les secteurs de l'industrie aux Etats-Unis ($137.9 milliards)

(b) Coûts annuels induits par les problèmes de corrosion dans les secteurs de l' infrastructure ($22.6 milliards)
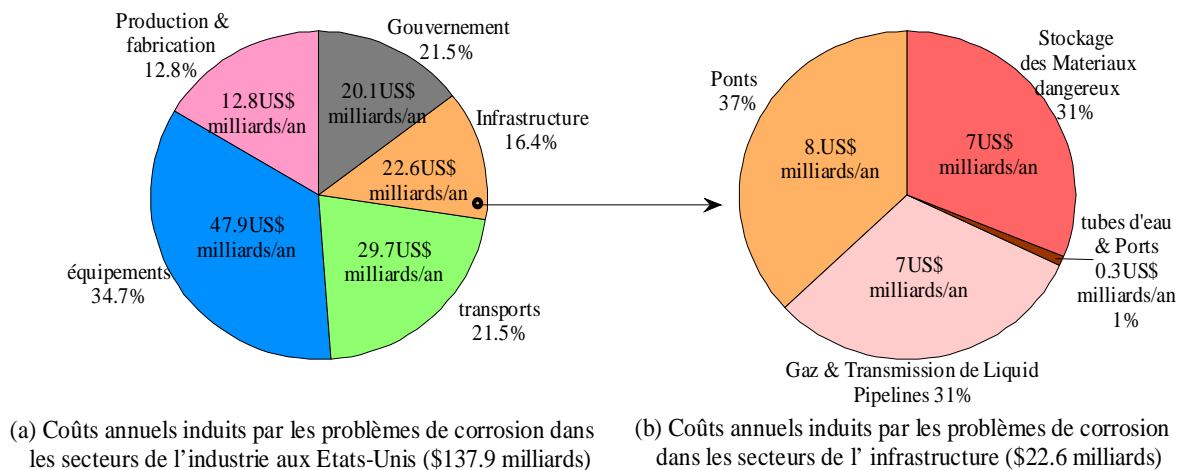
Figure 1.2: Coûts annuels induits par les problèmes de corrosion aux Etats-Unis [CC Technologies Laboratories Inc 2001].

Cette étude donne également des informations plus détaillées sur les 583000 ponts environ que comptent les Etats-Unis. Parmi eux, 200000 sont en acier, 235000 en béton armé, 108000 en béton précontraint et 40000 autres n'entrent pas dans ces catégories. Il ressort de l'étude que 15% de ces ponts doivent être considérés comme structurellement défaillants du fait de la corrosion des éléments de structure et des barres d'armatures. Le coût direct induit par la

corrosion est estimé à 8,3 milliards de dollars, avec dans le détail 3,8 milliards pour le remplacement sur 10 ans de ces ponts défaillants, 4 milliards pour la maintenance et 0,5 milliards dédiés à la repeinte des ponts métalliques.

Un autre facteur de dégradation très important vis-à-vis de la fiabilité des ponts est l'augmentation des charges d'exploitation dans le temps. Stewart et Rosowsky (1998) affirme qu'aux Etats-Unis que 45% des ponts considérés défaillants voient leur dégradation structurelle induite par un trafic routier inapproprié (augmentation à la fois des charges par essieu et des flux). Dans une autre étude consacrée aux ponts de la région de Victoria en Australie, Koay (2011) remarque que 70% d'entre eux ont été construits avant 1975 et qu'ils ont été dimensionnés pour supporter beaucoup moins de charges que les ponts conçus actuellement. Ces ponts voient donc leurs capacités plus rapidement dégradées dans leurs conditions de service. Une grande part de ces ponts nécessiterait un renforcement urgent voire, dans l'idéal, d'être remplacés afin de reprendre l'augmentation des chargements et des trafics de véhicules.

Le contrôle des ouvrages existants se fonde généralement sur trois étapes principales [Val *et al* 2000]. La première étape consiste en l'inspection sur site et la compilation de données statistiques. L'inspection est le plus souvent programmée avec une fréquence réglementée. Elle permet d'identifier les changements intervenus depuis la dernière inspection. Chen et Duan (2003) rapportent que le National Bridge Inspection Standard (NBIS) recommande de ne pas dépasser deux ans entre chaque inspection. Des mesures complémentaires et des tests peuvent être requis. Dans le cas d'ouvrages en béton armé dans un environnement à forte teneur en ions chlorures, aux premiers signes de dégradation ; fissures, délaminage ou éclatement de l'enrobage de béton, des essais partiellement ou non destructifs peuvent être conduits afin de déterminer l'état des performances des matériaux (en général, carottage et test ou utilisation du marteau de Schmidt afin d'estimer *in situ* la résistance en compression du béton), de contrôler certaines dimensions (détecteur électromagnétique afin de localiser et mesurer les profondeurs d'enrobage des barres d'acier) et de détecter les défauts majeurs (marteau de choc pour localiser les fissures ou vides internes, mesures de la résistivité pour l'estimation du niveau de corrosion des armatures) [Suo et Stewart, 2009].

La seconde étape, intégrée au contrôle des ouvrages existants, consiste en l'analyse structurale pour déterminer les performances globales. Cette analyse peut être conduite en adoptant une approche déterministe basée sur la comparaison directe entre valeurs de résistance et de sollicitation ou en privilégiant une approche probabiliste ou fiabiliste exprimant la performance de l'ouvrage en termes de probabilité de rupture. La troisième

étape, enfin, consiste en la prise de décision établie sur une comparaison entre le comportement réel du pont (basé sur les deux premières étapes d'inspection et d'analyse structurale) et les exigences des codes de dimensionnement appropriés. Alors, une décision pourra être prise entre le renforcement, et la technique à utiliser, ou bien le remplacement de l'ouvrage.

Le renforcement des ponts existants en béton armé constitue une alternative fréquemment considérées par les ingénieurs structure quand l'évaluation de leurs performances indique une baisse de leurs résistances de flexion ou au cisaillement. Comme évoqué précédemment, des dépenses considérables sont consacrées chaque année à la réparation de tabliers de ponts BA. Aux Etats-Unis, les sommes s'élèvent à 3 milliards de dollars par an alors que l'instauration de bonnes pratiques de maintenance permettrait de réduire ces montants par au plus 46% [CC Technologies Laboratories Inc 2001]. La méthode de renforcement la plus efficace, et la plus répandue, consiste en l'utilisation de renforts collés par l'extérieur. Depuis longtemps, des plaques en acier ont été collées sur les parties tendues ou sur les flancs de poutres en béton armé pour augmenter respectivement les résistances en flexion et au cisaillement. Depuis un vingtaine d'années maintenant, l'application externe de lamelles de polymères renforcés de fibres (PRF) a progressivement remplacée l'utilisation de plaques en acier. Les matériaux composites à base de PRF ont mobilisé l'attention de par leur forte résistance spécifique (définie comme le rapport entre la résistance et leur poids ou leur densité), leur facilité d'application, de manipulation et de transport, leur résistance vis-à-vis de la corrosion,… De plus, l'inconvénient du coût élevé de ces composites peut être compensé au regard des faibles coûts d'application et des coûts de maintenance sur le cycle de vie.

La dégradation des performances d'une structure devient un problème quand la marge de sécurité est trop réduite. L'approche traditionnellement utilisée pour déterminer le niveau sécurité qu'offre une structure méthode s'appuie sur un critère sur les contraintes, dans le domaine élastique, exprimé sous la forme :

$$\frac{\sigma_{appliquée}}{\sigma_{admissible}} \leq F \tag{1.1}$$

Où, $\sigma_{appliquée}$ et $\sigma_{admissible}$ représentent respectivement les composantes de contraintes appliquée et admissible. F est le facteur de sécurité.

L'équation Equation 1.1 peut s'exprimée également sous un autre formalisme impliquant la résistance de la section et les actions appliquées :

$$\frac{S_{\{L_i\}}}{R_{\{x_i\}}} \leq F \tag{1.2}$$

Où, R exprime la résistance de l'élément de structure considéré. Elle est fonction d'un vecteur de variables de dimensionnement notées $\{x_j\}$ qui peuvent être les propriétés mécaniques des matériaux ou les caractéristiques dimensionnelles de la section. S représente les actions appliquées sur l'élément de structure. Ce paramètre est fonction du vecteur des charges appliquées $\{L_i\}$: permanente, variable, dynamique,…etc.

Tout ou partie des composantes des vecteurs $\{x_j\}$ et $\{L_i\}$ peuvent être considérés de manière déterministe, c'est-à-dire par une valeur unique et déterminée par avance. Ce calcul déterministe pourra être privilégié quand les incertitudes ou variabilités des paramètres - chargements, propriétés matérielles, géométrie de la section – influençant la mesure de la fiabilité ou de la marge de sécurité d'une structure peuvent être négligées. Ce type d'approche peut être utile pour les calculs réalisés dans le domaine élastique. Toutefois, pour les hauts niveaux de chargements (i.e. si l'on se rapproche des états limites ultimes), ces approches déterministes ne sont pas satisfaisantes ni efficaces car il s'agit de prendre des décisions dans un contexte devenant incertain. Dans ce cas, on se tournera vers les méthodes plus pertinentes de type probabilistes ou fiabilistes. Ces démarches sont de plus en plus prônées aujourd'hui dans l'analyse des structures.

Selon la norme NF EN 13306 *Terminologie de la maintenance*, la fiabilité est « l'aptitude d'une entité à accomplir une fonction requise, dans des conditions données, durant un intervalle de temps donné ». Le terme fiabilité est également utilisé pour désigner la valeur de la fiabilité et peut être défini comme une probabilité. C'est alors la probabilité pour qu'une entité puisse accomplir une fonction requise, dans des conditions données, pendant un intervalle de temps donné. Dans le domaine des structures du génie civil, la fiabilité de tels systèmes peut être définie en termes statistiques comme la probabilité que la structure considérée assure un niveau de performance adapté (vis-à-vis de l'état limite ultime de résistance, de service ou d'un autre état limite) durant un temps déterminé (qui est le plus souvent celui de la vie de l'ouvrage). En ces termes, la fiabilité s'exprimera usuellement sous la forme d'un indice (β) ou d'une probabilité de défaillance (P_f).

La fonction définissant la limite entre sécurité et défaillance peut s'écrire :

$$R_{\{x_j\}} - S_{\{L_i\}} \leq 0 \tag{1.3}$$

Avant d'estimer la fiabilité en se basant sur les concepts probabilistes, il est nécessaire de choisir quelles seront les composantes des vecteurs $\{x_j\}$ et/ou $\{L_i\}$ qui seront considérés en tant que variables stochastiques : chacune d'entre elles sera définie par une valeur moyenne,

un écart-type et un type de distribution statistique. Ainsi, pour revenir aux indicateurs de la fiabilité, la probabilité de défaillance d'un élément de structure pourra s'exprimer :

$$P_f = \mathrm{Pr}\,ob\left(R_{\{x_j\}} - S_{\{L_i\}} \leq 0\right) \tag{1.4}$$

L'indice de fiabilité s'exprimant quant à lui :

$$\beta = -\Phi^{-1}\left(P_f\right) \tag{1.5}$$

Où, Φ^{-1} est la fonction inverse de la loi normale (ou gaussienne).

Généralement, les objectifs principaux des analyses probabilistes, au-delà de la seule évaluation de l'indice de fiabilité, consistent en l'établissement ou encore la calibration des facteurs de sécurité partiels impliqués dans les équations de dimensionnement.

Dans le code de dimensionnement, ces facteurs de sécurité se retrouvent dans le formalisme des fonctions d'états limites :

$$\phi R = \sum \gamma_i S_i \tag{1.6}$$

Où, ϕ est le facteur de sécurité partiel associé à la résistance R. γ_i est le facteur de sécurité partiel de la charge appliquée S_i correspondante.

Cette équation Equation 1.6 a été développée initialement au cours des années 60 pour une première application dans les codes de dimensionnement des structures en béton armé [Melchers 1999]. La calibration des facteurs de sécurité présents dans l'équation Equation 1.6 consiste à traiter le problème d'optimisation associé à l'équation Equation 1.4. L'objectif étant un indice de probabilité cible β_T (ou une probabilité de défaillance limite). Cet objectif de fiabilité est généralement évalué par des comités d'experts et dépend de nombreux facteurs comme le type de structure, son environnement, l'état limite considéré, le type et le mode de défaillance, les conséquences financières, en termes de sécurité,… La Figure 1.3 donne une vision générale des objectifs en termes de probabilité de défaillance exprimés par des experts pour différents secteurs industriels à risques se différenciant par leurs durées de vie [Lemaire *et al* 2009]. A titre d'exemple plus précis, l'indice de fiabilité à 50 ans dans le cas de l'état limite ultime sera donnée dans l'annexe C de l'Eurocode 0 (2001) avec une valeur cible de 3.8 (1.5 pour l'état limite de service ELS) ce qui correspond à une probabilité de rupture (en 50 ans) de 7.2×10^{-5} (7.0×10^{-2} à l'ELS).
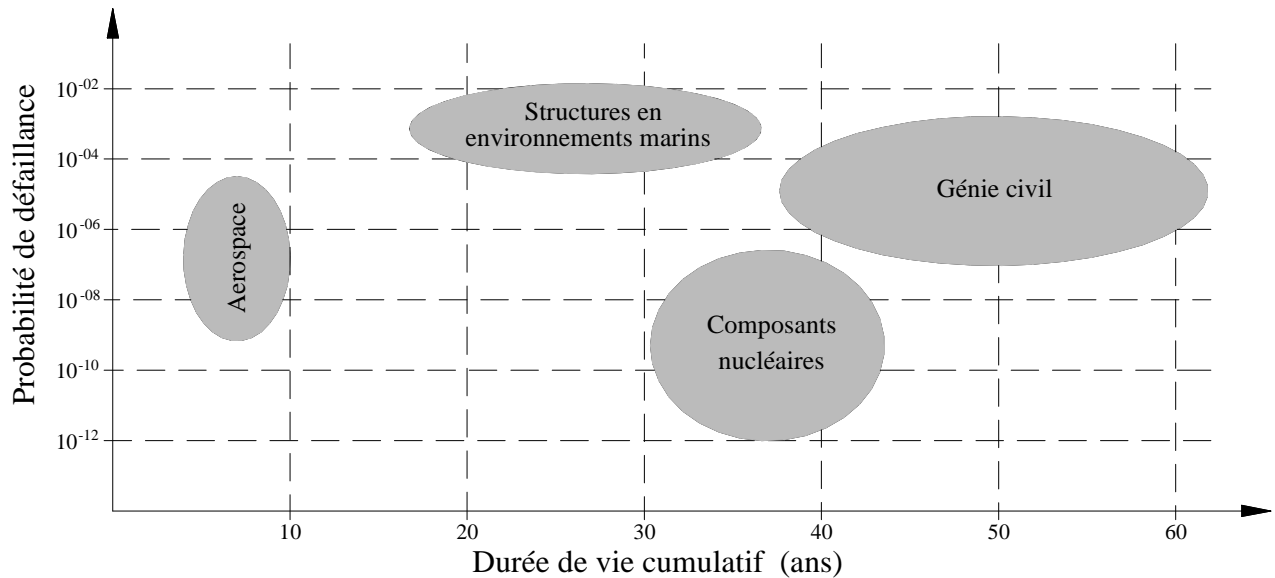
Figure 1.3 : Niveaux de fiabilité, exprimés en termes de probabilité de défaillance limites, pour diedfférents secteurs industriels [Lemaire *et al*, 2009].

Cet objectif de fiabilité doit être tenu dans le temps tel qu'attendu par la norme NF EN 13306 évoquée plus avant. L'étude de la fiabilité dans le temps ou « fiabilité dépendante du temps » implique généralement l'évaluation de la durée de service d'une structure sous l'influence de facteurs de dégradation associés aux chargements, aux propriétés matérielles et géométriques. La durée ou temps de service d'une structure peut être définie comme le temps pendant lequel une structure est apte à assumer certaines spécifications techniques ou d'assurer un certain niveau de fiabilité. L'analyse de la fiabilité dépendante du temps peut être menée à partir des Equations 1.3 et 1.4 en y implémentant des modèles de dégradation de la résistance et/ou d'augmentation des chargements dans le temps.

De nombreuses méthodes ont été développées afin d'estimer la fiabilité (pour un temps donné et/ou dépendante du temps) des structures. On peut citer les méthodes de fiabilité du premier et second ordre (plus connues sous leurs acronymes en anglais FORM pour First Order Reliability Method et SORM pour Second Order Reliability Method), ou encore celles s'appuyant sur les simulations Monte-Carlo. Les deux premières sont les plus couramment employées. Elles consistent en des méthodes d'approximation de la fonction d'état limite. La méthode dite Monte Carlo est basée sur la génération de nombres aléatoires ; elle sera plus précise mais requerra un grand nombre de simulations bien souvent trop consommatrices en temps de calculs [Lemaire, 2009 ; Melchers, 1999].

CADRE ET OBJECTIFS DE LA RECHERCHE

Le principal objectif de la présente étude est de conduire l'analyse de la fiabilité dépendante

du temps de poutres d'un pont en béton armé sujette à la corrosion par attaque des ions chlorures et soumise à l'augmentation des charges de trafic dans le temps. Les poutres en béton armé devront être renforcées quand l'indice de fiabilité aura été réduit à un niveau minimum autorisé (β_{min}). Le renforcement sera réalisé à l'aide de lamelles de PRF collées sur le dessous et les faces latérales de la poutre. Les états limites ultimes de résistance en flexion et au cisaillement et l'état limite de service (en déplacement) seront considérés dans l'étude. Pour le premier état limite de résistance en flexion, de multiples modes de défaillance sont considérés : rupture du béton en compression, décollement et rupture des lamelles de PRF en partie courante, la décohésion de l'enrobage et le décollement des lamelles de PRF depuis leurs extrémités.

L'analyse fiabiliste sera conduite en deux temps : une étude individuelle de chaque état limite et de chaque élément, suivie d'une analyse de la superposition des modes couplés ou concurrents de défaillance et de dégradation dans une étude à l'échelle du système, celle de la structure.

La présente recherche donc requiert que les efforts soient portés sur plusieurs aspects : les composites à PRF, sur l'analyse de la fiabilité dépendante du temps et sur l'analyse au niveau de la structure. La Figure 1.4 permet de visualiser le champ des compétences nécessitant d'être intégrée dans nos travaux. Chaque aspect s'imbrique avec les autres ; ceci illustre le besoin de traiter le problème dans son ensemble plutôt que de façon découplée. Chaque zone de ce diagramme, y compris au niveau des imbrications, permet d'identifier les sept éléments (et leurs sous-éléments) d'étude nécessaires à notre recherche.

1. **PRF:** Nature, propriétés, durabilité
2. **Fiabilité:** Variables aléatoires, états limites, méthode de fiabilité, modèles statistiques des chargements variables.
3. **Structure:** Modes de rupture, analyse structurale : modèles analytiques ou approches numériques (méthode des éléments finis), comportement des matériaux.
4. **PRF – Fiabilité:** Représentation statistique des propriétés du PRF ; moyenne, écart-type, loi de distribution.
5. **Fiabilité – Structure:** Méthode fiabiliste, méthodes d'analyse et leurs incertitudes.
6. **PRF – Structure:** courbes contrainte-déformation des PRF collés, modélisation du comportement des lamelles de PRF au sein du modèle de la structure.
7. **PRF – Fiabilité – Structure:** Valeurs minimum et cible de l'indice de fiabilité, modèles statistiques pour les matériaux, méthodes de fiabilité, modèles de dégradation, des charges variables appliquées, méthode d'analyse

Figure 1.4 : Les éléments d'étude à considérer pour l'analyse de la fiabilité dépendante du temps de poutres de ponts béton armé renforcées par composites de PRF.

Les principaux objectifs ou points clefs de la recherche consistent en :

1. la détermination d'un modèle probabiliste des propriétés variables dans le temps des aciers à partir d'une simulation de type Monte Carlo et d'un modèle probabilisé de corrosion induite par attaque des ions chlorures.

2. la détermination d'un modèle probabiliste des chargements variables du trafic à partir d'une simulation de type Monte Carlo s'appuyant sur les observations sur site de Nowak [Nowak 1993, 2004] et sur les hypothèses quant à la variation au cours des années des charges des camions.

3. la construction du profil de fiabilité (tracé de l'indice de fiabilité ou de la probabilité de défaillance en fonction du temps) de poutres BA dégradées et réparées par des PRF accompagnée de l'analyse de l'effet de la réparation sur la fiabilité. La fiabilité est calculée en appliquant la méthode de fiabilité de premier ordre (FORM) sur les équations simplifiées des codes de dimensionnement. La calibration des facteurs de sécurité partiels pourra en être déduite.

4. la proposition d'une méthode d'analyse de la fiabilité d'une structure couplant simulations de Monte-Carlo, Reseaux de Neurones Artificiels et Méthode des Eléments Finis (MOC – RENA – MEF). Cette approche pourra être validée en comparant ses résultats avec certains points du profil de fiabilité construit précédemment.

5. l'établissement de recommandations sur la base des résultats obtenus et sur la comparaison entre méthodes FORM et MOC-RENA-MEF.

ORGANISATION DU MANUSCRIT DE THESE

Le travail de thèse est présenté en trois parties en plus de celles consacrées à la présente introduction et à la conclusion générale. La première partie sera divisée elle-même en deux chapitres. Le premier d'entre eux consiste en un rappel et une revue quant à la dégradation des structures en béton armé par corrosion des barres d'acier sous l'effet des ions chlorures, quant aux mécanismes de pénétration des ions chlorures, de corrosion des renforts and de la fissuration de l'enrobage de béton. Le second chapitre sera quant à lui consacré à une discussion brève sur les méthodes de réparation des poutres en béton armé suivie d'une revue des techniques de renforcement à l'aide de PRF, de leurs propriétés, de leur durabilité pour finir par une étude du comportement des poutres renforcées ou réparées à l'aide de PRF et de leurs modes de défaillance.

La seconde partie est divisée en trois chapitres. Le premier sera consacré tout d'abord à la

modélisation structurale de poutres renforcées à l'aide de PRF. Cette première section fera le bilan des formules analytiques relevées dans la littérature existante et les codes de dimensionnement. Des détails pour chaque état limite – ultime et de service -, chaque mode de défaillance seront donnés. La suite du premier chapitre permettra d'introduire les principes et bases de la modélisation numérique – par la méthode des éléments finis – des poutres BA renforcées. Dans ce cadre, une brève description des modèles de comportement des matériaux constitutifs et des éléments de structure sera donnée. La modélisation par éléments suivis sera conduite sur un logiciel commercial (ABAQUS). Le deuxième chapitre de la partie II se concentrera sur l'explication de la construction de surfaces de réponse – établies en fonction des variables du dimensionnement – couplées avec des réseaux de neurones afin de simuler la réponse structurale. Dans ce chapitre nous présenterons de manière détaillée l'architecture interne de ces réseaux neuronaux. Le troisième chapitre introduira quant à lui les fondamentaux des approches stochastiques. Ce chapitre débute par la définition de termes principaux liés à l'analyse fiabiliste et par la présentation des méthodes pouvant être utilisées pour calculer les indices de fiabilité telles que les méthodes d'approximation des surfaces de réponse aux premier ou au second ordres et les techniques de simulation basées sur les réseaux de neurones. Ce chapitre se conclura sur le détail pas à pas de la procédure développée pour l'analyse de la fiabilité dépendante du temps.

La troisième et dernière partie de la thèse se divise en deux chapitres. Le premier se décompose en deux sections. La première vise à présenter dans le détail – dimensions du pont, valeurs caractéristiques des propriétés des matériaux, chargements appliqués et autres spécifications du dimensionnement - le cas étudié dans la suite de la recherche. La seconde section fait le bilan des variables amenées à être considérées comme stochastiques. Une étude de sensibilité permettra de justifier *in fine* la nature stochastique ou déterministe des différentes variables. Ceci réalisé, cette section se poursuit par l'évaluation des modèles probabilistes de la section des aciers (perte de section du fait de la corrosion) et des charges de trafic en fonction du temps. Le deuxième chapitre de la partie III se concentre sur l'analyse de la fiabilité dépendante du temps des poutres BA renforcées par des lamelles de PRF à fibres de Carbone (PRFC). Les profils de fiabilité en fonction du temps sont déterminés dans un premier temps en utilisant la méthode d'approximation du premier ordre (FORM) et en s'appuyant sur les équations analytiques reportées et validées par la littérature ou les codes de dimensionnement. Ces profils de fiabilité sont dans un second temps reconstruit en utilisant la simulation de Monte-Carlo par Tirages d'Importance seule (i.e. sans couplage avec réseaux neuronaux et calcul éléments finis). La comparaison des résultats permettra de juger de la

pertinence de l'approximation faite par la méthode FORM. Enfin, la méthode développée dans le cadre de la recherche, MOC-RENA-MEF, est utilisée pour recalculer certains points du profil (au temps de première mise en service du pont, au moment de la réparation et plusieurs points après la réparation).

Le dernier chapitre de l'étude contient les conclusions générales de cette étude. En plus, le chapitre contient des recommandations pour de futures recherches

INTRODUCTION:

GENERAL ASPECTS

Reinforced concrete structures make up an important part of the national infrastructures. It can be casted into a variety of shapes and finishings. Usually, it is durable, strong, and performing well throughout its service lifetime. However, RC structures behave inadequately over the time when placed in severe or aggressive environments (for example, structures in marine environments or under heavy traffic). Such environments could dramatically damage the concrete structure and decreasing its reliability through the service life.

Chlorides-induced corrosion that affects the reinforcing steel in concrete is also a major problem facing civil structures. A considerable research effort has been done to evaluate chlorides-induced corrosion effects. It has been found from these studies that corrosion causes deterioration in the properties as it reduces the area, yield strength and ultimate strain of steel rebars [Cairns *et al* 2005; Almusallam 2001]. Losses in the properties of steel rebars are the major corrosion deterioration factor that induces rapid aging of RC structures. Palsson & Mizra (2002) reported that up to 80% loss of cross-section areas for reinforcing a 40-years-old Canadian bridge demolished in 1999. In addition, the accumulation of corrosion products in steel/concrete interface causes losses of the bond between concrete and steel bars, cracking and spalling of the concrete cover [Lui & Weyers 1998; Li *et al* 2006]. Figure 1.1 shows typical examples of corrosion-induced damage: cracking and spalling of concrete cover. Loss of bonded between corroded bars and concrete is more hazardous in studying serviceability - deflection - limit state rather than the ultimate limit state. Field studies have shown that RC bridges at the time of severe cracking loss no more than 10-20% of its strength and the loss of safety is not significant [Stewart & Mullard 2007].
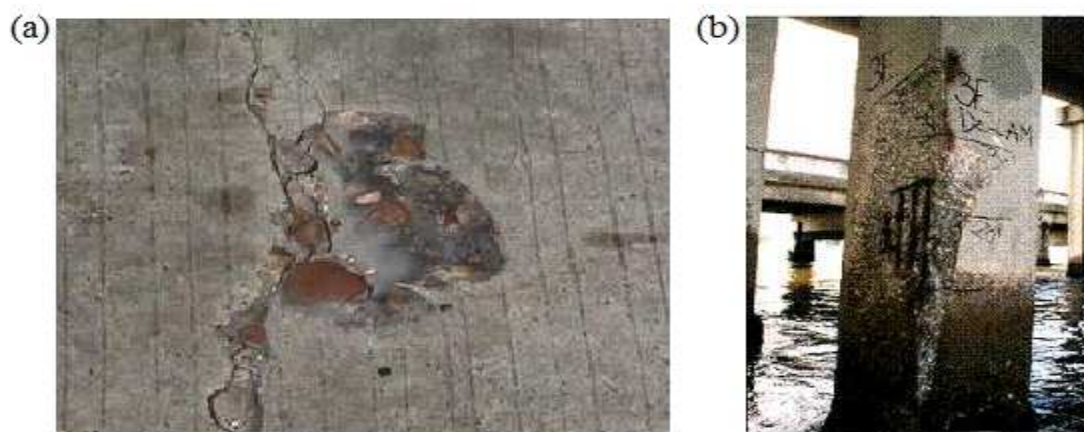
Figure 1.1: Damages induced by corrosion (a) concrete cracking (b) concrete spalling.

Regarding to corrosion cost, in a study conducted by [CC Technologies Laboratories Inc 2001] to determine the economic impact of corrosion for industry sectors, it was found that the total direct cost of corrosion in the USA is close to US$137.9 billion per year for all industrial categories; infrastructure, utilities, transportation, production & manufacturing and government. Direct cost of corrosion of infrastructure only was estimated to be 16.4% ($22.6 billion/year) of the total direct cost. Figure 1.2 presents the contribution of each sector in the infrastructure category.

(a) Annual cost of corrosion in industry categories in USA ($137.9 billion)

(b) Annual cost of corrosion in infrastructure sectors ($22.6 billion)
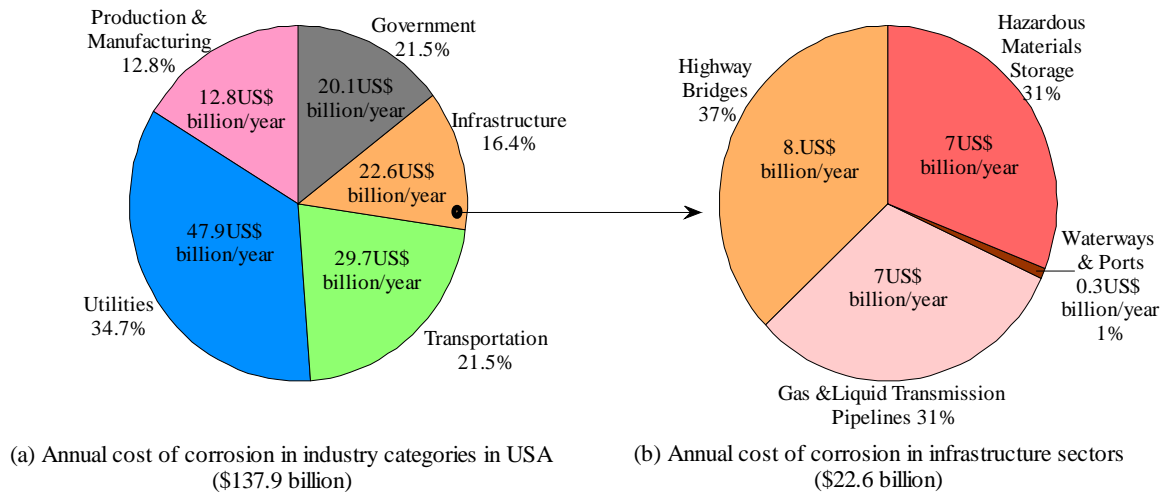
Figure 1.2: Annual cost of corrosion in USA [CC Technologies Laboratories Inc 2001].

According to the study, there are approximately 583,000 bridges in the U.S. Of this total, 200,000 are constructed of steel, 235,000 are conventional reinforced concrete, 108,000 are constructed using prestressed concrete and the balance is made with other construction materials. Approximately 15% of these bridges are structurally deficient because of corroded steel and steel reinforcement. Annual direct cost estimates total $8.3 billion, including $3.8 billion to replace deficient bridges over the next 10 years, $2 billion for maintenance and capital costs for concrete bridge decks and $2 billion for their concrete substructures, and $0.5 billion for maintenance painting of steel bridges.

Another deterioration factor of a great importance should be considered in studying the safety of bridges is the growth of live load over the time. Stewart & Rosowsky (1998) reported that in the USA there are approximately 45% of bridges that are currently deficient due to either structural deterioration and/or traffic inadequacy (increased traffic loads/volume). Koay (2011) reported that approximately 70% of the bridges in Victoria were built before 1975. They were designed to carry much lower loads than today's bridges and their capacities are being further reduced by deterioration in their condition. A high proportion of these bridges require strengthening and ideally replacement in order to meet the

ever increasing traffic volumes and heavier commercial vehicle loads.

Assessment of an existing bridge usually involves three main steps [Val *et al* 2000]. First is the site inspection and collection of statistical data. Inspection is often done usually on a regular basis to identify the changes that have occurred since previous inspection time. Regular intervals not exceeding 2 years as recommended by National Bridge Inspection Standard (NBIS) [Chen & Duan 2003]. Further measurements and testing may be required. For RC structures in chloride contaminated environment, the first sign of corrosion induced distress is cracking, delamination or spalling of concrete cover. Partial destructive or nondestructive techniques may be used to determine material properties (e.g., core testing or the use of Schmidt hammer to estimate in situ concrete compressive strength), element dimensions (e.g., electromagnetic cover-meter to located and measure cover of reinforcing bars) and detect defects (e.g., impact echo to locate large voids or delamination, half-cell potential and resistivity measurements to predict the likelihood of corrosion) [Suo & Stewart 2009]. Second is the structural analysis to determine the structural performance. Structural analysis may be performed deterministically (based on design load and resistance) or probabilistically (based on reliability or probability of failure). Third is the decision making based on a comparison between the actual bridge behavior (based on inspection and structural analysis) and appropriate code requirements, thus, a decision about appropriate strengthening technique or replacement can be made.

The strengthening of existing RC bridges is one of the current problems faced by the structural engineers when the strength evaluation indicates a decrease in flexural or shear strength. In general, strengthening takes place as the structural performance deteriorate throughout the service lifetime of the structure. In the recent years, the need for strengthening or rehabilitation of reinforced concrete structures had been increased, due to the aging of these structures, damage of these structures, modifications in design codes or to support higher vehicle loads. As previously mentioned, in the USA up to US$3 billion/year is spent on repair of RC bridge decks, however it is estimated that improved maintenance practices can reduce this amount by up to 46% [CC Technologies Laboratories Inc 2001]. The most power strengthening tool that had been widely used for reinforced concrete structures is the use of externally bonded reinforcements. Traditionally, steel plates have been bonded to tensioned surface or to the side of the RC beams to raise flexural or shear strengths respectively. However, over the last two decades the applications of fiber reinforced polymers (FRP) laminates as an external reinforcement have replaced the use of steel plates. FRP composites laminates have received more attention than steel plates due to their high strength-to-weight

ratio, ease of installation, transportation, corrosion resistance …etc. Although, FRP composites cost may be high, it can be offset by the low installation and long-term maintenance costs.

The degradation in the structure performance becomes a problem when the safety margin is too small. The traditional method to define structural safety is through a factor of safety, usually used in elastic stress analysis which require that

$$\frac{\sigma_{applied}}{\sigma_{permissible}} \leq F \tag{1.1}$$

where, $\sigma_{applied}$ and $\sigma_{permissible}$ are the applied and permissible stress components respectively. F is the safety factor. Equation 1.1 can be given also in the term of stress resultants (section resistance and the applied action), obtained by appropriate integration:

$$\frac{S_{\{L_i\}}}{R_{\{x_i\}}} \leq F \tag{1.2}$$

where, R is the resistance of the structural member and function of a vector of design variables $\{x_i\}$; such as material properties or section geometry. S is the applied actions on the structural member and function of a vector of the applied loads $\{L_i\}$: dead, live, impact, etc.

All or some of the components of $\{x_i\}$ and $\{L_i\}$ are expressed deterministically with their deterministic values. This approach was considered as a measure of the reliability or safety of a loaded structure within the elastic range, as, the uncertainties associated – in: loads, material properties, geometries – using the elastic ranges may be neglected. However, deterministic approaches are not efficient for decisions taken under uncertainty induced from high loading level (i.e., structure is close to the ultimate limit state), a more useful assessment and powerful tool is probabilistic or reliability analysis which is recently used in safety analysis.

According to NF EN 13306 *Maintenance Terminology standard*, reliability is « the ability of an item to perform a required function under given conditions during a given time interval». The term reliability is also used to denote the value of reliability and can be defined as a probability. It is then the probability for an entity to perform a required function, under stated conditions, for a given time interval. In the domain of civil engineering structures, reliability of structural systems can be defined in statistical term as the probability that the structure under consideration has a proper performance (strength, serviceability or other limit state) throughout its lifetime. In these terms, reliability is usually expressed in the form of reliability index (β) or probability of failure (P_f).

The safety limit state will be expressed as:

$$R_{\{x_i\}} - S_{\{L_i\}} \leq 0 \qquad (1.3)$$

In order to estimate the reliability using probabilistic concepts it is necessary to introduce some/all components of $\{x_i\}$ and/or $\{L_i\}$ as stochastic variables: each stochastic variable is expressed by mean value, standard deviation and a certain statistical distribution. Thus, the probability of failure of the structural element can be stated as:

$$P_f = \left(R_{\{x_i\}} - S_{\{L_i\}} \leq 0\right) \qquad (1.4)$$

The reliability index can be expressed as:

$$\beta = -\Phi^{-1}\left(P_f\right) \qquad (1.5)$$

where Φ^{-1} is the inverse standard normal function.

Generally, the major objectives of probabilistic analysis beside evaluating the reliability index is to calibrate the partial safety factors involved in limit state design equations that are recently reported in most design codes [e.g., AASHTO-LRFD 2007]. It takes the form,

$$\phi R = \sum \gamma_i S_i \qquad (1.6)$$

where, ϕ is the partial safety factor on the resistance R. γ_i is the partial safety factor on the corresponding applied load S_i.

Equation 1.6 was originally developed during the 1960s for reinforced concrete codes [Melchers 1999]. Calibration of partial safety factors associated in Equation 1.6 is based on optimizing equation 1.4 to reach a target reliability index β_T (e.g., AASHTO-LRFD requires $\beta_T=3.5$). Target reliability index is generally evaluated by expert or code committee and generally depends on many factors such as: type of structure, environment, limit state, type of failure, consequences of cost…etc. Figure 1.3 summarizes probabilities of failure estimated by experts in different industrial areas involving all the greatest risks, but with very different lifetimes [Lemaire *et al* 2009]. For more specified example, reliability index of 50 years in the case of ultimate limit state will be given in Appendix C of the Eurocode 0 (2001) with a target value of 3.8 (1.5 for serviceability limit state SLS) which corresponds to a probability of failure (in 50 years) of 7.2×10^{-5} (7.2×10^{-2} for SLS).

This objective of reliability must be held in time as expected by the standard NF EN 13306 as previously mentioned. Time-dependent reliability generally results in the evaluation of service lifetime for a certain structure under deterioration factors associated in loads, material properties and geometry of the structural element. The service lifetime of a structure can be defined as time during which the structure is able to meet specific technical requirements or a target reliability level. Time-dependent reliability analysis can be performed

using Equations 1.3 or 1.4 with certain deterioration models of the strength or/and the growth of loads over the time.
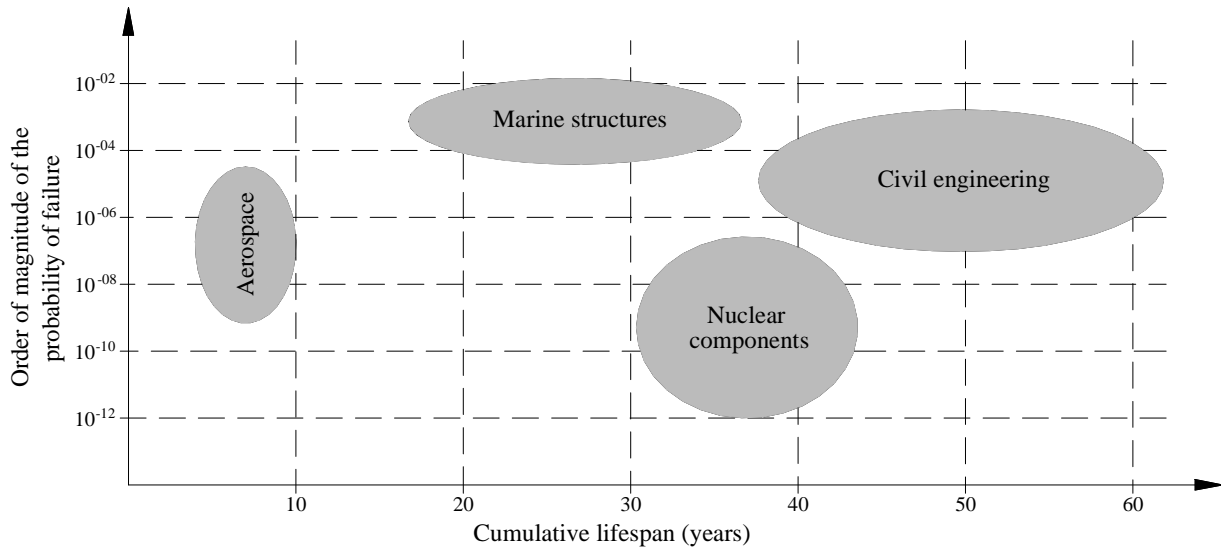
Figure 1.3: Level of probabilities estimated in different industrial branches [Lemaire *et al* 2009].

Many methods were developed to estimate the structural reliability such as First Order Reliability Method (FORM), second order reliability Method (SORM) and Monte-Carlo simulation methods (MC). The first two methods are the most common and they are considered as approximated methods but they required many differential calculations especially SORM. Monte-Carlo method (MC) is based on random number generation theory, but it needs a high number of simulations and it is considered time consuming [Lemaire *et al* 2009; Melchers 1999].

SCOPE AND RESEARCH OBJECTIVES

The main objective of present study is to perform a time variant reliability analysis of reinforced concrete bridge girder under chlorides-induced corrosion and growth of live load over the time. The concrete girder has to be strengthened when the reliability index of the girder is deteriorated to a minimum reliability index (β_{min}). The girder is strengthened using externally bonded FRP strengthening technique. The limit states considered in the study are: ultimate limit state (e.g. flexural and shear) and serviceability limit state (deflection). For flexural limit state, multiple failure modes were considered; concrete crushing, FRP debonding, FRP rupture concrete cover separation, and FRP end debonding.

Reliability analysis is divided into two steps: reliability analysis for each individual limit state, then, an overall reliability analysis for a system of these limits states. Generally, the study is exposed through three main categories: FRP composites, Time dependents reliability

analysis and structural analysis. Figure 1.4 identifies these categories with significant amounts of overlap. This represents the need to consider the problem as a whole, rather than as three independent categories. Each region on this diagram can be used to identify an aspect of developing a time-dependent reliability analysis of FRP strengthening RC beam. The significant domains associated with each portion of the diagram are given in Figure 1.4.

1. **FRP:** properties, types, durability.
2. **Reliability:** random variables, limit states, reliability method, statistical models of live load.
3. **Structure:** failure modes, analysis method; complete analytical approaches or numerical approaches (finite element method), material behavior.
4. **FRP-Reliability:** statistical presentation of FRP properties; mean, standard deviation, distribution.
5. **Reliability-Structure:** reliability method, analysis method, uncertainty in analysis method
6. **FRP-Structure:** stress-strain curve of FRP composites, method of modeling FRP composite in the structural model.
7. **FRP-Reliability-Structure:** target & minimum reliability value. Material statistical models, reliability methods, deterioration model, live load, analysis method

Figure 1.4: Components of Reliability Based Design for FRP Strengthening.

The specific objectives of the studies are as the following:

1. Evaluate a probabilistic model for the steel properties over the time using Monte-Carlo simulation based on a chlorides-induced corrosion model.

2. Evaluate a probabilistic model for the live load model using Monte-Carlo simulation based on Nowak's field observations [Nowak 1993; 2004] and on the truck variation over time proposed by Stewart & Rosowsky [Stewart & Rosowsky 1998].

3. Construct the reliability profile of FRP strengthened RC deteriorated girder and examine the effect of strengthening on the reliability reinforced concrete girder. Reliability was performed by applying the first order reliability method on the simplified design equations presented in design codes. This method is used to calibrate partial safety factor for the FRP composites.

4. Perform a reliability analysis using Monte-Carlo based on Neural Network application and finite elements method (MC-NN-FEM). The results will be compared with the results obtained in the previous step at certain points on the reliability profile.

5. Eventually, recommendations will be given based on the results obtained and the comparison between FORM and MC-NN-FEM algorithms.

THESIS OUTLINES

The manuscript is divided into three parts in addition to the present introductory part and a general conclusion. Part I is divided into two chapters. The first chapter of part I reviews the deterioration of the reinforced concrete structures under chlorides-induced corrosion of steel rebars embedded in concrete; chloride ingress, reinforcement corrosion, and concrete cover cracking. While the second chapter of part I presents a brief discussion about repairing methods of RC girders. Afterwards, the sections review FRP strengthening RC girders; FRP material - history, types, properties, fabrication, durability... etc - behavior of FRP strengthening RC girder, failure modes of FRP strengthening RC girder, and design codes.

Part II is divided into three chapters. The first Chapter of part II outlines the structural modeling of FRP strengthening RC girder. The first section of the chapter presents the analytical formulas used to model FRP strengthening RC girder which reported in previous studies and design codes. Explanations for each ultimate limit state – flexural and shear - and failure modes were introduced. The next section of the chapter introduces the principles and basics of numerical formulation - finite elements method - of FRP strengthening RC girder. In addition the section gives a brief description of material constitutive models and structural elements used to model FRP strengthened RC girder. Abaqus package commercial software was used to perform the finite elements analysis.

Chapter 2 of part II explains how to construct a response surface based on design variables to simulate the structural responses using neural network applications. Also, the chapter contains a description of the overall construction of architecture neural network and its individual components; inputs. Chapter 3 of part II presents stochastic approach aspects. The chapter starts with outlines of all the reliability definitions and principles of uncertainty modeling. The chapter also gives definitions and methods that could be used to calculate the reliability value such as first order reliability methods, second order reliability method, and simulation techniques based on neural networks applications. In addition, the chapter concludes the steps required to solve time-variant reliability analysis.

Part III integrates all aspects of the thesis by carrying out a numerical example. Part III is divided into two chapters. The first chapter of part III evolved three sections. The first section presents a detailed description of the design case assumed in the study; bridge dimensions, characteristic values of material properties, loads, and design specifications. The second section introduces all random variables that will be considered in the study based on a sensitive reliability analysis. The section also goes in details to evaluate the time dependent

probabilistic models for steel area and traffic loads over the time. The second chapter integrates on the time-dependent reliability analysis of CFRP strengthened RC girder. Reliability profiles over the time were drawn using first order reliability analysis (FORM) based on analytical design formulas and equations reported in design codes. The reliability profiles were constructed for the ultimate limit states discussed in the first chapter of part II: flexural limit state, CFRP end debonding based shear crack and shear limit state. Based on the results obtained using FROM method, sensitivity factors of the random variables were presented for the different limit states considered in the study. In addition, the chapter presents results of the reliability analysis using Monte-Carlo based on neural networks application and finite elements method MC-NN-FEM. The later analysis was performed at strengthening time. The aim of this analysis is to check the reliability using the finite element method which is considered the most power accurate tool in the analysis of structures. Furthermore, this chapter presents the results of the reliability analysis of serviceability limit state SLS (deflection) using MC-NN-FEM.

The last chapter of the study contains the general conclusions of this study including recommendations for future actions to be taken.

PART I:
LITERATURE REVIEW

PART I: LITERATURE REVIEW

Chapter I.1: Deterioration of RC structures

I.1.1 GENERAL

Chloride penetration in RC structures leading to reinforcement corrosion has been widely studied in recent publications [e.g., Stewart Al-Harthy 2008; Atadero & Karbhari 2007: Val & Trapper 2008]. The corrosion deterioration process can be divided into three main stages; initiation, propagation before cover cracking and propagation after cover cracking. This classification corresponds to the observed variation of corrosion current parameters through each stage. Initiation stage does not include losses in the strength of the RC section. Generally, corrosion causes extensive damages of RC structures, as it reduces the geometrical and mechanical properties of the steel bars leading to slow losses in the whole strength of the RC section after corrosion initiation. Rate of deterioration increases with time, this increase induces radial cracks in the concrete cover due to the accumulation of corrosion production at the steel/concrete interface. In addition, the formed crack in the concrete cover causes direct loss in the bond between the steel and concrete which eventually leads to overall collapse of the RC structure (see Figure I.1.1).
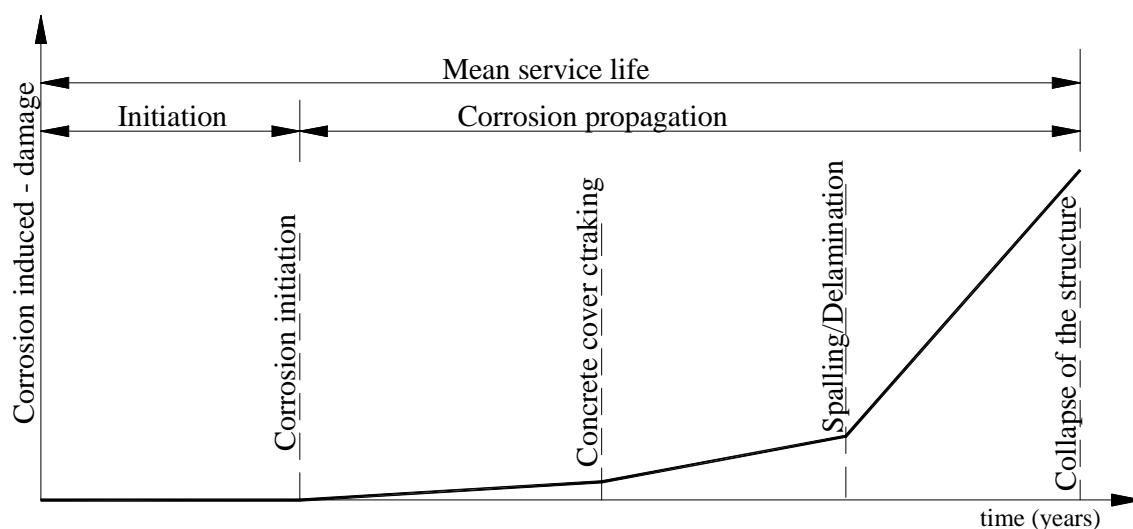
Figure I.1.1: Service life of reinforced concrete structures affected by corrosion.

Pitting and uniform corrosion are the most two common types of corrosion of steel reinforcement embedded in concrete. Pitting corrosion occurs when only a small area of steel loses its passive layer, usually due to high concentrations of Cl^- ions. Pitting corrosion is characterized by a large cathode area and a small anode area resulting in accelerated

corrosion. Uniform corrosion occurs when the pits grow together and when anode areas are large and the cathode areas are small. The corrosion rate of the latter is much slower when compared to pitting corrosion because of the lower cathode to anode ratio [Żemajtis 1998]. Val *et al* (2000) distinguish two types of pitting corrosion along bar length based on in site measurements of repaired bridges: coarse and fine pits which are characterized by corroded lengths ranges between 20-100 mm and 2-4 mm respectively.

The main objectives of this chapter are to review:

- The basics and principals of corrosion mechanism
- Chloride diffusion in concrete leading to initiation, propagation of corrosion process in addition to damages induced in the properties of reinforcement due to corrosion.
- Concrete cover cracking which results in updating of corrosion current

I.1.2 MECHANISM OF CORROSION OF STEEL IN CONCRETE

The strongly alkaline nature of concrete, due to $Ca(OH)_2$ with a pH of about 13, prevents the corrosion of the steel reinforcement by the formation of a thin protective film of iron oxide on the metal surface. This protection is known as passivity. However, if the concrete is permeable to the extent that soluble chlorides penetrate right up to the reinforcement while both water and oxygen are present, thus corrosion of reinforcement will take place. The passive iron oxide layer is destroyed when the pH falls below about 11.0. Corrosion of steel occurs because of the electro-chemical action which is usually encountered when two dissimilar metals are in electrical contact in the presence of moisture and oxygen. However, the same process takes place in steel alone because of differences in the electrochemical potential on the surface, which also leads to form a corrosion cell.

Basically, corrosion cell involved four components: anode, cathode, electrolyte and electrical connection. The anode usually corrodes by loss of electrons from electrically neutral metal atoms to form discrete ions. These ions may remain in solution or react to form insoluble corrosion products. The electrochemical process is often divided into primary electrochemical processes and secondary processes. The primary electrochemical processes starts when the concentration of the chloride at the corrosion cell reaches a critical threshold value, at this point the passive film is degraded by chloride ions or the pH reduced by carbonation, the metallic *Fe* at the anode is oxidized to form ferrous ions (Fe^{2+}):

$$Fe \rightarrow Fe^{2+} + 2e^-$$ (I.1.1)

The released electrons at the anode flow through the steel to the cathodic areas, as illustrated in Figure I.1.2 [Ahmed 2003]. The above reaction is initially balanced by cathodic

reaction of dissolved oxygen (O_2) to hydroxyl ions (OH):

$$2H_2O + O_2 + 4e^- \rightarrow 4OH^- \tag{I.1.2}$$
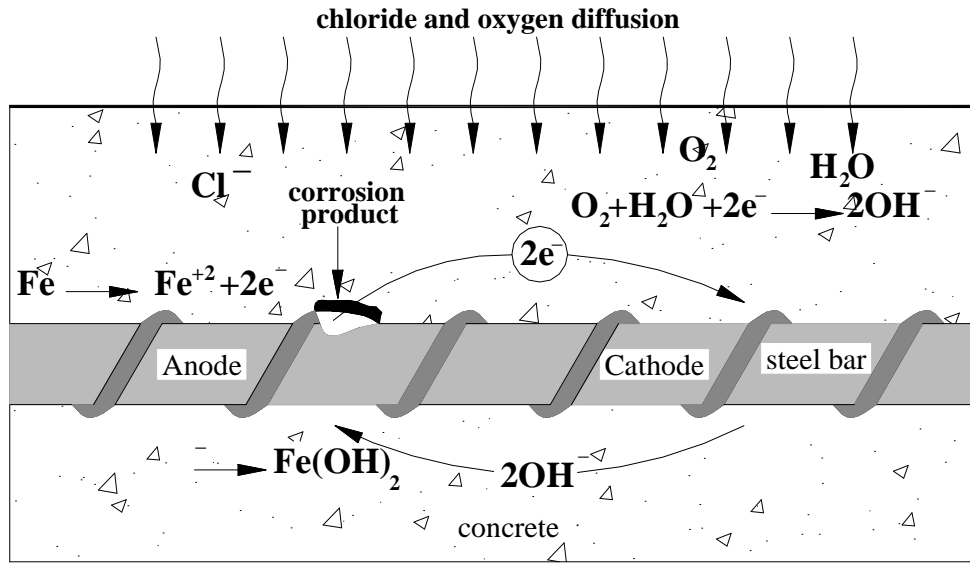
Figure I.1.2: Schematic illustration of corrosion mechanism of reinforcement in concrete.

The anodic product Fe^{2+} reacts with the cathodically formed hydroxyl ions to produce a ring of a white precipitate of ferrous hydroxide $Fe(OH)_2$:

$$Fe^{2+} + 2OH^- \rightarrow Fe(OH)_2 \tag{I.1.3}$$

In the secondary processes corrosion products are generated. Various corrosion products can be produced depending basically on the pH of the solution. The $Fe(OH)_2$ can be further converted to hydrated ferric oxide ($Fe_2O_3.H_2O$), also known as ordinary red-brown rust, and black magnetite (Fe_3O_4) preceded by the formation of green hydrated magnetite ($Fe_3O_4.H_2O$):

$$4Fe(OH)_2 + O_2 \rightarrow Fe_2O_3.H_2O + 2H_2O \tag{I.1.4}$$

$$6Fe(OH)_2 + O_2 \rightarrow Fe_2O_4.H_2O + 4H_2O \tag{I.1.5}$$

$$Fe_2O_4.H_2O \rightarrow Fe_3O_4 + H_2O \tag{I.1.6}$$
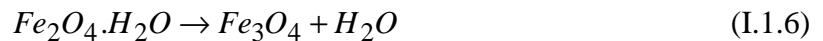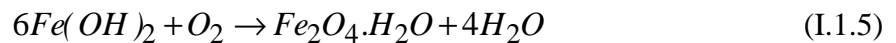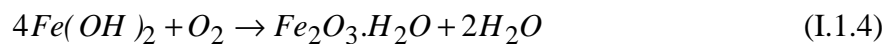
Most of forms of chemical reactions due to corrosion are affected by some factors. Such these factors may be classified into two major categories: external factors (mostly environmental) and internal factors (depend on the concrete and steel quality). Table I.1.1 presents a summary of these factors. It is well known that the different corrosion products have different densities and expansions volumes, as shown in Figure I.1.3.

Table I.1.1: Factors affecting corrosions mechanism [Ferreira 2004]

External factors	Internal factors
• Availability of oxygen and moisture at reinforcement level • Relative humidity • Temperature • Carbonation and penetration of acidic gaseous pollutants to the reinforcement level • Aggressive anions reaching the reinforcement level • Stray currents • Bacterial action	• Cement composition • Impurities in aggregates • Impurities in mixing and curing water • Admixtures • *w/c* ratio • Cement content • Aggregate size and grading • Construction practices • Concrete cover over reinforcing steel • Chemical composition and structure of the reinforcing steel • pH of the concrete porewater
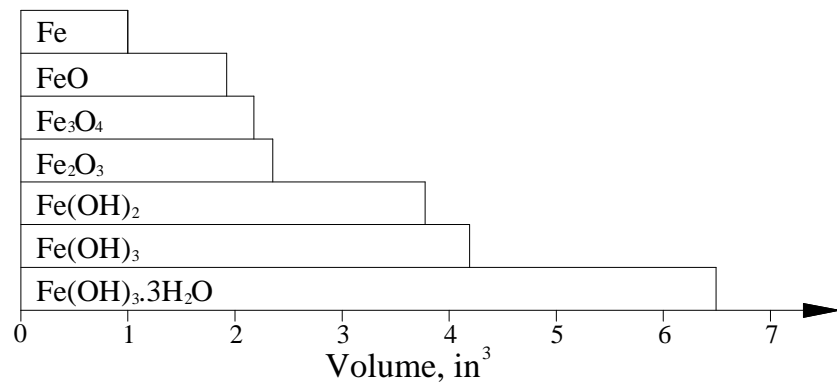
Figure I.1.3: Relative volumes of iron and its corrosion reaction products ($1in^3$=16.387) [Lui & Weyers 1998]

I.1.3 CORROSION INITIATION

In corrosion initiation stage the chloride ingresses into concrete. In many previous studies [e.g., Vu & Stewart 2000; Val & Trapper 2008: Bastidas-Arteaga *et al* 2008], chloride attack had been considered as a diffusion process of moisture through voids spread in concrete media, which is assumed also to be relatively moist. Based on the theory of diffusion, the diffusion process of chloride-ion through the concrete can be represented according to Fick's second law:

$$\frac{\partial C(x,t)}{\partial t} = D_{cl} \frac{\partial^2 C(x,t)}{\partial x^2}$$

(I.1.7)

where $C(x,t)$ is the chloride-ion concentration in concrete at the distance x (see Figure I.1.4) from the surface of concrete at the time t, and D_{cl} is the apparent (or effective) chloride diffusion coefficient of concrete. In this equation it assumed that: (1) concrete is a homogenous and isotropic material (2) the chloride surface concentration is constant C_s.

Equation I.1.7 has many solutions depending on the considered boundary conditions. The most common solutions used in the analysis of chloride diffusion in concrete is the one

considering that the chloride concentration equals to zero at time equals to zero and chloride ion concentration equals to $C(x,t)$ at time t. Thus, the chloride-ion concentration, $C(x,t)$, at depth x after time t is:

$$C(x,t) = C_s \left[1 - erf\left(\frac{x}{2\sqrt{D_{cl}t}} \right) \right] \qquad (I.1.8)$$

where, erf is the error function. D_{cl} is the chloride diffusion coefficient.

D_{cl} is not significantly affected by the source of chloride [Vu & Stewart 2000]. However, it is significantly influenced by time of exposure, temperature and relative humidity, and can be evaluated as follow [Val & Trapper 2008]:

$$D_{cl} = D_{cl,ref} \, f_{cl,T}(T) \, f_{cl,t}(t) \, f_{cl,h}(RH) \qquad (I.1.9)$$

where $D_{cl,ref}$ is a value of D_{cl} which corresponds to a reference temperature T_{ref}=298 K, at a critical relative humidity RH_c=0.75, and at a reference time t_{ref}=28 days. According to Val & Trapper (2008), the three functions in Equation I.1.9 were formulated as:

$$f_{cl,T}(T) = exp[U_c(1/T_{ref} - 1/T)/R] \qquad (I.1.10a)$$

$$f_{cl,t}(t) = (t_{ref}/t)^{m_{age}} \qquad (I.1.10b)$$

$$f_{cl,h}(RH) = [1 + (1 - RH)^4 / (1 - RH_C)^4]^{-1} \qquad (I.1.10c)$$

where T is the absolute temperature in Kelvin, U_c (=44.6±4.46 kJ/mol) is the activation energy, R (=8.314 J/mol Kelvin) is the universal gas constant, m_{age} (=0.15) is the aging coefficient, and RH is the relative humidity.

$D_{cl,ref}$ represents the concrete permeability and is influenced by mix properties (water-cement wc ratio, cement type, aggregate…etc), curing, compaction. Vu & Stewart (2000) compared a number of models developed to predict $D_{cl,ref}$ with field measurements; the authors recommended the following equation as the best descriptor of $D_{cl,ref}$.

$$D_{cl,ref} = 0.15 D_{H_2O} \frac{1 + \rho_c wc}{1 + \rho_c wc + \rho_c ac/\rho_a} \left(\frac{\rho_c wc - 0.85}{1 + \rho_c wc} \right)^3 \qquad (I.1.11)$$

where D_{H2O} is the chloride diffusion coefficient in an infinite solution (=50491.08 mm^2/year for $NaCl$), ac is the aggregate-cement ratio, wc is the water-cement ratio. ρ_c and ρ_a are the mass densities of cement and aggregates respectively.

Equation I.1.8 may be reorganized to find the penetration depth of chloride threshold aggressive front $D_{th}(t)$ in substitution of parameter x in Equation I.1.8, as

$$D_{th}(t) = 2\sqrt{D_{cl}t}\,\text{erf}^{-1}\left(1 - \frac{C_{th}}{C_s}\right) \qquad (I.1.12)$$

where, C_{th} is the value of the critical threshold chloride concentration for which the passive layer of steel is destroyed and the corrosion reaction begins. The term $D_{cl}t$ under the square root in Equation I.1.8 is calculated according to Equation I.1.13. Since temperature and humidity are time dependent, average monthly temperature and humidity profiles can be used to perform the integration using increment procedure and a time increment equals to one month [Luping & Gulkers 2007]:

$$D_{cl}(t) = D_{cl,ref}\,f_{cl,T}(T)\,f_{cl,t}(t)\,f_{cl,h}(RH) \qquad (I.1.13)$$

As far as the chloride surface concentration C_s is considered, used in Equation I.1.12, McGee (1999) has conducted a field-based study of 1158 bridge in Australian state of Tasmania. In this study, the author suggested that the surface chloride concentration C_s (in kg/m^3) as a function of distance from the coast (d in km) is

$$C_s(d) = \begin{cases} 2.95 & \text{if } d <= 0.1 \\ 1.15 - 1.81\log_{10}(d), & \text{if } 0.1 < d < 2.84 \\ 0.03 & \text{if } d > 2.84 \end{cases} \qquad (I.1.14)$$

Finally, from Equation I.1.12 it is possible to determine the corrosion initiation time (t_{ini}) which corresponds to the time required for $D_{th}(t)$ to reach the net concrete cover c as shown in Figure I.1.4. After this time we must consider corrosion propagation.
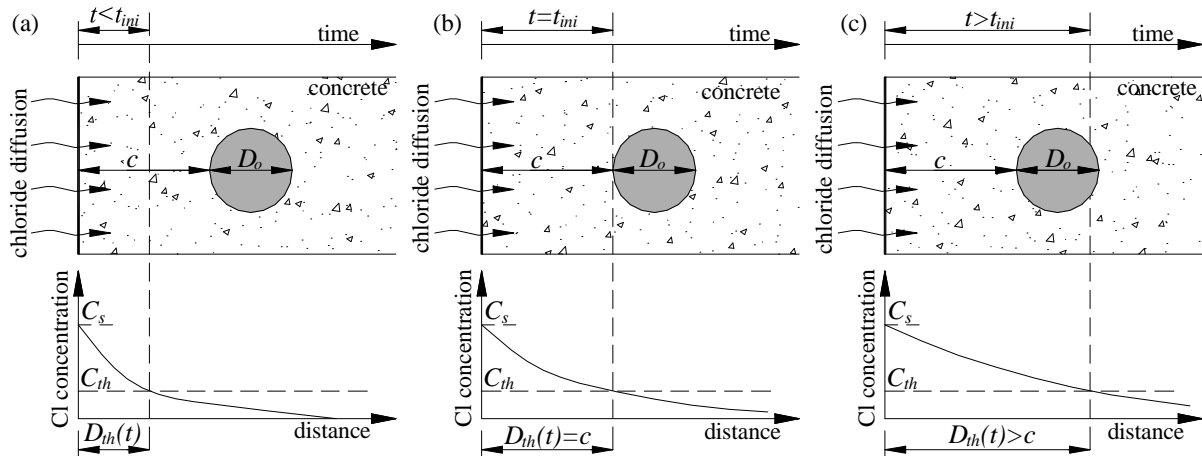
Figure I.1.4: Schematic illustration of chloride diffusion process induced corrosion initiation.

I.1.4 CORROSION PROPAGATION

According to Faraday's law of electrochemical equivalence, the corrosion current density, i_{corr}, of steel corrosion cell can be expressed as:

$$\frac{i_{corr}(t)}{n_{O_2}F} = J_c(t) \tag{I.1.15}$$

where $i_{corr}(t)$ is the current density of cathodic electrode at time t, $i_{corr}(t)$ can be expressed either as a corrosion current density (in $\mu A/cm^2$; the loss of metal per unit surface area) or per unit of time (in $\mu m/year$). The relationship between both units can be obtained by using Faraday's law for uniform corrosion (i.e. $1\mu A/cm^2 = 11.6\mu m/year$). n_{O_2} is the obtained electric number of oxygen molecules participating in chemical reaction ($n_{O_2}=4$), F is Faraday's constant, $F=96500\times10^4$ C/mol. $J_c(t)$ is the diffusion flow of O_2 on the steel surface at time t. Based on electrochemistric principle, the diffusion flow of matter A in matter B equals the product of diffusion coefficient of matter A in matter B with the first order derivative of concentration of matter A in the direction of diffusion, i.e.,

$$J_c(t) = D_{O_2}(t)\frac{\partial C(x)}{\partial x} \tag{I.1.16}$$

where $D_{O_2}(t)$ is the diffusion coefficient of O_2 (in $mm^2/year$) in concrete. $C(x)$ is the concentration of O_2 in a concrete of distance x, from surface, in the diffusion direction.

Diffusion of O_2 in concrete obeys Fick' first law [Liang *et al* 2005; Bastidas-Arteaga *et al* 2008]. Thus, the concentration of O_2, $C(x)$, varies linearly in the area of the diffusion layer from the maximum value on the concrete surface to the zero value at the chloride front $D_{th}(t)$ as given in the following Equation:

$$\frac{\partial C(x)}{\partial x} = \frac{C_{O_2} - C_{st}}{D_{th}(t)} \tag{I.1.17}$$

where C_{O_2} is the oxygen concentration on the concrete surface ($C_{O_2}=8.93\times10^{-10}$ mol/mm^3). C_{st} is the concentration of O_2 (in mol/mm^3) at the distance $D_{th}(t)$, thus, $C_{st}=0$. Substituting Equations I.1.16 & I.1.17 into Equation I.1.15 yields to the corrosion current i_{corr} ($\mu A/cm^2$) as:

$$i_{corr}(t) = \frac{n_{O_2}FD_{O_2}(t)C_{O_2}}{D_{th}(t)} \tag{I.1.18}$$

It can be observed from Equation I.1.18 that corrosion current decreases with increasing the depth $D_{th}(t)$ of critical chloride concentration (see also Figure I.1.5). This concept simulates the corrosion process in the nature as the corrosion rate in the nature after initiation tends to decrease with time as shown in Figure I.1.5. The main reason for the decrease of the corrosion rate is that the transportation of oxygen and moisture is retarded due to the dense

corrosion rust layer.

When the equilibrium between rates of consumption and transportation of oxygen is reached, the corrosion rate tends to be steady [Yuan *et al* 2009]. The continuous accumulation of rust layer at the concrete/steel interface induces cracks around the steel bar. These cracks start at the concrete/steel interface and propagate towards the concrete surface in the radial direction and eventually reach the concrete surface. The width of these cracks at the surface of the concrete, generally known as "*surface cracks width*", propagate with time. When the width of surface cracks reaches a critical value additional access of oxygen and moist occur, thus, corrosion process is reactivated. The time required for the width of surface crack of the concrete cover to reach the critical value (w_{cr}) is known as the time to severe cracking t_{sp} [Bastidas-Arteaga *et al* 2008]. Skai *et al* (1999) suggest that the value of w_{cr} ranges between 0.3-0.5 mm for durability limit state. Bastidas-Arteaga *et al* (2008) recommend a value of w_{cr} equals to 0.5mm. In the present study, w_{cr} will be taken equal to 0.3 mm.
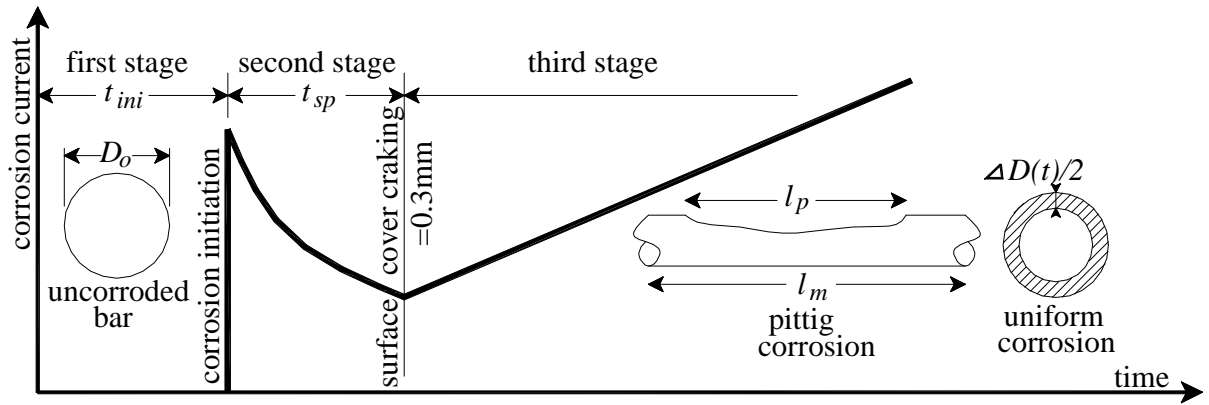
Figure I.1.5: Time-variant corrosion rate.

The above discussion explains the reason why considering the coefficient of oxygen diffusion as time-variant in Equation I.1.18. It is complex to model and predict corrosion rate activation due to cover cracking. Bastidas-Arteaga *et al* (2008) assumed that $D_{O_2}(t)$ becomes linearly time-dependent when $t > t_{sp}$. The authors consider that the oxygen concentration on the steel surface C_{nO_2} after t_n (with $t_n >>>> t_{sp}$; e.g. $t_n = 500$ years) coincides with the oxygen concentration at the concrete surface C_{O_2}. They substitute these values into Fick's second law to get oxygen diffusion coefficient $D_{nO_2}(t)$ at time t_n as:

$$D_{nO_2}(t) = c^2 \left/ 4t_n \left[erf^{-1}\left(1 - \frac{C_{nO_2}}{C_{O2}} \right) \right]^2 \right.$$

(I.1.19)

where, *c* is clear concrete cover in mm.

Finally, the time-variant oxygen diffusion can be expressed as:

$$D_{O_2}(t) = \begin{cases} D_{O_2,ref} & if\ t < t_{sp} \\ D_{O_2,ref} + \left(\dfrac{D_{O_2,ref} - D_{nO_2}}{t_{sp} - t_n} \right)(t - t_{sp}) & if\ t \geq t_{sp} \end{cases} \qquad (I.1.20)$$

The reference coefficient of oxygen diffusion before cover cracking $D_{O_2,ref}$ is assumed according to [Liang et al 2005; Bastidas-Arteaga et al 2008] as follow:

$$D_{O_2,ref} = 3.1536\ x10^5 \left(\frac{32.15}{f'_{cu}} - 0.44 \right) \qquad (mm^2/year) \qquad (I.1.21)$$

where, f_{cu}, $f'_{cu} = f'_c/0.8$, is the concrete cube compressive strength in MPa. But, the oxygen diffusion coefficient $D_{O_2}(t)$ is also assumed to vary with respect to the change in temperature T. Arrhenius relationship was used to express $D_{O_2}(t)$ as temperature dependent:

$$D_{O_2}(t,T) = D_{O_2}(t)\ exp\left[\frac{U_{O_2}}{R} \left(\frac{1}{T_{ref}} - \frac{1}{T} \right) \right] \qquad (I.1.22)$$

where T is the absolute temperature in Kelvin, R (=8.314 J/mol Kelvin) is the universal gas constant. U_{O_2} is the corresponding activation energy of the coefficient of oxygen diffusion which can be expressed as [Pour-Ghaz et al 2009]:

$$U_{O_2} = (-505wc^2 + 484.5wc - 94) \qquad (kj/mol) \qquad (I.1.23)$$

Middleton & Hogg (1998) and others have reported that concrete cover and concrete quality affect corrosion rates. Concrete quality is expressed as the value of water cement ratio (wc). When relative humidity is in the region of 70-85%, the oxygen availability at the cathode and the electrical resistivity of concrete are factors affecting corrosion rates [Yokozeki et al. 1997]. To isolate the effect of concrete quality (wc ratio) and concrete cover it is assumed that the corrosion rate is limited by the availability of oxygen at the steel surface [e.g. Arnon et al. 1997]. As such, the oxygen availability depends on concrete quality (wc ratio), cover and environmental conditions. Therefore, corrosion rate can be empirically expressed as a function of concrete quality (wc ratio) and concrete cover (c) based on an ambient relative humidity of 75% and temperature of 20°C [Vu & Stewart 2000]

$$i_{corr}(1) = \frac{37.8(1 + wc)^{-1.64}}{c} \qquad For\ \ t_{ini} \leq t \leq t_{ini} + 1\ year \qquad (I.1.24)$$

where $i_{corr}(1)$, in $\mu A/cm^2$, is the corrosion current through the first year since the time of

corrosion initiation. As mentioned previously, it is expected that the formation of rust product on the steel surface will reduce the diffusion of the iron ions away from the steel surface. Also, the area ratio between the anode and the cathode is reduced, and consequently the corrosion current will reduce with time; namely, rapidly during the first few years after initiation but then more slowly as it approached a nearly uniform level. Based on experimental data reported by [Liu & Weyers 1998; 1998[b]], Vu & Stewart (2000) proposed an empirical time-dependent corrosion rate model, which can be expressed as:

$$i_{corr}(t) = i_{corr}(1)0.85t^{-0.29} \qquad \text{For} \quad t \geq t_{ini}+1\text{year} \qquad (I.1.25)$$

However, the applicability of the model is limited to RC structures in environments having a relative humidity of 80%. In addition the model does not consider the increase in corrosions rate after cover cracking as shown in Figure I.1.5. If a high temperature is associated with the corrosion process, Arrhenius relationship can be applied such that:

$$i_{corr}(t,T) = i_{corr}(t)exp\left[\frac{U_{corr}}{R}\left(\frac{1}{T_{ref}} - \frac{1}{T}\right)\right] \qquad (I.1.26)$$

where T is the ambient absolute temperature in (Kelvin), T_{ref} is reference temperature (T_{ref}=293K), U_{corr} (=18.98 kJ/mol) is the activation energy of corrosion rate [Liu 1996], R is the universal gas constant.

The reduction in the diameter of corroded reinforcing bar ΔD in (mm) at time t greater than the corrosion initiation time t_{ini} ($t \geq t_{ini}$) is evaluated according to the following equation:

$$\Delta D(t) = 0.0232 \int_{t_{ini}}^{t} i_{corr}(t)dt \qquad (I.1.27)$$

Thus, the steel area as a function of the time can be determined as;

$$A_s(t) = \pi \frac{(D_o - \Delta D(t))^2}{4} \qquad (I.1.28)$$

Equation I.1.28 is valid for losses due to uniform corrosion as losses are to be uniform along bar length and perimeter. Another type of corrosion of a great importance has been considered in many studies (e.g. Bastidas-Arteaga *et al* 2009; Vu & Stewart 2000; Duprat 2007). This type of corrosion has a localized damage on the rebar surface. Val *et al* (2000) distinguish two types of pitting corrosion along bar length based on in-site measurements of repaired bridges: coarse pits which are characterized by length l_p ranges between 20-100 mm and fine pits ranges between l_p: 2-4 mm (see Figure I.1.5). The authors assumed that the

reinforcing bar pit area is constant over its length, thus the equivalent bar area is equal to

$$A_s(t) = \frac{\pi}{4}\left(D_o^2 - \Delta D(2D_o - \Delta D)\frac{l_m}{l_p} \right)$$ (I.1.29)

where l_p is the length of the pit, and l_m (=105mm) is the bar length of in-site measurement of corrosion current. The choice of l_m value corresponds to maximum pit length observed in the survey [Val *et al* 2000].

It is worth mentioning that corrosion does not affect the steel area only, but its actions also change the steel properties with time; yield strength, ultimate strength and ultimate strain [Cairns *et al* 2005; Almusallam 2001]. According to Cairns *et al* (2005), it can be assumed that yield strength, ultimate strength and ultimate strain are linearly proportional to the reduced cross-sectional area $A_s(t)$ such that:

$$f_y(t) = (1 - \alpha_y Q_{corr})f_{yo}$$ (I.1.30)

$$f_u(t) = (1 - \alpha_u Q_{corr})f_{uo}$$ (I.1.31)

$$\varepsilon_u(t) = (1 - \alpha_{u,s} Q_{corr})\varepsilon_{uo}$$ (I.1.32)

where $f_y(t)$, $f_u(t)$ and $\varepsilon_u(t)$ represent the yield strength, ultimate tensile strength and elongation corresponding to ultimate strength at a time t, based on the bar properties, respectively; f_{yo}, f_{yo} and ε_{uo} represent yield strength, ultimate tensile strength and elongation of non-corroded bar. Q_{corr} is the average section loss; $Q_{corr}=100A_s(t)/A_{so}$. α_y, α_u and $\alpha_{u,s}$ are empirical factors. Cairns *et al* (2005) review 12 experimental studies which report average value of the empirical factors up to 0.01. Herein, the empirical factors were taken equal to 0.005 according to recommendation given by [Stewart & Al-Harthy 2008].

I.1.5 CRACKING OF CONCRETE COVER

Generally, corrosion products (rust) at the steel concrete interface have volume higher than the consumed metal in corrosion process (see Figure I.1.3). Therefore, the continuous accumulation of these products initiates tensile stress in the concrete cover, these stresses are in the tangential direction due to the pressure $P_s(t)$ in the radial direction induced by the corrosion rust. Radial cracks are initiated – at the steel/concrete interface – and propagate in the concrete cover when the tangential tensile stresses reach the tensile strength of the concrete. Thus, the time to severe cracking (t_{sp}) can be expressed as [Vu *et al* 2005]:

$$t_{sp} = t_{1st} + t_{ser}$$ (I.1.33)

where t_{1st} is the time to crack initiation, t_{ser} is the time since crack propagation to the reach

critical crack width (w_{cr}).

Once corrosion starts corrosion products begin to be produced and accumulate over the time at the concrete/steel interface. Lui & Weyers (1998) assume that the rate of rust production is inversely proportional to the rust layer thickness around the steel bar, of diameter D, such that:

$$dW_r(t)/dt = k_p/W_r(t) \qquad (I.1.34)$$

where $W_r(t)$ is the mass of corrosion products (mg/mm) at a time t (years). k_p is the rate of rust production which is related to the rate of metal loss and can be expressed as:

$$k_p = 0.105(1/\alpha_r)\pi D i_{corr}(t) \qquad (I.1.35)$$

in which α_r is a ratio expressing the molecular weight of steel divided by the molecular weight of corrosion products and related to the type of corrosion products: α_r=0.523 if corrosion product is $Fe(OH)_3$ and α_r=0.622 if corrosion product is $Fe(OH)_2$; an average value may be taken equals to 0.57 [Lui & Weyers 1998]. Substituting Equation I.1.35 into Equation I.1.34 and integrating, the mass of corrosion products can be expressed as:

$$W_r(t) = \sqrt{2\int_0^t 0.105(1/\alpha_r)\pi D i_{corr}(t)dt} \qquad (I.1.36)$$

Expansion of the accumulated rust layer around the steel bar over the time induces internal radial compression stresses. These stresses take place when the rust layer fully fills the porous band around the steel bar. It is well known that embedded rebars and the surrounding concrete behave as thick ring [Lui & Weyers 1998; Li *et al* 2006] as shown in Figure I.1.6. In this figure d_o is the thickness of porous band around the steel bar. The inner and outer radii of the thick ring are $a=(D+2d_o)/2$ and $b=c+a$ respectively. According to Lui & Weyers (1998), the critical mass of corrosion products that full fill the porous zone can be expressed as:

$$W_{cr} = \frac{\pi \rho_{st}\rho_{rust}}{\rho_{st} - \alpha_r\rho_{rust}}[d_o D + (D + 2d_o)t_{crit}] \qquad (I.1.37)$$

ρ_{rust} is density of corrosion products, ρ_{st} is density of steel. t_{crit} represents the thickness of corrosion product required to initiate the radial stresses:

$$t_{crit} = \frac{cf_{ct}}{E_{c,eff}}\left(\frac{b^2 + a^2}{b^2 - a^2} + \nu_c\right) \qquad (I.1.38)$$

where f_{ct} is the tensile strength of the concrete. $E_{c,eff}$ is the effective elastic modulus of the

concrete where $E_{c,eff}=Ec/(1+\varphi_{cr})$. E_c is the elastic modulus of the concrete. φ_{cr} is the creep coefficient of concrete, $\varphi_{cr}=2$. v_c is the Poisson's ratio of the concrete, $v_c=0.2$.

(a)   *(b)*   *(c)*
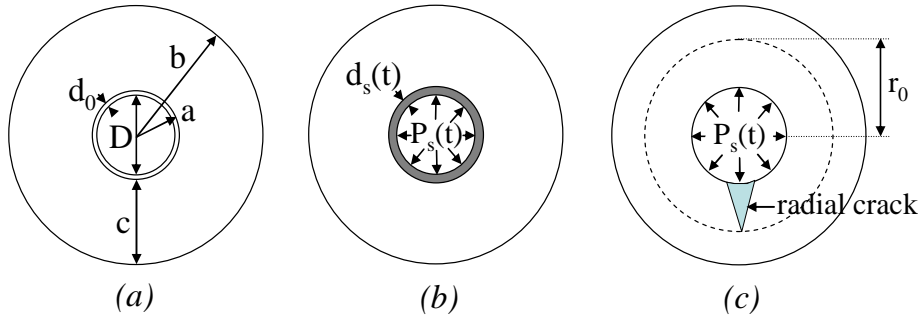
Figure I.1.6: Corrosion induced cover cracking Scheme [Li *et al* 2006].

The thickness of rust layer $d_{rust}(t)$ that induces compression radial stresses $P_s(t)$ at steel/concrete interface can then be determined as [Lui & Weyers 1998; Li *et al* 2006]:

$$d_{rust}(t) = \begin{cases} 0 & For \quad W_r(t) < W_{cr} \\ \dfrac{W_r(t)}{\pi(D+2d_o)}\left(\dfrac{1}{\rho_{rust}} - \dfrac{\alpha_r}{\rho_{st}}\right) & For \quad W_r(t) \geq W_{cr} \end{cases} \qquad (I.1.39)$$

Thus, the time required to initiated radial cracks t_{1st} may be calculated such that: $d_{rust}(t)= t_{crit}$ or $W_r(t) =W_{cr}$.

Based on experimental fitting of accelerated corrosion tests, Vu *et al* (2005) propose a model to calculate the time to crack propagation (t_{ser}) which can be defined as the time since crack initiation to reach a the critical surface crack width (w_{cr}). The authors found that the time to crack propagation can be expressed as function of the concrete quality as given in following equation,

$$t_{ser(acc)} = A(c/wc)^B \qquad (I.1.40)$$

where the concrete quality is expressed as the ratio between the concrete cover and the water-to-cement ratio (c/wc). The constants A and B in Equation I.1.40 were fitted for three values of critical surface crack width (w_{cr}); $w_{cr}=0.3$, 0.5 and 1 mm:

$$t_{ser(acc)} = \begin{cases} A=65 \quad \& \quad B=0.45 \quad for \quad w_{cr}=0.3mm \\ A=225 \quad \& \quad B=0.29 \quad for \quad w_{cr}=0.5mm \\ A=700 \quad \& \quad B=0.23 \quad for \quad w_{cr}=1.0mm \end{cases} \qquad (I.1.41)$$

The tests were carried out using a corrosion rate $i_{corr(exp)}$ 100 μA/cm^2.

A correction factor (k_R) was deduced to relate the $t_{ser(acc)}$ with the real corrosion rate $i_{corr(real)}$:

$$k_R \approx 0.95 \left[exp \left(-\frac{0.3i_{corr(exp)}}{i_{corr(real)}} \right) - \frac{i_{corr(exp)}}{2500 i_{corr(real)}} + 0.3 \right] \qquad (I.1.42)$$

Therefore, the real time from crack initiation to crack propagation to reach the critical surface crack width in years is:

$$t_{ser} = k_R \frac{0.0114}{i_{corr(real)}} t_{ser(acc)} \qquad (I.1.43)$$

The model was developed on the basis that the corrosion current is constant, however Stewart & Suo (2009) recommended the model for both corrosion rates; variant and invariant, and only for 16mm diameter reinforcing bars. To generalize the model for additional bar diameters, t_{sp} given by Equation I.1.43 is increased by 50% and reduced by 25% for bars with diameter of 10 and 13 mm respectively [Stewart & Suo 2009].

Li *et al* (2006) derive a full analytical model to predict the time to severe cracking. As previously discussed the growth of the ring of corrosion products exerts an outward pressure $P_s(t)$ on the concrete at the interface between the rust band and concrete. Under this expansive pressure, radial cracks begin to form and propagate in the radial direction. The crack divides the concrete thick-wall cylinder into two co-axial cylinders: inner cracked and outer cracked ones, as shown in Figure I.1.6c. For the outer uncracked concrete cylinder, the theory of elasticity still applies. Because of the symmetry there is no tangential displacement, the model assume the radial displacement $u(r)$ in the uncracked cylinder satisfies Timoshenko & Goodier (1970) equation given below:

$$\frac{d^2 u(r)}{dr^2} + \frac{1}{r}\frac{du(r)}{dr} - \frac{u(r)}{r^2} = 0 \qquad (I.1.44)$$

The solution of Equation I.1.44 takes the form,

$$u(r) = c_1(r_o)r + \frac{c_2(r_o)}{r} \qquad (I.1.45)$$

where the coefficients $c_1(r_o)$ and $c_2(r_o)$ are a function of r_o because it varies between a and b. Thus, the radial and tangential stresses can be expressed as follows:

$$\sigma_r(r) = \frac{E_{c,eff}}{1-v_c^2} \left[(1+v_c)c_1(r_o) - \frac{(1-v_c)c_2(r_o)}{r^2} \right] \qquad (I.1.46)$$

$$\sigma_\theta(r) = \frac{E_{c,eff}}{1-v_c^2} \left[(1+v_c)c_1(r_o) + \frac{(1-v_c)c_2(r_o)}{r^2} \right] \qquad (I.1.47)$$

According to Li *et al* (2006), the behavior of the inner cracked concrete cylinder is based

on many assumptions: cracks are smeared and uniformly distributed on the circumference of the cracked cylinder; concrete is a quasi-brittle material; fracture mechanics is applied to determine the stress distribution in the cracked cylinder; the cracking in the radial direction makes the concrete an anisotropic material locally in the vicinity of cracks; there exists a residual tangential stiffness at each point on the cracked surface along the radial direction which depends on the tangential strain of that point which is a function of the radial coordinate r. The residual tangential stiffness is constant along the cracked surface, i.e., on the interval [a, r_0], and represented by $\alpha E_{c,eff}$, where α (<1) is referred to as tangential stiffness reduction factor which can be determined as follows [Bažant & Planas 1998]

$$\alpha = \frac{f_{ct} \exp\left[-\gamma(\overline{\varepsilon_\theta} - \overline{\varepsilon_\theta^c})\right]}{E_{c,eff}\,\overline{\varepsilon_\theta}}$$

(I.1.48)

where $\overline{\varepsilon_\theta}$ is the average tangential strain over the cracked surface. $\overline{\varepsilon_\theta^c}$ is the average tangential cracking strain . γ is a material constant. Based on these assumptions, the radial displacement $u(r)$ in the uncracked cylinder satisfies:

$$\frac{d^2 u(r)}{dr^2} + \frac{1}{r}\frac{du(r)}{dr} - \alpha\frac{u(r)}{r^2} = 0$$

(I.1.49)

where the solution of Equation I.1.49 can be in the form of:

$$u(r) = c_3(r_o)r^{\sqrt{\alpha}} + c_4(r_o)r^{-\sqrt{\alpha}}{}_2$$

(I.1.50)

where the coefficients $c_3(r_o)$ and $c_4(r_o)$ are related to r_o. Thus, the corresponding radial and tangential stresses respectively are:

$$\sigma_r(r) = \frac{\sqrt{\alpha}E_{c,eff}}{1-v_c^2}\left[(1+v_c)c_3(r_o)r^{(\sqrt{\alpha}-1)} - (1-v_c)c_4(r_o)r^{(-\sqrt{\alpha}-1)}\right]$$

(I.1.51)

$$\sigma_\theta(r) = \frac{\sqrt{\alpha}E_{c,eff}}{1-v_c^2}\left[(1+v_c)c_3(r_o)r^{(\sqrt{\alpha}-1)} + (1-v_c)c_4(r_o)r^{(-\sqrt{\alpha}-1)}\right]$$

(I.1.52)

The four constants $c_1(r_o)$, $c_2(r_o)$, $c_3(r_o)$, $c_4(r_o)$ and consequently the strength reduction factor α can be found by applying the boundary conditions for the concrete cylinder: $\sigma_r(b)|_{outer}=0$, $u_r(a)|_{inner} = d_{rust}(t)$, $u_r(r_o)|_{inner} = u_r(r_o)|_{outer}$ and $\sigma_r(a)|_{outer} = \sigma_r(a)|_{inner}$.

Eventually, the crack will propagate to the surface of the concrete cylinder. At a time t the crack penetrates to the concrete surface, thus, the concrete cylinder fractures completely and the outer cylinder is vanished. In this case, $r_o = b$, as the concrete cylinder is completely cracked. Equation I.1.49 is the governing equation for the displacement, but the solution must

be different as the boundary conditions have changed, consequently the solution of Equation I.1.49 for completely cracked concrete cover can be expressed in the form of;

$$u(r) = c_5 r^{\sqrt{\alpha}} + c_6 r^{-\sqrt{\alpha}} \tag{I.1.53}$$

The two constants c_5 and c_6 can be determined by applying the boundary conditions: $\sigma_r(b) = 0$ and $u_r(a) = d_{rust}(t)$. The corresponding average tangential strain can be expressed as follows:

$$\overline{\varepsilon_\theta} = \frac{1}{b-a}\int_a^b \varepsilon_\theta(r)dr = \frac{1}{b-a}\int_a^b (c_5 r^{\sqrt{\alpha}-1} + c_6 r^{-\sqrt{\alpha}-1})dr =$$

$$= \frac{(b^{\sqrt{\alpha}} - a^{\sqrt{\alpha}})(c_5 + c_6/(ab)^{\sqrt{\alpha}})}{\sqrt{\alpha}(b-a)} \tag{I.1.54}$$

The stiffness factor for completely cracked concrete cover

$$\alpha = \frac{f_{ct}\, exp\left\{-\gamma\left[(b^{\sqrt{\alpha}} - a^{\sqrt{\alpha}})(c_5 + c_6/(ab)^{\sqrt{\alpha}})/\sqrt{\alpha}(b-a) - \frac{1}{b-a}\Omega\right]\right\}}{\dfrac{E_{c,eff}(b^{\sqrt{\alpha}} - a^{\sqrt{\alpha}})(c_5 + c_6/(ab)^{\sqrt{\alpha}})}{\sqrt{\alpha}(b-a)}} \tag{I.1.55}$$

where $\Omega = \int_a^b \left(c_1(r) + \dfrac{c_1(r)}{r^2}\right)dr$. The crack width on the concrete surface of the concrete cylinder can be determined as:

$$w_c(t) = 2\pi b\left[\varepsilon_\theta(b) - \varepsilon_\theta^{e,m}(b)\right] \tag{I.1.56}$$

where $\varepsilon_\theta^{e,m}(b)$ is the maximum elastic strain, at $r=b$, expressed as [Timoshenko & Goodier 1970]:

$$\varepsilon_\theta^{e,m}(b) = \frac{\sigma_{\theta,m}(b) - \nu_c \sigma_r(b)}{E_{c,eff}} \tag{I.1.57}$$

where $\sigma_{\theta,m}(b)$ is the maximum tangential stress at $r=b$. As $\sigma_r(b)=0$ and $\sigma_{\theta,m}(b)=f_{ct}$, eventually the crack width w_c is given by:

$$w_c(t) = \frac{4\pi d_{rust}(t)}{(1-\nu_c)(a/b)^{\sqrt{\alpha}} + (1+\nu_c)(b/a)^{\sqrt{\alpha}}} - \frac{2\pi b f_{ct}}{E_{ef}} \tag{I.1.58}$$

The time to severe cracking t_{sp} can be obtained using the above describe cover craking model in an incremental time procedure, in which, the time to severe cracking t_{sp} is the time that corresponds to the surface crack width of the concrete cover, based on Equation I.1.58, to reach a certain critical value w_{cr}. The model is fully detailed in [Li et al 2006] and verified by

the authors with experimental results reported in [Andrade *et al* 1993] (see Figure I.1.7).
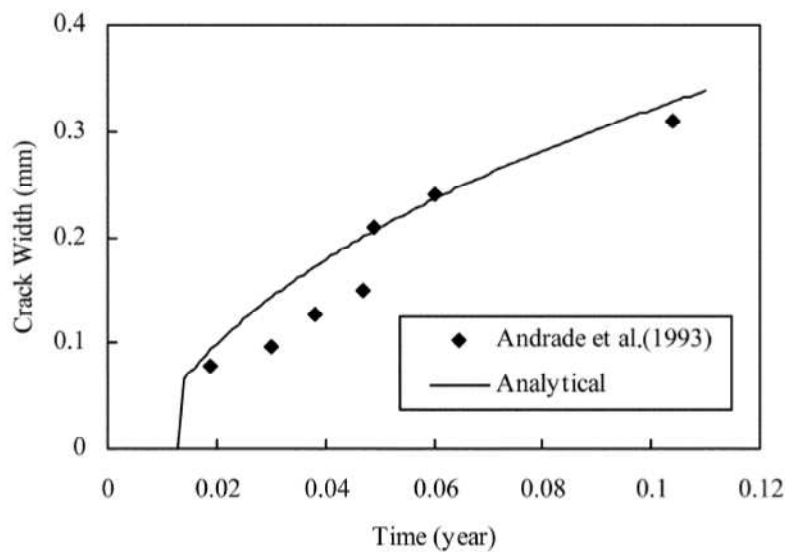
Figure I.1.7: Experimental verification of crack width over time [Li *et al* 2006].

In the present study, Li *et al* (2006) model's was used to predict the time to severe cracking, as the model is a full analytical formula which gives a robust correlation with experimental results as shown in Figure I.1.7, while Vu *et al* (2005) model's is an imperial formula and used only with a limited number of bar diameters. In addition, Vu *et al* (2005) model's was fitted on the assumption that the corrosion current is constant value which contradicts the realistic case that takes place in the nature. Herein, the corrosion current presented by Equations I.1.18 & I.1.20 was used in the reliability analysis as the model consider the activation in corrosion process after cracking of the concrete cover. While the corrosion model presented by Equations I.1.24-I.1.26 does not considered activation process in corrosion after cover cracking.

Figure II.1.8 presents the results of applying the corrosion model (Equation I.1.18) based on Li *et al* (2006) cover cracking model's (Equation I.1.58) and the corresponding activation of oxygen diffusion after cover cracking (Equation I.1.20). The corrosion current and the area of a steel bar, with diameter of 25mm, embedded in concrete with a clear cover of 30mm were calculated for a time period equals to 100 years. Based on the result, it could be concluded that the considering activation of oxygen diffusion after cover cracking has a significant effect on the corrosion current and the corresponding are of the steel bar.
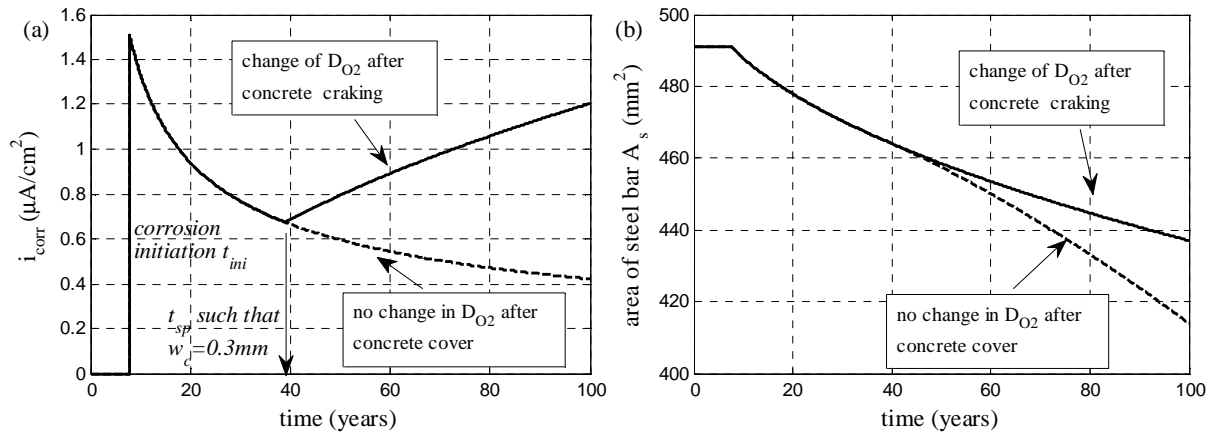
Figure I.1.8: Effect of cover cracking on corrosion activity, (*fc*=30MPa, *c*=30mm, *D*=25mm, C_s=3.05 kg/m³, and C_{th}=0.9 kg/m³, and $w_{c,lim}$=0.3mm)

I.1.6 CORROSION ACTIVITY IN FRP STRENGTHENED RC STRUCTURES

Strengthening of RC section using FRP composite laminates may be used to compensate the losses in strength due to corrosion of reinforcement. From the other side FRP strengthening may affect corrosion activity after strengthening. In an experimental study implement by Gadve *et al 2009*, circular reinforced concrete specimens were casted and their reinforcements were subjected to corrosion current, then the pre-corroded specimen were fully wrapped using two FRP composite types; glass and carbon. Finally, the wrapped specimens were exposed to further corrosion. Mass losses in reinforcing bars were determined after corrosion. It was found that, in most worth corrosion loss, the fully wrapping of the specimens using GFRP and CFRP sheets significantly reduce the mass loss due to corrosion by 4.8 and 3.8% respectively with respect to control specimen. GFRP composite have seemed to have impeded the corrosion more than CFRP. This may be due to the higher electrical resistance of the glass fiber. However, it may be recalled that the thickness of glass fiber sheets is higher than that of the carbon fiber sheet in field application. Therefore, in this experiment a thicker glass fiber sheet was used. Moreover, the choice of sheet in field application depends on several other factors such as the required stiffness, strength, durability…etc. Therefore, the choice of fiber may be made based on all those factors along with their relative resistance to corrosion. However, the study may not be considered as a realistic case for the corrosion activity in FRP strengthened RC beams due to the fully wrapping if FRP sheets, as beams are never fully wrapped through strengthening process.

Masoud & Soudki (2006) test ten large scale RC beams. The test beams fall into four groups. The first group; control; included a test specimen that was neither corroded nor repaired to serve as reference for this program. The second group; corroded unrepaired;

included three specimens that were corroded to three different degrees of corrosion: minor, medium and severe. A reinforcement mass loss of 5.5% was used to define a minor degree of corrosion, whereas mass losses of 9.5% and 12.5% were used to define medium and severe degrees of corrosion, respectively. Each degree of corrosion was induced in one specimen of this group. The third group; FRP repaired (short-term); included two specimens that were corroded to a mass loss of about 5.5%, and then repaired with FRP sheets. The fourth group; FRP repaired (long-term); included four specimens that were corroded to a mass loss of about 5.5%, and then repaired with FRP sheets. After repair, these last four specimens were exposed to further corrosion (medium and severe degrees of corrosion) to examine their long-term performance. Two FRP repair schemes were utilized for the repair process. The first (scheme I) included wrapping the cross-section of the specimen with U-shaped GFRP sheets. The second (scheme II) included flexural strengthening of the specimen with CFRP sheets in addition to wrapping the cross-section with U-shaped GFRP sheets. FRP repair schemes I and II are shown in Figure I.1.9.

Results of study have shown that the average mass losses of the repaired beams of the fourth group are 5.5, 9, and 10.5% for minor, medium and severe degree of corrosion respectively. In addition the measurements of mass loss for the beams repaired using scheme I and those repaired using scheme II were almost identical. Consequently, it can be concluded that the CFRP sheets provided for flexural strengthening in repair scheme II had a negligible effect on the corrosion activity, and the observed reduction in mass losses of the fourth group with respect to the second group is due to the GFRP wrapping.
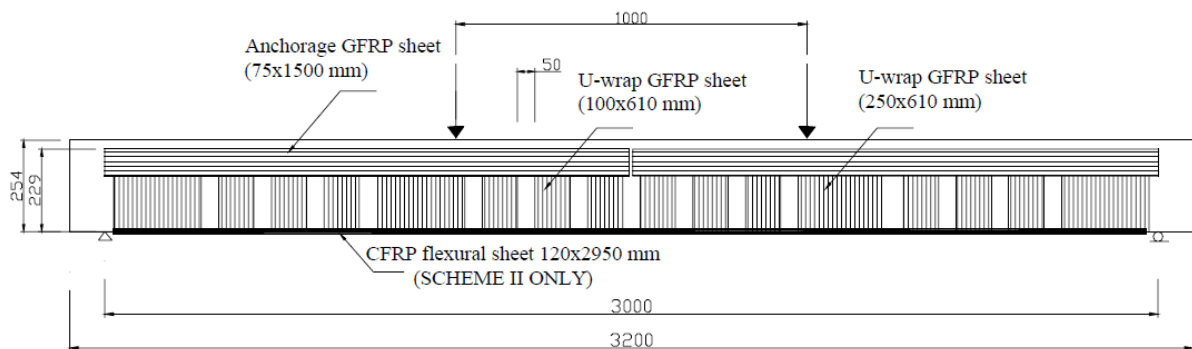
Figure I.1.9: FRP repair schemes I and II [Masoud & Soudki 2006].

I.1.7 CONCLUSIONS

The following conclusions are drawn from the present chapter:

1. This chapter presents and discusses all the stages, and the basic principles that control each stage, of the RC deterioration process due to corrosion of reinforcement bars embedded in concrete element.

2. Chloride penetration is modeled by a diffusion/convection process. This process depends on many mechanical and environmental factors such as concrete quality, temperature, relative humidity, chlorides concentration…etc.

3. Chloride-induced RC deterioration is a complex process is controlled by diffusion, electrochemical current, mechanical properties of concrete. The RC deterioration due to corrosion process results from the interaction between: (1) chloride penetration, (2) losses in reinforcement area, (3) losses in the mechanical properties of reinforcement and (4) concrete cracking induced reactivation of corrosion current and consequently corrosion process.

4. FRP strengthening of RC element has no effect on corrosion activity.

PART I: LITERATURE REVIEW

Chapter I.2: Strengthening of RC beams using FRP composites

I.2.1 INTRODUCTION

Reinforced concrete structures are often subjected to a decrease in stiffness and resistance over the time. The maintenance of existing RC bridges is one of the current problems faced by the structural engineers when the strength evaluation indicates a decrease in flexural or shear strength. The decrease of strength may take place due to many factors such as corrosion of steel rebars, fatigue… etc. Inspection and evaluation of the damages that may affect reinforced concrete structures capacity is an important work to check their reliability for future periods, their needs for strengthening or replacement in case that the strengthening is not useful. In some cases strengthening of concrete structures is to be implemented not only due to the harms affecting the RC structures but also to increase their capacity to support additional live loads. Generally, strengthening of a structure is required to:

1. Support additional loads: due to the growth of traffic loads over the time on the lanes bridges, or due to the change of the use of building.
2. Structural damage due to corrosion of the bars in RC and deterioration of concrete.
3. Structural damage due to exceptional events as explosions, fire and crashes.
4. Changes of the structural system.
5. Design or manufacturing defects.
6. The need to reduce tensions, deformations or crack spacing.
7. Increasing of ultimate strength and of stiffness.

In the past, the increase in strength has been provided by casting additional reinforced concrete, dowelling in additional reinforcements or externally post-tensioning the structures. More recently, attaching steel plates to the surface of the tension zone by use of adhesives and/or bolts has been used to strengthen concrete structures. Even more recently, the use of Fiber Reinforced Plastics has been developed using the same basic technique as for steel-plate bonding [e.g., Arya *et al* 2002]. The most frequent application fields of using externally bonded FRP laminates as strengthening tool are shown in Figure I.2.1 [Rochdi 2004]:

- Flexural strengthening of RC beams or slabs (1).

- Shear strengthening of RC beams (2).
- Repairing of Diagonal of masonry walls (3).
- Confinement of RC or masonry columns (4).
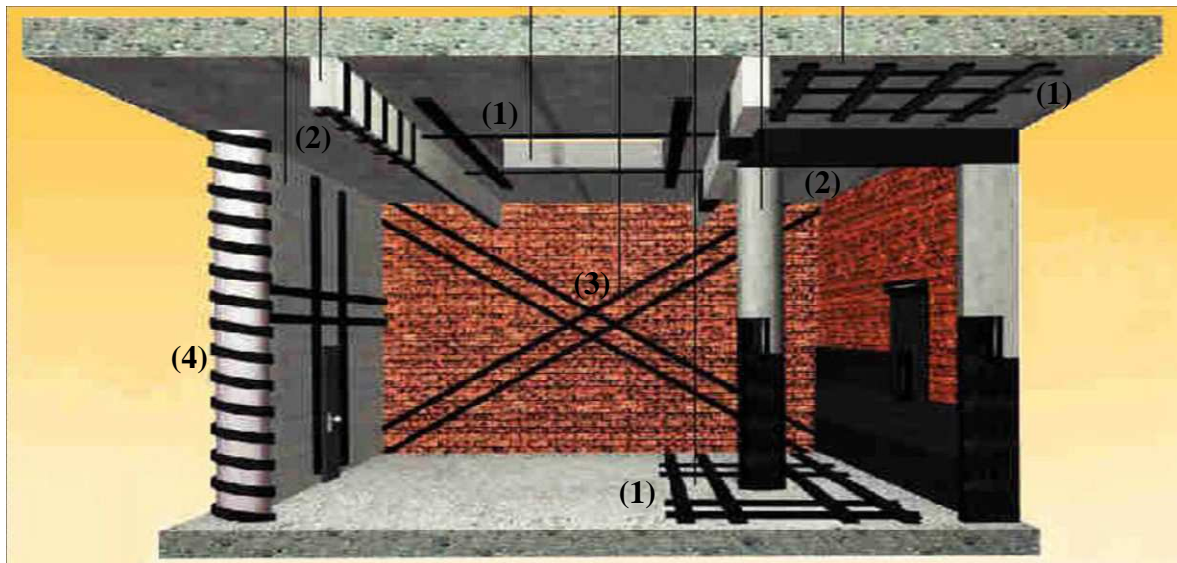
Figure I.2.1: Typical applications of FRP in the strengthening of RC structures.

Economic issues are the major cause of the awareness of the importance of maintenance process, thus, the development of strengthening techniques. Traditional strengthening techniques have shown their limits in long-term behavior (e.g., corrosion of steel), as the profitability of a strengthening technique is conditioned by the durability of strengthening material. Research in the field of strengthening has been oriented towards the use of new materials capable to satisfy various criteria required for the strengthening process. One of these materials is FRP composites were restricted for long time to military applications and the aviation industry, then, used in the field of Civil Engineering. Several reasons allowed composite materials to be only restricted for long time to military applications and the aviation industry. Among these reasons is the industrial development of the composites through the last three decades and the crisis passed in the aviation industry since the early 90's [Rochdi 2004] which result in reducing prices of the composites. In addition, the field of civil engineering requires too much labor. The cost of labor in developed countries has become high enough so the price of raw materials no longer plays the role of "key economic criteria". This implies that the price of the composite is no longer causes a disability, especially for applications in repair and reinforcement [Hamelin 1998]. As shown in Figure I.2.2, applications of FRP composites in civil engineering for about 25 years has become widespread throughout the international community, groups industrial and research laboratories.
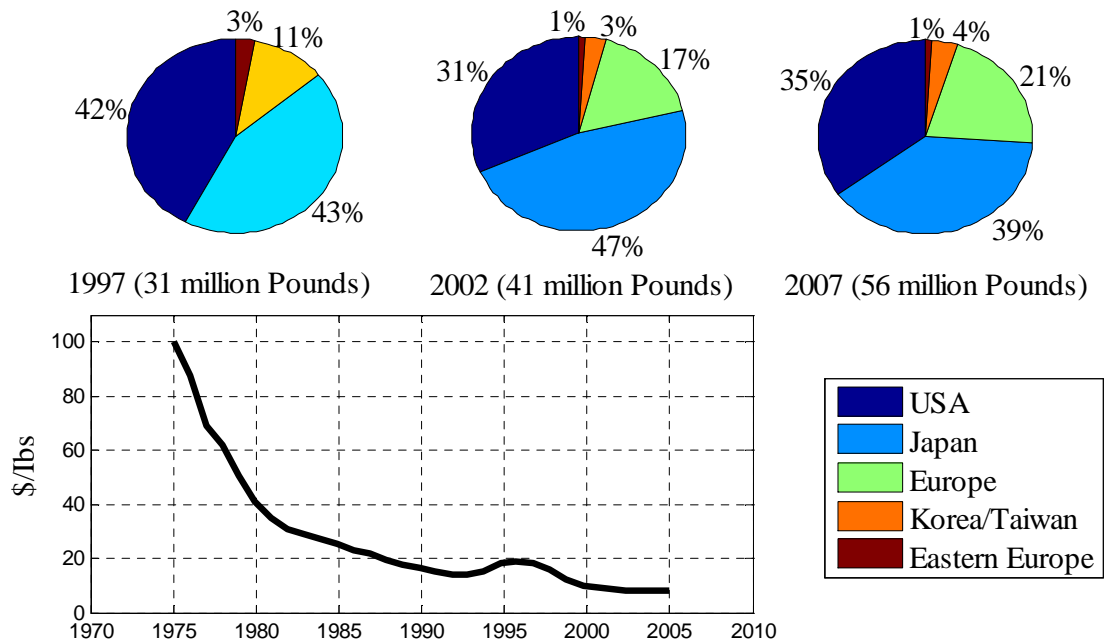
Figure I.2.2: Evolution of world production of composites & effects on price [Rochdi 2004].

I.2.2 STRUCTURAL REPARATION METHODS OF RC BEAMS

I.2.2.1 Reparation by bolted steel attachments

Reparation by bolted steel attachments consists of attaching steel plates or other steel shapes to the tension face of the RC beam as shown in Figure I.2.3. Prefabricated channels are an effective substitute when rolled sections of the required size are not available. For beams with inadequate in shear strength, combinations of steel bars – on the sides of beam – and channels bolted to the concrete beam may be added to improve shear capacity as shown in Figure I.2.3b. Advantages of this method are that rolled channels are available in a variety of sizes and require little additional preparation prior to attachment. From other side, bolting may be an expensive and time-consuming method. Moreover, a destructive work is required as holes have to be drilled through the old concrete.

(a) Flexural strengthening   (b) Shear strengthening
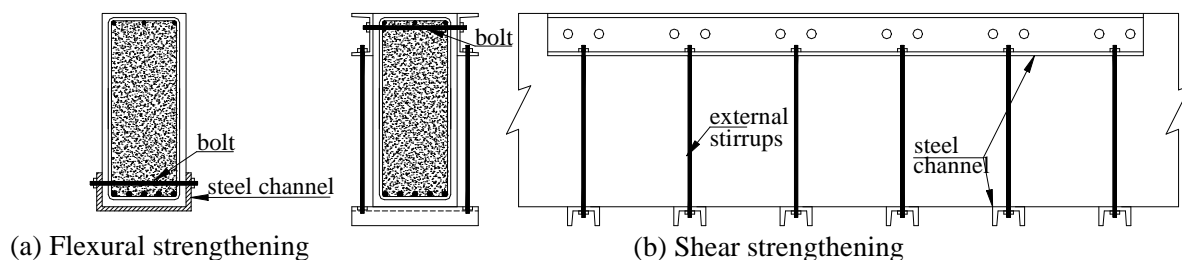
Figure I.2.3: Reparation of RC beams using bolted steel attachments.

I.2.2.2 Reparation by concrete projection

Another method of increasing flexural capacity of RC beams is to adjacently project new

amounts of concrete to the old section. The new part contains the required amount of longitudinal steel reinforcements. Stirrups should also be added to provide additional shear reinforcement and to support the new longitudinal rebars as shown in Figure I.2.4. The major difficulty of this technique is that it requires destructive works on the existing concrete elements to produce holes and to rough concrete surface which is needed to ensure the bond between the new and existing concrete. In addition, it leads to a remarkable increase in the cross section of the concrete elements which may affect the architecture shape.
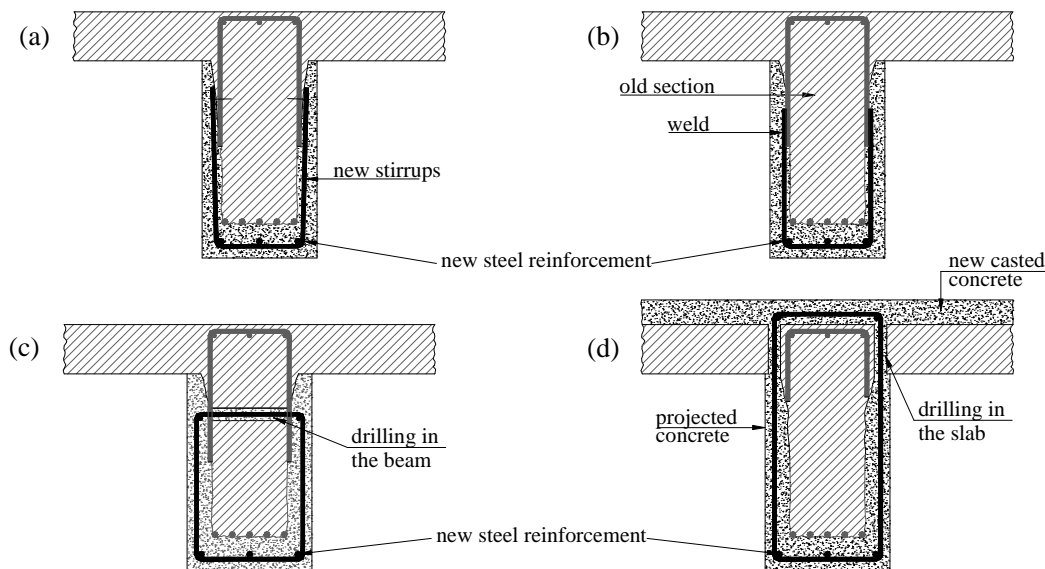
Figure I.2.4: Reparation of RC beams by concrete projection.

I.2.2.3 Reparation by post-tensioning

Since the 1950s, post-tensioning has been applied as a strengthening method in many configurations to almost all common bridge types. Prestressed tendons can be used to increase both shear and the flexural strengths of RC beams, as prestressing process allows applying certain stress intensities in defined directions in the concrete element. Tendons can be used for various types of concrete structures (e.g., such as bridges, buildings, tanks) and with many configurations according to the position of the tendons; internal or external. External post-tensioning is characterized by low friction loss of tension force in the tendons. For shear strengthening, the prestressed tendons are added in a vertical or inclined orientation and may be placed either within the beam web or outside the web as shown in the Figure I.2.5a. The longitudinal tendon configuration shown in Figure I.2.3b, which is used for flexural strengthening, has been applied with the objective of controlling the longitudinal axial stresses in bridge members and consequently undesirable displacements could be reduced or reversed. Various tendon configurations could be considered; straight, bent and curved. The axial force, shear force and bending moment effects due to post-tensioning have enough versatility in

application so as to meet a wide variety of strengthening requirements. Probably this strengthening technique can reverse the undesirable behavior in an existing bridge rather than provide a simple patching effect. For both these reasons, post-tensioning has become a very commonly technique in repair and strengthening of RC structures. The principal disadvantage of using post-tensioning as a strengthening technique is that it increases the allowable stress range by the magnitude of the applied post-tensioning stress. If maximum advantage is taken of the increased allowable stress range, the factor of safety against ultimate load will be reduced. Thus, the ultimate load capacity will not increase at the same rate as the allowable-stress capacity. Also, at the location of anchorages and brackets where tendons are attached to the bridge structure, there are high local stress concentrations that require special design considerations. In addition, all these attachments require corrosion protection because they are generally in locations that can be subjected to saltwater runoff or salt spray.

(a) Shear strengthening   (b) Flexural strengthening
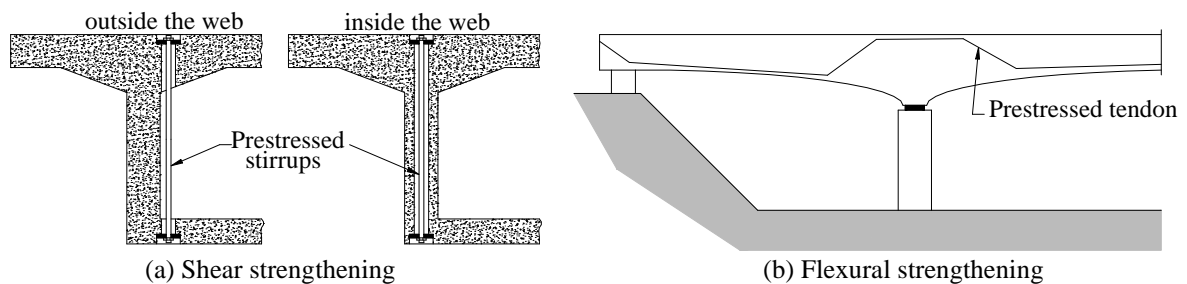
Figure I.2.5: Reparation of RC beams by post-tensioning additions.

I.2.2.4 Reparation by bonding steel plates

The flexural and shear strengths of RC beams can be significantly increased using externally bonded steel plates to their tension face using a certain adhesive material such as epoxy (see Figure I.2.6). This technique has been used to strengthen deficient RC structures since the 1960s [Chen & Teng 2001]. Steel plates required for shear strengthening may be bonded in vertical or inclined direction. The major disadvantages of this technique are the corrosion of the steel, increase in weight of the repaired element and installation.
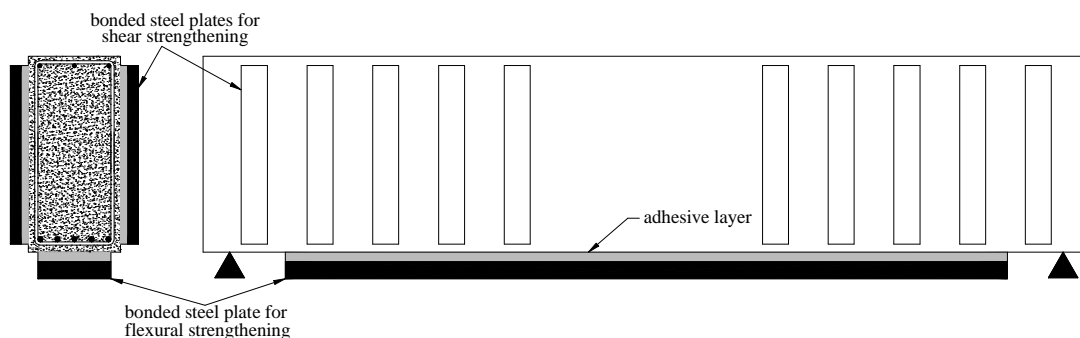
Figure I.2.6: Reparation of RC beams using bonded steel plates.

I.2.3 STRENGTHENING BY MEANS OF FRP BONDED LAMINATES

I.2.3.1 General Aspects

Recently, fiber-reinforced polymer FRP laminates have increasingly been used to replace steel plates due to their superior properties. Strengthening of RC elements by externally bonded Fiber Reinforced Plastic FRP materials is one of the most widely adopted solutions for retrofitting existing structures. Most applications are related to shear and flexural reinforcement as bonded steel plates. National and international code provisions for the design of elements strengthened with FRP Externally Bonded Reinforcements (EBR) are being issued worldwide [e.g., ACI Committee 440.2R; Fib bulletin 14]. FRP laminates may be used in different lengths, schemes and multiple layers. FRP strengthening can be applied to any RC structural element (such as: beams, columns, slabs, shear walls …etc) and all types of RC structures (such as: typical concrete structures, bridges, parking …etc).

Many types of FRP composites were produced and used for the purpose of externally bonded strengthening techniques of RC elements such as carbon (CFRP), glass (GFRP)…etc. This may gain a wide variety in material properties (strength and modulus) used in strengthening. The FRP plates may be stressed or unstressed. In addition, their ends can be anchored using bolts or FRP U-wrapped bonded laminates in the transverse direction. Various schemes for FRP strengthened RC girders are presented in Figures 2.5 & 2.6 for flexural and shear design respectively.

(a) Non-anchorage FRP end laminates (b) Anchorage FRP end laminates using bolts

(c) Anchorage FRP end laminates using U wrapped laminates
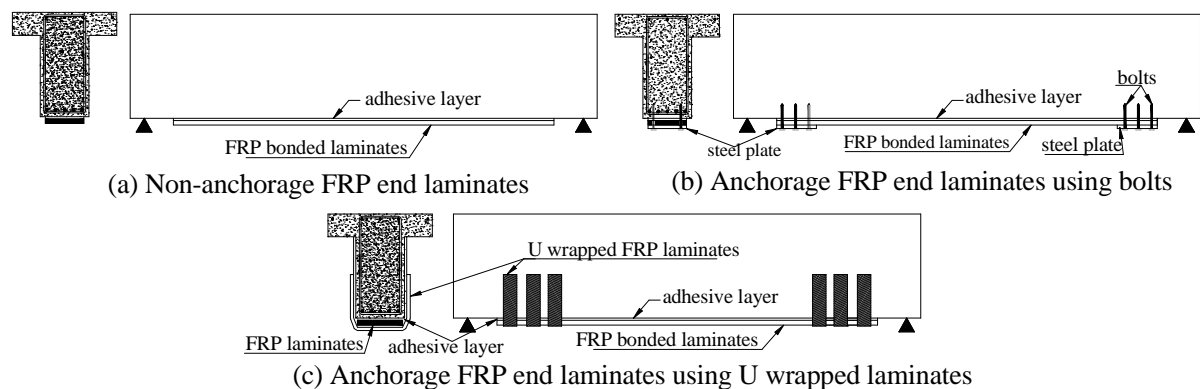
Figure I.2.7: Reparation of RC beams using bonded FRP composite plates: flexural design.

(a) Side bonding   (b) U wrapping

(c) Full wrapping   (d) U wrapping with anchorage
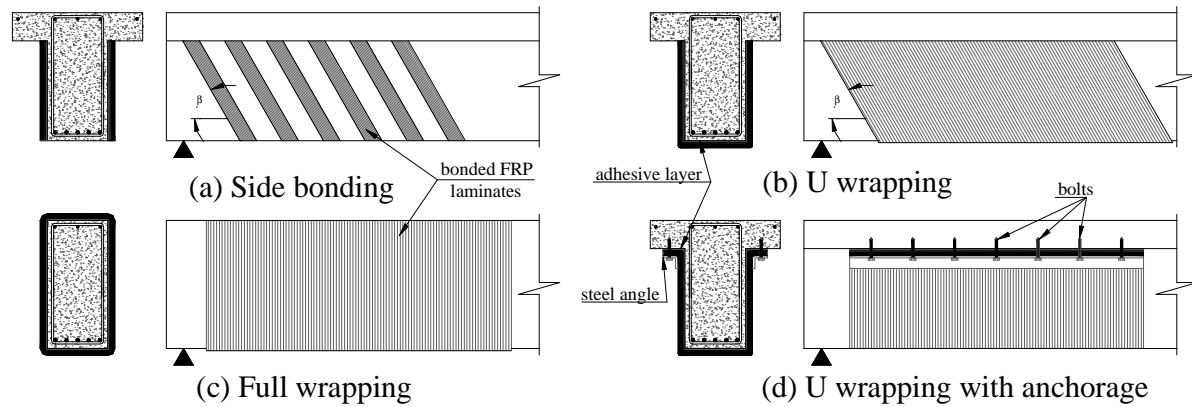
Figure I.2.8: Reparation of RC beams using bonded FRP composite plates for shear design.

A large number of projects have been carried out to demonstrate the use of this composite in the rehabilitation of reinforced and prestressed concrete structures. These advanced materials may be applied to the existing structures to increase any or several of the following properties [Balaguru *et al* 2009]:

- Axial, flexural, or shear load capacities.
- Ductility for improved seismic performance.
- Improved durability against adverse environmental effects.
- Increased fatigue life.
- Stiffness for reduced deflections under service and design loads.

Composites have been used by the space and aerospace communities for over six decades and the use of composites by the civil engineering community spans about three decades. In the composite system, the strength and the stiffness are primarily derived from raw fibers and the matrix that binds the fibers together to form composites. Composites are known for their high specific strength, high stiffness and corrosion resistance. Repair and retrofit are still the predominant areas where FRPs are used in the civil engineering community. The field is relatively young and, therefore, there is considerable ongoing research in this area. The wide range of strengthening using bonded FRP laminates to the surface of the concrete elements as be seen as an advantage and opportunity for the knowledgeable designer to tailor the strengthening scheme to the need of the particular structure.

I.2.3.2 History of FRP materials in civil engineering

FRP composites are the latest version of the very old idea of making better composite material by combining two different materials which can be traced back to the use of straw as reinforcement in bricks used by ancient civilizations (e.g. Egyptians in 800). The development of FRP reinforcement can be found in the expanded use of composites after World War II: the

automotive industry first introduced composites in early 1950s and since then many components of today's vehicles are being made of composites. The aerospace industry began to use FRP composites as lightweight material with acceptable strength and stiffness which reduce the weight of aircraft structures such as pressure vessels and containers. Today's modern jets use large components made out of composites as they are less susceptible to fatigue than traditional metals. Others industries like naval, defense and sporting goods have used advanced composite materials on a widespread basis: pultrusion offered a fast an economical method of forming constants profile parts and pultruded composites were being used to make golf clubs and fishing poles. Although, the civil engineering was not the first domain in using composites materials, but the FRP strengthening techniques have been widely used in recent years in civil infrastructures such as columns, beams, or slabs since their first application in the 1960s [Diagana *et al* 2003].

I.2.3.3 Raw materials of FRP composites

FRP composites comprise fibers of high strength and a polymer matrix that binds these fibers to form a composite structural component as shown in Figure I.2.9. Fibers are organized in parallel direction through the resin. Fiber consists of several filaments with diameters ranging from 5 to 25μm. These filaments are generally of carbon or glass which provides strength and stiffness, in a matrix (resin) such as polyester, vinylester or epoxy which provides the transfer of stresses and strains between the fibers. These fibers are indefinitely long. Both raw fibers and resin are produced under high temperatures in industrialized processes that require highly specialized equipment and control.
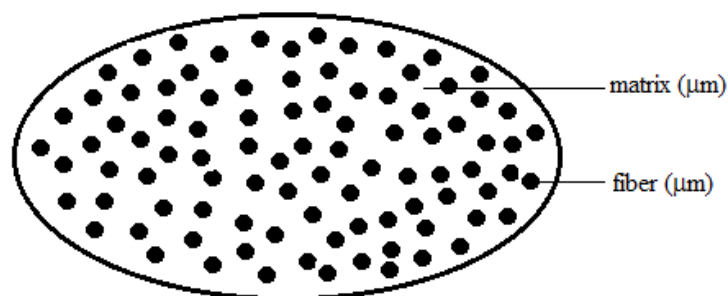
Figure I.2.9: Components of composite.

I.2.3.3.1 Types of fibers

As mentioned previously, the role of fiber in FRP composite is to resist the applied load acting on the composite system. Fiber volume fraction ranges between 20-70% and depends on the matrix type and fiber configuration [Varastehpour 1996]. The properties of the resulting composite present considerable variations. The most known typical types of fiber

reinforcements used in composite industry are glass, carbon, and aramid. Table I.2.1 presents the mechanical properties of these types.

Table I.2.1: Properties of common fiber types used in civil engineering [Varastehpour 1996; Bank 2006].

Type of fiber		Density (g/cm^3)	Tensile strength (MPa)	Modulus of elasticity (GPa)	Elongation at rupture (%)	Maximum temperature of use (^{o}C)
Glass:	C-glass	2.6	3310	69	4.8	
	D-glass	2.1	2410	52	4.6	770
	E-glass	2.5	3400	75	4.8	550
	R-glass	2.5	4400	80	5.5	650
	S-glass	2.5	4800	84	5.4	650
Carbon:	SM	1.70	3700	250	1.2	2500
	IM	1.80	4800	250	1.4	
	HS	1.90	3000	500	0.5	2000
	UHM	2.10	2400	800	0.2	
Aramid:	Kevlar 29 HR	1.44	3620	83	4	400
	Kevlar 49 HR	1.44	3620	131	2.8	425
	Kevlar 149 UR	1.47	3470	186	2	

HR: high resistance. UR: Ultrahigh resistance. SM: Standard modulus. IM: Intermediate modulus. HS: High strength. UHM: Ultra-high modulus.

Glass fiber:

Glass fiber is the most common of all reinforcing fibers used in composites. Diameter of glass fiber filaments ranges in between 5 and 24 μm. The two most common types of glass fibers used in the fiber-reinforced polymers industry are electrical glass (E-glass) and structural glass (S-glass). Other less common types include chemical glass (C-glass) and alkali-resistant glass (AR-glass). The most economical and widely used reinforcement in polymer matrix composites is E-glass as it offers good strength properties at a very low cost. It accounts for more than 90% of all glass fiber reinforcements. S-glass has the highest tensile strength among all the glass fibers and was originally developed for missile casings and aircraft components. Cost of S-glass is considerably higher than E-glass. C-glass is utilized in corrosive environments where chemical stability is desired. It provides greater corrosion resistance to acids than E-glass. Its primary use is in surface coatings of laminates used in chemical and water pipes and tanks. Specifically developed for use in concrete, AR-glass is used in applications requiring greater chemical resistance to alkaline chemicals, such as in cement substrates and concrete [Balaguru *et al* 2009].

Carbon fiber:

Carbon fibers are used in structural engineering applications today in FRP strengthening sheets and fabrics, in FRP strengthening strips and in FRP prestressing tendons. Carbon fiber

is a solid semi-crystalline organic material and is produced in grades known as standard modulus, intermediate modulus, high strength and ultrahigh modulus (SM, IM, HS, and UHM). Carbon fibers have diameters ranges between 5 and 10 μm. Due to their two dimensional atomic structure, carbon fibers are considered to be transversely isotropic and have different properties in the longitudinal direction of the atomic array than in the transverse direction. The longitudinal axis of the fiber is parallel to the graphitic planes and gives the fiber its high longitudinal modulus and strength.

Aramid fiber:

Third, aramid fiber are synthetic organic polymer fibers and generally known as "Kevlar". Kevlar was commercially introduced in 1972 (by DuPont in USA) and is currently available in three different types [Varastehpour 1996]:

- Kevlar 49 has high tensile strength and modulus and is intended for use as reinforcement in composites.
- Kevlar 29 has about the same tensile strength, but only about two-thirds the modulus of Kevlar 49. This type is primarily used in a variety of industrial applications.
- Kevlar 149 has the extreme modulus value.

The specific modulus in Table I.2.1 is simply the modulus of the material divided by the material density and is a measure of the stiffness of a material per unit weight. Kevlar has been extremely successful in a variety of applications including premium tire cords, marine cordage, military body armor, oxygen bottles, high-pressure rocket casings, propeller blades and in engine cowlings and wheel pants of aircraft, which are subjected to damage from flying gravel [Balaguru *et al* 2009]. To compare between the different fibers types, Table I.2.2 presents the relative cost of different fiber types with respect to glass fiber of type Glass-E. In addition, an overall comparison evolves advantages and disadvantages of glass, carbon and aramid fibers are presented in Table I.2.3

Other fibers that are now in the development phase for use in FRP products for structural engineering include thermoplastic ultrahigh molecular-weight (UHMW) polyethylene fibers and polyvinyl alcohol (PVA) fibers. PVA fibers have been used in FRP bars and FRP strengthening sheets in Japan. UHMW short fibers are being used in the development of ductile fiber-reinforced cements (FRCs) but have not yet been used in FRP products for structural engineering. Inorganic basalt fibers, produced in Russia and the Ukraine, may be seen as future applications of FRP products in structural engineering, due to their superior corrosion resistance and similar mechanical properties to glass fibers. Natural fibers such as hemp, sisal and flax, as well as bamboo fibers, have been used in experimental

applications to produce FRP composites, but no commercial FRP products are available that contain these fibers at this time. It is anticipated that FRP products in structural engineering that will be developed in the first half of the twenty-first century will probably use more of these natural fibers as sustainability and recyclability become more important drivers in the construction industry.

Table I.2.2: Relative cost of certain fiber with respect to glass-E [Varastehpour 1996]

Type of fiber	Relative cost
Glass-E	1
Glass-C	2
Glass-D	15
Glass-R or S	4
Kevlar 29	8
Kevlar 49	12
Carbon, high resistance	13
Carbon, high modulus	60

Table I.2.3: Advantages and disadvantages common fiber types in civil engineering domain.

fiber	advantages	disadvantages
glass	• Optimum mechanical properties-to-cost ratio • High tensile strength • Chemical resistance • High temperature resistance. [Varastehpour 1996]	• Low tensile modulus • Sensitivity to abrasion while handling, • Relatively low fatigue resistance. Brittleness. • Sensitive to moisture especially in the presence of salts and alkalinity.
carbon	• Very durable in hot & moist environments. • Perform well under fatigue and impact loads. • Very low coefficient of thermal expansion in the longitudinal direction. • Have good Chemical properties in the ambient temperature. • Behavior of carbon fiber under high temperature is conditioned by matrix type, as no matrix can resist this temperature, thus carbon matrix is developed for this reason [Varastehpour 1996]	• Carbon fibers thermally and electrically conductive with respect to other types. • Care must be taken when they are used in contact with metallic materials, as a galvanic corrosion cell can develop due to the electro-potential mismatch between the carbon fiber and most metallic materials. Some studies have suggested that this can lead to degradation of the polymer resin.
aramid	• Have the lowest specific gravity. 43% and 20% lighter than glass and carbon fibers respectively. • Have the highest tensile strength-to-weight ratio. • High strength. • Offer good resistance to abrasion and impact, chemical and thermal degradation. [Balaguru *et al* 2009]	• Low compressive strength. • Degrade when exposed to ultraviolet light. • Considerable difficulty in machining and cutting. So, ultrasonic tools are needed to cut materials containing or composed of aramid fibers

I.2.3.3.2 Types of matrix

The matrix plays a major role in the composite as it influences the inter-laminar shear between fibers. Furthermore, the ability to manufacture the composite and the defects within it depends strongly on the matrix's physical and thermal characteristics [Balaguru *et al* 2009].

Generally, There are two types of matrix; organic and inorganic. Organic matrices - known as resins or polymers - are the most widespread used today. Polymers can be classified into two types according to the effect of heat on their properties. The first type is the thermoplastics which soften with heating and eventually melt, hardening again with cooling. This process of crossing the softening or melting point can be repeated as often as desired without any noticeable effect on the material properties in either state. Typical thermoplastics include nylon, polypropylene, polycarbonate, and polyether-ether ketone (PEEK). The second type is the thermosets which are formed from a chemical reaction when the resin and hardener (or catalyst) are mixed and then undergo a nonreversible chemical reaction to form a hard, infusible product. In some thermosets, such as phenolic resins, volatile by-products are produced. Other thermosetting resins, such as polyester and epoxy, cure by mechanisms that do not produce any volatile by-products and, thus, are much easier to process. Once cured, thermosets will not become liquid again if heated, although above a certain temperature their mechanical properties will change significantly. The most common resins used in the field of civil engineering are epoxy resins. In some cases polyester or vinyl resins can be used. A brief description of each resin is presented in the following sections [Balaguru *et al* 2009].

Polyester resins:

Polyester resins are the most economical and widely used resin, especially in the marine industry. Nearly half a million tons of this material are used annually in U.S in composite applications. Polyester resins can be formulated to obtain a wide range of properties ranging from soft and ductile to hard and brittle. At ambient temperature the resin is usually solid. A solvent must be added to Polyesters to reduce its viscosity and to facilitate the impregnation of the fibers. Their advantages include low viscosity, low cost and fast cure time. The most significant disadvantage of polyesters is their high volumetric shrinkage. In addition, the chemical resistance and mechanical properties of the polyester are not as good as epoxy.

Vinylester resins:

Vinylester resins are more flexible and have higher fracture toughness than cured polyester resins. The handling and performance characteristics of Vinylester are similar to polyesters. Some advantages of the Vinylester, which may justify their higher cost, include better chemical and corrosion resistance, hydrolytic stability, and better physical properties, such as tensile strength as well as impact and fatigue resistance. It has been shown that a 0.5 to 1.5 mm thick layer of a Vinylester resin matrix can provide an excellent permeation barrier to resist blistering in marine laminates.

Epoxy resin:

Epoxy resins are a broad family of materials that provide better performance as compared to other organic resins. Aerospace applications use epoxy resins almost exclusively, except when high temperature performance is a key factor. The maximum working temperature of Epoxies is depends on the type but is typically below 60 $^{\circ}$C. However epoxy resins with higher working temperatures are available. Usually there are no limits on the minimum temperature. The high cost of epoxies, long cure time, and handling difficulties are the principal Disadvantages. Table I.2.4 concludes the advantages and disadvantages of the most widely used organic resins in civil engineering applications; polyester, vinylester, and epoxy [Balaguru *et al* 2009]. In addition, the principal mechanical properties of these resins are given in Table I.2.5 [Marouani 2007].

Table I.2.4: Advantages and disadvantages of resin types used in civil engineering.

Resin type	Advantages	Disadvantages
Polyesters	• Easy to use • Lowest cost of resins available	• Only moderate mechanical properties • High styrene emissions in open molds • High cure shrinkage • Limited range of working times
Vinylester	• Very high chemical/ environmental resistance • Higher mechanical properties than polyesters • High mechanical and thermal properties	• Post-cure generally required for high properties • High styrene content • Higher cost than polyesters • High cure shrinkage
Epoxies	• High water resistance • Long warning times available • Temperature resistance up to 140°C wet /220°C dry • Low cure shrinkage	• More expensive than Vinylester • Corrosive handling • Critical mixing

Table I.2.5: Mechanical properties of resins (organic type).

Resin type	Density (g/cm^3)	Modulus of elasticity (GPa)	Tensile strength (MPa)	Rupture elongation %	Temperature resistance ($^{\circ}$C)
Polyesters	1.2	2.9-3.1	50-60	2-3	120
Vinylesters	1.1	3.4-3.5	70-85	2-5	100-140
Epoxies	1.1-1.4	3	50-120	3-8	50-200

I.2.3.4 Common terms of fabrics

Fabric is defined as an assembly process of long fibers to produce a flat sheet of one or more layers of fibers, these layers are held together by mechanical interlocking of the fibers themselves or with secondary material to bind these fibers together. Fabric types are categorized by the orientation of the fibers used, and by the various construction methods used to hold the fibers together. The weight of a dry fabric is usually represented by its area density. Each fabric has its own pattern, often called the construction, and is an *x*, *y* coordinate system (see Figure I.2.10). Some of the yarns run in the direction of the roll (*y*-axis or 0°) and

are continuous for the entire length of the roll. These are the warp yarns and are usually called "*ends*". The *y*-axis is the long axis of the roll and is typically 30–150 m. The short yarns, which run crosswise to the roll direction (*x*-axis or 90°), are called the "*fill*" or "*weft*" yarns (also known as picks). Therefore, the *x*-direction is the roll width and is usually 1-3 m. Fabric *count* refers to the number of warp and fill yarns per inch. It is important to note that warp yarns are counted in the fill direction, while fill yarns are counted in the warp direction. Two other important terms are drape and bias. Drape refers to the ability of a fabric to conform to a contoured surface, and bias represents the angle of the warp and weft threads, usually 90°.
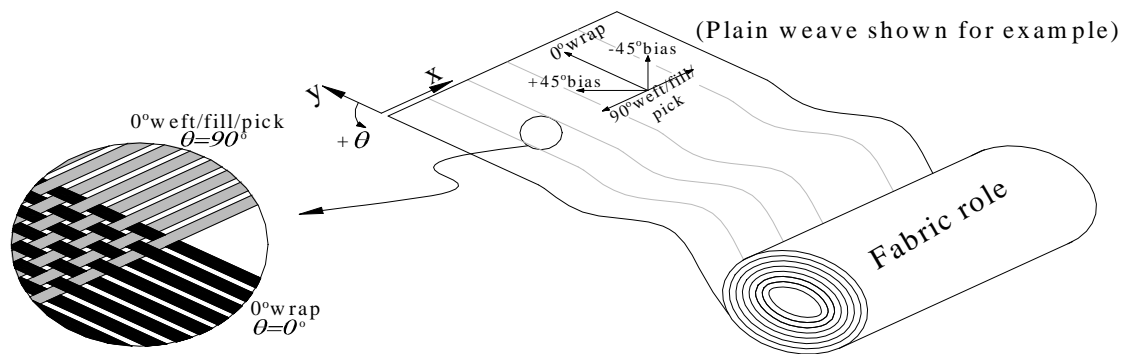
Figure I.2.10: Fabric orientation.

Unidirectional fabrics: A fabric made with a weave pattern designed for strength in only one direction is termed unidirectional. The pick count of a unidirectional fabric is very small and most of the yarns run in the warp direction. Pure unidirectional construction implies no structural reinforcement in the fill direction, although enough warp fibers are included in the weave to ensure ease of handling. Unidirectional fabrics are commonly manufactured in tape form or narrow rolls (less than a few inches wide).

Weave The weave describes how the warp and fill yarns in a fabric are interlaced. Weave determines the ability to drape and the isotropy of strength (some weaves are biased to the warp or fill direction). Figure I.2.11 presents the most popular weaves: plain, twill, basket weave, harness satin, and crowfoot satin [Balaguru *et al* 2009].
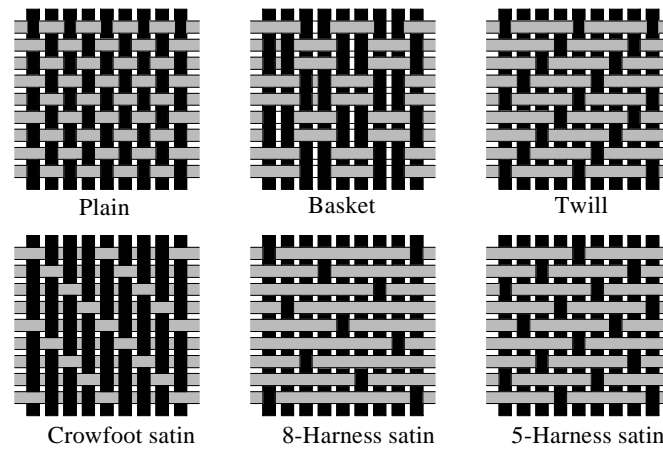
Figure I.2.11: Basic weave types [Balaguru *et al* 2009].

Hybrid fabrics: The term hybrid refers to a fabric that has more than one type of structural fiber in its construction. In a multi-layer laminate, if the properties of more than one type of fiber were required, then it would be possible to provide this with two fabrics, each ply containing the fiber type needed. However, if low weight or extremely thin laminates are required, a hybrid fabric will allow the two fibers to be incorporated in just one layer of fabric instead of two. Hybrids are most commonly found in 0/90° woven fabrics. The most common hybrid combinations are as follows:

- Carbon/aramid: The high impact resistance and high tensile strength of the aramid fiber combines with the high compressive and tensile strengths of carbon. Both fibers have low density but relatively high cost.

- Aramid/glass: The low density, high impact resistance and tensile strength of aramid fiber combines with the good compressive and tensile strength of glass, coupled with its lower cost.

- Carbon/glass: Carbon fiber contributes high tensile and high compressive strengths, high stiffness, and reduces the density, while glass reduces the cost.

Multi-axial fabrics: Multi-axial fabrics, also known as non-woven, non-crimped, stitched or knitted have optimized strength properties because of the fiber architecture. Stitched fabrics consist of several layers of unidirectional fiber bundles held together by a nonstructural stitching thread, usually polyester. The fibers in each layer can be oriented along any combination of axes between 0 and 90°. Multiple orientations of fiber layers provide a quasi-isotropic reinforcement. The entire fabric may be made of a single material, or different materials can be used in each layer. A layer of strands mat may also be incorporated into the construction. A schematic drawing of a typical knitted biaxial fabric is shown in Figure I.2.12a.
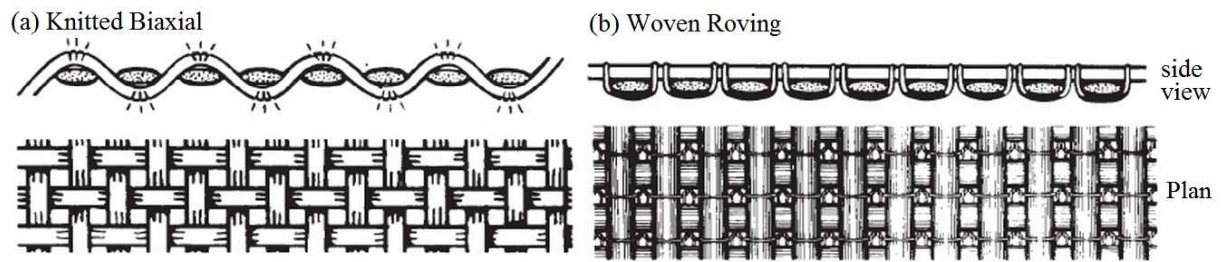
Figure I.2.12: (a) Knitted biaxial fabric (b) Woven roving [Balaguru *et al* 2009].

Conventional woven fabrics are made by weaving fibers in two perpendicular directions (warp and fill). However, weaving bends the fibers, reducing the maximum strength and stiffness that can be achieved. Stitched fabrics can be relatively expensive compared to woven fabrics. For over half a century, the stitched fabrics have been traditionally used in boat hulls. Other applications include wind turbine blades, light poles, trucks, buses and underground storage tanks. Currently, these fabrics are used in bridge decks and column repair projects.

Woven roving: Woven roving reinforcement consists of flattened bundles of continuous strands in a plain weave pattern with slightly more material in the warp direction. To form the material, roving is woven into a coarse, square, lattice-type, open weave as shown in Figure I.2.12b. Woven roving provides great tensile and flexural strengths and a fast laminate build-up at a reasonable cost. Woven roving is more difficult to wet-out than chopped strand mat however, and because of the coarse weave, it is not used where surface appearance is important. When more than one layer is required, a layer of chopped strand mat is often used between each layer of roving to fill the coarse weave.

I.2.3.5 Fabrication/installation method of FRP composites

It is well known that fiber and matrix type largely influence the overall mechanical properties of a composite. However, the final properties of a composite produced from these materials are also a function of the way in which the materials are prepared and processed. Two main manufacturing methods are used to produce FRP composite material products for the use in structural engineering. The First method is an automated industrialized process, developed in the early 1950s, and called pultrusion method. The FRP products are produced in a factory and shipped to the construction site for fabrication and installation or erection. The pultrusion process is used to manufacture FRP reinforcing bars, FRP strengthening strips, and FRP profiles. The pultrusion process is the most cost-competitive method for producing high-quality FRP parts for use in structural engineering. It is used to generate long lengths of material with high unidirectional strengths. Figure I.2.13 shows a photograph of typical FRP pultruded parts used in structural engineering.
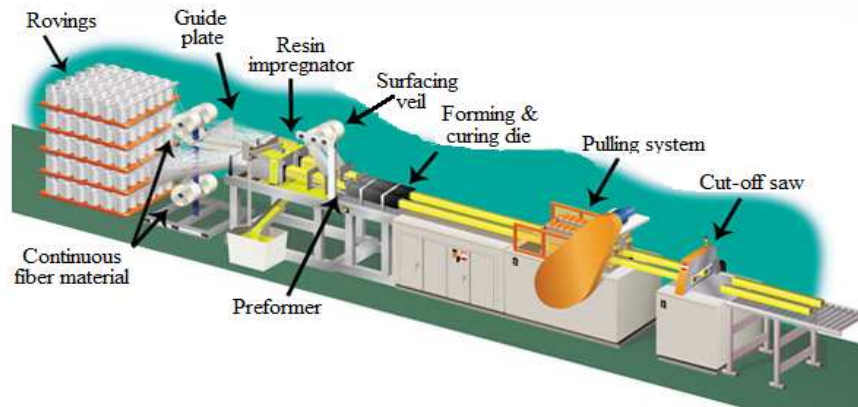
Figure I.2.13: Pultrusion line for FRP production [Balaguru *et al* 2009].

A pultruded part has structural shapes with open or closed cross-section such as a plates, wide-flange, hollow tube...etc. The cross section does not require having a constant thickness throughout. Although there is great flexibility in the shape, thickness variation, and size of the part cross section, the cross section must remain constant along its length. In addition, the part must be straight and cannot be cured into a curved shape. A pultruded part can be produced to any desired length. Modifications to the pultrusion process have been developed for varied cross sections or for producing curved parts.

To produce FRP pultruded element, dry fibers impregnated with a low-viscosity liquid thermosetting polymer resin are guided into a heated chrome-plated steel die, where they are cured to form the desired FRP cross section. The FRP is cured as the material is pulled through the die by a pulling apparatus. The entrance to the die is typically cooled to prevent premature curing of the resin system. After exiting the die and extending past the pullers, the part is cut to length by a diamond blade cutoff saw. The length of the heated steel die is typically from 500 to 1000 mm. The die is often heated in two or three separate regions along its length to different temperatures from 90 to 180°C in order to develop the best curing conditions for the type of resin system used in the part. More detail about pultrusion process can be found in [Bank 2006].

The second method is a manual method, which is generally known as hand layup, wet layup or laminating. It is the original method used to produce FRP composites and dates back to the development of FRP materials in the 1940s. The method is extremely flexible and can be used over a wide range of sizes and shapes. It is also used to make a variety of FRP products; laminates or panels of FRP composites. Although, the method is simple, a significant degree of skill and good quality control are required to produce a high-quality FRP part. The FRP product is manufactured at the construction site. Fabric is cut to the appropriate

size and is placed on a mold layer by layer, resin being applied to each layer by pouring, brushing/rolling or spraying, prior to placement of the next layer. Entrapped air is removed from the fibrous assembly and resin impregnation of the reinforcement is achieved through the manual application of pressure using rollers. This method has become commonplace throughout the composites industry for a number of reasons:

- Easy to teach and have been used widely for many years.

- Very economical since large expensive equipment is not needed.

- A wide variety of fibers and resins are compatible with this method.

However, this method can lend itself to a host of problems, especially if air voids remain within the composite. These air voids can eventually form cracks, which can propagate throughout the composite. This will result in a debonding failure in which the bond between FRP layers breaks down, allowing the composite layers to separate. Not only will this lead to a significant reduction in strength, but it will also allow adverse environmental conditions to penetrate and attack the surface of the FRP layers. Often to reduce air voids in the manually fabricated FRP composites, a vacuum bag is used to apply further pressure on the impregnated assembly leading to a higher level of fabric compaction with lower void content. A wide range of thermosets can be used in this process under both ambient and heated conditions with impregnation being more uniform and easier when the resin viscosity is low. Volume fractions achievable are based on the level of compaction achieved with levels just reaching 35% without the use of a vacuum bag and up to 55% being obtained with a vacuum bag under specific conditions. Other noteworthy disadvantages include the following [Balaguru *et al* 2009]:

- Resin mixing, laminate resin content and overall laminate quality are strongly dependent upon the skills of the laborers.

- Hand lay-up is a very slow and labor-intensive process.

- Health and safety risks may be posed when handling resins. Since the fabric must be impregnated by hand, the resins have a low viscosity to facilitate easier wet-out of the fabric. Unfortunately, the lower viscosity of the resins also means that they are more like to penetrate clothing and harm the skin. In addition, lower viscosity resins generally have lower mechanical and thermal properties.

- Greater variability from part to part and even within the same part in the produced FRP composites.

The process is widely used to fabricate jackets/wraps directly onto columns for the

purpose of seismic retrofit/strengthening and for placement of fabric strips onto concrete as a mode of external strengthening (see Figure I.2.14).

Figure I.2.14: Use of wet layup for installation of a fiber-reinforced polymer.

FRP laminates, pultruded or wet layup, are bonded to the structural elements chemically through adhesives. Chemical bonding is the most practical because:

- It does not induce stress concentrations,
- It does not damage neither the base material nor the composite
- Easier than mechanical devices to be installed.

The most suitable adhesive for composite materials is the epoxy resin based adhesives. The adhesive is made of a two component mix. The principal component is constituted of organic liquids containing epoxy groups, rings composed of an oxygen atom and two carbon atoms. A reagent is added to the above mix to obtain the final compound. The adhesive adhere to the materials to be bonded through interlocking and the formation of chemical bonds. The preparation of the surfaces to be bonded plays a key role for the effectiveness of the adhesive. Treatment of the surfaces is aimed to have a clean surface, free of any contaminant like: oxides, powders, oils, fat and moisture. The surface is then generally treated chemically to achieve stronger chemical bonds and always mechanically to obtain a rough surface for interlocking. Cleaning is performed using solvents and abrasion through sand blast is used for preparation of a rough surface. The surface of pre-impregnated laminates is often ready for the application of the adhesive and protected by a tape to be removed right before the application.

Porous surfaces require a priming coat, which must be compatible with the adhesive. The method of applying the adhesive depends on the structural configuration. Generally hand

methods are used, though machines have been developed for wrapping columns. For plates, a layer of adhesive is usually applied to the plate while fabrics are usually pre-impregnated. The materials are then applied to the prepared concrete. Sufficient pressure is applied with rollers to ensure a uniform adhesive layer and to expel any entrapped air. For complex surface geometries where preformed plates cannot conform: vacuum-assisted resin infusion can be used to form the composite in-situ, the fibers are applied to the structure dry, The area is sealed with a rubber sheet and vacuum used to draw in the resin.

I.2.3.6 Mechanical properties of FRP composites

To design a structure with an FRP composite, a structural engineer must have knowledge of the physical, and especially, the mechanical properties of the FRP material being used in the design. There are two ways to determine the properties of an FRP composite for use in design. The first is via theoretical calculations, and the second is via experimental measurements. Since an FRP composite is an inhomogeneous material, it can be characterized theoretically and experimentally on a number of different levels. An FRP composite material can be characterized on one of four levels: (1) the fiber level, (2) the lamina level, (3) the laminate level, and (4) the full-section level [Bank 2006]. As strengthening of RC beams using externally bonded FRP laminates requires FRP laminates of unidirectional type, therefore, fiber level is detailed below, and there is no need to focus on the last three levels (the lamina level, the laminate level, and the full-section). For this fiber-level analysis, a micro-mechanic model can be used. The model is based on the rule of mixtures, and used to:

- Relate mass or weight fractions of the constituents to their volume fractions.
- Estimates the modulus and strength of unidirectional composites.
- Approximate the longitudinal strength and longitudinal modulus of a fiber sheet material by ignoring the mechanical contribution of the matrix material in the longitudinal direction.

In the micromechanics model, the final properties of FRP composites depend on the basic properties of each constituent (fiber and matrix). Figure I.2.15 gives a typical presentation of the stress strain diagram of FRP composite and its primary components: fiber and matrix. The physical and mechanical properties of the fiber and matrix constituents need to be known. They are usually obtained by experimental methods. The matrix and fibers are assumed as isotropic and linear elastic materials. The resistance of fibers cannot be specified as a single value. Experimentally, a wide dispersion is recorded in the strength of fiber as shown in Figure I.2.16. It was proven that the dispersion of results for a given fiber length is about 10-

20%. In addition, the average fiber strength decreased gradually as its length increases. The variability can be attributed to a number of factors such as material and specimen preparation, gripping, system alignment, testing temperature, void content, testing environment and rate of loading [Rochdi 2004].
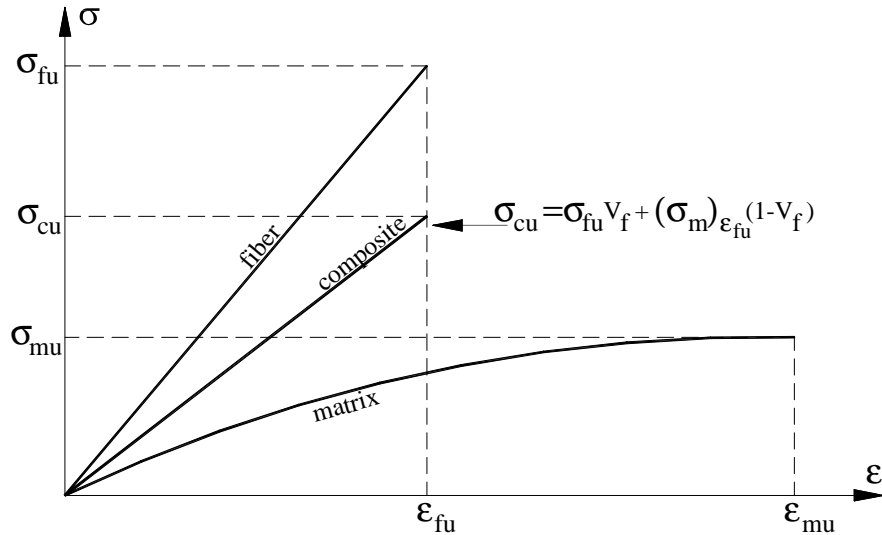
Figure I.2.15: Stress-strain (σ-ε) relations for different components of FRP composite.
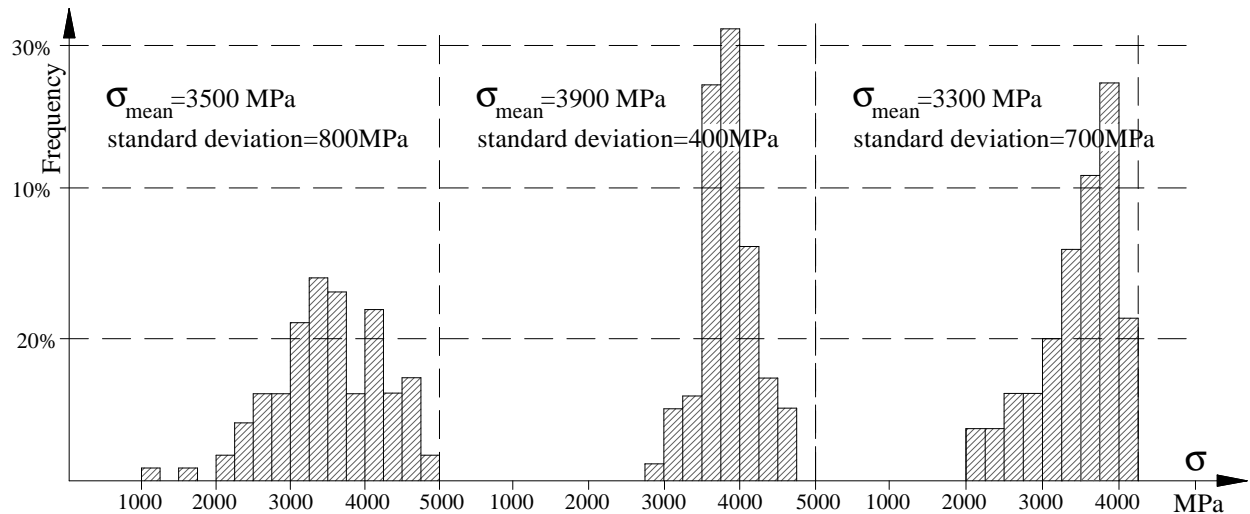
Figure I.2.16: Examples of the dispersion of fiber strength (σ) [Rochdi 2004].

The unidirectional composite ply has two preferred directions as shown in Figure I.2.17: the longitudinal direction (L) and transverse direction (T). Unidirectional ply of a planar FRP composite material contains all of its fibers aligned in one direction. In a unidirectional composite material, fibers are most often distributed in certain randomness rather than following a regular arrangement. Experimental tests of the matrix material results in: modulus (E_m), Poisson's ratio (v_m), shear modulus (G_m) and volume fraction (V_m). While for fibers results in: modulus (E_f), Poisson's ratio (v_f), shear modulus (G_f) and volume fraction

(V_f). Thus, the four independent engineering characteristics of an orthotropic (or transversely, isotropic) unidirectional FRP composite (E_x, E_y, E_s, v_x) can be estimated at a first approximation by the following rule-of-mixtures equations:

$$E_x = v_f E_f + v_m E_m \qquad (I.2.1)$$

$$\frac{1}{E_y} = \frac{v_f}{E_f} + \frac{v_m}{E_m} \qquad (I.2.2)$$

$$\frac{1}{E_s} = \frac{v_f}{G_f} + \frac{v_m}{G_m} \qquad (I.2.3)$$

$$v_x = v_f v_f + v_m v_m \qquad (I.2.4)$$

$$v_y E_x = v_x E_y \qquad (I.2.5)$$

where E_x is the longitudinal modulus in the fiber direction, E_y the transverse modulus perpendicular to the fiber direction, E_s the in-plane shear modulus, v_x the longitudinal (or major) Poisson ratio, and v_y the transverse (or minor) Poisson ratio. V_f can be related to V_m as: $V_f = 1 - V_m$.

Finally, the longitudinal tensile strength of a unidirectional composite, σ_{cu}, which is dominated by the properties of the fiber, can be estimated at a first approximation by (see also Figure I.2.12):

$$\sigma_{cu} = \sigma_{fu} V_f + \sigma_{fu}(1 - V_f) \qquad (I.2.6)$$
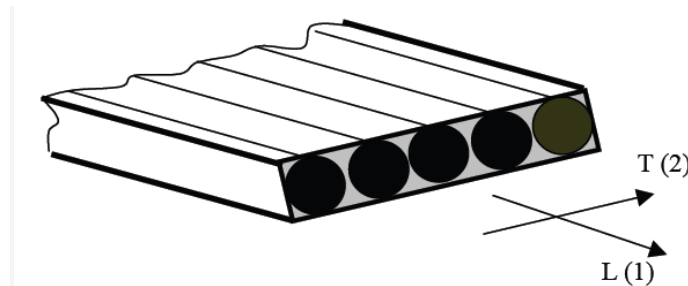
Figure I.2.17: Unidirectional composite ply.

The overall behavior of the FRP composite given by Equation I.2.6 can be determined experimentally. Many standards organizations around the world publish standard test methods for FRP composite materials; among these is the American Society for Testing and Materials [ASTM 2006]. ASTM (2006) is the most widely used guideline to determine the in-plane tensile properties of FRP composite. The tensile samples were mounted in self-aligning grips mechanical testing machine and continuously loaded in tension. Various failure modes were observed to take place. The American Society for Testing and Materials devised a standard failure code system as shown in Figure I.2.18. Although these failure codes cover most tensile

failures, not all failure modes will conform to these standard representations. The failure code for a particular specimen consists of three separate categories or characters, each denoted by a letter value. The first character represents the nature or type of failure, while the second characterizes the failure area. The third character distinguishes the failure location. Table I.2.6 presents a summary of the characters and their related description..
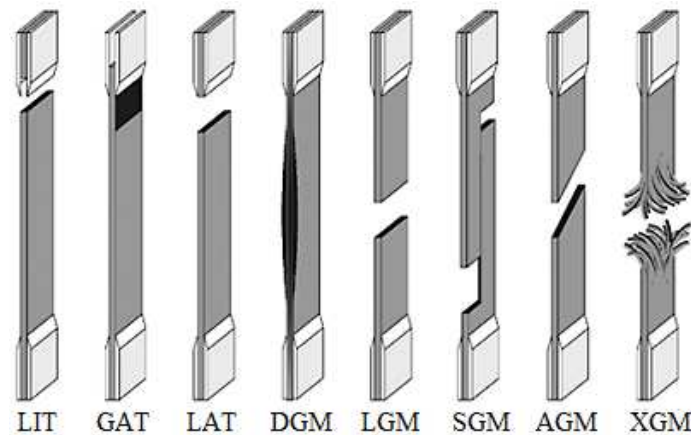
Figure I.2.18: Example of FRP failure codes.

Table I.2.6: Failure codes for tensile specimens [ASTM 2006]

First character		Second character		Third character	
failure type	code	failure area	code	failure location	code
Angled	A	Inside grip/tab	I	Bottom	B
Edge delamination	D	At grip/tab	A	Top	T
Grip/tab	G	<1 W from grip/tab	W	Left	L
Lateral	L	Gage	G	Right	R
Multi-mode	M(xyz)	Multiple areas	M	Middle	M
long Splitting	S	Various	V	Various	V
eXplosive	X	Unknown	U	Unknown	U
Other	O				

I.2.3.7 Advantages and disadvantages of FRP of strengthening technique.

All structural problems have more than one technical solution. Structural engineers could differentiate between strengthening techniques according to economical and structural evaluations such as cost, required service life, weight of the elements after strengthening, deformations...…etc. Two major comparisons could be done when comparing FRP strengthening of RC structures with other techniques. The first is to compare strengthening using bonded attachments plates (steel or FRP composites) with non-bonded techniques that require addition of bolted steel attachments concrete projection or post-tensioning which are previously discussed. Non-bonded techniques require a lot destructive works on the existing concrete elements to produce holes for anchors and also to produce a rough concrete surface to ensure bond between the new which will be casted adjacently to the existing concrete

element. Also, these techniques increase remarkably the own weight of the strengthened elements and its cross section may affect the architecture shape. From other side, non-bonded strengthening methods do not allow to use the structure during strengthening period while all these disadvantages does not exist for in FRP externally bonded strengthening methods that concern concrete elements.

Secondly, the most recent technique that is noteworthy when comparing FRP strengthening technique with other techniques is the use of external bonded steel plates. The emergence of FRPs in the civil engineering industry has been driven by their numerous advantages over steel and can be concluded as follow [Concrete Society 2004; Täljsten 2002; FIB 2001; ACI Committee 440],

- Steel plates require maintenance painting – to resist corrosion - and may incur traffic disruption. In contrast, FRPs do not suffer from corrosion, thus composite plates will not require such maintenance, reducing the whole life cost of this system.

- The high strength and stiffness to weight ratios of FRPs mean that a smaller weight of FRP needs to be applied as compared to steel plate bonding. Thus, composite plates may be less than 10% of the weight of steel of the same ultimate strength.

- This low weight reduces transportation costs, significantly eases installation, even in tight spaces, and can eliminate the need for scaffolding as it may be installed from mobile platforms, reducing traffic impact. The low weight also means that FRPs add only a small amount to the structure's dead load. This allows more of the strengthening to be useful to the structure and also makes FRPs a repair option when significant additional weight could cause failure.

- FRPs are typically applied in thin strips, resulting in very little change in the structural profile, an important feature on bridges or other structures that require clearances for vehicles or machinery.

- The way that FRPs are manufactured also provides useful properties. By designing the placement of the reinforcing fibers, properties such as strength and modulus can be controlled in different directions. This allows the strengthening to act only in the needed direction, preventing it from changing the structural behavior in unintended ways. Because they are made from long thin fibers.

- FRPs are very easy to handle. They can be made to wrap around curves and to accept the irregularities in concrete surfaces.

- FRPs can be manufactured in long lengths, eliminating the need for splices, and can be

cut to length on site, eliminating sizing errors in the manufacturing stage.

- Composite plates are a low conductor of heat when compared with steel, thus reducing the effect fire has on the underlying adhesives, and thus the FRPs system remains effective for a much longer period than steel plate bonding.

- Composite plates do not require extensive jacking and support systems to move and hold in place. The adhesives alone will support the plate until curing has taken place. In contrast, fixing of steel plates constitutes a significant proportion of the works costs.

In contrast FRPs have numerous disadvantages. Unidirectional FRP materials are characterized by linear elastic behavior; this lack of yielding can result in less ductile structures. FRP materials are very susceptible to damage from impact or vandalism, and as such need to be protected. FRPs susceptibility to high temperatures and fire has hindered their use for enclosed structures, which is why the majority of their use to date has occurred in bridges and other outdoor applications. Though FRPs do not exhibit corrosion, they are not immune to environmental impacts and do suffer degradation due to moisture, temperature, and UV rays. This disadvantage is of particular importance because there is currently little long-term information on the durability of composites in exposed environments. The initially high material cost of FRPs is also a drawback to many engineers, however, due to the cost advantages in transportation, installation and the long lifespan offered by composites. The cost of a whole strengthening project can be comparable or even less than the same project strengthened with steel plates.

I.2.4 BEAMS STRENGTHENED BY FRP LAMINATES

I.2.4.1 Flexural behavior and design of FRP strengthened beam

The role of the composite in retrofitted beam is similar to that of ordinary steel reinforcement. The composite enhances both the stiffness and strength of the beam. Methods of analysis for ordinary RC can be easily generalized to include FRP composite laminates. Accordingly, the gain in the structural capacity of the strengthened beam is generally significant. Figure I.2.19 shows the theoretical typical load–deflection curves of RC girder and FRP strengthened RC girders using externally bonded technique. According to the figure, the ultimate load of the RC beam is approximately equals to the yield load value. While for FRP strengthened RC beam the ultimate load is much higher than the yield load. This can explained by the gained hardening effect due to the boned FRP laminates. This hardening, and consequently the ultimate load, increases as the thickness t_{FRP} of the bended FRP laminate increases.
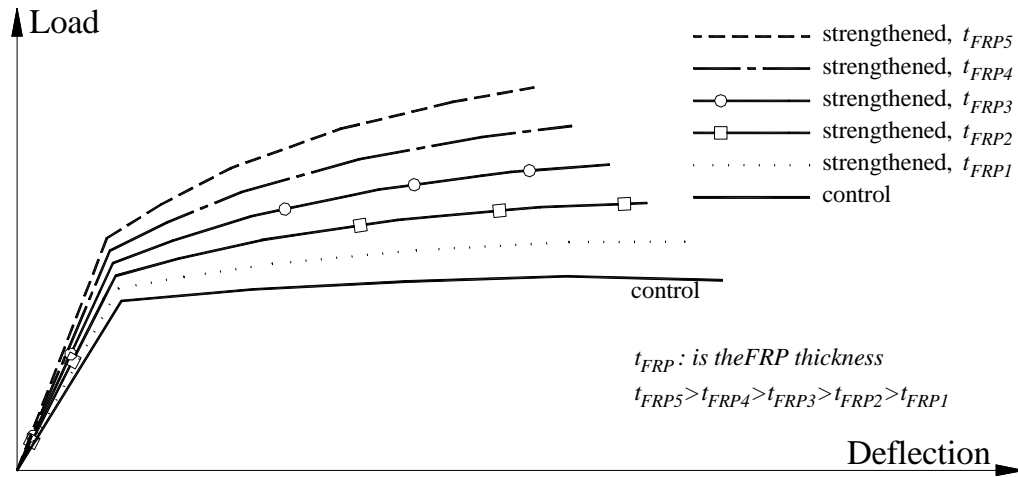
Figure I.2.19: Load versus deflection curves of control and FRP strengthened RC beams.

According to the typical load–deflection curve, presented by solid line in Figure I.2.20, of FRP strengthened RC beam may be divided into three main parts [Varastehpour 1996; Ferrier 1999; Balaguru *et al* 2009]:

- The first part ends with cracking load at point (1) which refers to the maximum moment of uncracked concrete section. At this stage concrete strains in the tension part range between 0.0002-0.0003. The concrete section at point (2) acts as a cracked section. Points (1 & 2) approximately give the same load. The horizontal distance is due to the reduction in the stiffness as the RC section is transformed to the cracked case.

- The second part lies between points (2) and (3). This part can be considered as linear segment. The tensile steel rebars at point (3) are fully yielded.

- The third part lies between points (3) and (4) in which the later point represents the ultimate load or the failure load.
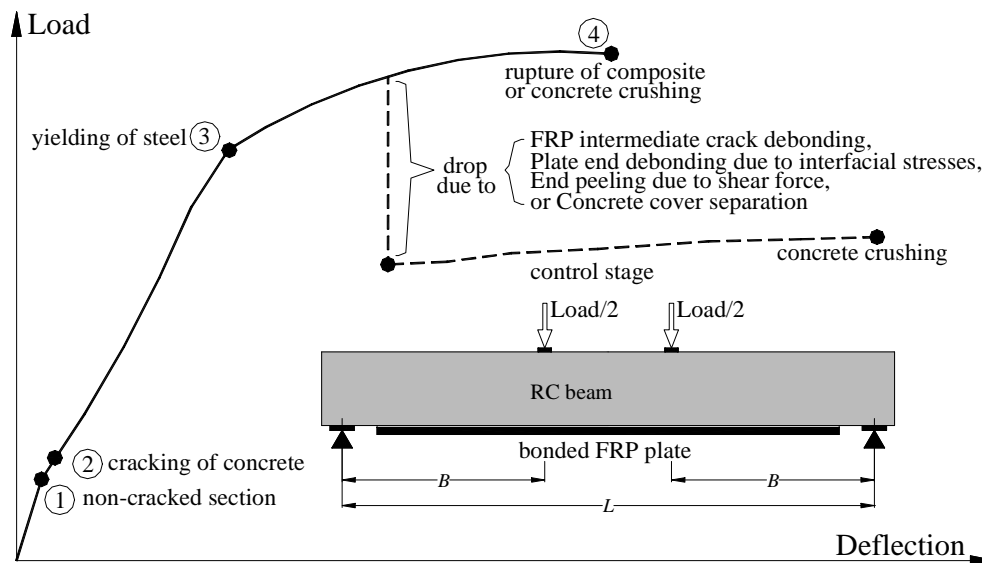
Figure I.2.20: Typical load - deflection curve for FRP strengthened RC beam.

The ultimate load of non-strengthened RC beam is nearly equal to the yielding load and the curve after yielding is almost horizontal line and no significant increase in capacity can be observed. The ultimate load of the strengthened beam is much higher than the yielding load. This increase can be explained by the effect of composite material which starts to effectively maintain the stiffness after yielding of steel reinforcements [Schilde & Seim 2007]. The typical load–deflection curves for FRP strengthened RC beam shown in Figure I.2.19 is based mainly on the assumption that there is a full bond action between concrete and FRP laminates and that the beam will fail by concrete crushing or FRP rupture.

However, researchers have observed that the real capacity is limited by modes of failure not observed in ordinary RC beams. These failure modes are often brittle, involving delamination of the FRP, debonding of concrete cover layer and shear collapse. Failure can occur at loads significantly lower than the theoretical strength of the retrofitted system. Specific failure criteria are therefore required for the analysis of these systems. Load deflection, presented by dashed line in Figure I.2.20, shows the effect of such these modes of the load-deflection of FRP strengthened RC beams. The curve is characterized by a sudden drop in stress after delamination of FRP plate followed by a residual strength equals to the strength of non strengthened beam. The curve is also valid for debonding of FRP composites and concrete cover separation as the stiffness of FRP composites is lost after FRP debonding.

ACI Committee 440 reported that strengthening of RC beams using externally bonded FRP laminates increases the resistance by 10-160%. From other part, the ductility and serviceability requirements may be reduced by 5-40%. The ultimate flexural capacity of FRP strengthened RC member can be calculated based on assumptions similar to those made for

concrete members reinforced with steel bars. Most design international codes [e.g., ACI 440.2R-02; Fib Bulletin 14; Concrete Society 2004] assume that the planes section before loading remains plane after loading. Nonlinear stress-strain (σ-ε) constitutive relations can be considered for concrete (see Figure I.2.21a). The concrete tensile strength can be totally neglected. Steel reinforcements present an elastic perfect plastic behavior, while FRP composite is assumed to be linear elastic until failure as shown respectively in Figures I.2.21b & I.2.21c.

(a) Concrete   (b) reinforcement steel   (c) FRP composites
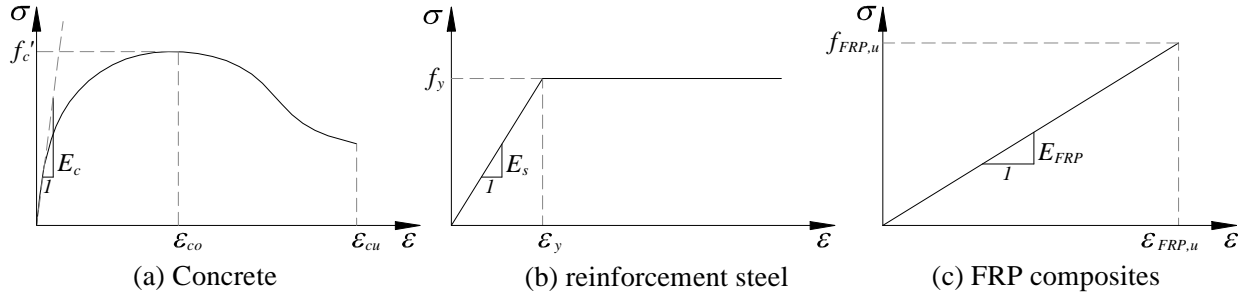
Figure I.2.21: Strain-strain (σ-ε) curve for material used in FRP strengthened RC member.

In addition, the concept of concrete block shown in Figure I.2.22 remains under consideration. Internal forces in concrete, compression steel, tensile steel, and FRP plate can be expressed as given in Equations I.2.7-I.2.10 respectively.

$$F_c = \int b_c f_c(\varepsilon_c)dx \tag{I.2.7}$$

$$F_s = A_s f_s \tag{I.2.8}$$

$$F_{sc} = A_{sc} f_{sc} \tag{I.2.9}$$

$$F_{FRP} = b_{FRP} t_{FRP} f_{FRP} \tag{I.2.10}$$

and the governing internal stability equation is

$$F_c + F_{sc} = F_s + F_{FRP} \tag{I.2.11}$$

where A_s and A_{sc} corresponds to the area of tensile and compression steel rebars respectively. f_c is the concrete stress which corresponds to a concrete strain (ε_c) at distance (x) measured from the extreme compression stress applied to the concrete as shown in Figure I.2.22. f_s and f_{sc} are the tensile and compression stresses in steel rebars respectively and can be taken as follow:

$$f_s = \begin{cases} f_y & \text{for } \varepsilon_s > \varepsilon_y \\ E_s \varepsilon_s & \text{for } \varepsilon_s \leq \varepsilon_y \end{cases} \tag{I.2.12}$$

where, E_s, f_y, and ε_y are the elastic modulus, yield stress and yield strain of steel rebars

respectively. f_{FRP} is the stress in composite laminates and is taken equal to

$$f_{FRP} = (\varepsilon_{FRP} - \varepsilon_{FRP,exist})E_{FRP} \qquad (I.2.13)$$

where, E_{FRP} is the modulus of FRP composites, ε_{FRP} is the strain in FRP composites according to the strain diagram shown in Figure I.2.22 and $\varepsilon_{FRP,exist}$ is the existing substrate FRP strain and taken equal to the maximum tensile strain – due to permanent loads – of RC section; before applying FRP strengthening. Based on beam theory the ultimate bending moment (M_u) of FRP strengthening RC section can be evaluates according to Equation I.2.14.

$$M_u = \int b_c f_c(\varepsilon_c)(c-x)dx + A_s f_s(d_s - c) + A_{sc} f_{sc}(c - d_{sc}) + b_{FRP} t_{FRP} f_{FRP}(d_{FRP} - c_{comp}) (I.2.14)$$

The evaluation of Equation I.2.14 depends on the failure mode which may take place; concrete crushing, FRP rupture, FRP debonding. More detail will be given in the following sections.

(a) FRP strengthened RC section   (b) Strain diagram   (c) Internal forces diagram
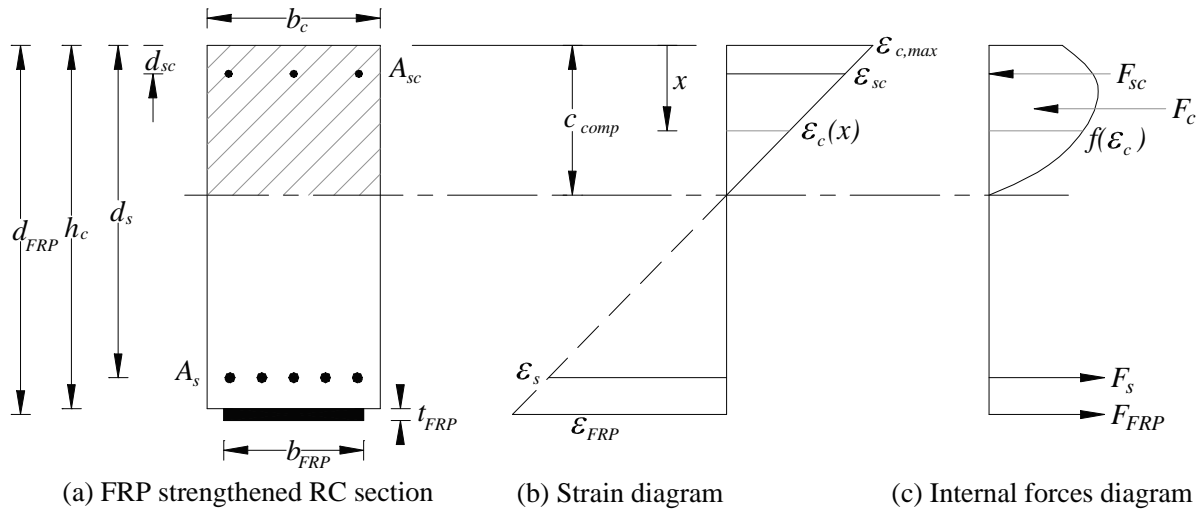
Figure I.2.22: Strain distribution of FRP strengthened RC flexural member.

I.2.4.2 Failure modes of flexural strengthened RC beam by FRP laminates

In the last two decades, the behavior of FRP strengthened RC beams has been well studied in a significant numbers of experimental and numerical publications. Different failure modes have been observed, which can be classified into two types according to the location of the occurrence along the beam. First, modes occur at positions of maximum moments. Such modes are concrete crushing, FRP mid span debonding (due to flexural cracking or flexural-shear cracking) and FRP rupture. Second, failure modes occur at plate-ends. Such modes are interfacial shear stress induced FRP end-debonding, concrete cover separation and FRP end-debonding based shear crack). Figure I.2.23 presents positions and types of these failure modes which can possibly take place [Esfahania *et el* 2007; Oehlersa *et el* 2003]. The following subsections give detailed explanations about each failure mode.
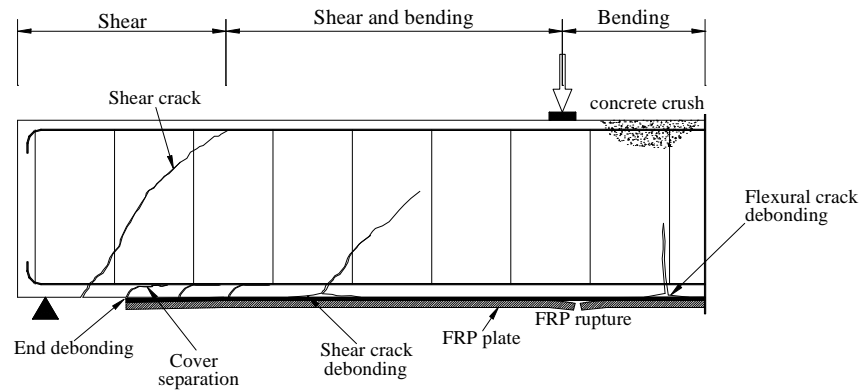
Figure I.2.23: Possible failure modes of FRP strengthened RC beam under four point bending.

I.2.4.2.1 Concrete crushing

Concrete crushing failure mode is the principal failure mode in RC structures and takes place before or after yielding of steel reinforcements. The ultimate moment is calculated when the maximum applied concrete compressive strain ($\varepsilon_{c,max}$) equals to the ultimate concrete strain (ε_{cu}). Concrete crushing failure mode is considered as brittle failure mode (see Figure I.2.24).

Figure I.2.24: Concrete crushing of FRP strengthened RC beam [Esfahania et el 2007].

I.2.4.2.2 FRP rupture

FRP rupture failure mode is related to the longitudinal applied strain in FRP composites (ε_{FRP}). Since the concrete strain may not reach its ultimate strain value before the FRP strain reaches its ultimate value ($\varepsilon_{FRP,u}$) causing a cut in the FRP plate as shown in Figure I.2.25. Two possible behaviors may take place. The first is fiber rupture followed directly by concrete crushing, as the concrete strain is nearly closed to concrete crushing strain. In this case no residual strength remains after FRP rupture and the load-deflection curve is the same as in concrete crushing (see Figure I.2.19). The second is FRP rupture followed by a vertical drop in the beam strength and the residual strength equals to the strength of non-strengthened beam as shown in Figure I.2.20.

FRP rupture failure mode may frequently occur in two cases. First, FRP rupture occurs as RC beam is strengthened with small amounts of FRP laminates. Second, the RC beam is strengthened with anchorage end FRP laminates using a system of bolts as shown in Figure I.2.7b.
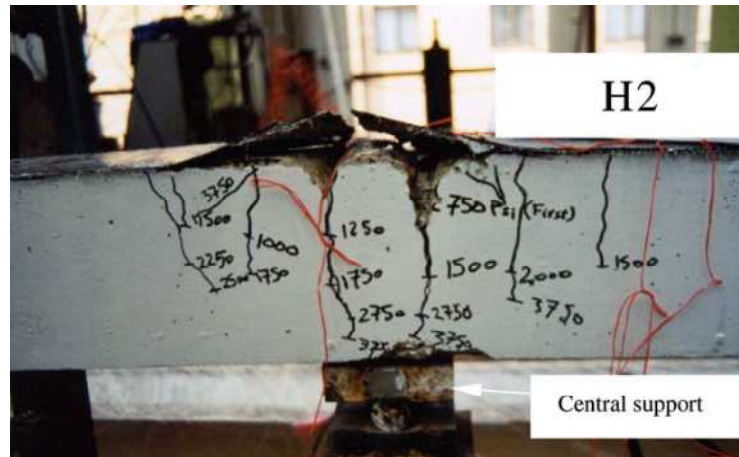
Figure I.2.25: Tensile rupture of the FRP plate bonded to RC beam [Ashour *et al* 2004].

I.2.4.2.3 FRP intermediate crack debonding

It is well known that reinforced concrete elements behave under small amounts of loads as an elastic element. Concrete and steel around the neutral axis affect significantly the stiffness of the beam. Increasing the loads initiate micro cracks in concrete subjected to tension, while the overall performance of the RC element is still considered elastic. Thus, the concrete section should be analyzed as cracked section and concrete in tension zones can be totally neglected. The induced cracks are to be approximately uniformly spaced in the longitudinal direction of the beam. Adhesive near cracked zones is subjected to a concentration of interfacial stresses due to the discontinuity – induced by cracks – of concrete elements near the adhesive layer. Generally, it takes place after initiation and propagation of micro flexural or flexural/shear cracks along the RC beam. While the loads continue to increase on the beam, these cracks tend to induce high interfacial stresses at the conjunction zone between the adhesive layer and the tips of the cracks, thus, resulting in initiation and propagation of slip along the interface as shown in Figure I.2.26. Slips may occur at concrete-adhesive or FRP-adhesive interface. The slip begins to propagate towards the nearest plate end of the FRP plate as shown in Figure I.2.26 & I.2.27. Then, the beam is transformed into a non-strengthened beam leading to a vertical drop in the strength giving a load-deflection curve similar to that shown in Figure I.2.20.

(a) Intermediate crack debonding (b) Diagonal crack debonding
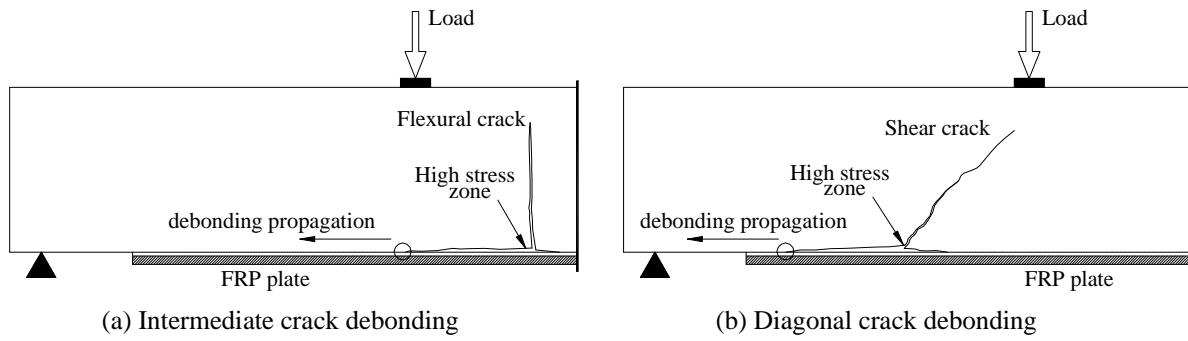
Figure I.2.26: Flexural and flexural/shear crack debonding, [Esfahania *et al* 2007].
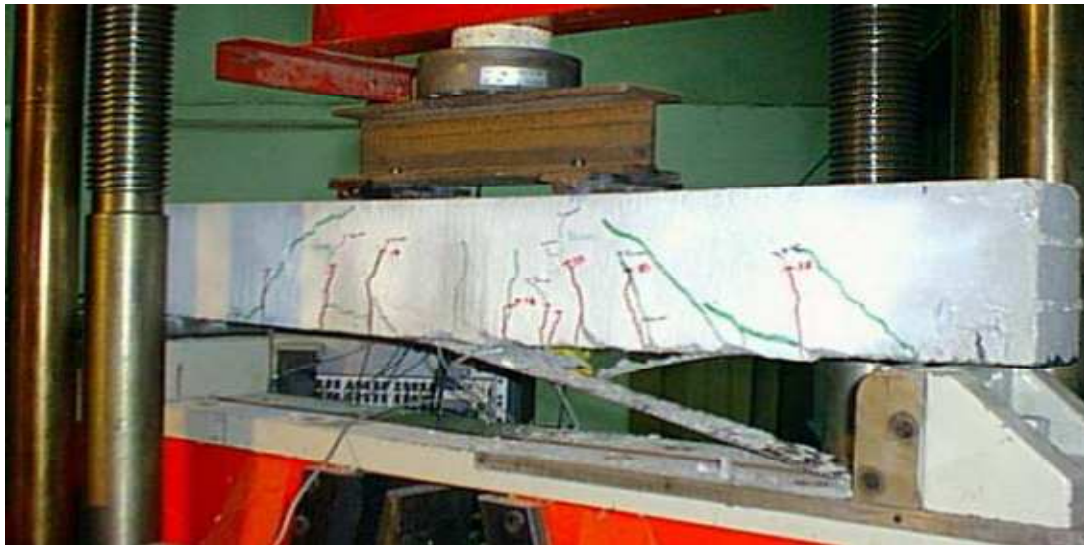
Figure I.2.27: FRP strengthened RC beam, FRP intermediate crack debonding [Ferrier 1999].

Experimentally, FRP debonding due to intermediate cracking is the most frequently failure mode that affects passively the capacity of FRP strengthened RC beams, so there is a need to understand the nature of the debonding failure due to the interfacial shear stresses induced near cracks. Debonding failure may occur at three planes; at contact surface between the soffit FRP plate and the adhesive layer, within the adhesive layer or at the contact surface between adhesive layer and concrete beam. Figure I.2.28 shows the free body diagram of a longitudinal segment with length (dx) of the FRP strengthened RC beam, where $M_{(x)}$, $N_{(x)}$ and $V_{(x)}$ present the bending moment, normal force and shearing force respectively at a distance x measured from the end of FRP plate. There are two types of interfacial stresses [Smith & Teng 2001; Tounsi & Benyoucef 2007]: normal stress $\sigma(x)$ in the vertical direction and shear stress $\tau(x)$ in horizontal direction. Classical beam theory fails to predict the values of these stresses. In other hand, the finite elements method is calculations waste. Particularly, several relatively simplified approximated closed form solutions for the interfacial stresses have been developed [e.g., Smith & Teng 2001; Tounsi & Benyoucef 2007; Täljsten 1977]. Generally, these models aims to calculate the interfacial shear $\tau(x)$ and normal stresses $\sigma(x)$ induced

between concrete, adhesive, and FRP composite plate using the following governing differential equations,

$$\tau(x)=G_a\left(\frac{du(x,y)}{dy}+\frac{dv(x,y)}{dx}\right) \tag{I.2.15}$$

$$\sigma(x)=\frac{E_a}{t_a}\left[v_2(x)-v_1(x)\right] \tag{I.2.16}$$

where G_a, E_a, t_a are the shear modulus, elastic modulus and thickness of the adhesive layer. $u(x,y)$ and $v(x,y)$ are the horizontal and vertical displacements respectively at any point in the adhesive layer. Adherents 1 and 2 in Figure I.2.28 express concrete and FRP elements respectively. The analytical approach is based on elastic behavior of the concrete, FRP composites, adhesive layer and steel reinforcement. Interfacial stresses are considered invariant across the width and the thickness of the adhesive layer. Deformations of adherents 1 and 2 are due to bending and axial actions. No slip is allowed at the interface of the bond (i.e. there is a perfect bond at the adhesive-concrete interface and at the adhesive-plate interface). Solution of Equation I.2.15 & I.2.16 results in the interfacial shear and normal stresses as:

$$\tau(x)=A\cosh(\lambda x)+B\sinh(\lambda x)+mV_T(x) \tag{I.2.17}$$

$$\sigma(x)=e^{-\beta x}\left[C\cos(\beta x)+D\sin(\beta x)\right]-n_1\frac{d\tau(x)}{dx}-n_2 q \tag{I.2.18}$$

where q is the uniform load applied to the concrete beam segments if exist, $V_T(x)$ is the total applied shearing force acting at the distance (x) measured from the end of FRP plate,

$$\lambda^2=\frac{G_a b_{FRP}}{t_a}\left(\frac{(y_1+y_2)(y_y+y_2+t_a)}{E_1 I_1+E_2 I_2}+\frac{1}{E_1 A_1}+\frac{1}{E_2 A_2}\right), \qquad m_1=\frac{G_a}{t_a\lambda^2}\left(\frac{y_1+y_2}{E_1 I_1+E_2 I_2}\right),$$

$$n_1=\left(\frac{y_1 E_2 I_2+y_2 E_1 I_1}{E_1 I_1+E_2 I_2}\right), \quad n_2=\frac{E_2 I_2}{b_{FRP}(E_1 I_1+E_2 I_2)}, \quad \beta=\sqrt[4]{\frac{E_a b_{FRP}}{4t_a}\left(\frac{1}{E_1 I_1}+\frac{1}{E_2 I_2}\right)}, \text{ and. } b_{FRP} \text{ is the }$$

width of the soffit plate. E_i, A_i, and I_i are the elastic modulus, cross-sectional area and second moment of area of adherent (i.e. $i=1, 2$). y_1 and y_2 are the distances from the bottom adherent 1 and the top of adherent 2 to their respective centroid. A, B, C, and D are the integration constants which will be found by applying certain boundary conditions depending on the loading and supporting system.
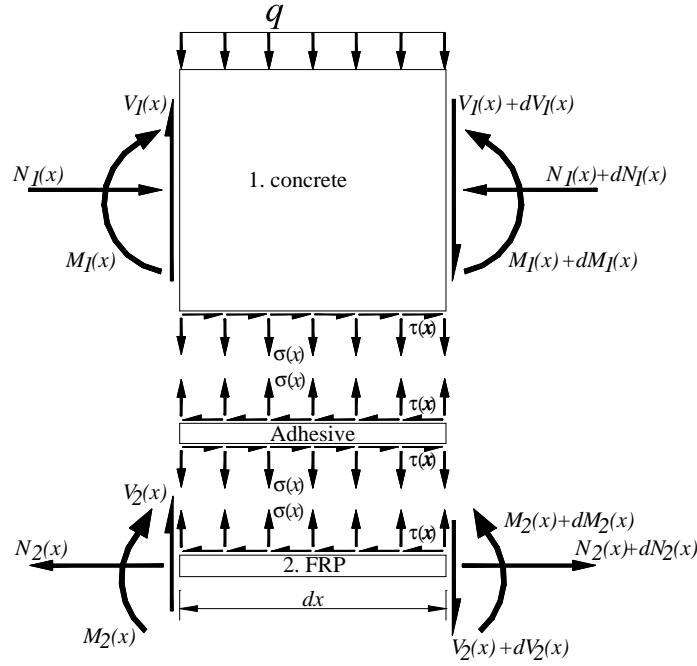
Figure I.2.28: Differential segment of FRP strengthened RC beam.

Other similar closed form approaches to calculate the interfacial stresses and their distribution across the longitudinal direction of the beam due to intermediate flexural crack or flexural shear crack were derived by Wang J. [2006; 2008]. The two studies assume a linear elastic behavior for concrete and FRP plate. Slip between concrete and the FRP plate is considered through a bilinear relationship for interfacial shear stress-slip model of the adhesive layer.

From a practical point of view, all interfacial stress analysis developed to predict debonding failure mode has two main disadvantages:

- Many differential calculations are required.
- The analysis is based on the elastic behavior of FRP strengthened RC beam, and nonlinearity in concrete is completely neglected.

Similar analytical models were developed in many publications to simplify the calculation for FRP debonding failure mode. It was assumed that the behavior of the FRP plate bonded to the concrete beam between two cracks is similar to the debonding behavior of FRP plate bonded to a concrete prism. Length of the concrete prism is equal to half the distance between the two flexural cracks as shown in Figure I.2.29. The tension force induced in FRP plate due to external loading ($P_{FRP,u}$) applied on the FRP strengthened RC beam is simulated by tension force applied directly to the FRP plate bonded to the concrete prism. Such these analytical models are called *analysis of bonded joints*. This bonded joint contains a continuity of one element and discontinuity of the other one; i.e. at the plate end the concrete element is

continuous and the composite plate is discontinuous, while the elements between cracks the composite plate is continuous and the cracked concrete is discontinuous. Performance of bonded joint was studied analytically and experimentally in many previous studies. Table I.2.7 summarizes the analytical models developed to calculate the ultimate strain that if applied to FRP plate causes debonding ($\varepsilon_{FRP,d}$) [Schilde & Seim 2007; Chen & Teng 2001; Lu *et al* 2005; Sharma *et al* 2006; Maalej & Bian 2001; Ali *et al* 2008; Yao *et al* 2005; Yuan *et al* 2004]. These modes will be compared in chapter II.1, based on experimental results, in order to find the most accurate one which will be used in the reliability analysis, in terms of robustness.
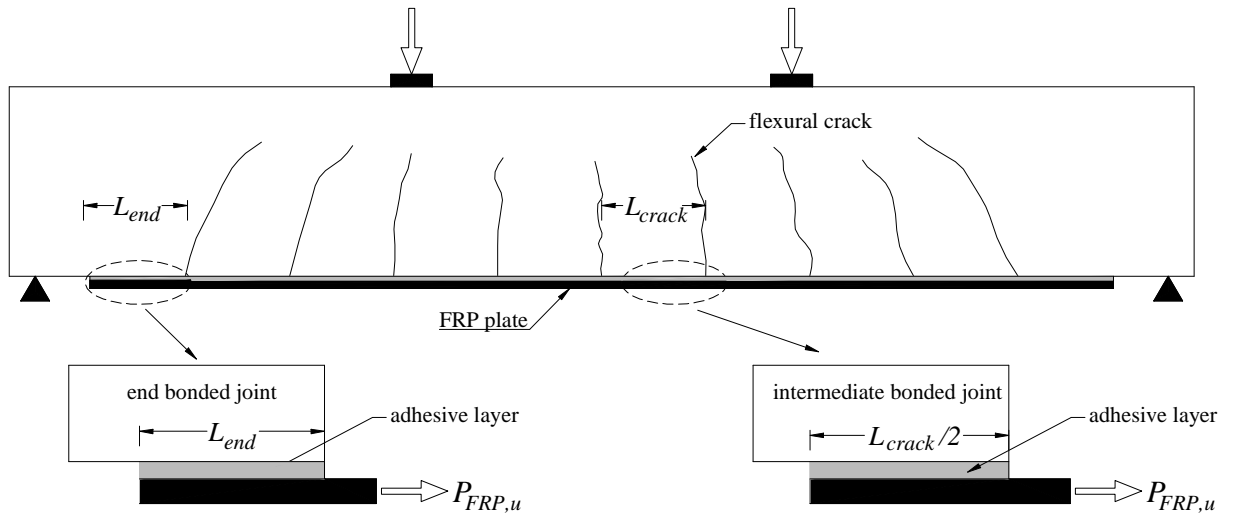
Figure I.2.29: Location of bonded joints in cracked FRP strengthened RC beam.

Table I.2.7: Debonding strain ($\varepsilon_{FRP,d}$) of FRP plate bonded to concrete prism, bonded joint, reported in previous studies and design provisions (SI units).

Neubauer & Rostasy (1997) model, applied in Fib Bulletin 14 (method 1):

$$\varepsilon_{FRP,d} = 0.64k_b\sqrt{\frac{f_{ctm}}{t_{FRP}E_{FRP}}}\begin{cases}1 & if\ L \geq L_e \\ \dfrac{L}{L_e}\left(2-\dfrac{L}{L_e}\right) & if\ L < L_e\end{cases} \text{ ,where} \qquad k_b = \sqrt{1.125\frac{2-b_{FRP}/b_c}{1+b_{FRP}/400}}\ ,$$

$$L_e = \sqrt{\frac{E_{FRP}t_{FRP}}{2f_{ctm}}}$$

Chen & Teng (2001) model:

$$\varepsilon_{FRP,d} = \alpha\beta_w\beta_l L_e b_{FRP}\sqrt{\frac{f_c'}{t_{FRP}E_{FRp}}} \text{ where } \alpha=0.427 \text{ for bonded joint, } \alpha=1.1 \text{ for beams, } L_e = \sqrt{\frac{E_{FRP}t_{FRP}}{\sqrt{f_c'}}}\ ,$$

$$\beta_w = \sqrt{\frac{2-b_{FRP}/b_c}{1+b_{FRP}/b_c}}\ , \beta_l = \begin{cases}1 & if & L \geq L_e \\ \sin\left(\dfrac{\pi L}{2L_e}\right) & if & L < L_e\end{cases}$$

Teng *et al* (2004) model:

$$\varepsilon_{FRP,d} = 0.54k_b\frac{f_{ct}}{\sqrt{E_{FRP}t_{FRP}}}\ , \text{ where } k_b = \sqrt{\left(2.25-\frac{b_{FRP}}{b_c}\right)\bigg/\left(1.25+\frac{b_{FRP}}{b_c}\right)}$$

Taljsten (1994) model:

$$\varepsilon_{FRP,d} = \sqrt{\frac{2G_f}{(1+\alpha_T)E_{FRP}t_{FRP}}}\ , \text{ where, } G_f = 0.644\left(f_c'\right)^{0.19}\ , \alpha_T = \frac{E_{FRP}t_{FRP}}{E_c h_c}$$

Lu *et al* (2005) model:

$$\varepsilon_{FRP,d} = \beta_w\sqrt{\frac{2G_f}{E_{FRP}t_{FRP}}}\ ,$$

where $\beta_w = \sqrt{\dfrac{2-b_{FRP}/b_c}{1+b_{FRP}/b_c}}$, $\lambda_2 = \sqrt{\dfrac{\tau_f}{(s_f-s_o)E_{FRP}t_{FRP}}}$, $\tau_f = 1.5\beta_w f_{ct}$, $s_f = \dfrac{2G_f}{\tau_f}$, $s_o = 0.0195\beta_w f_{ct}$

$a = \dfrac{1}{\lambda_2}\arcsin\left[0.99\sqrt{\dfrac{(s_f-s_o)}{s_f}}\right]$, $L_e = a + \dfrac{1}{\lambda_1}\ln\dfrac{\lambda_1+\lambda_2\tan(\lambda_2 a)}{\lambda_1-\lambda_2\tan(\lambda_2 a)}$, $\beta_l = \begin{cases}\dfrac{L}{L_e}\left(2-\dfrac{L}{L_e}\right) & if & L \geq L_e \\ \sin(\dfrac{\pi L}{2L_e}) & if & L < L_e\end{cases}$

Yuan *et al* (2004) model:

$$\varepsilon_{FRP,d} = \frac{\tau_f}{\lambda_2 t_{FRP}E_{FRP}}\left[\frac{\lambda_2}{\lambda_1}\tanh[\lambda_1(L-a)]\cos(\lambda_2 a)+\sin(\lambda_2 a)\right]$$

where $\lambda_1 = \sqrt{\dfrac{\tau_f}{s_o}\left(\dfrac{1}{E_{FRP}t_{FRP}}+\dfrac{b_{FRP}}{b_c E_c h_c}\right)}$ $\lambda_2 = \sqrt{\dfrac{\tau_f}{(s_f-s_o)}\left(\dfrac{1}{E_{FRP}t_{FRP}}+\dfrac{b_{FRP}}{b_c E_c h_c}\right)}$,

$L_e = a + \dfrac{1}{\lambda_2}\ln\dfrac{\lambda_1+\lambda_2\tan(\lambda_2 a)}{\lambda_1-\lambda_2\tan(\lambda_2 a)}$, $\tau_f = 1.5\beta_w f_{ct}$, $s_f = \dfrac{2G_f}{\tau_f}$, $G_f = 0.308\beta_w^2\sqrt{f_{ct}}$, $s_o = 0.0195\beta_w f_{ct}$,

If $L\geq L_e$ $a = \dfrac{1}{\lambda_2}\arcsin\left[0.97\sqrt{\dfrac{(s_f-s_o)}{s_f}}\right]$ else a is found by solving $\tanh[\lambda_1(L-a)] = \dfrac{\lambda_2}{\lambda_1}\tan(\lambda_2 a)$ iteratively

Sharma *et al* (2006) model:

$$\varepsilon_{FRP,d} = \begin{cases} \dfrac{f_c' K_{crit} \beta_w (L/t_{FRP})}{(L_{b,crit}/t_{FRP}) E_{FRP}} & \text{if} \quad L/t_{FRP} < L_{b,crit}/t_{FRP} \\[3mm] \dfrac{f_c' K_{crit} \beta_w}{E_{FRP}} & \text{if} \quad L/t_{FRP} \geq L_{b,crit}/t_{FRP} \end{cases}$$

$$L_{b,crit}/t_{FRP} = 0.0089 x^3 - 0.439 x^2 + 7.8645 x$$

$$x = \frac{E_{FRP}^{0.25} f_{FRP}^{0.125}}{t_{FRP}^{0.5} f_c^{0.25}}, \ \beta_w = \sqrt{\frac{2 - b_{FRP}/b_c}{1 + b_{FRP}/b_c}}, \ K_{crit} = 1{,}277 \frac{L_{b,crit}/t_{FRP}}{\beta_w}$$

ACI Committee 440:

$$\varepsilon_{FRP,d} = \kappa_m \varepsilon_{FRP,u}, \ \text{where} \ \kappa_m = \begin{cases} \dfrac{1}{60\varepsilon_{FRP,r}}\left(1 - \dfrac{E_{FRP}t_{FRP}}{360{,}000}\right) & \text{for} \ E_{FRP}t_{FRP} \leq 180{,}000 \\[3mm] \dfrac{1}{60\varepsilon_{FRP,r}}\left(\dfrac{90{,}000}{E_{FRP}t_{FRP}}\right) & \text{for} \ E_{FRP}t_{FRP} > 180{,}000 \end{cases}$$

Fib 2001, method 2:

$$\varepsilon_{FRP,d} = c_1 \sqrt{\frac{\sqrt{f_c' f_{ct}}}{E_{FRP}t_{FRP}}} \ , \ \text{where} \ c_1 = 0.23 \ \text{for CFRP}.$$

Fib 2001, strain limiting method:

$$\varepsilon_{FRP,d} = \begin{cases} 0.0065 & \text{for concentred loads} \\ 0.0085 & \text{for distributd loads} \end{cases}$$

JSCE 2001:

$$\varepsilon_{FRP,d} = \sqrt{\frac{2G_f}{E_{FRP}t_{FRP}}} \ , \ \text{where} \ G_f = 0.5 \text{N/mm in absence of test values.}$$

Concrete Society 2004 TR 55:

$$\varepsilon_{FRP,d} = 0.5 k_b \sqrt{\frac{f_{ct}}{E_{FRP}t_{FRP}}} \ , \ \text{where} \ k_b = 1.06 \sqrt{2 - \frac{b_{FRP}}{b_c} \Big/ 1 + \frac{b_{FRP}}{400}} \geq 1$$

Concrete Society 2004 TR 55, strain limiting:

$$\varepsilon_{FRP,d} = \begin{cases} 0.006 & \text{for concentred loads} \\ 0.008 & \text{for distributd loads} \end{cases}$$

CNR DT 200:

$$\varepsilon_{FRP,d} = 0.484 \sqrt{\frac{k_b \sqrt{f_{ct} f_c'}}{E_{FRP}t_{FRP}}} \ , \ \text{where} \ k_b = 1.06 \sqrt{2 - \frac{b_{FRP}}{b_c} \Big/ 1 + \frac{b_{FRP}}{400}} \geq 1$$

L is the available bond length of the FRP laminates which equals to $L_{crack}/2$ and L_{end} for an intermediate and end concrete prism respectively (see Figure I.2.29). L_e is the effective length of the bonded FRP laminates. f_c' is the concrete compressive strength. f_{ct} is the tensile strength of the concrete. f_{ctm} is the mean tensile strength of the concrete. b_c and h_c is the width and the depth of the concrete prism/beam respectively. G_f is interfacial fracture energy. b_{FRP} and t_{FRP} are the width and the thickness of FRP laminates respectively. E_{FRP} is the modulus of the FRP laminates. $\varepsilon_{FRP,u}$ is the rupture strain of the FRP laminates which equals to $f_{FRP,u}/E_{FRP}$. $f_{FRP,u}$ is the ultimate strength of the FRP laminates.

The derivations of the models presented in Table I.2.7 were based on the assumption that both concrete prism and FRP plate behave as elastic materials until failure. Failure may occur in the adhesive layer or in a small depth in the concrete element. Interfacial shear stress–slip relation through the adhesive layer may be different from model to model and may take different shapes such as linear elastic relation till failure, bi-linear relation or bi-parabolic

relation. Various bond-slip models used in analytical previous studies are shown in Figure I.2.30. The area under the bond–slip curve is the interfacial fracture energy G_f. Once the value of G_f is known it can be used regardless of the exact shape of the bond-slip curve as the ultimate load $P_{FRP,u}$ depends on the interfacial fracture energy but not on the shape of the bond-slip curve. However, experimental results indicate that the bilinear curve which features a linear ascending branch followed by a linear descending branch provides a close approximation [Yuan et al 2004].

Some factors in the models reported in Table I.2.7 are based on regression analysis of experimental data beside the analytical derivation of the models. The main objective of studying the bonded joint is to obtain the ultimate load carried by the cross-section of FRP plate $P_{FRP,u}$. Thus, FRP ultimate debonding strain $\varepsilon_{FRP,d}$ can be calculated by dividing $P_{FRP,u}$ by the plate area A_{FRP} and FRP modulus E_{FRP}. The minimum value between the ultimate debonding strain $\varepsilon_{FRP,d}$ – based on bonded joint concept - and the FRP rupture strain $\varepsilon_{FRP,r}$ – discussed in the previous section - will be assumed to be the control strain $\varepsilon_{FRP,u}$ in FRP plates bonded to concrete beam as expressed in Equation I.2.14. Failure in the composite FRP plate is assumed to take place when the applied strain in the FRP plate ε_{FRP} exceeds the control value.

$$\varepsilon_{FRP,u} = \min \begin{cases} \varepsilon_{FRP,d} \\ \varepsilon_{FRP,r} \end{cases} \qquad (I.2.19)$$
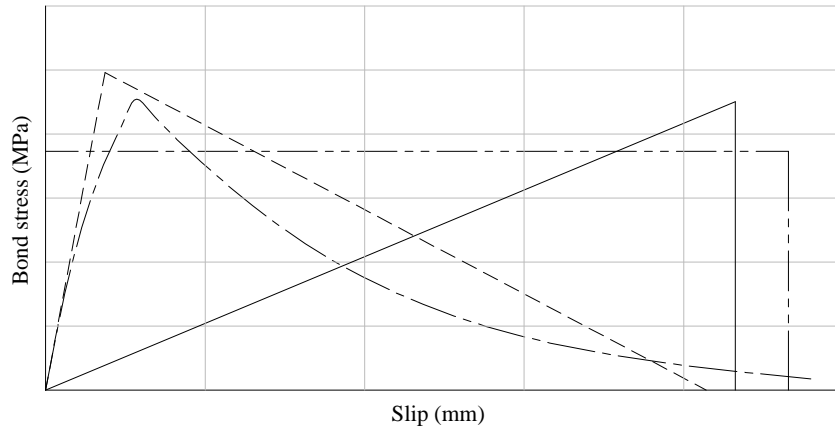
Figure I.2.30: Bonding-slip curves from existing bond-slip models [Yuan et al 2004].

I.2.4.2.4 Plate end debonding due to interfacial shear stress.

Plate end region is subjected to interfacial stresses concentration. The concentration of the interfacial shear stresses tends to form a failure surface between concrete and the adhesive layer, FRP plate and adhesive layer or in the adhesive layer itself. Generally, the analytical models used to calculate the interfacial shear stresses at the end of composite plate are based

on Equations 15 & 16. Concrete and FRP composite are assumed to have an elastic behavior. Adhesive layer is assumed to show a linear normal stress-strain relation. However, a certain shear stress–slip relation through the adhesive layer may be assumed as; linear elastic relation till failure, bi-linear relation, bi-parabolic relation…etc. Debonding failure of this form is initiated near the end of the FRP plate and propagates towards the middle of the beam (see Figure I.2.31). This failure is only likely to occur when the pate is significantly narrower than the beam section (as otherwise failure tends to occur by concrete cover separation) [Teng & Chen 2007].
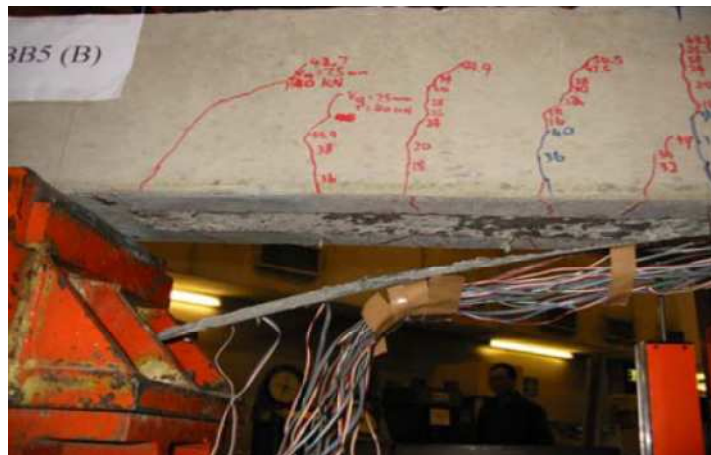
Figure I.2.31: FRP-plated RC beam; FRP end interfacial debonding [Teng & Chen 2007].

Figure I.2.32 presents a typical plot of the interfacial stresses across the longitudinal direction of the FRP plate [Smith & Teng 2001]. Interfacial stresses distributions can be determined by substitution the boundary and loading conditions of the plated beam into Equations I.2.15 & I.2.16. Thus, the constants included in the Equations I.2.17 & I.2.18 can be obtained. Based on the results obtained by Smith & Teng (2001), it can be concluded that; the bending and axial deformations in the beam and the FRP plate respectively are the dominant actions determining the interfacial stresses, including the peak values occurring at the plate end. Interfacial normal stress is seen to change sign at a short distance from the plate end.
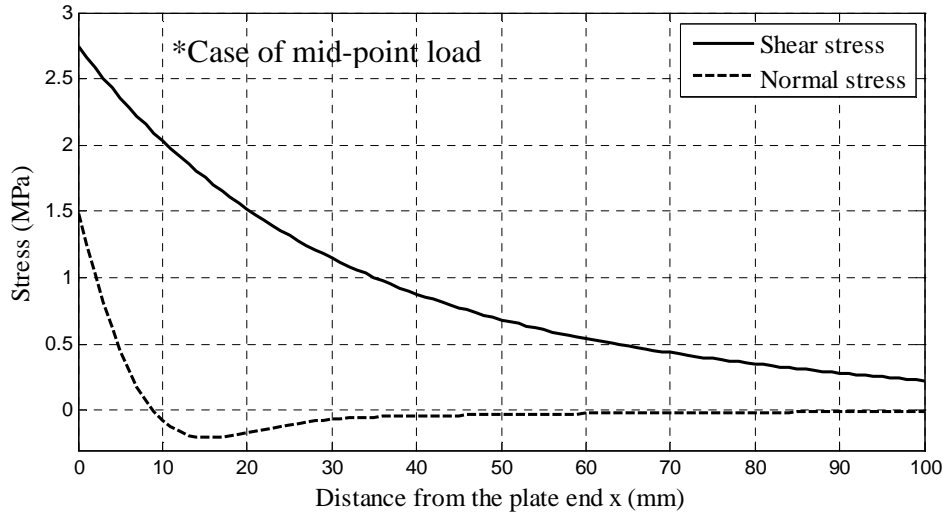
Figure I.2.32: Typical interfacial stress distributions at plate end [Smith & Teng 2001].

However, there is a difficulty to apply such these closed-form derivations to a practical case, as the model was derived to simply boundary and load conditions. In recent publication, simplified formulas were developed to calculate the interfacial stresses – shear and normal - at the plate end. Ziraba *et al* (1994) proposed formulas to calculate the peak interfacial shear and normal at the plate end according to the following equations,

$$\tau = \alpha_1 f_{ct}\left(\frac{C_{R1}V_o}{f_c'}\right)^{5/4} \tag{I.2.20}$$

$$\sigma = \alpha_2 C_{R2}\tau \tag{I.2.21}$$

where,

- $C_{R1} = \left[1+\left(\frac{K_s}{E_{FRP}b_{FRP}t_{FRP}}\right)^{1/2}\frac{M_o}{V_o}\right]\frac{b_{FRP}t_{FRP}}{I_{trc,FRP}b_a}\left(d_{FRP}-x_{trc,FRP}\right)$

- $C_{R2} = t_{FRP}\left(\frac{K_n}{4E_{FRP}I_{FRP}}\right)^{1/4}$

- $K_s = \frac{E_a b_a}{t_a}$

- $K_n = \frac{G_a b_a}{t_a}$

α_1 and α_2 are empirical multipliers calibrated from numerical studies for RC beams strengthened plates. E_a, G_a, b_a, and t_a are the modulus of elasticity, shear modulus, width and thickness of the adhesive layer respectively. $x_{trc,FRP}$ is the distance from the compression face to the neutral axis of the plated section transformed to concrete. I_{FRP} is the second moment of

area of the FRP plate only. d_{FRP} is the distance from the compression face to centroid of the plate. $I_{trc,FRP}$ is the second moment of area of the cracked plated section. Mohr-Coulomb failure criterion is used to define the critical stress state at the plate end:

$$\tau + \sigma \tan \phi \leq C \tag{I.2.22}$$

where, C and ϕ are the coefficient of cohesion and the angle of internal friction respectively. $\alpha_1 = 35$, $\alpha_2 = 1.1$ and $\phi = 28$ for $a/h < 3$ where h is the depth of the beam, a is the distance for the plate end to the nearest support. The value of the coefficient C ranges between 4.8 to 9.5 MPa, ($C = 7.15$ MPa as an average). Finally, substitution of Equations I.2.13 & I.2.14 into Equation I.2.22 gives an expression for the shearing force in the beam, at the plate end, to cause plate end interfacial debonding:

$$V_{db,end} = \frac{f_c'}{C_{R1}} \left[\frac{C}{\alpha_1 f_{ct} (1 + \alpha_2 C_{R2} \tan \phi)} \right] \geq V_o \tag{I.2.23}$$

where, V_o is the applied shearing force on the RC beam at the plate end.

Varastehpour (1996) also developed a model to calculate the interfacial stresses. The model is based on Mohr-Coulomb failure criterion given in Equation I.2.22. C and ϕ are calibrated based on laboratory shear test samples that failed by debonding. Average values were suggested: $C = 5.4$ MPa and $\phi = 33^o$. the shear stress and normal stress required in Mohr-Coulomb equation are expressed as:

$$\tau = 0.5 \sqrt{\beta} (\lambda V_o)^{3/2} \tag{I.2.24}$$

$$\sigma = C_{R2} \tau \tag{I.2.25}$$

The shearing force in the beam, at the plate end to cause debonding, can then be determined as:

$$V_{db,end} = \frac{1.6 \tau_{max}^{2/3}}{\lambda \beta^{1/3}} \geq V_o \tag{I.2.26}$$

where,

- $\lambda = \dfrac{t_{FRP} E_{FRP}}{I_{trc,FRP} E_c} \left(d_{FRP} - x_{trc,FRP} \right)$

- $\beta = \dfrac{1.26 \times 10^5 B}{h^{0.7} t_{FRP} E_{FRP}}$

- $\tau_{max} = \dfrac{5.4}{1 + C_{R2} \tan 33^o}$

where, B is the shear span of the beam. The above described two models can be used when the adhesive is not strong enough, as the normal and shear interfacial stresses induce a crack

within the adhesive layer. The crack is initiated at the end of the plate and propagates toward the second end of the plate as shown in Figure I.2.33a.

Another type of failure criterion is associated at plated end where debonding can take place when the adhesive is strong enough. Failure occurs at the concrete-adhesive interface or in few millimeters through the concrete cover and closed to the plate (see Figure I.2.33b). Tumialan *et al* (1999) evaluate the maximum principle stress as function of three stresses values: the peak interfacial shear stress $\sigma(x)|_{x=0}$, the peak interfacial normal stress $\tau(x)|_{x=0}$ and the applied tensile stress in the concrete in the longitudinal direction σ_l at the end of the plate:

$$\tau(x)\big|_{x=0} = \overline{C}_{R1}\frac{E_{FRP}}{E_c}V_o \tag{I.2.27}$$

$$\sigma(x)\big|_{x=0} = C_{R2}\tau_{(x=0)} \tag{I.2.28}$$

$$\sigma_l = \frac{M_o}{I_{trc,FRP}}(h_c - x_{trc,FRP}) \tag{I.2.29}$$

where,

- $\overline{C}_{R1} = \left[1+\left(\dfrac{K_s}{E_{FRP}b_{FRP}t_{FRP}}\right)^{1/2}\dfrac{M_o}{V_o}\right]\dfrac{b_{FRP}t_{FRP}}{I_{trc,c}b_a}\left(d_{FRP} - x_{trc,c}\right)$

- C_{R2} is taken the same as in Ziraba *et al* (1994) model's given in page 87.

where, M_o is the applied bending moment at the end of the plate. Here, $x_{trc,c}$ and $I_{trc,c}$ are the distance from the compression face to the natural axis and the second moment of area of the uncracked section transformed to concrete. The value σ_l is assumed as the concrete segment near the plate end has approximately no bending moment and the segment is uncracked. The authors assumed that failure takes place when the maximum principal stress (σ_1) exceeds the tensile strength of the concrete (f_{ct}), σ_1 is calculated according to the following equation:

$$\sigma_1 = \left[\frac{\sigma_l+\sigma(x)\big|_{x=0}}{2}+\sqrt{\left(\frac{\sigma_l-\sigma(x)\big|_{x=0}}{2}\right)^2+\tau(x)^2\bigg|_{x=0}}\right] \le f_{ct} \tag{I.2.30}$$

Equation I.2.30 is used to calculate the maximum shearing force causes delamination between concrete and adhesive $V_{del,end}$. The present authors adopted a trial and error procedure evolving iterating on a load until Equation I.2.30 is satisfied. Finally, the maximum shearing force that must be applied is taken equal to the minimum of ($V_{db,end}$ or $V_{del,end}$)

(a) weak adhesive   (b) Strong adhesive
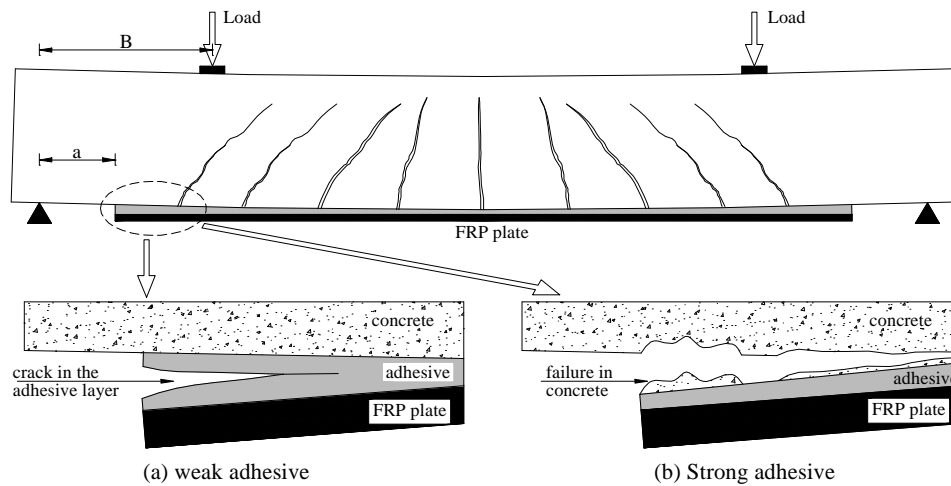
Figure I.2.33: Possible failures at plate end due to interfacial stress concentration.

Due to the complexity of all the calculation of the interfacial stress and the rare nature of the interfacial delamination failure at plate end, many design codes [e.g. Fib Bulletin 14 and Concrete Society TR 55] avoid such these calculations. It can be safely dimensioning the plate near the support by evaluating the position of un-cracked FRP strengthened RC section along the longitudinal direction of the beam, thus, the FRP plate must be extended after this position to a distance ($L_{act,FRP}$) greater than the effective bond length (L_e) of the soffit plate. L_e is taken according to the concept of bonded joint described previously. Different values of L_e are reported in Table I.2.1 for different design codes and previous publications.

I.2.4.2.5 FRP End-peeling due to shear crack.

It is worth mentioning that critical diagonal shear cracks are formed in RC beam as the applied shearing force reaches the shear capacity of the beam, thus, a rigid body displacement across the critical diagonal crack takes place. End peeling of FRP plate bonded to RC beam rarely takes place but it may occur at the intersection between shear crack and end of FRP plate bonded to the RC beam. This type of debonding is strongly related to the rigid body displacement across the critical diagonal crack caused by the lack of design of shear capacity of the beam. The formed vertical displacement causes debonding of plate by very rapid crack starting from the lower edge of the diagonal crack - point (B) - and propagates towards the end of the plate - point (C) - as seen in Figure I.2.34.

.
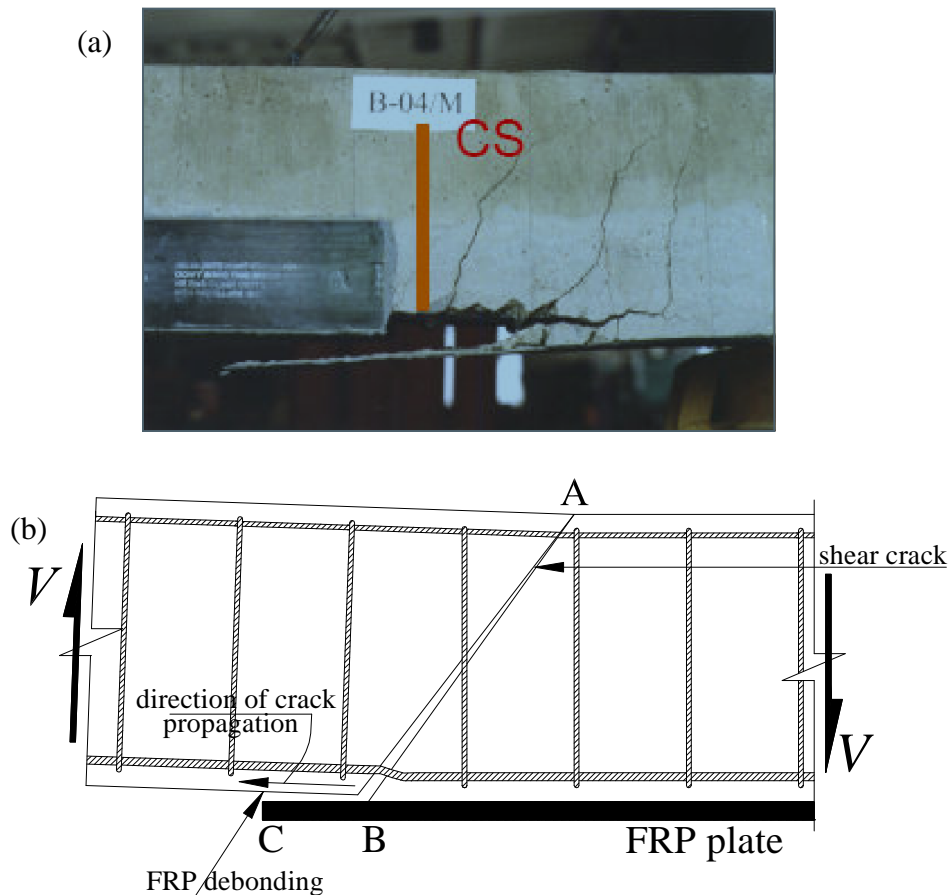
Figure I.2.34: Shear crack induced plate end peeling off [Ali *et al* 2005].

FRP end debonding based shear crack is based on the thickness of the FRP near the plate end, as the vertical displacement induces bending (or dowel action) of the plate. Since the dowel action is not very significant for thin sheets [Pham & Al-Mahaidi 2004]. Many analytical models were derived to safely prevent such this type of failure. The common feature of these models is that the debonding failure strength is assumed to be related to the shear strength of the concrete section, while steel shear reinforcement does not or partially contribute. Thus, the models assume that debonding may be totally eliminated by limiting the applied shearing force at the plate end to the end peeling shear strength ($V_{peel,end}$). Table I.2.8 presents a review of the analytical models reported in previous publications and design codes. These modes will be compared in chapter II.1, based on experimental results, in order to find the most accurate one which will be used in the reliability analysis, in terms of robustness.

.

Table I.2.8: End peeling (FRP end-debonding) based shear crack models.

Oehlers Model [Oehlers 1992; Oehlers & Moran 1996][1]

$$M_{db,f} = \frac{E_c I_{tr,c} f_{ct}}{0.901 E_{FRP} t_{FRP}}$$

$$V_{db,s} = V_c = [1.4 - d_s/2000] b_c d_s (\rho_s f_c')^{1/3}, \text{ where } 1.4 - d_s/2000 \geq 1.1$$

Based on test results, failure creation follows:

$$\frac{M_{db,end}}{M_{db,f}} + \frac{V_{db,end}}{V_{db,f}} \leq 1.17, \text{ and } M_{db,end} \leq M_{db,f}, V_{db,end} \leq V_{db,f}$$

Smith & Teng Model [Smith & Teng 2003]

failure creation follows:

$$0.4 \frac{M_{db,end}}{M_{db,f}} + \frac{V_{db,end}}{V_{db,f}} \leq 1 \quad \text{if} \quad V_{db,end} \leq 0.6 \geq V_{db,f}$$

$$\frac{M_{db,end}}{M_{db,f}} \leq 1 \qquad \qquad \text{if} \quad V_{db,end} < 0.6 V_{db,f}$$

Teng & Yao Model [Teng & Yao 2007]

$$M_{db,f} = \frac{0.488 M_{uc}}{(\alpha_{flex} \alpha_{axial} \alpha_w)^{1/9}} < M_{uc}$$

$$V_{db,s} = V_c + V_p + \varepsilon_{v,e} V_s,$$

failure creation follows:

$$\left(\frac{M_{db,end}}{M_{db,f}}\right)^2 + \left(\frac{V_{db,end}}{V_{db,f}}\right)^2 \leq 1$$

where,

$$\alpha_{flex} = \frac{E_c I_{trc,c} - E_c I_{trc,o}}{E_c I_{trc,o}}, \alpha_{axial} = \frac{E_{FRP} t_{FRP}}{E_c d_s}, \alpha_w = \frac{b_c}{b_{FRP}} \leq 3, V_s = \frac{A_{sv} f_{y,sv} d_s}{s_v}, \varepsilon_{v,e} = \frac{10}{(\alpha_{flex} \alpha_E \alpha_t \alpha_w)^{1/2}},$$

$$\alpha_E = E_{FRP}/Ec, \alpha_t = \sqrt[3]{t_{FRP}/d_s}$$

Jansze Model [Jansze1997][1]

failure creation is related to the critical shear force that causes debonding $V_{ds,end}$:

$$V_{db,end} = (\tau_{PES}) b_c d_s$$

where,

$$\tau_{PES} = 0.18 \sqrt[3]{3 \frac{d_s}{B_{mod}}} \left(1 + \sqrt{\frac{200}{d_s}}\right) \sqrt[3]{100 \rho_s f_c'},$$

$$B_{mod} = \sqrt[4]{\frac{(1 - \sqrt{\rho_s})^2}{\rho_s} d_s a}. \text{ If } B_{mod} > B \text{ of the beam then an average value of the modified shear span is}$$

assumed: $(B_{mod} + B)/2$

Ahmed & van Gemert Model [Ahmed & van Gemert 1999]

failure creation is related to the critical shear force that causes debonding $V_{ds,end}$:

$$V_{db,end} = (\tau_{PES} + \Delta \tau_{PES}) b_c d_s$$

where,

$$\Delta \tau_{PES} = \tau_{PES} b_c d_s \left(\frac{S_s}{I_s b_{FRP}} - \frac{S_{frp}}{I_{FRP} b_a}\right) + 6188.5 \left(\frac{\tau - 4.121}{b_c d_s}\right)$$

$$\tau = \left(0.15776 \sqrt{f_c'} + \frac{17.2366 \rho_s d_s}{B}\right) + 0.9 \frac{A_{sv} f_{y,sv}}{s_v b_c}$$

Blaschko *et al* (1998)

$$V_{db,end} = [1.6 - d_s/1000] b_c d_s (1.2 + 40 \rho_l) 0.18 (f_c')^{1/3}, \text{ where, } \rho_l = \frac{A_s + E_{FRP} t_{FRP} b_{FRP}/E_s}{b_c d_s}$$

Teng *et al* model [Teng *et al* 2002][2]

$$V_{db,end} = 1.4\left[1.4 - d_s / 2000\right]b_c d_s (\rho_s f_c')^{1/3}, \text{ where } 1.4 - d_s / 2000 \geq 1.1, \frac{M_{db,end}}{M_u} \leq 0.67$$

Sharma *et al* (2008)

$$V_{db,end} = \frac{M_u}{B + (h_c - c_{comp})\cot\alpha}$$

Where, $\cot\alpha =, \dfrac{B}{1-2h_c+c_{comp}} \pm \sqrt{\left(\dfrac{B}{1-2h_c+c_{comp}}\right)^2 - \dfrac{2s_v M_u}{P_{b,crit}(h_c - c_{comp})^2 (1-2h_c + c_{comp})}}$,

$$P_{b,crit} = \begin{cases} 1.277 L f_{ct} b_{FRP} & \text{if} \quad L/t_{FRP} < L_{b,crit}/t_{FRP} \\ 1.277 L_{b,crit} f_{ct} b_{FRP} & \text{if} \quad L/t_{FRP} \geq L_{b,crit}/t_{FRP} \end{cases}$$

$L_{b,crit}/t_{FRP}$, see Sharma *et al* model [Sharma *et al* 2008] in Table I.2.7

Colotti *et al* (2006)

$$V_{db,end} = b_c d_v \psi_i \left[\phi + \alpha - \sqrt{(\phi+\alpha)^2 - 2\phi\beta} \right]$$

where, $d_v = 0.9 d_s$, $\alpha = B/d_v$, $\beta = (B-a)/d_v$, $\phi = U_y / p_i$, $U_y = \min(b_m \tau_u; f_{ct} l_c b_c / 5 d_{sc})$,

$b_m = 0.5(b_{FRP} + b_c)$, $\tau_u = 2.77 + 0.06(f_c' - 20)$, $\psi_i = \dfrac{A_{sv} f_{yv}}{s_v}$, $l_c = 50 + 0.25 k_1 k_2 \phi_l / \rho_r$,

$\rho_r = \dfrac{A_s}{2.5 b_c (h_c - d_s)}$, k_1=0.8, k_2=0.5, ϕ_l is the diameter of the longitudinal bar.

$I_{trc,c}$ is cracked second moment area of the plated section transformed to concrete. $\rho_s = A_s / b_c d_s$ is tensile steel ratio. $M_{db,end}$ and $V_{db,end}$ are applied bending moment and shearing force at the plate end. M_{uc} is the unplated concrete section ultimate moment. $I_{trc,o}$ is the cracked second moment area of the RC section transformed to concrete. V_c, V_p, and $\varepsilon_{v,e} V_s$ are the contributions of concrete, soffit plate and shear reinforcement to the beam's shear capacity, respectively. A_s is the tension steel reinforcement area, A_{sv}, s_v, $f_{y,sv}$ are the total cross sectional area, the longitudinal spacing and yield stress of the stirrups, respectively. d_s is the depth of the steel reinforcements. S_{FRP} and S_s are the first moment of area of the FRP plate and that of equivalent steel plate about the neutral axis for the cracked plated transformed to concrete; the equivalent steel plate is one that has same total tensile capacity and width as that of the FRP plate, but with an equivalent thickness assuming that the yield stress is 550 MPa. I_{FRP} and I_s are the second moment of area of cracked plated section transformed to concrete with an FRP plate and an equivalent steel plate respectively. b_{FRP} and b_a are the widths of the FRP and adhesive respectively. b_c is the width of RC beam. B is the shear span of the beam. M_u if the bending moment capacity of strengthened cross section. c_{comp} depth of neutral axis at ultimate stage (see Figure I.2.22)
[1] Cited in [Smith & Teng 2002[a]]. [2] Cited in [Aram *et al* 2008]

I.2.4.2.6 Concrete cover separation

In the last two sections, the conventional debonding of plate-end and their previously proposed models were discussed. The significant characteristic of these failure modes are that there is only a very thin layer of concrete attached on the debonded FRP strips and the concrete cover stays essentially intact in the vicinity of the FRP plate. Beside these conventional failure modes, concrete cover separation is frequently observed in experimental studies of FRP strengthened RC beams as shown in Figure I.2.35. In many investigations [Smith & Teng 2002[b]], it is suggested that failure of concrete cover is initiated by the formation of a crack at the end of the FRP plate due a high stress concentration caused by the abrupt termination of the FRP plate. The crack propagates at the level of the tension

reinforcement and then progresses horizontally along the level of the steel reinforcement, thus resulting in the separation of concrete cover.

Figure I.2.35: FRP-plated RC beam: cover separation failure mode [Teng & Chen 2007].

In an effort to identify the load capacity of a strengthened RC beam with this failure mode, many studies have been carried out and many models have been proposed. In these models, failure is strongly related to the flexural crack spacing formed in the concrete cover [Smith & Teng 2002[a]; Gao *et al* 2005; Aprile & Feo 2007]. Concrete teeth between adjacent cracks form a system which resists to the interfacial shear stresses induced between plate and concrete surface as shown in Figure I.2.36. These teeth behave as cantilever under the action of horizontal shear stresses at the base of the beam. Shear stresses lead to tensile stresses at the roots – point (A) - of the teeth that exceed the tensile strength of the concrete, thus failure occurs at the steel-concrete cover interface. Table I.2.9 presents the existing models developed to express the concrete cover separation failure mode. These modes will be compared in chapter II.1, based on experimental results, in order to find the most accurate one which will be used in the reliability analysis, in terms of robustness.
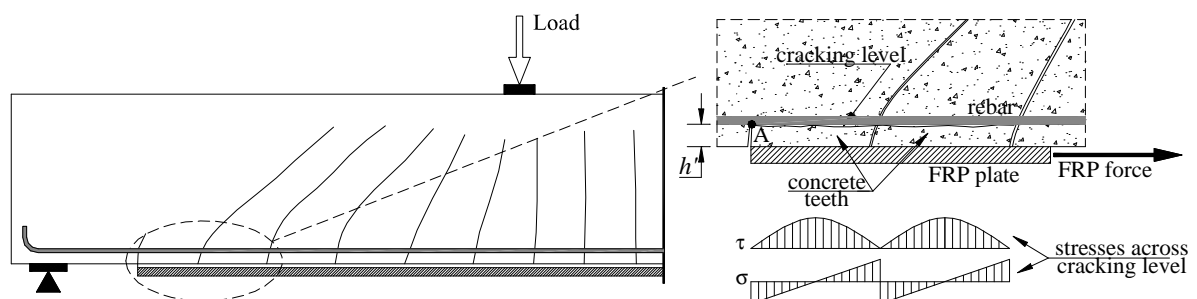

Figure I.2.36: Concrete cover separation failure mode.

Table I.2.9: Concrete cover separation models.

Ziraba *et al* model [Ziraba *et al* 1994]
Shear force causes concrete cover separation:

$$V_{db,end} = V_c + kV_s$$

where,

$$V_c = 0.1667(\sqrt{f_c'} + 100\rho_s)b_c d_s \,,\; V_s = \frac{A_{sv}f_{y,sv}d_s}{s_v}\,,\; k = 2.4e^n\,,\; n = -0.08 \times 10^6 C_{R1}C_{R2}\,,$$

$$C_{R1} = \left[1 + \left(\frac{K_s}{E_{FRP}b_{FRP}t_{FRP}}\right)^{1/2}\frac{M_o}{V_o}\right]\frac{b_{FRP}t_{FRP}}{I_{trc,FRP}b_a}\left(d_{FRP} - x_{trc,FRP}\right), C_{R2} = t_{FRP}\left(\frac{K_n}{4E_{FRP}I_{FRP}}\right)^{1/4}\,,$$

$$K_s = \frac{E_a b_a}{t_a}\;\; K_n = \frac{G_a b_a}{t_a}$$

Raoof & Zhang Model [Raoof & Zhang 1996; Zhang *et al*.1995; Raoof & Zhang 1997][1]

The minimum stress in the soffit plate $\sigma_{s,min}$ required to cause flexural cracking and failure of the cover teeth:

$$\sigma_{s,min} = \tau_{min}L_P / t_{FRP}$$

$$\tau_{min} = \frac{f_{ct}L_{min}b_c}{6h'b_{FRP}}$$

L_P is the min(L_{P1},L_{P2}). L_{P1}; the length of the soffit plate in the shear spans of the beam as indicated in figure 2.15

$$L_{P2};\begin{cases} l_{min}(21 - 0.25l_{min}) & \text{for } l_{min} \le 72mm \\ 3l_{min} & \text{for } l_{min} > 72mm \end{cases}\,,\; l_{min} = \frac{A_e f_{ct}}{u(\sum O_{bars} + b_{FRP})}\,,\; f_{ct} = 0.36\sqrt{f_{cu}}\,,\; u = 0.28\sqrt{f_{cu}}$$

Wang & Ling Model [Wang & Ling 1998][1]

The minimum stress in the soffit plate $\sigma_{s,min}$ required to cause flexural cracking and failure of the cover teeth:

$$\sigma_{s,min} = \tau_{min}L_P / t_{FRP}$$

$$\tau_{min} = \frac{f_{ct}L_{min}b_c}{6h'b_{FRP}}$$

L_P is the min(L_{P1},L_{P2}). L_{P1}; the length of the soffit plate in the shear spans of the beam as indicated in figure 2.15

$$L_{P2};\begin{cases} l_{min}(21 - 0.25l_{min}) & \text{for } l_{min} \le 72mm \\ 3l_{min} & \text{for } l_{min} > 72mm \end{cases}\,,\; l_{min} = \frac{A_e f_{ct}}{u_s \sum O_{bars} + u_{FRP}b_{FRP}}\,,\; f_{ct} = 0.36\sqrt{f_{cu}}$$

$$u_s = 0.313\sqrt{f_c'}\,,\; u_{FRP} = 1.96\text{ MPa.}$$

Raoof & Hassanen Model [Raoof & Hassanen 2000][1]

Model I (upper pound model):

The minimum stress in the soffit plate $\sigma_{s,min}$ required to cause flexural cracking and failure of the cover teeth:

$$\sigma_{s,minu} = \tau_{minu}L_{P,u} / t_{FRP}$$

$$\tau_{minu} = \frac{f_{ct}L_{minu}b_c}{6h'b_{FRP}}$$

$L_{P,u}$ is the min($L_{P1},L_{P2,u}$). L_{P1}; the length of the soffit plate in the shear span of the beam, indicated in figure 2.15

$$L_{P2,u};\begin{cases} l_{min}(24 - 0.5l_{min}) & \text{for } l_{min} \le 40mm \\ 4l_{min} & \text{for } l_{min} > 40mm \end{cases}\,,\; l_{min,u} = \frac{A_e f_{ct}}{u(\sum O_{bars} + b_{FRP})}\,,\; f_{ct} = 0.36\sqrt{f_{cu}}\,,\; u = 0.28\sqrt{f_{cu}}$$

Model II (lower pound model):

The minimum stress in the soffit plate $\sigma_{s,min}$ required to cause flexural cracking and failure of the cover teeth:

$$\sigma_{s,minl} = \tau_{minl}L_{P,l} / t_{FRP}$$

$$\tau_{min,l} = \frac{f_{ct}L_{min,l}b_c}{6h'b_{FRP}}$$

$L_{P,l}$ is the min($L_{P1},L_{P2,l}$). L_{P1}; the length of the soffit plate in the shear span of the beam, indicated in figure 2.15

$$L_{P2,l};\begin{cases} l_{min}(11.6 - 0.17l_{min}) & \text{for } l_{min} \le 56.5mm \\ 2l_{min} & \text{for } l_{min} > 56.5mm \end{cases}\,,\; l_{min,l} = \frac{A_e f_{ct}}{u_s \sum O_{bars} + u_{FRP}b_{FRP}}\,,\; f_{ct} = 0.36\sqrt{f_{cu}}\,,$$

$u_s = 0.28\sqrt{f_{cu}}$, u_{FRP}=0.8 MPa.

Aprile & Feo model [Aprile & Feo 2007]
The mean crack spacing:

$$L_{cmt} = L_{cm}/\sin\theta$$

where,

$$L_{cm} = 1.7\left[2h^{'} + 0.2\frac{h_c - x_{trc,FRP}}{0.25h^{'}}\frac{\Phi_s}{\rho_{s,eff}\,\omega}\right], \quad \omega = \frac{n_s\rho_{s,eff} + n_f\rho_{f,eff}}{n_s\rho_{s,eff}}, \quad \theta = \arctan\sqrt{\frac{\psi + \dfrac{p}{f_{cm}}}{1 - \left(\psi + \dfrac{p}{f_{cm}}\right)}} \leq 45^o$$

$$\psi = \rho_{sv}\frac{f_{ym}}{f_{cm}}, \quad \rho_{sv} = \frac{A_{sv}}{b_c s_v}.$$

Maximum applied stress at the end of the plate causes rip-off the concrete cover:

$$\sigma_{f,\max} = \frac{f_{ctm}b_c L_{cmt}^2}{6h^{'}b_{FRP}t_{FRP}}$$

V_c, V_p, and V_s are the contributions of concrete, soffit plate and shear reinforcement to the beam's shear capacity respectively. A_s is the tension steel reinforcement area, A_{sv}, s_v, $f_{y,sv}$ are the total cross sectional area, the longitudinal spacing and yield stress of the stirrups, respectively. M_o and V_o are applied bending moment and shearing force at the plate end. A_e is twice the distance from the centroid of the tension reinforcement to the base of RC beams multiplied by the width of the RC beam. ΣO_{bars} is the total perimeter of the tension reinforcing bars. h' is the net area of the height of the concrete cover measured from the base of the reinforcement to the base of the RC beam. l_{min} is the stabilized crack spacing in RC beam. f_{cu} is the concrete cube compressive strength; $0.8f'_c$. $I_{trc,FRP}$: is cracked second moment area of the plated section transformed to concrete. $x_{trc,FRP}$ is the neural axis depth of the plated beam transformed to concrete. h_c is the total depth of the concrete section. d_{FRP} is the distance for the compression face in the plated beam to the centroid the FRP plate. Φ_s is the longitudinal steel rebar diameter. $\rho_{s,eff}$ is the steel reinforcement ratio to the effective area of the concrete in tension ($\rho_{s,eff}=A_s/2b_c h'$). $\rho_{f,eff}$ is the FRP reinforcement ratio to the effective area of the concrete in tension ($\rho_{f,eff}=b_{FRP}t_{FRP}/2b_c h'$). d_s is the depth of the steel reinforcements. I_{FRP} and I_s are the second moment of area of cracked plated section transformed to concrete with an FRP plate and an equivalent steel plate respectively. b_{FRP} is the width of the FRP. b_c is the width of RC beam. B is the shear span of the beam. n_s and n_f are the steel and composite homogenization factors. p is the maximum compression stress of the concrete section due to bending. f_{ym} and f_{cm} are the mean yield stress of steel and the compressive stress of concrete respectively. f_{ctm} is the mean tensile strength of the concrete.
[1] Cited in [Smith & Teng 2002a].

I.2.4.3 Shear strength of FRP strengthened RC girder

Since 1990s, tests on a wide variety of shear strengthening schemes have been undertaken with the goal to increase shear capacity of RC beams. Shear is actually a very complex problem and is not completely solved for simple RC beams. However, to find a reasonable method to estimate the contribution of externally bonded FRP in shear is not an easy task. Several researchers have published design equations and analytical models to specifically evaluate FRP shear strengthening of RC beams. In all these models, the shear strength V of a FRP-strengthened RC beam is evaluated by assuming that the contribution of concrete V_c, internal steel stirrups V_s and the contribution of external FRP strips/sheets V_f are additive so that the design equation can be written as follow:

$$V = V_c + V_s + V_{FRP} < 0.66\sqrt{f'_c}\,b_c d_s \qquad (I.2.31)$$

Steel and concrete contributions were calculated according to the ACI code as given by

Equations I.2.32 and I.2.33.

$$V_c = 0.17 b_c d_d \sqrt{f_c} \qquad (I.2.32)$$

$$V_s = \frac{A_{sv} f_{yv} d_s}{s_s} \qquad (I.2.33)$$

where, A_{sv}, s_s, and f_{yv} are area, spacing and yield strength of internal shear reinforcements. The common methods of shear strengthening using FRP composites include: side bonding, U-jacketing and wrapping. Both FRP strips and continuous sheets along the axis of beam, FRP strips/sheets may also be oriented at different angles (β) as seen in Figure I.2.37.

Available experimental data indicate that almost all beams strengthened by wrapping failed due to FRP rupture (although debonding most likely occurs first, FRP rupture controls the shear capacity in this case). Some beams strengthened by U-jacketing also failed in this mode. In contrast, almost all beams strengthened by side bonding only and most strengthened by U-jacketing failed due to FRP debonding. The developments of practical and reliable design equations for the shear strengthening of RC members through FRP are still hindered by three aspects that still remain not perfectly understood. The first aspect regards the shear resisting mechanism that develops when FRP strips/sheets are side bonded to the elements, rather than U-jacketing or fully wrapped around. The second aspect regards the correct evaluation of the FRP transverse strengthening contribution to the total shear capacity. The third aspect regards the evaluation of the relative contributions to the shear capacity of concrete, steel stirrups and FRP at ultimate.

Different assumptions were used on the existing proposed models to calculate the FRP contribution. Such these assumptions are:

- Failure may take place due to FRP rupture or debonding.

- FRP composite and the stirrups behave similarly.

- Based on experimental fitting, shear contribution of the FRP is limited by the effective strain/stress in the composite – a reduction factor for the effective stress/strain is used in some models.

- Considering strain limitations due to shear crack opening and loss of aggregate interlock.

- Analyzing the stress distribution in the FRP along the shear crack.

- Distribution of forces in FRP strengthened RC beam follows the truss model concept.

Table I.2.6 presents an overview of the existing theoretical models to predict the contribution of FRP strips/sheets shear capacity. These modes will be compared in chapter

II.1, based on experimental results, in order to find the most accurate one which will be used in the reliability analysis, in terms of robustness.
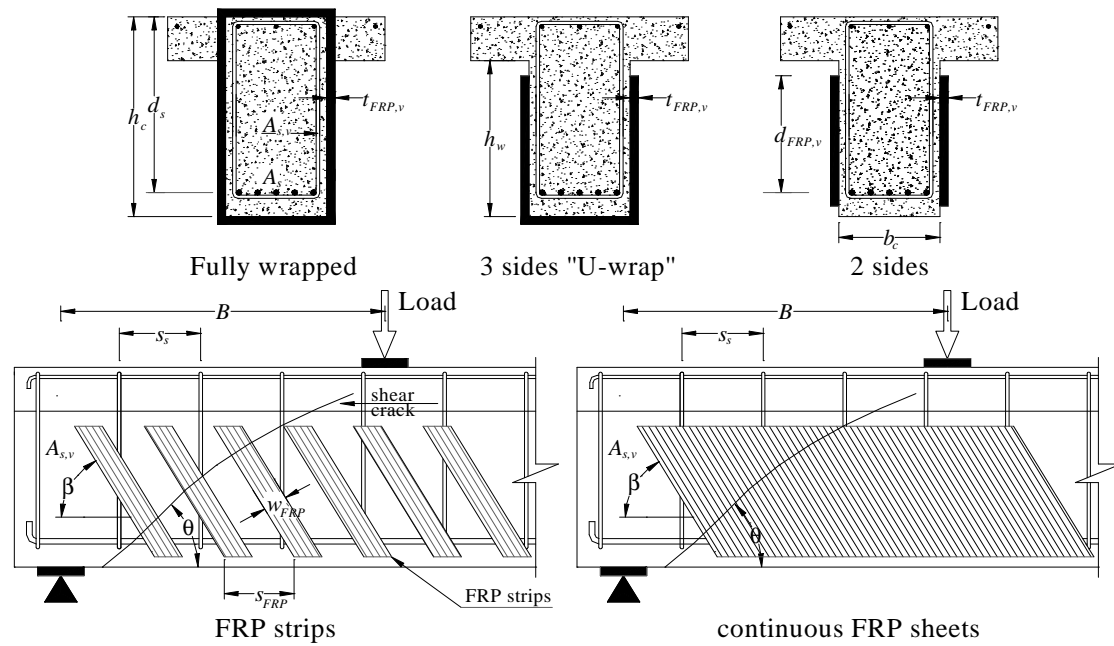
Figure I.2.37: Typical wrapping schemes and dimensional variables for shear strengthening.

Table I.2.10: Existing shear capacity models of FRP strengthened RC beam.

Chaallal *et al* models [Chaallal *et al* 1998]

$$V_{FRP} = 2\tau_{avg}\left(\frac{w_{FRP}h_{FRP,v}}{2}\right)\frac{(\sin\beta + \cos\beta)}{s_{FRP}}d_s$$

where,

$$\tau_{avg} = \frac{2.7}{1+k_1\tan 33^o}, \quad k_1 = t_{FRP,v}\left[\frac{k_n}{4E_{FRP,v}I_{FRP,v}}\right]^{1/4}, \quad k_n = E_d b_a / t_a$$

Triantafillou &Antonopoulos model [Triantafillou & Antonopoulos 2000]

$$V_{FRP} = \varepsilon_{FRP,e}E_{FRP}\rho_{FRP,v}b_c d_s(\sin\beta + \cos\beta) \text{ under the constraints } V = V_c + V_s + V_{FRP} < 0.66v_{co}f_c'b_c d_s$$

where,

$$\varepsilon_{FRP,e} = \begin{cases} 0.17\,\varepsilon_{FRP,uv}\left(\dfrac{f_c^{2/3}}{E_{FRP,v}\rho_{FRP,v}}\right)^{0.3} & \text{for fully wrapped scheme} \\[3mm] \min\left\{65x10^{-5}\left(\dfrac{f_c^{2/3}}{E_{FRP,v}\rho_{FRP,v}}\right)^{0.56}, \ 0.17\,\varepsilon_{FRP,uv}\left(\dfrac{f_c^{2/3}}{E_{FRP}\rho_{FRP,v}}\right)^{0.3}\right\} & \text{for sides and U - jacket} \\[3mm] 0.48\varepsilon_{FRP,uv}\left(\dfrac{f_c^{2/3}}{E_{FRP,v}\rho_{FRP,v}}\right)^{0.48} & \text{for anchorage wrapped scheme} \end{cases}$$

E_{FRP} is the modulus in GPa. $f_c = v_{ca}f_c'$. $v_{co} = 0.7 - f_c'/200 \geq 0.5$

Matthys & Triantafillou model [Matthys & Triantafillou 2000]

$$V_{FRP} = \varepsilon_{FRP,e}E_{FRP,v}\rho_{FRP,v}b_c d_s(\sin\beta + \cos\beta)$$

where,

$$\varepsilon_{FRP,e} = \begin{cases} 0.72\varepsilon_{FRP,uv}e^{-0.0431\Gamma f} & \text{for beams fully wrapped with CFRP} \\ 0.56\varepsilon_{FRP,uv}e^{-0.0455\Gamma f} & \text{for 2 or 3 sides laminated with CFRP} \end{cases}, \quad \Gamma_f = \frac{E_{FRP,v}\rho_{FRP,v}}{f_c^{2/3}(B/d_s)}$$

$f_c = v_{ca}f_c'$. $v_{co} = 0.7 - f_c'/200 \geq 0.5$

Khalifa & Nanni model [Khalifa & Nanni 2000]

$$V_{FRP} = \frac{w_{FRP}t_{FRP,v}f_{f,e}(\sin\beta + \cos\beta)d_{FRP,v}}{s_{FRP}}$$

where,

$$f_{f,e} = Rf_{FRP,uv}$$

R is a reduction factor depending on the governing failure mode; either mode I which represents FRP rupture or Mode II which represents FRP debonding.

$$R = \begin{cases} 0.5622\left(\rho_{FRP,v},E_{FRP,v}\right)^2 - 1.2188\left(\rho_{FRP,v},E_{FRP,v}\right) + 0.778 & \text{for mode I} \\[3mm] \dfrac{f_c^{,2/3}w_{f,e}}{\varepsilon_{FRP,u}}\left[738.93 - 4.06(E_{FRP}t_{FRP})\right]x10^{-6} & \text{for mode II} \end{cases} \leq \frac{0.006}{\varepsilon_{FRP,uv}}$$

$$w_{f,e} = \begin{cases} d_{FRP,v} - L_e & \text{for U- wrapped scheme} \\ d_{FRP,v} - 2L_e & \text{for side scheme} \end{cases}, \quad L_e = \min\{6.134 - 0.58\ln(t_{FRP,v}E_{FRP,v}) \text{ or } 75mm$$

Chen & Teng model [Chen & Teng 2003; Lu *et al* 2008]

$$V_{FRP} = 2f_{f,e}h_{FRP,e}t_{FRP,v}w_{FRP}\frac{(\cot\theta + \cot\beta)\sin\beta}{s_{FRP}}$$

where,

$h_{FRP,e} = z_b - z_t$, $z_t = d_{FRP,t}$, $z_b = 0.9d_s - (h_c - d_{FRP})$, $f_{FRP,e} = D_{FRP}\sigma_{FRP,\max}$, $\sigma_{FRP,\max} = \min\begin{cases} f_{FRP,uv} \\[3mm] 0.427\beta_w\beta_L\sqrt{\dfrac{E_{FRP,v}\sqrt{f_c'}}{t_{FRP,v}}} \end{cases}$

$$D_{FRP} = \begin{cases} \dfrac{2}{\pi\lambda}\dfrac{1-\cos\dfrac{\pi\lambda}{2}}{\sin\dfrac{\pi\lambda}{2}} & \text{if } \lambda \geq 1 \\[4mm] 1-\dfrac{\pi-2}{\pi\lambda}\sin\dfrac{\pi\lambda}{2} & \text{if } \lambda < 1 \end{cases}, \beta_w = \sqrt{\dfrac{2-w_{FRP}/(s_{FRP}/\sin\beta)}{1+w_{FRP}/(s_{FRP}/\sin\beta)}}, \beta_L = \begin{cases} 1 & \text{if } \lambda \geq 1 \\[2mm] \sin\dfrac{\pi\lambda}{2} & \text{if } \lambda < 1 \end{cases}, \lambda = \dfrac{L_{\max}}{L_e},$$

$$L_e = \sqrt{\dfrac{E_{FRP,v}t_{FRP,v}}{\sqrt{f_c'}}}, L_{\max} = \begin{cases} \dfrac{h_{FRP,e}}{\sin\beta} & \text{for U jackets} \\[4mm] \dfrac{h_{FRP,e}}{2\sin\beta} & \text{for side plates} \end{cases}.$$
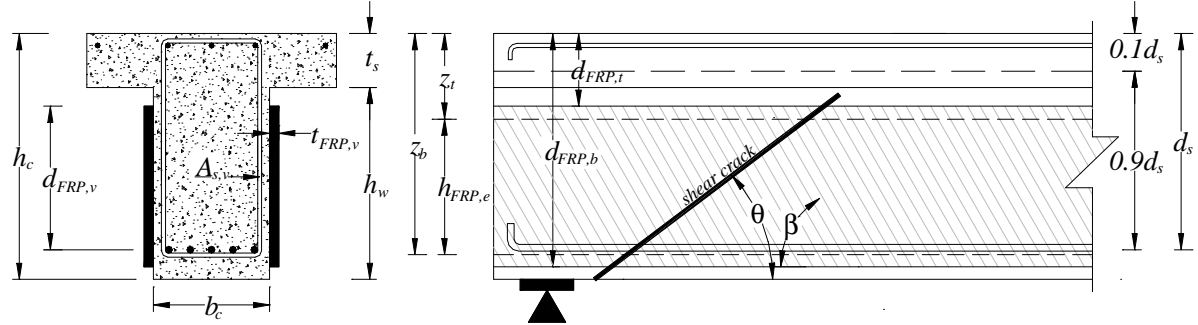
z_b and z_t are the co-ordinates of the top and bottom end of the effective FRP composites. $d_{FRP,t}$ and $d_{FRP,b}$ are the distances from the compression face of the beam to upper and the lower edges of FRP composite respectively.

Ye *et al* model [Ye *et al* 2005].

$$V_{FRP} = K_{FRP}\tau h^2_{FRP,e} w_{FRP}\dfrac{(\sin\beta+\cos\beta)}{s_{FRP}}$$

where,

$$K_{FRP} = \varphi_{FRP}\dfrac{\sin\beta\sqrt{E_{FRP,v}t_{FRP,v}}}{\sin\beta\sqrt{E_{FRP,v}t_{FRP,v}}+0.3f_{ct}h_{FRP,e}}, \quad \varphi_{FRP} = \begin{cases} 1.3 & \text{for U jackets} \\ 1.0 & \text{for side plates} \end{cases}, \quad \tau=1.2\beta_w f_{ct}$$

$$\varepsilon_{f,e} = \varepsilon_{f,\inf}\begin{cases} 0.96(1\text{-}e^{-\lambda/0.79}) & \text{for U jackets} \\ 0.77(1\text{-}e^{-\lambda/0.62}) & \text{for side plates} \end{cases}, \quad \lambda = \dfrac{h_{FRP,e}}{2L_e\sin\beta}, \quad L_e = 1.33\dfrac{\sqrt{E_{FRP}t_{FRP,v}}}{f_{ct}},$$

$$\varepsilon_{f,\inf} = \beta_w\sqrt{\dfrac{0.616\sqrt{f_{ct}}}{E_{FRP,v}t_{FRP,v}}}, \quad \beta_w = \sqrt{\dfrac{2.25-w_{FRP}/(s_{FRP}/\sin\beta)}{1.25+w_{FRP}/(s_{FRP}/\sin\beta)}}$$

$h_{FRP,v}$ is taken according to [Chen & Teng 2003; Lu *et al* 2008]

ACI committee 440 model

$$V_{FRP} = 2\varepsilon_{FRP,e}E_{FRP,v}h_{FRP,e}t_{FRP,v}w_{FRP}\dfrac{(\sin\beta+\cos\beta)}{s_{FRP}}$$

where,

$$\varepsilon_{FRP,e} = \begin{cases} 0.004 \leq 0.75\varepsilon_{FRP,uv} & \text{for fully wrapped member} \\ k_v\varepsilon_{FRP,uv} \leq 0.004 & \text{for U-wraps or sides} \end{cases}, \quad k_v = \dfrac{k_1k_2L_e}{11.9\varepsilon_{FRP,uv}} \leq 0.75$$

$$L_e = \dfrac{23{,}300}{\left(E_{FRP,v}t_{FRP,v}\right)^2}, \quad k_1 = \left(\dfrac{f_c'}{27}\right)^{2/3}, \quad k_2 = \begin{cases} \dfrac{d_{FRP,v}-L_e}{d_{FRP,v}} & \text{for U jackets} \\[4mm] \dfrac{d_{FRP,v}-2L_e}{d_{FRP,v}} & \text{for side plates} \end{cases}$$

Carolin & Täljsten model [Carolin & Täljsten 2005]

$$V_{FRP} = \eta\varepsilon_{cr}E_{FRP,v}t_{FRP,v}r_{FRP}z\dfrac{\cos\alpha}{\sin\theta}$$

where,

$$\alpha = \theta + \beta - 90, \; \varepsilon_{cr} = \min \begin{cases} \varepsilon_{FRP,uv} \\ \varepsilon_{c,max}\sin^2(\alpha+\beta), \\ \varepsilon_{bond}\sin^2(\alpha+\beta) \end{cases} r_{FRP} = \begin{cases} \sin\beta & \text{for continuous wrapping} \\ \dfrac{w_{FRP}}{s_{FRP}} & \text{for discrete strips} \end{cases}$$

$$\varepsilon_{bond} = \frac{1}{t_{FRP,v}E_{FRP,v}}\sqrt{2t_{FRP,v}E_{FRP,v}G_f}\begin{cases}\sin(\omega L_{cr}) & \text{if } L \le L_{cr} \\ 1 & \text{if } L \le L_{cr}\end{cases}, \; L_{cr} \le \frac{\pi}{2\omega}, \; \omega = \sqrt{\frac{\tau_{max}^2}{2t_{FRP,v}E_{FRP,v}G_f}},$$

$$\tau_{max} = 3.5 f_c^{'0.19}, \; G_f = 0.644 f_c^{'0.19}$$
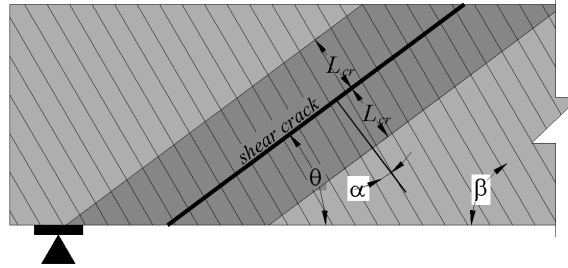
Failure angle θ is 45° and uniform distribution for the strain across the section is assumed, thus factor equal $\eta=1$. $\varepsilon_{c,max}$ is the maximum allowable strain to achieve concrete contribution, $\varepsilon_{c,max}$, e.g. concrete contribution due to aggregate interlocking. If the concrete contribution is not included in the shear bearing capacity the limiting parameter $\varepsilon_{c,max}$ can be ignored. L is the available bond length.

Monti & Liotta model [Monti & Liotta 2007]

$$V_{FRP} = \begin{cases} 0.9d_s f_{fed}\, 2t_{FRP,v}(\cot\theta+\cot\beta)\dfrac{w_{FRP}}{p_{FRP}} & \text{U or fully wrapped} \\[3mm] \min(0.9d_s,h_w)f_{fed}\,2t_{FRP,v}\dfrac{\sin\beta}{\sin\theta}\dfrac{w_{FRP}}{p_{FRP}} & \text{side scheme} \end{cases}$$

where,

$$L_e = \sqrt{\frac{E_{FRP,v}t_{FRP,v}}{2f_{ct}}}, \; f_{fdd} = 0.8\sqrt{\frac{2E_{FRP,v}\Gamma_{EK}}{t_{FRP,v}}}, \; \Gamma_{EK} = 0.03k_b\sqrt{f_c' f_{ct}}, \; k_b = \sqrt{\frac{2-(w_{FRP}/s_{FRP})}{1+(w_{FRP}/400)}} \ge 1$$

$$f_{fdd}(l_b) = \begin{cases} f_{fdd} & \text{if } l_b \ge l_e \\ f_{fdd}\dfrac{l_b}{l_e}\left(2-\dfrac{l_b}{l_e}\right) & \text{if } l_b < l_e \end{cases} \quad f_{f,u}(l_b,\delta_e,r_c) = \begin{cases} f_{fdd} + \left\langle \phi_R f_{FRP,uv} - f_{fdd}\right\rangle & \text{if } l_b \ge l_e \\ f_{fdd}(l_b) + \left\langle \phi_R f_{FRP,uv} - f_{fdd}(l_b)\right\rangle\delta_e & \text{if } l_b < l_e \end{cases},$$

$$\delta_e = \begin{cases} 0 & \text{free end} \\ 1 & \text{end around a corner} \end{cases}, \quad \phi_R = 0.2 + 1.6\frac{r_c}{b_c}, \; \text{with; } 0 \le rc/bw \le 0.5$$

$$f_{fed} = \begin{cases} f_{fdd}(l_b)\dfrac{z_{rid,eq}}{\min\{0.9d_s,h_c\}}\left(1+0.6\sqrt{\dfrac{l_{eq}}{z_{rid,eq}}}\right)^2 & \text{for S wrapped strips} \\[3mm] f_{fdd}(l_b)\left[1-\dfrac{1}{3}\dfrac{l_e\sin\beta}{\min\{0.9d_s,h_c\}}\right] & \text{for U wrapped strips} \\[3mm] f_{fdd}(l_b)\left[1-\dfrac{1}{6}\dfrac{l_e\sin\beta}{\min\{0.9d_s,h_c\}}\right] + \dfrac{1}{2}(\phi_R f_{FRP,d}-f_{fdd}(l_b))\left[1-\dfrac{l_e\sin\beta}{\min\{0.9d_s,h_c\}}\right] & \text{for U wrapped strips} \end{cases}$$

$$z_{rid,eq} = \min(0.9d_s,h_c) - \left(l_e - \frac{s_{FRP}}{f_{fdd}(l_b)/E_{FRP,v}}\right)\sin\beta$$

$f_{FRP,d}$ is the design ultimate strength of the FRP. ϕ_R is a factor considering the corner effect in case of U-jacket or fully wrapped laminates. r_c is the corner rounding radius. l_b is the available bond length. $\langle.\rangle$ denotes that the bracketed expression is zero if negative.

Aprile & Benedetti model [Aprile & Benedetti 2004]

$$V = \min\{V_v + V_l + V_d\} + V_c$$

$$V_v = \frac{z}{\tan\theta}\left(\frac{A_{sv}f_{y,v}}{s_s} + \frac{2w_{FRP}t_{FRP,v}f_{FRP,uv}}{s_{FRP}}\right), V_l = \frac{A_s f_y + b_{FRP}t_{FRP}f_{FRP,u}}{\dfrac{1}{\tan\theta} + \dfrac{B}{z}}, V_d = \frac{0.6f_c'b_c z}{\tan\theta + \cot\theta}$$

$$\theta = \arctan\sqrt[4]{\frac{1 + \dfrac{1}{n_s\rho_s + n_{FRP}\rho_{FRP}}}{1 + \dfrac{1}{n_{sv}\rho_{sv} + n_{FRP,v}\rho_{FRP,v}}}}$$

Failure angle θ ranges between 30° to 60°.

Colotti & Spadea model [Colotti & Spadea 2011]

$$V_{FRP} = 2t_{FRP,v}w_{FRP}\Delta f_{fed}\frac{(\sin\beta + \cos\beta)}{s_{FRP}}$$

where,

$$f_{fed} = \begin{cases} \min(D_{fb}\sigma_{f,\max}, 0.625f_{FRP,uv}) & \text{for side plqtes or U- jackets} \\ 0.625f_{FRP,uv} & \text{for complete wrapping} \end{cases}$$

$$\Delta = 0.9d_s\cot\theta, \qquad \sigma_{f,\max} = 1.014\beta_L\beta_w\sqrt{\frac{E_{FRP,v}f_c'^{0.236}}{t_{FRP,v}}} \le f_{FRP,v}, \qquad \beta_L = \begin{cases} 0.96 & \text{if } \lambda \ge 1 \\ \lambda(1.92 - 0.96\lambda) & \text{if } \lambda \ge 1 \end{cases},$$

$$\beta_w = \begin{cases} 1 & \text{if } s_{FRP} < w_{FRP} + 7.4 \\ 1 + \dfrac{7.4}{w_{FRP}} & \text{if } s_{FRP} \ge w_{FRP} + 7.4 \end{cases}, \lambda = \frac{L_{\max}}{L_e}, \quad L_{\max} = \begin{cases} h_{FRP,v} & \text{for U- jackets} \\ \dfrac{h_{FRP,v}}{2} & \text{for side plates} \end{cases}, \quad L_e = \sqrt{\frac{E_{FRP,v}t_{FRP,v}}{f_c'^{0.236}}},$$

$$D_{fb} = \begin{cases} \dfrac{0.654 + 0.965(\lambda - 1)}{0.96\lambda} & \text{if } \lambda \ge 1 \\ 0.1812\lambda + 0.4 & \text{if } \lambda < 1 \end{cases}$$

General notations:

$$\rho_s = \frac{A_s}{b_c z} \;;\; \rho_{s,v} = \frac{A_{sv}}{b_c s_s} \;;\; \rho_{FRP} = \frac{b_{FRP}t_{FRP}}{b_c z} \;;\; \rho_{FRP,v} = \frac{2w_{FRP}t_{FRP,v}}{b_c s_{FRP}}$$

A_s	Area of the longitudinal steel.
A_{sv}	Area of the steel stirrups.
f_y	Yield strength of the longitudinal steel.
$f_{y,v}$	Yield strength of the steel stirrups
$I_{FRP,v}$	Moment of inertia of the FRP plate used for shear strengthening.
$h_{FRP,v}$	Total height of FRP strip used for shear strengthening.
$d_{FRP,v}$	Effective depth of shear FRP; $= d_s$ for rectangular section, $= d_s$-slab thickness for T section)
$E_{FRP,v}$	Young's modulus of the FRP used for shear strengthening.
$f_{FRP,uv}$	Ultimate strength of FRP composite used for shear strengthening.
$f_{FRP,u}$	Ultimate strength of FRP composite used for flexural strengthening.
$\varepsilon_{FRP,uv}$	Ultimate strain of FRP composite used for shear strengthening.
w_{FRP}	Width of the FRP strips.
s_{FRP}	Spacing between FRP strips.
s_s	Spacing between steel stirrups.
$t_{FRP,v}$	Thickness of the FRP strips.
β	Inclination angle of the FRP strips.
d_s	Depth of the steel rebars measured from the compression face to the centroid of tensile steel.
θ	Angle between the critical shear crack and the longitudinal axis of the beam.
B	Shear span of the beam.
z	Flexural lever arm.
n_s	Homogenization coefficient of the flexural steel reinforcement.
n_{FRP}	Homogenization coefficient of the flexural FRP composites.
n_{sv}	Homogenization coefficient of the shear steel reinforcement.
$n_{FRP,v}$	Homogenization coefficient of the shear FRP composites.

I.2.4.4 Codes and specifications

Establishment of design provisions requires specification of material properties for use in design. There are currently several different design guidelines for the use of FRP in strengthening [e.g. Fib 2001; Concrete Society TR 55; ACI Committee 440]. All of these guidelines use a similar approach to specifying composite properties for design. They generally neglect the modulus, most merely implying that the mean value should be chosen, while a few specify modulus-specific safety factors, and instead place emphasis on the ultimate tensile strength or strain. The general approach to determine a design value for composite strength is to define the "*characteristic value*" as a certain percentile of test results, with most guidelines specifying a minimum of 20 to 30 tests. Factors, varying for the different guideline, are intended to account for environmental effects, manufacturing specifics or testing procedures. They are then applied to this "characteristic value" to reach the final value for design. Often, instead of specifying a percentile, guidelines give an equation similar to Equation I.2.34 where the characteristic value, x_c, is calculated as the mean, μ_x, less a constant, n, times the standard deviation, σ_x. COV expresses the coefficient of variation; as $\text{COV} = \sigma_x/\mu_x$.

$$x_c = \mu_x - n\sigma_x \qquad\qquad (\text{I.2.34a})$$

$$x_c = \mu_x(1 - n\text{COV}_x) \qquad\qquad (\text{I.2.34b})$$

The constant, n, varies by specification; however by fitting statistical distribution for the tested data, the percentile of the distribution specified by Equation I.2.34 or the value of n implied by a certain percentile can be computed, allowing direct comparison of the different guidelines. Table I.2.11 shows this comparison for ultimate tensile strength. When necessary a Normal distribution is used to relate the specified percentile to a value of n. As FRP is assumed to have linear-elastic behavior, these relations would apply equally to the ultimate rupture strain, assuming that the modulus has a constant value.

Table I.2.11: Specifying the characteristic value for FRP strength.

Guideline	n
ACI Committee 440	3
The Concrete Society TR55	2
Canadian highway bridge design code CHBDC 2006 [1]	1.64
ISIS Canada [1]	3
JSCE 2001	3
Fib 2001	1.64

[1] Cited in Atadero & Karbhari 2009

The value of the coefficient n is considered as the first or initial safety factor that must be

applied to specify the characteristic strength of FRP composite. Other safety factors are assumed to account for the possible environmental degradations of the FRP materials throughout the lifetime of the strengthening. For example, the ACI Committee 440 provision recommends the use of an environmental reduction factor, C_E; thus the design value of FRP composite strength equals to the characteristic strength of FRP composite multiplied by coefficient C_E. For carbon fiber materials subjected to exterior exposure, which is typical for most bridge structures, a value of C_E of 0.85 should be used. While, the design ultimate strain of the FRP material, $\varepsilon_{FRP,u}$ can be calculated by dividing the calculated design strength of the FRP by the average elastic modulus, E_{FRP}, reported by the manufacturer.

The final level of safety is provided through the partial safety factors included in Load-Resistance-Factor-Design LRFD approach. In this approach, load actions are increased and strength is reduced, by multiplying the corresponding characteristic (nominal) values with the partial safety factors. Two forms of LRFD approach are often used in design provisions.

The first approach, involved in ACI Committee 440 guideline, can be expressed as:

$$\gamma_{DL}DL + \gamma_{WL}WL + \gamma_{LL}LL + \gamma_{IL}IL \leq \phi R_n(x_c, x_s, \psi_{FRP}x_{FRP}) \qquad (I.2.35)$$

where γ_{DL}, γ_{WL}, γ_{LL} and γ_{IL} are load factors for dead, wearing surface, live, impact loads respectively. DL, WL, LL, and IL are the nominal values of dead, wearing surface, live, impact load actions (bending moment/shearing force) respectively. ϕ is a general resistance factor applied to the full nominal resistance. R_n is the nominal strength (bending moment/shearing force) which is function of concrete contribution x_c, steel contribution x_s, FRP contribution x_{FRP}. ψ_{FRP} is the resistance safety factor specific to FRP composite. These contributions are function of the design values of material properties and the dimensions of RC section.

The second approach, involved in Fib 2001, Concrete Society and TR 55 guidelines, can be expressed as:

$$\gamma_{DL}DL + \gamma_{WL}WL + \gamma_{LL}LL + \gamma_{IL}IL \leq R_n(x_c(\psi_c), x_s(\psi_s), x_{FRP}(\psi_{FRP})) \qquad (I.2.36)$$

In this approach, material contributions are function of the dimensions of FRP strengthened RC section, design values of the strengths of each material (yield strength of the steel, concrete compressive strength, rupture strength of the composite) and specific factors of these strengths (concrete factor ψ_c, steel factor ψ_s, FRP composite factor ψ_{FRP}).

I.2.5 FRP durability

In certain environments such as costal zones, a wide number of structures are in contact with water. Generally, water has an effect on the geometry and on mechanical properties of the

materials that are used in these structures. For example, the amounts of water absorbed through concrete voids in RC structures result in corrosion of steel rebars. Similarly to concrete FRP composites have the ability to absorb amounts of water. However, degradation mechanism of the mechanical properties of FRP composite due to water absorption is still unclear unlike the corrosion mechanism of steel. Recently, there are many studies developed to simulate and evaluate degradation of FRP composite due to water absorption [e.g., Karbhari & Abanilla 2007; Karbhari 2007; Marouani 2007]. The majority of these studies evaluate absorption of water in FRP using Fickian response in conjunction with accelerated tests. Considering FRP plate with finite dimension and thickness L as shown in Figure I.2.38. Fick's first law (1855) is used to express the diffusion flux (J: in mol/mm^2.s) as function of the concentration gradient:

$$J = -D \frac{\partial c}{\partial x} \tag{I.2.37}$$

where, D is the diffusion coefficient in mm^2/s. c is the moisture concentration at a position x.
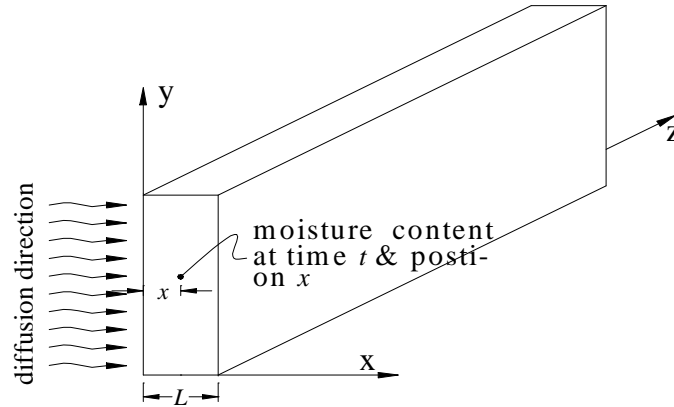
Figure I.2.38: Mass absorption vs. time according to Fickian response.

Fick's second law is used to predict how diffusion changes moisture concentration with time and can be expressed for three dimensional diffusion mechanisms as:

$$\frac{\partial c}{\partial t} = -D_x \frac{\partial^2 c}{\partial x^2} + D_y \frac{\partial^2 c}{\partial y^2} + D_z \frac{\partial^2 c}{\partial z^2} \tag{I.2.38}$$

where, D_x, D_y and D_z are the diffusion coefficients in x, y, z directions. Diffusion process thought FRP plate can be simulated as unidirectional diffusion problem. As the diffusion in y and z direction is very slow with respect to x direction and has negligible effect, thus Equation I.2.38 can be reduced to:

$$\frac{\partial c}{\partial t} = -D_x \frac{\partial^2 c}{\partial x^2} \tag{I.2.39}$$

Assuming the boundary conditions: $t=0$; $0<x<L$; $c=c_o$, and $t\geq0$; $x=L$; $c=c_\infty$, thus, solution of Equation I.2.39 can be given as [Marouani 2007]:

$$\frac{c_\infty - c_{x,t}}{c_\infty - c_i} = \frac{4}{\pi} \sum_{n=0}^{\infty} \left\{ \frac{1}{2n+1} \sin\left(\frac{(2n+1)\pi x}{L} \right) \exp\left(-\frac{(2n+1)^2 \pi^2}{L^2} D_x t \right) \right\} \qquad (I.2.40)$$

where c_o and c_∞ are initial and equilibrium moisture concentration respectively. $c_{x,t}$ is the moisture concentration at time t and distance x measured for the surface of the plate. n is an integer. The total weight of the absorbed water by the FRP plate at a time t can be obtained by integrating $c_{x,t}$ over the thickness of the plate L and the area A_f that is subjected to the flow:

$$M_t = \int_{-L/2}^{L/2} A_f c_{x,t} dx \qquad (I.2.41)$$

Thus, if we note the % gain in moisture uptake M_t and M_∞ at times t and after infinite time respectively, thus, we can obtain:

$$\frac{M_t}{M_\infty} = 1 - \frac{8}{\pi^2} \sum_{n=0}^{\infty} \frac{1}{(2n+1)^2} \exp\left(-\frac{(2n+1)^2 \pi^2}{L^2} D_x t \right) \qquad (I.2.42)$$

Figure I.2.39 represents the mass of absorbed versus time according Fickian response.
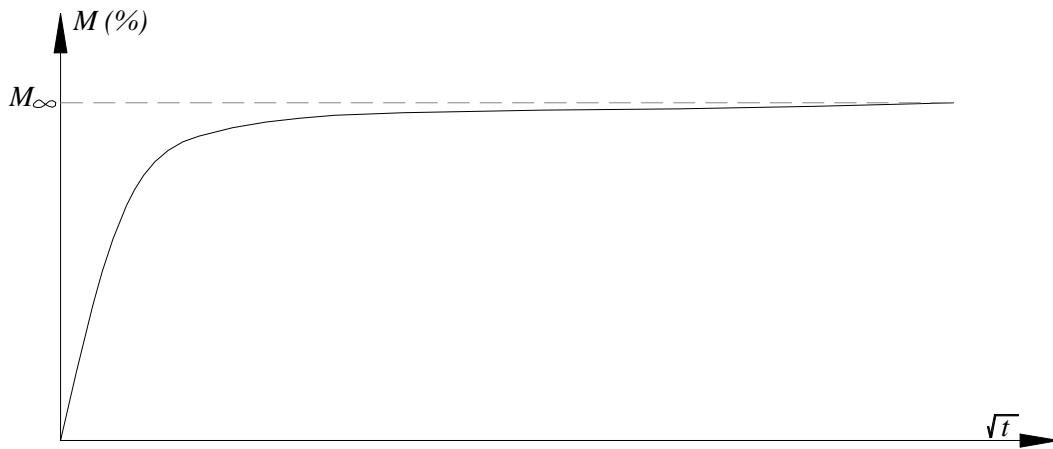
Figure I.2.39: Diffusion in FRP composite plate.

Sometimes, it is useful to use simplified formulas especially in determining the diffusion coefficient in the nature. Marouani (2007) reported three values used to determine D_x:

$$\frac{M_t}{M_\infty} = \frac{4}{L} \sqrt{\frac{D_x t}{\pi}} \qquad \text{For } M_t/M_\infty < 0.5 \qquad (I.2.43a)$$

$$D_x = \frac{0.05}{(t)_{1/2}} L^2 \qquad \text{For } M_t/M_\infty = 0.5 \qquad (I.2.43b)$$

$$\frac{M_t}{M_\infty} = 1 - \frac{8}{\pi^2} \exp\left(-\frac{(2n+1)^2 \pi^2}{L^2} D_x t\right) \quad \text{For } M_t/M_\infty > 0.5 \qquad \text{(I.2.43c)}$$

Equation I.2.43 is used to determine D_x is based on the hypothesis that the FRP sample is rectangular. The gain of moisture can be determined as: $M = (m_{wet} - m_{dry}) \times 100 / m_{dry}$, where, m_{dry} is the dry weight of the FRP plate. m_{wet} are the gain in weight of FRP plate due to water uptake. According to many experimental studies [i.g., Marouani 2007; Karbhari and Abanilla 2007]. The above described analysis is used to determine the gain in moisture as function of time using the actual value of D_x. It is proven that the value of diffusion coefficient increases with the temperature of exposure. Arrhenius relationship is strongly recommended to evaluate D_x at a temperature T_2 with respect to reference temperature T_1:

$$D_x = D_{xo} \exp\left(\frac{-E_a}{K}\left\{\frac{1}{T_2} - \frac{1}{T_1}\right\}\right) \qquad \text{(I.2.44)}$$

where, D_{xo} is the diffusion coefficient at T_1, R is the universal gas constant (8.3143 J/mol K). T_1 and T_2 are in Kelvin scale.

Accelerated tests are used to predict the properties of FRP composites (strength or modulus) as function of gain of moist absorbed by FRP specimen and time ($P = f(M_t, t)$): the properties of FRP samples subjected to constant immersion in de-ionized water are measured through time intervals. Then, the time-evolution of the moisture profile within the same grade of FRP under natural conditions (real conditions of moisture) and assuming the Fickian response described above. The final step leads us to express a % gain of moist weight M_t under real moisture exposure as a function of time (%moist = $f(t)$). From these two steps, it is finally possible to express the evolution of performance as a function of time under real moist conditions ($P = f(t)$).

Karbhari & Abanilla (2007) have formulated a simplified durability model based on Arrhenius' acceleration law and Fickian response previously described. The authors express the long-term performance $P(t)$ (strength or modulus) of FRP composites as:

$$\left(\frac{P(t)}{P_0}\right) - B = A.\ln(t) \qquad \text{(I.2.47)}$$

Where P_0 is the performance at time equals to zero. Different sizes (2, 6, 12 layers) of wet layup carbon/epoxy (for external strengthening) specimens were used. Exposure conditions of the accelerated tests range between 2 to 3 years. For the used FRP grade, the authors fit the constants A and B, thus, the long-term properties (the ultimate strength $f_{fu}(t)$ and modulus

$E_f(t)$) for the case of FRP composites with two layers can be expressed as:

$$\left(\frac{f_{fu}(t)}{f_{fu0}}\right) - 1.0607 = -0.03366\ln(t) \tag{I.2.48a}$$

$$\left(\frac{E_f(t)}{E_{f0}}\right) - 1.0607 = -0.0418\ln(t) \tag{I.2.48b}$$

where, f_{fuo} is the initial CFRP ultimate strength, E_{fo} is the initial CFRP modulus, t is the time in days. Here the values of constants B_{fu} and B_{Ef} are not equal to the unity because the parameters of the formula were obtained by fitting experimental data. According to the authors, this is considered acceptable since an assessment of predictive accuracy of the model shows reliable predictions of the model especially for long periods of exposure conditions.

I.2.6 CONCLUSIONS

Recently, strengthening of RC structures using FRP composite materials had been proven as the most power strengthening tool. This was evident and justified in various extreme solicitations (e.g. corrosion, shock, seismic …etc) as FRP materials characterized by their high resistance and specific rigidity, anticorrosive nature, low specific weight, high cycle fatigue life …etc with respect any other strengthening material. FRP Composite materials used in civil engineering domain may be classified into three categories: glass, carbon and aramid. Each of these types has different ranges of strengths and rigidities, this provide a wide variety of the mechanical properties required for strengthening process. A brief discussion of possible strengthening techniques is reviewed in the present chapter. The chapter also includes a detailed discussion of the history, use, fabrication, installation, durability, properties, advantages and disadvantages of FRP composite laminates.

FRP strengthened RC beams were extensively studied, different failure modes were observed: concrete crushing, FRP intermediate crack debonding, FRP rupture, FRP-end interfacial debonding, concrete cover separation, FRP-end debonding based shear crack.. There are many analytical and empirical models were proposed in the literature to predict the ultimate behavior of the FRP strengthened RC beams. The chapter reviews these models for the different failure mode. Also, this chapter presents detail of specifying the mechanical properties of FRP materials required for calculation and design method of FRP strengthened RC beam in diffident guidelines [e.g. Fib 2001; Concrete Society TR 55; ACI Committee 440].

PART II:
STRUCTURAL RELIABILITY OF FRP-STRENGTHENED RC BEAM

PART II: STRUCTURAL RELIABILITY OF FRP STRENGTHENED RC BEAM

Chapter II.1: Modeling of FRP strengthened RC beam.

II.1.1 GENERAL

The first step towards the probabilistic analysis is to establish the limit state functions which compare the strength to the load effect through a safety margin (Equation II.1.1). The limit state functions or failure modes can be considered of three types. The first is the ultimate limit state which corresponds to the maximum load carrying capacity. Such capacities are related to e.g. formation of a mechanism in the structure: excessive plasticity, rupture due to fatigue and instability (buckling). The second type is the conditional limit state which corresponds to the load-carrying capacity if a local part of the structure has failed. A local failure can be caused by an accidental action or by fire. The conditional limit state can be related to e.g. formation of a mechanism in the structure, exceedance of the material strength or instability. The third type is serviceability limit states which are related to normal use of the structure, e.g. excessive deflections, local damage or excessive vibrations. The fundamental quantities which characterize the behavior of a structure are called the *design variables*. Typical examples of design variables are loads, dimensions and materials properties.

The general form of the so-called safety margin can be expressed as:

$$g(R,S) = R - S \geq 0 \qquad\qquad (\text{II.1.1})$$

where R is the strength (flexural/shear) of the FRP strengthened RC section which is function of design or basic variables. For example, in case of FRP rupture, R is equal to the ultimate flexural strength due to FRP rupture. S is the load action (e.g. bending moment) due to the applied dead, live, impact loads…etc.

Flexural strength R of FRP strengthened RC section is determined using sectional analysis method. It is proven to be a practical and accurate technique for computing the ultimate flexural capacity of RC section [El-Tawil *et al* 2001]. As shown in Figure II.1.1, fiber section analysis of a composite cross-section entails discretization of the section into many small layers (fibers) for which the constitutive models are based on uniaxial stress-strain relationships. Each region represents a fiber of material running longitudinally along the member and can be assigned one of several constitutive models representing concrete, FRP

laminates or reinforcing steel.

The main assumptions employed in the fiber section method are:

- Plane sections are considered to remain plane after bending. It is generally accepted that this assumption is reasonable even into the inelastic range. Measurements of strains along the height show that this assumption is good for beams strengthened with FRP laminates [Inoue *et al* 1995]

- Perfect bond is assumed between concrete and other materials (steel reinforcement and FRP laminates).

- Shear deformations are neglected as the fiber section method is limited to long thin members whose behavior is dominated by flexure.

(a) FRP strengthened RC section   (b) Strain diagram   (c) Internal forces diagram
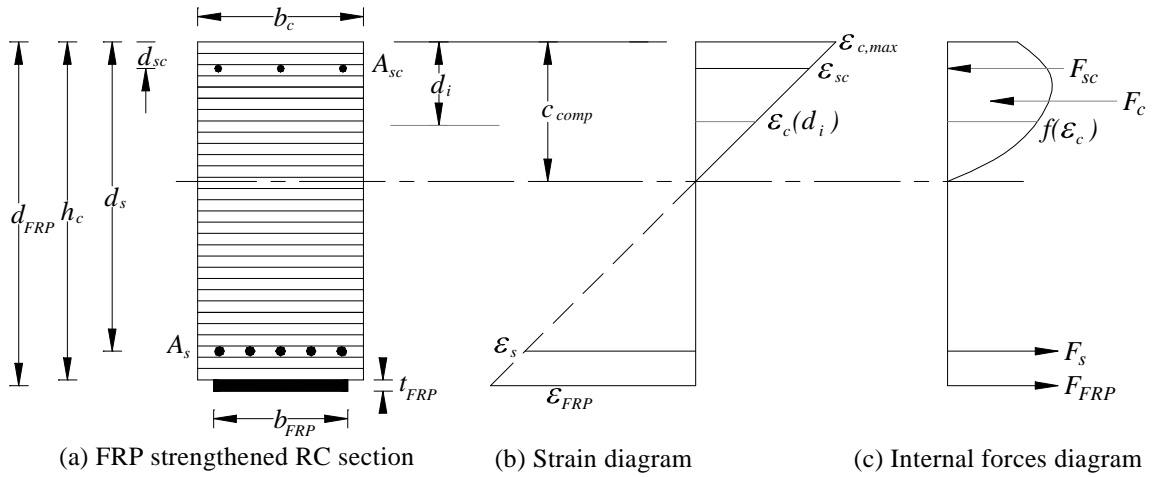
Figure II.1.1: Strain distribution of FRP strengthened RC flexural member

The constitutive properties for the components materials are shown in Figure II.1.2. The stress-strain response of the FRP is assumed to be elastic-perfectly brittle. In practical cases, stress analysis of FRP laminates in FRP strengthened RC beams generally involves evaluation of the existing substrate FRP strain ($\varepsilon_{FRP,exist}$). This strain is evaluated at the interface between concrete surface and FRP laminates due the effect of permanent loads on the RC section, thus, the stress in FRP laminates bonded to concrete beam can be calculated as:

$$f_{FRP} = (\varepsilon_{FRP} - \varepsilon_{FRP,exist})E_{FRP} \qquad (\text{II.1.2})$$

where, E_{FRP} is the modulus of FRP composites. ε_{FRP} is the strain in FRP composites according to the strain diagram shown in Figure II.1.1.

The stress-strain relationship for steel reinforcements is assumed elastic-perfectly plastic and can be expressed analytically as:

$$f_s = \begin{cases} f_y & \text{for } \varepsilon_s > \varepsilon_y \\ E_s \varepsilon_s & \text{for } \varepsilon_s \leq \varepsilon_y \end{cases} \tag{II.1.3}$$

where, E_s, f_y, and ε_y are the elastic modulus, yield stress and yield strain of steel rebars respectively.

A nonlinear stress-strain relationship is assumed for concrete material, the compressive stress-strain curve is taken according to the Model Code MC90 as given in Equation II.1.4.

$$\sigma_c = \frac{E_c \dfrac{\varepsilon}{f_c'} - \left(\dfrac{\varepsilon}{\varepsilon_o}\right)^2}{1 + \left(E_c \dfrac{\varepsilon}{f_c'} - 2\right)\dfrac{\varepsilon}{\varepsilon_{co}}} \tag{II.1.4}$$

where f_c is the compressive strength, E_c represents the initial tangent modulus of the concrete, ε_{co} indicates the strain corresponding to the peak stress of the concrete. The tensile strength of the concrete is neglected.

(a) Concrete (b) reinforcement steel (c) FRP composites
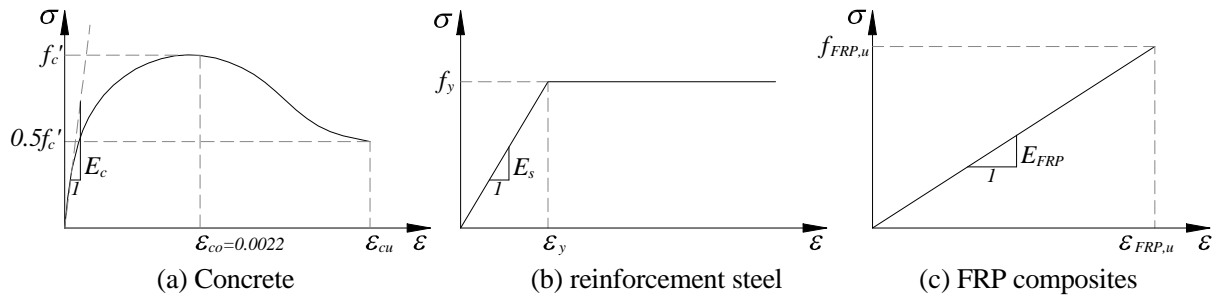
Figure II.1.2: Strain-strain (σ-ε) curve for material used in FRP strengthened RC member

In their general discretized form, the cross-sectional forces are determined as stress resultants according to the following general equations:

$$F_X = \sum_{i=1}^{n} \sigma_i A_i = 0 \tag{II.1.5}$$

$$M_u = \sum_{i=1}^{n} \sigma_i A_i d_i \tag{II.1.6}$$

where F_x is the summation of axial stress resultants. M_u is the ultimate bending moment of the section. Evaluation of F_x and M_u depends on the ultimate control strains in the materials; concrete, steel or FRP composites. A_i is the area of layer or fiber i. d_i is the distance between the centroid of the fiber i and the top of the FRP strengthened RC section. n is the total number of the section fibers. i is a positive integer representing the fiber or layer of the FRP strengthened RC section: tensile steel area or compression steel area, FRP laminates or any layer of the concrete as shown in Figure II.1.1. Equation II.1.5 is a nonlinear equation

including the depth of the neutral axis c as an unknown. An iterative Newton-Raphson algorithm can be used to determine the value of c that permit to verify Equations II.1.5 & II.1.6.

II.1.2 MODELING OF FRP STRENGTHENED RC BEAM; SIMPLIFIED FORMULAS

II.1.2.1 Modeling of flexural limit state

II.1.2.1.1 Concrete crushing and FRP rupture failure mode

The ultimate bending moment in the flexural limit state which corresponds to concrete crushing failure mode, see Figure II.1.3, can be determined by limiting the maximum concrete strain ($\varepsilon_{c,max}$) to the failure concrete strain (ε_{cu}) (see Figure II.1.1 & II.1.2). Thus, Equations II.1.4 & II.1.5 can be expressed as:

$$F_X = \frac{b_c h_c}{n} \sum_{i=1}^{n} \sigma_{c,i}(\varepsilon_i) + A_s \sigma_s + A_{sc} \sigma_{sc} + b_{FRP} t_{FRP} (\varepsilon_{FRP} - \varepsilon_{FRP,exist}) E_{FRP} = 0 \quad \text{(II.1.7)}$$

$$M_u = \frac{b_c h_c}{n} \sum_{i=1}^{n} \sigma_{c,i}(\varepsilon_i) d_i + A_s \sigma_s d_s + A_{sc} \sigma_{sc} d_{sc} + b_{FRP} t_{FRP} (\varepsilon_{FRP} - \varepsilon_{FRP,exist}) E_{FRP} d_{FRP} \quad \text{(II.1.8)}$$

where ε_i, f_s, f_{sc} and ε_{FRP} are determined according to the linear strain distribution (see Figure II.1.1 & II.1.2) considering that $\varepsilon_{c,max} = \varepsilon_{cu}$. M_u is the resistance part R in Equation II.1.1.

As far FRP rupture failure mode is concerned, the ultimate bending moment can be determined by substituting the FRP strain ε_{FRP} by $\varepsilon_{FRP,u}$ in Equations II.1.5 & II.1.6 such that:

$$F_X = \frac{b_c h_c}{n} \sum_{i=1}^{n} \sigma_i(\varepsilon_i) + A_s f_s + A_{sc} f_{sc} + b_{FRP} t_{FRP} (\varepsilon_{FRP,u} - \varepsilon_{FRP,exist}) E_{FRP} = 0 \quad \text{(II.1.9)}$$

$$M_u = \frac{b_c h_c}{n} \sum_{i=1}^{n} \sigma_{c,i}(\varepsilon_i) d_i + A_s \sigma_s d_s + A_{sc} \sigma_{sc} d_{sc} + b_{FRP} t_{FRP} (\varepsilon_{FRP,u} - \varepsilon_{FRP,exist}) E_{FRP} d_{FRP} \quad \text{(II.1.10)}$$

where ε_i, f_s, and f_{sc} are determined according to the linear strain distribution (see Figures II.1.1 & & II.1.2).
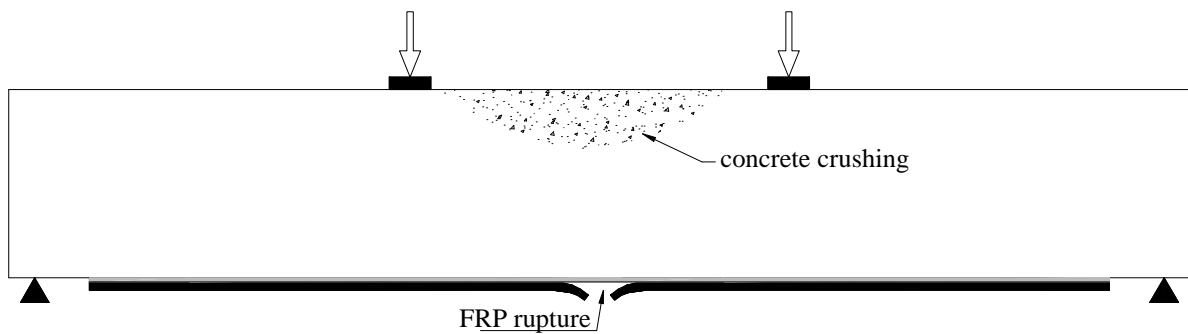
Figure II.1.3: Concrete crushing and FRP rupture failure modes.

In order to ensure the accuracy of such simplified equations, we compare the theoretical

ultimate load ($P_{u,th}$) using Equations II.1.9 & II.1.10 to the experimental values ($P_{u,exp}$) obtained for tested RC beams. A dataset containing 49 tested beams were collected from [Esfahani *et al* 2007; Toutanji *et al* 2006; Bogas & Gomes 2007; Ceroni 2010; Aram *et al* 2008; Zoghmar 1998; Grace *et al* 2002; Hashemi *et al* 2009; Maalej & Bian 2001]. All the beams in the dataset have failed only by concrete crushing or FRP rupture. The beams were simply supported and tested symmetrically under four-point loading test. Details of tested beams are given in Appendix A.1. Figure II.1.4 presents the scatter distribution of the ultimate load results obtained experimentally ($P_{u,exp}$) and those obtained theoretically ($P_{u,th}$) using the above described model. It can be noted that the beam theory can predict the ultimate strength for both concrete crushing and FRP rupture failure modes. The average value of $P_{u,exp}/P_{u,th}$ is 1.066 with a standard deviation of 0.1306. Coefficient of correlation R_c between the experimental and theoretical values was calculated and found equal to 0.9798.
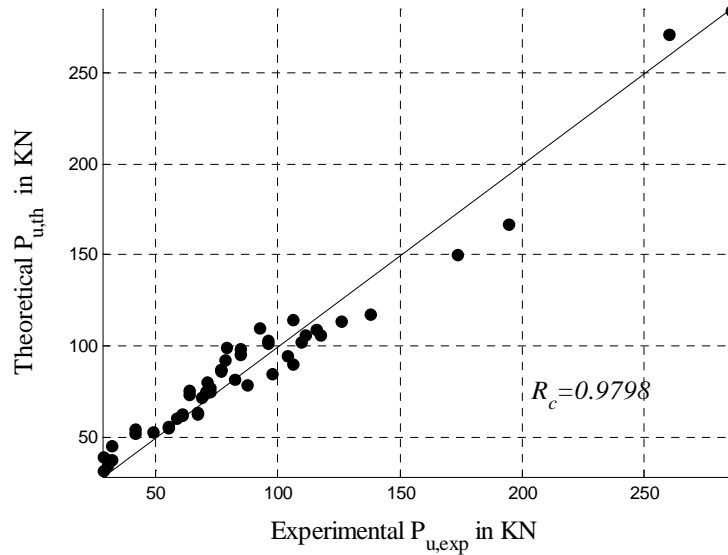
Figure II.1.4: Verification of beams theory for concrete crushing and FRP rupture failure mode. P_u is the ultimate load applied on the beam. R_c is the coefficient of correlation.

II.1.2.1.2 FRP intermediate crack debonding failure mode

FRP intermediate crack debonding failure mode takes place when flexural cracks are spread in FRP strengthened RC beams (see Figure II.1.5). The ultimate bending moment in the flexural limit state corresponding to FRP intermediate crack debonding can be determined by limiting the maximum FRP strain (ε_{FRP}) to the ultimate debonding strain ($\varepsilon_{FRP,d}$). Thus, Equations II.1.5 & II.1.6 can be expressed as:

$$F_X = \frac{b_c h_c}{n} \sum_{i=1}^{n} \sigma_i(\varepsilon_i) + A_s f_s + A_{sc} f_{sc} + b_{FRP} t_{FRP} (\varepsilon_{FRP,d} - \varepsilon_{FRP,exist}) E_{FRP} = 0 \quad \text{(II.1.11)}$$

$$M_u = \frac{b_c h_c}{n} \sum_{i=1}^{n} \sigma_{c,i}(\varepsilon_i)d_i + A_s \sigma_s d_s + A_{sc} \sigma_{sc} d_{sc} + b_{FRP} t_{FRP} (\varepsilon_{FRP,d} - \varepsilon_{FRP,exist}) E_{FRP} d_{FRP} \quad \text{(II.1.12)}$$

where ε_i, f_s, and f_{sc} are determined according to the linear strain distribution (see Figure II.1.1) assuming that $\varepsilon_{FRP} = \varepsilon_{FRP,d}$.
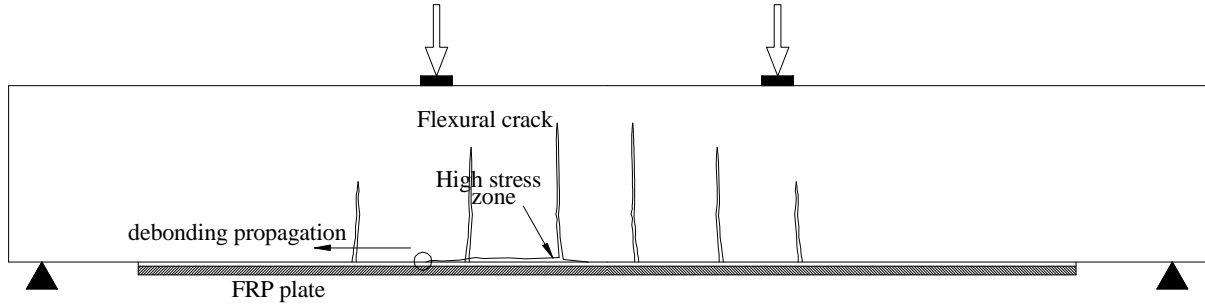
Figure I.1.5: Intermediate crack debonding failure mode.

Two verifications were carried out to choose an accurate analytical formula of $\varepsilon_{FRP,d}$ through the formulas reviewed in previous studies and reported in Table I.2.7. The first is to verify the ultimate load applied (P_u) to a FRP plate bonded to concrete prism using the models given in Table I.2.7. The theoretical predictions of the ultimate bond tensile force (P_u) are compared with 245 tests results of a dataset reported in [Lu *et al* 2005; Chen & Teng 2001; Yao *et al* 2005]. Dimensions and material properties of the tested FRP plates bonded to concrete prisms are detailed in Appendix A.2. Figure II.1.6 shows a scatter distribution of the ultimate load results obtained experimentally ($P_{u,exp}$) and those obtained theoretically ($P_{u,th}$) using the debonding models given in Table I.2.7. According to the figure, it can be noted that the theoretical values obtained using the debonding model proposed by Chen & Teng (2001) give the best scatter distribution with experimental values with coefficient of correlation (R_c) of 0.9646. In addition, statistical moments (i.e. mean and standard deviation) of $P_{u,exp}/P_{u,th}$ of the models were reviewed in Table I.2.7 can also be compared (see Table II.1.1). As can be seen in this table, Chen & Teng (2001) model can be chosen as the best predictor of the ultimate debonding load applied to FRP plate bonded to concrete prism.
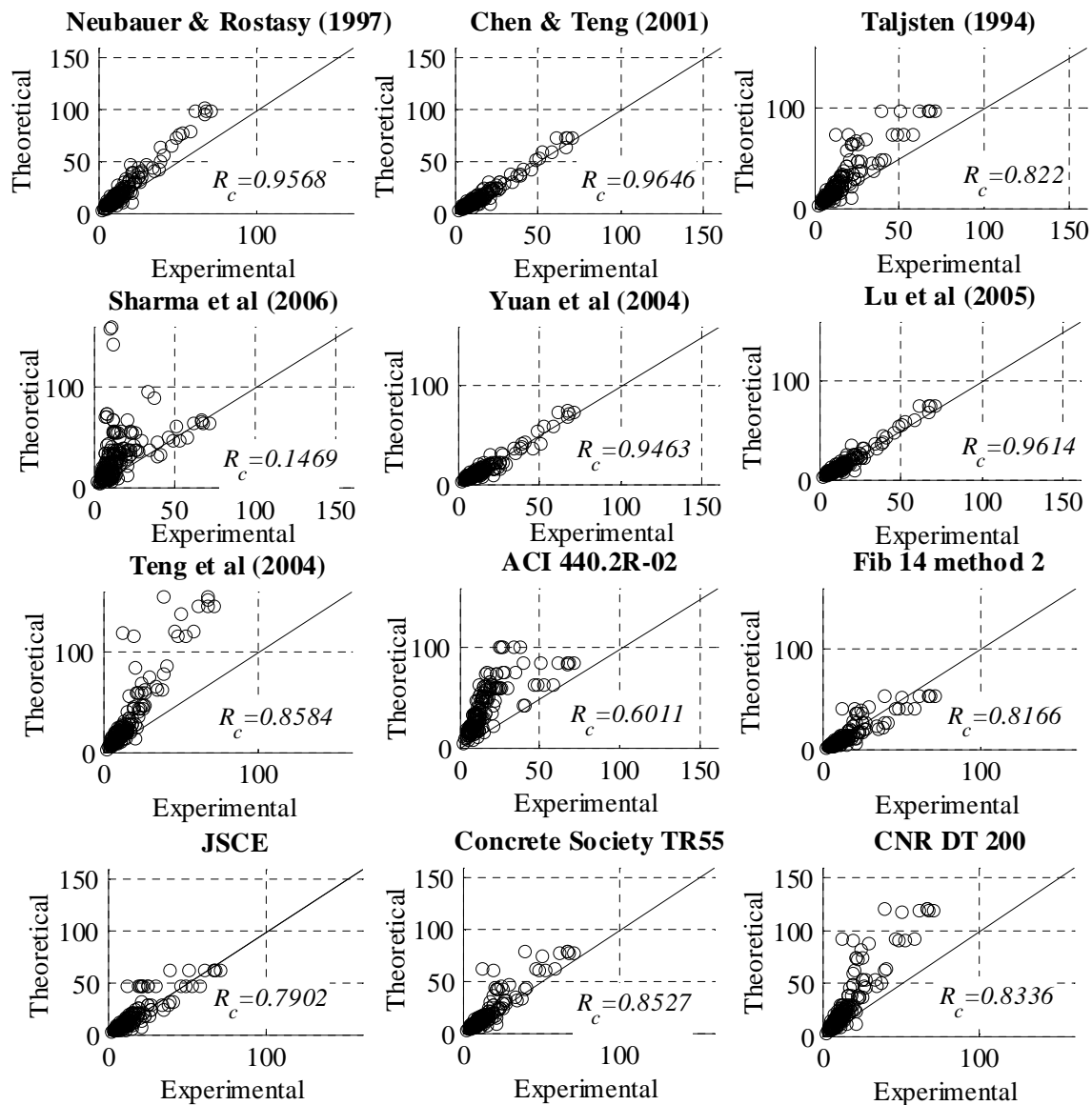
Figure II.1.6: Verification test of bond strengths (P_u in KN) versus predictions of existing bond strength models given in Table I.2.7. R_c is the coefficient of correlation.

Table II.1.1: Mean and standard deviation of $P_{u,exp}/P_{u,th}$ of the FRP plated bonded to concrete prism of debonding models reviewed reported in Table I.2.7.

Model	Mean of ($P_{u,exp}/P_{u,th}$)	Standard deviation of ($P_{u,exp}/P_{u,th}$)
Neubauer & Rostasy (1997)	0.8079	0.2141
Chen & Teng (2001)	1.0557	0.1904
Taljsten (1994)	0.7188	0.2810
Sharma *et al* (2006)	0.6188	0.5310
Yuan *et al* (2004)	1.0522	0.2083
Lu *et al* (2005)	1.0247	0.2012
Teng *et al* (2004)	0.6399	0.2627
ACI 440.2R-02	0.4271	0.3676
Fib 14 method 2	1.5680	0.2986
JSCE	1.1192	0.2901
Concrete Society TR55	1.0044	0.2444
CNR DT 200	0.6745	0.2744

The second verification was performed using a dataset of 58 tested beams collected from [Bogas & Gomes 2007; Aram & Czaderski 2008; Pham & Al-Mahaidi 2004; Teng *et al* 2003; Ceroni 2010; Yao & Teng 2007; Maalej & Leong 2005; Zoghmar 1998]. All the beams of the dataset have failed only by FRP intermediate crack debonding. The beams were simply supported and tested symmetrically under four-point loading test. Details of the tested beams are given in Appendix A.3. The ultimate debonding loads applied on the beams were calculated using Equations II.1.11 & II.1.12 in conjunction with the debonding models given in Table I.2.7. Figure II.1.7 shows the scatter distribution of the ultimate load results obtained experimentally ($P_{u,exp}$) and those obtained theoretically ($P_{u,th}$). It can be noted that the model proposed by Chen & Teng (2001) gives the best scatter distribution between the experimental and theoretical results. Coefficient of correlation between the experimental and theoretical values – using Chen & Teng (2001) model - was calculated and found equal to 0.958. In addition, the mean and the standard deviation of ($P_{u,exp}/P_{u,th}$) of the models reviewed in Table I.1.2 are given II.1.7. Results also confirm that Chen & Teng (2001) model can catch the minimum variation with all the studied models.

According to the two verifications, it can be concluded that Chen & Teng (2001) give the most accurate prediction of ultimate debonding load applied to FRP strengthened RC beams. Thus, we recommend using Chen & Teng (2001) model in the reliability analysis.
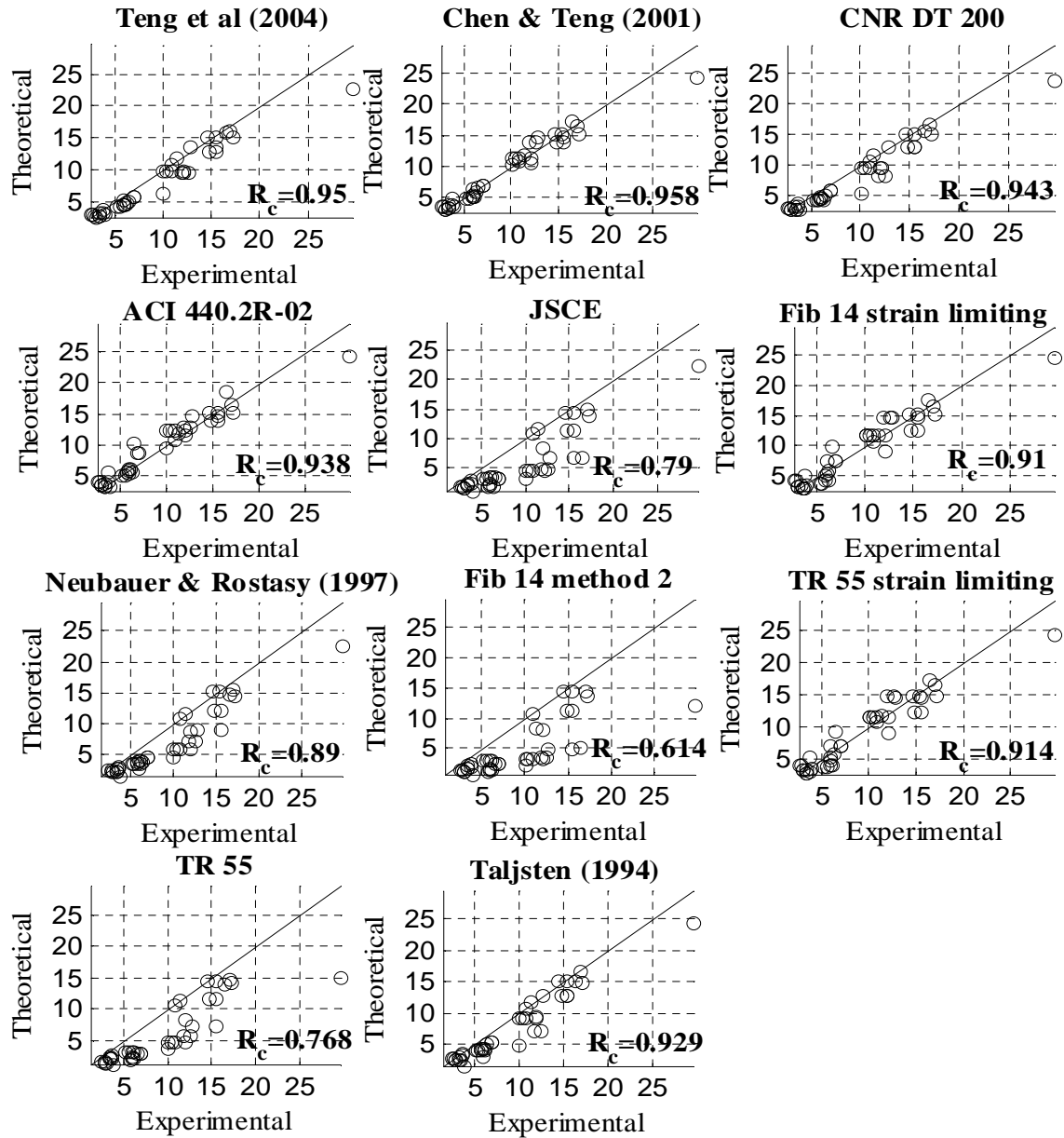
Figure II.1.7: Theoretical and experimental FRP debonding loads (P_ux10^{-1} in KN) applied on the beam. R_c is the coefficient of correlation.

Table II.1.2: Mean and standard deviation of $P_{u,exp}/P_{u,th}$ of the FRP strengthened RC beams.

Model	Mean of $(P_{u,exp}/P_{u,th})$	Standard deviation of $(P_{u,exp}/P_{u,th})$
Teng et al (2004)	1.2238	0. 1434
Chen & Teng (2001)	1.0234	0. 1170
CNR DT 200	1.1815	0. 1533
ACI Committee 440	0.9818	0. 1792
JSCE (2001)	1.9346	0. 3626
Fib (2001), limiting strain	0.9862	0. 2297
Neubauer & Rostasy (1997)	1.4812	0. 2156
Fib (2001), method 2	2.4249	0. 4123
Concrete Society TR55 limiting strain	0.9998	0. 2358
Concrete Society TR55	1.8733	0. 2969
Taljsten (1994)	1.2692	0. 2353

II.1.2.1.3 Modeling of plate end debonding based-shear crack failure mode

The basic principle of plate end debonding based shear crack failure mode is the movement of two adjacently rigid concrete blocks (§ I.2.3.2.5). These two concrete blocks are separated by a shear crack as shown in Figure II.1.8. Table I.2.8, in chapter I.2, reviews the available models proposed in literature to predict FRP end debonding based shear crack failure mode. All the reviewed models are based on limiting the applied shearing force (V_{app}) at the end of the plate to a critical value ($V_{db,end}$), thus, the limit state can be expressed as:

$$V_{app} - V_{db,end} = 0 \qquad (II.1.13)$$

In order to validate the accuracy of these models, 15 tested beams were collected from [Ahmed et al 2001; Pham & El-Mahaidi 2004; Ceroni 2010; Ali 2005]. Dimensions and material properties of these beams are given in Appendix A.4. All the beams were simply supported and tested symmetrically under four-point loading test. All the beams in the dataset have failed only by FRP end debonding based shear crack. The critical shear values ($V_{db,end}$) were calculated using the end debonding models given in Table I.2.8. Figure II.1.9 shows the scatter distribution of these critical shear values obtained experimentally and those obtained theoretically.
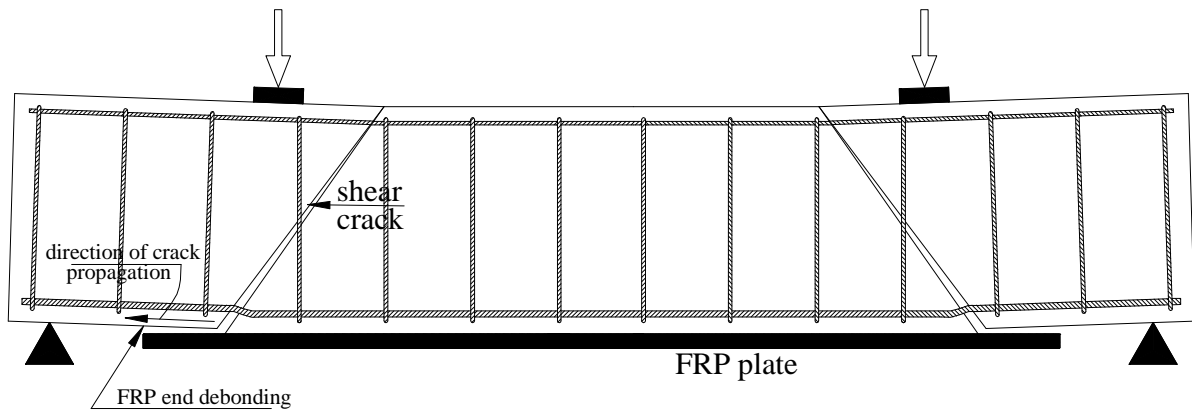
Figure II.1.8: Shear crack induced plate end debonding failure mode.

Despite of the low number of the available tests in literature, as FRP end debonding based shear crack barely takes place, Ahmed & Van-Gemert (1999) model gives the best scatter distribution between the experimental and theoretical results. Coefficient of correlation between the experimental and theoretical values for this model was found equal to 0.928. Table I.1.3 reports the mean and the standard deviation of (experimental/theoretical) ratio of the critical shear force ($V_{db,end}$) calculated using the models reviewed in Table I.2.8. It can be concluded that Ahmed & Van-Gemert (1999) gives the most accurate prediction of the critical

shear force ($V_{db,end}$) of FRP end debonding based shear crack. Thus, we recommend, in the present study, using Ahmed & Van-Gemert (1999) model in the reliability analysis.
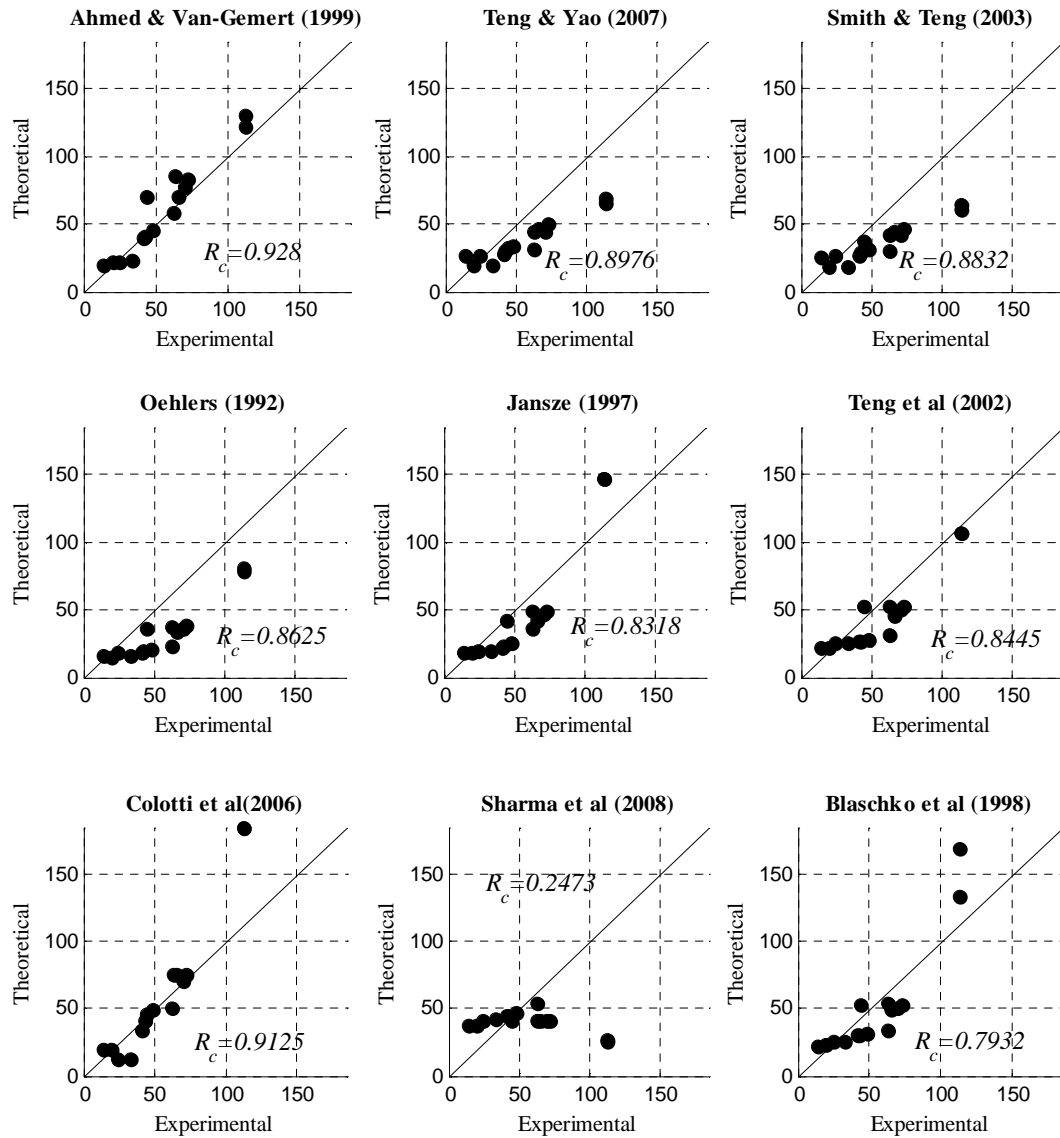
Figure II.1.9: Theoretical and experimental shear capacity FRP end debonding based shear crack loads ($V_{db,end}$ x10^{-1} in KN). R_c is the coefficient of correlation.

Table II.1.3: Mean and standard deviation of $V_{db,end,exp}/ V_{db,end,th}$ of the FRP strengthened RC beams.

Model	Mean of ($V_{db,end,exp}/ V_{db,end,th}$)	Coefficient of variation ($V_{db,end,exp}/ V_{db,end,th}$)
Ahmed & van Gemert (1999)	0.9548	0.2082
Teng & Yao (2007)	1.4108	0.2574
Smith & Teng (2003)	1.4794	0.2649
Oehlers (1992) [1]	1.7803	0.2784
Jansze (1997) [1]	1.3791	0.2949
Teng *et al* (2002) [2]	1.2766	0.2959
Colotti *et al* (2006)	1.1047	0.4748
Sharma *et al* (2008)	1.5150	0.8074
Blaschko *et al* (1998)	1.1707	0.2972

[1] Cited in [Smith & Teng 2002[a]]. [2] Cited in [Aram *et al* 2008]

II.1.2.1.4 Modeling of interfacial FRP end debonding & cover separation failure modes.

Interfacial stress concentration at the end of FRP plate causes separation of the plate from the concrete surface. Failure may take place in the adhesive layer or in small depth in the concrete cover as shown in Figure II.1.10. Interfacial plate end debonding failures were observed in RC beams bonded with a steel plate on which a considerable research had been already accumulated before to become popular for FRP plates. Through the literature review of the experimental data of FRP strengthened RC beams, reported in previous studies, FRP interfacial end debonding failure mode was not recorded as it is infrequent failure mode [Smith & Teng 2002[a]]. Therefore, it is difficult to differentiate between the reviewed FRP end debonding due to interfacial stresses models – Ziraba *et al* (1994), Varastehpour (1996) and Tumialan *et al* (1999) – reported in § I.2.11.4. From other side, several researchers have investigated that a significant decrease in the magnitude of interfacial stresses can be achieved by considering the three following recommendations:

1. Tapering the thickness of the FRP material and using fillet adhesive at the FRP plate edge [Allan *et al* 1988; Price & Moulds 1991; Adams *et al* 1986].
2. Placing the cut-off point of the FRP plate closed to the support.
3. Using transverse FRP U-wrapped laminates around the FRP longitudinal plates or anchorage the using steel bolts as shown in Figures I.2.7b & I.2.7c respectively.

Accordingly, we neglect the interfacial FRP end debonding failure mode assuming the above assumptions in the design of FRP strengthened RC beams.

(a) weak adhesive; failure in adhesive; layer

(b) Strong adhesive; failure in concrete-adhesive interface
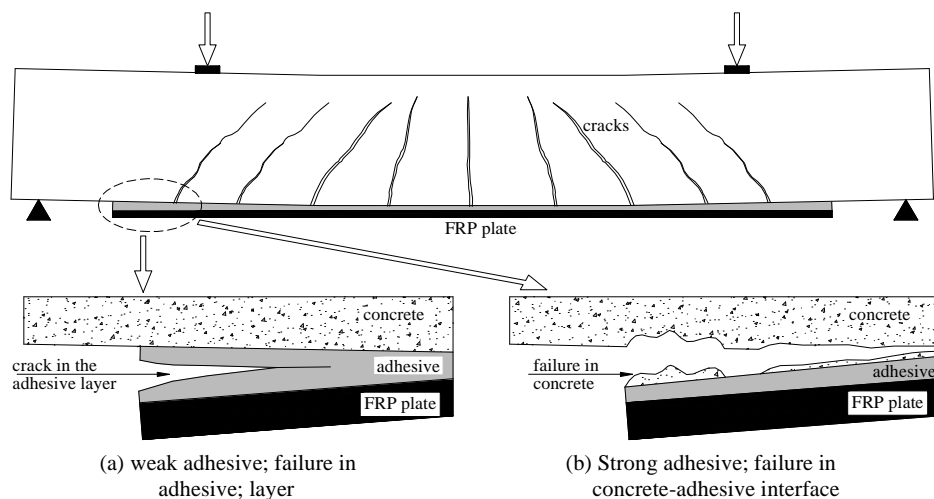
Figure II.1.10: FRP interfacial end debonding failure mode.

In what concerns concrete cover separation failure mode, it takes place at steel reinforcement depth level due to the excessive tensile force in the FRP plate as shown in

Figure II.1.11. Concrete cover separation failures were frequently observed in many experimental studies. Six analytical models, proposed to cover failure, were reviewed in Table I.2.9. In order to validate the accuracy of these models, 47 tested beams were collected from [Maalej & Bian 2001; David *et al* 1999; Garden *et al* 1997; Nguyen *et al* 2001; Ahmed et al 2001; Ahmed & Van-Gemert 1999; Beber *et al* 2001; Smith & Teng 2002[b]]; dimensions and material properties are given in Appendix A.5. All the beams were simply supported and tested symmetrically under four-point loading test. All the beams in the dataset have failed only by concrete cover separation. The ultimate load values (P_u) were calculated using the concrete cover separation models given in Table I.2.9.
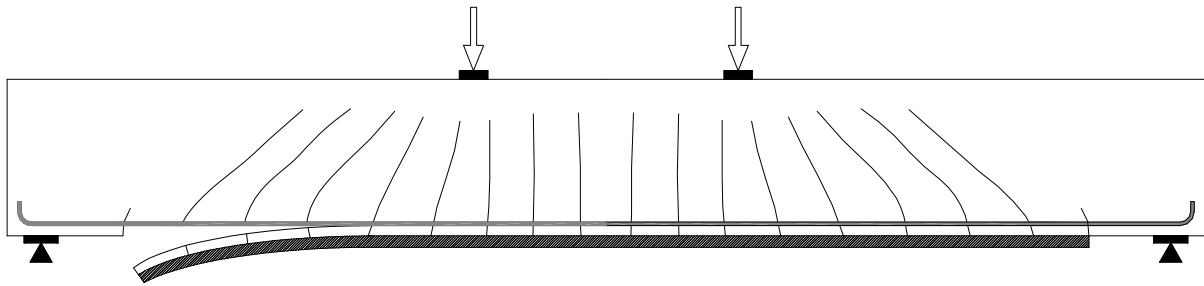
Figure II.1.11: Concrete cover separation failure mode.

Figure II.1.12 shows the scatter distribution of the values obtained experimentally and those obtained theoretically. It could be concluded that concrete cover separation models, reviewed in Table I.2.9, give a bad scatter distribution and cannot give a safe predictions of the concrete cover separation failure mode. In addition, a lower correlation factors between experimental and theoretical result were recorded. Thus, the reviewed models could not be used as an accurate tool to predict concrete cover separation failure mode. From other side, the reported cover separation models were proposed only for symmetrical four loading case and there are not enough informations about how they can be applied to general loading cases. But, similarly to interfacial FRP end debonding failure mode, the above three assumptions are considered to diminish concrete cover separation failure mode. So we neglected theses failure modes in the reliability analysis.
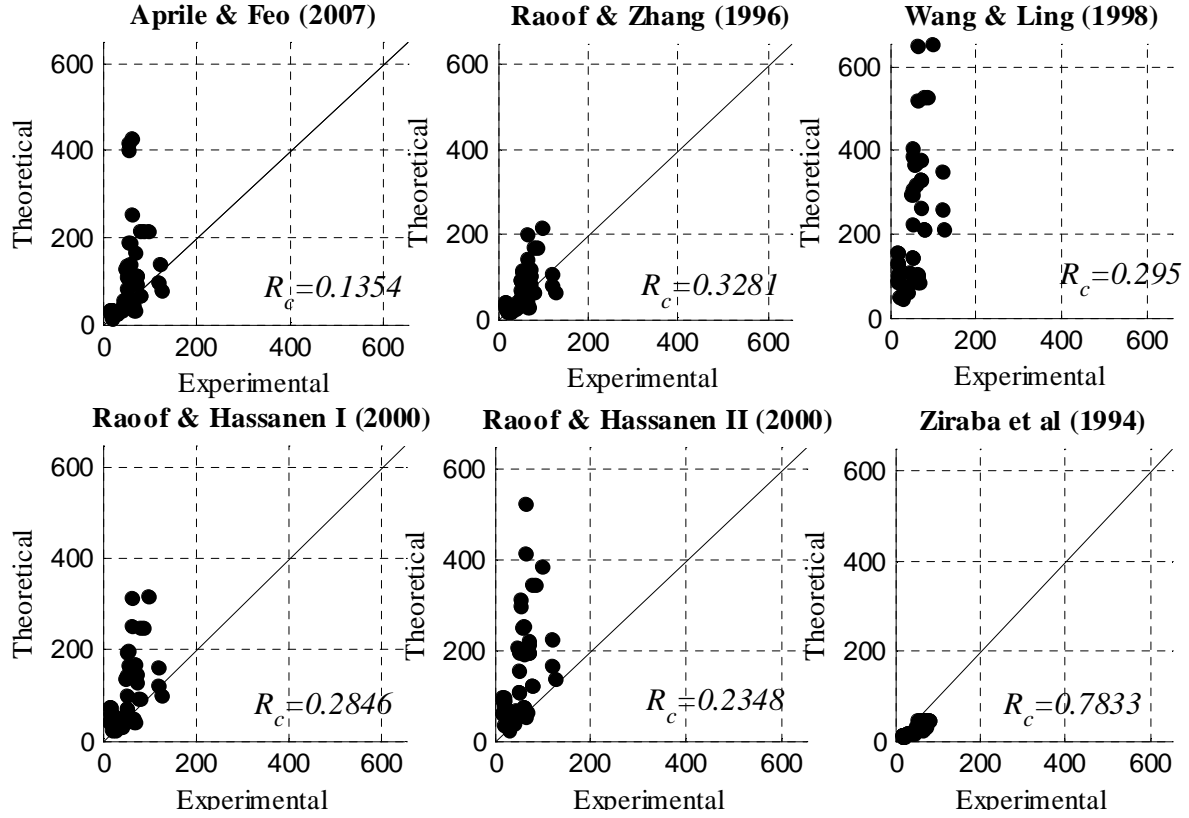
Figure II.1.12: Theoretical and experimental shear capacity concrete cover separation loads ($P_u/2$ in KN). R_c is the coefficient of correlation.

II.1.2.2 Modeling of shear limit state

The shear strength *V* of a FRP-strengthened RC beam is evaluated by assuming that the contribution of concrete V_c, internal steel stirrups V_s and the contribution of external FRP strips/sheets V_f are additive so that:

$$V = V_C + V_S + V_{FRP} < 0.66\sqrt{f_c'}b_c d_s \tag{II.1.14}$$

Steel and concrete contributions were calculated according to the ACI code as given by equations 1.19 and 1.20.

$$V_c = 0.17 b_c d_d \sqrt{f_c} \tag{II.1.15}$$

$$V_S = \frac{A_{sv}f_{yv}d_s}{s_s} \tag{II.1.16}$$

where, A_{sv}, s_s, and f_{yv}, are area, spacing and yield strength of internal shear reinforcements.

The contribution of external bonded FRP laminates for shear strengthening has to be chosen within the models given in Table I.2.10. A complete dataset containing 159 experiments was collected from [Kim *et al* 2008; Jayaprakash *et al* 2008; Taljsten & Elfgren

2000; Barros & Dias 2003; Khalifa & Nanni 2000; Triantafillou 1980; Kamiharako *et al* 1997; Umezu 1997; Taerwe 1997; Diagana *et al* 2003; Norris *et al* 1997; Challal *et al* 1998; Chajes *et al* 1995; Triantafillou 1998; Khalifa *et al* 1998; Deniaud & Cheng 2001; Park *et al* 2001; Pellegrino & Modena 2002; Täljsten 2003; Adhikary *et al* 2004; Carolin & Täljsten 2005; Dias & Barros 2008; Sas 2008] and used to verify the accuracy of the shear models. All the studies consider an initially repaired simply supported beam with symmetrically four-points loading tests, with various schemes FRP shapes. Failure mode for all data collected is the shear mode. All details of repaired beams; dimensions and material properties for concrete, steel and FRP were tabulated in Appendix A.5. Shear capacity was calculated using Equation II.1.13 and the models give the FRP contribution shown in Table I.2.10.

Figure II.1.13 shows the scatter distribution of the ultimate FRP shear contribution obtained experimentally ($V_{FRP,exp}$) and those obtained theoretically ($V_{FRP,th}$) using shear capacity models given in Table I.2.10. The accuracy of the model proposed by Chaallal (1998) cannot be checked since the values of the thickness and strength of the adhesive are not available for most of the experimental studies presented in the dataset (Appendix A.5). Within these models, Triantafillou & Antonopoulos (2000) model, recommended also by Fib Bulletin 14 provisions, gives a good scatter distribution between $V_{FRP,exp}$ and $V_{FRP,th}$ with coefficient of correlation 0.957. The mean and the standard deviation of ($V_{FRP,exp}/V_{FRP,th}$) of the shear models are given in Table II.1.4. Triantafillou & Antonopoulos (2000) model is a good candidate to achieve the minimum variation in the obtained results comparing to the other models. From this point of view we can consider this model in the reliability analysis.
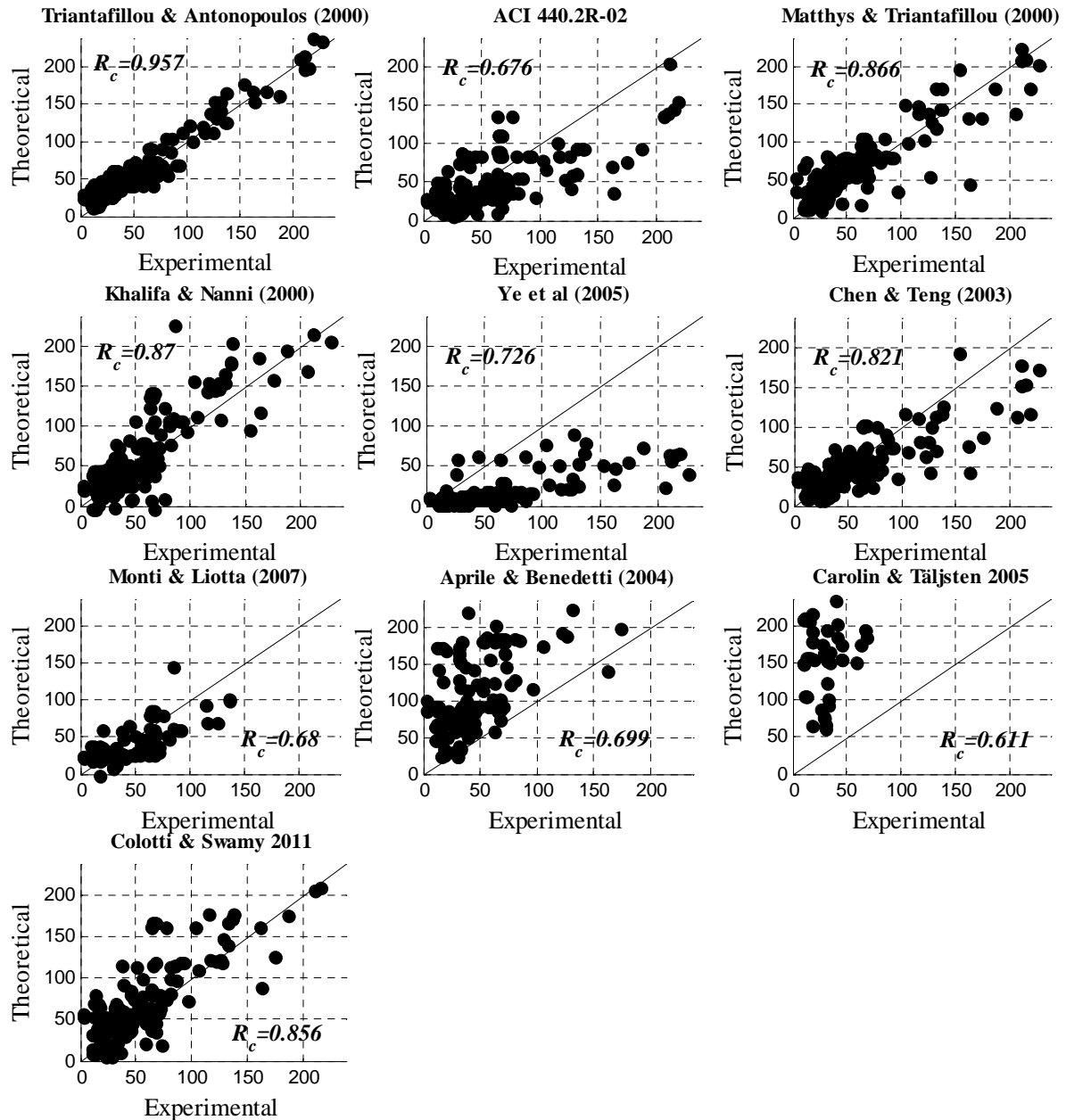
Figure II.1.13: theoretical and experimental shear capacity (V_ux10^{-1} in KN) of RC beams strengthened using FRP laminates for shear. R_c is the coefficient of correlation.

Table II.1.4: Mean and standard deviation of ($V_{FRP,exp}/V_{FRP,th}$) of FRP strengthened RC beams.

	Mean of ($V_{w,exp}/V_{w,th}$)	Coefficient of variation ($V_{w,exp}/V_{w,th}$)
Triantafillou & Antonopoulos (2000)	0.916	0.275
Matthys & Triantafillou (2000)	0.916	0.504
Khalifa & Nanni (2000)	0.714	2.617
Chen & Teng (2003)	1.264	0.696
Ye *et al* (2005)	7.649	12.98
Carolin & Täljsten (2005)	0.209	0.121
ACI 440.2R-02	1.440	1.039
Colotti & Spadea (2011)	1.009	0.757
Aprile & Benedetti (2004)	0. 448	0.258
Monti & Liotta (2007)	1.703	1.028

II.1.3 NUMERICAL SIMULATION OF FRP STRENGTHENED RC BEAM

II.1.3.1 Introduction

Reinforced concrete externally bonded with FRP is considered as a type of heterogeneous composite structure consisting of three major components: concrete, reinforcing steel and FRP. The composite poses a highly nonlinear analysis challenge that involves complications such as extensive cracking, local effects and failure modes. A general approach to model such a problem is to select a suitable numerical approach to treat the response of each component separately and then obtain their combined effects by imposing the condition of material continuity. Thus, a complete analysis includes: selecting a suitable numerical method, modeling each material using appropriate laws and modeling the interaction between the materials. The three main numerical solution procedures are: finite difference method (FDM), boundary element method (BEM), and finite element method (FEM).

The FEM offers a powerful and general numerical tool for studying structural behavior of reinforced concrete structures. Cracking, tension stiffening, non-linear material properties, interface behaviors and other effects previously ignored or treated in a very approximate manner by analytical or empirical methods can be modeled rationally using FEM. The reliability of the method is largely dependent on the accuracy with which the model simulates the actual behavior and geometrical characteristics of the prototype structure. Where simple analytical methods are not feasible for the solution of complex civil engineering problems, the FEM offers an effective, versatile and reliable approach to handle such cases. Abaqus/explicit [Abaqus manual] has been used in our research to calculate the behaviour of the FRP strengthened RC beams. This FEM package includes a large variety of material models and elements including facilities necessary for this particular subject.

II.1.3.2 Constitutive models

II.1.3.2.1 Concrete

In the last decades, many constitutive models which can predict the behavior of concrete, including cracks and crushing have been developed. Two approaches are available in Abaqus to predict the behavior of concrete: smeared crack and plastic damage models. The plastic damage model was selected for this study since it has higher potential for convergence compared to the smeared crack model [Abaqus manual]. The concrete plastic damage model assumes that the two main concrete failure mechanisms are cracking and crushing. Crack propagation is modeled by using continuum damage mechanics, stiffness degradation.

The plastic damage model requires the values of elastic modulus, Poisson's ratio, the plastic damage parameters and description of compressive and tensile behavior. The five plastic damage parameters are the dilation angle, the flow potential eccentricity, the ratio of initial equi-biaxial compressive yield stress to initial uniaxial compressive yield stress, the ratio of the second stress invariant on the tensile meridian to that on the compressive meridian and the viscosity parameter that defines viscoplastic regularization. The values of the last four parameters were recommended by the Abaqus documentation for defining concrete material and were set to 0.1, 1.16, 0.66, and 0.0, respectively. The dilation angle and Poisson's ratio were chosen to be 35° and 0.2, respectively [Chen *et al* 2010]. Another important thing is to represent the stress-strain curve for concrete in an accurate way. For a given concrete characteristic compressive strength, the concrete stress-strain curve in compression can be described using the concrete model reported in Model Code Mc90 (see Equation II.1.2).

The stress-strain curve can be defined beyond the ultimate stress, into the strain-softening regime. The compressive inelastic strain, $\widetilde{\varepsilon}_{0c}^{in}$, is defined as the total strain minus the elastic strain, $\widetilde{\varepsilon}_{0c}^{in} = \varepsilon_c - \varepsilon_{0c}^{el}$, as illustrated in Figure II.1.14 [Abaqus manual].
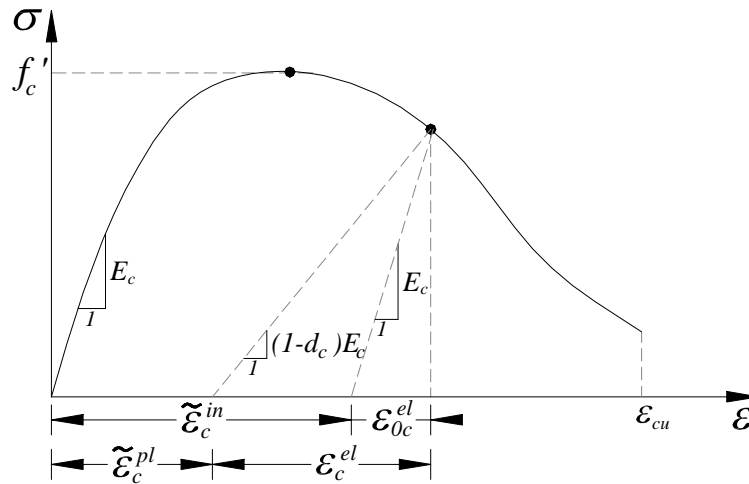
Figure II.1.14: Response of concrete to uniaxial loading in compression [Abaqus manual].

In what concerns the concrete behavior in tension, it has been modeled using a linear elastic approach until cracking initiated at tensile strength. After crack initiation, the softening will start. The post-failure behavior for direct straining is modeled with tension stiffening, which permits to define the strain-softening behavior for cracked concrete. Linear, bilinear or exponential function can be used to fit the tension-softening curve as shown in Figure II.1.15 [Coronado & Lopez 2006].
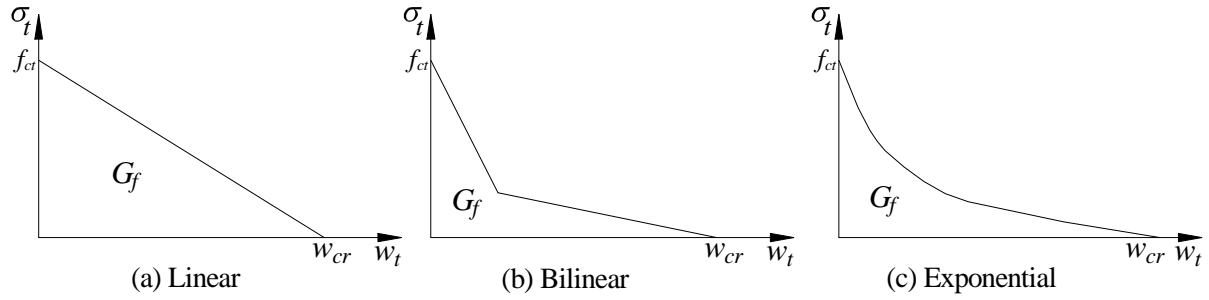
Figure II.1.15: Softening of concrete under uniaxial tension [Coronado & Lopez 2006].

Exponential relation was used in this study as recommended in many studies [i.e. Chen *et al* 2010; Coronado & Lopez 2006]. Formula reported in [Chen *et al* 2010] was used:

$$\frac{\sigma_t}{f_{ct}} = \left[1 + \left(c_1 \frac{w_t}{w_{cr}}\right)^3\right] e^{\left(-c_2 \frac{w_t}{w_{cr}}\right)} - \frac{w_t}{w_{cr}}\left(1 + c_1^3\right) e^{(-c_2)} \tag{II.1.19}$$

$$w_{cr} = 5.14 \frac{G_f}{f_{ct}} \tag{II.1.20}$$

where c_1=3.0 and c_2=6.93 are constant determined from tensile tests of the concrete. σ_t is the tensile stress normal to the crack direction. w_t is the crack opening displacement as shown in Figure II.1.16. f_{ct} is the concrete tensile strength of the concrete. G_f (N/mm) is the fracture energy and may be estimated from the following equation [Coronado & Lopez 2006]:

$$G_f = 2.5\alpha_o \left(\frac{f_c'}{0.051}\right)^{0.46} \left(1 + \frac{d_a}{11.27}\right)^{0.22} (wc)^{-0.3} \tag{II.1.21}$$

where α_o=1.44 for crushed or angular aggregate diameter. d_a (mm) is the maximum aggregate size. In the present study it will be assumed that d_a=32mm. w_c=0.45 is the water-to-cement ratio in the concrete mix.
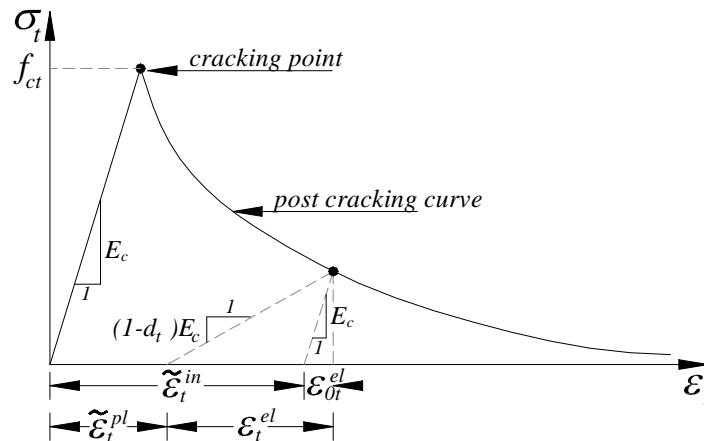
Figure II.1.16: Response of concrete to uniaxial loading in tension [Abaqus manual].

The stress-displacement curve defined by Equations II.1.19 - II.1.21 (also see Figure II.1.16) can be transformed into stress-strain curve according to the crack band defined by the following equation [Bazant 1983]:

$$w_t = \int_{h_c} \varepsilon_{cr} dh \qquad \text{(II.1.22)}$$

where ε_{cr} is the cracking strain. h_c is the width of the crack band.

In Abaqus, the crack band width is defined as the characteristic crack length of an element. Recommendation for estimating crack band width was adopted in [Chen *et al* 2010]. For instance, the characteristic crack length of a plane stress four-node square element was taken to be $\sqrt{2}e$, where e is the side length of the element. Thus, the cracking strain can be expressed as $\varepsilon_{cr} = w_t / \sqrt{2}e$. Tension stiffening is required in the concrete damage plasticity model. It is possible to specify tension stiffening by means of a post-failure stress-strain relation or by applying a fracture energy cracking criterion. The degradation of the elastic stiffness is characterized by two damage variables, d_t and d_c, which are assumed to be functions of the plastic strains. The damage variables can take values from zero, representing the undamaged material, to one, which represents total loss of strength. Linear relationship between the damage variable and stress will be assumed in the present study.

II.1.3.2.2 Reinforcing steel

The constitutive model used to simulate the steel reinforcement was the classical metal elastic-perfectly plastic model as shown in Figure II.1.2. The input for the steel model includes elastic modulus and yield stress. Perfect bond between the steel reinforcement and the concrete was assumed.

II.1.3.2.3 FRP composites

For FRP laminates, linear elastic behavior up to failure was assumed as shown in Figure II.1.2. Elastic modulus and tensile strength were needed for the simulations.

II.1.3.2.4 FRP-Concrete interface

Two different models were used to represent the interface between concrete and FRP plate. In the first model the interface was modeled as a perfect bond between the FRP and the concrete while in the second it was modeled using a cohesive zone model. The former model is used to simulate FRP rupture or concrete crushing failure mode while the latter is used to simulate debonding failure modes. In the direction parallel to the interface, a simple bilinear bond–slip

model softening behavior was employed to simulate the real FRP-to-concrete bond behavior. The bond-slip relationship is written in terms of the effective traction τ and effective opening displacement δ. Figure II.1.17 shows a graphic interpretation of the model. The interface is modeled as a rich zone of small thickness and the initial stiffness K_0 is defined as [Obaidat *et al* 2010]:

$$K_o = \frac{1}{\dfrac{t_i}{G_i} + \dfrac{t_c}{G_c}}$$ (II.1.23)

where t_i is the resin thickness, the value used for this study was t_i=1mm. t_c is the effective thickness of concrete whose deformation forms part of the interfacial slip. Lu *et al* (2005) found that effective thickness of concrete 5mm provides the best prediction of the bond-slip curve. Thus, the thickness of concrete was assumed to equal 5mm throughout the study. G_i and G_c are the shear modulus of resin and concrete respectively.
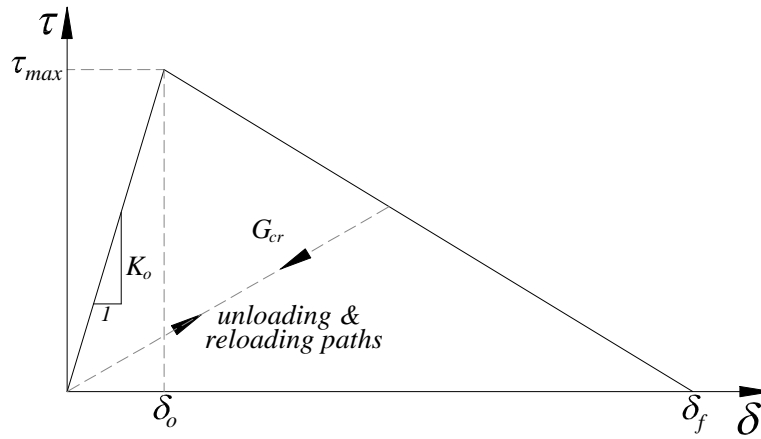
Figure II.1.17: bond–slip constitutive law of the adhesive layer [Obaidat *et al* 2010].

According to Figure II.1.17, it is obvious that the relationship between the tension stress and effective opening displacement is defined by the stiffness, K_0, the local strength of the material, τ_{max}, and a characteristic opening displacement at fracture, δ_f. When τ_{max} is achieved, the stress transfer decreases linearly to zero. The area under the curve is defined as the interfacial fracture energy, G_c. This model is capable of simulating the bond behavior regardless of whether debonding occurs within the concrete substrate or within the adhesive layer.

Equation II.1.24, [Obaidat *et al* 2010], provides an upper limit for the maximum shear stress, τ_{max}, giving τ_{max}=3MPa in this case:

$$\tau_{max} = 1.5\beta_w f_{ct}$$ (II.1.24)

where

$$\beta_w = \sqrt{\left(2.25 - \frac{b_{FRP}}{b_c}\right) \Big/ \left(1.25 + \frac{b_{FRP}}{b_c}\right)}$$

and b_{FRP} is the width of the FRP plate, b_c is the width of the concrete beam.

Based on the numerical simulations employed by [Obaidat *et al* 2010], it had been proved that the value, τ_{max}=3MPa, is too high, since CFRP rupture or concrete crushing induced the failure, instead of the CFRP debonding that occurs the experimental studies. Hence, τ_{max} is recommended to be reduced to 1.5MPa. For fracture energy, G_{cr} was taken equal to 0.09J/mm^2 as recommended by [Obaidat *et al* 2010].

The initiation of damage was assumed to occur when a quadratic traction function involving the nominal stress ratios reached the value one. This criterion can be represented by

$$\left\{\frac{\sigma_n}{\sigma_n^0}\right\}^2 + \left\{\frac{\tau_s}{\tau_s^0}\right\}^2 + \left\{\frac{\tau_t}{\tau_t^0}\right\}^2 = 1 \qquad \text{(II.1.25)}$$

where σ_n is the cohesive tensile and τ_s and τ_t are shear stresses of the interface. *n*, *s*, and *t* refer to the direction of the stress component in case of three dimensional problem. Direction *t* or *s* is neglected in case of two dimensional problems (see Figure II.1.18). The values used for this study were $\sigma_n^0 = f_{ct}$ and $\tau_n^0 = \tau_t^0 = 1.5\text{MPa}$. Interface damage evolution was expressed in terms of energy release. The description of this model is available in [Abaqus manual]. The fracture criterion model reported in [Abaqus manual] is particularly useful when the critical fracture energies during deformation purely along the first and the second shear directions are the same; i.e., $G_s^C = G_t^C$. It is given by:

$$G_n^C + \left(G_s^C - G_n^C\right)\left\{\frac{G_y}{G_g}\right\} = G^C \qquad \text{(II.1.26)}$$

where $G_y = G_s + G_t$, $G_g = G_n + G_s$ and η are the material parameters. G_n, G_s and G_t refer to the work done by the traction and its conjugate separation in the normal, the first and the second shear directions, respectively. The values used in this study are $G_n^C = 0.09\text{J/mm}^2$ and $G_t^C = G_s^C = 0.09\text{J/mm}^2$ and $\eta = 1.45$.
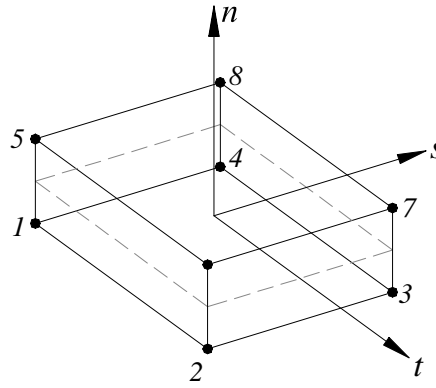
Figure II.1.18: 3-Dimensional cohesive Element [Abaqus manual].

Normal to the interface, the behavior is assumed to be linear elastic with normal stiffness estimated from the stiffness of the adhesive layer. This treatment is based on the observation that the interfacial stress normal to the FRP-to-concrete interface is small and has little effect on debonding failure [Chen *et al* 2010].

II.1.3.3 Choice of Elements

The of finite element modeling were performed into two steps. First, an overall model was used to obtain the load actions – bending moments and shearing forces in beams - of a RC bridge, see Figure II.1.20. The bridge deck was simulated using shell elements (S4) available in Abaqus elements library. While the beams of a RC bridge were simulated using beam element. The applied dead and surface - Asphalt - loads are simulated as uniform distributed loads on the concrete shells, while truck loads where simulated as point loads. Second, the RC beams were modeled as a two dimensional finite element representation as shown in Figure II.1.21. The applied loads on the beams obtained from the first step where used to study the flexural and the shear behaviors of the RC beam more accurately. In this case the concrete was modeled using the plane stress elements (CPS4R) available in Abaqus elements library. The element incorporates the crack band model for modeling its cracking behavior as explained in the section II.1.3.2.1. Both the steel and the FRP reinforcement were modeled using truss elements (T2D2). Perfect bond was assumed between concrete and all types of steel reinforcement; tensile steel, internal steel stirrups and compression steel. Interface between the concrete and the FRP plate was modeled using 2-D cohesive elements with four points (COH2D4) as shown in Figure II.1.21. The applied loads were simulated as point loads on the upper edge of the concrete.
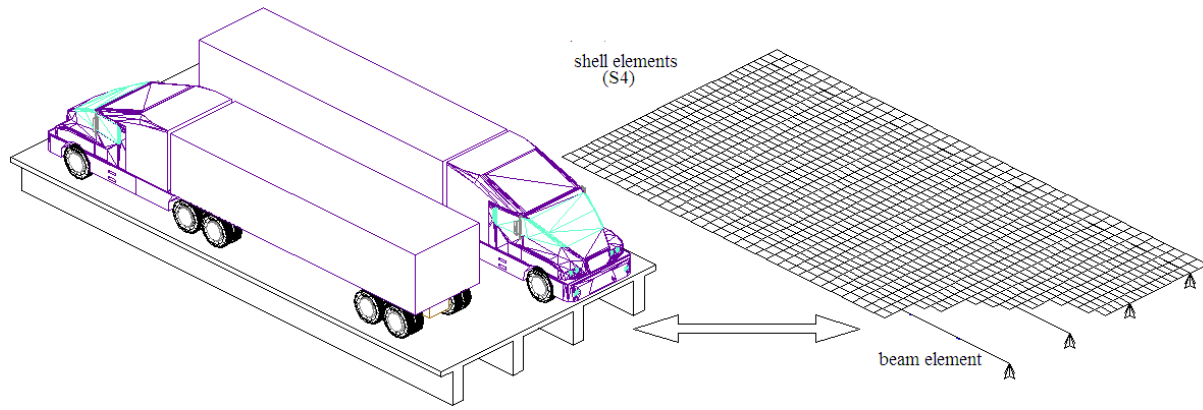
Figure II.1.20: Overall modeling of RC bridge.
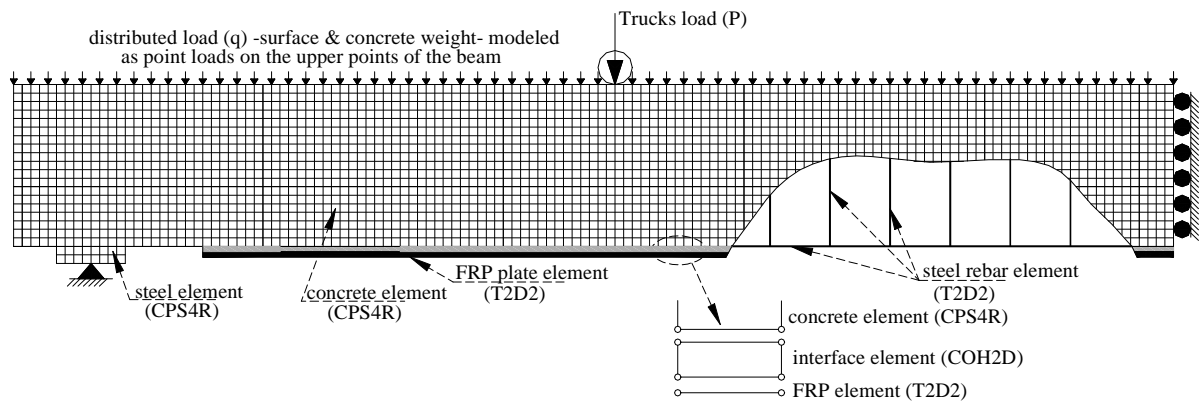
Figure II.1.21: Modeling of RC beam.

Abaqus is a general finite element program. Two nonlinear solution procedures are available in Abaqus program; standard/implicit and explicit. Implicit procedure includes the ability to simulate both static and dynamic structural problems. While explicit procedure is available only to structural dynamic problems. Material degradation and failure often lead to severe convergence difficulties in implicit analysis procedure; as cracking of concrete causes such a problem; tensile cracking makes the material stiffness a negative value. In the present study the implicit model was used to simulate the overall modeling of the bridge (concrete deck and beams), as the implicit model does not contain convergence problem in concrete when simulated using shell and beam elements. In the other side, Abaqus/explicit is a quasi-static method which is characterized by the absence of a global tangent stiffness matrix, which is required with implicit methods. Since the state of the model is advanced explicitly, iterations and tolerances are not required [Bahtui 2008]. Therefore, Abaqus/explicit procedure is more reasonable to be used when simulating the RC beam as a plane grid of plane stress and truss elements as shown in Figure II.1.21. The quasi-static response was attained by keeping the kinetic energy level below 1% of the total energy level of the whole model. However, because Abaqus/explicit is a dynamic analysis program, oscillatory response was

inevitable even in the quasi-static solution. The quasi-static results were generally obtained when the time step periods were greater by 5 times or more than the slab natural period [Abdullah 2007]. The curve was at last smoothened using the smoothing function available in ABAQUS/explicit to eliminate the oscillation effect while it keeps all amplitudes and trend of curves intact.

II.1.3.4 Verifications

Simulation of FRP strengthened RC elements using FEM were employed in many previous studies such as: Hiu *et al* (2006), Obidat *et al* (2010) and Chen *et al* (2010). The studies include reviews of FRP strengthened RC beams tested using four-points loading test and numerical simulation of these beams. Examining the load deflection curves of the simulated and tested beams shows that the FEM models are capable of predicting the structural behavior of FRP strengthened RC beams, since a very good agreement between the experimental and numerical simulation results is observed. Corondo & Lopez (2006) employ several numerical simulations of 11 tested FRP strengthened RC beams. The beams include specimens failed by different failure modes: concrete crushing, FRP debonding and FRP rupture. Results of the study present a good agreement between results experimental and numerical simulations. In addition, the authors investigate additional numerical simulations to show the sensitivity of the structural behavior of the FRP strengthened RC beam with respect to four parameters of the concrete: tensile strength, fracture energy, tension softening and angle of dilation.

Results of the sensitivity analysis performed by [Corondo & Lopez 2006] conclude that the value of the concrete tensile strength has no significant effect on the peak load and the failure mode, while a slight increase in the stiffness had been observed with respect to the tensile strength of the concrete. The type of the concrete tension softening model (linear, bilinear and Exponential), shown in Figure II.1.15, a slight effect on the peak load and deflection is observed. In addition, beams failed by concrete crushing are insensitive to changes in the concrete fracture energy. The failure mode and the peak load of beams failed by plate debonding are significantly affected by the magnitude of the concrete fracture energy, as low values of the concrete fracture energy results in premature plate debonding. Moreover, beams failed by concrete crushing are insensitive to changes in the concrete angle of dilation. In contrast, the failure mode and the peak load of beams failed by plate debonding are significantly affected by the angle of dilation, as low angle of dilation results in plate debonding. Conversely, high angle of dilation increases the peak load. Very good results are attained when using an angle of dilation of 30°.

II.1.4 CONCLUSIONS

The present chapter was divided into two main parts:

The first part outlines the most important failure modes that will be considered in the reliability analysis and the most accurate model that can predict the ultimate capacity of the FRP strengthened RC beams. Two flexural limit states were considered; flexural and shear limit states. For flexural limit state, four of six flexural failure modes were considered: concrete crushing, FRP rupture, FRP intermediate crack debonding and FRP end debonding based shear crack. While two failure modes will be neglected: FRP interfacial end debonding and concrete cover separation. These two failure mode can be avoided using some design considerations (e.g. using anchoraged end laminates).

The second part gives all the principles of the Abaqus finite elements software – materials, elements, modeling…etc – used to simulate the structure performances. Such these performances are considered as the first step towards the reliability analysis based neural network applications which will be discussed in the following chapters.

Part II: Structural reliability of FRP strengthened RC beam

Chapter II.2: Structural analysis using neural networks applications

II.2.1 GENERAL

In the reliability analysis, if the performance function is known with an analytical explicit function of design variables, the reliability analysis can be preformed easily. Certain deterministic calculations (such as the calculation using finite elements or finite differences methods) cannot be obtained from an explicit analytical form of the performance function. In this case, methods such as surface response method and the neural network applications are used to approximate the analytical form of the performance function.

The response surface method is used to approximate the structural performance by an analytical expression. The choice of polynomial approximation is classic in the structural reliability. A polynomial of the second order is realized from the non-linearity of the exact, or reference, performance in certain ranges of the design variables. The following surface response quadratic function was used to approximate the structural performance (y) as function of the design variables (x_i, i=1, 2, ...n):

$$y = a_o + \sum_{i=1}^{n} a_i x_i + \sum_{i=1}^{n} \sum_{j=1}^{n} b_{ij} x_i x_j \tag{II.2.1}$$

where a_o, a_i and b_{ij} are coefficients found from a number of reference structural performances obtained using the finite elements method by a given values of a dataset of the variables x, using a regression based on the least square method. Generally, application of the response surface method is used in iterative procedure.

Surface response quadratic function was used in many structural reliability applications with an acceptable accuracy [Soares *et al* 2002; Massih 2007; Gavin & Yau 2008; Wong *et al* 2005]. However, surface response method may have two main disadvantages. First, all its applications are recommended with a small number of random variables, typically 3-5. If larger number of random variables are considered (number of variables in our case is 6-8), the time cost of generation of the response surface would probably blow up. Second, the accuracy

may be completely lost especially in case of performance function with high nonlinearity.

Recently, neural networks work as powerful interpolation tools were used instead of quadratic response functions to approximate the structural performance function, as the neural network can produce reliable output values for any input at low time cost. In the present study, we use the neural network applications to perform the reliability analysis to avoid time cost and accuracy problems that may probably be produced when using response surface method.

II.2.2 INTRODUCTION TO NEURAL NETWORKS

Artificial neural networks are computational models broadly inspired by the organization of the human brain. The most important features of a neural network are its abilities to learn, to associate, and to be error tolerant. Unlike conventional problem solving algorithms, neural networks can be trained to perform a particular task. This is done by presenting the system with a representative set of examples describing the problem, namely pairs of input and output samples; the neural network will then extrapolate the mapping between input and output data. After training, the neural network can be used to recognize data that is similar to any of the examples shown during the training phase. As an important intelligent computation method, neural network has been applied to a wide range of applications such as: curve fitting, pattern classification, nonlinear system identification…etc. At the most abstract level, a neural network can be thought of as a black box, where data or inputs is fed in on one side, processed by the neural network which then produces an output. Although a neural network can usually process any kind of data, e.g. qualitative or quantitative information, the data fed into the neural network should be preprocessed (e.g. filtered, transformed) to enable faster training and better performance. In fact, the selection, preprocessing, and coding of information is one of the main issues to deal with when working with neural networks. Figure II.2.1 shows the functionality of the neural network.
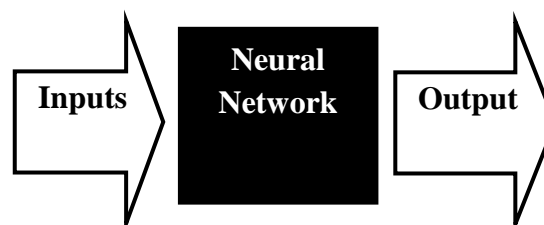
Figure II.2.1: Neural network.

A closer look at the black box reveals that its interface to the outside world consists of an input layer and an output layer of neurons. The neurons are the processing units within the

neural network and are usually arranged in layers. The information is propagated through the neural network layer by layer, always in the same direction. Besides the input and output layers there can be other intermediate layers of neurons, which are usually called hidden layers. Neural networks may have more than one output, but in our cases we will perform the analysis considering neural networks with one output. Figure II.2.2 illustrates the simplified architecture of a neural network.
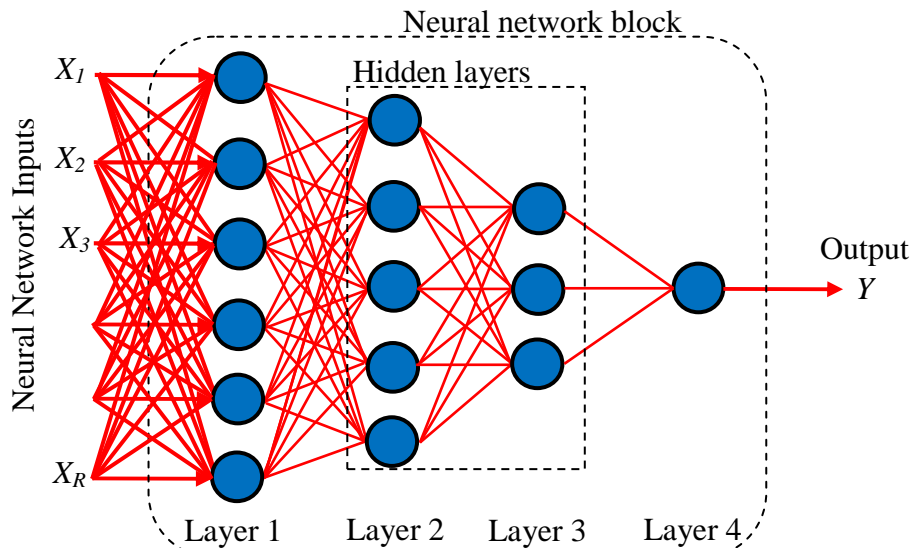
Figure II.2.2: General Architecture of Neural Network.

II.2.3 ELEMENTS OF SIMPLE NEURON

A neuron collects information from all preceding neurons relative to the flow of the information and propagates its output to all the neurons in the following layer. The output of each preceding neuron p is modulated by a corresponding weight vector (w) and bias b before affecting the activity of the neuron. This process is realized by the formula, where $n=w^Tp+b$ represents the activity of the neuron. This activity is then modified by activation or transfer function $f(.)$ and becomes the final output of the neuron $a=f(n)=f(w^Tp+b)$. This signal is then propagated to the neurons of the next layer. Figure II.2.3 depicts this process. Connections are the paths between neurons where all the information flows within a neural network. Often the neurons of two succeeding layers are fully interconnected, but there might exist additional connections going to further layers or even missing connections between certain neurons.
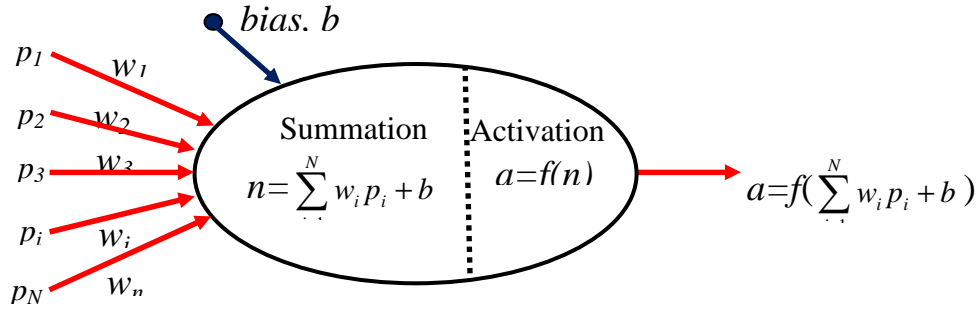
Figure II.2.3: Single neural components.

II.2.3.1 Inputs values, weights and biases

Each connection is equipped with an individual weight vector and bias that modifies the signal flow on the respective connection. The weight works as a factor by which the output of the preceding neuron is multiplied. The bias works as a fine adjustment by which the product of weight and output from the preceding layer is added. This means that information is stored and distributed within a neural network and even minor destruction of some of the weights and biases will have large effect on the recall of learned information.

II.2.3.2 Activation function

Activation functions, known also as transfer functions, are the processing units of a neuron. These functions can be linear or non-linear. Four of the most common transfer functions are depicted in Figure II.2.4:
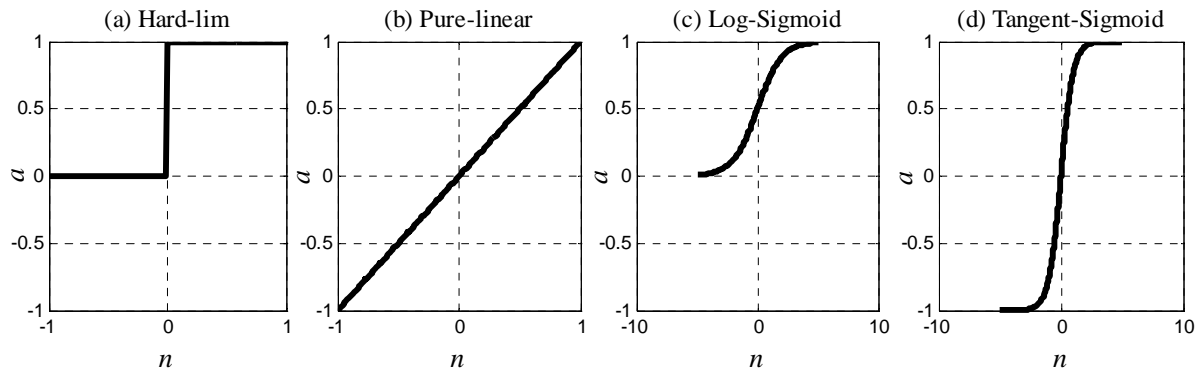
Figure II.2.4: Activation functions.

The mathematical formulation of the above functions is given as follows:

Hard-lim: $a = \begin{cases} 0 & \text{if } n < 0 \\ 1 & \text{if } n \geq 0 \end{cases}$

Pure-linear: $a = n$

Log Sigmoid: $a = \dfrac{1}{1 + e^{-n}}$

Tangent Sigmoid: $a = \dfrac{e^n - e^{-n}}{e^n + e^{-n}}$

II.2.4 MULTI-LAYER NEURAL NETWORK

Multi-layer neural network represents a generalization of the single neuron as described in Figure II.2.2. The capability of multi-layer neural network stems from the non-linearity that exists in neural cells. The general structure of the neural network consists of three types of layer:

- Input Layer: A layer of neurons that receives information from external sources, and passes this information to the network for processing.

- Hidden Layer: A layer of neurons that receives information from the input layer and processes them in a hidden way. It has no direct connections to the outside world (inputs or outputs). Each of the hidden layers involves a number of neural cells, each of these neural cells is connected with all the neural cells in the previous and the following layers in the neural network.

- Output Layer: A layer of neurons that receives processed information and sends output signals out of the system.

As shown in Figure II.2.5, the inputs of the first layer and output of the last layer are the input variables and the desired output respectively. The inputs of an intermediate layer are the outputs of the previous layer. For instance, in case of ultimate limit state, the input of the neural network may be the material properties (e.g. steel, concrete and/or FRP modulus/strength), dead load, live load, geometrical dimensions of the beam…etc. while the corresponding output is the maximum strain in steel, concrete or FRP material. The same inputs may be considered in case of severability limit state considering the desired output is the maximum deflection of the beam.

Connections between the neural cells are represented by the weights. Bias acts on a neuron as an offset, its function is to provide a threshold for the activation of neurons. The bias input is connected to each of the hidden and output neurons in a network. The output vector a of layer (i) can be expressed as:

$$a^i = f^i(w^i_{S^i R^i} a^{i-1} + b^i) \tag{II.2.2}$$

where a^{i-1} is the output vector of the previous layer. $w^i_{S^i R^i}$ is weight matrix between layer (i) and (i-1), the size – rows and columns - of the weight matrix is equal to $S^i R^i$. S^i is the number

of neural cell in the layer (i). R^i is the inputs number of the layer (i). b^i is the bias vector with length equals to S^i. f^i is a vector, with length S^i, comprising the non-linear activation functions of the layer (i).

The phase when sample patterns of a certain problem are presented to a neural network is called the training phase. During training, the weights and biases of the neural network are adjusted so as calculated output match desired output (i.e. theoretical or reference value of output). Generally, training depends on the type of the neural network and on the problem it is aiming to solve; either a supervised or an unsupervised method can be used for adapting the weights. In both cases however, training starts with a recall where the input is propagated through the neural network and all its neurons change their activity accordingly. A supervised training is typically chosen when the neural network is able to map input to desirable output patterns. This requires that the output to a given input is known. After the recall phase, the calculated output of the neural network is compared to what the resulting actual output pattern should be. The observed difference is used to adapt the weights and biases.

The adaptation of the weights starts at the output neurons and continues downward toward the input layer in a looping algorithm called Back-propagation (see Figure II.2.6). The weight and bias adaptation for one pattern often does not correct the neural network's faulty response completely, but improves it. Then the next input pattern is chosen and the whole process is repeated until the overall response of the neural network is satisfying. Many iterations are required to train small networks, even for a simple problem. In the present study, the maximum time required to train neural networks was observed about 3 to 4 minutes using Matlab neural network toolbox. It is important to define the point where the training is terminated, because sometimes it is possible to over-train a neural network. Namely, at some point the neural network starts to memorize exactly the training examples with their inherent noise and later on it will not be able to generalize from the trained examples to new patterns presented during supervision recall.
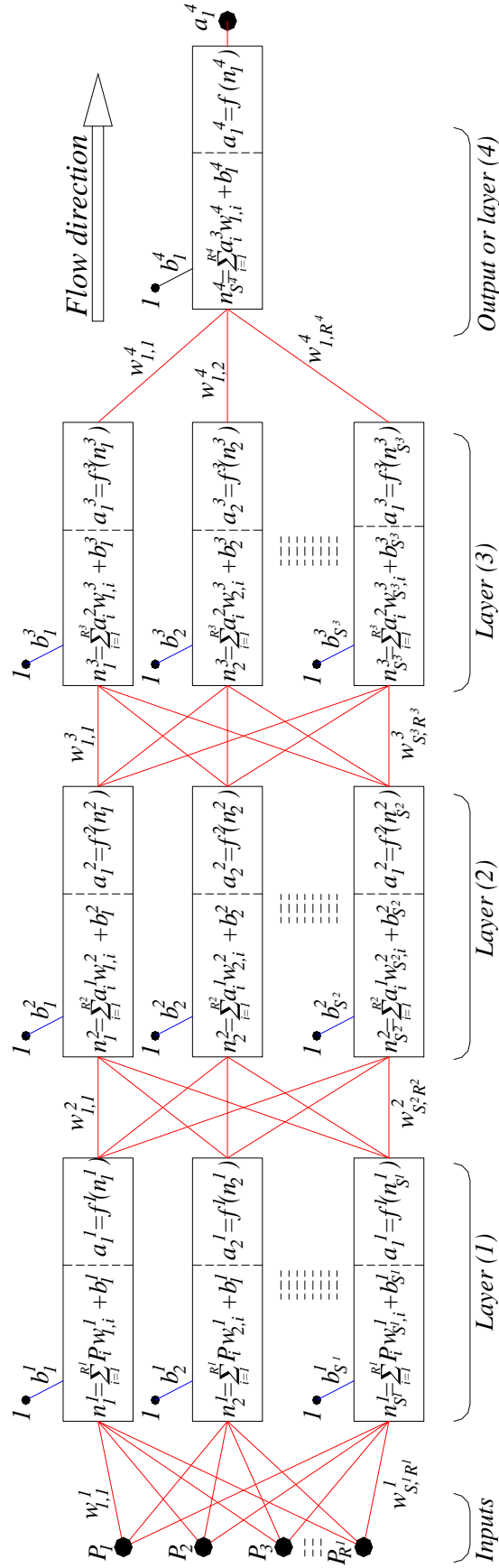
Figure II.2.5: Multi-layer neural networks.

The objective of the learning process is to train the network so that the application of a set of inputs produces the desired or at least a consistent set of outputs. During training the network weights gradually converge to values such that each input vector produces the desired output vector. The learning of a neural network is composed of two passes: forward pass and backward pass. In the forward pass, the input signal propagates through the network in a forward direction, on a layer-by-layer basis with the weights fixed with any initial values. Next, the network evaluates the errors between the desired output vector and the actual output vector. While in the backward pass, the measured error is propagated in a backward manner. The weights are adjusted based on an error-correction rule. This process is generally referred to as "error back-propagation" or back-propagation for short. The adjusted weights and biases are then used to start a new cycle. A back-propagation cycle, also known as an epoch, in a neural network is illustrated in Figure II.2.6. For a finite number of epochs the weights and biases are shifted until the deviations from the outputs are minimized.
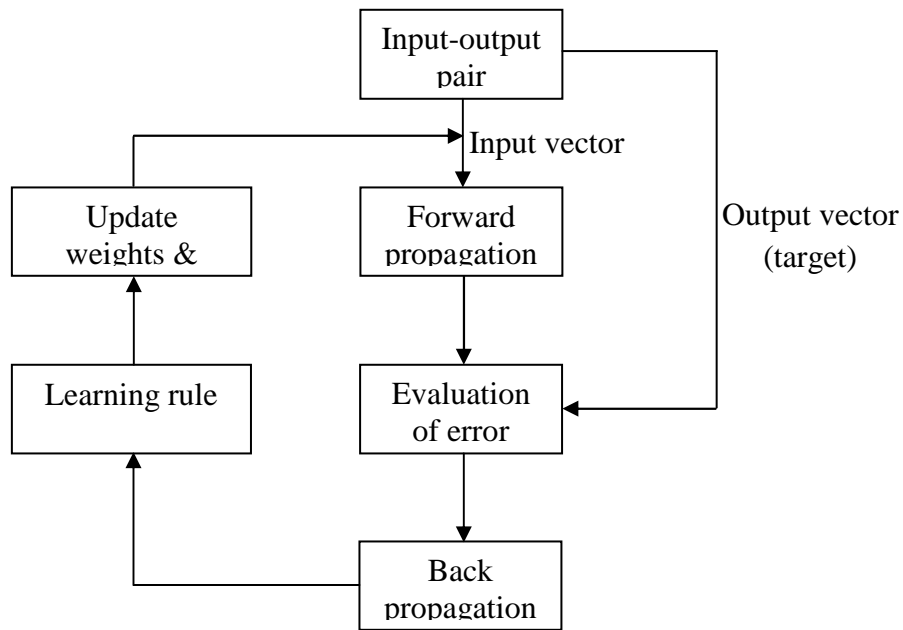
Figure II.2.6: Back-Propagation Cycle.

II.2.5 DEFINING OF A NEURAL NETWORK PATTERN

II.2.5.1 Architecture of a neural network

Generally, there are two main characteristic values must be known before training the neural network: (1) number of hidden layer in the neural network and (2) the number of neural cells in each of these layers. The choice of the number of hidden layer depends on the size of input/output vector, size of training, validation and test datasets and the non-linearity of the

problem. One rule proposed by Lachetermacher & Fuller (1995), suggests that the number of the hidden layers n^{HL} for one output is a function of the number of training samples n_{TR} and of the number of input variables n_{iv}: $0.11n^{TR}<n^{HL}(n_{iv}+1)<0.3n_{TR}$. For limited number of data within the training dataset, it leads conservatively to one hidden layer. However, neural network with two hidden layers are necessary to represent an arbitrary decision boundary to arbitrary accuracy with rational activation functions and can approximate any smooth mapping to any accuracy. There is currently no theoretical reason to use neural networks with any more than two hidden layers.

The next question is related to the neural network architecture is the choice of the number n^{NL} neurons in each of the hidden layers. The choice of neurons number is not a straightforward question. Using too few neurons in the hidden layer will result in under-fitting: the neural network is unable to adequately detect the signals in a complicated data set. Using two many neurons in the hidden layers on the contrary will result in over-fitting; the neural network has so much information processing capacity that the limited amounts of information contained in the training set is not enough to train all of the neurons in the hidden layers and the time required may inadequately increase. So, it is necessary to find a balance between too many and too few neurons in the hidden layers. Examples of rules for determining the correct number of neurons in the hidden layers as a function of the input and output variables are cited by [Heaton 2005; Costea & Nastac 2005]:

$$n^{NL} \in \left[n_{ov}, n_{iv} \right] \quad \text{(Assuming that } n_{iv} > n_{ov}) \quad \text{(II.2.3a)}$$

$$n^{NL} = \frac{2}{3} n_{iv} + n_{ov} \quad \text{(II.2.3b)}$$

$$n^{NL} \leq 2 n_{iv} \quad \text{(II.2.3c)}$$

$$\sqrt{n_{iv} n_{ov}} - 2 \leq n^{NL} \leq \sqrt{n_{iv} n_{ov}} + 2 \quad \text{(II.2.3d)}$$

Upadhyaya & Eryurek (1992) propose a relation between the total number of the weight n^w and the number of training samples $n^w = n_{TR}.\log_2(n_{TR})$. These rules provide a starting point but, definitely, the choice of neural network architecture will generally come down to trial and error procedure.

II.2.5.2 Matlab neural network toolbox

Matlab (version 2011a) neural network toolbox was used to establish the structural response function based neural network algorithm. Matlab (version 2011a) neural network toolbox allows changing the transfer function at each layer. Neural networks using matlab neural

network toolbox can be constructed, trained, validated, tested and used according to the six following steps:

1.   ***Input and output data processing***. Matlab neural network accepts input data and the output data are organized in two matrixes; input matrix [*X*] and output matrix [*Y*]. Length of [*X*] and [*Y*] equals to the number of the available training samples n_{TR}. Matlab automatically processes the inputs and output dataset through processing functions as shown in Figure II.2.7. These functions transform the input and target values you provide into values that are better suited for network training. Such these function is '*mapminmax*' which normalize the input/output data to fall in the range [-1,1]. Required matlab code to perform data processing can be writing in the following syntax:

```
[pn,ps]=mapminmax(X);
[tn,ts]=mapminmax(Y);
```

Another function can be used is '*mapstd*' which is used to normalized the data to have o have zero mean and unity variance, where [*pn*] and [*tn*] are the processed input and output matrices respectively. *ps* and *ts* are the process settings that allow consistent processing of values for input and output dataset respectively.
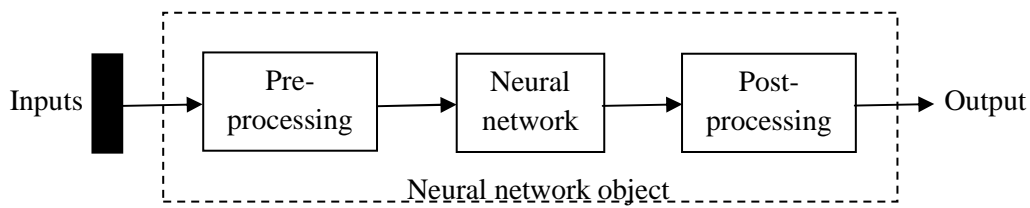
Figure II.2.7: Pre/Post-processing of input/output dataset.

2.   ***Network creation***. Feed forward neural network can be constructed using the command '*newff*' as:

```
Net1=newff(minmax(pn),minmax(tn),[6,3],{'logsig','logsig'},'trainbr');
```

The above syntax must contain the input and the processes matrices. In addition the number of the layer and the neurons number in each layer must be defined. The length of the matrix [6,3] express the number of the hidden layer in the neural network, while the value of each element in this matrix gives the number neurons in each layer. For instance, the above code establishes a neural network '*Net1*' with two layers. The first layer composed of six neurons with '*logsig*' transfer function. The second layer composed of three neurons with '*logsig*' transfer function. The term '*trainbr*' assign the Bayesian regularization train algorithm to perform training process. This algorithm updates weights and biases values according to Levenberg-Marquardt optimization method. There are about twelve back propagation training algorithms available in Matlab neural network toolbox. Try and error was used to differentiate

between these training algorithms. It was found that '*trainbr*' is the best training algorithm that could reach training the network in minimum required time.

3.   ***Data division***. Dataset must be dividing into three different categories; training, validation and testing as follow.

```
Net1.divideFcn ='dividerand';
Net1.divideParam.trainRatio=0.7;
Net1.divideParam.valRatio=0.15;
Net1.divideParam.testRatio=0.15;
```

where the option '*Net1.divideFcn*' specify the dividing function of the dataset available for neural network Net1. Matlab provides different dividing functions such as '*dividerand*' which divide the dataset in random procedure. Dividing functions are controlled by three parameters. These parameters assign the ratio of each division. The default ratios are 0.6, 0.2 and 0.2 for training, validation and testing division respectively.

4.   ***Initialize the weights and biases.*** Before starting training of the network. Initial values of weights and biases associated in the network (Net1) must be specified. Matlab automatically initiate weights and biases through the following command:

```
init(Net1);
```

5.   ***Train the network.*** Matlab neural network toolbox allows to the performance of the network during training process by using the following code:

```
net.trainParam.showWindow=true;
```

During training, there are two methods to evaluate the error in the output values obtained by the network with respect to the target output values. The first is the mean square error performance function '*mse*'. The second is the summation of square error performance function '*sse*'. The latter method was used in the present study and can be performed in matlab using the following syntax:

```
net.performFcn='sse';
```

Generally, training process required two parameters types. The first is general tainting parameters. These parameters are required to stop training process when any of them is reached. The following code lines present these parameters with a brief definition after comment Matlab sign '*%*',

```
net.trainParam.epochs=1000;      % maximum number of epochs to train
net.trainParam.time=120;         % maximum time to train in seconds
net.trainParam.goal=0.0001;      % Performance goal of 'sse' function
net.trainParam.min_grad=1e-20;   % Minimum performance gradient
net.trainParam.max_fail=10;      % Maximum validation failures
```

Figure II.2.8 shows the neural network window, the window shows that the data has been divided using the '*dividerand*' function, and the Bayesian regularization '*trainbr*' training method has been used with the summation of square error '*sse*' performance function. Matlab terminates the analysis as the performance function reaches the goal value. In addition, the analysis will be ended when the training time, gradient or the number of validation checks reaches a specific value even the performance goal function did not be reached. As presented in the above Matlab code lines: the training will be terminated if the time of the training or number of validation checks reaches 120 seconds or 10 respectively. The number of validation checks represents the number of successive iterations that the validation performance fails to decrease. Also, the magnitude of the gradient and the number of validation checks are used to terminate the training. The gradient will become very small as the training reaches a minimum of the performance. Thus, if the magnitude of the gradient is less than 1e-20, the training will stop.
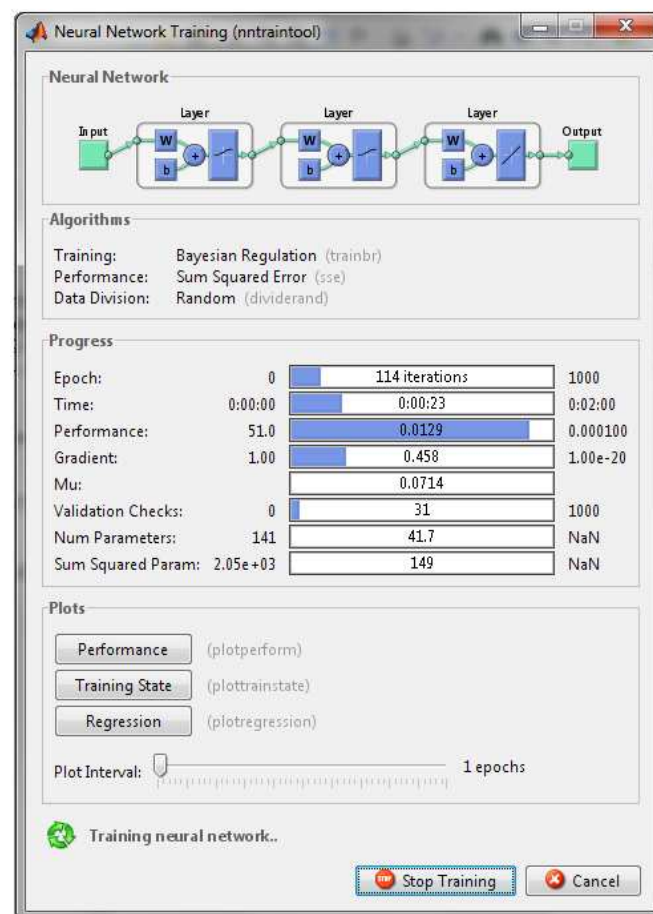
Figure II.2.8: neural network training window.

The second type of training parameters are depends on the optimization method of the training algorithm used to train the network. Herein, the parameters that should be associated

with the training algorithm are as follow:

```
net.trainParam.mu=0.005;        % Marquardt adjustment parameters
net.trainParam.mu_dec=0.1;      % decrease factor for mu
net.trainParam.mu_inc=10;       % increase factor for mu
net.trainParam.mu_max=1e10;     % maximum value for mu
```

'*train*' function is used to start training process. As shown in the following matlab code, '*train*' function takes three parameters: the initially created neural network, input data and output processes dataset. The output of '*train*' function is the trained neural network.

`Net1=train(Net1,pn,tn);` Figure II.2.9 presents the result network training. The three axes represent the training, validation and testing data. The dashed line in each axis represents the perfect result (i.e. outputs=targets). The solid line represents the best fit linear regression line between outputs and targets. The R value is the coefficient of correlation between the outputs and targets. As shown in the graph, the training data indicates a very good fit. The validation and test results also show R values that greater than 0.95.
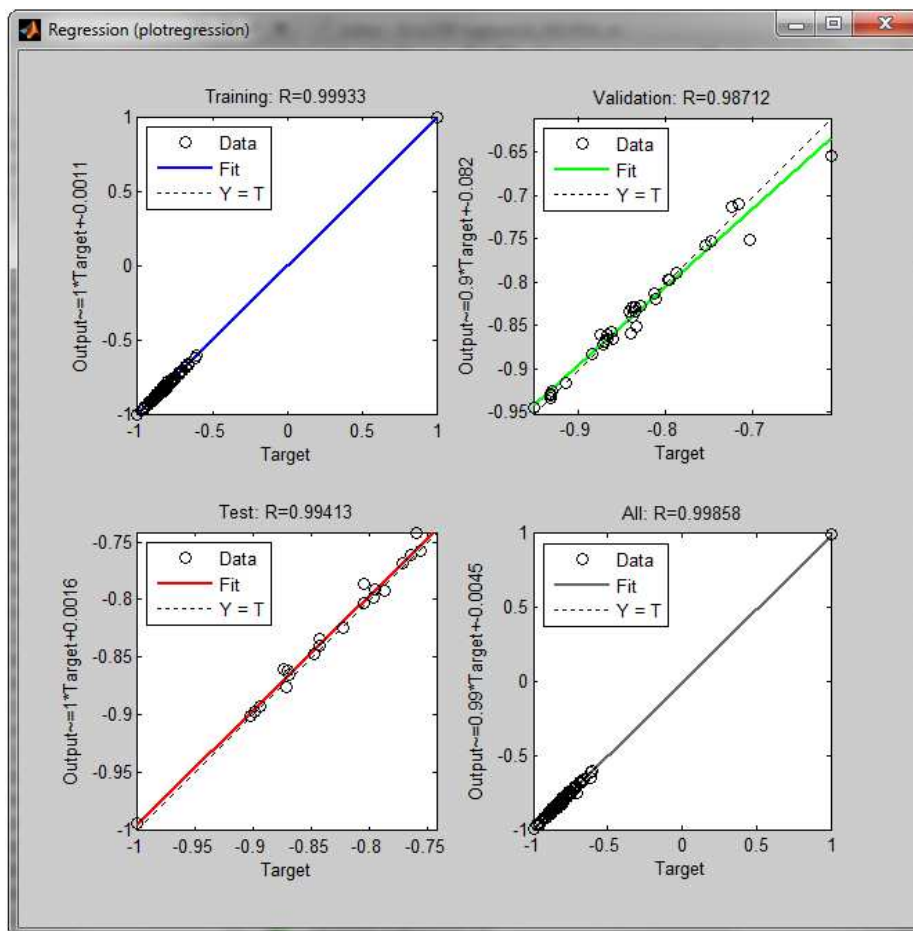
Figure II.2.9: Neural network training, validation and testing results.

6.   ***Using of the network.*** If a new data D want to be simulated using the trained neural network, the following statement can be used to calculate the corresponding outputs. D may

be a set of variables:

```
Res=mapminmax('reverse',sim(net,mapminmax('apply',D',ps)),ts);
```

II.2.5.3 design of experiments

Although, the neural network is capable to predict a certain response, the accuracy of the predicted responses are strongly related to the training dataset. Thus, the values of inputs to be simulated using the network should be within the range of the training dataset. The purpose of this section is to focus on the concept of design of experiments required to define the range of dataset used for training process. Generally, the experimental design is able to prepare a proper plane to sample the response levels at different values of the inputs variables. For simplicity, the experiments are usually initiated around the mean values of the design variables (input of the neural network).

There are several experimental designs available for the responses assigned. Such these experimental designs methods are the factorial design [Faravelli 1989; Bucher & Bourgund 1990; Maymon 1993; Wong *et al* 2005]. However, it should be noted that, in factorial design the total number of experiments increase exponentially with the number of the random variables. As a result it leads to unacceptably high computational costs. In order to reduce the number of experiments, Bucher & Bourgund (1990) proposed a design that consists of the axial points only, where the total number of experiments is $2n+1$: n is the number of input or random variables. For convenience, this design is termed as "$2n+1$ axial-point" design in the present study. Schematic representation of $2n+1$ axial-point is shown in Figure II.2.10 for a two design variables. The axial points that lie along the axis x_i can be represented as:

$$x_i^r = x_i^o \pm h_i \sigma_i \qquad \qquad \text{(II.2.4)}$$

where r is the experimental point number on the axis x_i (excluding the centre point). x_i^o is the centre point of the evaluation. σ_i is the standard deviation of the random variable i. h_i is a user-defined parameter.
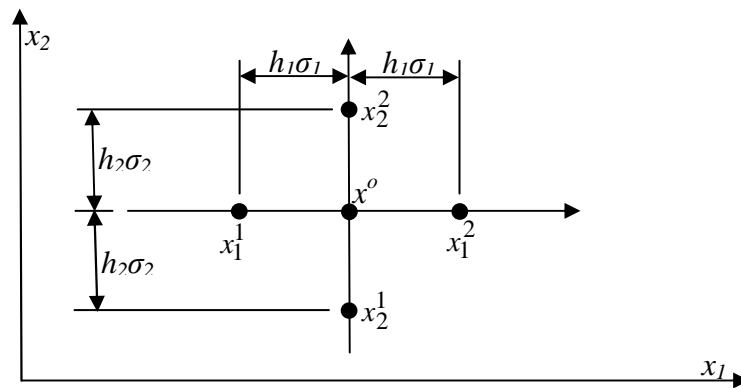
Figure II.2.10: *2n+1* axial point design.

It has been suggested that the centre point is set to the mean values of the random or input variables as an initial guess in the reliability problem [Bucher & Bourgund 1990]. The purpose of the reliability analysis based neural network is to verify the reliability index β obtained using First Order Reliability Method (FORM). β index corresponds the co-ordinates of the most probable design point obtained by FORM which will be explained in the next chapter. Thus in our case, the x_i^o vector will be equal to the co-ordinates of the most probable design point [Lemaire *et al* 2009]. Another experimental design scheme known as factorial design, called also hyper-cube, with order 2^n is shown in Figure II.2.11b [Soares *et el* 2002]. The advantage of this scheme is the capability to generate interactions between the sampling axes. In the present study, the mixed design Figure II.2.11c was used to reach more accurate responses obtained by the neural network. In addition, multiple levels of the mixed design were considered, each of these levels is constructed with different values of h; herein, we assume that the value of the parameter h ranges between 1~5.

(a) $2n+1$ axial design   (c) 2^n factorial design   (b) $2n+1$ & 2^n Mixed
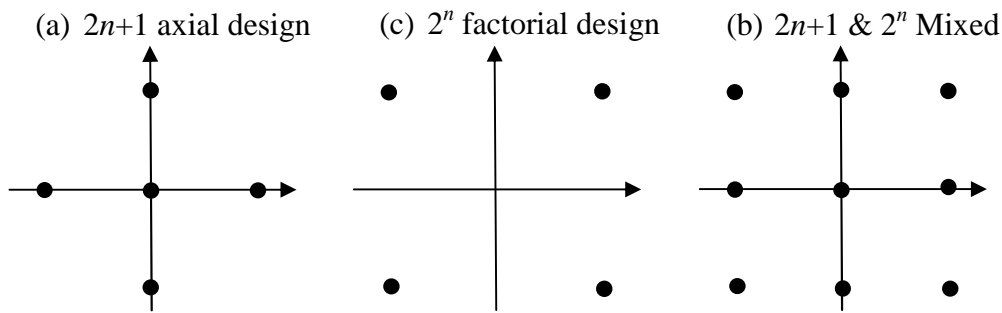
Figure II.2.11: Different sampling methods.

In the present study, neural networks were used to approximate the values of the structural responses. As they were used to predict:

- Loading actions (bending moment or shearing forces) in a certain point in the RC beam
- Strains in different positions of FRP strengthened RC beam: in concrete, adhesive layer and FRP material
- Deflection required for the serviceability limit state function at mid span of the RC beam.

II.2.6 CONCLUSIONS

Surface response method is the most widely regression tool. It is used to represent an explicit function of a structural response based on providing a dataset of reference responses and their corresponding variables. However, the accuracy of response surface method is limited by certain factors such as the number of variables, non-linearity nature of the problem. Thus, neural network applications were used recently instead of the response surface method, as neural network can provide an acceptable accuracy even with high number of variables and high nonlinearity.

The purpose of this chapter was to introduce all the basic fundamentals and the necessary aspects required to establish a structural response function using neural network applications. For example we touched the each individual component, general architecture, training, validation and testing of a neural network.

An important aspect, covered here, that is prior to the establishment of a neural network is the concept of design of experiments. Basically, this concept is an important step that is used to define the each point of the dataset required to train the neural application. Two methods of experiments, axial and hyper-cube, design were used together to provide a robust regression tool. In addition the chapter presents the brief details about the use of Matlab neural network toolbox provided in Matlab software.

PART II: STRUCTURAL RELIABILITY OF FRP STRENGTHENED RC BEAM

Chapter II.3: Structural reliability aspects

II.3.1 DEFINITIONS

II.3.1.1 General

For many years it has been assumed in design of structural systems that both loads and strengths are deterministic values. The strength of an element was determined in such a way that it exceeded the load with a certain margin. The ratio between the strength and the load was denoted the safety factor. This number was considered as a measure of the reliability of the structure. In codes of practice for structural systems values for loads, strengths and safety factors are prescribed. These values are traditionally determined on the basis of experience and engineering judgment. However, in new codes partial safety factors are used. Characteristic values of the uncertain loads and resistances are specified and partial safety factors are applied to the loads and strengths in order to ensure that the structure is safe enough. The partial safety factors are usually based on experience or calibrated to existing codes or to measures of the reliability obtained by probabilistic techniques.

Reliability of structural systems can be defined as the probability that the structure under consideration has a proper performance throughout its lifetime. Reliability methods are used to estimate the probability of failure. An important step in a reliability analysis is to decide which quantities should be modeled by stochastic variables and which should be modeled by deterministic parameters. The stochastic variables are denoted as $X=(X_1,\ldots, X_n)$. Typical examples of basic variables are loads, strengths, dimensions and materials. The basic variables can be dependent or independent. Structural reliability problem may have different types of uncertainty such as: loading, geometrical, material and analysis uncertainties. Generally, methods to measure the reliability of a structure can be divided in four groups [Ditlevsen & Madsen 1996]:

- *Level I methods*: The uncertain parameters are modeled by one characteristic value, as for example in codes based on the partial safety factor concept.

- *Level II methods*: The uncertain parameters are modeled by the mean values and the standard deviations, and by the correlation coefficients between the stochastic

variables. The stochastic variables are implicitly assumed to be normally distributed. The reliability index method is an example of a level II method.

- *Level III methods*: The uncertain quantities are modeled by their joint distribution functions. The probability of failure is estimated as a measure of the reliability.

- *Level IV methods*: In these methods the consequences (cost) of failure are also taken into account and the risk (consequence multiplied by the probability of failure) is used as a measure of the reliability. In this way different designs can be compared on an economic basis taking into account uncertainty, costs and benefits.

Level I methods can e.g. be calibrated using level II methods, level II methods can be calibrated using level III methods, etc. Level II and III reliability methods are considered in these notes. Level IV is out the scope of the present of the study.

II.3.1.2 Random variable

There are many ways to specify probabilistic characteristics of systems under uncertainty. Random variables are measurable values in the probability space associated with events of experiments. Accordingly, random vectors are sequences of measurements in the context of random experiments. A random variable X takes on various values x within the range -$\infty<x<\infty$. A random variable is denoted by an uppercase letter, and its particular value is represented by a lowercase letter. Random variables are of two types: discrete and continuous. If the random variable is allowed to take only discrete values, x_1, x_2, x_3,....,x_n, it is called a discrete random variable. On the other hand, if the random variable is permitted to take any real value within a specified mathematical expression, it is called a continuous random variable. Data description using maximum and minimum values only is not sufficient. Additional parameters are needed to accurately describe the properties of the variable mathematically. In this section, elementary statistical formulas and random variable are briefly described in order to facilitate an introduction to the following sections.

Mean: This is the most likely value of the observations. For a random variable, X, the mean value, μ_X, is defined as:

$$\mu_x = \frac{1}{n}\sum_{i=1}^{n} X_i \tag{II.3.1}$$

where n is number of observations, and X_i is the set of observations.

1. *Standard deviation*: Standard deviation, σ_X, estimates the dispersion of data from the mean value and can be expressed as:

$$\sigma_x = \sqrt{\frac{\sum\limits_{i=1}^{n} X_i - n\mu_X^2}{n-1}} \tag{II.3.2}$$

Another expression used to measure dispersion of a random variable is the variance (V_X) which equals to σ_X^2.

2. ***Coefficient of Variation***: Coefficient of variation, V_X is calculated as

$$CoV_X = \frac{\sigma_x}{\mu_X} \tag{II.3.3}$$

3. ***Bias***: Bias, λ_X is the ratio between the mean μ_X to the nominal value of the variable X.

$$\lambda_X = \frac{\mu_X}{X_n} \tag{II.3.4}$$

where, X_n is the nominal value of variable.

4. ***PDF & CDF functions***: If a large number of observations or data records exist, then a *frequency diagram* or *histogram* can be drawn. A histogram is constructed by dividing the range of data into intervals of approximately similar size and then constructing a rectangle over each interval with an area proportional to the number of observations that fell within the interval as shown in Figure II.3.1. The histogram is a useful tool for visualizing characteristics of the data such as the spread in the data and locations. If the rectangular areas are normalized so that the total sum of their areas is unity, then the histogram would represent the probability distribution of the sample population, and the ordinate would represent the probability density. The probability that a randomly chosen sample will fall within a certain range can be calculated by summing up the total area within that range. In this sense, it is analogous to calculating mass as density times volume where

Probability=Probability density x *Interval size* (II.3.5)
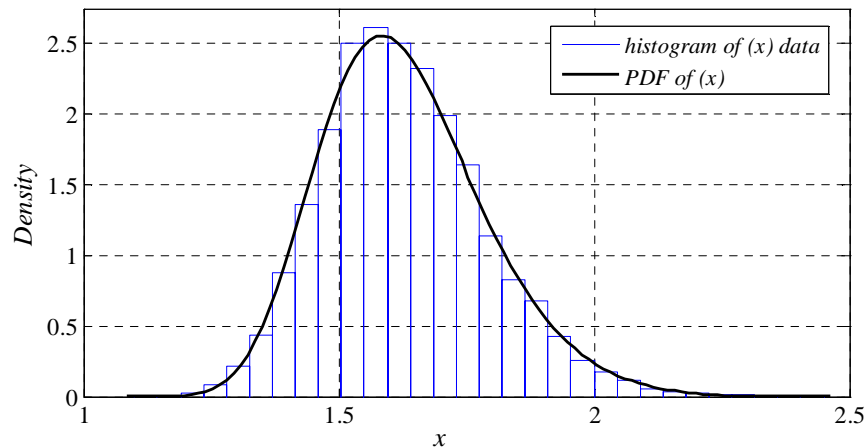
Figure II.3.1: Histogram of random variable x.

There are an infinite number of values a continuous variable can take within an interval, although there is a limit on measurement resolution. One can see that if the histogram was constructed with a very large number of observations and the intervals were to become infinitesimally small as the number of observations grew, the probability distribution would become a continuous curve. The mathematical function that describes the distribution of a random variable over the sample space of the continuous random variable, X, is called the probability density function *PDF* and designated as $f_X(x)$ (see Figure II.3.1). The *PDF* is only defined for continuous random variables. If an interval $[a,b]$ of the random variable x is specified as shown in Figure II.3.2, the probability of X falling between $[a,b]$ is obtained by integrating the *PDF* over this interval as :

$$p(a < X < b) = \int_a^b f_X(x)dx \qquad (II.3.6)$$
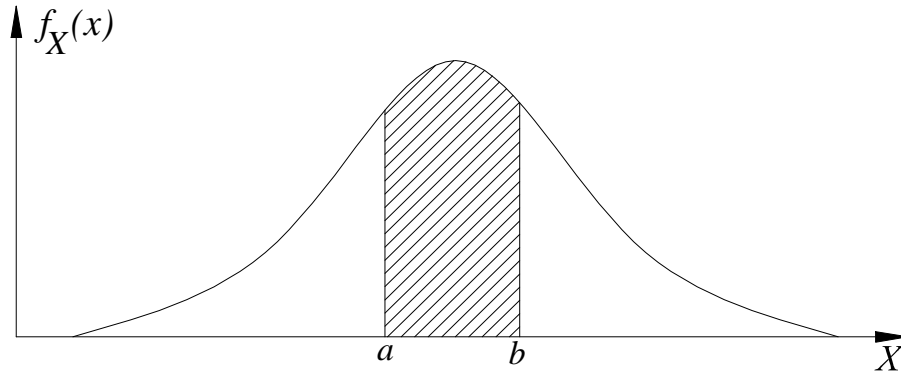
Figure II.3.2: *PDF of X.*

Another way to describe the probability distribution for both discrete and continuous random variables is the Cumulative Distribution Function (*CDF*), $F_X(x)$. The *CDF* is defined for all values of random variables X from $-\infty$ to ∞. For a certain value x_1 of a random variable X the *CDF* is equal to the probability that X is less than or equal to a realized value x. Figures II.3.3a & b show graphical representation of the *PDF* and the corresponding *CDF* function of random variable X respectively. For a continuous random variable, $F_X(x)$ is calculated by integrating the *PDF* for all values of X less than or equal to x:

$$F_x(X) = \int_{-\infty}^x f_X(x)dx \qquad (II.3.7)$$

A Cumulative Distribution Function is everywhere non-negative and the summation of all probabilities over the entire design space is equal to 1; i.e. 100% probability. The probability for X falling between $-\infty$ and x_1 is referred to as *CDF*:

$$p(-\infty < X < x_1) = F_X(x_1) = \int_{-\infty}^{x_1} f_X(x)dx \tag{II.3.8}$$
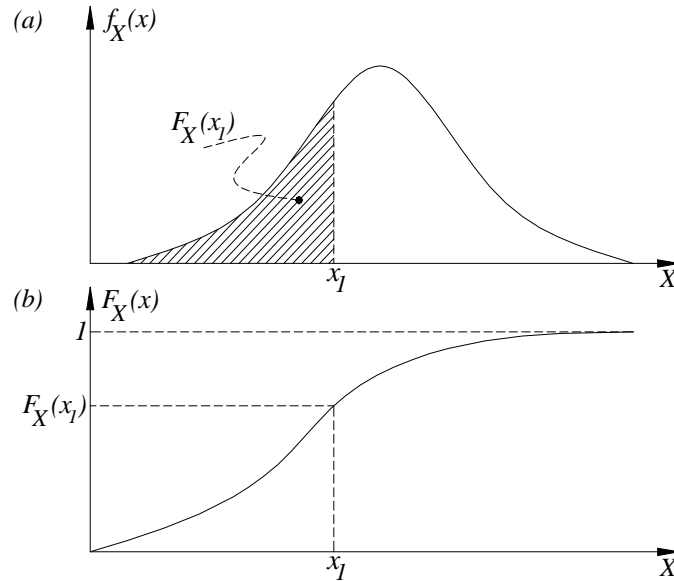
Figure II.3.3: Histogram of random variable *x*.

In evaluating structural reliability, several types of probability distributions are used to model the design or random variables. Selection of the distribution function is an essential part of obtaining probabilistic characteristics of structural systems. The selection of a particular type of distribution depends on:

- The nature of the problem

- The underlying assumptions associated with the distribution

- The shape of the *PDF* and *CDF* curves obtained after estimating data

- The convenience and simplicity afforded by the distribution in subsequent computations

The most common distribution is the Normal, also known as Gaussian, distribution. The *PDF* for normal random variable *X* are expressed mathematically as:

$$f_X(x) = \frac{1}{\sigma_X \sqrt{2\pi}} \exp\left[-\frac{1}{2}\left(\frac{x - \mu_X}{\sigma_X}\right)^2\right] \tag{II.3.9}$$

where μ_X and σ_X denote the mean and standard deviation of the variable *X*, respectively, and *X* is identified as $N(\mu_X, \sigma_X)$. The density function and corresponding parameters of normal distribution are shown in Figure II.3.4. The *PDF* of the Gaussian distribution is also known as a *bell curve* because of its shape in the graph. The Gaussian distribution is symmetric with respect to the mean and has inflection points at $x = \mu_X \pm k\sigma_X$, where *k* is any positive number.

The areas under the curve within one, two, and three standard deviations are about 68%, 95.5%, and 99.7% of the total area, respectively.
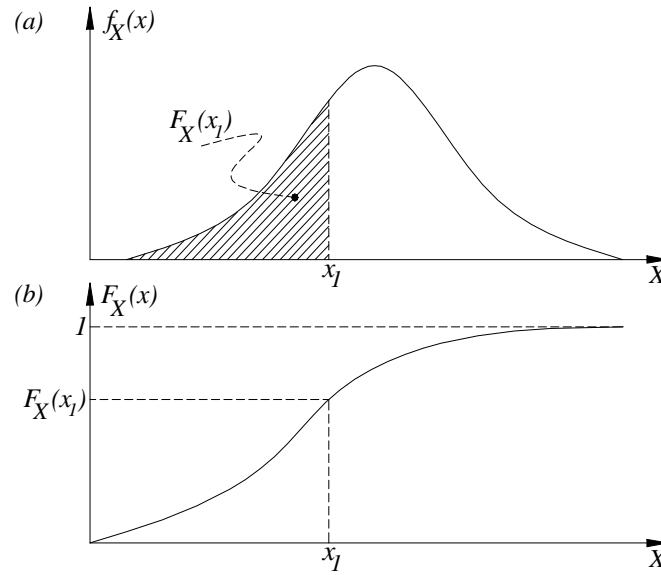
Figure II.3.4: Normal Density Function.

The Gaussian distribution can be normalized by defining a new dataset u_1, u_2, u_3,...,u_n based on the basic dataset x_1, x_2, x_3,…,x_n. Normalization is carried out using: $u_i=(x_i-\mu_X)/\sigma_X$ and yields the standard normal distribution $N(0,1)$. The density function of a standard normally distributed variable U is given by:

$$f_X(x) = \frac{1}{\sqrt{2\pi}} \exp\left(\frac{-u^2}{2}\right) \tag{II.3.10}$$

There is no closed-form solution for the *CDF* of a Normal random variable but tables have been developed to provide values of the *CDF* for the special case in which $\mu_X=0$ and $\sigma_X=1$. These tables can be used to obtain values for any general normal distribution. For convince, the notations $\Phi(x,\mu_X,\sigma_X)$ and $\phi(x,\mu_X,\sigma_X)$ expresses the *CDF* and *PDF* values receptively of a normal random variable (X) with mean (μ_X), and standard deviation (σ_X), while $\Phi(x)$ and $\phi(x)$ expresses the *CDF* and *PDF* values receptively of the variable (X) with standard normal distribution; $\mu_X=0$ & $\sigma_X=1$.

There are many types of density distribution such as Log-Normal, Uniform, Extreme Value… etc. Any random variable must be defined using its individual parameters and density distribution. In most cases, such these parameters are related mathematically to the mean and the standard deviation of the variable. Properties and parameters of all other probability distributions used in the present study are given in Appendix B. In the present study, Matlab statistics toolbox was used to perform all the required statistical calculation

such as:

- The statistical properties of random variable such as mean, standard deviation, etc.

- Calculation the *CDF* and *PDF* values for a random variable.

- Fitting the distribution of a random variable based on a large dataset of this variable.

It is meant by fitting the distribution for given observations of a random variable is to choose a certain distribution and the corresponding parameters of this distribution. Matlab software was used to the maximum possible distribution that can accurately simulate these observations of the random variable. To be able to decide which distribution is better for a particular random variable, the difference between actual observation values and the fitted theoretical distribution values is quantified. The Chi-Square test is often used to assess the "goodness-of-fit" between an obtained set of frequencies in a random sample and what is expected under a given statistical hypothesis. The steps to be followed to determine the most accurate distribution of a random variable are given in Appendix B.

5.   ***Coefficient of correlation***: statistical analysis of dataset of two random variables may show a correlation between them. For two datasets, $(x_1, x_2, x_3,...., x_n)$ and $(y_1, y_2, y_3,...., y_n)$ of two random variables *X* are *Y* are given, the coefficient of correlation between two random variables $(\rho_{X,Y})$ can be estimated as:

$$\rho_{X,Y} = \frac{1}{1-n} \frac{\left(\sum_{i=1}^{n} X_i Y_i\right) - n\mu_X \mu_Y}{\sigma_X \sigma_Y} \qquad \text{(II.3.11)}$$

where *n* is the number of samples in the dataset. μ_X and μ_Y are the mean values of *X* and *Y* respectively. σ_X and σ_Y are the standard deviation of *X* and *Y* respectively.

II.3.1.3 Isoprobabilistic transformation

The calculation of reliability index β requires transformation *T* of the random variable vector {*X*} from the physical variable space to standard, centered and independent variables which will be discussed in this section. As previously defined that, the reliability of a structural element is defined by the knowledge of the limit state $G(x_1, x_2, x_n)=0$ which is function of a chosen random design variables and other deterministic design variables, the later are called limit state function parameters. A representation of the limit state function – for a simplified case with two variables – in the physical variable space is given in Figure II.3.5a. As shown, the limit state separate the physical variable domain into two sub-domains, the safety domain and the failure domain which can be expressed as $G(x_i)>0$ and $G(x_i)\leq0$ respectively.

The measure of the reliability index must be performed in a standardized Gaussian space as given in Figure II.3.5b [Lemaire *et al* 2009]. Thus, the limit state $G(x_i)$ must be redefined using the standardized space $H(u_i)$ instead of the physical space using the transformation T. Each corresponding variable u_i in the standardized apace are non-dimensional and must be represented as standard normal variable with $\mu_u=0$ and $\sigma_u=1$:

$$u_i = T_i(x_i) \rightarrow H(u_i) = G(T_j^{-1}(x_i)) \qquad \text{(II.3.12)}$$

(a) Physical space   (b) Standardized space
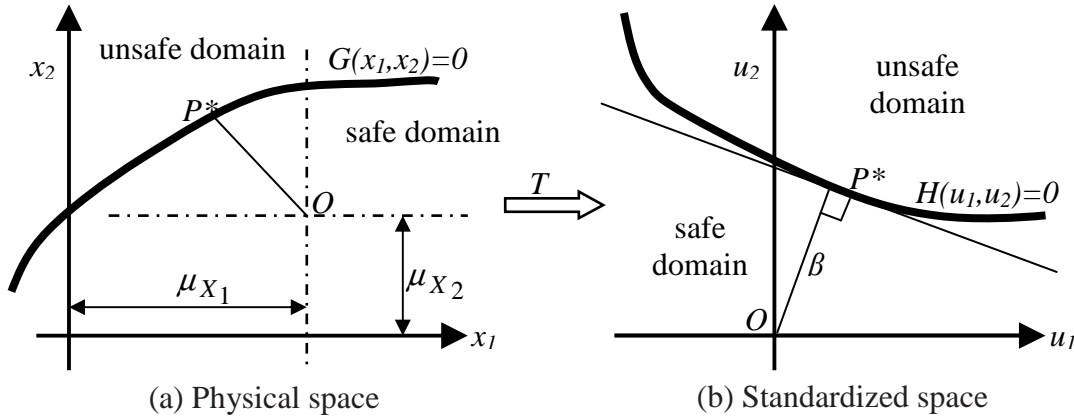
Figure II.3.5: Transformation of physical space into standardized space

Transformation depends on the correlation between the variables. For non-correlated variables X_i with a distribution $F_{Xi}(x_i)$, it is possible to express transformation T by writing the equality of cumulative density functions for variables x_i and u_i and hence the isoprobabilistic transformation:

$$x_i \xrightarrow{\ T\ } u_i \ \text{ defined by: } \ \Phi(u_i) = F_{X_i}(x_i) \qquad \text{(II.3.13)}$$

and therefore:

$$x_i \xrightarrow{\ T\ } u_i = \Phi^{-1}\left(F_{X_i}(x_i)\right) \qquad \text{(II.3.14)}$$

If F_{X_i} is invertible for any value of x_i, the inverse transformation is defined as:

$$u_i \xrightarrow{\ T^{-1}\ } x_i = F_{X_i}^{-1}\left(\Phi(u_i)\right) \qquad \text{(II.3.15)}$$

Differentiating the equality of probabilities, Equation II.3.13, for variables x_i and u_i leads to,

$$\frac{d\Phi(u_i)}{du_i} du_i = \frac{dF_{X_i}(x_i)}{dx_i} dx_i \qquad \text{(II.3.16)}$$

Thus,

$$\phi(u_i)du_i = f_{X_i}(x_i)dx_i \qquad \text{(II.3.17)}$$

and finally,

$$\frac{dx_i}{du_i} = \frac{\phi(u_i)}{f_{X_i}(x_i)} = \frac{\phi(\Phi^{-1}(F_{X_i}(x_i)))}{f_{X_i}(x_i)}$$ (II.3.18)

Based on the above described transformation, Table II.3.1 represents the random variable x_i as function of the normalized variable u_i and the corresponding differentiation dx_i/du_i for all the distribution types used in the present study. All the parameters associated in the different distributions are given in Appendix B.

Isoprobabilistic transformation of correlated variables from the physical space to centered normalized space requires more mush calculation than isoprobabilistic transformation of un-correlation variables. The first step towards isoprobabilistic transformation of two correlated variables, X_1 and X_2 with coefficient of correlation ρ, is to transform them into a centered and normalized correlated variables, Y_1 and Y_2, using equations II.3.15 & II.3.18. Thus, the transformations can be expressed as:

$$y_i \xrightarrow{\ T^{-1}\ } x_i = F_{X_i}^{-1}(\Phi(y_i))$$ (II.3.19)

$$\frac{dx_i}{dy_i} = \frac{\phi(y_i)}{f_{X_i}(x_i)} = \frac{\phi(\Phi^{-1}(F_{X_i}(x_i)))}{f_{X_i}(x_i)}$$ (II.3.20)

The two variables new, Y_1 and Y_2, are still correlated with the same coefficient of correlation ρ. The next step is to decorrelate Y_1 and Y_2. An alternative way to define the transformation from the u-space to the intermediate y-space is to use the Nataf transformation method. This transformation is in general only an approximate transformation. A new correlation coefficient ρ_o in y-space is obtained as [Lemaire *et al* 2009]:

$$\rho = \int_{-\infty}^{\infty} \int_{-\infty}^{\infty} \frac{x_1(y_1) - \mu_{x_1}}{\sigma_{x_1}} \frac{x_2(y_2) - \mu_{x_2}}{\sigma_{x_2}} \phi_2(y_1, y_2, \rho_o) dy_1 dy_2$$ (II.3.21)

where ϕ_2 is 2-dimensional normal density, with zero means, unit standard deviations and the coefficient of correlation ρ_o as:

$$\phi_2(y_1, y_2, \rho_o) = \frac{1}{2\pi\sqrt{1-\rho_o^2}} \exp\left[-\frac{y_1^2 - 2y_1 y_2 \rho_o + y_2^2}{2(1-\rho_o^2)}\right]$$ (II.3.22)

The solution of Equation II.3.21 to obtain the correlation ρ_o is available in many statistical text books [i.e. Lemaire *et al* 2009]. Eventually, the transformation from y-space to the centered, normalized and decorrelated u-space is obtained as:

$$y_1 = u_1$$ (II.3.23a)

$$y_2 = \rho_o u_1 + \sqrt{1 - \rho_o^2}\, u_2 \qquad\qquad (II.3.23a)$$

Table II.3.1: Transformation from physical space to normalized space.

Distribution type	$u_i \xrightarrow{\;T^{-1}\;} x_i$ & dx_i/du_i	parameters
Normal	$x_i = u_i \sigma_X + \mu_X$ $\dfrac{dx_i}{du_i} = \sigma_X$	μ_X, σ_X
Log-Normal	$x_i = \exp\!\left(u_i \sigma_{\ln(X)} + \mu_{\ln(X)}\right)$ $\dfrac{dx_i}{du_i} = \sigma_{\ln(X)} x_i$	$\mu_{\ln(X)}$, $\sigma_{\ln(X)}$
Weibull	$x_i = \alpha\left\{-\ln\left[1 - \Phi(u_i)\right]\right\}^{1/\beta}$ $\dfrac{dx_i}{du_i} = \dfrac{\alpha}{\beta}\dfrac{\phi(u_i)}{\left[1 - \Phi(u_i)\right]}\left\{-\ln\left[1 - \Phi(u_i)\right]\right\}^{(1-\beta)/\beta}$	α, β
GEV	$x_i = m + \dfrac{s}{k}\left\{\left[-\ln\left(\Phi(u_i)\right)\right]^{-k} - 1\right\}$ $\dfrac{dx_i}{du_i} = s\dfrac{\phi(u_i)}{\Phi(u_i)}\left[-\ln\left(\Phi(u_i)\right)\right]^{-k-1}$	k, m, s
Uniform	$x_i = (b-a)\Phi(u_i) - a$ $\dfrac{dx_i}{du_i} = (b-a)\phi(u_i)$	a, b
Bi-Model	The value of x_i for a known value of u_i can be obtained using numerical solution of the following equation: $r\Phi(x, \mu_{1X}, \sigma_{1X}) - (1-r)\Phi(x, \mu_{1X}, \sigma_{1X}) = \Phi(u_i)$ $\dfrac{dx_i}{du_i} = \dfrac{\phi(u_i)}{r\phi(x, \mu_{1X}, \sigma_{1X}) - (1-r)\phi(x, \mu_{1X}, \sigma_{1X})}$	μ_{1X}, μ_{2X}, σ_{1X}, σ_{2X}, r

All the parameters associated in each distribution are given in Appendix B.

II.3.2 MESURE OF RELIABILITY

In a limit-state design, the design of structures is checked for all groups of limit-states to ensure that the safety margin between the maximum likely loads and the weakest possible resistance of the structure is large enough. The limit states that have been defined in the structural codes are:

• Serviceability limit state (SLS), defined as the limit between the states where the performance of the structure is acceptable and the state where the structure is no longer serviceable. Normally associated with economical consequences. Examples of SLS are deflection, onset of corrosion, crack widths, spalling, vibrations, aesthetics, etc.

- Ultimate limit state (ULS), defined as the limit between the states where the structure is no longer serviceable and the state where the structure has collapsed, for example, due to excessive material degradation. Examples of ULS are collapse, buckling, and loss of instability of the structure.

Each failure mode may be controlled by a set of design criteria. Limit-state design criteria are developed based on ultimate strength as well as use of the reliability methods. The design criteria have traditionally been expressed in the format of Working Stress Design (WSD) (or Allowable Stress Design, ASD), where only one safety factor is used to define the allowable limit. However, in recent years, there is an increased use of the Load and Resistance Factored Design (LRFD) that comprises of a number of load factors and resistance factors reflecting the uncertainties and safety requirements. A general safety format for LRFD design may be expressed as:

$$\sum \gamma_i S_i \leq \phi \sum R \qquad\qquad (II.3.24)$$

where S_i and γ_i are the load value (e.g. dead, live, …etc) and its corresponding load factor respectively. R is the resistance (capacity) of the structural element. ϕ is a general resistance factor applied to the resistance. Basically, reliability analysis requires expressing the limit state function without the load or resistance factors. Thus, the limit state function for the purpose of reliability analysis can be expressed as

$$G(R,S) = R - S \leq 0 \qquad\qquad (II.3.25)$$

R and S involved a high uncertainty due to the variations exited in load and material propertied. The simplest mathematical model for describing the event 'failure' comprises a load variable S and a resistance variable R. If R and S are independent of time, the event 'failure' can be expressed as follows:

$$\{\text{failure}\} = \{R < S\} \qquad\qquad (II.3.26)$$

The concept of structural reliability is illustrated in Figure II.3.6, where load and strength are both modeled as random variables. Failure occurs when load exceeds strength. Denoting the probability density function for load and strength as $f_S(x)$ and $f_R(x)$ respectively, $F_S(x)$ and $F_R(x)$ are the *CDF* of the load and strength respectively. The failure probability P_f may then be expressed as [Lemaire *et al* 2009]:

$$P_f = P(R < S) = \int_{-\infty}^{\infty} P(R \leq x)P(x \leq S \leq x + dx) = \int_{-\infty}^{\infty} F_R(x)f_S(x)dx \qquad (II.3.27)$$

Alternatively the probability of failure can be evaluated by

$$P_f = \int_{-\infty}^{\infty} P(x \le R \le x+dx)P(S \ge x) = \int_{-\infty}^{\infty} f_R(x)\big(1-F_S(x)\big)dx = 1 - \int_{-\infty}^{\infty} f_R(x)F_S(x)dx \qquad \text{(II.3.28)}$$
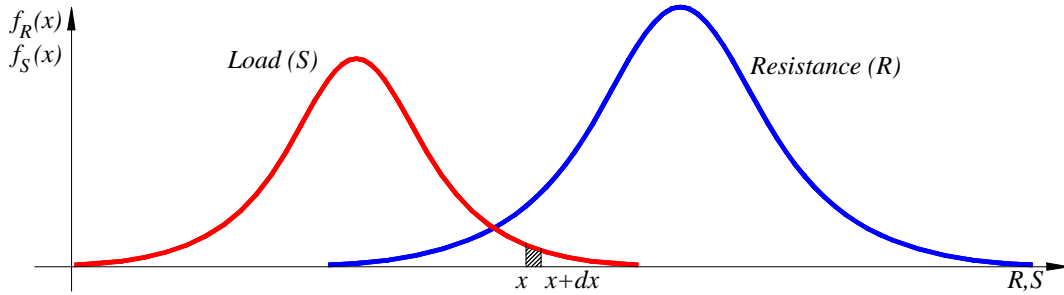
Figure II.3.6: Densities of *R* and *S*.

Reliability index of structure is a measure of its safety level which takes into account the uncertainties inherent in the design variables. The first definition of this index was in 1969 by Cornell (called also Cornell index $\beta_{Cornell}$). This index expresses the ratio between the mean of the performance function *G, G=R-S,* and its standard deviation. As *R* and *S* are random variables with mean values μ_R and μ_S respectively and with standard deviations σ_R and σ_S respectively. If *R* and *S* are non-correlated variables with normal distributions Cornell index can be expressed as:

$$\beta_{Cornell} = \frac{\mu_R - \mu_S}{\sqrt{\sigma_R^2 + \sigma_S^2}} \qquad \text{(II.3.29)}$$

Due to simplicity of determining Cornell reliability index it was frequently adopted by the authors to perform reliability analysis of RC structures (e.g. [Pham & Al-Mahidi 2008]). The major drawback of the index of Cornell is that its value depends on the form of the performance function in case of nonlinear limit states or variables with non normal distribution. For example if the same performance function is defined in two different methods, *G=R-S* or *G=R/S*-1, two values of reliability index are obtained [Massih 2007].

There are many sources of uncertainties that affect the resistance (*R*) and loading (*S*) models. The possible sources of uncertainty in (*R*) model can be divided into three categories:

  ➢ Geometrical uncertainties: these are the uncertainties in the overall dimensions of the member which can affect the cross-sectional area, moment of inertia… etc.

  ➢ Material uncertainties: the uncertainties associated with material properties are uncertainties in the strength of the material, the modulus of elasticity …etc.

  ➢ Model uncertainties: the uncertainty resulting from approximate methods of analysis.

Each of these uncertainty sources has its own statistical properties; i.e. bias, coefficient of variation, and distribution type. While uncertainty exist in loads are generally depend on the

type of the loads such as self weight of the element, surface loads, truck loads…etc.

II.3.3 ESTIMATION OF RELIABILITY

II.3.3.1 First order reliability method

The First Order Reliability Method (FORM) provides a practical scheme of computing small probabilities of failure at high dimensional space spanned by the random variables in the problem. FORM is based on a first order Taylor Series expansion of the limit state function, which approximates the failure surface by a tangent plane at the point of interest as shown in Figure II.3.5b. It is not always possible to find a closed form solution for a non-linear limit state function or a function including more than two random variables. Hence, to convert a non-linear limit state function into simple polynomials, Taylor series is used. The expansion of a function, $f(X)$ at a certain point "a" is given by;

$$f(X) = f(a) + (X-a)f'(a) + \frac{(X-a)^2}{2}f''(a) + \cdots\cdots\cdots\frac{(X-a)^n}{n!}f^n(a) \quad \text{(II.3.30)}$$

FORM uses this expansion to simplify the limit state function, $g(X_1, X_2, \ldots, X_n)$ by considering the expansion of the Taylor series after truncating terms higher than the first order. The expansion is done at the design point P^*, called also the most probable failure point (see Figure II.3.5b). To overcome the non-invariance of the index of Cornell, Hasofer & Lind (1974) defined the reliability index β as the length of vector OP^* (Figure II.3.5b). This definition is the most widely used in the structural reliability application applications. Calculation of the reliability index is thus reduced to the resolution, in standardized space, of the following optimization problem [JCSS 2001]:

$$\beta = OP^* = \min\{d(u_k)\} = \min\left(\sqrt{\sum_{i=1}^{n} u_i^2}\right), \text{ under the constraint } H(u_k) \leq 0 \quad \text{(II.3.31)}$$

where u_K is the vector of random variables in the normal, centered and non-correlated u-space. There are several algorithms to search the reliability index [Lemaire 2009] such as first order algorithms (i.e. Hasofer-Lind-Rackwitz-Fiessler first order), second order algorithms (i.e. Newton method and sequential quadratic programming method) and hybrid algorithms. These algorithms are based on iterative processes that require the calculation of partial derivatives of the performance function. In the present study Hasofer-Lind-Rackwitz-Fiessler *HLRF* is used to solve the optimization problem, given by Equation II.3.31, as it is the most frequently used in the literature. Figure II.3.7 present a graphical representation of Hasofer-Lind-Rackwitz-Fiessler algorithm.
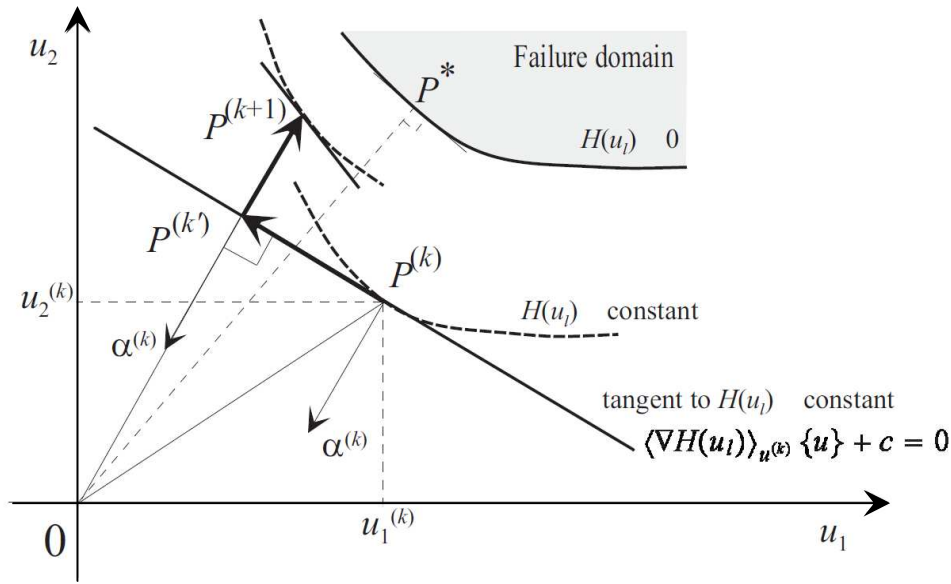
Figure II.3.7: graphical representation of Hasofer-Lind-Rackwitz-Fiessler algorithm.

Hasofer-Lind-Rackwitz-Fiessler algorithm can be summarized by the following steps:

1. Define the appropriate limit-state function $G(x_1, x_2, \ldots x_n)$.

2. Transformation of all the random variables from physical x-space to a normalized, centered and non-correlated u-space

3. Substitution of transformed variables, x_i, $i=1, 2, \ldots n$, into the limit state defined x-space to obtain the limit state in u-space; $H(u_1, u_2, \ldots u_n)$.

4. Choosing a starting point $\{u\}^{(k)}$, setting first iteration as $k=0$, generally the origin of the space in the absence of specific information.

5. Evaluate the limit-state function $H(u_l^{(k)})$

6. Calculate the limit state gradient $\{\nabla H(u_l)\}^{(k)}$ and its norm $\| \nabla H(u) \|^{(k)}$, then deducing $\{\alpha\}^{(k)}$ as:

$$\{\alpha\}^{(k)} = \frac{\{\nabla H(u)\}^{(k)}}{\| \nabla H(u) \|^{(k)}} \qquad (II.3.32)$$

7. Calculate the reliability index $\beta^{(k)}$ as follow:

$$\beta^{(k)} = -\left(\langle u \rangle^{(k)} \{\alpha\}^{(k)} \right) + \frac{H(u)^{(k)}}{\|\nabla H(u)\|_{(k)}} \qquad (II.3.33)$$

where the convention $\langle a \rangle$ returns zero 0 if $a<0$, and a if $a \geq 0$.

8. Calculate $\{u\}^{(k+1)}$ as follow:

$$\{u\}^{k+1} = \beta^{(k)} \{\alpha\}^{(k)} \qquad (II.3.34)$$

9. If $\left|\{u\}^{k+1} - \{u\}^k\right| \leq \varepsilon$ stop the calculation; otherwise set $k=k+1$ and go to step 2.

After convergence, it could be verified that $\{u\}^{(k+1)}=\{u\}^{(k)}$ and $H(u_l^{(k)}) = 0$. The algorithm is stopped according to a criterion calculated either from a norm of vector $\{u\}$, for example, $\left|\{u\}^{k+1} - \{u\}^k\right| \leq \varepsilon$ or, better still, from a tolerance on all the components of the vector $\{u\}$. From the properties of the u-space (normalized, centered and non-correlated) it can be concluded that it follows immediately rotational symmetry about the origin. Thus the probability of failure can be determined as,

$$P_f \approx \Phi(-\beta) \qquad\qquad (\text{II.3.35})$$

where $\Phi(\cdot)$ is the distribution function of the reduced centered normal distribution.

The computed α_i values, calculated in step 6, provide the sensitivity of the reliability index with respect to u_i. Figure II.3.8 shows graphical representation of α_i values which called also directional cosines at the design point. Sensitivity factors have two major purposes. First, these sensitivity factors show the contributions of the random variables to the safety-index or probability of failure. Second, the sign of the sensitivity factor shows the relationship between the performance function and the physical variables. A positive α_i means that the performance function $H(u_1, u_2, ... u_n)$ decreases as the random variable increases, and a negative factor means $H(u_1, u_2, ... u_n)$ increases as the random variable increases.
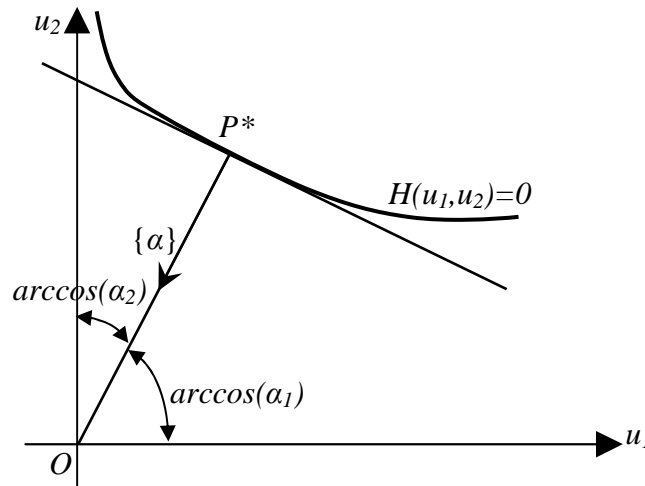
Figure II.3.8: Graphical representation of direction cosines at the design point.

The importance of evaluating sensitivity factors is to identify the influence of its variation on the reliability index and to select the most significant variables. The physical meaning of α_i implies the relative contribution of each random variable to the reliability index (Figure

II.3.8). For example, the larger the α_i value is, the higher the contribution towards the reliability index. This is due to

$$\alpha_1^2 + \alpha_2^2 + \alpha_3^2 + \cdots\cdots\alpha_n^2 = 1 \tag{II.3.36}$$

From the definition of β as the distance from the origin to the limit-state surface, $H(u_1, u_2, \dots u_n)=0$, it follows that

$$\alpha_i = \frac{\partial \beta}{\partial u_i} = \frac{\partial}{\partial u_i}\sqrt{u_1^2 + u_2^2 + u_3^2 \cdots\cdots + u_n^2} = -\frac{u_i}{\beta} \tag{II.3.37}$$

The FORM algorithm described above as used to perform reliability analysis of the limit stat function $G(x_i)=R-S=0$, where R and S in this case are the resistance of the structural element and the corresponding applied action (bending moment or shearing force) respectively. The resistance R is to be calculated using the proposed simplified designed formulas for the limit states, failure mode, reported in chapter II.1.

II.3.3.2 Simulation Method

II.3.3.2.1 Pseudo-random number generation

Generation of pseudo-random numbers is at the root of all simulation methods. The most widely used method for generating a series x_i is based on the calculation of the remainder of a division by an integer m; the most common expression is written in the form:

$$x_{i+1} = (ax_i + c)(\bmod m) \tag{II.3.38}$$

where the multiplier a, the increment c and the denominator m are non-negative integers; mod is the operator of integer division: A (mod B)= the remainder from the integer division of A by B. The previous notation is equivalent to:

$$x_{i+1} = (ax_i + c)k_i \qquad \text{with} \qquad k_i = \text{integer}\left(\frac{ax_i + c}{m}\right) \tag{II.3.39}$$

in which the operator integer(.) indicates the integer part of the division. The number obtained, x_i, belongs to the interval $[0,m[$. In order to have a number v_i belonging to the interval $[0, 1[$, it is sufficient to divide by m: $v_i=x_i/m$.

The generated numbers (v_i; $i=1,2,\dots n$) follow a uniform distribution within the indicated interval: $[0, 1[$. It is clear that such procedure is periodic. Each period is lower than or equal to m and contains a maximum of m distinct numbers. In order to ensure a significant number of non-repeated values, it is necessary to choose the largest possible m. For a general stochastic variable x with a distribution function is $F_X(x)$. The variable x, defined by:

$$x_i = F_X^{-1}(v_i) \tag{II.3.40}$$

Herein, the described pseudo-random number generation method, described above, was performed using Matlab statistic toolbox.

II.3.3.2.2 Classical Monte-Carlo simulation Method

Classical Monte-Carlo simulation is considered to be the simplest and most robust method for the evaluation of the probability of failure. In addition, the method is general and did not depend on the shape of the limit state function. From other side, it represents the most expensive methods as it required a huge number of simulations. The principle of simulation methods is to carry out a random sampling in the variable space, which could be physical or standardized. For each of the samples, the limit state function is evaluated to conclude whether its configuration lie in the safety domain or the failure domain. The steps of the procedure are as follow:

1. Define the appropriate limit-state function $G(x_1, x_2, …..x_n)$.
2. Transformation of all the random variables from physical x-space to a normalized, centered and non-correlated u-space using the Isoprobabilistic transformation explained in section II.3.1.3.
3. Substitution of transformed variables, x_i, $i=1, 2, ...n$, into the limit state $G(x_1, x_2, …..x_n)$ defined x-space to obtain the limit state function $H(u_1, u_2, ….. u_n)$ in u-space.
4. Choosing an appropriate sampling number N_s. Generally, the value of N_s depends on the required accuracy of the simulation.
5. Generation of a random vectors, U_i, i=1,2,…n, with normal distribution having a mean value and standard deviation equal to 0 and 1 respectively. Figure II.3.9 presents a graphical representation of Monte-Carlo simulations in case of two variables.
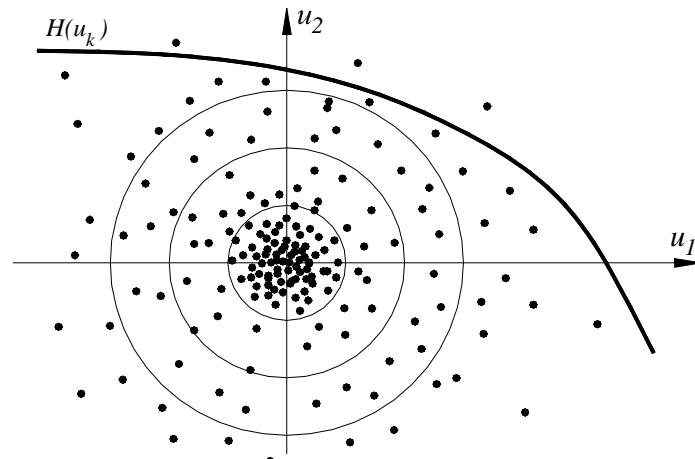
Figure II.3.9: Classical Monte-Carlo simulations in case of two variables.

6. For each simulation case, calculate the value of the limit state function $H(u_1,u_2,...u_n)^r$, $r=1,2,...N_s$.

7. Depending on the case, a vector of indicators, $I_D(H(u))$, is evaluated according to,

$$I_D^r(H(u)) = \begin{cases} 0 & \text{if} \quad H(u) > 0 \\ 1 & \text{if} \quad H(u) \le 0 \end{cases}, \quad \text{where} \quad r = 1,2,....N_s \quad (\text{II.3.41})$$

8. Evaluate the probability of failure P_f,

$$P_f = \frac{1}{N_s} \sum_{r=1}^{N_s} I_D^r(H(u)) \quad (\text{II.3.42})$$

9. The coefficient of variation of the estimate equals to [Lemaire *et al* 2009],

$$\text{cov} = \sqrt{\frac{1 - \widehat{P}_f}{N_s \widehat{P}_f}} \quad (\text{II.3.43})$$

where $\widehat{P}_f$ is the estimate of P_f. For an objective $cov=0.1$ and a probability $P_f=10^{-n}$, we obtain $N_s=10^{n+2}$. For example if a probability of failure P_f of a value greater than 0.001, $n=3$, therefore $N_s=10^5$ simulation is required. The convergence is given by the [Shooman 1968] formula

$$s = 1.96 \sqrt{\frac{1 - \widehat{P}_f}{N_s \widehat{P}_f}} \quad (\text{II.3.44})$$

This percentage corresponds to a probability of 95% that the exact value of P_f belongs to the interval $\widehat{P}_f (1 \pm s)$: this is the 95% confidence interval. The corresponding reliability index β can be determined using the inverse of Equation II.3.26; $\beta=-\Phi^{-1}(P_f)$, where $\Phi^{-1}(\cdot)$ is the *CDF* inverse of reduced centered normal distribution.

II.3.3.2.3 Importance sampling Monte-Carlo simulation method

Classical Monte-Carlo method required a huge number of sampling (i.e. calculation time is very important) especially with small values of probability of failure P_f. Monte-Carlo Importance Sampling (MC-IS) simulation is more effective, it requires sampling number N_s less than the sampling number required using the classical Monte-Carlo simulation. Basically, the weight of the probability of failure is generally located in the vicinity of the design point $P*$, thus in this method, original sampling density is translated at the design point $P*$ to concentrate the sampling in the region of the highest density of the failure zone defined by $H(u)=0$ (Figure II.3.10). In this way the standard error of the estimate of P_f can be reduced significantly. The center of the sampling is calculated using the FORM method cited in

section II.3.3.1. Accordingly, the integral to be evaluated is given in the form [Melchers 1999]:

$$P_f = \int_{R^n} I_D \frac{\phi(u_k)}{\varphi(u_k)} \varphi(u_k) du_1 du_2 du_3 \cdots du_n \qquad \text{(II.3.45)}$$

where $\varphi(u_k)$ is a new density function of the sampling at the deign point. A first solution is to choose for this function a reduced normal density $\varphi(u_k)$ centered at the design point u_k^*.

$$\varphi(u_k) = \frac{1}{(2\pi)^{n/2}} \exp\left(-\frac{(u_i - u_i^*)^2}{2}\right) \qquad \text{(II.3.46)}$$

Thus, probability of failure is estimated as:

$$P_f = \frac{1}{N_s} \sum_{r=1}^{N_s} \left(I_D^r \exp\left(-\sum_{i=1}^{n} u_i^* u_i^{(r)} - \frac{\beta^2}{2}\right) \right) \qquad \text{(II.3.47)}$$

At each simulation case r, the indicator I_D^r is evaluated according to,

$$I_D^r(H(v)) = \begin{cases} 0 & \text{if} \quad H(v) > 0 \\ 1 & \text{if} \quad H(v) \le 0 \end{cases}, \quad \text{where} \quad r = 1,2,....N_s \qquad \text{(II.3.48)}$$

where $v^{(r)} = u_i^{(r)} + u_i^*$. β is reliability index obtained using FORM method, given by $\sqrt{\sum_{i=1}^{n} (u_i^*)^2}$, u_i^* are the co-ordinates of the design point P^* in u-space. $u_i^{(r)}$ is a generated vector of random variable i ($i=1,2,…n$) with normal distribution, mean value ($=0$) and standard deviation ($=1$). r being the number of the sample ($r=1,2,… N_s$). The coefficient variation estimate of P_f is given by the usual definition:

$$\text{cov}(\widehat{P}_f) \approx \frac{1}{N_s - 1} \left[\frac{1}{N_s} \sum_{r=1}^{N_s} \left(I_D^f \left(\frac{\phi(u_k)}{\varphi(u_k)}\right)^2 \right) - P_f^2 \right] \qquad \text{(II.3.49)}$$

Finally, Monte-Carlo importance sampling (MC-IS) gives satisfactory results if point P^* has been well identified and if there are no secondary minima at neighboring distances.
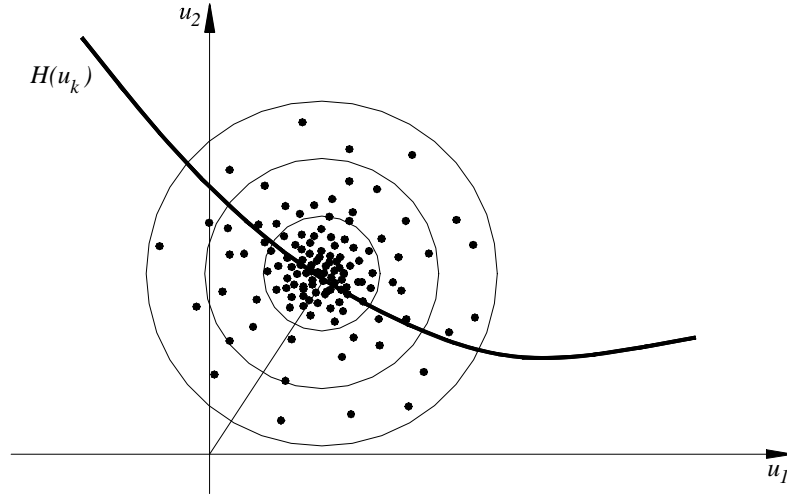
Figure II.3.10: Classical Monte-Carlo simulations in case of two variables.

II.3.3.2.4 Monte-Carlo simulation based Neural networks

It has been presented in pervious chapter that the neural network (NN) applications can be used to predict the structural response within corresponding ranges of the network inputs. Thus, NN was used to establish an explicit form to predict structural responses. Such these responses may be strains, stresses or deflection. The first layer contains as many neurons as there are design variables and the last layer contains a number equal to that of the performance functions. In our cases the neural network was used to predict only one output. Monte-Carlo technique was used to perform the reliability analysis based neural networks. Monte-Carlo based Neural Networks (MC-NN) is performed according to the following steps:

1. Selection of the random variable, considered in MC-NN, is based on the importance factors α_i obtained using FORM method: i.e. random variables considered in FROM method and have small values of α_i will not be considered in MC-NN as they have a negligible effect on the reliability index β.

2. Limit state function may have different form from that used in FROM method which can be expressed as

$$G(x_i) = R - S \qquad (II.3.50)$$

where R and S in this case of MC-NN are ultimate material failure strain and the corresponding induced strain due to the applied loads respectively; i.e. R is ultimate FRP composite strains $\varepsilon_{FRP,u}=f_{FRP,u}/E_{FRP}$ and S is the FRP strain induced due to the applied loading. $f_{FRP,u}$ and E_{FRP} are the strength and the modulus of the FRP composites respectively. Each S and R may evolve random variables. The neural network was used to predict the S values.

3. Implementation of isoprobabilistic transformation of the design variables and the limit state function from x-space to u-space.

4. Preparation of the dataset required to train, validate and test the neural networks. The co-ordinates of each point, in the u-space, in the dataset are determined according to mixed experiments design explained in section II.2.4. Center of the dataset required for neural network origin of the design space for classical Monte-Carlo simulation or the co-ordinates of the design point $P*$ for Importance sapling Monte-Carlo simulation (see Figure III.3.11).

   Structural response for each point, with coordinated $(x_1, x_2, …x_n)$ in x-space, in the dataset was implemented using finite element analysis.

5. Construction of the neural network NN: number of hidden layers, number neuron in each layer and the activation function used in each layer.

6. Training, validation and testing of the neural network based on the dataset obtained in step 4.

7. Perform classical Monte-Carol or Monte-Carol Importance Sampling using the Neural Network around the point $P*$ and calculating the probability of failure P_f, thus the reliability index $\beta_{MC\text{-}IS\text{-}NN}$; $\beta= \beta=-\Phi^{-1}(P_f)$, where $\Phi^{-1}(\cdot)$ is the *CDF* inverse of reduced centered normal distribution.

8. Comparison the two reliability index $\beta_{MC\text{-}NN}$ and β_{FORM} obtained form FROM and MC-NN methods respectively.
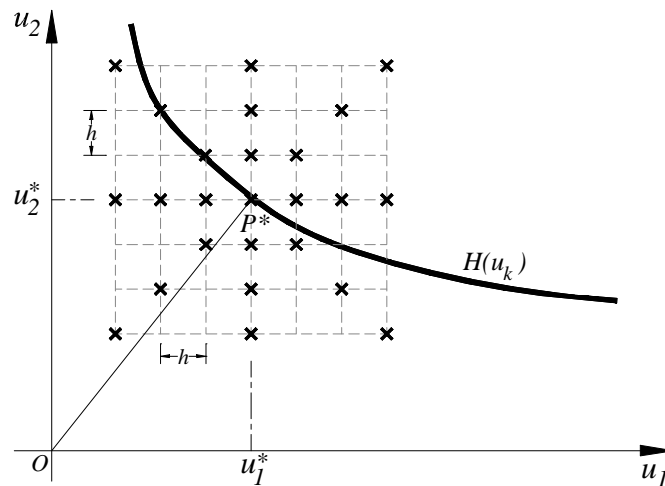
Figure II.3.11: Successive designs of experiment; case of two variables.

II.3.4 TIME VARIANT RELIABILITY ANALYSIS

The performance function, expressed with a limit state $G(t)=R(t)-S(t)$, is to be analyzed in

steps over time steps. To perform a time variant reliability analysis, probabilistic models for the resistance and the loads are evaluated at each time step. In the present study, it is assumed the resistance of the RC section before applying FRP strengthening is deteriorated over the time due to corrosion of steel reinforcement, while after strengthening it is assumed that the properties, FRP modulus and strength, of the FRP laminates deteriorate due to aging affect. The most important factor that affects the reliability of RC highway bridges is the growth of truck loads over the time. Probabilistic models for steel area and the truck loads are developed based on Monte-Carlo simulation technique which will be presented in the next chapter.

Figure II.3.12 shows the relation between both the resistance and the loads with respect to the time. It could be noted that the structure after construction time, $t \approx 0$, could maintain the lowest value of the probability of failure. This can be deduced from that the interaction between the *PDF* of both the resistance and the loads are the minimum at this stage. Lowest probability of failure must satisfy the condition that it is higher that a target, $P_{f,target}$, value proposed by provisions or design codes. As shown in Figure II.3.12, this interaction increase over the time causing a growth of the probability of failure. In general, the measure of risk associated with the specific event of $R(t)<S(t)$ can be expressed as the probability of failure $P_f(t)$ of that event, or generically as:

$$P_f = P\big(R(t) < S(t)\big) \tag{II.3.51}$$
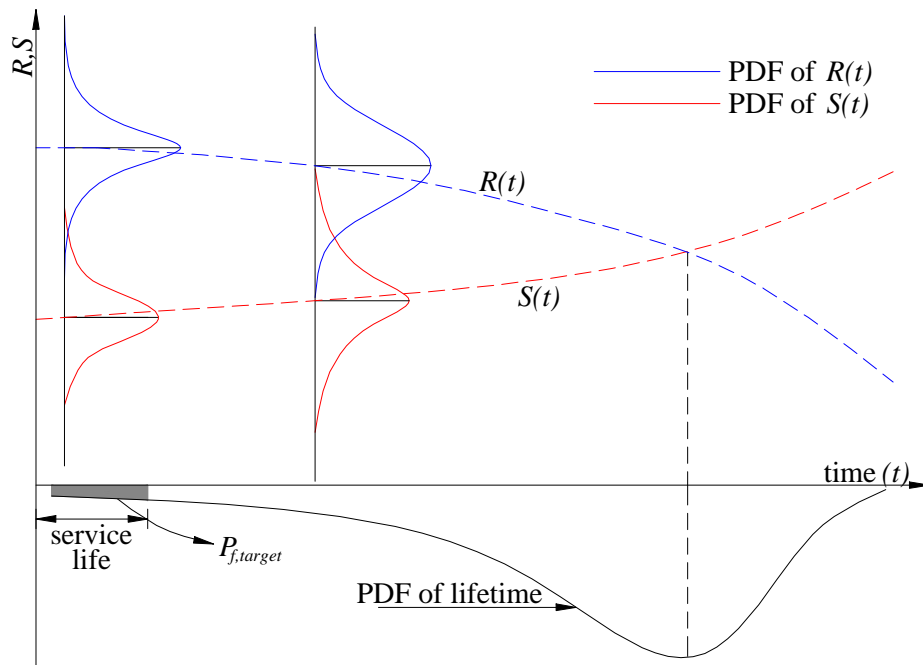
Figure II.3.12: schematic representation of time variant reliability analysis and lifetime concept.

If the resistance and the loads model are expressed probabilistically at each time step, thus,

the reliability index or the probability of failure can be determined as time dependent using any reliability method such as Cornell method, FORM method, Monte-Carlo simulation…etc. growth of the probability of failure over the time such that it reach a minimum or critical value leads to strengthening of the deteriorated structural element to maintain it over the target value again. The period that the probability of failure, as a function of time $P_f(t)$, of the structure undergoes for the target probability of failure, $P_{f,target}$, to the critical probability of failure, $P_{f,critical}$, is defined as the service life of the structure. More explanation and calculation algorithms of lifetime are presented in the next chapter.

II.3.5 RELIABILITY OF STRUCTURAL SYSTEM

Structural design is, at present, primarily concerned with component behaviour. Each limit state equation is, in most cases, related to a single mode of failure of a single component. However, most structures are system of structural components. There are two fundamental systems, see Figure. II.3.13:

1. A series system is a system which fails if one or more of its components fail, i.e. the probability of failure of series system composed of limit states g_i, $i=1,2,..m$, is:

$$P_f^{sys} = P\left(\bigcup_{i=1}^{m} \{g_i(X) \le 0\} \right) = P\left(\bigcup_{i=1}^{m} \{g_i(T(U)) \le 0\} \right) \tag{II.3.52}$$

   where $T(U)$ is the isoprobabilistic transformation of the random variables vector X from x-space to the normalized space u-space.

2. A parallel system is a system which fails when all its components have failed, i.e. the probability of failure of parallel system composed of limit states g_i, $i=1,2,..m$, is:

$$P_f^{sys} = P\left(\bigcap_{i=1}^{m} \{g_i(X) \le 0\} \right) = P\left(\bigcap_{i=1}^{m} \{g_i(T(U)) \le 0\} \right) \tag{II.3.53}$$

(a) series system   (b) parallel system
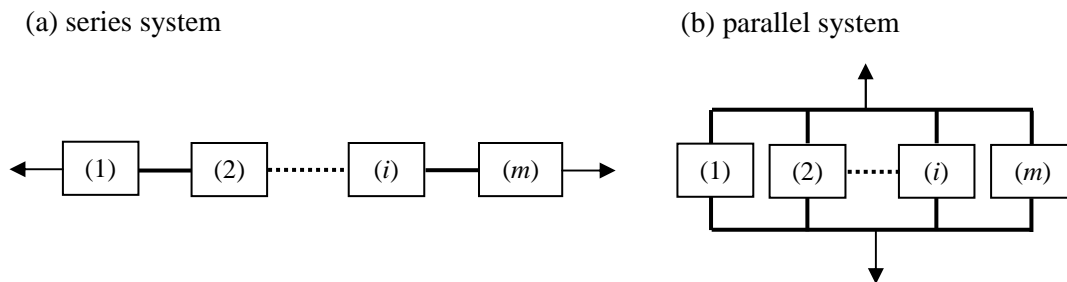
Figure II.3.13: Schematic representation of series and parallel systems.

Structural system may consist of subsystems combinations. These subsystems may be

either series or parallel. Common system combinations, which will be used in our case, are the series combination of parallel systems, see Figure II.3.14.
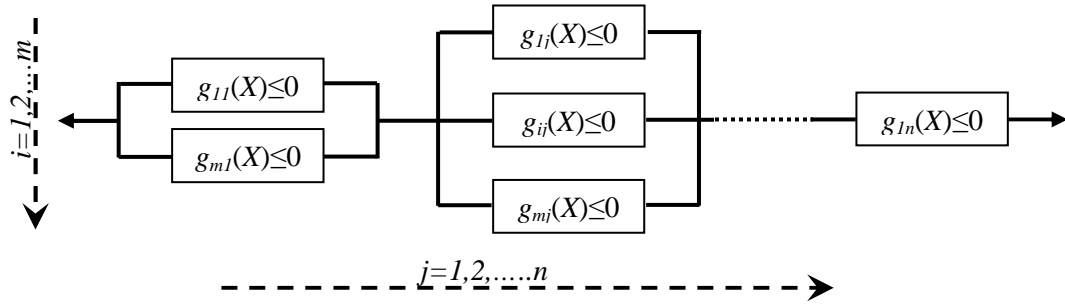
Figure II.3.14: Representation of a series system of parallel systems.

By combining Equations III.3.52 and III.3.53, the probability of failure of such system becomes:

$$P_f^{sys} = P\left(\bigcup_{i=1}^{n}\left[\bigcap_{j=1}^{m}\{g_i(X)\le 0\}\right]_j\right) = \left(\bigcup_{i=1}^{n}\left[\bigcap_{j=1}^{m}\{g_i(T(U))\le 0\}\right]_j\right) \qquad (II.3.54)$$

II.3.6 CONCLUSIONS

A literature review was presented in this chapter. This first part presents an introductory definition to the reliability index of a structural system, the sources of uncertainty in engineering structures and levels of reliability analysis. Moreover, this part outlines all the primary aspects required to completely define a random variable such as mean, standard deviation, *PDF*, *CDF*, coefficient of correlation, distribution …etc. Isoprobabilistic transformation of random variables, correlated or non-correlated, between physical and normalized space were presented in details for different types of distributions such as Lognormal, Weibull, …etc.

The second part gives brief definitions of the main limit states (ultimate and serviceability) considered in the reliability analysis and Load & Resistance Factored Design LRFD concept used in recent design codes. Theses limit states can be simply defined as the difference between the strength and applied actions. Limit state function based random variables leads to express the probability of failure, as a measure of reliability, as the probability that the strength is lower than applied action.

The third part of this chapter presents all the reliability analysis methods used in the present study. The notations and the mathematical expressions of the performance function, reliability index, probability of failure and the methods of calculations of the reliability index. Cornell and Hasofer-Lind (using FORM method) reliability indices were presented. We also presented Monte-Carlo simulation methods used to calculate the probability of failure, thus, the corresponding reliability index. Two Monte-Carlo methods were reported; classical and importance sampling. In the present study, these methods were used in conjunction with the neural network applications and finite element method. In addition, the reliability of structural system concept is presented. This concept will enable in exalting the reliability index or probability of failure when more the one limit state are coupled in the reliability analysis, as FRP strengthened RC beam involved multiple failure modes which may take place independently as presented in chapter I.2

This final part of this chapter focused on the concept of time-variant reliability analysis which used to figure the reliability index as time dependent. In this case the limit states are involved random variables that may change with time causing deterioration of the reliability index over that time. In the present study, we focused on the reliability of FRP strengthened RC beams of a high way bridges constructed in coastal zones. Thus, three deterioration models were assumed affecting the reliability index over the time: corrosions models was

assumed to affect the yield strength reinforcement and its area, growth of truck loads over the time was assumed to affect the live loads actions (shear and bending moment) and FRP properties (strength and modulus) are affected by aging and moisture attack. This can be helpful tool in evaluating the service life of RC highway bridges

PART III:

NUMERICAL

APPLICATION AND

RESULTS

PART III: NUMERICAL APPLICATION AND RESULTS.

Chapter III.1: Stochastic model of design variables.

III.1.1 INTRODUCTION

The proposed developments presented in previous parts have been used to: (1) improve knowledge about the deterioration phenomenon; corrosion of steel rebars and growth of live loads over the time and (2) evaluate the reliability of existing FRP strengthened RC beams. Therefore, the analytical and numerical formulations of the models described in chapter II.1 as well as the methodology for the reliability analysis presented in chapters II.2 and II.3 were implemented using a scientific computing program. Given the complexity of the problem, this chapter presents a practical application to illustrate the benefits of the model and to evaluate the statistical parameters of the random variables.

This section presents the details of the design case considered in our study. Our case is an interior girder of a simply supported RC highway bridge presented in Figure III.1.1. The span of the girder is 10m. The girder has been designed according to the AASHTO standard (2007). In addition to the dead loads, a truck wheel load is applied on the deck of the bridge. The design loads, correspond to a HL-93 live load reported in AASHTO specifications. The RC beam considered was designed to achieve a reliability index equals to 3.5 which is the target value proposed in AASHTO specifications.
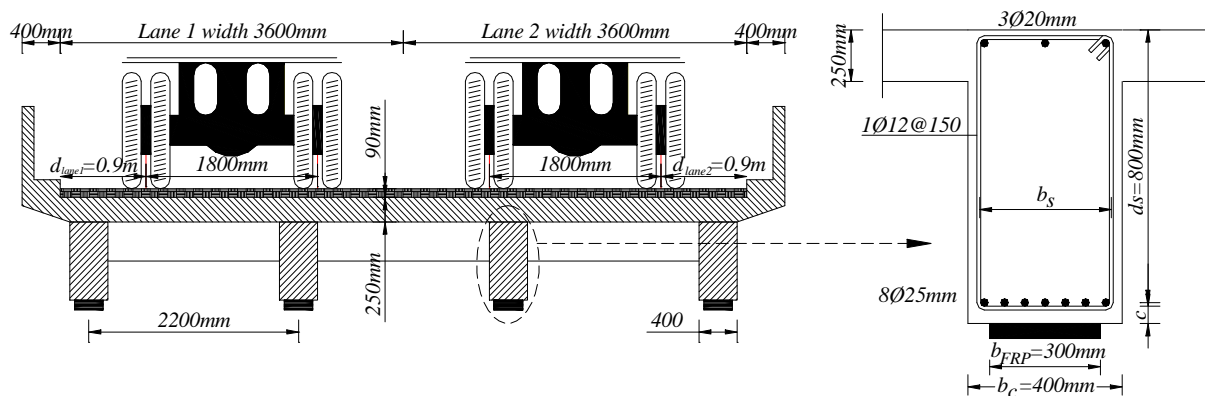
Figure III.1.1: Bridge cross-section and trucks position; Reinforcements and dimensions details of the interior beam

The objectives of this chapter are:

1. to present the geometrical and material probabilistic design variables considered in our case.

2. to evaluate the probabilities of corrosion initiation, cover cracking and to evaluate a time-dependent probabilistic model of steel area based on the corrosion model proposed in chapter I.1.

3. to present the probabilistic models of dead loads and time-dependent live load.

Table III.1.1presents all the deterministic parameters required in the reliability analysis. Such these parameters were considered in many studies as deterministic values since their variation does not affect the reliability analysis [e.g. Bastidas-Arteaga *et al* 2009]. From other side, there are no probabilistic models for these parameters found in the review.

Table III.1.1: Deterministic material constant.

Variable	Value	Units	Description
E_s	201300	MPa	Elastic steel modulus
γ_c	22	kN/m^3	Specific weight of concrete
γ_p	18	kN/m^3	Specific weight of Asphalt pavement
v_c	0.2	---	Concrete Poisson ratio
d_o	12.5x10^{-3}	mm	Thickness of porous band around steel bar
ρ_{steel}	78.5	kN/m^3	Density of steel
ρ_{rust}	36	kN/m^3	Density of corrosion rust
ρ_c	29	kN/m^3	Density of cement
ρ_a	26	kN/m^3	Density of aggregate
ac	5.14	---	Aggregate to cement ratio
m_{age}	0.15	---	aging coefficient [Val & Trapper 2008]

III.1.2 PROBABILISTIC MODELS FOR DESIGN VARIABLES

III.1.2.1 Environmental, material, geometrical and model error variables

In fact, Reliability analysis requires descriptors of the statistical variation of the variables involved in design formulas. Reliability analysis is often conducted on the basis of load and resistance concept. However, data about the resistance of FRP strengthened RC member at the member level are not directly available. Simulation or calculation required to express member resistance will be based on the exact descriptions of all the influencing variables.

In the present section the statistical variation of these variables is presented in term of the mean/bias, standard deviation/coefficient of variation and the corresponding distribution. Generally, we divide the variables in four categories: (1) environmental, (2) material and geometrical, (3) structural model error, (4) loading. Figure III.1.2 presents an overall scheme of reliability calculation and all the random variables considered.
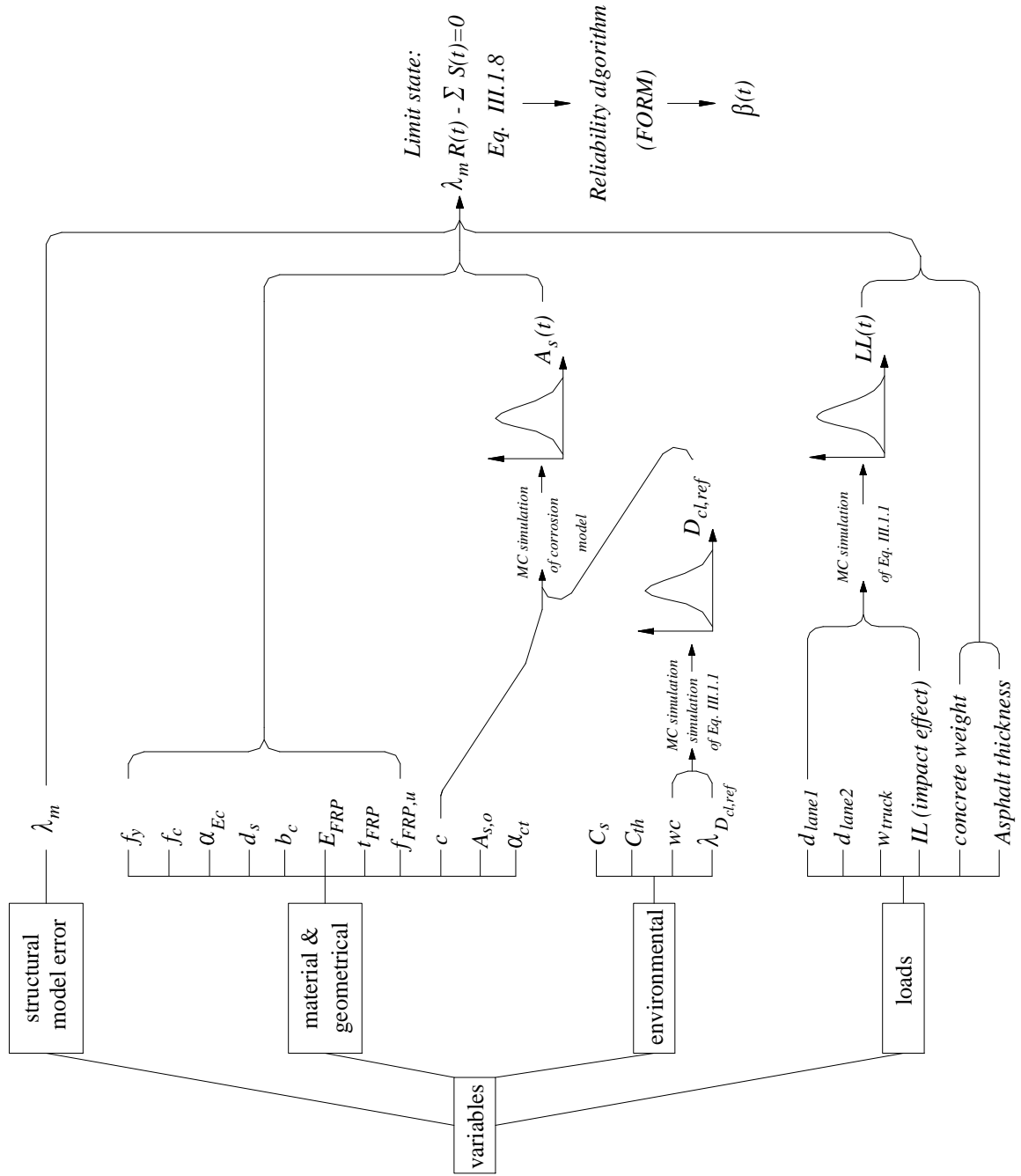
Figure III.1.2: Categories of random variables

Environmental

The probabilistic models of environmental variables are given in Table III.1.2. It is worthy to notice the high variability of surface chloride concentration C_s (coefficient of variation around 50%). C_s data reported in this table were obtained from a field survey of 1158 bridges in Australian state of Tasmania [McGee 1999]. This study appears to be the most comprehensive for the bridges in different environmental conditions. It expresses the value of C_s as a function of the distance from the coastal as given in Equation I.1.14. In our case, we chose an extreme value of chloride surface concentration C_s (=3).

The reference chloride diffusion coefficient $D_{cl,ref}$ is an important material parameter that has been considered as random variables in many studies [e.g. Stewart & Rosowsky 1998; Vu & Stewart 2000; Bastidas-Arteaga *et al* 2009]. It is reported that $D_{cl,ref}$ is influenced by many factors (mix, curing, compaction…etc) and is not significantly affected by the source of chlorides [Vu & Stewart 2000]. In our study, we use the model proposed by Papadakis *et al* (1996) which is reported in [Vu & Stewart 2000] and expressed by Equation I.1.11. This model was used and recommended in many studies [e.g. Bastidas-Arteaga *et al* 2009].

In order to compute a probabilistic model, i.e. to select the accurate density distribution, for $D_{cl,ref}$ from Equation I.1.11, Monte-Carlo simulation and Kolmogorov-Smirnov test (KS-test) with a level of significance of 5% were carried out.

ρ_c and ρ_a were considered as deterministic parameters (see Table III.1.1) because it is difficult to reach their probabilistic models [Vu & Stewart 2000; Bastidas-Arteaga *et al* 2009].

Uncertainty in the values obtained using Equation I.1.11 is assumed as a random variable called model error in the reference chloride diffusion coefficient $\lambda_{D_{cl,ref}}$. Thus, the final form of Equation I.1.11 can be re-expressed as:

$$D_{cl,ref} = \lambda_{D_{cl,ref}} 0.15 D_{H_2O} \frac{1+\rho_c wc}{1+\rho_c wc + \rho_c ac/\rho_a} \left(\frac{\rho_c wc - 0.85}{1+\rho_c wc} \right)^3 \qquad \text{(III.1.1)}$$

The statistical parameters of this variable are presented in Table III.1.2.

Water-cement ratio *wc* is assumed as random variables normally distributed with mean value 0.45 and coefficient of variation 0.05 according to [Atadero & Karbhari 2007]. Figure III.1.3 presents the density of the generated reference chloride diffusion coefficients $D_{cl,ref}$ obtained using Monte-Carlo simulation. The KS-test results indicate that generalized extreme value (GEV) distribution can best fit the generated data with statistical parameters (scale; -0.1021, shape; 17.0195, location; 46.5274).

As presented in chapter II.2, any random variable *X* can be expressed by three important statistical parameters; mean value μ_X, standard deviation σ_X and the density distribution function *PDF*. However, μ_X and σ_X can be replaced by the bias λ_X and CoV_X, respectively, as:

$$\lambda_X = \frac{\mu_X}{X_n} \qquad \text{(III.1.2)}$$

$$CoV_X = \frac{\sigma_X}{\mu_X} \qquad \text{(III.1.3)}$$

where X_n is the nominal value of a variable *X*. The statistical parameters given in Table III.1.2 are expressed in term of λ_X and CoV_X. Otherwise they will be given in term of μ_X and σ_X in

parentheses.

Table III.1.2: Probabilistic parameters of random variables.

Variable	Distribution	Units	Nominal	λ^a(mean)	$CoV^b(\sigma^c)$	Source
c	Log-Normal	mm	25:5:45	1	0.2-0.1	[Duprat 2007]
e_c	Normal	mm	0	(0)	(5)	[Duprat 2007]
b_s	Normal	mm	348:10:368	1	(5)	[Duprat 2007]
C_s	Log-Normal	kg/m^3	3.0	1	0.5	[Vu & Stewart 2000]
C_{th}	Uniform	kg/m^3	0.9	1	0.19	[Bastidas-Arteaga *et al* 2009]
wc	Normal	m^2/s	0.45	1	0.05	[Atadero & Karbhari 2007]
Model error ^{d} Eq III.1.1	Normal	---	1	1	0.2	[Val *et al* 2000]
Model error ^{d} i_{corr}	Normal	---	Eq I.1.18	1	0.2	[Vu & Stewart 2000]

$^a\lambda$; bias value, ^bCoV; coefficient of variation, $^c\sigma$ standard deviation. ^{d} denotes that the model error is multiplicative. c is the concrete cover of tensile steel. e_c is the stirrup eccentricity. b_s is the stirrup width. C_s is the surface chloride concentration. C_{th} is the critical chloride concentration. wc is the water cement ratio. i_{corr} is the corrosion current.
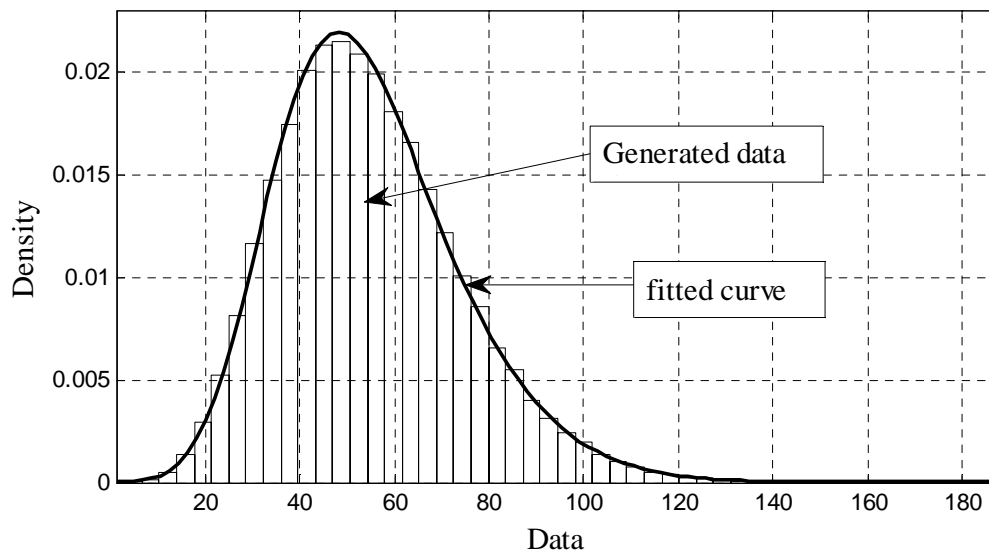
Figure III.1.3: Density of generated reference chloride diffusion coefficients $D_{cl,ref}$ and the fitted GEV distribution.

Material and Geometrical

The statistical parameters for material properties (concrete, steel and FRP properties) and geometry are provided in Table III.1.3. Concrete properties are often considered as random variables which involved high uncertainty values. Many sources contribute to the variation in concrete properties (e.g. material proportions and properties, methods of mixing, transporting, placing, curing and testing). The most comprehensive study that provides statistical models of concrete properties is proposed by [Mirza & MacGregor 1976]. The authors have defined three levels for describing the *CoV* of concrete strength: 0.10-0.15 for good control, 0.15-0.20 for average control and above 0.20 for poor control. The Normal distribution is appropriate for modeling concrete compressive strength for *CoV* values up to 0.15-0.20. Beyond this range the Log-Normal distribution provides a better fit for the tail regions [Mirza &

MacGregor 1976]. In the present design example, we assume that the mean compressive strength, in-situ, of the concrete equals to 35 MPa with average control. Thus *CoV* of 0.15 with Normal distribution can be assumed as presented in Table III.1.3.

In order to take into account the dependency of concrete compressive strength at 28 days f_c with both concrete tensile strength f_{ct} and the concrete modulus E_c, it is assumed that herein f_{ct} and E_c can be expressed via f_c as $f_{ct} = \alpha_{ct} f_c^{2/3}$ and $E_c = \alpha_{Ec} (0.1 f_c)^{1/3}$ respectively [Model Code 1990]. According to Val *et al* (2000), it is assumed that f_c and both the coefficients α_{ct} and α_{Ec} can be considered as independent random variables.

The gain in concrete properties with time was considered according to the formulas proposed in Model code(1990):

$$f_c^{'}(t) = f_c^{'} \exp\left\{ 0.25\left[1 - \left(\frac{28}{t}\right)^{1/2} \right] \right\} \tag{III.1.4}$$

$$E_c(t) = E_c \sqrt{\exp\left\{ 0.25\left[1 - \left(\frac{28}{t}\right)^{1/2} \right] \right\}} \tag{III.1.5}$$

where t is the time in days.

It is known that, externally bonded FRP is applied in two ways. One way is through adhesive bonding of pre-manufactured FRP strips. These strips are manufactured in a controlled factory setting resulting in more uniform material with higher levels of material performance characteristics. When pre-manufacturing FRP strips are applied to an existing structure the adhesive layer between the concrete and FRP is likely to be the most significant source of uncertainty. The second technique for the application of externally bonded FRP material is through field-manufacture FRP materials, called also wet-layup FRP (see § I.2.2.5). The latter method, which is considered in the present study, is the most widely used as it is very flexible and can be applied to variety of geometric configurations, whereas pre-manufacture strips cannot be significantly bent.

When the FRP is manufactured on site, various sources of uncertainties impact the final properties of FRP material, resulting in a higher level of uncertainty with respect to the first technique. Such these sources are due to: fiber fabric itself, resin, manufacturing conditions, curing methods and curing conditions, handling process, number of layers…etc.

Atadero *et al* (2005) have studied the variability of CFRP properties (thickness t_{FRP}, modulus E_{FRP} and strength $f_{FRP,u}$). The study is based on statistical analysis of tensile tests of

wet-layup FRP panels of 457 mm length and 152 mm width. Tested panels were fabricated at thicknesses of 1, 2 and 3 layers. Each panel was cured and cut in a number of coupons with length of 254 mm and width of 25.4 mm. Total number of coupons for each thickness equals to 29. Coupons were tested in uniaxial tension test following ASTM D3039. Results of the study conclude that FRP modulus and strength are statistically correlated to the total CFRP thickness. Thus, these correlations must be considered in the reliability analysis or CFRP properties must be normalized from thickness before applying the reliability analysis.

In addition, the statistical distributions of CFRP strength, modulus and thickness were fitted by the authors using Chi-square test. Normal, Lognormal, Weibull and Gamma distributions were compared to choose the best descriptor of the data distribution of FRP properties. Lognormal, Weibull and Lognormal distributions were found as the best descriptors for CFRP modulus, strength and thickness respectively.

In order to catch more accurately the influence of the number of layers, Atadero & Karbhari (2009) have analyzed statistically the results of five FRP datasets fabricated from different FRP types. Through each dataset the number of layers was taken equals to 1, 2, 3 and 4. Fabricated FRP specimens in the datasets were tested according to ASTM D3039. Through the obtained results, it can be observed that the CFRP number of layers has insignificant effect on the mean value of E_{FRP}, while the mean value of $f_{FRP,u}$ decreases with respect to the number of layers by 0, 2, 11, and 23% (as average between the datasets reported in [Atadero & Karbhari 2009]) for 1, 2, 3, and 4 layers respectively. In our case, we will consider these reductions in the mean value of FRP strength with respect to the number of layers. Statistical models of CFRP properties used in the present study were considered from the normalized data provided by Atadero & Karbhari (2009).

Table III.1.3: Probabilistic parameters of geometrical and material random variables.

Variable	Distribution	Units	Nominal	λ^{a}(mean)	$CoV^{b}(\sigma^{c})$	Source
f'_c	Normal	MPa	34.5	1	0.15	[Plevris et al 1995]
α_{ct}	Normal	---	0.3	1	0.15	[Val et al 2000]
α_{Ec}	Normal	---	2.15×10^{4}	1	0.08	[Val et al 2000]
f_y	Normal	MPa	414	(460)	(46.2)	[Vu & Stewart 2000]
d_s	Normal	mm	700	(700-4.7)	(12.7)	[Plevris et al 1995]
b_c	Normal	mm	400	(400+2.54)	(3.658)	[Plevris et al 1995]
s_s	Normal	mm	200	1	0.1	[Duprat 2007]
$A_{s,o}$	Normal	mm^{2}	490.87	0.97	0.024	[Atadero & Karbhari 2007]
E_{FRP}	Lognormal	GPa	51.7	1	0.2	[Atadero & Karbhari 2007]
$f_{FRP,u}$	Weibull	MPa	620.5	1	0.15	[Atadero & Karbhari 2007]
t_{FRP}	Lognormal	mm	1	0.05	[Atadero & Karbhari 2007]

f'_c is the concrete compressive strength. α_{ct} and α_{Ec} are the random parameters in concrete tensile strength and modulus respectively. d_s is the steel depth. b_c is the beam width. s_s is the stirrups spacing. $A_{s,o}$ is the original area of tensile steel bar. $A_{sv,o}$ is the original area of one branch of shear stirrup. E_{FRP} and $f_{FRP,u}$ are the modulus and the strength of FRP material respectively. t_{FRP} is the thickness of the FRP material.

Structural model error

If the statistics of resistance are derived based on test results there is no need to consider error in the modeling process because no model is used. However, when the statistics of resistance are based on probability distributions of the variables contributing to resistance and analytical or empirical models relating those variables to the resistance, a random variable considering the accuracy of the model should be used.

Depending on how the reliability problem is formulated it may be appropriate to include a random variable that considers the error between the theoretical results used to describe the resistance and the results from actual member tests. For example, the structural model error of the flexural limit state λ_{flex} can be expressed as:

$$\lambda_{flex} = \frac{M_{u,\exp}}{M_{u,th}} \tag{III.1.6}$$

where $M_{u,exp}$ and $M_{u,th}$ are the experimental and the theoretical ultimate bending moment values respectively. For any other limit state function $M_{u,exp}$ and $M_{u,th}$ are replaced by its corresponding experimental and theoretical values.

Ellingwood *et al* (1980) formulated the structural model error as a Normal random variable with a mean value equal to the average value of the ratio of the experimental resistance to the theoretical resistance. The coefficient of variation of model error, CoV_m, is calculated as:

$$CoV_m = \sqrt{CoV_{T/C}^2 - CoV_{test}^2 - CoV_{spec}^2} \tag{III.1.7}$$

where $CoV_{T/C}$ is the coefficient of variation of the ratio of tested to calculated strengths, CoV_{test} is the uncertainty in the measured loads during testing and CoV_{spec} is due to errors from strength differences between the test cylinders and the test structure and variations in dimensions of the test structure. The typical values for CoV_{test} are about 0.02-0.04 (average value can be considered) and the values for CoV_{spec} are about of 0.04.

With model error formulated in this manner the limit state function $g(x)$ can be formulated as:

$$g(x) = \lambda_m R - \sum S_i \tag{III.1.8}$$

where λ_m is the random variable representing structural model error for a certain limit state m (i.e. m denotes the considered limit state; flexural, shear…etc). R is the corresponding resistance of the considered limit state. $\sum S_i$ represents the summation of random loading actions; dead, trucks and impact.

For all the limit states considered in our study, the mean value λ_m and the coefficient of variation $CoV_{T/C}$ of a tested dataset and its theoretical evaluation were given in Chapter II.1. Table III.1.4 concludes the model error for the different failure modes considered in the present study. According to Ellingwood *et al* (1980) Normal distribution can be assumed.

Table III.1.4: Probabilistic parameters structural model error λ_m

Limit state	$CoV_{T/C}$	CoV_{test}	CoV_{spec}	CoV_m	λ_m
For flexural limit state:					
❖ Concrete crushing & FRP rupture	0.1306	0.03	0.04	0.1206	1.066
❖ FRP intermediate crack debonding	0. 1170	0.03	0.04	0.1058	1.0234
❖ FRP end-debonding based shear crack	0.2082	0.03	0.04	0.2021	0.9548
For shear limit state:					
❖ Non-strengthened RC beam[a]	---	---	---	0.125	1.15
❖ Strengthened RC beam: Triantafillou & Antonopoulos model (2000)	0.275	0.03	0.04	0.270	0.919
Finite element simulation[b]	---	---	---	0.045	1.01

[a] and [b] were obtained from [Vu & Stewart 2000; Duprat 2007] and [Vu & Stewart 2000] respectively.

III.1.2.2 Probabilistic Steel area model

Evaluation of steel damage in term of loss of area during time using the following proposed simulation could obviate many complicated differential calculations required for the FORM algorithm which is used in reliability analysis. Monte-Carlo random number generation in conjunction with the corrosion model proposed in chapter I.1 has been used to represent a time dependent steel area probabilistic model. The model was obtained according to the following steps:

1. Based on the statistical parameters of environmental variables (C_s, C_{th}, c, ….etc), a vector for each variable was generated using Monte-Carlo simulation technique. Each vector contains 5×10^5 cases.

2. Each ith case of these vectors was combined and simulated in the following flow diagram, of corrosion modeling, shown in Figure III.1.4 to obtain the corrosion initiation time t_{ini}, time of severe cracking of the concrete cover t_{sp} and steel area at each time increment $A_s(t)$. The model has been run for a total lifetime equals to 100 years.
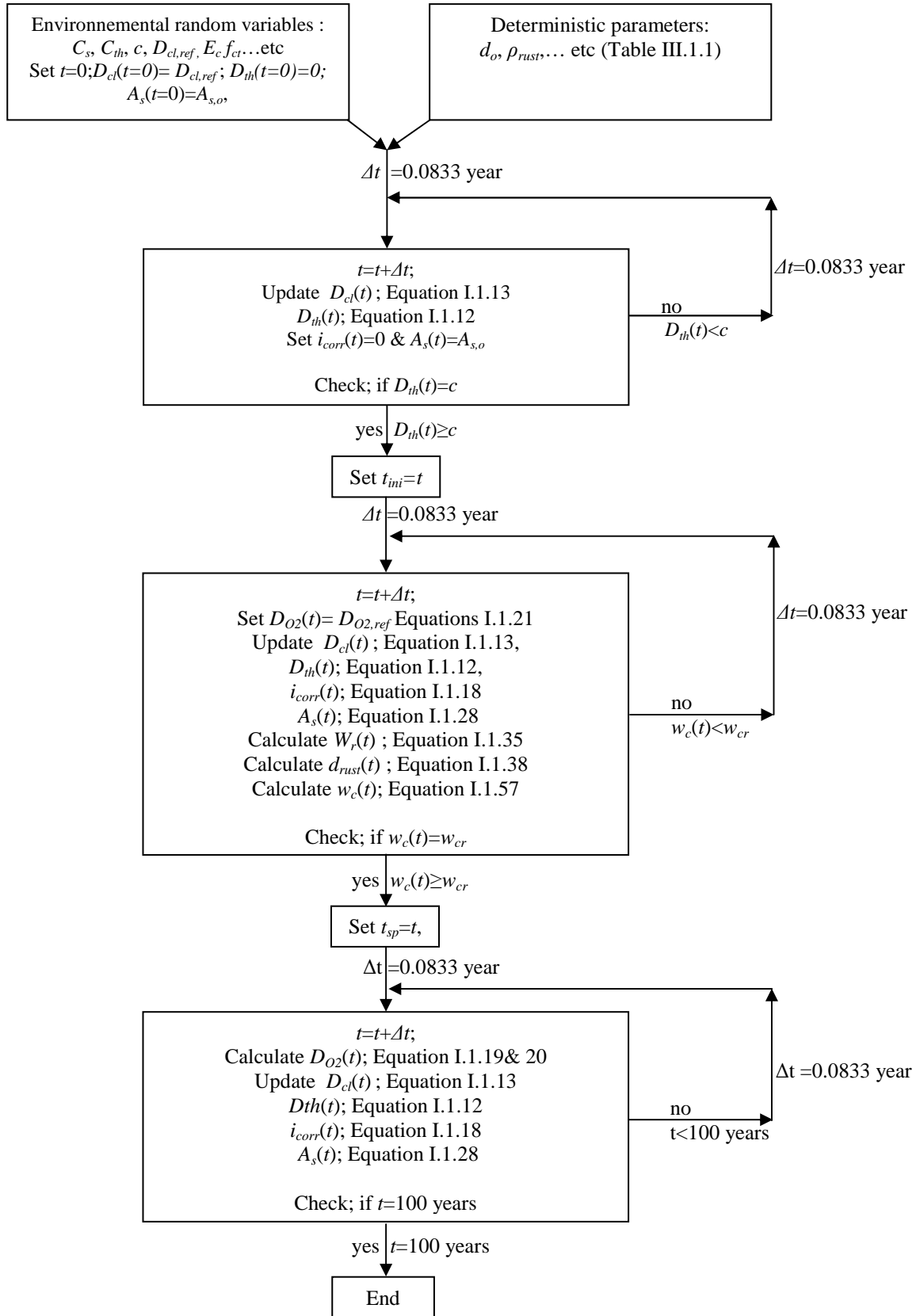
Figure III.1.4: Flow diagram of corrosion model.

3. For all the simulated cases, results of Monte-Carlo simulation indicate that both the time to corrosion initiation t_{ini} and the time to severe cracking of the concrete cover t_{sp} are Log-

Normally distributed. Test of Kolmogorov-Smirnov (KS) with a significance level of 5% was used as selection criterion. Figures III.1.5 & III.1.6 present the plots of the fitted distributions and their corresponding statistical properties, mean and standard deviation, for both bottom steel and stirrups respectively
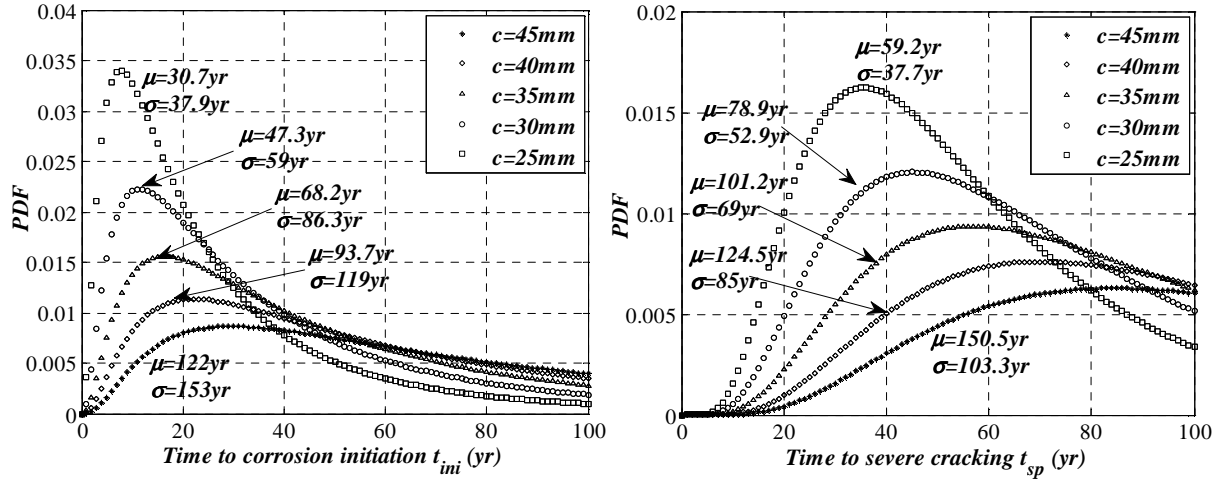
Figure III.1.5: *PDF* of time to corrosion initiation and concrete cover severe cracking; bar diameter equals to 25 mm. μ and σ are the mean and the standard deviation respectively. *c* is the concrete cover.
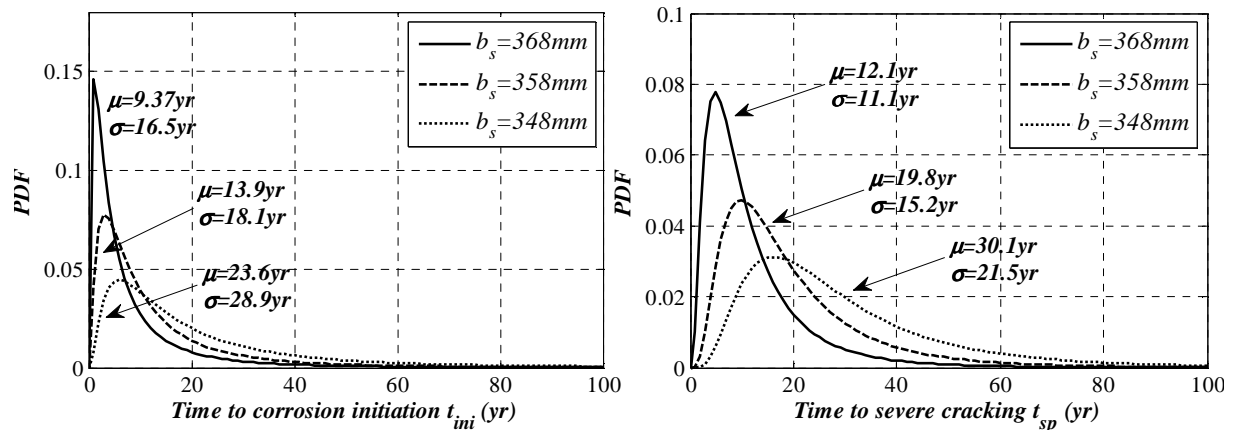
Figure III.1.6: *PDF* of time to corrosion initiation and concrete cover severe cracking; bar diameter and beams width equals to 12 mm and 400 mm respectively. μ and σ are the mean and the standard deviation respectively. b_s is the width of steel stirrups (see Figure III.1.1).

4. The distribution of the corroded steel areas $A_s(t)$ was plotted in Figures III.1.7 & III.1.8 at different ages (1, 50, 100 years). It can be noted that the steel area density function changes with time from Normal distribution with two parameters $N(\mu,\sigma)$ – assumed at initial ages – to a Bi-modal distribution which can be fitted with five parameters (μ_1,σ_1, μ_2,σ_2, and ρ) according to Equation III.1.9.

$$f_{As}(x,t) = \rho_{(t)}\,\Phi(x,\mu_{1(t)},\sigma_{1(t)}) - (1-\rho_{(t)})\,\Phi(x,\mu_{2(t)},\sigma_{2(t)}) \qquad \text{(III.1.9)}$$

where, $\mu_{i(t)}$ is the mean value, $\sigma_{i(t)}$ is the standard deviation, $\rho_{(t)}$ is the mixture ratio, and Φ

is the normal density function.

These parameters were evaluated at each time increment. The generated density distribution in Figures III.1.7 & III.1.8 may simulate the corrosion process in the nature: there is a probability that the steel rebar may be still non-corroded or that corrosion takes place at latter ages. It means that a proportion of the generated cases are not corroded or corrosion will take place after the considered lifetime, i.e. t_{ini} >>>>100 years. Such these cases are characterized by high values of concrete cover/critical chlorides concentration and small values of coefficient of chlorides diffusion/surface chlorides concentration.

Matlab software nonlinear fitting toolbox was used to fit the distribution parameters of Equation III.1.6 based on dataset obtained. Fitting algorithm was focused on a range of the generated data corresponds to a range [-2.0~0.5] in the standard normalized space; space which requires probabilistic transformation for all the random variable considered in the limit state. This transformation de-correlates variables from their individual statistical distributions and physical dimensions to standard normal distribution for each variable. The choice of latter range depends on the contribution of steel bar area u_{As} in safety index β (chapter II.2). Preliminary reliability analysis show that u_{As} contributes -0.2 to -1.4 of the safety index, satisfying the considered range of fitting algorithm.
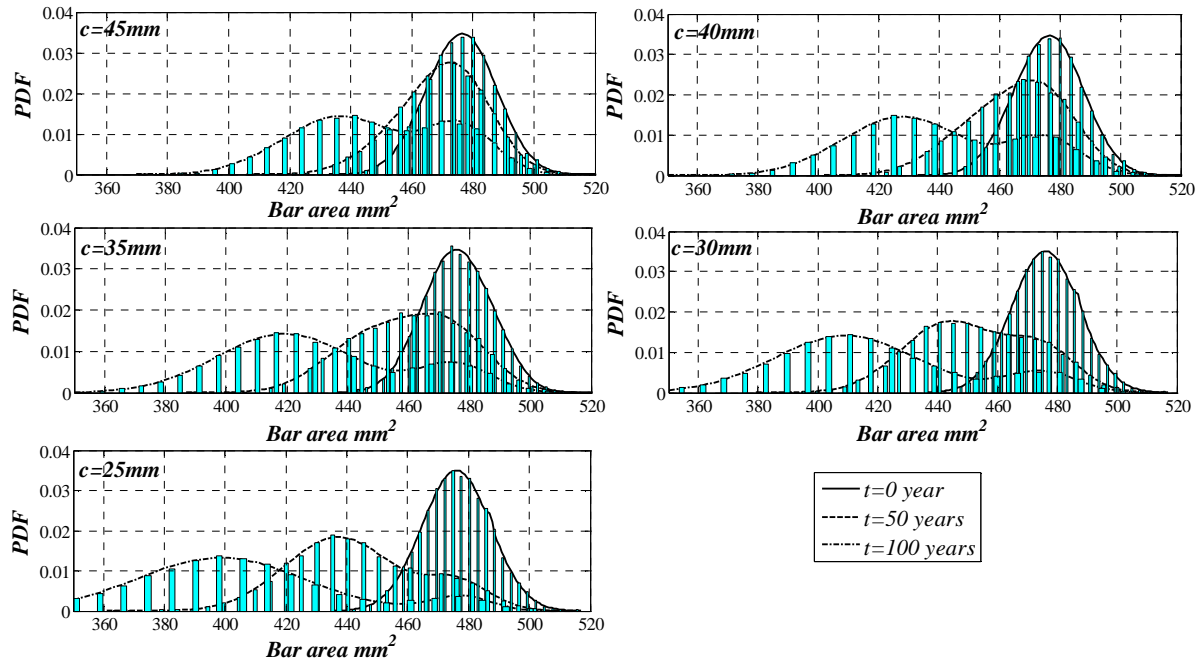
Figure III.1.7: *PDF* of tensile steel area, original bar diameter equals to 25 mm (A_s=490 mm^2). *c* is the concrete cover.
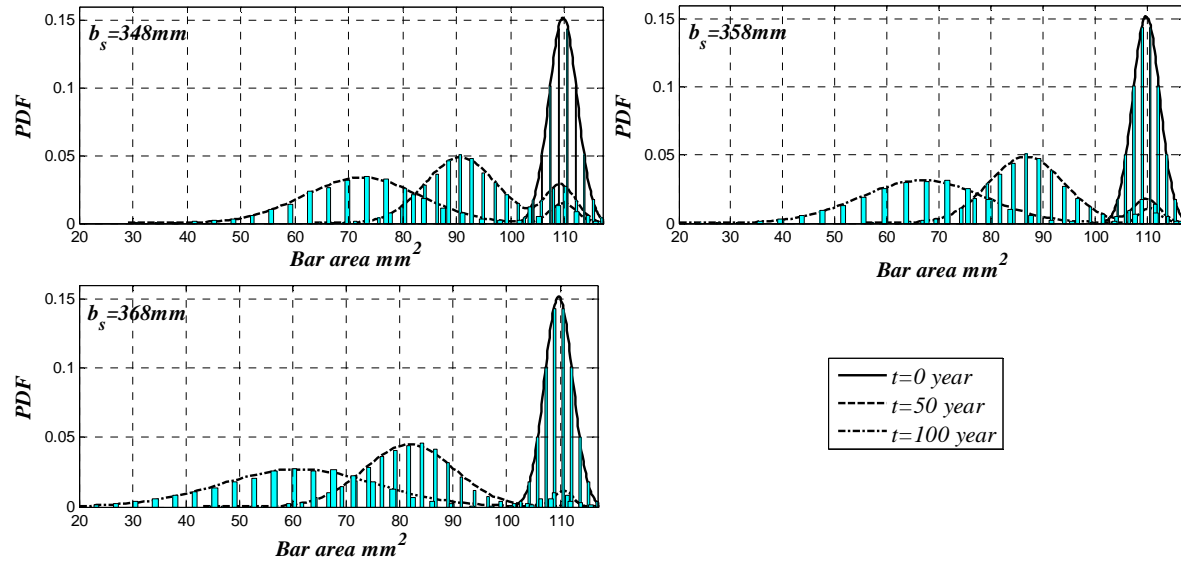
Figure III.1.8: *PDF* of steel stirrup area, original bar diameter equals to 12 mm (A_{sv}=113 mm^2). b_s is the width of the steel stirrups from centre to centre (see Figure III.1.1).

It is important to mention that corrosion model shows the influence of the temperature and relative humidity. According to Val & Trapper (2008), an aging coefficient of 0.15 must be considered in Equation I.1.10b. To understand the effect of these factors on the time to corrosion initiation and severe cracking of concrete cover, five cases were simulated in the above detailed corrosion model (see Table III.1.5). So as to take accurately into account the influence of the temperature and relative humidity, we propose to consider their monthly profiles shown in Figure III.1.9a and carrying out the simulations of their influence on the time to corrosion initiation t_{ini} and the time to severe cracking t_{sp} (Figure III.1.9b and III.1.9c)

Table III.1.5: Effect of environmental factors.

Case	Environmental factor		
	Temperature	Relative humidity	Aging coefficient
(a)*	x	x	x
(b)			
(c)	x		
(d)		x	
(e)			x

* Reference case. x denotes the environmental factor is considered in the corresponding case.

PDF of the simulation results of the five cases were plotted in Figure III.1.9. It can be noted that considering temperature only (case c) can significantly accelerate both corrosion initiation time and severe cracking time by 49% and 28% respectively with respect to case b (neglecting environmental factors).

In contrast, relative humidity (case d) and aging coefficient (case e) delay initiation time and severe cracking time 237-162% and 211-4% respectively with respect to (case c).

This reflects the importance of considering the actual variation of these factors on the corrosion process. Therefore, these factors were considered in all the simulated cases to reach more accurate time-variant probabilistic simulation.
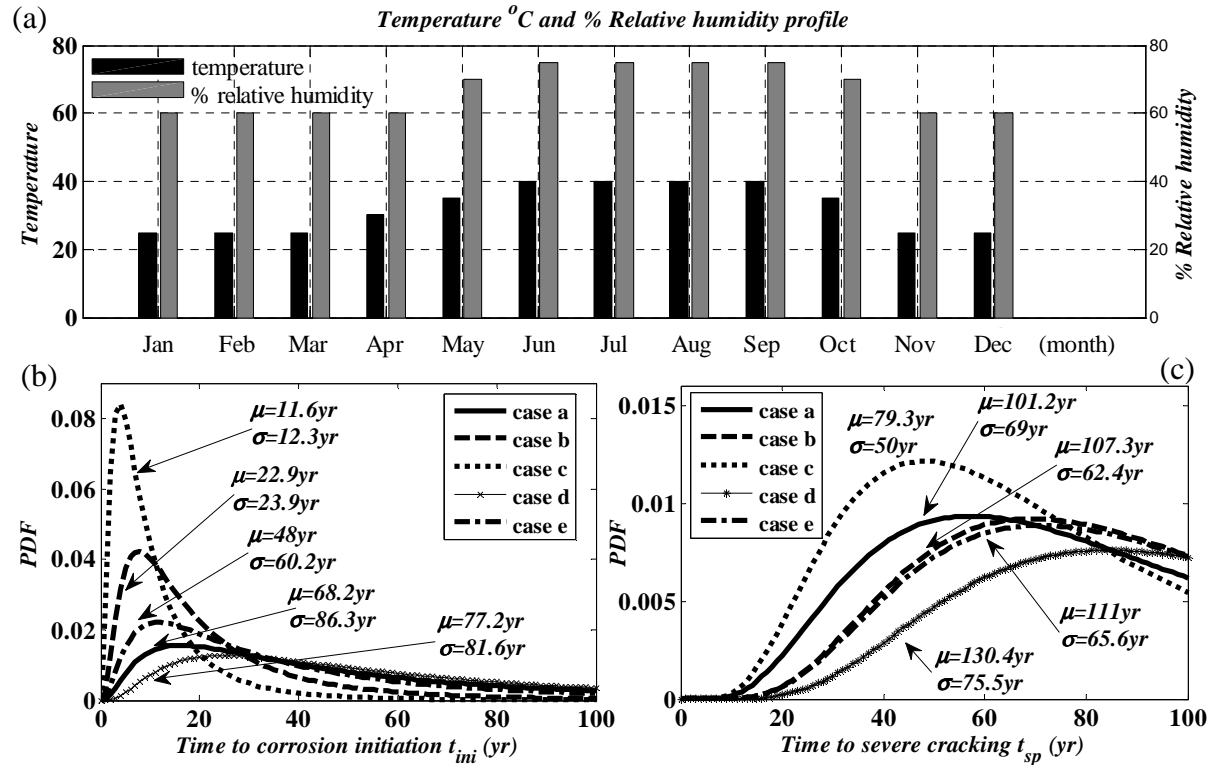
Figure III.1.9: Effect of environmental conditions on time to corrosion initiation and severe cracking of concrete cover. c=40 mm and bar diameter equals to 25 mm.

III.1.2.3 Probabilistic Live loads model

III.1.2.3.1 Probabilistic Truck model

There are many Live load models for highway bridges. The most comprehensive study was carried out by [Hong & Nowak 1991; Nowak 1993]. The models were derived from an extensive truck survey; weigh-in-motion observation and others. This survey covered about 9250 heavy trucks recorded within two weeks. The data base includes truck configuration (number of axles and axle spacing) and weights (axle loads and gross vehicle weight). For each truck in the survey, actions (bending moments and shear forces) were calculated for wide ranges of spans (9 to 60m).

The main fallout of their study is the expression of the statistical model for truck weight which was finally recommended in many reliability studies [e.g. Vu & Stewart 2000]. In the present study we consider the same statistical properties of the truck proposed by Hong & Nowak (1991). It was assumed that truck weight follows a Normal distribution with initial

mean value μ_{Wo} (=250 KN) and standard deviation σ_{Wo} (=100 KN). Gross truck weight distribution between axles and axle's spacing were adopted as for a standard HS20 truck proposed in [AASHTO-LRFD 2007]. The nominal truck dynamic effect was taken as a fraction of the gross truck weight; 0.15 for a single truck and 0.1 for two trucks side-by-side [AASHTO-LRFD 2007; Vu & Stewart 2000]. However, Nowak's model neglects the increase in live load - traffic volume and weight - over the time and the average daily truck traffic *ADTT* was assumed constant (*ADTT*=1000 trucks/day in one direction). In the present study we will consider that the live load model is time and *ADTT* dependent.

Highway Traffic survey studies confirm that traffic load volume and weight increase with time. Vu & Stewart (2000) suggested that the mean truck weight and the corresponding standard deviation are time dependent:

$$\mu_W(t) = \mu_{Wo}(1 + \lambda_w)^t \qquad (III.1.10)$$

$$\sigma_W(t) = \sigma_{Wo}(1 + \lambda_w)^t \qquad (III.1.11)$$

where λ_w is the annual increase of truck weight (=0.005).

The average daily truck traffic can be expressed as:

$$ADTT(t) = ADTT_{initial}(1 + \lambda_v)^t \qquad (III.1.12)$$

where λ_v is the annual increase in traffic volume (which ranges between 1-3% taken 2.3% as an average value [Vu & Stewart 2000]) and $ADTT_{initial}$ is the initial average daily truck number at construction time of the bridge.

ADTT can be assumed as a fraction of the total traffic flow, this fraction depends on the class (rural, urban... etc) of the highway [AASHTO-LRFD 2007]. Five values of $ADTT_{initial}$ were considered in the 50, 250, 500, 750 and 1000 trucks/day. Such these values can simulate the level of traffic amount on the bridge.

Extreme truck events (i.e. bending moments or shearing forces) induced in the girders are affected by four variables [Nowak 1993; Nowak 2004];

1. Truck model.
2. Impact factor.
3. Variation in transverse traffic position d_{lane} through bridges lanes (see Figure III.1.1). For standard 3.6 m wide lane, d_{lane} is approximated by a Log-Normal distribution with coefficient of variation 0.33 and mean value of 900 mm measured from the edge of the lane to the centre line of the outermost vehicle wheel.
4. Multiple presence of fully correlated heavy truck side-by-side on bridge deck traffic lanes (two lanes in the present study).

Nowak (1993) has observed that on average a truck is on the bridge simultaneously with another truck (side-by-side) about every 15 trucks/crossings. For these simultaneous occurrences, the author observes that:

- Every 10th time of side-by-side trucks are partially correlated (with regard to weight). The weights of side-by-side trucks have a coefficient of correlation equals to about 0.5.

- Every 30th time of side-by-side the trucks are fully correlated (i.e. have approximately the same weight).

The later observation is the most important because the girder extreme effects, bending moments or shearing forces, due to the crossing trucks are function of the fully correlated side-by-side trucks on the bridge. For example if *ADTT*=250 truck/day, there are 203 cases/year of simultaneous presence of fully correlated trucks (number of simultaneous presence cases *N*=365*ADTT*/450 case/year).

Kozikowski (2009) proposes another field survey including two sites in Florida and New York cities. The total number of records equals to 1,654,004 and 1,594,674 in Florida and New York respectively in 12 months. Multiple presences were filtered. Different correlation between the trucks side-by-side on the bridge were recorded and analyzed through the surveyed data. The authors have performed a statistical analysis of the side-by-side trucks on the bridge. They found that about 1259 and 1874 trucks in the first lane are fully correlated - with respect to gross vehicle weight - with trucks passed in the adjacent lane Florida and New York respectively.

In order to take into account the multiple truck presences in evaluating the extreme effects (e.g. bending moment), extreme value analysis is required. Rationally, the way to analyze the extreme value of a variable over a period is based on the knowledge of *CDF* of the maximum value of this variable over a shorter basic period. Then, assuming that the maximum effect in each basic period is an independent variable equally distributed in all periods [Crespo-Minguillon & Casas 1997], thus the *CDF* of the extreme value over the long period can be expressed as:

$$F_n(x) = \left[F_1(x)\right]^N \qquad \text{(III.1.13)}$$

where F_n is the *CDF* of the maximum effect in *N* basic periods, F_1 is the *CDF* of the maximum effect in one basic period.

In our case, Equation III.1.13 was employed to find the *CDF* of extreme event based on the *CDF* of an individual truck such that:

$$F_n(w,t) = \left[\Phi\left(\frac{w - \mu_W(t)}{\sigma_W(t)} \right) \right]^{N(1+\lambda_v)^t} \qquad \text{(III.1.14)}$$

where t is the time in years. Φ is the *CDF* of the standard normal distribution. $\mu_W(t)$ and $\sigma_W(t)$ were defined in Equations III.1.10 & III.1.11 respectively. N, in this case, is the number of crossings (side-by-side) heavily loaded fully correlated trucks per year. λ_v is the expected annual growth in the traffic volume (λ_v=0.023).

According to Nowak's (1993) observations, N will be taken as a ratio of $ADTT_{initial}$. Based on the probabilistic transformation discussed in § II.3.1.3 (Equation II.3.13), Equation III.1.14 can be transformed from the physical space to the normalized U-space such that:

$$w = \sigma_W(t)\Phi^{-1}\left[\Phi(u)^{\left(\frac{1}{N(1+\lambda_v)^t}\right)} \right] + \mu_W(t) \qquad \text{(III.1.15)}$$

The above observations were used to obtain a live load probabilistic model during the bridge lifetime. Table III.1.6 presents the required statistical parameter of the random considered variables. It is assumed that the increase in traffic volume takes place at each year increment and that traffic simulation from year to the next is statistically independent. Consequently, simulations can be treated separately for each time increment [Crespo-Minguillon & Casas 1997; Vu & Stewart 2000].

Table III.1.6: Probabilistic parameters of loads random variables.

Variable.	Distribution	Units	Nominal	λ^a	CoV^b	Cource
Model error	Normal	---	1	0.98	0.07	[Nowak 2004]
d_{lane}	Log-Normal	mm	900	1	0.33	[Nowak 2004]
concrete weight	Normal	depend on analysis		1.05	0.1	[Nowak 1993]
Asphalt thickness	Normal	mm	90	1	0.25	[Nowak 1993]
Truck load w	Normal	kN	250	1	0.4	[Val *et al* 2000]
Impact factor (*IL*)	Normal	---	0.1	1	0.8	[Val *et al* 2000]

[a]λ; bias value, [b]CoV; coefficient of variation.

III.1.2.3.2 Probabilistic structural error model

Two theoretical methods can be used to determine truck event (bending moment or shearing force). The first is the simplified formulas of girder distribution factors reported in bridges design codes [e.g. AASHTO-LRFD 2007] which involved high values of uncertainty, as shown by their statistical parameters (bias λ_d and variation coefficient CoV_d equal to 0.93 and 0.12 respectively). The second is to use sophisticated methods such as the finite element analysis which was used in our case, because it provides a robust prediction tool of the

structural truck events. In addition, uncertainty given in the first method can be decreased to $\lambda_d =0.98$ and $cov_d=0.07$ [Nowak 2004]. Recent field tests have confirmed that the girder distribution factor can be treated as a Normal random variable [Nowak 2004].

III.1.2.3.3 Overall live load Probabilistic model

In order to decrease the number of random variables of the live load, the impact factor (*IL*) and the truck weight given in Table III.1.6 were assumed statistically independent [Val *et al* 1998]. Consequently *IL* and *w* can be merged in one variable which has a mean value and coefficient of variation of 275 kN and 0.408 respectively (e.g. 250x(1+0.1)= 275 kN & $\sqrt{0.4^2 + 0.08^2} = 0.408$).

In our research, three key points were used to develop a live load model: (1) Monte-Carlo random number generation, (2) finite element analysis and (3) neural network applications. For each *ADTT* value and at each time increment (e.g. one year), the following steps were performed to develop the probabilistic model of the extreme effects, based on Nowak's (1993) observations:

1. A dataset of the live load random variables is prepared. The dataset consists of 810 combinations of d_{lane} and *w* (see Table III.1.7). Ranges of d_{lane} and *w* have been chosen such that all the expected generated values will be within the minimum and the maximum values of these ranges. For each case of the dataset, different values d_{lane} were considered for each lane. According to Nowak (1993), we also made the assumptions that extreme event induced in the girder takes place when two trucks (side-by-side) are on the bridge; these two trucks are then fully correlated. In other words these trucks have a coefficient of correlation equals to the unity. Consequently, the two side-by-side trucks have the same weight *w*. Finally variations in dead load, surface load and material properties were neglected, as they are expected to have insignificant effect on the live load model.

Table III.1.7: Range of live load variables and corresponding range of the analyzed actions.

Variable.	Units	Range	Remarks
d_{lane}	Mm	0:200:1600	Range for each lane
Extreme truck weight including impact *w*	kN	400:100:1300	The range for the two lanes
Corresponding extreme bending moment	kN.m	20.154:109.471	
Corresponding extreme shearing forces	kN	156.43:464.92	

2. Finite element analysis program Abaqus is used to analyze each case in the dataset. Bridge deck is simulated using shell and beam elements for bridge slab and beams respectively (see Figure III.1.10). For each case the mid span bending moment and the support shear force were recorded. Appendix D.1 gives an example of input file for a case within the

prepared dataset (case number 810).
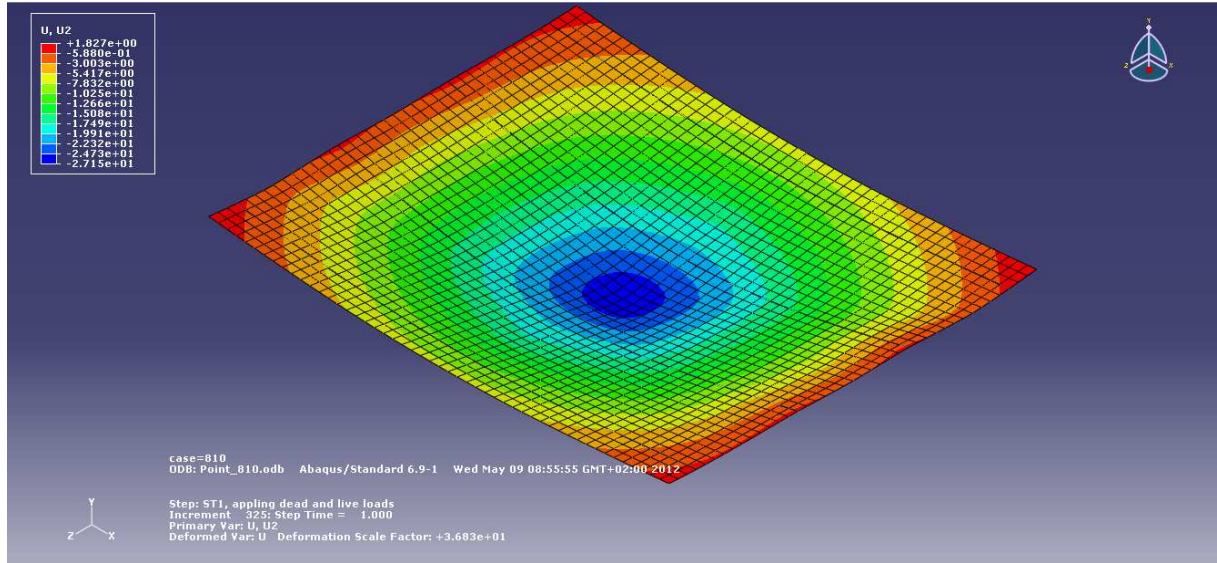
Figure III.1.10: Deformed shape of bridge deck; d_{lane} 1600mm for first and second lane, extreme weight of side-by-side trucks equals to 1300 KN. (case number 810)

3. Based on the dataset prepared in first step and their corresponding actions, a neural network were constructed, trained, validated and tested. Figure III.1.11 presents the inputs of the neural network. Output of the neural network are actions induced in the interior girder of the bridge deck; maximum bending moment and shearing force. This neural network used to predict additional actions.
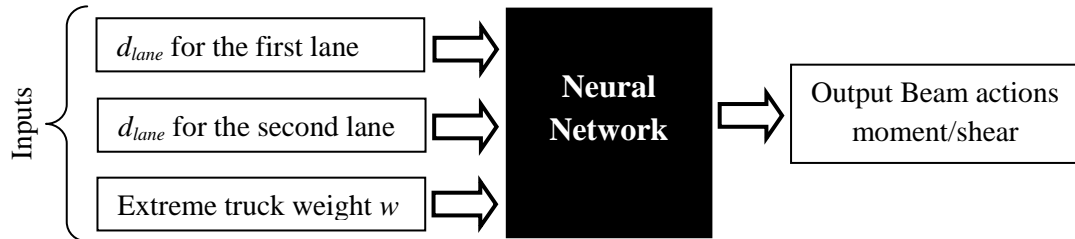
Figure III.1.11: Inputs and outputs of neural network used to predict extreme actions in the interior girder of the bridge deck.

In order to provide a visual presentation of the accuracy of the neural network constructed in this step, Figure III.1.12 present a scatter distributions of the beam actions extrapolated using neural networks and real values obtained using non-linear finite elements analysis. It can be noted that the application of neural network application provides a robust predictor for the response of the bridge deck (coefficient of correlation R =0.999).

4. Based on the individual distribution of each variable (see Table III.1.5 and Equation III.1.9), Monte Carlo technique is used to generate 10^5 values of these variables. Thus 10^5 extreme actions (shear and bending moment) are calculated using the neural network

constructed in the previous step.

5. The *PDF* of the extreme events for a certain actions (bending moment or shearing force) were fitted by continuous distribution. Many statistical distributions were examined using Kolmogorov-Smirnov test (KS-test) with a level of significance of 5%. The KS-test results indicate that both Log-Normal and Generalized Extreme Value (GEV) distributions can best fit the generated data. Then, KS-tests are carried out for these two distributions with level of significance lower than 5%. It is finally found that the Log-Normal distribution is still valid contrary to the GEV distribution. Thus, we choose Log-Normal distribution to simulate the extreme bending moments and shearing forces.
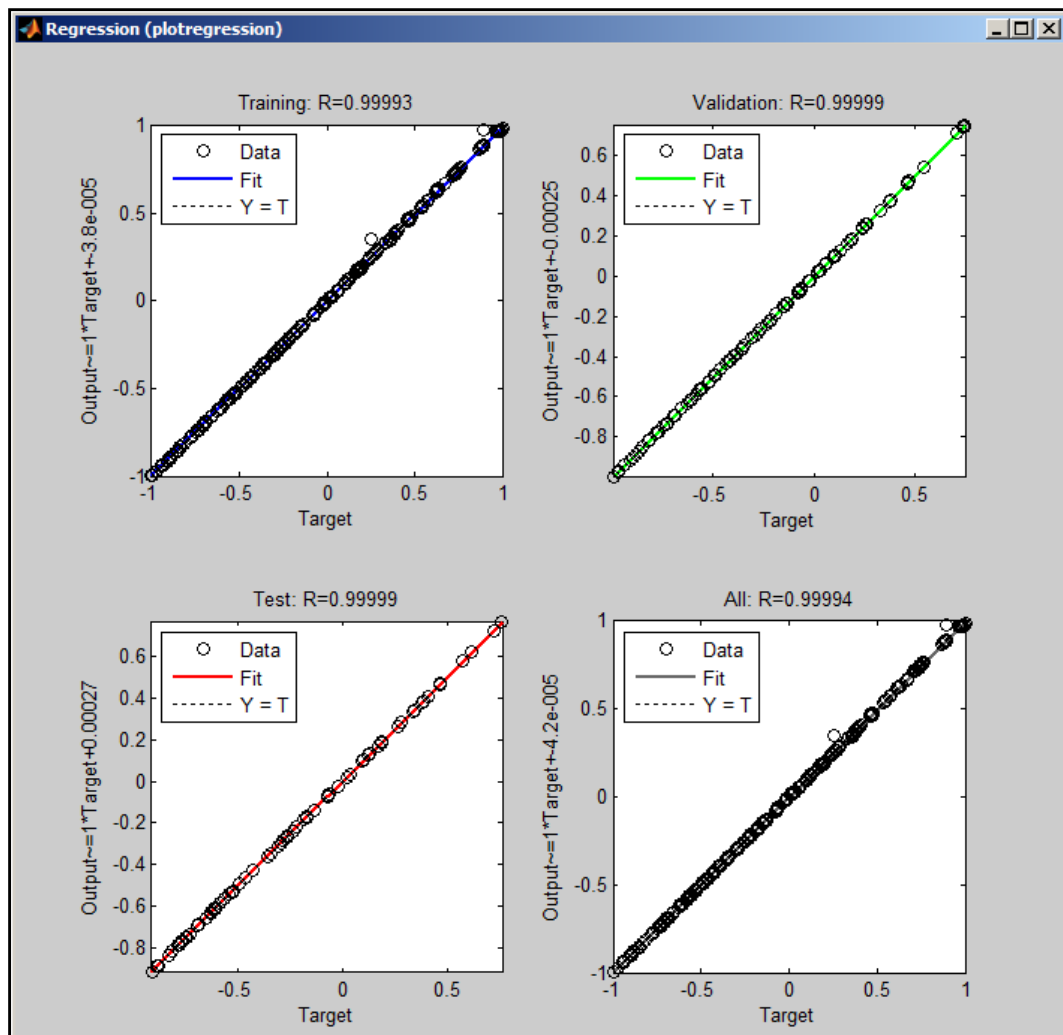
Figure III.1.12: Scatter distribution of target and predicted actions (810 cases), bending moment, obtained using neural network.

Figures III.1.13 & III.1.14 show samples of simulation results for extreme bending moment and shearing force induced in an intermediate girder respectively. Results shown in the figure are normalized in term of bias; i.e. extreme actions were divided by the nominal action obtained by the AASHTO specifications. Nominal AASHTO actions were obtained

considering the two trucks of standard HS20 type which were positioned on the bridge lanes such that d_{lane}=900 mm. The proposed model was used to fit the live load probabilistic model at a time increment equals to one year. For the time dependent reliability analysis, the parameters of the Log-Normal distribution between the two time increments were obtained using linear interpolation between these increments. According to Figures III.1.13 & III.1.14, increasing the *ADTT* value increases slightly the actions biases. Growth of live load over time increases dramatically these biases and the dispersion of the generated data.
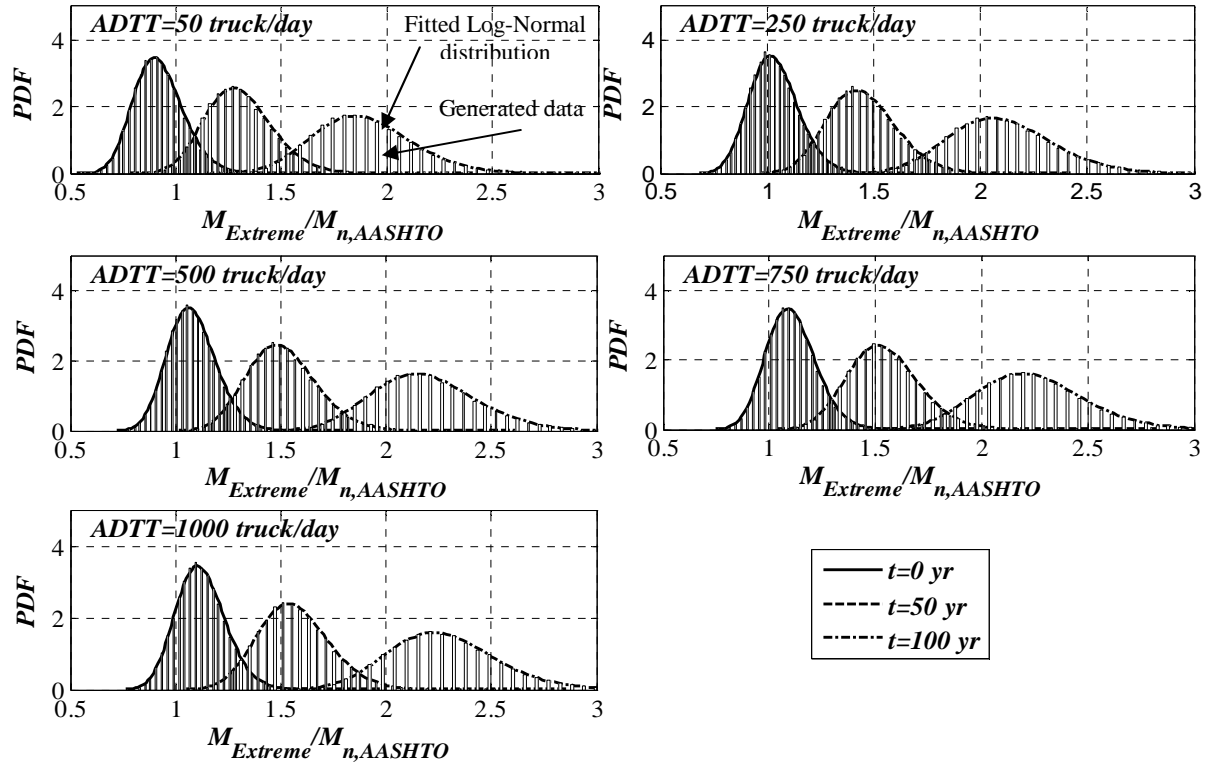
Figure III.1.13: Probability density distribution of extreme generated bending moments bias ($M_{extreme}/M_{n,AASHTO}$); $M_{extreme}$ is the extreme bending moment and $M_{n,AASHTO}$ is the nominal bending moment based on AASHTO specifications.
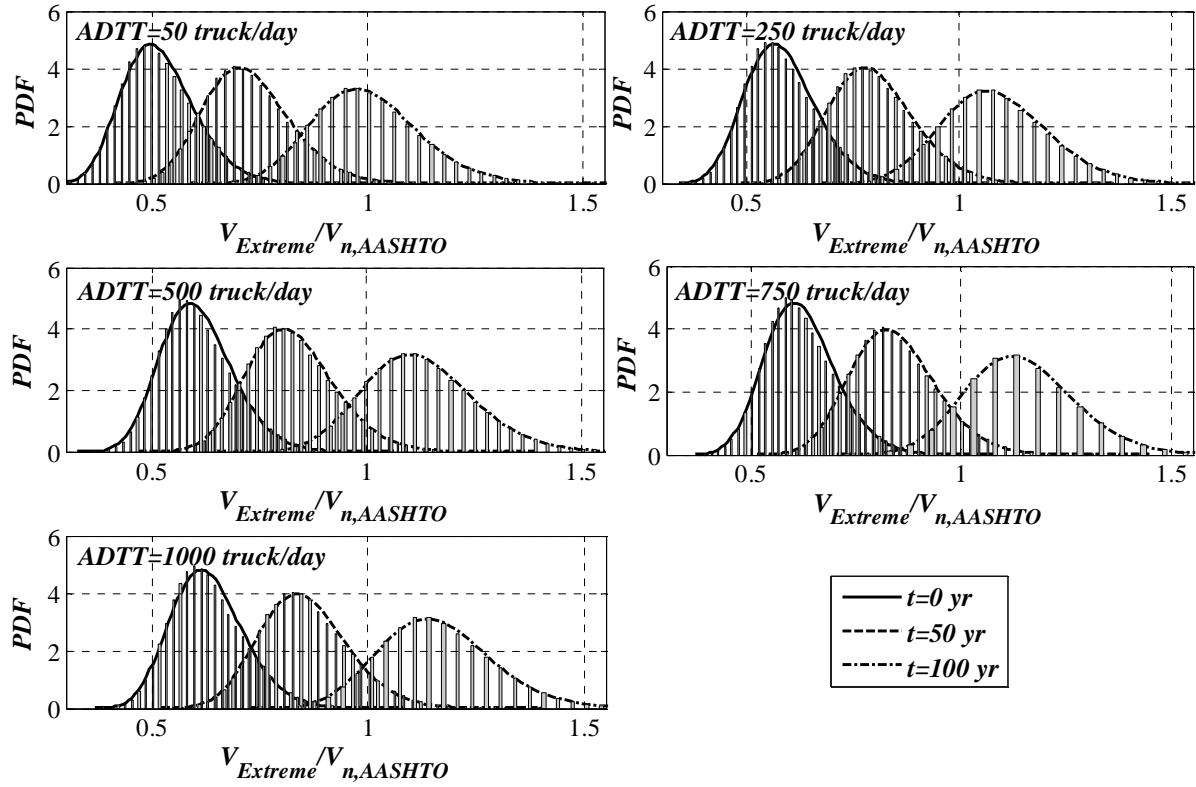
Figure III.1.14: Probability density distribution of extreme generated shearing forces bias ($V_{extreme}/V_{n,AASHTO}$); $V_{extreme}$ is the extreme shearing force and $V_{n,AASHTO}$ is the nominal shearing force based on AASHTO specifications

In order to clarify the effect of the variations inherited to the four random variables (d_{lane1}, d_{lane2}, w and structural model error) involved in the proposed model, five cases were simulated using the trained neural network. The five cases are:

1. A reference case at time 50 years with *ADTT*=1000 truck/day (all the variables are probabilistic ones with distributions given in Table III.1.7)

2. The reference case considering d_{lane1} as deterministic value equals to 900 mm

3. The reference case considering d_{lane2} as deterministic value equals to 900 mm

4. The reference case considering structural model error as deterministic value equals to unity

5. The reference case considering w – extreme truck weight including impact effect - as deterministic value equals to 850.487 kN. This value is calculated using Equation III.1.15 with u=0.

The *PDF* of the generated data were plotted in Figure III.1.15. It can be noted that only three variables have a significant effect on the *PDF* of the live load model. Such these variables are d_{lane1}, w and structural model error. While the truck position in the second lane d_{lane2} has no effect on the live load model, since *PDF* of the reference case 1 and the case 3 are identical as shown in Figure III.1.15. Thus, this variable can be considered as deterministic value equals

to its nominal value (d_{lane2}=900 mm) in the subsequent reliability example.
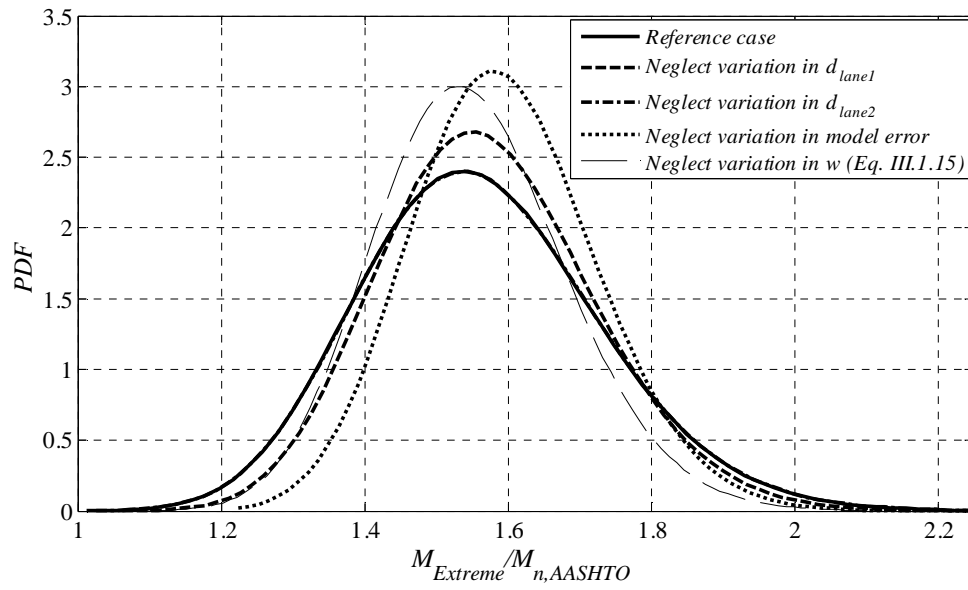
Figure III.1.15: Sensitivity of the live load model to its random variables, time=50 years and *ADTT*=1000 truck/day.

III.1.3 CONCLUSIONS

This chapter presents the parameters of the probabilistic models of all the variables considered in the reliability analysis. These variables were divided in four categories: environmental, material, geometrical and loading. Monte-Carlo simulation technique was used in conjunction with a corrosion model to obtain a time-dependent probabilistic model of steel corrosion. Different values of concrete cover ranges between 25 to 45 mm were considered. A Kolmogorov-Smirnov test (KS-test) with a level of significance of 5% was used to fit the distribution of the generated data. Log-Normal distribution was found to be the best predictor of time to corrosion initiation t_{ini} and severe cover cracking t_{sp}. While Bi-modal distribution was found to be the best predictor for the steel area over the time after corrosion initiation.

In addition, the chapter presents a time-variant live load model; the growth of traffic load over the time is considered in both weight of heavy trucks and traffic volume ($ADTT$, Average Daily Truck Traffic; truck/day). The model is based on Nowak's (1993) field observations. These observations include truck weight, position of the truck through the traffic lane and the number of simultaneous presence of two adjacent trucks on the bridge deck. 810 combination cases were analyzed using a Finite elements program. These combinations and their corresponding responses, bending moments or shearing forces, were used to train, validate and test a neural network. Monte-Carlo simulation technique was used to provide vectors of live load variables and their structural responses using the trained neural network. Kolmogorov-Smirnov test (KS-test) with a level of significance of 5% was used to fit the distribution of the generated data. Log-Normal and Generalized Extreme Value (GEV) distributions were found to be the best predictors of structural actions due to truck loads. Log-Normal distribution was used to perform the reliability analysis. Various values of $ADTT$ were considered (50 – 1000 truck/day).

PART III: NUMERICAL APPLICATION AND RESULTS.

Chapter III.2: Results of reliability analysis.

III.2.1 INTRODUCTION

Time dependent probabilistic steel area and live load models developed in the previous chapter were used to perform a reliability analysis of the interior girder shown in Figure III.1.1. The other geometrical and material random variables are presented in Table III.1.3. In addition, the structural model errors for the different limit states considered are given in Table III.1.4. Reliability analysis, of FRP strengthened RC beam, presented in the present chapter is divided into two main parts. The first is the reliability analysis based on FORM algorithm and simplified limit states formulas proposed in previous studies. The second is the reliability analysis using Monte-Carlo simulation based on Neural Network applications MC-NN. Dataset required to train neural network were determined using finite element method. The considered beam was designed such that the reliability index, at time t=0, is greater than the target reliability index required for AASHTO specifications: β_T=3.5. FRP strengthening was assumed to take place at the time when the reliability index reaches a minimum value β_{min} (=3).

III.2.1 RELIABILITY ANALYSIS BASED ON FORM METHOD

III.2.1.1 Flexural limit states

Time dependent reliability analysis was performed for flexural limit state of RC beam. In a first step, we consider only the growth of live load over the time and no corrosion deterioration. Five values of Average Daily Truck Traffic were considered $ADTT$=50, 250, 500, 750 and 1000 truck/day. These values can simulate the traffic volume aggressiveness effect on bridge reliability. The reliability index as a function of time is shown in Figure III.2.1. It can be noted that the reliability index profile is not significantly affected by the $ADTT$ value. Indeed, the differences of reliability indexes between $ADTT$=50 and $ADTT$=1000 equal to 0.211 and 0.626 at times equals to 0 and 100 years respectively. The figure also shows that the reliability profile is significantly affected by the growth of live load over the time and the girder is reliable for more than 50 years (e.g. for t<50 years, β>β_{min}).

While for the last 50 years, the girder is still in moderate reliable conditions ranges between 1.929 and 2.555.
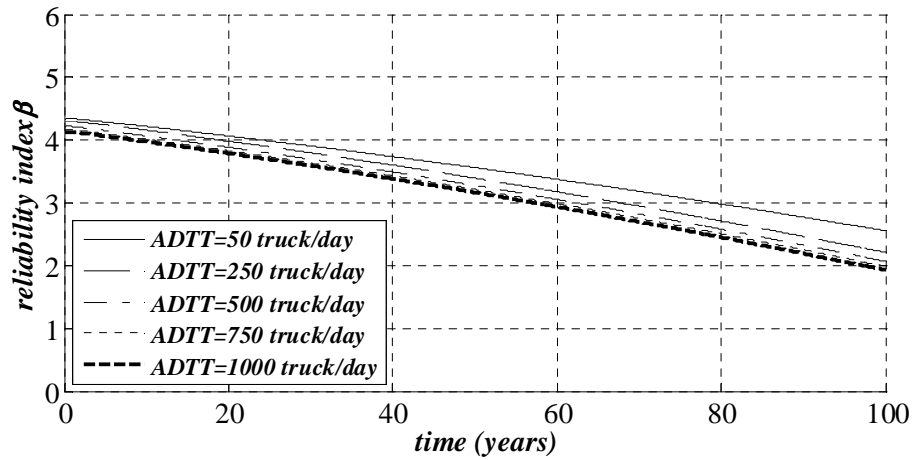
Figure III.2.1: Effect of live load on reliability profile of RC beam for flexural limit state (No corrosion).

In order to evaluate the effect of coupling the live load growth with corrosion effect. Both uniform and pitting corrosion models, presented in chapter I.1, were also considered. For an *ADTT* value equals to 500 trucks/day taken as an example, reliability analysis were conducted to assess the influence of the concrete cover on reliability index. Five values of concrete cover *c* were considered: 25, 30, 35, 40 and 45 mm. Results were plotted in Figure III.2.2. According to the results, growth of live load is more significant in deteriorating reliability index at high cover values *c*; 35:45 mm. While pitting corrosion, at *c*=25:30mm, is more hazardous than live load growth. In addition, pitting corrosion is potentially more hazardous in all cases than uniform corrosion; it is significantly accelerates time to strengthening. From a practical point of view concrete cover of 40 mm is required for aggressive marine environment according to the prEN 10080 (1999). Consequently, it can be observed that when coupling growth of live load effect with either pitting or uniform corrosion the beam is still reliable for about 45 years (e.g. for *t*<45 years $\beta>\beta_{min}$). Figure C.1 to C.4, in Appendix C, present the reliability profile for all the analyzed combinations of *c* and *ADTT*.
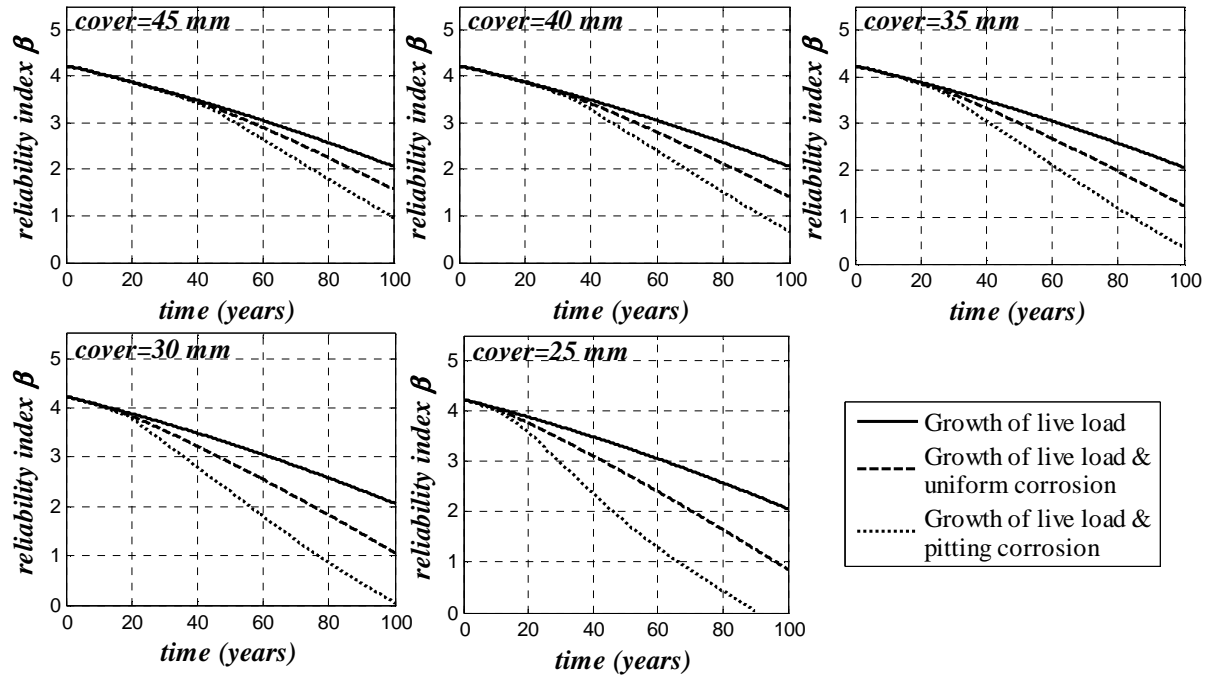
Figure III.2.2: Reliability profiles of RC beam for flexural limit state under corrosion deterioration and growth of live load (*ADTT*=500 trucks/day).

In order to generalize the relationship between the concrete cover and the time to strengthening, reliability analysis were conducted for all the possible combinations between the concrete cover and the *ADTT* values. Time to strengthening was evaluated for each combination of *c* and *ADTT*. Results were plotted in Figures III.2.3. It can be noted that the relation between *c* and the time to strengthening is linear for all *ADTT* values. In most cases, the beam under uniform corrosion maintains reliability index for a time more than 40 years. From the other side, pitting corrosion accelerates this time of about 30%. For a choosen cover value, time to strengthening for uniform corrosion is more senstive to the *ADTT* than pitting corrosion with respect to *ADTT*.
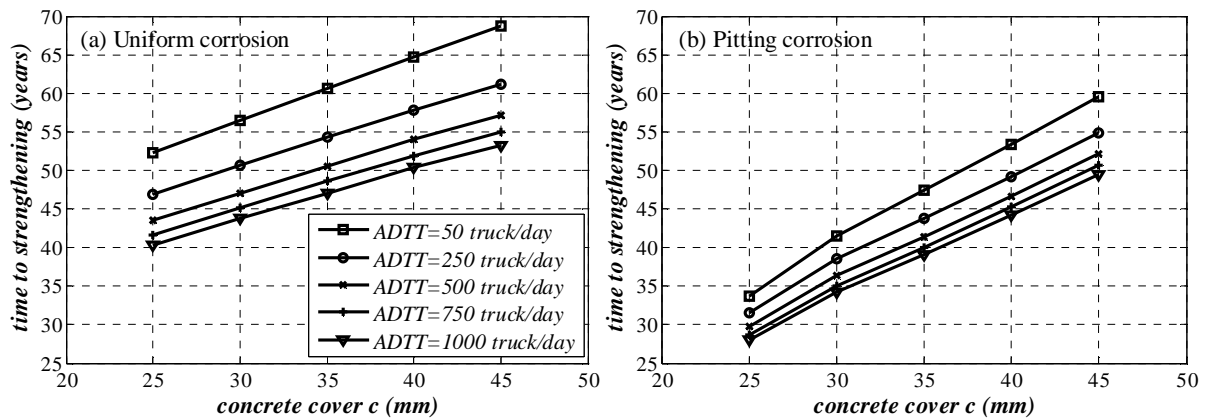
Figure III.2.3: Relation between cover *c* and time to strengthening, flexural limit state.

As the scope of the present study extends beyond reliability of deteriorated RC beams

towards FRP strengthening, we discuss in the following paragraphs the effect of FRP repairing on the reliability profile.

Herein, we assume that corrosion activity will not be affected by FRP strengthening scheme, as it was proven in previous studies that FRP strengthening does not affect corrosion process of steel reinforcement embedded in concrete (see § I.1.7). The reliability analysis was implemented assuming that strengthening process will take place at a time such that reliability index reaches a minimum value β_{min}=3. Two layers of the CFRP laminates with thickness equal to 1.27 mm/layer are considered. Width of the FRP plate is taken equal to 300 mm.

Two strengthening options were assumed:

1. Non-anchoraged end FRP laminates. The controlled bending moment $M_{u,min}$ can be expressed as:

$$M_{u,\min} = \min\left(M_{u,cc}, M_{u,FRP,r}, M_{u,FRP,d}\right) \qquad \text{(III.2.1)}$$

where $M_{u,cc}$ is the ultimate bending moment due to concrete crushing failure mode. $M_{u,FRP,r}$ is the ultimate bending moment due to FRP rupture. $M_{u,FRP,d}$ is the ultimate bending moment due to FRP intermediate crack debonding (see § II.1.2.1).

2. Anchoraged end FRP laminates. The controlled bending moment $M_{u,min}$ can be expressed as:

$$M_{u,\min} = \min\left(M_{u,cc}, M_{u,FRP,r}\right) \qquad \text{(III.2.2)}$$

Analysis results of all the combinations of c and $ADTT$ values are presented in Appendix C (Figures C.5-C.8). For all the cases, results of analysis have shown that the controlled failure mode after strengthening is limited by the CFRP strain; FRP rupture strain or FRP intermediate crack debonding strain (depending on wither the CFRP ends are anchoraged or not). While concrete crushing in our case was not the control failure mode after strengthening although the tension steel is in yield domain, this returns to that the total amounts of steel and FRP reinforcement ratio after strengthening is not beyond the limiting ratio that causes concrete crushing.

For the non-anchoraged FRP laminates, it is found that the debonding failure mode is the controlled mode; FRP rupture and concrete crushing are yet occurred. While For anchoraged FRP laminates rupture failure mode was found to be the control failure mode, concrete crushing did not occur.

Figure III.2.4 shows a result sample of the reliability analysis of the strengthened girder with c=30 mm & $ADTT$=500 truck/day. The most important characteristic in this figure is that anchoraged FRP laminates is more effective in increasing reliability index than non-

anchorage end laminates. In other words, FRP rupture failure mode provides more reliability than intermediate cracking FRP debonding, as reliability index of strengthened beam controlled by FRP rupture failure modes is approximately twice the reliability index of FRP strengthened beam controlled by FRP debonding.

In addition it can be observed that rate of deterioration in the reliability profile after strengthening is the same for both strengthened and non-strengthened beams. Accordingly, the additional service life provided after strengthening for FRP anchoraged laminates is approximately twice that for non-anchoraged FRP laminates if FRP durability effect is neglected. Although the time to strengthening is not the same for uniform and pitting corrosion, the increase in the reliability index takes the same value. We can conclude that the vertical increase in the reliability index does not depend on the deterioration level the reliability profile.
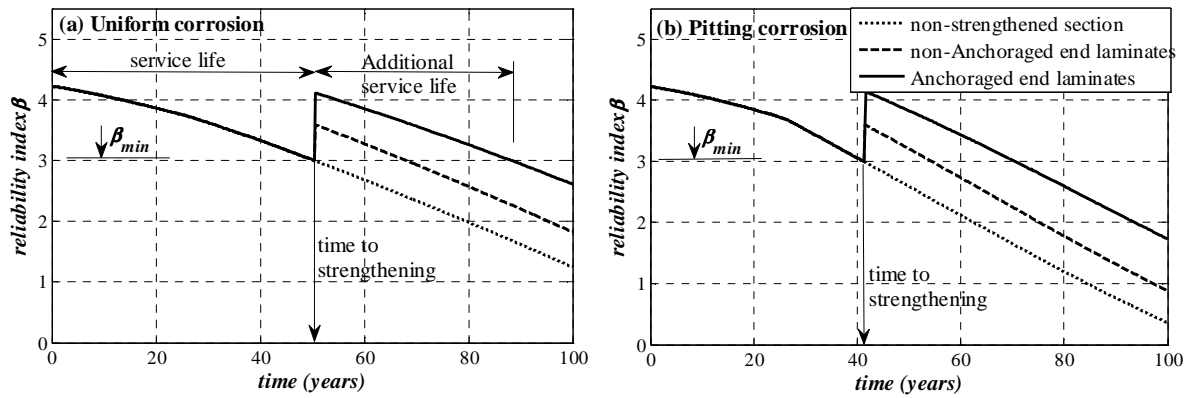
Figure III.2.4: Reliability profiles of FRP strengthened RC beam for flexural limit state under corrosion deterioration and growth of live load (*ADTT*=500 truck/day; *c*=30mm).

Although, concrete crushing did not occur after strengthening, this cannot be generalized in most FRP strengthening cases. We try the analysis with another CFRP material properties reported in [Atadero & Karbhari 2009]. For simplicity, the above CFRP properties used in the previous discussion and reported in Table III.1.3 are denoted as the ones of material type A, while the other CFRP material [from Atadero & Karbhari 2009] is denoted as material type B. Probabilistic model of both FRP material properties are given in Table III.2.1.

Results of the two cases are plotted in Figure III.2.5. According to the results of FRP non-anchoraged laminates, both cases A and B are controlled by intermediate crack debonding failure mode. Although the modulus of FRP type B is about 1.373 times the modulus of the FRP type A, there is no significant difference between their reliability profiles. As far as FRP anchoraged laminates are concerned beams fail by concrete crushing and FRP rupture for material types A and B respectively. The latter FRP material type gives lower deterioration

rate than the former, this may returns to its high mechanical properties with respect to FRP material type A.

Table III.2.1: Probabilistic parameters of FRP material types A and B.

Type	Variable	Distribution	Units	Nominal	λ^a(mean)	$CoV^b(\sigma^c)$	Source
A	E_{FRP}	Lognormal	GPa	51.7	1	0.2	[Atadero & Karbhari 2007]
	$f_{FRP,u}$	Weibull	MPa	620.5	1	0.15	[Atadero & Karbhari 2007]
	t_{FRP}	Lognormal	mm	1.27	1	0.05	[Atadero & Karbhari 2007]
B	E_{FRP}	Lognormal	GPa	71	1	0.25	[Atadero & Karbhari 2009]
	$f_{FRP,u}$	Weibull	MPa	1160.23	1	0.12	[Atadero & Karbhari 2009]
	t_{FRP}	Lognormal	mm	1.0891	1	0.09	[Atadero & Karbhari 2009]

E_{FRP}, $f_{FRP,u}$ and t_{FRP} are the modulus, strength and thickness of FRP material respectively.
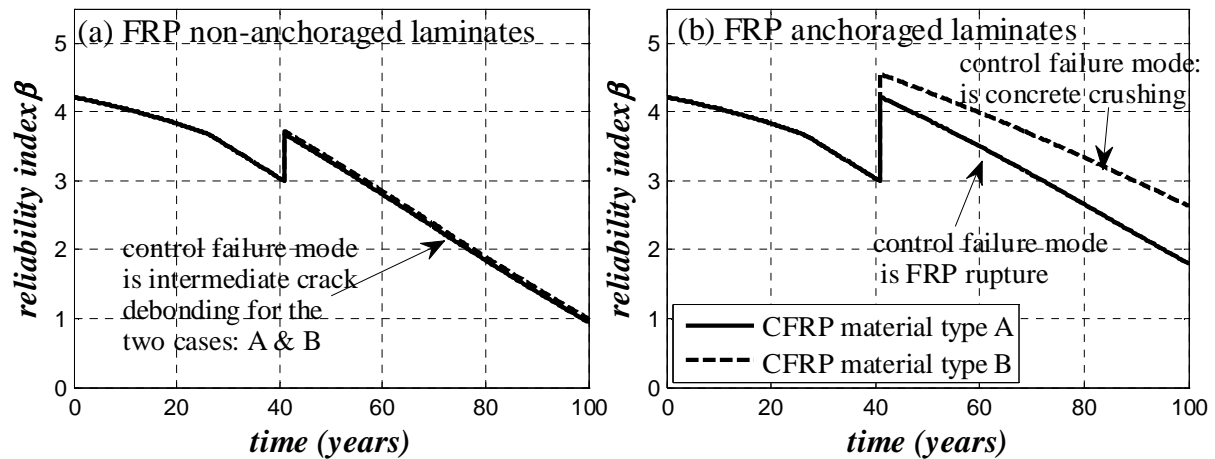
Figure III.2.5: Comparison of flexural limit state reliability profiles of interior RC beam strengthened with FRP materials A and B, pitting corrosion and growth of live load are considered (*ADTT*=500 truck/day; *c*=30mm).

Considering the effect of FRP durability on the reliability profile of FRP strengthened RC beams after time to strengthening, deterioration in the mechanical properties of the FRP composite material were assumed according to the durability model proposed by Karbhari & Abanilla (2007) (see § I.2.4 and Equation I.2.48). Figure III.2.6 presents the reliability profiles of FRP strengthened RC beam taking into account FRP durability. It can be noted that FRP durability has no effect on the reliability profile when the control failure mode is FRP debonding (case of non-anchoraged FRP laminates).

In contrast, rupture failure mode (for FRP anchoraged laminates) is significantly affected by FRP durability as it reduces the additional service life by 26%. However, the remaining additional service life is still longer than that provided when non-anchoraged FRP laminates is used. For example, in Figure III.2.6, for β_{min}=2, we can obtain a service life of 83.42 and 92.83 years respectively for non-anchoraged and anchoraged laminates. Thus, it can be concluded that the design of FRP strengthened beam using anchoraged FRP laminates is more effective than non-anchoraged laminates for the same FRP thickness. This effectiveness takes place in both reliability aspect and additional service life provided after strengthening.
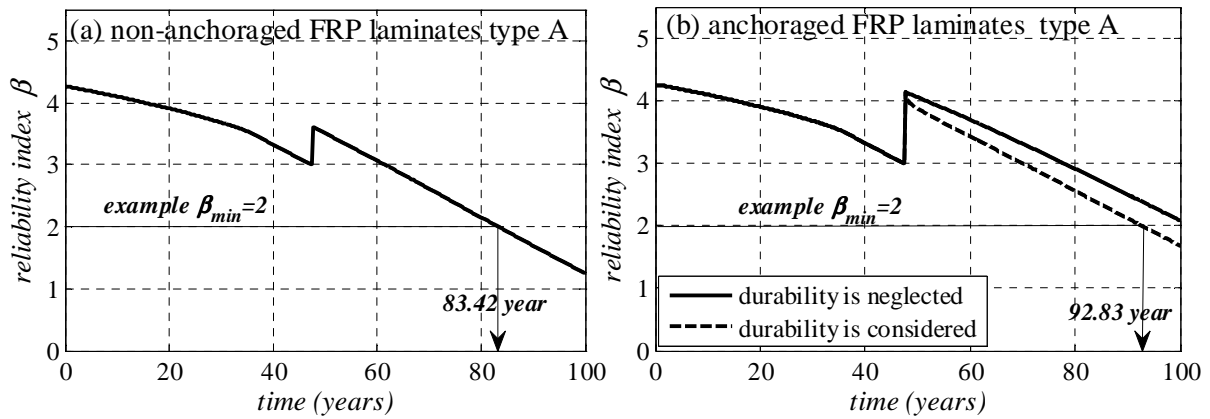
Figure III.2.6: Flexural limit state reliability of FRP strengthened RC beam under uniform corrosion deterioration, growth of live load, FRP durability ($ADTT$=500 truck/day; c=30mm).

The two cases compared above, in Figure III.2.5b, were reanalyzed considering durability effect as shown in Figure III.2.7. It can be noted that degradation of FRP properties, due to aging effect, does not change the control failure mode if it started initially with FRP rupture (Figure III.2.7a). As far as material type B is concerned, starting initially with concrete crushing, FRP durability consideration results in a vertical drop in reliability profile after strengthening as shown in Figure III.2.7b. This drop leads to a change in the control failure mode from concrete crushing to FRP rupture. Considering FRP durability has no effect on reliability if it is controlled by concrete crushing failure mode, while a significant deviation is observed in the reliability part of the profile which is controlled by FRP rupture failure mode.
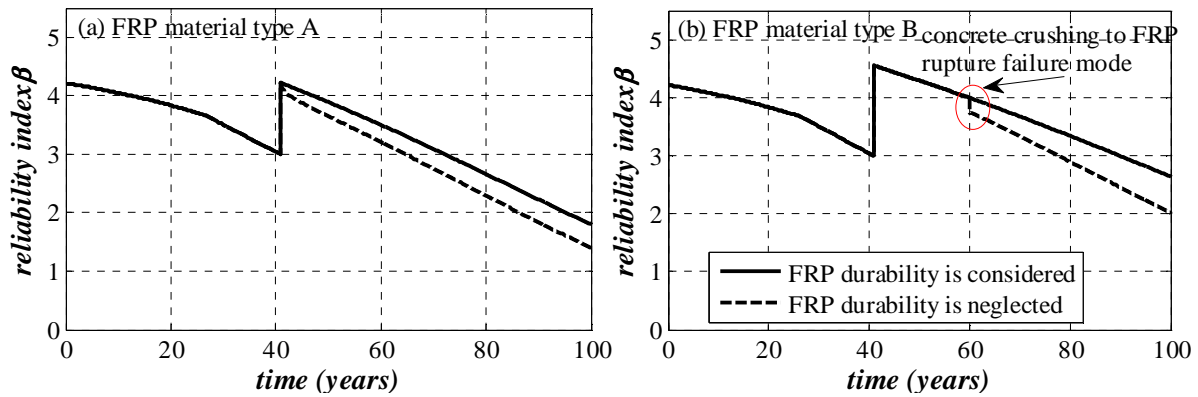
Figure III.2.7: Durability effect on FRP anchorage laminates flexural limit state reliability, strengthened with FRP materials A and B, pitting corrosion and growth of live load are considered ($ADTT$=500 truck/day; c=35 mm).

One of the main advantages of reliability analysis using FORM method is the possible direct calculation of the sensitivity factor of the design variables provided throughout the analysis (Equation II.3.32). These sensitivity factors reflect the random variables contributions on the reliability index. Generally, sensitivity factor of a random variable takes value ranges between -1 to 1. Values of sensitivity factors closed or equal to zero reflects that

their corresponding random variables have no effect on the reliability index and can be considered as deterministic values in the limit state. Importance of any random variable increases as the absolute value of its sensitivity factor increases towards the unity. Consequently we can judge which of these variables can be considered as random variables or as deterministic parameter in the limit state. Results of the sensitivity analysis were reported in Appendix C - Tables C1-C3 – for all c and *ADTT* values. Results were reported in terms of maximum and minimum values. The results indicate that:

- For non-strengthened beams (Table C.1): yield strength, live load, dead load, steel area and structural model error have a major influence on limit state reliability. While geometrical properties, concrete compressive strength and concrete modulus have insignificant effect on limit state reliability.

- For FRP strengthened beams with FRP intermediate crack debonding failure mode (Table C.2): yield strength, live load, dead load, steel area and structural model error have a major influence on limit state reliability. While cross-section dimensions, concrete properties and FRP properties have insignificant effect on limit state reliability.

- For FRP strengthened beam with FRP rupture failure mode (Table C.3): yield strength, live load, dead load, steel area, FRP strength and structural model error have a major influence on limit state reliability. While cross-section dimensions, concrete properties and FRP modulus have insignificant effect of limit state reliability.

In order to visualizes these factors as function of time, Figures III.2.8 shows the sensitivity factors of the flexural limit state of FRP strengthened RC beam with, as an example, concrete cover equals to 30 mm and under *ADTT*=500 truck/day.

The figures show the variation of sensitivity factors over the time due to corrosion of reinforcement and growth of live load over the time. It can be noted that growth of live load does not affect sensitivity factors over the time for non-strengthened beam (see Figure III.2.8a). A high variation in the sensitivity factor of steel area A_s and yield strength f_y is observed when coupling live load growth with corrosion especially of pitting type (see Figure III.2.8c and Figure III.2.8f).

For the case of FRP anchoraged laminates, a sudden drop takes place in yield strength sensitivity factor. This can be due to the fact that the FRP plate is stressed to its ultimate capacity, rupture capacity, leading to a decrease in steel contribution to the limit state (see for example Figure III.2.8h).

As previously mentioned, the control failure mode of the anchoraged laminates are FRP

rupture and concrete crushing for FRP material type A and B respectively. In order to show the effect of the control failure mode after strengthening on the sensitivity factors, Figure III.2.9 gives the sensitivity factors of the two cases. It can be noted that the major significant changes between the two cases are limited to the sensitivity factors of the FRP properties (strength, modulus and thickness):

- The sensitivity factor of FRP strength equals to zero when concrete crushing is the control failure mode (case FRP material type B).

- A significant increase over time in the sensitivity factor of the FRP modulus when concrete crushing is the control failure mode (case FRP material type B). In addition, the FRP strength sensitivity factor direction is changed from negative with FRP material type A to positive with FRP material type B.

- A slight increase is observed in the sensitivity factor of the FRP thickness.
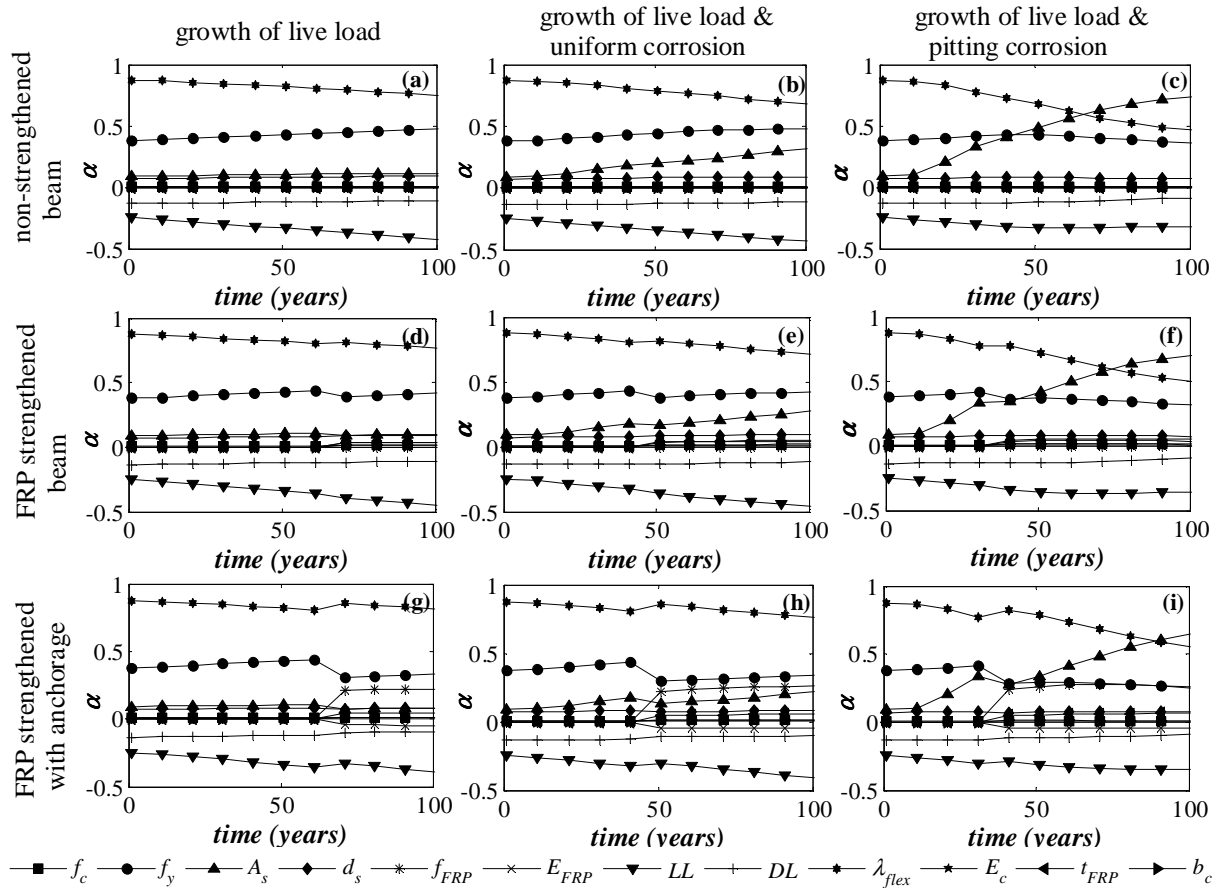
Figure III.2.8: Time dependent flexural limit state sensitivity factors α of FRP strengthened RC beam for (*ADTT*=500 truck/day; *c*=30mm).
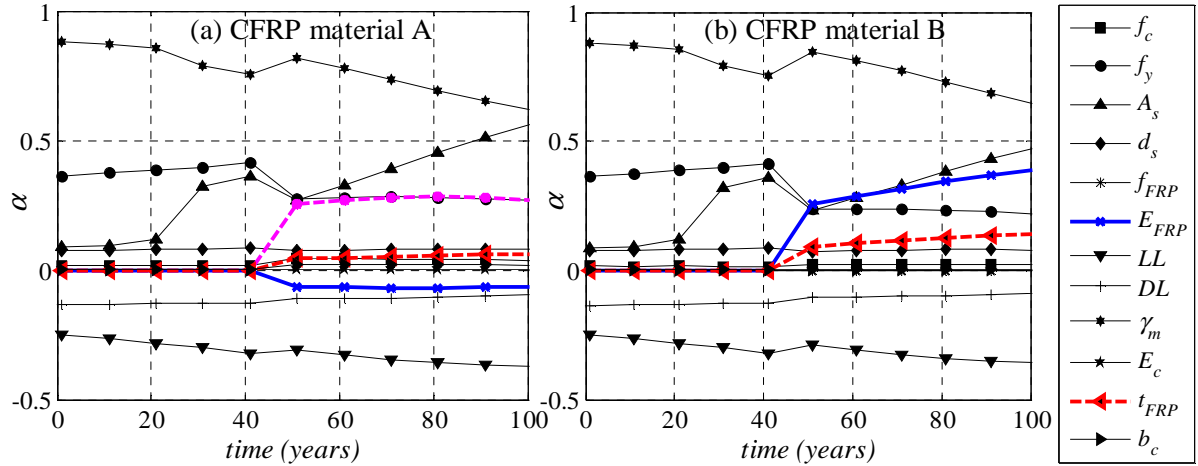
Figure III.2.9: Time dependent flexural limit state sensitivity factor α of FRP strengthened RC beam with anchorage laminates. (*ADTT*=500 trucks/day; *c*=30 mm).

III.2.1.2 Safety factors for flexural limit state

In an early study proposed by Plevris *et al* (1995), the authors suggested a specific reduction factor ($\psi = 0.8$) for the CFRP contribution to strengthened element resistance. However the study was limited to concrete crushing failure mode assuming full composite action; the authors neglected mid span CFRP debonding and FRP rupture. In a recent publication, by Pham & Al-Mahaidi (2008), discuses the reliability of strengthened beams considering multiple types of failure modes: CFRP rupture, intermediate crack debonding and end debonding. Atadero & Karbhari (2007) have studied the reliability versus time of CFRP strengthened concrete beams considering uniform corrosion and FRP durability. The authors focused on the importance of the statistical properties of CFRP material on a CFRP safety factor, which had been calibrated for various targets reliability indices. However, the authors neglect the structural model error which has important effect on the reliability index. Moreover, the study does not take into account the growth of live load over time.

The traditional format of Load and Resistance Design Factors LRFD that must be satisfied in design of FRP strengthened RC section can be expressed as:

$$\gamma_D DL + \gamma_w WL + \gamma_L LL \le \phi R(.......,\psi_{FRP}\, X_{FRP}) \qquad (III.2.3)$$

where γ_D, γ_W, and γ_L are load factors for dead and wearing surface and live loads respectively. *DL*, *WL* and *LL* are the bending moments due to asphalt wearing surface load, concrete weight and live load respectively. ϕ is the global safety factor. *R* is the nominal resisting bending moment. ψ_{FRP} is FRP partial safety factor. X_{CFRP} is the FRP contribution to resistance.

In the present section we focus on the effect of partial safety factors ϕ and ψ_{FRP} on the reliability index β of the FRP strengthened RC beam. Ranges of ϕ (0.6-0.875) and ψ_{FRP} (0.6-1) were considered.

For each combination of ϕ and ψ_{FRP}:

- Time dependent reliability analysis was performed to calculate time to strengthening of the RC beams assuming $ADTT$=500 truck/day; c=25mm (taken as an example).

- At time to strengthening, the thickness of FRP laminates t_{FRP} is calculated such that Equation III.2.3 is satisfied using in incremental procedure; an initial value of t_{FRP} is assumed. This value is increased incrementally until the resistance part in Equation III.2.3 reaches the loading part. Characteristic values of FRP properties (strength and modulus) required in Equation III.2.3 are calculated according to ACI 440.2R-02.

- Once Equation III.2.3 is satisfied the reliability index is calculated using FORM method for the flexural limit state function (Equation III.1.8).

The two FRP types A and B given in Table III.2.1 were considered. FRP width was taken equal to 300 mm. The reduction of FRP strength as function of number of FRP layers is considered (see § III.1.2.1).

Figures III.2.9 to III.2.12 give results of two strengthening schemes: anchoraged and non-anchoraged FRP end laminates. It can be observed, for a specific required target reliability index that the corresponding partial safety factors are not identical for anchoraged and non-anchoraged FRP laminates. For example, considering FRP material type A with partial safety factors (ϕ=0.8 & ψ_{FRP}=0.9) produces a reliability index β of 4.13 and 3.66 for anchorage and non-anchorage FRP laminates respectively. This point has not been treated in previous studies or in design codes, as previous calibration studies do not differentiate between the two cases.

In addition, it can be noted that the deterministic solution of LRFD and probabilistic solution of the limit state did not induce the same failure mode. In other words, deterministic analysis of LRFD equation probably fails to predict the true failure mode. Accordingly, the probabilistic analysis is an essential tool when multiple failure modes are considered to take place.

In term of deeper analysis of the results, lower values of ϕ ($<$0.7) are not preferable; indeed, un-conservative FRP amounts is required especially for non-anchoraged FRP laminates (see Figure III.2.11b). In addition, it can be noted that for high values of ϕ and ψ_{FRP}, the two strengthening schemes may required a same values of the FRP thickness since the control failure mode is FRP rupture.

According to the results, it can be recommended that probabilistic analysis is an essential step in the analysis of FRP strengthened RC because the failure mode changes with respect to the thickness, strength and modulus of the FRP material. These failure modes cannot be exactly predicted using deterministic analysis of the LFRD equation especially for non-

anchoraged system as shown in Figures III.2.11 and III.2.13.
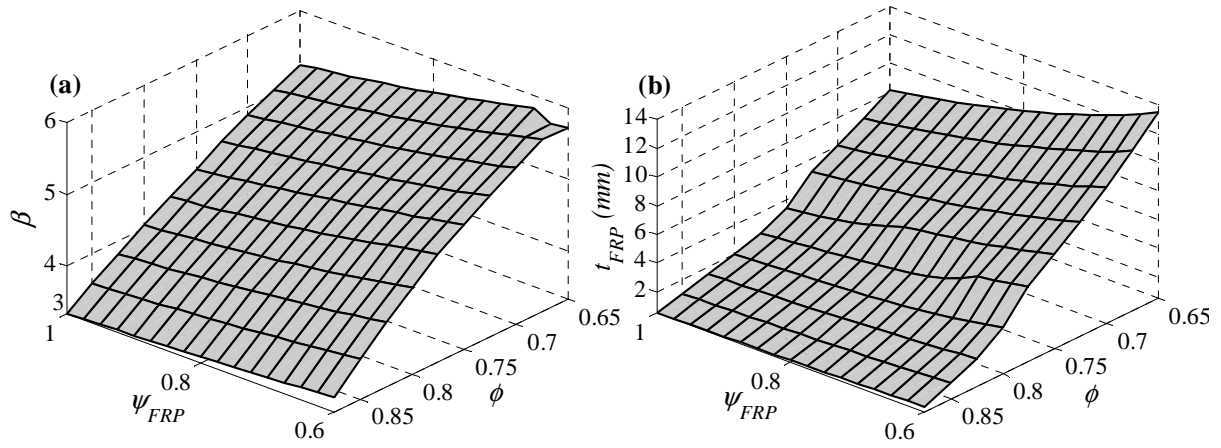
Figure III.2.10: Reliability index and FRP thickness as function of partial factors assuming anchoraged FRP laminated. FRP rupture is the control failure mode in all the cases (FRP material A).
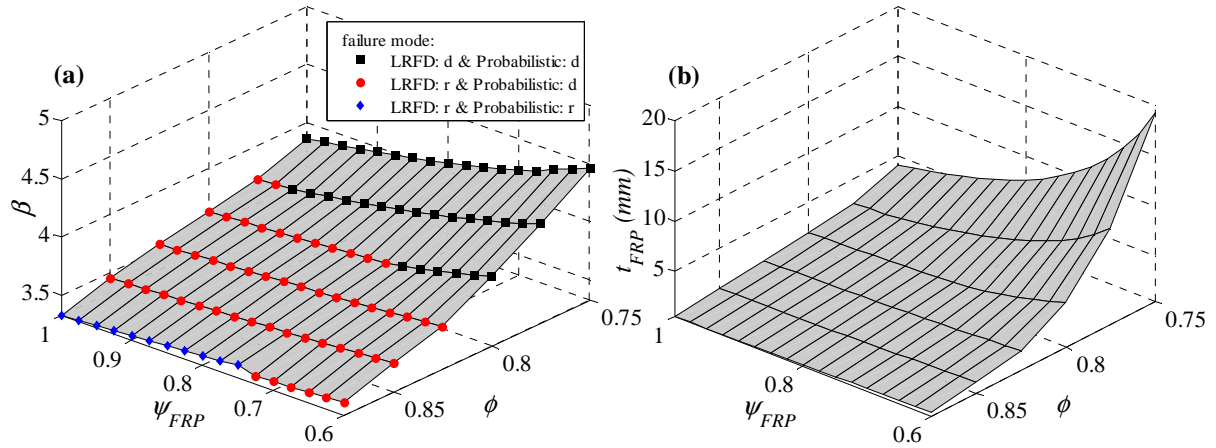
Figure III.2.11: Reliability index and FRP thickness as function of safety factors assuming non-anchoraged FRP laminated. r & d denotes FRP rupture and FRP debonding failure modes respectively (FRP material A).
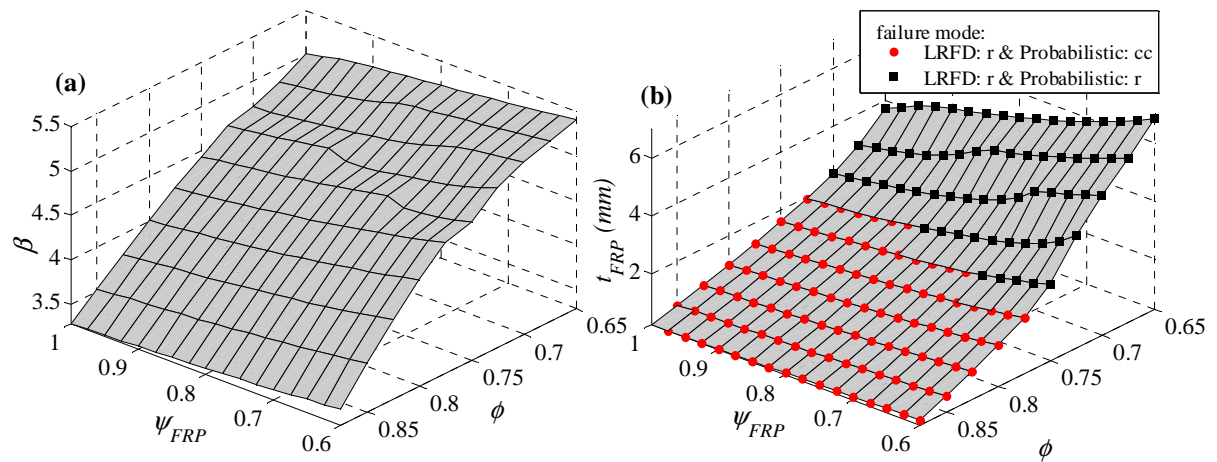
Figure III.2.12: Reliability index and FRP thickness as function of partial factors assuming anchoraged FRP laminated. cc & r denote concrete crushing and FRP rupture failure modes respectively (FRP material B).
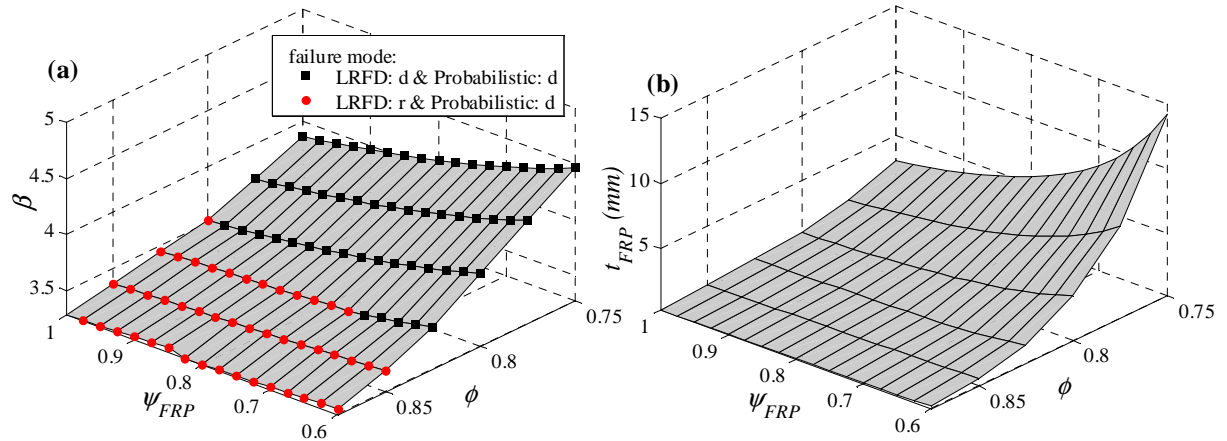
Figure III.2.13: Reliability index and FRP thickness as function of safety factors assuming non-anchoraged FRP laminated. d denotes FRP debonding failure mode (FRP material B).

III.2.1.3 Plate end debonding based shear crack

The second limit state that may take place when applying flexural FRP strengthening is the FRP end-debonding based shear crack. The resistance term in equation III.1.8 is calculated according to the debonding shear capacity $V_{db,end}$ proposed by [Ahmed & van Gemert 1999] (see § II.1.2.1.3 & Table I.2.8). Thus, the limit state given in Equation III.1.8 can be expressed as:

$$g(x) = \lambda_{db,end}V_{db,end} - \sum S_i \qquad \text{(III.2.4)}$$

where $\lambda_{db,end}$ is the structural model error, given in Table III.1.4, which is obtained according to § II.1.2.1.3. $\sum S_i$ denotes the summation of applied shearing forces which are taken equal to the summation of applied dead and live shear forces at the plate end. Applied shearing forces due to dead load include surface asphalt and concrete weights. While shearing forces due to live loads including impact factor will be calculated according to the live load model proposed in chapter III.1.
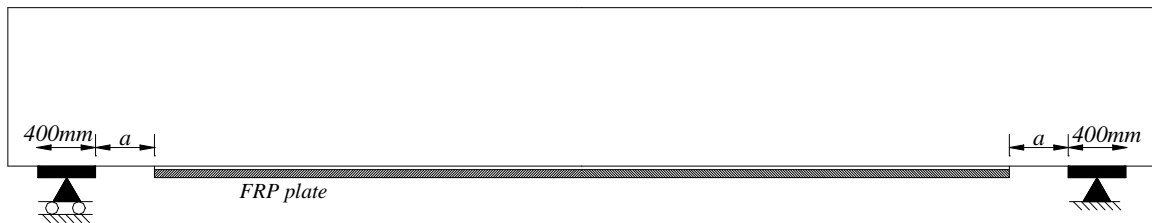
Figure III.2.14: Position of FRP plate end from beam support.

Reliability analysis was conducted according to the limit state expressed by Equation III.2.4. It is assumed that the plate-end is shifted about 50 mm from the support as shown in Figure III.2.14. Two layers of the CFRP laminates with thickness equal to 1.27 mm/layer are considered. Width of the FRP plate is equal to 300 mm.

In a first step, we consider that the deterioration takes place due to corrosion only and live load growth will be neglected. Figure III.2.15 presents the reliability profile of flexural limit state and the corresponding debonding based shear crack limit state. It can be noted that the present limit state is slightly affected by deterioration due to corrosion (pitting or uniform); i.e. there is a small variation on the β index versus cover c form with cover affects deterioration.

In a second step, we perform the reliability analysis of the present limit state considering deterioration due to corrosion and growth of live load. Results were plotted in Figure III.2.16. It can be noted that the *ADTT* has a slight effect on the reliability profile of FRP debonding based shear crack. In addition, growth of live load over time has a significant effect on reliability. However, the limit state reliability is still at considerable values (between 1.9 and 2.16 after 100 years).
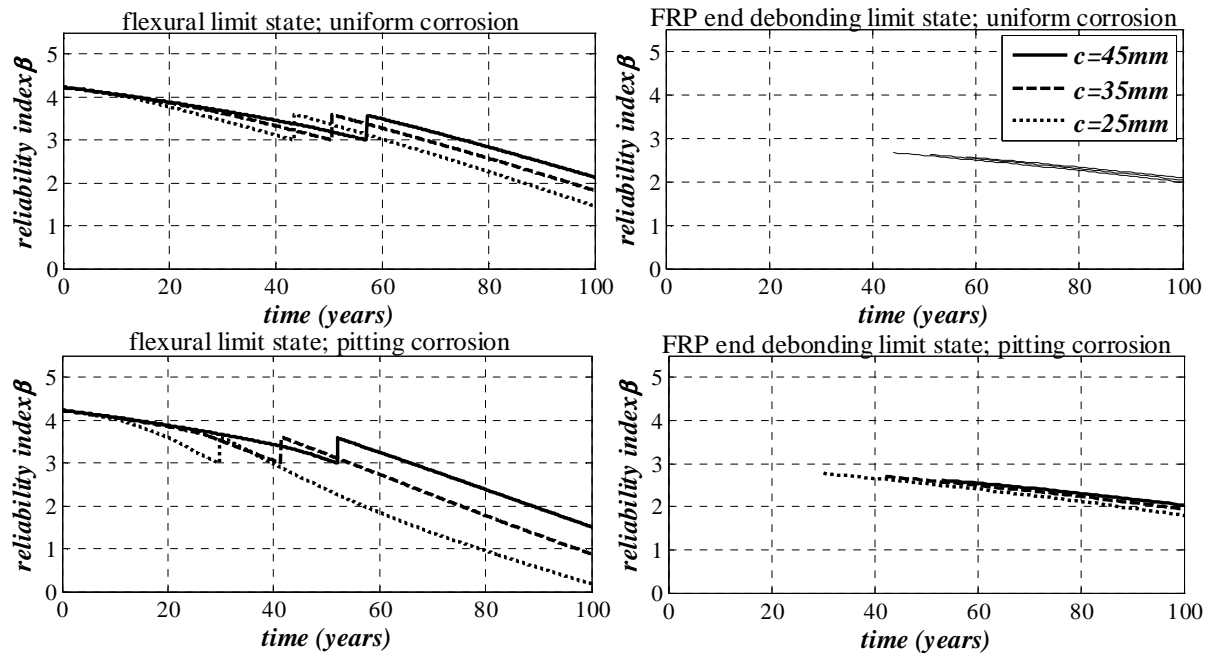
Figure III.2.15: FRP debonding based shear crack reliability profiles under corrosion deterioration (*ADTT*=500 truck/day).
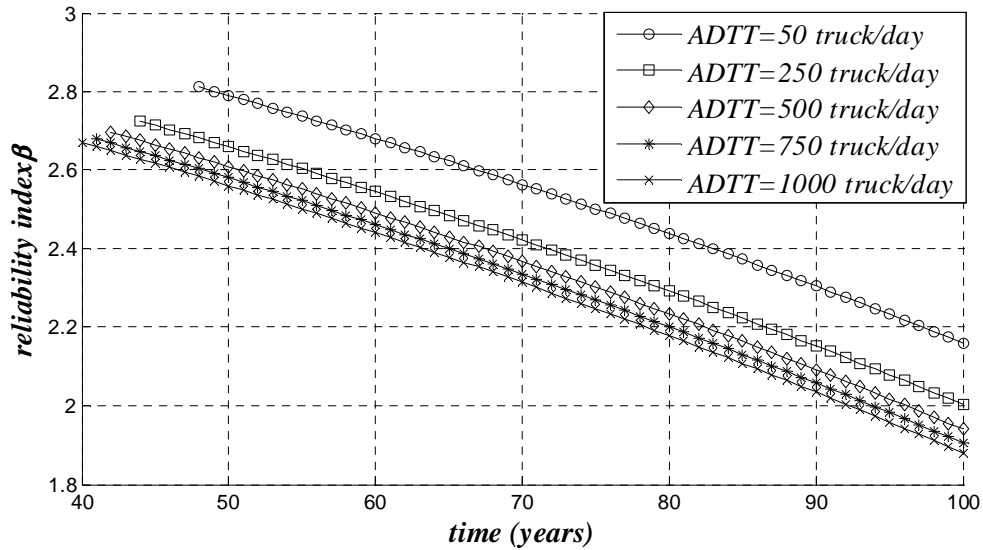
Figure III.2.16: FRP debonding based shear crack reliability profiles under corrosion deterioration and growth of live load over time (c=35 mm).

In order to take into account the effect of the distance a on the reliability of FRP debonding based shear crack limit state, three values of the distance a was considered: 50, 250 and 500 mm. Reliability analysis were performed for the three values of the distance a. Results were plotted in term of reliability profile as shown in Figure III.2.17. It can be observed that the distance a have a high significant impact on the reliability profiles; indeed, the increase in the distance a decreases dramatically the reliability. Finally, it can be concluded from Figures III.2.15-III.2.17 that the concrete cover c and the *ADTT* have no significant effect on the deterioration rate of the reliability of FRP end debonding based shear capacity limit state. However, a has a significant effect; i.e. reliability profile is very sensitive to a. Thus, the distance a should be closed to 0 to reduce its risk on the safety.
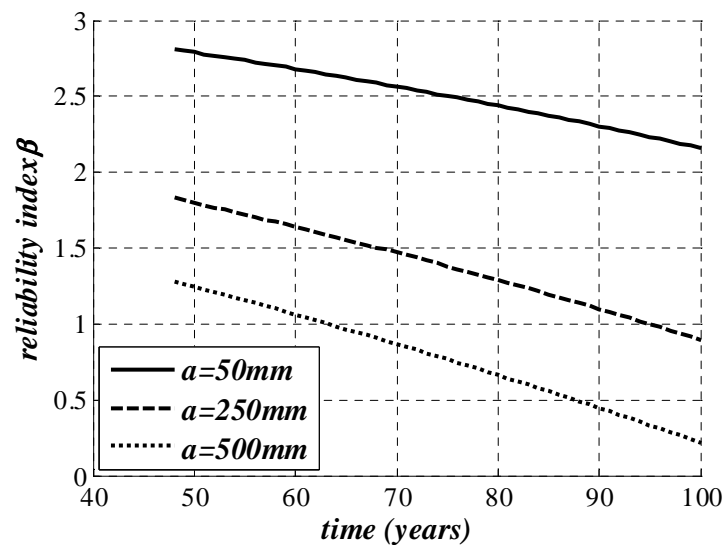
Figure III.2.17: Effect of distance a – see Figure III.2.12 - on FRP debonding based shear crack reliability profiles (c=35mm & *ADTT*=500 truck/day).

To sum up, Table III.2.2 presents the sensitivity factors of FRP end debonding based shear crack limit state. It can be observed that most of the random variables have sensitivity factor value close to zero. This can reflect that these variables have not any effect on the reliability of end debonding limit state. Consequently, such these variables can be considered as deterministic in the reliability analysis. However, concrete compressive strength, localized corroded steel bar area, dead load, live load and structural model error are important factor in reliability analysis.

Structural model error $\lambda_{db,end}$ has the highest sensitivity factor as it involved high coefficient of variation equals to 0.2021 (see chapter II.1). If we consider this variable reduced by 25% and 50% this may increase the reliability index by 32% and 83% respectively. This can reflect the accuracy required in the statistical parameters of the structural model error. Actually, only small dataset composed of 15 experimental cases was found in the review. This cannot enable to provide accurately parameters. In order to check the accuracy of the reliability analysis using the present structural model error, the latter section may provide more accurate reliability prediction using finite element analysis and Monte-Carlo simulation.

Table III.2.2: Minimum & maximum values of relative importance factor of design variable on β; case of FRP end debonding based shear crack

Variable	Deterioration factor		
	Growth of live load only	Growth of live load & uniform corrosion	Growth of live load & pitting corrosion
f_c	0.140:0.116	0.149:0.107	0.154:0.099
E_c	0.004:0.003	0.004:0.003	0.004:0.003
A_s	0.024:0.020	0.077:0.028	0.341:0.033
d_s	0.028:0.024	0.030:0.022	0.031:0.020
b_c	0.031:0.026	0.034:0.024	0.038:0.023
A_s	0.000	0.000	0.000
E_s	0.000	0.000	0.000
s_v	0.000	0.000	0.000
A_{sv}	0.000	0.000	0.000
f_{yv}	0.000	0.000	0.000
E_{FRP}	0.000	0.000	0.000
$f_{FRP,u}$	0.000	0.000	0.000
DL	-0.055:-0.056	-0.056:-0.059	-0.056:-0.061
LL	-0.188:-0.219	-0.180:-0.231	-0.172:-0.238
$\lambda_{db,end}$	0.973:0.963	0.974:0.956	0.976:0.893

III.2.1.4 Shear limit states

The simple formula used to evaluate the shear strength *V* of a FRP-strengthened RC beam is based on adding shear strength of RC beam (V_c+V_s) to the contribution of external FRP strips V_{FRP} (see Equation I.2.31). We assume that the shear limit state $g(x)$ can be expressed as:

$$g(x) = \lambda_{sh,RC}(V_c + V_s) + \lambda_{sh,FRP}V_{FRP} - \sum S_i \qquad \text{(III.2.5)}$$

where V_c and V_s are evaluated according to Equation I.2.32 and I.2.33 respectively. V_{FRP} is calculated considering the model proposed by Triantafillou & Antonopoulos (2000) as given in Table I.2.10. $\lambda_{sh,RC}$ and $\lambda_{sh,FRP}$ are the structural model error of the shear strength of RC beam and FRP strips respectively which are given in Table III.2.1. The second term in Equation III.2.5 takes place only after to strengthening. $\sum S_i$ is summation of the applied shear forces due to dead and live loads. Shear force due to live load is considered according to the live load model proposed in chapter III.1.
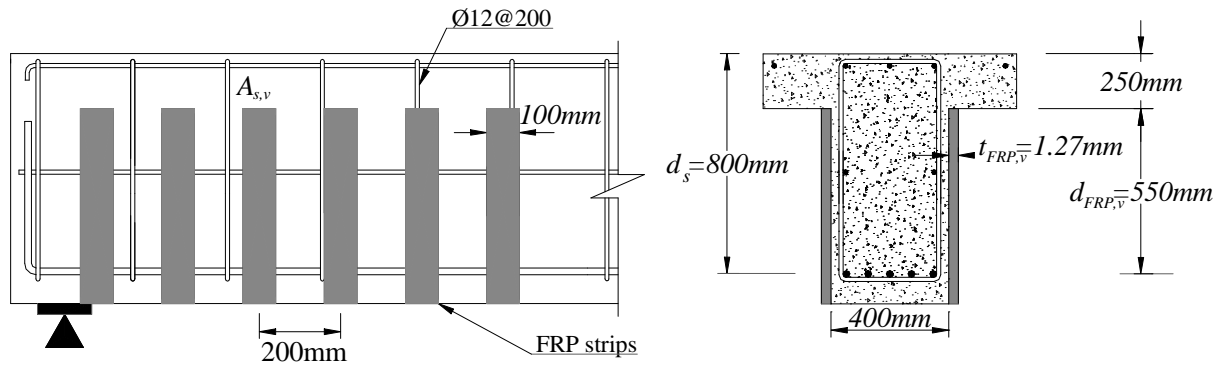
Figure III.2.18: Geometrical dimension of FRP shear strengthening.

In a first step, we consider the effect of live load growth over the time on the reliability profile of RC beam. Dimension and configuration of FRP strips assumed in strengthening process is presented in Figure III.2.18. Results are presented in Figure III.2.19. It is shown that *ADTT* gives a slight effect on the reliability profile; i.e. the differences of β index between values of *ADTT* are small. Although a considerable reduction can be observed in the reliability index over the time, the RC beam still has a high reliability index. Accordingly, strengthening process is not required in this case. This can be explained by high initial reliability index of the RC beam. Examining the two Figures III.2.1 & III.2.19 reflects that the rate of deterioration of the shear limit state is slightly higher than flexural limit state, as they give rate of deterioration equal to 0.016/year and 0.018/year for the former and the latter respectively.
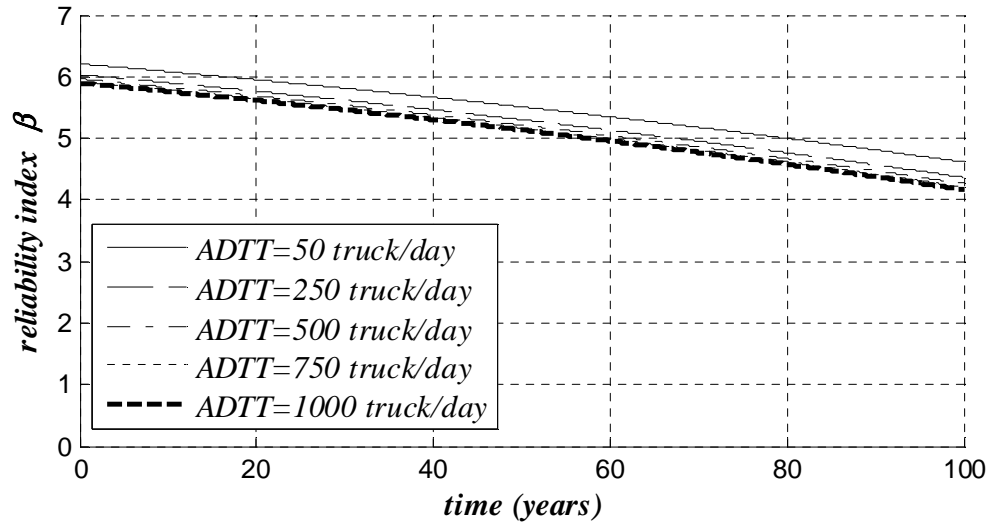
Figure III.2.19: Time-dependent reliability index of shear limit state of RC beam under growth of live load over time.

In the second step, we perform reliability analysis considering deterioration due to both corrosion and growth of live load over the time. Five values of *ADTT* were considered: 50, 250, 500, 750, 1000 truck/day. Three values of stirrups width b_s were considered: 348, 358 and 368. b_s is the distance between the centers of the two branches of the stirrups (see Figure III.1.1). All the Results of the analyzed cases were plotted in Figure C.9 and C.10 (see Appendix C).

Samples of results were plotted in Figure III.2.20 for an *ADTT* value equals to 500 truck/day. According to the results, pitting corrosion is potentially more hazardous in all cases than uniform corrosion. In addition, uniform corrosion causes a level of deterioration equals to that when considering live load growth only. Thus rate of deterioration in reliability profile is approximately doubled (from about 0.16 year to 0.32/year). It can be also noted that reliability profiles can be assumed linear after corrosion initiation time when considering uniform corrosion or/and growth of live load. This cannot be generalized to pitting corrosion, as the rate of deterioration decreases with time beca use under high level of corrosion deterioration the RC beam still retains the shear concrete contribution V_c which is not affected by corrosion process.
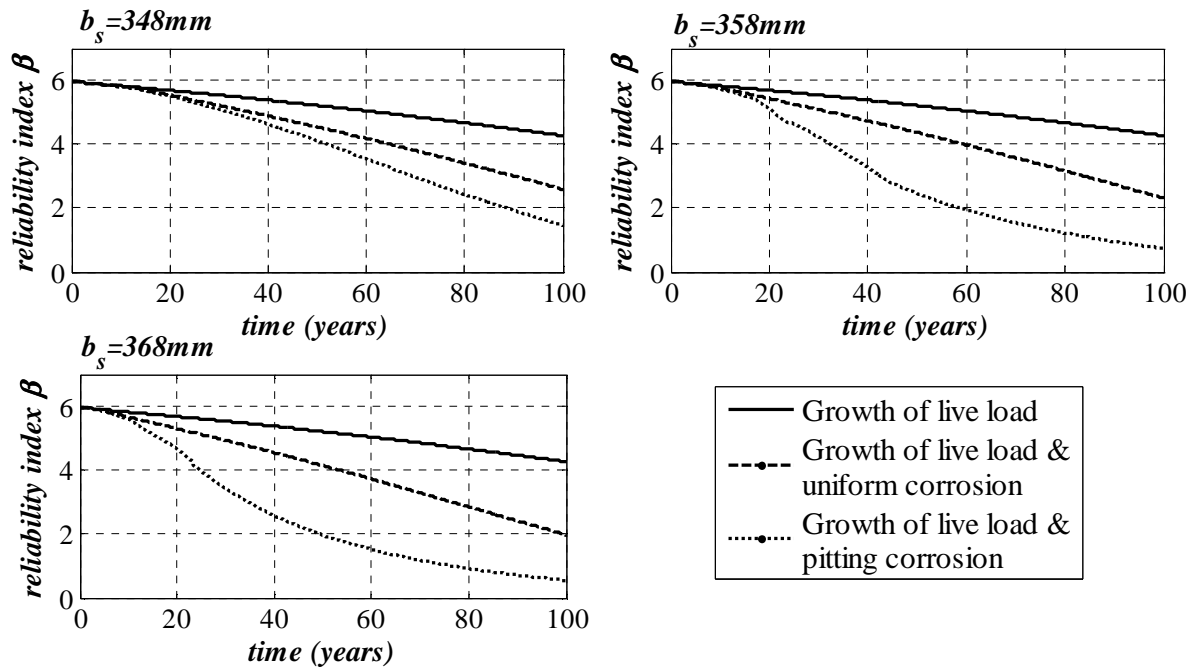
Figure III.2.20: Time-dependent reliability index of shear limit state of RC beam under growth of live load over time and corrosion (*ADTT*=500 truck/day).

The reliability analysis was performed taking into account FRP strengthening of the RC deteriorated beam. Although the used model [Triantafillou & Antonopoulos 2000] can predict both FRP rupture and FRP debonding failure modes, the observed failure mode in all the analyzed cases is FRP rupture and FRP debonding did not occur. Results were presented in term of time dependent reliability index as shown in Figure III.2.21. It can be noted that applying FRP strengthening with FRP strips with dimensions and configuration shown in Figure II.2.14 can effectively increase the reliability of the beam. This increase approximately ranges between 1.05-1.3. However, the major advantage of FRP strengthening is the significant decrease in deteriorated rate after strengthening. Indeed, the beam still retains a reliability index after strengthening greater than the minimum value β_{min} (=3.0) along the considered lifetime (=100 years).

Finally, in order to evaluate the effect of FRP durability on the strengthened RC beam, the reliability analysis were performed considering FRP aging in addition to corrosion and growth for live load. Deterioration in the mechanical properties of the FRP composite material were assumed according to Karbhari & Abanilla (2007) (see § I.2.4 and Equation I.2.48). Results, of b_s=368mm & *ADTT*=50 truck/day, are presented in Figure III.2.22. As shown in the Figure the degradation in the FRP properties due to FRP durability has an insignificant effect on the reliability index.
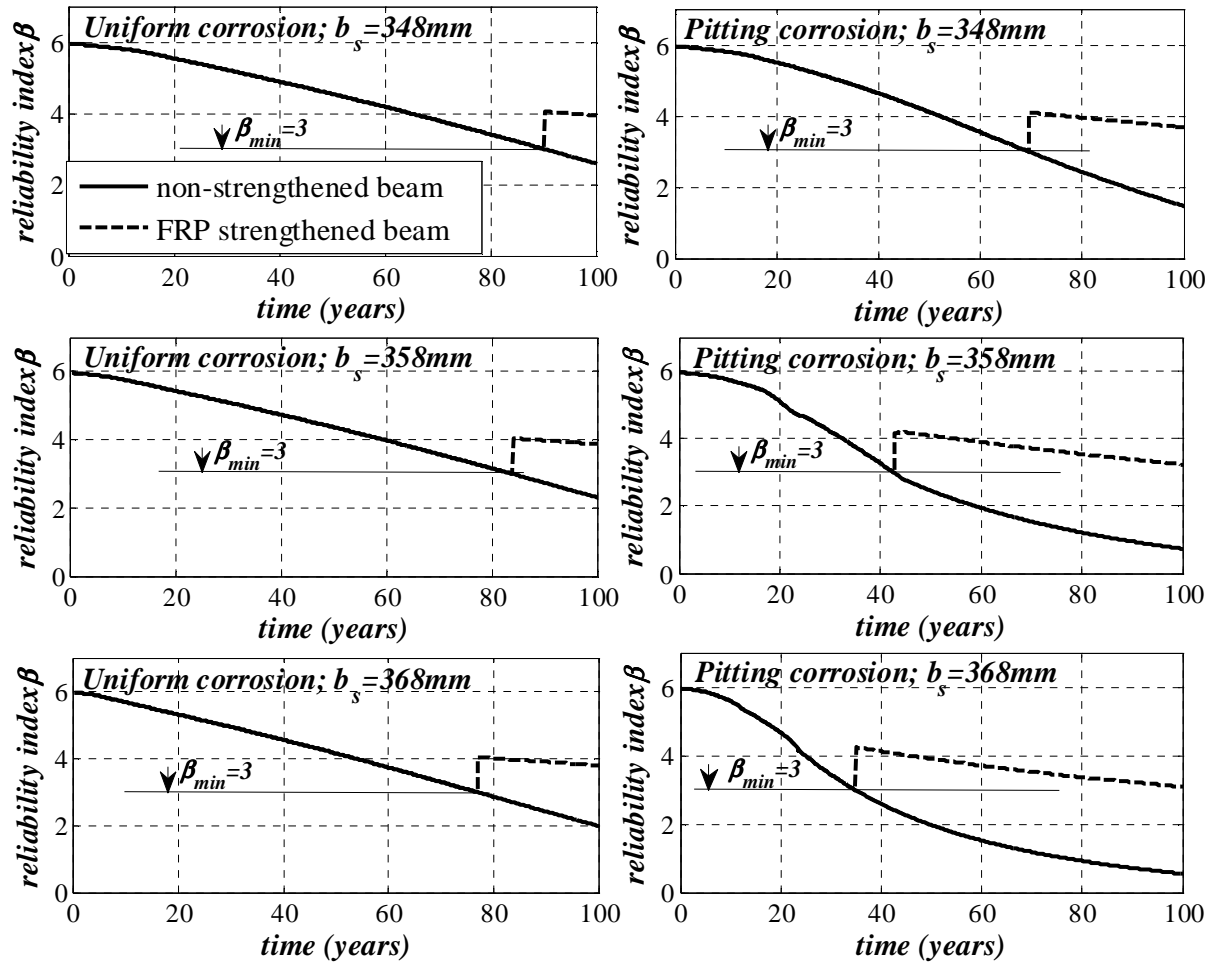
Figure III.2.21: Time-dependent β of shear limit state of FRP shear strengthened RC beam under growth of live load over time and corrosion (*ADTT*=500 truck/day).
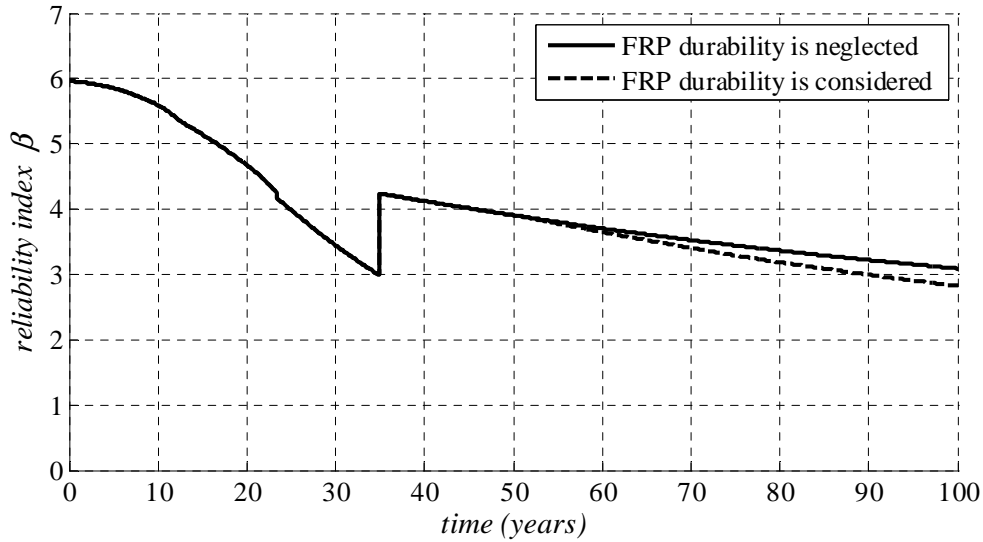
Figure III.2.22: Durability effect on time-dependent reliability index of shear limit state, both growth of live load and corrosion are considered (b_s=368 mm & *ADTT*=500 truck/day).

Sensitivity factors of all the analyzed cases are presented in Tables C.4 & C.5 (see Appendix C). The tables present the sensitivity factors in term of the maximum and minimum values observed for each random variable over the consider lifetime. Figure III.2.23 presents a graphical presentation of the sensitivity factors over the time. It can be noted that:

- For un-strengthened RC beam (Figures III.2.23a and III.2.23b): compressive strength f_c, stirrups spacing s_v, live load *LL*, dead load *DL*, stirrups area A_{sv} and the model error of RC shear contribution $\lambda_{sh,RC}$, are the most important factors. While all the other values involved in the limit state insignificantly affect the limit state.

- For FRP strengthened RC beam (Figure III.2.23c and III.2.23d): live load *LL*, stirrups area A_{sv} the model error of shear RC contribution $\lambda_{sh,RC}$ and the model error of FRP shear contribution are the most important factors. A significant decrease is observed in sensitivity factors of compressive strength f_c, stirrups spacing s_v, dead load *DL*. While all the other values involved in the limit state insignificantly affect the limit state especially those that corresponds to the FRP properties: modulus, strength and thickness.
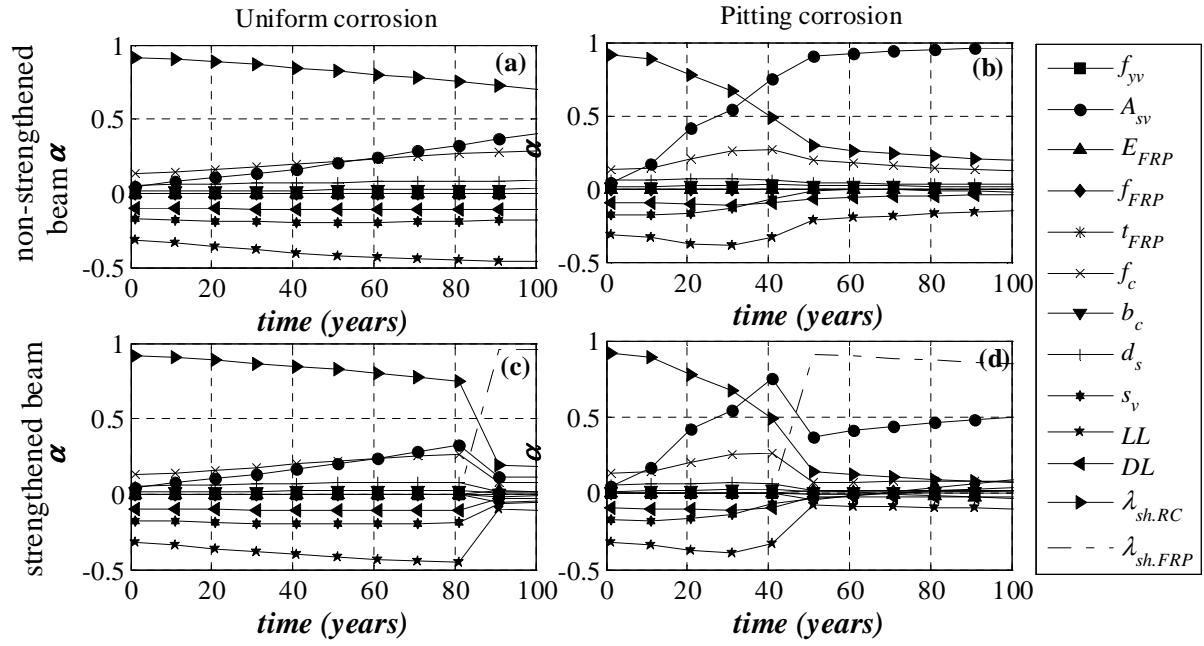
Figure III.2.23: Time dependent sensitivity factor of shear limit state under growth of live load over time and corrosion (b_s=358 mm & *ADTT*=500 truck/day).

III.2.2 RELIABILITY ANALYSIS BASED ON MONTE-CARLO SIMULATION

III.2.2.1 General

In many cases of structural responses calculation using simplified formulas cannot catch the accurate behavior. In our study, this has been achieved in many cases such as: serviceability limit state (deflection), cover separation…etc. Thus, we try to use a more efficient tool such as finite element method. It is well known that Finite Element Method FEM is the most robust tool used to provide structural responses. But it is difficult to perform explicitly reliability analysis based FORM method and FEM as many differentiations of the desired structure response with respect to random variables are required. From the other side Monte-Carlo Simulation MCS technique based on NN and FEM is computationally costly because in most cases MCS uses about 10^4 simulations at minimum. In addition FEM is computationally costly especially with concrete structures. Therefore, NN can be used to construct an explicit structural response function based on a limit number of FEM simulations. Thus this function can be coupled with MC to perform the reliability analysis. The computation procedure of Monte-Carlo based Neural Networks and Finite Element Method MC-NN-FEM is proposed in Figure III.2.24.
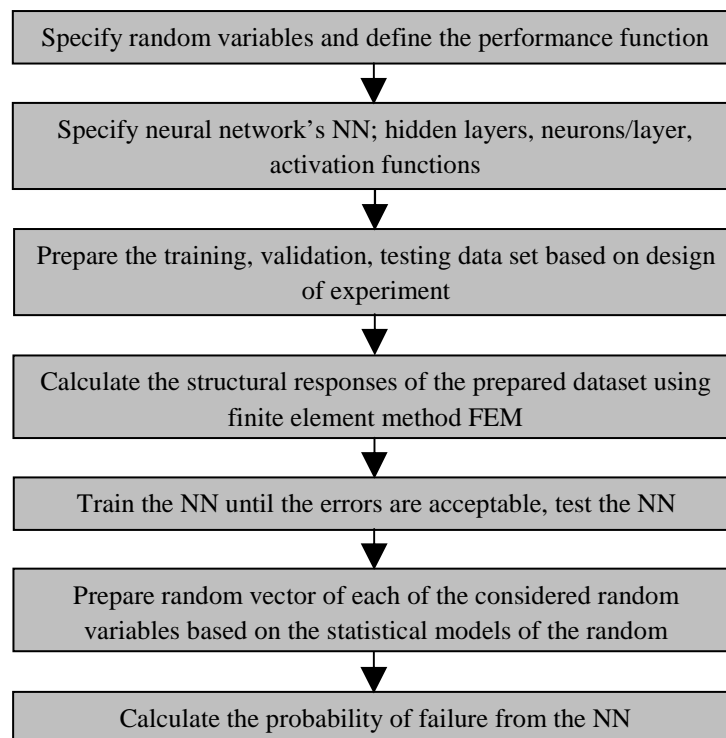
Figure III.2.24: Flow chart of MC-NN-FEM

In the following sections we use MC-NN-FEM techniques to perform the reliability analysis in order to:

- Express the reliability for serviceability limit state (beams deflection)

- Assess the reliability limit states obtained using simplified formulas

  1. Flexural limit state which involved concrete crushing, intermediate crack FRP debonding and FRP rupture failure modes.

  2. FRP end debonding based shear crack limit state.

  3. Shear limit state

- Conduct reliability analysis of cases that simplified formulas cannot be used (concrete cover separation).

III.2.2.2 Reliability of serviceability limit states

The serviceability limit state considered in the present study is given in terms of deflection limit for the interior beam of bridge deck under truck load (see Figure III.1.1). The objective of this limit is to prevent, albeit indirectly, excessive vibrations of the bridge. According to AASHTO specifications, the deflection Δ_w of the bridge under truck load should not exceed a limiting value $\Delta_{w,lim}$ equals to 1/800 of its span. Serviceability limit state can be defined in term of the limit state function containing the limiting deflection $\Delta_{w,lim}$ as:

$$g(x) = \lambda_{FEM} \Delta_w - \Delta_{w,\lim} \qquad \text{(III.2.6)}$$

where λ_{FEM} is the structural model error in the responses obtained using FEM (see Table III.1.4). For the beam under consideration, with span of 10.8 m, $\Delta_{w,lim}$=13.5 mm. In the following, we will perform the reliability of serviceability limit state expressed by Equation III.2.6 using MC-NN-FEM.

Val *et al* (1998) perform a reliability analysis of serviceability limit state (deflection) of RC bridge under corrosion. Many variables were assumed in the study such as geometrical dimensions, material properties and loading random variables. Results of the study have shown that concrete compressive strength f'_c, steel area A_s, dead load LL and extreme truck weight w are the most important variables that significantly affect the reliability results. Based on these conclusions, we consider the same variables in addition to the structural model error λ_{FEM} and the position of the truck in the first lane d_{lane1} (see Figure III.1.1). While the position of the truck in the second lane d_{lane2} is assumed as deterministic value (=900mm), as it has been proven - § III.1.2.3.1 - that this variable has insignificant effect on the beam bending moment and consequently the beam deflection.

Neural network is adapted to be function of five variables only: f'_c, A_s, DL, w and d_{lane1} as shown in Figure III.2.25. While λ_{FEM} is a multiplicative variable to the responses obtained using NN. A dataset of the NN variables were prepared according to the design of

experiments concept discussed in § II.2.5.3. Denoting number of NN variables as *n*, dataset required to train, validate and test were obtained based on two design of experiment concept: ($2n+1$ axial point design) and (2^n factorial design). Four values of the parameter h_i (1, 2, 3 and 4) in Equation II.2.4. Thus, of 169 design points are required. In this case, the x^o vector will be equal to the co-ordinates of origin point space of design variables (see Figure II.2.10 & Equation II.2.4).
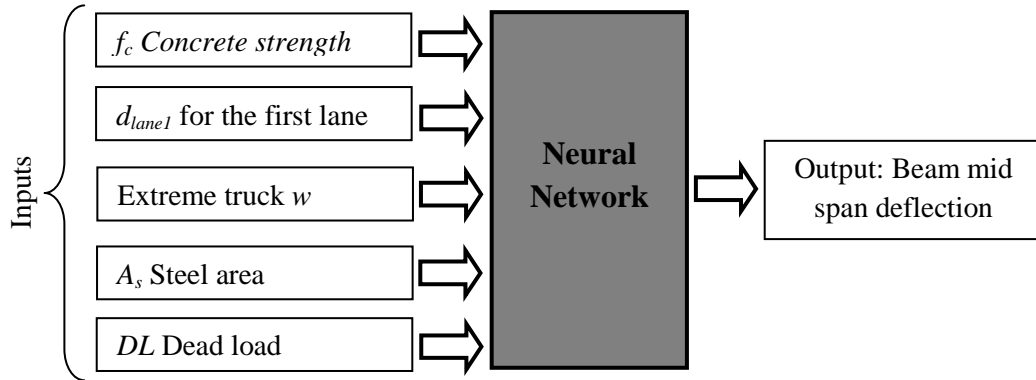
Figure III.2.25: Inputs and outputs of neural network used to predict extreme actions in the interior girder of the bridge deck.

Concrete slab and beams were simulated using shell element S4. Embedded steel option is used to simulate slab reinforcement. While all other steel part were simulated using link element T3D2. A sample of Abaqus input file of the dataset is reported in Appendix D.2. Figure III.2.26 gives visualized results of the bridge deflection of this case.
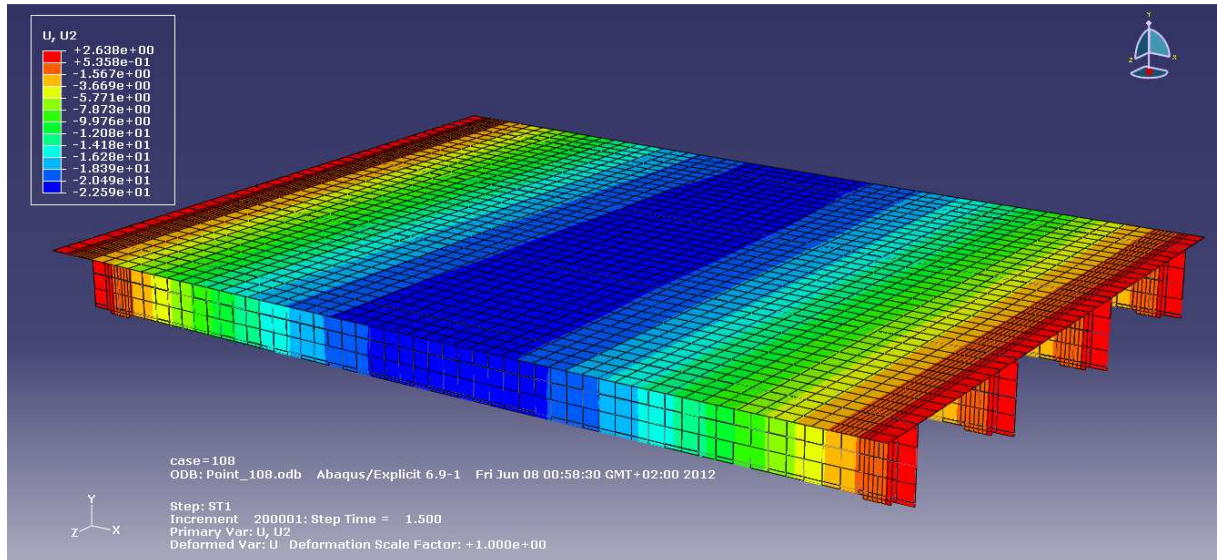
Figure III.2.26: Example of deflection results of FEM simulation (see Abaqus input file given in D.2)

Due to the difficulty of using the proposed reliability method (MC-NN-FEM) at various time increment across the full age considered (100 year), MC-NN-FEM was considered for

the following six datasets: (1) for RC beam at time $t=0$ year, (2) for RC beam at $t=50$ years (3) for RC beam at $t=100$ years, (4) for FRP strengthened RC beam at $t=40$ years, (5) for FRP strengthened RC beam at $t=70$ years, (6) for FRP strengthened RC beam at $t=100$ years. Figure III.2.27 presents example of the NN training, validating, testing results of a dataset used (FRP strengthened RC beam at 40 years). It can be noted that the neural network is capable to give a robust predictions of the beam deflection based on the trained dataset (correlation factor is close to 1).
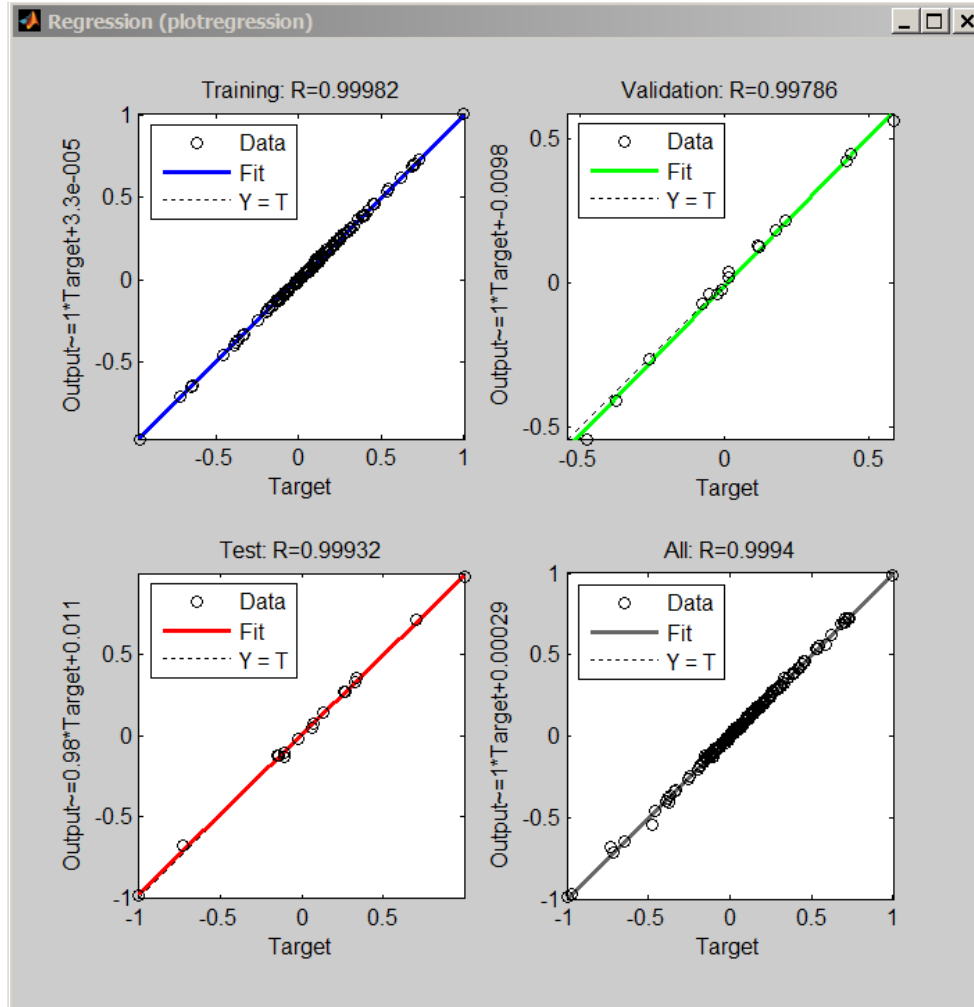
Figure III.2.27: Scatter distribution of target and predicted deflections (169 cases) of NN trained, validated and testing dataset.

Once the neural network is trained, validated and tested, MC-NN-FEM is performed to evaluate the probability of failure P_f and accordingly the reliability index β is calculated as: $\beta=-\Phi^{-1}(P_f)$, where Φ^{-1} is the cumulative density function of the standard normal distribution. All the studies cases were performed assuming that $c=40$ mm. Number of simulations N_s is an important aspect of MC simulation which must be known before performing the reliability analysis. In the present limit state we assume that N_s equals to 5×10^4. Equation II.3.43 was

used to calculate the coefficient of variation of the estimated probability of failure.

Figure III.2.28 presents the reliability index as function of the number of sampling. It can be noted that the assumed number of sampling is sufficient to predict accurately the reliability index, as the coefficient of variation of the estimated probability of failure was calculated and found to be equal to 0.0601.

In order to show the effect of the *ADTT* on the reliability index, reliability analysis was performed - at time equals to zero - considering various values of *ADTT*. Results were plotted in Figure III.2.29. According to the results it can be observed that the *ADTT* have a significant effect on the reliability index. In addition, the chosen beam dimensions satisfy the requirement of SLS (deflection), as the beams gives reliability index, for all *ADTT* of consideration, greater than the target, β_{Target}=1.7, value recommended by probabilistic design code [JCSS 2001]. This value corresponds to normal relative cost of safety measure.
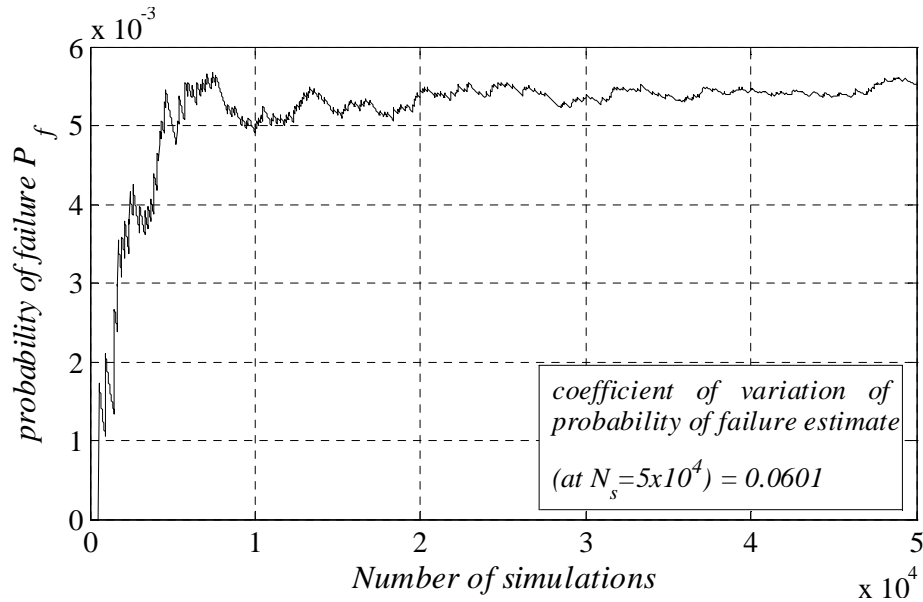
Figure III.2.28: Probability of failure vs. number of simulations (time=0).
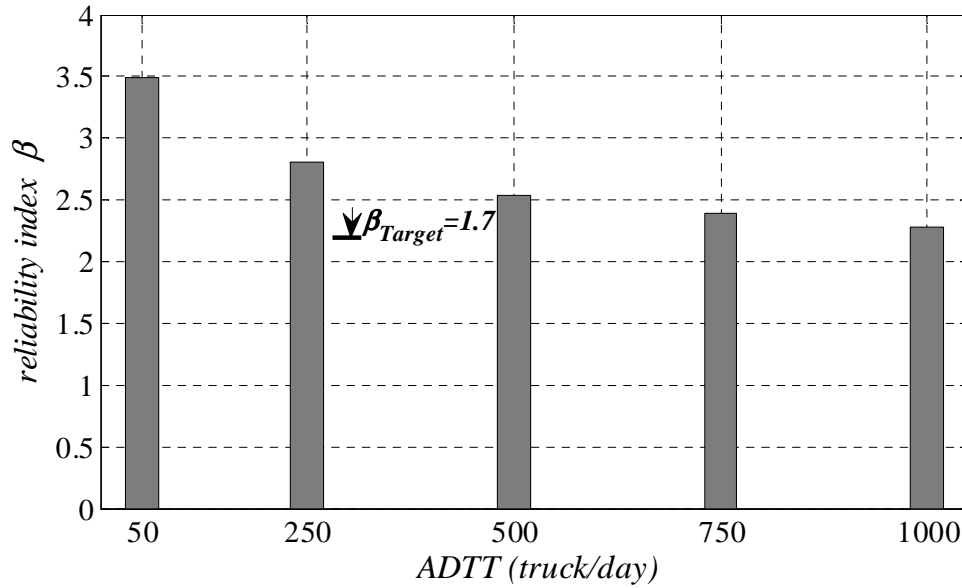
Figure III.2.29: Effect of the *ADTT* value on the initial probability of failure (*t*=0 year).

Based on the six datasets presented in above discussion, two NN were constructed. The first was trained, validated and tested using datasets prepared for RC beam. While the second was trained, validated and tested using the datasets prepared for FRP strengthened RC beams. These NNs were used to predict the deflection of RC and FRP strengthened RC beam respectively. In order to establish a time dependent reliability index profile, MC-NN-FEM is performed at various time increments. Time to strengthening was evaluated such that the reliability index reaches a minimum value equals to β_{min}=1.0.

Results of RC beam were plotted in Figure III.2.30. Results indicate that SLS are significantly affected by corrosion especially of pitting type. However the SLS still gives reliable performance of more than 80% of the considered age. In addition, growth of live load dramatically decreases reliability index.
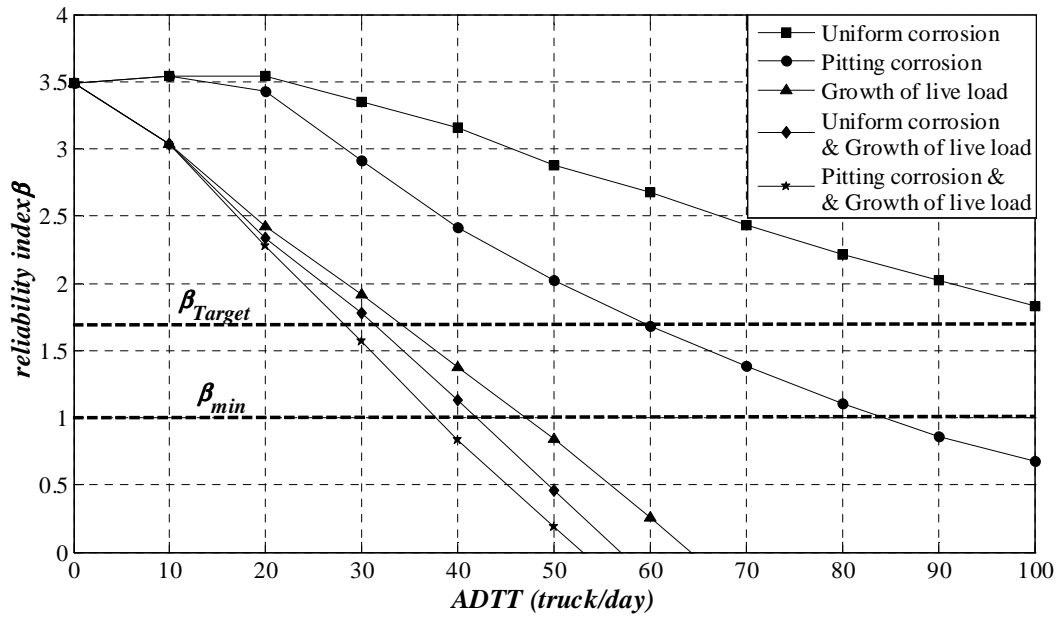
Figure III.2.30: Time dependent reliability for SLS, *ADTT*=50trucks/day & *c*=40mm.

Results of applying FRP strengthening were plotted in Figure III.2.31. It can be noted that FRP strengthening slightly increases the reliability index. The vertical increase in the reliability index is strongly affected by the growth of live load.
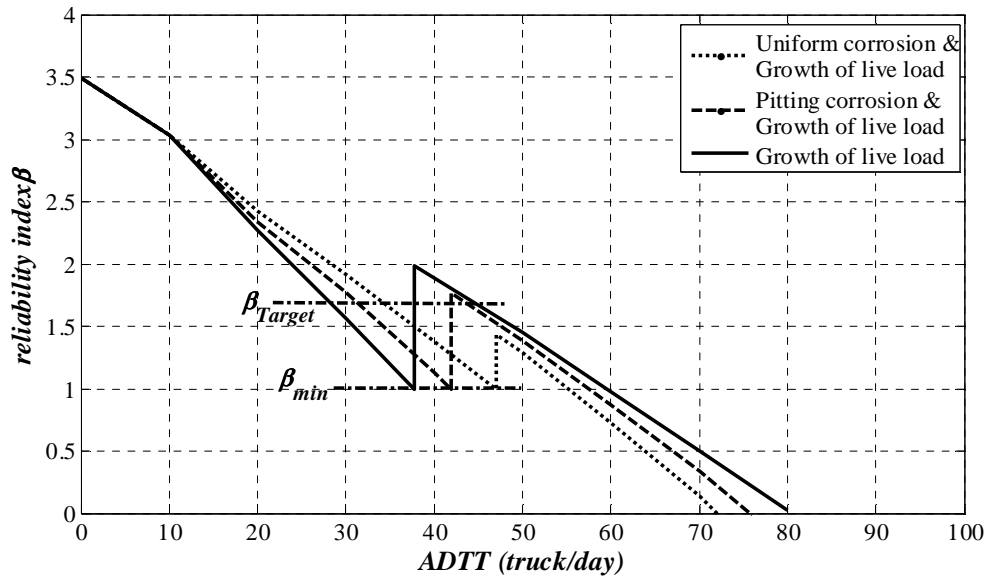
Figure III.2.31: Effect of the *ADTT* value on the initial probability of failure.

The statistical distribution of the generated deflections was fitted. Many statistical distributions were examined using Kolmogorov-Smirnov test (KS-test) with a level of significance of 5%. The KS-test results indicate that Log-Normal distributions can best fit the generated data. Figure III.2.32 presents examples of fitted distributions. It can be observed that applying FRP strengthening can effectively enhance the SLS; it decreases the mean value of the deflection probabilistic model. However, this enhancement in the deflection mean value

could not reach the initial mean (at t=0 year) value. In addition, it can be noted that FRP strengthening improve the standard deviation of the deflection model, as a high decrease is achieved due to FRP strengthening (σ_Δ=0.585 mm for FRP strengthened RC beam after 37.7 years versus σ_Δ=1.2592 mm for non-strengthened RC beam at 37.7 years).
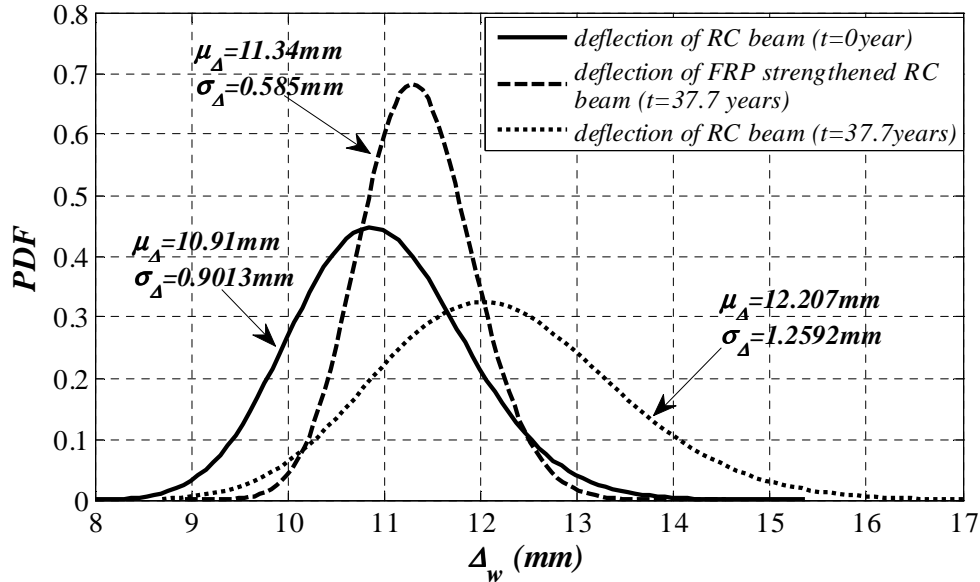
Figure III.2.32: Fitted *PDF* of beam deflection in (mm) distribution Effect of the *ADTT*=50 truck/day & *c*=40 mm.

In order to show the effect of the variation of the considered random variables on the reliability index, various runs of the proposed MC-NN-FEM was performed at time to strengthening. At each run the variation of certain of the considered variables is neglected. Results are presented in Table III.2.3. It can be concluded that most of the considered variables have a significant effect of the reliability index. However, steel area has insignificant effect after strengthening as the FRP area can compensate the steel losses due to corrosion. This variable can be considered as deterministic value after applying strengthening.

Table III.2.3: Effect of neglecting variation in random variables involved in SLS on the reliability index β at time to strengthening (=37.7 years), under pitting corrosion effect and growth of live load (*c*=40 mm & *ADTT*=50 trucks/day).

Neglected variable	Reliability index β (RC beam)	Reliability index β (Strengthened beam)
All variables are considered (reference case)	0.99692	1.98810
w (extreme truck weight including impact effect)	1.23401 (+23.8%)	2.49714 (+25.6%)
d_{lane1} (position of the truck in the first lane)	0.99241 (-0.50%)	2.50055 (+25.8%)
A_s (steel area)	1.36835 (+37.3%)	1.98919 (0.000%)
f'_c (concrete compressive strength)	1.17649 (+18.0%)	2.56091 (+28.8%)
DL (dead load)	1.19012 (+19.4%)	2.56762 (+29.1%)
λ_{FEM} (finite element analysis structural model error)	1.15230 (+15.6%)	2.61818 (+31.7%)

III.2.2.3 Reliability of flexural limit states

In the present section we perform the reliability analysis using Monte-Carlo simulation based on Neural Networks and Finite Element Method MC-NN-FEM technique which aims at estimating the reliability index of the seven possible failure modes that may take place when applying FRP flexural strengthening to a deteriorated RC beam.

Such these failure modes are presented in §II.1.2; they are: (1) concrete crushing of RC beam, (2) concrete crushing of FRP strengthened RC beam, (3) FRP rupture, (4) FRP Intermediate Crack IC debonding, (5) concrete cover separation, (6) FRP end debonding based shear crack, and (7) FRP end debonding based interfacial shear stresses.

The main objective of using MC-NN-FEM technique is to:

- Verify the results obtained using FORM method based on simplified design formulas obtained in § III.2.1.1 and III.2.1.3 [mainly through MC].
- Evaluate the reliability index for the two failure modes which analytical formulas proposed in the literature fail to predict accurately the limit state response (see § II.1.2.1.4), namely: (5) concrete cover separation for which we will consider two configurations ((5a) without anchoraged plate and (5b) with anchoraged plate), and (7) FRP end debonding due to interfacial shear stresses failure modes (at plate end) [mainly through FEM].
- Calculate the reliability index for all the failure modes of FRP strengthened RC beam as a system of failure modes [mainly trough NN].

The developments below will deal, as an example, with the case of a RC beam with a concrete cover c of 40 mm, under $ADTT = 500$ trucks/day, $C_s = 3$kg/m^3, submitted to pitting corrosion. Using FORM method, the time to strengthening was found to be 46.67 years.

We must first remind that MC-NN-FEM technique cannot be performed with high number of variables (e.g. 12 variables in case of flexural limit state). Therefore, the number of these variables should be reduced. Thus, we preliminary carry out a sensitivity analysis using FORM (§ III.2.1.1 and III.2.1.3). Table III.2.4 represents the sensitivity factors of the flexural limit states and, accordingly, we can chose the most important variables that must be considered as random variables; here, the ones with a sensitivity factor are greater than 0.1. After this choice it is necessary to assess its impact in terms of accuracy of reliability index estimation. It was found that the neglected variables (i.e. we neglect the random character of the variables) have no significant effect on the reliability index and their variation can be

totally neglected in the reliability analysis; e.g. the reliability index of flexural FRP strengthened RC beam of non-anchoraged laminates equals to 3.591 when considering all the variables and 3.607 when neglecting variables which have sensitivity factor less than 0.1.

Table III.2.4: Sensitivity factors using FORM method.

		Failure mode		
		Concrete Cover Separation		FRP end debonding due to interfacial shear stresses
		Flexural with anchoraged plate	Flexural with non-anchoraged plate	
Sensitivity factor α_i	f_c	0.01	0.01	0.11
	f_y	0.29	0.37	Nc
	A_s	0.26	0.32	0.04
	d_s	0.07	0.08	0.02
	$f_{FRP,u}$	0.23	0.00	Nc
	E_{FRP}	-0.04	0.04	Nc
	LL	-0.29	-0.34	-0.18
	DL	-0.11	-0.13	-0.07
	λ_m	0.83	0.78	0.97
	E_c	0.00	0.00	0.01
	t_{FRP}	0.04	0.04	Nc
	b_c	0.01	0.02	0.03
	s_v	nc	nc	0.00
	A_{sv}	nc	nc	0.00
	$f_{y,v}$	nc	nc	0.00

nc denotes that the variable was not considered in the corresponding limit state

For each individual failure mode within those presented in the first paragraph of this section, the proposed MC-NN-FEM reliability procedure can be summed up as presented in the following steps:

1. Choose the random variables according to their sensitivity factors as mentioned above. Table II.2.5 presents all the considered variables in each limit state. Concrete tensile strength f_{ct} has been taken here as random variable since some failure modes directly depend on this value: e.g. concrete cover separation.

Table III.2.5: Reliability results of MC-NN-FEM of flexural limit states.

Failure mode	Limit state variables	Neural Network variables
Concrete crushing of RC beam	$f_y, A_s, LL, DL, f_c, \lambda_m$	f_y, A_s, LL, DL, f_c
Concrete crushing of FRP strengthened RC beam	$f_y, A_s, LL, DL, f_c, \lambda_m$	f_y, A_s, LL, DL, f_c
FRP rupture	$f_y, A_s, LL, DL, f_{ct}, f_{FRP,u}, E_{FRP}, \lambda_m$	f_y, A_s, LL, DL, f_{ct}
FRP intermediate crack debonding	$f_y, A_s, LL, DL, f_{ct}, \lambda_m$	f_y, A_s, LL, DL, f_{ct}
Concrete cover separation	$f_y, A_s, LL, DL, f_{ct}, \lambda_m$	f_y, A_s, LL, DL, f_{ct}
FRP end debonding based shear crack	$f_y, A_s, LL, DL, f_c, f_{ct}, \lambda_m$	A_s, LL, DL, f_c, f_{ct}
FRP end debonding due to interfacial stresses[*]	$f_y, A_s, LL, DL, f_{ct}, \lambda_m$	f_y, A_s, LL, DL, f_{ct}

[*] Probability of failure of this failure mode could not be reached through the Monte-Carlo simulation.

2. Prepare a dataset of chosen variables according to the concept of design of experiments (see § II.2.5.3). The prepared dataset is required for Neural Networks training process.

Five values of the parameter h_i (number of standard deviation intervals from mean value) 1 to 5, required in Equation II.2.4, were assumed. The total size of the dataset will be calculated according to ($2n+1$ & 2^n) mixed design concept (see § II.2.5.3); n is the number of variables required for NN. Thus, size of dataset corresponds to 211 cases. Figure III.2.33 shows a graphical 2-dimensional representation of the design points around the origin of the u-space.
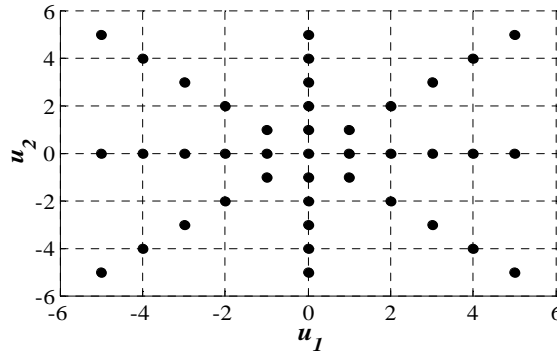
Figure III.2.33: 2-dimensional representation of the design points.

3. Carry out a probabilistic transformation of the prepared dataset of the chosen variables from the u-space to x-space.

4. Carry out a Finite Element Modeling of FRP strengthened RC beam, including all variable combinations prepared in the dataset, using Abaqus software to evaluate the required structural responses. Table III.2.6 gives the required responses for each limit state and the corresponding form of the limit states. Structural model error of FEM is given in Table III.1.4.

Table III.2.6: Form of limit states and the required responses.

Failure mode	Required FEM response	Limit state form
• Concrete crushing of RC beam	Max compression concrete strain at mid span $\varepsilon_{c,max}$	$g=\lambda_{FEM}\,\varepsilon_{c,max}-\varepsilon_{c,u}=0$
• Concrete crushing of FRP strengthened RC beam	Max compression concrete strain at mid span $\varepsilon_{c,max}$	$g=\lambda_{FEM}\,\varepsilon_{c,max}-\varepsilon_{c,u}=0$
• FRP rupture	Max tensile FRP strain $\varepsilon_{FRP,max}$	$g=\lambda_{FEM}\,\varepsilon_{FRP,max}-f_{FRP,u}/E_{FRP}=0$
• FRP intermediate crack debonding	Max damage value in cohesive element near the pre-cracked zone: $d_{coh,max}$	$g=\lambda_{FEM}d_{coh,max}-1=0$
• Concrete cover separation	Max tensile concrete strain at steel level near the plate end $\varepsilon_{ct,max}$	$g=\lambda_{FEM}\,\varepsilon_{ct,max}-f_{ct}/E_c=0$
• FRP end debonding based shear crack	Max tensile concrete strain near plate end $\varepsilon_{ct,max}$	$g=\lambda_{FEM}\,\varepsilon_{ct,max}-f_{ct}/E_c=0$
• FRP end debonding due to interfacial stresses	Max principle tensile stress in adhesive layer at plate end $f_{coh,max}$	$g=\lambda_{FEM}f_{coh,max}-f_{ct}=0$

Max; maximum.

In order to simplify the FEM modeling, dead load were applied as uniform distributed load, while truck loads were applied as two concentrated loads. Longitudinal distance

between the two concentrated loads equals to the distance between the truck axles (standard truck SH20 AASHTO 2007). Values of dead and live load were adopted such that the induced bending moment in the beam is equal to the applied bending moment using the load models proposed in section § III.1.2.3.1.
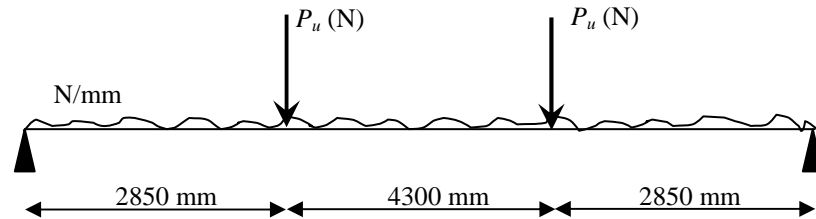
Figure III.2.34: Example of FEM outputs of FRP strengthened RC beam.

Due to symmetry of the beam geometries and loading, one half of the beam has been analyzed. The beam is modeled as a 2-dimensional problem. Plane stress element CPS4R is used to simulate concrete. 2-dimensional cohesive element COH2D4 is used to simulate adhesive layer between concrete and FRP plate. 2-dimensional truss element T2D2 is used to simulate steel reinforcement and FRP plate. In order to obtain results of sufficient accuracy, a very fine mesh was used near plate end and near mid span of the beam as shown in Figure III.2.35. A vertical pre-crack was modeled by making a gap of 0.1 mm width and 10 mm depth between the continuum elements. An example of input Abaqus file is given in Appendix D.3 (case 155). Figures III.2.35a and III.2.35b present result samples of longitudinal and vertical stresses respectively.
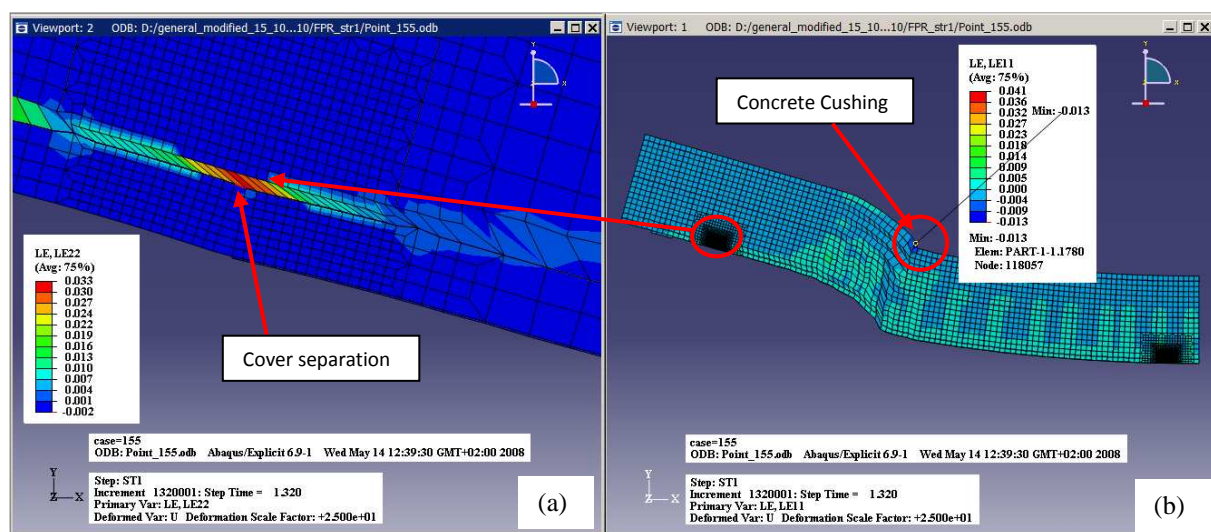
Figure III.2.35: Example of FEM outputs of FRP strengthened RC beam.

After analyzing the all the FEM cases required for each limit state, the structural responses

were evaluated.

5. For each limit state, a NN with two hidden layers is constructed. The first layer contains between 4 to 7 neurons, while the second layer contains between 2 to 5 neurons. The exact number of neurons in each layer is adopted using try and error procedure. The prepared dataset and responses is used to train and test the neural network. Eventually, all the terms of the limit states given in Table III.2.6 are known and the limit states formula is constructed. Figure III.2.36 gives an example of a neural network input and output required to predict cover separation failure mode.
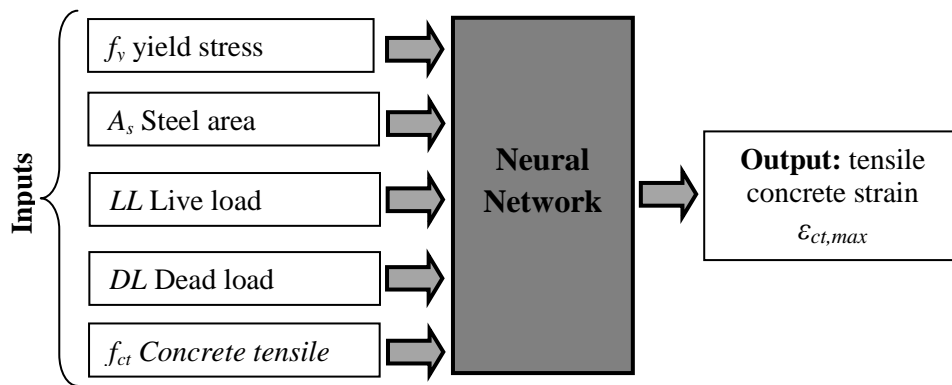
Figure III.2.36: Inputs and output of neural network used to predict maximum tensile concrete strain at steel level near the plate end (Concrete cover separation limit state).

6. Once the NN validated for each limit state, Monte-Carlo simulation technique was used to generate a random vector of the random variables (for each limit state). Size of sampling is taken equal to 10^6 simulations in order to provide a sufficient accuracy in term of β index calculation. All the combinations of the generated random variables are simulated in the NN to obtain the corresponding structural responses. Thus, the limit state can be evaluated and the probability of failure P_f can calculated according to Equations II.3.41 and II.3.42. Eventually, the reliability index can be determined such that: $\beta = -\Phi^{-1}(P_f)$

Table III.2.7 gives the calculated probability of failure and reliability index obtained using MC-NN-FEM technique for all the considered limit states. In addition, the table presents the reliability indices obtained using FORM method β_{FORM}. It can be noted that MC-NN-FEM technique is capable to predict the reliability index for most of these failure modes. However, on one hand, the technique fails to calculate the reliability index of FRP end debonding based

interfacial shear stresses failure mode because this failure did not take place for all sampling combinations. From the other hand, results obtained using FORM method are very conservative and approximately closed to those obtained using MC-NN-FEM technique.

Table III.2.7: Reliability results of MC-NN-FEM of flexural limit states.

Failure mode	P_f	$\beta_{MC\text{-}NN\text{-}FEM}$	β_{FORM}
1. Concrete crushing of RC beam	0.001	3.08728	3.00
2. Concrete crushing of FRP strengthened RC beam	0.000064	3.83028	did not occur
3. FRP rupture	0.000015	4.17347	4.138 (anchoraged case)
4. FRP intermediate crack debonding	0.00025	3.47862	3.591 (non-anchoraged case
5. Concrete cover separation	0.0016	2.95645	No structural model valid
6. FRP end debonding based shear crack	0.0074	2.43905	2.653
7. FRP end debonding due to interfacial stresses*	$\ll 10^{-6}$	$\gg -\Phi^{-1}(10^{-6})$	No structural model valid

*Probability of failure of this failure mode could not be reached through the Monte-Carlo simulation. P_f is the Probability of failure. β is the Reliability index

As mentioned in the beginning of the present paragragh III.2.2.3, one of the main objectives of MC-NN-FEM technique is to calculate the reliability index for all the failure modes of FRP strengthened RC beam as a system of failure modes. One of the major advantages for Monte-Carlo simulations technique is its ability to give an accurate value the probability of failure of structural system $P_{f,sys}$ (or β_{sys}), while FORM gives the probability of failure of a structural system in term of upper and lower bounds of β_{sys}.

The proposed MC-NN-FEM technique was used to evaluate the β_{sys}. Two structural systems were analyzed:

1. Failure of strengthening contribution of FRP plate: however the beam in this case is still valid as RC beam. Probability of failure depends on the failure modes numbers 3, 4, 5, 6 and 7 for non anchoraged FRP plate and failure mode number 3 for anchoraged laminates (see Table III.2.6). All these failure modes act as series system and the probability of failure can be calculated according to Equation II.3.52.

2. Overall failure of the FRP strengthened RC beam: failure is based on two different failure scenarios linked as series system. First, concrete crushing failure of FRP strengthened RC beam (failure mode number 2). Second, a coupled of one or more of failure modes numbers 3, 4, 5, 6 and 7 simultaneously with the failure mode number 1. These failure scenarios are known as series system of parallel systems and can be presented as shown in Figure III.2.37. The probability of failure is calculated according to Equation II.3.54.
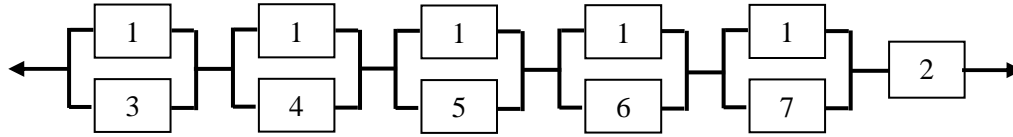
Figure III.2.37: Overall flexural failure scenarios of FRP strengthened RC beam.

Simulation results are presented in Figure III.2.38. It can be observed that failure of FRP contribution of anchoraged FRP plate catches a small value of reliability with respect to anchoraged one: e.g. estimated about 37.5% of the anchoraged system. This reduction is due to the high number of failure modes included in the series system. However, the overall collapse of the FRP strengthened RC beams still catches a high reliability for both anchoraged and non-anchoraged FRP plate. This is due to the advantages of the parallel links between all the FRP plate failure modes and the concrete crushing failure mode of RC beam because the concept of the FRP strengthened RC beam overall failure is not directly related to the failure of FRP plate, but to the concrete crushing of the RC beam. However, attention should be taken into consideration for anchoraged cases because we neglect the failure in the anchoraged tools itself which may probably lead to a reduction in reliability of anchoraged system. From this point of view, non-anchoraged FRP plate can be considered as strong as anchoraged system, although, the high number of failure modes involved in the anchoraged system.
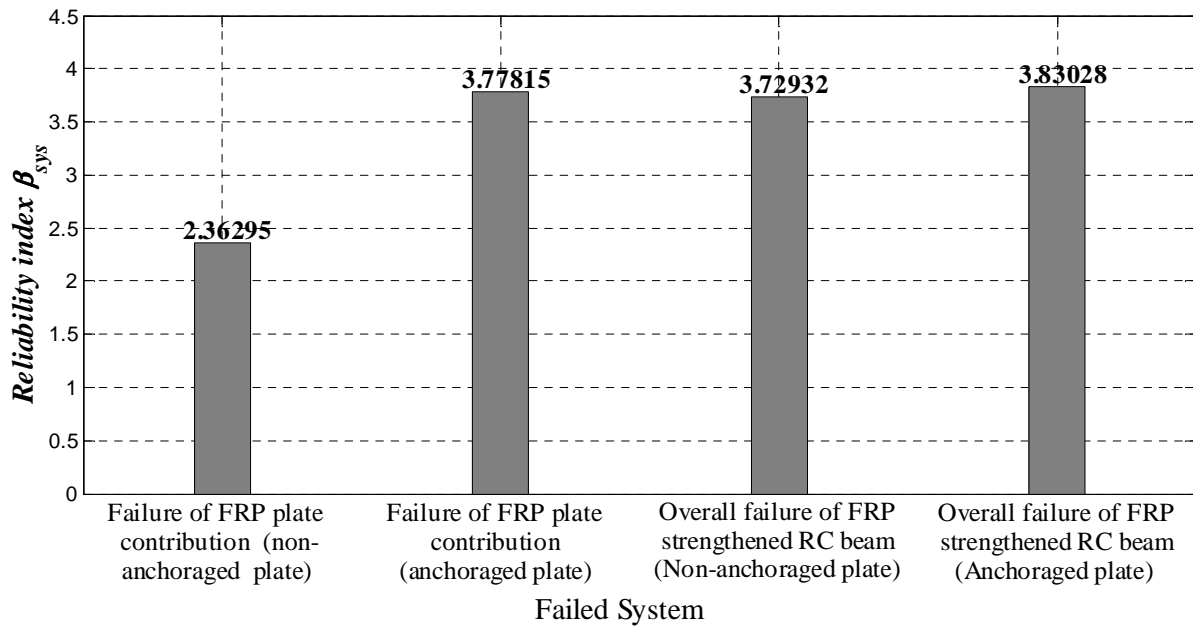
Figure III.2.38: Reliability index β_{sys} of flexural limit states system using MC-NN-FEM.

III.2.3 CONCLUSIONS

This chapter presents a numerical application of the model devolved in our study. The chapter is mainly divided into two parts. The first part of the chapter is related to the reliability analysis of FRP strengthened RC beam based on FORM method. Limit states and failure modes were expressed using analytical design formulas reported in literature and design codes. The second part of the chapter presents the results of reliability analysis based on Monte-Carlo MC simulation technique. Structural response required in limit sates was obtained using Neural Networks NN application. Datasets, of structural response, required to train, validate and test were obtained using Finite element analysis.

The main conclusions are:

1. The results of the numerical example indicate that reliability of RC beams is highly influenced by growth of live load over time. While, Average Daily Truck Traffic *ADTT* has a slight effect on the reliability profile.

2. Pitting corrosion has a significantly effect on the reliability profile. In contrast uniform corrosion slightly affects the reliability profile.

3. Flexural FRP strengthening effectiveness, in term of reliability index increase, depends on the control failure mode after strengthening; the three possible failure modes: concrete crushing, FRP rupture and FRP debonding can provide reliability index increase of about 1.6, 1.2 and 0.6 respectively. These failure modes depend on material properties and the strengthening scheme: anchoraged or non-anchoraged.

4. FRP durability has approximately no effect on the reliability index when the control failure mode is FRP debonding or concrete crushing. However, FRP durability shows a considerable effect on the reliability index when the failure mode is FRP rupture.

5. FRP strengthening design equations, reported in codes, give only one value for FRP specific safety factor for all expected failure mode: concrete crushing, FRP rupture and FRP debonding. In the present study it was found that the specific FRP safety factor depends on the control failure mode after strengthening.

6. Flexural strengthening does not affect the rate of deterioration of flexural reliability index, while shear strengthening decreases dramatically the rate of deterioration of shear reliability index.

7. Serviceability Limit State SLS (deflection) is strongly affected by growth of live load and the *ADTT* value. FRP flexural strengthening of RC beam can effectively increase the reliability index in case of RC beams degraded by corrosion. In contrast, a slight increase is observed in case of growth of live load.

GENERAL CONCLUSIONS

General conclusions.

SUMMARY

The research was conducted to assess the effectiveness, in the perspective of reliability, of externally bonded FRP strengthening of deteriorated RC highway bridge girders due to coupled effects of corrosion and live load growth. The following notes summarize the main topics considered in our study:

1. Corrosion of RC structures is and remains a complex deterioration process that can be represented by diffusion, electrochemical and mechanical principles given that the whole process includes interactions between various phenomena (i.e. chloride penetration, corrosion of reinforcement steel and concrete cracking). The discussion of the state-of-the-art in lifetime modeling in relation to each phenomenon taken separately states that:

   Chloride penetration is a diffusion/convection process modeled by an analytical solution of Fick's law. The analytical solution involves temperature and relative humidity and is based on error function. Additionally, the effective diffusion rate at any point in time can be projected using available diffusion decay models (aging effect on chloride diffusion).

   Corrosion of steel reinforcement is governed by electrochemical principles and can be measured in term of corrosion rate which is affected by temperature, oxygen availability and concrete electrical resistivity. Furthermore, the kinematics of corrosion rate can change when the RC member is cracked.

   Concrete cracking is induced by the accumulation of corrosion products in the steel/concrete interface. There are analytical and numerical approaches to estimate the time to concrete cracking initiation and the crack growth. Since there is good agreement between experimental measures and results obtained for the analytical models, there are implemented as it is in this study to determine the length of this stage.

   Monte-Carlo simulation technique based corrosion model was used to provide time-dependent steel area, time to corrosion initiation and time to cover cracking statistical models. Time-dependent Bi-modal distribution was found the best descriptor of steel area distributions. Log-Normal distribution was found the best descriptor for both times to corrosion initiation and cover cracking.

2. Live load uncertainties are important factors which must be considered in structural reliability estimation especially for highway bridges, as loading involves considerable random variables with high uncertainty: truck weight, truck positions with bridges lanes, traffic volume and number of simultaneous presence of trucks (side-by-side). Based on Nowak's field observations and the theory of extreme event, a live load probabilistic model has been developed using finite element analysis, neural network and Monte-Carlo simulation. The model takes into account growth of truck weight and daily traffic over years. Moreover, structural responses (i.e. bending moment or shearing force) were obtained using finite element modeling of the bridge deck. Thus, the uncertainty in girder distribution factor, given in design codes, can be reduced. Log-Normal and Generalized Extreme Value distributions (GEV) were found the best descriptors of the developed live load model.

3. FRP strengthened RC beam involves more failure modes than RC beam. Such these failure modes are as follow:

   - Concrete crushing

   - FRP intermediate crack debonding

   - FRP rupture

   - FRP end debonding based shear crack

   - FRP end debonding based interfacial shear stresses.

   - Concrete cover separations.

   The structural behavior of FRP strengthened RC beams has been simulated using two methods. The first is based on the simplified analytical formulas reported in previous studies or in design codes. Chapter I.1 gives a brief description of analytical formulas of these failure modes. In order to choose the most accurate formula for each failure mode, results of experimental datasets have been compared with the theoretical evaluations of these formulas. The second method is based on numerical simulations using finite element method.

4. The reliability is measured in term of the reliability index or the probability of failure. The main advantage of the reliability analysis is to consider the uncertainty included in the design variables. The main sources of uncertainties are related to: (1) environmental properties; e.g. chloride concentration, diffusion coefficient…etc (2) material and geometrical properties, (3) loads and (4) structural model error. In accordance with the main objectives of this research, Load and Resistance Factor

Design (LRFD) concept has been used to establish the limit state functions required to perform the reliability analysis. All the aspects of reliability analysis have been presented in Chapter II.3: e.g. definition of random variables, *PDF* and *CDF* functions of the used distributions, probabilistic transformations…etc.

5. Two reliability methods were used. The first is first order reliability method FORM method which is an approximated method. Limit state functions are explicitly expressed using the design codes analytical formulas related to failure modes. The second method is based on Monte-Carlo simulation which is used in conjunction with Finite Element Method (FEM). In this case, the limit state functions are expressed using Neural Network (NN) technique. This technique has been used to avoid the explicit formulation of the limit state function using FEM, as it is considered time cost. The datasets required to train, validate and test the NN are obtained using finite element method. The two reliability methods are finally compared in terms of accuracy and calculation time. Three limit states have been considered: (1) flexural ultimate limit state, (2) shear ultimate limit state and (3) serviceability limit state (deflection).

CONCLUSIONS

In accordance with the main objective of this thesis which is, as mentioned above, to assess the effectiveness, in the perspective of reliability, of FRP strengthening of deteriorated RC girders due to coupled effects of corrosion and live load growth, the following conclusions have been drawn:

1. *ADTT* value has a slight effect on the reliability index ultimate limit state (flexural or shear).

2. Reliability profiles (time-evolution of reliability index) of FRP strengthened RC girders designed for flexural and shear limit states are significantly affected by the growth of live load over time. However, the RC girders are considered as reliable for more than 50 years.

3. Growth of live load is more significant in deteriorating reliability index of RC beams. However, pitting corrosion is more hazardous than live load growth when concrete cover *c* does not satisfy the corrosion protection requirement (i.e. $c \leq 30$mm)

4. Pitting corrosion is potentially more hazardous in all cases than uniform corrosion, as the later has a slight effect on the deterioration of the reliability profile. One must also notice that both pitting and uniform corrosions do not affect beam reliability for about 40 years. Additionally, corrosion has no significant effect on the reliability for end debonding failure mode.

5. Concrete crushing is not the most frequent failure mode after strengthening. Instead, FRP debonding or FRP rupture may occur after strengthening. This depends on the FRP properties used in the strengthening and on the interface between concrete and FRP.

6. The effectiveness of the FRP strengthening on reliability depends on the control failure mode after strengthening. The maximum increase in the reliability index due to FRP strengthening takes place if the control failure mode is concrete crushing or FRP rupture. While FRP debonding gives the lower effectiveness compared to the concrete crushing or FRP rupture.

7. FRP durability (expressed in term of mechanical properties reduction) has no effect on the time-dependent reliability index when the control failure mode after strengthening is concrete crushing or FRP debonding. However, a considerable reduction in the reliability is observed when the control failure mode is the FRP rupture.

8. If the control failure mode after strengthening is the concrete crushing, reduction in FRP properties due to aging may cause a change of failure mode toward FRP rupture.

9. Unlike reliability for flexural ultimate limit state that is strongly affected by corrosion or growth of load, FRP end debonding based shear crack limit state is quite affected by growth of live load. However, the beam reliability index is still of sufficiently considerable value.

10. The end distance between the plate end and the support has a high effect on the reliability index of FRP end debonding based shear crack limit state.

11. FRP strengthening has no effect of the rate of deterioration before and after strengthening. While this rate dramatically decreases in case of shear strengthening.

12. FRP durability slightly affects the reliability of the shear limit state.

13. Artificial neural networks technique provides a robust tool to formulate a response function required to predict the structural behaviors of bridge deck.

14. *ADTT* value has a considerable effect on the reliability analysis of serviceability limit state (deflection).

15. FRP flexural strengthening can increase efficiently the reliably index due to corrosion damage: pitting or uniform. However, this increase in the reliability index is strongly affected by the growth of live load.

16. For a given target reliability index the corresponding partial safety factors are not identical for anchorage and non-anchorage FRP laminates cases.

17. In most cases, deterministic resolution of LRFD and probabilistic analysis of the limit state equations did not produce the same failure mode. Thus, it appears that probabilistic analysis is an essential step toward a more accurate prediction of the control failure mode when multiple failure modes are probable.

18. High values of partial safety factors (ϕ and ψ_{FRP}) produce the same FRP amounts for both anchoraged and non-anchoraged FRP laminates because the control failure mode is FRP rupture in both cases.

OUTLOOKS AND RECOMMENDATIONS FOR FUTURE RESEARCH

Based on the findings of this study, we can suggest at least six areas in which further research is needed to enhance the proposed models:

1. To study the effect of concrete and FRP interface durability on the reliability profile of FRP strengthening RC element.

2. To look for the optimal time to strengthening based on life-cycle performance and costs analysis of RC beams considering the random variability of material properties, loads, section dimensions, model errors, chloride penetration and corrosion rates,…

3. To calibrate partial safety factors for the design of FRP strengthened RC beam as a function of required service life after strengthening, updated target reliability index and/or minimum expected cost.

4. To study the coupled fatigue effects on the reliability profile of FRP strengthened RC beams (fatigue can damage the compression zone of the concrete, FRP laminates, etc).

5. To perform reliability analysis considering the effect of corrosion induced cover cracking on bond between FRP laminates and concrete surface.

6. To focus on the reliability estimation of degraded FRP-concrete multi-material components subjected to aging effect based on accelerated life test concept.

Conclusions générales

RESUME

L'objectif de la recherche était de vérifier l'efficacité, sous l'angle de la fiabilité, du renforcement par collage extérieur de PRF de poutres béton armé de type pont autoroutier dégradées sous les effets couplés de la corrosion et de l'augmentation des chargements d'exploitation. Les principaux sujets traités dans notre étude sont repris dans les points qui suivent.

1. La corrosion des structures en béton armé est et reste un processus de dégradation complexe qui relève des principes de la diffusion, électrochimiques et mécaniques dans la mesure où le processus, dans son ensemble, met en jeu des interactions entre phénomènes multiples (c.-à-d. pénétration des ions chlorures, corrosion des aciers de renforcement et fissuration du béton). L'analyse de l'état de l'art relatif aux modèles de dégradation et de durée de vie vis-à-vis de chacun de ces phénomènes nos amène à conclure que :

   La pénétration des ions chlorures est un processus de diffusion/convection qui peut être modélisé par une formulation analytique de la loi de Fick. Cette solution analytique intègre l'influence de la température et de l'humidité relative et est basée sur la fonction erreur. En complément, le taux effectif de diffusion à un temps quelconque peut être déterminé à l'aide de modèles validés de décroissance de la diffusion (effet du vieillissement sur la diffusion des ions chlorures).

   La corrosion des renforcements en acier est gouvernée par des phénomènes électrochimiques et sera mesurée par un taux de corrosion qui peut être influencé par la température, la quantité d'oxygène and par la résistivité électrique du béton. En outre, la cinématique du taux de corrosion peut évoluer dés que l'élément de structure en béton armé est fissuré.

   La fissuration du béton intervient à la suite de l'accumulation de produits de la corrosion à l'interface entre les barres d'acier et le béton. Des approches analytiques ou numériques existent afin d'estimer le temps de (première) fissuration et de modéliser la croissance des fissures. Comme il existe une bonne corrélation entre les mesures d'essais et les résultats obtenus par le biais des modèles analytiques de la littérature, ces derniers seront utilisés tels quels dans notre étude.

   La technique de simulation dite de Monte Carlo est appliquée sur le modèle de

corrosion afin de déterminer les lois de distribution statistique de l'aire des barres d'acier corrodées (loi évoluant au cours du temps), du temps d'initiation de la corrosion et du temps de fissuration. Des lois bimodales dont les paramètres évoluent avec le temps seront déterminées pour décrire les distributions de la section des aciers. Une loi Log-normale a été identifiée comme étant, quant à elle, la plus en adéquation à la fois pour les temps d'initiation de la corrosion et de fissuration.

2. Les incertitudes et variations liées aux charges variables, et notamment de trafic, constituent des paramètres importants qui doivent être pris en compte dans le cadre d'un travail d'estimation de la fiabilité structurale. Ceci est spécialement vrai dans le cas des ponts autoroutiers où une forte dispersion des variables aléatoires est identifiée : sur le poids des camions, leur position vis-à-vis des voies de circulation du pont, sur le volume du trafic et le nombre de passages simultanés de camions (côte à côté). En s'appuyant sur les observations de Nowak et sur la théorie des valeurs extrêmes, un modèle probabiliste des charges variables de trafic routier a été développé en associant méthode des éléments finis, réseaux de neurones et simulation de Monte Carlo. Ce modèle prend en compte la croissance du poids des camions et du trafic journalier au fil des années. Enfin, les réponses structurales (c.-à-d. le moment fléchissant et l'effort tranchant) sont déterminées à l'aide d'une modélisation par éléments finis du pont autoroutier. En conséquence, l'incertitude quant au traduite par les coefficients de sécurité, donnés dans les codes de dimensionnement, peut être réduite.

3. Une poutre béton armé renforcée par matériau composite à base de PRF est confrontée à plus de rupture qu'une poutre en béton armé seule. Ces modes de rupture à considérer sont les suivants:

- Ecrasement du béton dans la zone comprimée
- Décollement du matériau composite en partie courante au voisinage des fissures de flexion
- Rupture du matériau composite
- Décollement du matériau composite à ses extrémités au voisinage des fissures de cisaillement
- Décollement du matériau composite à ses extrémités par rupture de l'interface composite sur béton par cisaillement inter-laminaire

- Séparation de l'enrobage.

Le comportement structural de poutres béton armé renforcées à l'aide de PRF a été simulé en utilisant deux méthodes. La première s'appuie sur des formules analytiques simplifiées extraites de travaux antérieurs ou de codes de dimensionnement. Le Chapitre I.1 donne une description succincte des formulations analytiques des modes de rupture évoqués ci avant. Et, avec pour enjeu de sélectionner les formulations les plus adaptées à chaque mode de rupture, les résultats extraits de bases de données expérimentales ont été confrontés aux valeurs théoriques établies pour chaque formule. La seconde méthode s'appuie quant à elle sur des simulations numériques par éléments finis.

4. La fiabilité est mesurée en termes d'indice de fiabilité ou de probabilité de défaillance. La caractéristique ainsi que l'avantage principale de l'analyse fiabiliste est de prendre en compte les incertitudes liées aux variables de conception ou de dimensionnement. Les sources principales d'incertitudes se retrouvent dans : (1) les propriétés environnementales (par exemple, la température ou l'humidité), (2) les propriétés des matériaux et géométriques, (3) les sollicitations et (4) l'erreur du modèle structural. Cadrant avec les principaux objectifs fixés, le concept de dimensionnement basé sur le calcul des facteurs de résistance et de charge[1] a été repris en vue d'établir les fonctions d'état limite requises pour conduire l'analyse fiabiliste. Tous les aspects et développements relatifs à cette analyse ont été présentés dans le Chapitre II.3 : par exemple, la définition des variables aléatoires, les fonctions de densité de probabilité (*PDF*) et cumulative des probabilités (*CDF*) des distributions statistiques utilisées, les transformations probabilistes, etc.

5. Deux approches fiabilistes sont adoptées. La première se fonde sur la méthode d'approximation dite de fiabilité du premier ordre (ou méthode FORM pour First Order Reliability Method). Les fonctions d'état limite sont dans ce cas exprimées de manière explicite de par l'utilisation des formulations analytiques, issues des codes règles de dimensionnement, des modes de défaillance. La seconde méthode s'appuie quant à elle sur la simulation de Monte Carlo associée à la technique des réseaux de neurones artificiels. Les bases de données nécessaires à l'apprentissage, à la validation et à la généralisation des réseaux de neurones sont bâties à partir de simulations numériques par éléments finis. Les deux approches sont finalement confrontées sur la

---

[1] plus connu sous son acronyme anglais LRFD pour Load and Resistance Factor Design

base de la précision et de la vitesse des calculs. Dans nos travaux, trois familles d'états limites sont considérés : (1) l'état limite ultime en flexion, (2) l'état limite ultime en cisaillement et (3) l'état limite de service en déplacement.

CONCLUSIONS

Vis-à-vis de l'objectif principal de la thèse qui était, nous l'avons rappelé plus haut, de vérifier l'efficacité, sous l'angle de la fiabilité, du renforcement par PRF de poutres béton armé dégradées sous les effets de la corrosion et de l'augmentation des chargements d'exploitation, nous pouvons tirer les conclusions suivantes :

1. Le trafic moyen journalier de poids lourds (Average Daily Truck Trafic ou *ADTT* en anglais) présente un effet modéré sur l'indice de fiabilité exprimé pour l'état limite ultime (en flexion ou en cisaillement).

2. Les profils de fiabilité (évolution de l'indice de fiabilité avec le temps) de poutres béton armé renforcées par PRF aux états limites ultimes en flexion et en cisaillement sont affectés de manière significative par la croissance des chargements autoroutiers au cours du temps. Toutefois, les poutres en béton armé sont considérées comme étant fiables pour au moins une cinquantaine d'années.

3. La croissance des chargements est le facteur le plus sensible vis-à-vis de la diminution de l'indice de fiabilité de poutres en béton armé. Il apparait toutefois que la corrosion par piqûres (pitting corrosion en anglais) est plus critique que la croissance des chargements dés lors que l'enrobage c des barres d'acier ne satisfait pas les exigences requises de protection (c.à.d. $c \leq 30mm$).

4. La corrosion par piqûres est potentiellement plus critique que la corrosion généralisée (uniform corrosion en anglais) ; cette dernière ayant un effet modéré sur la dégradation du profil de fiabilité. Il faut également retenir que les deux types de corrosion n'impactent pas la fiabilité de la poutre avant une quarantaine d'années. En outre, la corrosion n'a pas d'effet significatif en terme de fiabilité pour le mode de rupture par décollement des extrémités du composite en PRF.

5. L'écrasement par compression du béton ne constitue pas le mode de rupture le plus probable suite au renforcement par PRF contrairement aux décollements du PRF voire de sa rupture. Au final, le mode dépend des propriétés du PRF de renforcement et de celles de l'interface béton sur PRF.

6. L'efficacité du renforcement par PRF sur la fiabilité dépend du mécanisme qui contrôle la rupture. L'apport du renforcement en termes d'indice de fiabilité est maximal si le dimensionnement est tel qu'il puisse conduire aux modes de défaillance par écrasement du béton dans la zone de compression ou par rupture du PRF. A contrario, les modes de défaillance par décollements du PRF diminuent l'efficacité du

renforcement.

7. Le vieillissement du PRF (qui s'exprime par une diminution de ses propriétés mécaniques) n'a pas d'effet notable sur la variation de l'indice de fiabilité dans le temps quand les mécanismes qui contrôlent la rupture de la poutre sont l'écrasement du béton dans la zone de compression ou le décollement du béton. Par contre, une diminution considérable de la fiabilité est observée quand le mode de défaillance est celui de la rupture du PRF.

8. Si le dimensionnement avant réparation est conduit au pivot B, le mode de défaillance après réparation peut évoluer dans le temps vers la rupture du PRF du fait des diminutions des propriétés mécaniques dû au vieillissement.

9. Alors que la fiabilité vis-à-vis de l'état limite ultime en flexion est considérablement impactée par la corrosion ou la croissance des chargements de trafic, celle exprimée pour l'état limite associé au décollement du matériau composite à ses extrémités au voisinage des fissures de cisaillement l'est très peu. Toutefois, l'indice de fiabilité des poutres reste à des valeurs suffisamment importantes.

10. La distance entre l'extrémité du composite et l'appui a une influence forte vis-à-vis de l'indice de fiabilité pour l'état limite associé au décollement des extrémités du PRF au voisinage des fissures de cisaillement.

11. Le renforcement par PRF n'a pas d'effet sur la pente exprimant la dégradation de l'indice de fiabilité dans le temps calculée avant et après réparation. Cette pente sera au contraire très affectée dans le cas d'un renforcement additionnel vis-à-vis de l'effort tranchant.

12. Le vieillissement du PRF impacte modérément la fiabilité à l'état limite ultime en cisaillement.

13. La technique des réseaux de neurones artificiels constitue une approche robuste de formulation d'une fonction de réponse dont l'analyse permet de prédire les comportements structuraux de tabliers de ponts.

14. Le trafic moyen journalier de poids lourds a une influence considérable sur l'analyse de la fiabilité à l'état limite de service (en déplacements).

15. Le renforcement par PRF vis-à-vis de la flexion peut augmenter efficacement l'indice de fiabilité après corrosion, par piqûres ou généralisée. Toutefois, cette augmentation de l'indice de fiabilité est fortement impactée par la croissance des chargements de trafic.

16. Pour un indice de fiabilité cible donné, les coefficients de sécurité partiels

correspondants doivent être différenciés selon que les stratifiés de PRF sont ancrés ou non.

17. Dans la plupart des cas, le traitement déterministe du dimensionnement par le calcul des facteurs de résistance et de charge (méthode LRFD) et la résolution probabiliste des équations d'états limites n'amène pas au même mode de défaillance. Il apparait ainsi que l'analyse probabiliste consiste une étape essentielle vers une prédiction plus pertinente du mode prédominant de défaillance quand plusieurs modes sont probables.

18. De fortes valeurs des coefficients de sécurité partiels (ϕ and ψ_{FRP}) amènent à des quantités similaires de PRF à la fois pour des renforcements ancrés ou non car le mode de défaillance prédominant est la rupture du PRF dans les deux cas.

PERSPECTIVES ET RECOMMANDATIONS POUR DES FUTURES RECHERCHES

A partir des résultats de notre étude, nous pouvons suggérer au moins six directions vers lesquelles continuer la recherche afin d'améliorer les modèles proposés :

1. Etudier l'impact de la durabilité du béton et de son interface avec le PRF sur le profil de fiabilité d'éléments en béton armé renforcés par le biais de PRF.

2. Rechercher le meilleur délai avant renforcement en se basant sur l'analyse de la performance et du coût du cycle de vie des poutres en béton armé en intégrant le caractère aléatoire des propriétés matérielles, des chargements, des dimensions des sections, des erreurs de modèles, des taux de pénétration des ions chlorures, de corrosion,…

3. Calibrer les coefficients de sécurité partiels pour le dimensionnement d'une poutre béton armé renforcée par PRF en fonction de la durée de vie attendue après le renforcement, un indice de fiabilité cible actualisé et/ou un coût global minimum engendré.

4. Etudier les effets de couplage avec la fatigue sur le profil de la fiabilité de poutres béton armé renforcées par PRF (la fatigue endommageant le béton dans la zone comprimée, endommageant le PRF, etc.).

5. Analyser par une approche fiabiliste l'effet des fissures de l'enrobage dues à la corrosion sur l'adhérence entre le PRF stratifié et la surface du béton.

6. Se concentrer sur l'estimation de la fiabilité sous l'effet du vieillissement de composants multi-matériaux à base de béton et de composites en PRF à partir du concept des essais accélérés.

REFERENCES

REFERENCES

AASHTO-LRFD Bridge Design Specifications. 2007. American Association of State Highway Transportation Officials. Washington DC 20001.

ABAQUS 6.9. 2009. ABAQUS user's manual.

Abdullah R, Paton-Cole V P and Easterling W S. 2007. Quasi-static analysis of composite slab, Malaysian Journal of Civil Engineering 19(2): 91-103.

ACI Committee 440. 2002. ACI 440.2R-02: Guide for the design and construction of externally bonded FRP system for strengthening concrete structures. Farmington Hills, MI: ACI 2002.

Adams R D, Atkins R W, Harris J A and Kinloch A J. 1986. Stress analysis and failure properties of carbon-fibre-reinforced-plastic/steel double-lap joints. Journal of Adhesion 20: 29-53.

Adhikary B B, Mutsuyoshi H, and Ashraf M. 2004. Shear strengthening of reinforced concrete beams using fiber-reinforced polymer sheets with bonded anchorage. ACI Structural Journal 101(5): 660-68.

Ahmed A. 2003. Reinforcement corrosion in concrete structures, its monitoring and service life prediction – a review. Cement & concrete Composites, 25: 459-71.

Ahmed O, Gemert D V and Vandewalle L. 2001. Improved models for plate-end shear of CFRP strengthened RC beams. Cement& Concrete Composites 23: 3-19.

Ahmed O and Van Gemert D. 1999. Behaviour of RC beams strengthened in bending by CFRP laminates, In: Proceedings of the eighth international conference on advanced composites for concrete repair.

Allan R C, Bird J and Clarke J D. 1988. Use of adhesives in repair of cracks in ship structures. Materials Science and Technology 4: 853-859.

Ali M S, Oehlers D J and Bradford M A. 2005. Debonding of steel plates adhesively bonded to the compression faces of RC beams. Construction and Building Materials 19: 413-422.

Ali M S M, Oehlers D J, Griffith M C, and Seracino R. 2008. Interfacial stress transfer of near surface-mounted FRP-to-concrete joints. Engineering Structures 30: 1861-68.

Almusallam A A. 2001. Effect of degree of corrosion on the properties of reinforcing steel bars. Construction and Building Material 15: 361-68.

Andrade C, Sanjuan M A, Recuero A and Rio O. 1993. Calculation of chloride diffusivity in concrete from migration experiments in non-steady state conditions. Cement and Concrete

Research 24(7): 1214-28.

Aprile A and Benedetti A. 2004. Coupled flexural-shear design of R/C beams strengthened with FRP. Composites: Part B 35: 1–25.

Aprile A and Feo. 2007. Concrete cover rip-off R/C beams strengthened with FRP composites. Composites: Part B 38:759-71

Aram M R, Czaderski C and Motavalli M. 2008. Debonding failure modes of flexural FRP-strengthened RC beams. Composites: Part B 39: 826-41.

Arya C, Clarke J L, Kay E A and O'Regan P D. 2002. TR 55: Design Guidance for Strengthening Concrete Structures Using Fibre Composite Materials: A Review. Engineering Structures 24: 889-900

Arnon B, Sidney D and Neal S B. 1997, Steel Corrosion in Concrete: Fundamentals and Civil Engineering Practice, E & FN Spon, London.

Ashour A F, El-Refaie S A and Garrity S W. 2004. Flexural strengthening of RC continuous beams using CFRP laminates. Cement & Concrete Composites 26: 765-775.

ASTM International D3039/D3039M-00, standard test method for tensile properties of polymer matrix composite materials. Annual book ASTM standards 2000. West Conshohocken, PA: ASTM International.

Atadero A A and Karbhari V M. 2007. Calibration of resistance factor for reliability based design of externally-bonded FRP composites. Composites Part B 39(4): 665-79.

Atadero A A and Karbhari V M. 2009. Sources of uncertainties and design values for field-manufactured FRP. Composites Structures 89:83-93.

Atadero A A, Lee L and Karbhari V M. 2005. Consideration of material variability in reliability analysis of FRP strengthened bridge decks. Composites Structures 70: 430-43.

Bahtui A. 2008. Development of a Constitutive Model to Simulate Un-bonded Flexible Riser Pipe Elements. Ph.D thesis, Brunel University.

Bank C L. 2006. COMPOSITES FOR CONSTRUCTION: Structural Design with FRP Materials. John Wiley & Sons, New Jersey, USA, 567p.

Balaguru P, Nanni A, and Giancaspro J. 2009. FRP Composites for Reinforced and Prestressed Concrete Structures; A guide to fundamentals and design for repair and retrofit. *Taylor & Francis's Structural Engineering: Mechanics and Design series*, New York, USA, 334p.

Barros J A O and Dias S J E. 2003. Shear Strengthening of reinforced concrete beams with laminte strips of CFRP. Proceedings of the International Conference Composites in Construction – CCC2003, Italia, September: 289-294.

Bastidas-Arteaga E, Bessolette P, Chateauneuf A and Sanchez-Silva M R. 2009. Probabilistic lifetime assessment of RC structures under coupled corrosion deterioration processes, Structural safety 31: 84-96.

Bastidas-Arteaga E, Sanches-Silva M, Chateauneuf A and Sanchez-Silva M R. 2008. Coupled reliability model of biodeterioration, chloride ingress and cracking for reinforced concrete structures. *Structural Safety* 30: 110-29.

Bazant Z P. 1983. Crack band theory for fracture of concrete. Materials & Constructions journal (16)93: 155-77.

Bažant Z P & Planas J. 1998, Fracture and Size Effect in Concrete and Other Quasibrittle Materials, CRC Press, 640p.

Beber A J, Filho A C and Campagnolo J L. 1999. Flexural strengthening of R/C beams with CFRP sheets, In: Proceedings of the eighth international conference on advanced composites for concrete repair.

Blaschko M, Mierdermeier R and Zilch K. 1998. Bond failure modes of flexural members strengthened with FRP. Proceedings of 2nd International Conference on Composites in Infrastructures, Tucson: 315–27

Bogas J A and Gomes A. 2007. Analysis of the CFRP flexural strengthening reinforcement approaches proposed in Fib bulletin 14. Construction and Building Materials 22: 2130-40.

Bucher C G and Bourgund U. 1990. A fast and efficient response surface approach for structural reliability problems. Journal of structural Safty 7: 57-66.

Cairns J, Plizzari. G A, Du Y, Law D W, and Franzoni C. 2005. Mechanical Properties of Corrosion-Damaged Reinforcement. ACI material journal 102(4): 256-64.

Carolin A and Täljsten B. 2005. Theoretical study of strengthening for increased shear bearing capacity. Journal of Composites for Construction, 9(6): 497-506.

CC Technologies Laboratories Inc. 2001. Corrosion Costs and Preventive Strategies in the United States. Reported by Federal Highway Administration (FHWA). Office of Infrastructure Research and Development. Publication No: FHWA-RD-01-156.

Ceroni F. 2010. Experimental performance of RC beams strengthened with FRP materials. Construction and Building Materials 24: 1547-59.

Chajes M J, Januszka T F, Mertz D R, Thomson Jr T A and Finch Jr W W. 1995. Shear strengthening of reinforced concrete beams using externally applied composite fabrics. ACI Structural Journal 92(3): 295-303.

Chaallal O, Nollet, M J, and Perraton D. 1998. Strengthening of reinforced concrete beams with externally bonded fibre-reinforced-plastic plates: design guidelines for shear and

flexure. Canadian Journal of Civil Engineering, 25: 692-708.

Challal O, Nollet M J and Saleh K. 1998. Use of CFRP strips for flexure and shear strengthening of RC members. Proceedings of the Second International Conference on Composites in Infrastructure, Tucson, AZ, USA: 49–60.

Chen G M, Chen J F and Teng J G. 2010. On the finite element modeling of RC beams shear-strengthened with FRP. Construction and Building Materials 32: 13-26.

Chen J F and Teng J G. 2001. Anchorage strength model for FRP and steel plates bonded to concrete. Journal of Structural Engineering 127 (7): 784-91.

Chen J F and Teng J G. 2003. Shear capacity of FRP strengthened RC beams: FRP debonding. Construction and Building Materials 17: 27–41.

Chen W and Duan L. 2003. Bridges Engineering: Construction and Maintenance. Taylor & Francis Group, LLC, United States: 236p.

CNR-DT 200, Consiglio Nazionale Delle Richerche. 2004. Istruzioni per la Progettaazione. I'Esecuzione ed il Controllo di Interventi di Consolidamento Statico mediante I'utilizzo di Compositi Fibrorinforzati. Rome, Italy, 164pp.

Colotti V and Spadea G. 2006. Unified model to predict flexural and shear behaviour of externally bonded RC beams. The Arabian Journal for Science and Engineering 1C(31):3-18.

Colotti V and Spadea G. 2011. Unified analytical approach for determining shear capacity of RC beams strengthened with FRP. Engineering Structures 33: 827-842.

Concrete Society. 2004. Design Guidance for strengthening concrete structures using fibre composite materials. Concrete Society Technical Report 55, Second Edition, Camberley, Surrey, UK, 102p.

Coronado C A, and Lopez M M. 2005. Sensitivity analysis of reinforced concrete beams strengthened with FRP laminates. Cement & Concrete Composites 28: 102-14.

Costea A and Nastac I. 2005 .Assessing the predictive performance of artificial neural network-based classifiers based on different data preprocessing methods, distributions and training mechanisms. Intelligent Systems in Accounting, Finance and Management 13(4): 217-250

Crespo-Minguillon C & Casas J R. 1997. A comprehensive traffic load model for bridge safety checking. Journal of Structural Safety 19(4): 339-59.

David E, Djelal C, Ragneau E and Bodin F B. 1999. Use of FRP to strengthen and repair RC beams: experimental study and numerical simulations, In: Proceedings of the eighth international conference on advanced composites for concrete repair.

References

Deniaud C, and Roger Cheng J J. 2001. Shear behaviour of reinforced concrete T-beams with externallybonded fibre-reinforced polymer sheets. ACI Structural Journal, 98(3): 396-94.

Diagana C, Li A, Gedalia B and Delmas Y. 2003. Shear strengthening with CFF strips. Engineering Structures 25: 507-16.

Dias S J E and Barros J A O. 2008. Shear strengthening of T cross section reinforced concrete beams by near surface mounted technique. Journal Composites for Construction, 12(3): 300-11.

Ditlevsen O and Madsen H O. 1996. Structural Reliability Methods. First edition published by John Wiley & Sons Ltd, Chichester, 373p.

Duprat F. 2007. Reliability of RC beams under chloride-ingress. Construction and Building materials 21: 1605-1616.

Ellingwood B, Galambos T V, MacGregor J G and Cornel C A. 1980. Development of a probability based load criterion for American National standard A58. Washington, DC: National Bureau of Standards: 222p.

El-Tawil S, Ogunc C, Okeil A and Shahway M. 2001. Static and fatigue analysis of RC beams strengthened with CFRP laminates. Journal of Composites for Construction (5)4: 258-267.

Esfahani M R, Kianoush M R and Tajari A R. 2007. Flexural behavior of reinforced concrete beams strengthened by CFRP sheets. Engineering Structures 29: 2428-44.

Eurocode 0. 2001. Basis of Structural Eurocodes. Eurocode 0, En 1990.

Ferreira R M. 2004. Probability-based durability analysis of concrete structures in marine environment. Ph.D thesis, University of Minho: 268p.

Ferrier E. 1999. Comportement de l'interface composite-beton sous des sollicite et en fatigue oligocyclique. Application au calcul prévisionnel de la durabilité de poutres BA reinforeés. Ph.D thesis, Claude Bernard Lyon 1 university, France, 263p.

Faravelli F. 1989. Response-surface approach for reliability analysis. Journal of Engineering Mechanics ASCE 115(12): 2763-81.

Fib Fédération international du béton 2001. Externally bonded FRP reinforcement for RC structures. Technical Report, Bulletin 14, Task Group 9.3 FRP, Lausanne, Switzerland: 130p.

Gadve S, Mukherjee A and Malhotra S N. 2009. Corrosion of steel reinforcement embedded in FRP wrapped concrete. Construction and Building Material 23: 153-161.

Gao B, Leung C K Y, and Kim J. 2005. Prediction of concrete cover separation failure for RC beams strengthened with CFRP strips. Engineering Structures 27: 177-89.

References

Garden HN, Hollaway LC and Thorne AM. 1997. A preliminary evaluation of carbon fibre reinforced polymer plates for strengthening reinforced concrete members. Proceedings of the Institution of Civil Engineers: Structures and buildings 123:127–42.

Gavin H P and Yau S C. 2008. High-order limit state functions in the response surface method for structural reliability analysis. Structural Safety 30: 162-79.

Grace N F, Abdel-Sayed G and Ragheb W F. 2002. Strengthening if concrete beams using innovative ductile fiber-reinforced polymer fabric. ACI Structural Journal 99(5): 692-700.

Hamelin P. 1998. Composite infrastructure applications: concept, design, and durability control and prediction. Journal of Composites Technology and Research, ASTM.

Hashemi S H, Maghsoudi A A and Rahgozar R. 2009. Bending Response of HSRC Beams Strengthened with FRP Sheets. Transaction A: Civil Engineering, Sharif University of Technology (16)2: 138-46.

Hasofer A M and Lind N C. 1974. Exact and invariant second-moment code format. Journal of Engineering Mechanics, ASCE 100(1): 111-21.

Heaton J. 2005. Introduction to Neural Networks for Java. 2nd Edition, Heaton Research, 440p.

Hiu H, Karbhari V M and Wu Z. 2006. Diagonal marco-crack induced debonding mechanisms in FRP rehabilitated concrete. Composites: Part B 37: 627-41

Hong A S and Nowak A S. 1991. Bridge live loads. Journal of Structural Engineering ASCE 117(9): 2757-67.

Inoue S, Nishibayashi S, Kuroda T and Omata F. 1995. Fatigue Strength and Deformation Characteristics of Reinforced Concrete Beams Strengthened with Carbon Fiber-Reinforced Plastic Plate. Transactions of the Japan Concrete Institute 17: 149-156.

Jayaprakash J, Abdul-Samad A, Abbasovich A A and Ali A M A. 2008. Shear capacity of pre-cracked and non pre-cracked reinforced concrete shear beams with externally bonded by bi-directional CFRP strips. Construction and Building Materials 22: 1148-65.

JCSS. 2001. Probabilistic model code. The Joint Committee on Structural Safety.

JSCE 2001. Japan Society of Civil Engineers. Recommendations for Upgrading of Concrete Structures with use of Continuous Fiber Sheets. Concrete Engineering Series 41, Tokyo, 250p.

Kamiharako A, Maruyama K, Takada K and Shimomura T. 1997. Evaluation of shear contribution of FRP sheets attached to concrete beams. Proceedings of the III International Symposium Non Metallic (FRP) Reinforcement for Concrete Structures, Japan: 467-74.

Karbhari V M. and Abanilla M A 2007. Design factors, reliability, and durability predictions

of wet layup carbon/epoxy used in external strengthening. Composites: Part B 38: 10-23.

Karbhari V M. 2007. Durability of composites for civil structural applications. Woodhead Publishing Limited, Cambridge, England: 366p.

Khalifa A, Gold W, Nanni A and Abdel-Aziz M J. 1998. Contribution of externally bonded FRP to shear capacity of RC flexural members. Composite Construction, 2(4): 195–202.

Khalifa A and Nanni A. 2000. Improving shear capacity of existing RC T-section beams using CFRP composites. Cement & Concrete Composites 22: 165-74.

Kim G, Sim J and Oh H. 2008. Shear strength of strengthened RC beams with FRPs in shear. Construction and Building Materials 22: 1261-70.

Koay Y C. 2011. FRP composites for strengthening bridges in Victoria. 4th international conference in durability and sustainability of fiber reinforced polymer (FRP) composites for construction and rehabilitation CDCC'2011 Canada Québec: 433-41.

Kozikowski M. 2009. WIM Based Live Load Model for Bridge Reliability. Ph.D thesis, University of Nebraska, at Lincoln, USA: 363p.

Lachtermacher G and Fuller J D. 1995. Back Propagation in time series forecasting. Journal of forecasting 14(4): 381-393.

Lemaire M, Chateauneuf A and Mitteau J. 2009. Structural Reliability. John Wiley & Sons, Inc. United States: 511p

Li C, Melchers R E, and Zheng J. 2006. Analytical model for corrosion-Induced Crack Width in Reinforced Concrete Structures. ACI Structural Journal 103(4): 479-87.

Liang M, Jin W, Yang R and Huang N. 2005. Predeterminate model of corrosion rate of steel in concrete. Cement and Concrete Research 35: 1827-33.

Liu Y. 1996. Modeling the Time-to-Corrosion Cracking of the Cover Concrete in Chloride Contaminated Reinforced Concrete Structures. Ph.D thesis, Virginia Polytechnic Institute and State University, Blacksburg, Virginia: 117p.

Lui Y and Weyers R E. 1998. Modeling the Time-to-Corrosion Cracking in Chloride Contaminated Reinforced Concrete Structures. ACI Material Journal 95(6): 675-681.

Liu Y and Weyers R E. 1998*. Modeling the dynamic corrosion process in chloride contaminated concrete structures. Cement and Concrete Research, 28: 365-79.

Luping T and Gulkers J. 2007. On the mathematics of time-dependent apparent chloride diffusion coefficient in concrete. *Cement and Concrete Research* 37: 589-595.

Lu X Z, Chen J F, Ye L P, Teng J G, and Rotter J M. 2008. RC beams shear-strengthened with FRP: stress distribution in the FRP reinforcement. Construction and Building Materials 23: 1544-54.

Lu X Z, Teng J G and Jiang L P. 2005. Bond-slip models for FRP sheets/plates bonded to concrete. Composites: Part B 27: 920-37.

Maalej M and Bian Y. 2001. Interfacial shear stress concentration in FRP-strengthened beams". Composite structure, 54: 417-26

Masoud S and Soudki K. 2006. Evaluation of corrosion activity in FRP repaired RC beams. Cement & Concrete Composites 28: 969-977.

Massih D Y A. 2007. Analyse du comportement des fondations superficielles filantes par des approches fiabilistes. Ph.D thesis, Nantes University, Faculté des sciences et des techniques, 267p.

Matlab R2011a. 2011. Matlab user' manual, version 7.12.0.

Matthys S and Triantafillou T C. 2000. Shear and torsion strengthening with externally bonded FRP reinforcement. In: Reality A, Cisenza E, Manfredi G, Nanni N, editors. Procedings of the international workshop on composite construction, Capri, Italy, July 20-21: 203-10

Maymon G. 1993. Probability of failure of structures without a closed-form failure function. Computer Structures 49(2): 301-13.

McGee R. 1999. Modeling of durability performance of tasmanian bridges. In: Melchers R E and Stewart M G editors. ICASP8 applications of statistics and probability in civil engineering, 1: 297-306

Melchers R E. 1999. Structural reliability analysis and prediction. John Wiley & Sons Ltd. New York, United States: 437p.

Middleton C R and Hogg V. 1998, Review of Deterioration Models Used to Predict Corrosion in Reinforced Concrete Structures, CUED/D - STRUCT/TR.173, Cambridge University.

Mirza S A and MacGregor J G. 1976. A Statistical Study of Variables Affecting the Strength of Reinforced Normal Weight Concrete Members. Structural Engineering Report No. 58; Department of Civil Engineering, Alberta University, Edmonton, Alberta, Canada: 133p.

Marouani M S. 2007. Approche expérimental du vieillissement des matériaux composites à matrice polymère utilises dans la réparation et/ou le renforcement des ouvrage d'art. Ph.D thesis, Claude Bernard-Lyon1 University, 265p.

Model Code 1990, CEB-FIP. London: Thomas Telford Services Ltd. 460p.

Monti G and Liotta M A. 2007. Test and design equation for FRP strengthening in shear. Construction and Building Materials 21: 799-809.

Neubauer U. and Rostasy F S. 1997. Design aspects of concrete structures strengthened with externally bonded CFRP plates. Proceedings of the International Conference on Structural

References

Faults and Repairs, Edinburgh, ECS Publications, 109-118.

NF EN 13306. 2001. Maintenance Terminology standard. European Standard. 57p.

Norris T, Saadatmanesh H and Ehsani MR. 1997. Shear and flexural strengthening of R/C beams with carbon fiber sheets. Journal of Structural Engineering, ASCE:123(7):903–11.

Nowak A S. 1993. Live load model for high way bridges. Structural Safety 13: 53-66.

Nowak A S. 2004. System reliability models for bridge structures. BULLETIN OF THE POLISH ACADEMY OF SCIENCE, TECHNICAL SCIENCE, 52(4): 321-328.

Obidat Y T, Heyden S and Dahlbilom O. 2010. The effect of CFRP and CFRP/concrete interface models when modeling retrofitted RC beams with FEM. Composite Structures 92: 1391-1398.

Oehlersa D J, Park S M, and Ali M S M. 2003. A structural engineering approach to adhesive bonding longitudinal plates to RC beams and slabs. Composites: Part A 34: 887–97.

Palsson R and Mizra M S. 2002. Mechanical response of corroded steel reinforcement of abandoned concrete bridges. ACI structural journal, 99(2): 157-62.

Park SY, Naaman AE, Lopez MM and Till RD. 2001. Shear strengthening effect of R/C beams using glued CFRP sheets. Proceedings of the International Conference on FRP Composites in Civil Engineering, Hong Kong, China, vol. 1: 669–76.

Pellegrino C and Modena C. 2002. Fiber reinforced polymer shear strengthening of reinforced concrete beams with transverse steel reinforcement. Composites Constructions, 6(2): 104-11.

Pham H and Al-Mahaidi R. 2004. Experimental investigation into flexural retrofitting of reinforced concrete beams using FRP composites. Composites Structures 66: 617-625.

Pham H P and Al-Mahidi R. 2008. Reliability analysis of bridge beams retrofitted with fibre reinforced polymers. *Composite Structures* 82: 177-84.

Plevris, N., Triantafillou, T., and Veneziano, D. 1995. Reliability of RC members strengthened with CFRP Laminates. Journal of Structural Engineering 121(7): 1037-44.

Pour-Ghaz M, Isgor O B, and Ghods P. 2009. The effect of temperature on the corrosion of steel in concrete. Part 2: Model verification and parametric. Corrosion science 51: 426-43.

Price A and Moulds R J. 1991. Repair and strengthening of structures using plate bonding. Construction and Building Materials 5(4): 189-192.

prEN 10080-1 1999. Steel for the reinforcement of concrete – Weldable steel – Part 1 – General requirement, CEN, Brussels, 1999.

Rochdi E. 2004. Contribution à l'analyse du comportement mécanique de dalles en béton arme renforcées par matériaux composites. Ph.D thesis, Lyon 1 University: 232p.

Sas G. 2008. FRP shear strengthening RC beams and walls. Ph.D thesis, Luleå University of Technology, Sweden: 202p

Schilde K and Seim W. 2007. Experimental and numerical investigation of bond between CFRP and concrete. Construction and Building Materials: 21: 709-26.

Sharma S K, Ali M S M, Goldar D and Sikdar P K. 2006. Plate-concrete interfacial bond strength of FRP and metallic plated concrete specimens. Composites: Part B 37: 54-63.

Sharma S K, Ali M S M, Goldar D and Sikdar P K. 2008. Investigation of critical diagonal crack debonding in plated RC beams. Composites: Part B 39: 570-84.

Shooman M L. 1968. Probabilistic Reliability: An Engineering Approach. McGraw-Hill Book Co, New York.

Skai K, Shimomura T and Sugiyama. 1999. Design of concrete structures in the 21st century. In: the proceeding of the international conference - controlling concrete degradation.

Smith S T and Teng J G. 2001. Interfacial stresses in plated beams. Journal of Engineering Structures 23: 857-71.

Smith S T and Teng J G. 2002[a]. FRP-strengthened RC beams. I: review of debonding strength models. Journal of Engineering Structures 24: 385-95

Smith S T and Teng J G. 2002[b]. FRP-strengthened RC beams II: assessment of debonding strength models. Journal of Engineering Structures 24: 397-417.

Smith S T and Teng J G. 2003. Shear debonding failure of FRP-plated RC beams. Advances in Structural Engineering 6(3): 183-199.

Soares R C, Moahmed A, Venturini W S and Lemaire M. 2002. Reliability analysis of non-linear reinforced concrete frames using the response surface method. Reliability Engineering and System Safety 75: 1-16.

Stewart M G and Al-Harthy A. 2008. Pitting corrosion and structural reliability of corrosion RC structures: Experimental data and Probabilistic analysis. Reliability Engineering and System Safety 93: 373-82.

Stewart M G and Mullard J A. 2007. Spatial time-dependent reliability analysis of corrosion damage and the timing of first repair of RC structures. Engineering Structures, 29: 1457-65.

Stewart M G and Rosowsky D V. 1998. Time-dependent reliability of deteriorating reinforced concrete bridge decks. Structural Safety 20: 91-109.

Stewart M G and Suo Q. 2009. Extent of spatially variable corrosion damage as an indicator of strength and time-dependent reliability of RC beams. Engineering Strucutres, 31: 189-207.

References

Suo Q and Stewart M G. 2009. Corrosion cracking prediction updating of deteriorating RC structures using inspection information. Reliability Engineering and System Safety, 94: 1340-48.

Taerwe L, Khalil H and Matthys S. 1997. Behavior of R/C beams strengthened in shear by external CFRP sheets. Proceedings of the III International Symposium Non Metallic (FRP) Reinforcement for Concrete Structures, Japan: 483-90.

Täiljsten B. 1994. Plate bonding: Strengthening of existing concrete structures with epoxy bonded plates of steel or fibre reinforced plastics. Doctoral thesis, Luleå University of Technology, Sweden.

Täiljsten B. 1997. Strengthening of beams by Plates bonding. Journal of materials in civil engineering 9(4): 206-212.

Tajlsten B. 2002. FRP Strengthening of Existing Concrete Structures – Design Guidelines. Lulea University Printing Office, Lulea, Sweden.

Täljsten, B. 2003. Strengthening concrete beams for shear with CFRP sheets. Construction and Building material, 17: 15-26.

Täiljsten B and Elfgren L. 2000. Strengthening concrete beams for shear using CFRP-materials: evaluation of different approach methods. Composite: Part B 31: 87-96.

Teng J G, and Chen J F. 2007. Debonding failures of RC beams strengthened with externally bonded FRP reinforcement: behavior and modeling. Proceeding of Asia-Pacific Conference on FRP in Structures (APFIS-2007): 33-42

Teng J G, Lu X Z, Ye L P and Jiang J J. 2004. Recent Research on Intermediate Crack Induced Debonding in FRP Strengthened Beams. Proceedings of the 4th International Conference on Advanced Composite Materials for Bridges and Structures, Calgary, Alberta: 1-12.

Teng J G and Yao J. 2007. Plate end debonding in FRP plated RC beams-II: strength model. Structural Engineering. Engineering Structures 29: 2472–2486

Timoshenko S P & Goodier J N. 1970, Theory of Elasticity, McGraw-Hill Book Co., New York, 400p.

Tounsi A and Benyoucef S. 2007. Interfacial in externally FRP-plated concrete beams. International Journal of Adhesion & Adhesives 27: 207-15.

Toutanji H, Zhao L and Zhang Y. 2006. Flexural behavior of reinforced concrete beams externally strengthened with CFRP sheets bonded with an inorganic matrix. Engineering Structures 28: 557-66.

Triantafillou T C. 1980. Shear strengthening of reinforced concrete beams using epoxy-

bonded FRP composites. ACI Structural Engineering 95(2): 107-15.

Triantafillou T C. 1998. Shear strengthening of reinforced concrete beams using epoxy-bonded FRP composites. ACI Structal Journal, 5(2): 107-115.

Triantafillou T C and Antonopoulos C P. 2000. Design of concrete flexural members strengthened in shear with FRP. Journal of Composites for Construction, 4(4): 198-205.

Tumialan G, Belarbi A and Nanni A. 1999. Reinforced concrete beams strengthened with CFRP composites: failure due to concrete cover delamination. Department of Civil Engineering, Center for Infrastructure Engineering Studies, Report No. CIES-99/01, University of Missouri-Rolla, USA.

Umezu K, Fujita M, Nakai H and Tamaki K. 1997. Shear behavior of RC beams with aramid fiber sheets. Proceedings of the III International Symposium Non Metallic (FRP) Reinforcement for Concrete Structures, Japan: 491-98.

Upadhyaya B R and Eryurek E. 1992. Application of neural network for sensory validation and plant monitoring. Nuclear Technology 97(2): 170-176.

Val D V, Stewart M G and Melchers R E. 1998. Effect of reinforcement corrosion on reliability of highway bridges. Journal of Engineering Structures 20(11): 1010-19.

Val D V, Stewart M G and Melchers R E. 2000. Life-Cycle Performance of RC Bridges Probabilistic Approach. Computer-Aided Civil Infrastructure Engineering 15: 14-25.

Val D V and Trapper P A. 2008. Probabilistic evaluation of initiation time of chloride-induced corrosion. Reliability Engineering and System Safety 93: 364-372.

Varastehpour E. 1996. Optimization du Reinforcement des ouvrage en beton arme par des materiaux composite. Ph.D thesis, Claude Bernard Lyon 1 University. 216p.

Vu K A T and Stewart M G. 2000. Structural reliability of concrete bridges including improved chloride-induced corrosion models. Structural safety 23: 313-33.

Wang J. 2006. Cohesive zone model of intermediate crack-induced debonding of FRP-plated concrete beam. International Journal of Solids and Structures 43: 6630-48.

Wang J. 2008. Nonlinear fracture mechanics of flexural-shear crack induced debonding of FRP strengthened concrete beams. International Journal of Solids and Structures 45:2916-36.

Wong S M, Hobbs R E and Onof C. 2005. An adaptive response surface method for reliability analysis of structures with multiple loading sequences. Structural Safety 27: 287-308.

Yao J, Teng J G, and Chen J F. 2005. Experimental study on FRP-to-concrete bonded joints. Composites: Part B 36: 99–113.

Ye L P, Lum X Z, and Chen J F. 2005. Design proposals for debonding strengths of FRP

strengthened RC beams in the Chinese Design Code. Proceedings of International Symposium on Bond Behavior of FRP in Structures, Hong Kong, China.

Yokozeki K, Motohashi K, Okada K and Tsutsumi, T. 1997, 'A rational model to predict the service life of RC structures in a marine environment', Fourth CANMET/ACI International Conference on Durability of Concrete, SP170-40: 778-799.

Yuan H, Teng J G, Seracino R, Wu Z S, and Yau J. 2004. Full-range behavior of FRP-to-concrete bonded joints. Engineering Structures 26: 553-65.

Yuan Y, Ji Y, Jiang J. 2009. Effect of corrosion layer of steel bar in concrete on time variant rate. Materials and Structures, 42:1443-1450. doi:10.1617/s11527-008-9464-9.

Żemajtis J. 1998. Modeling the Time to Corrosion Initiation for Concretes with Mineral Admixtures and/or Corrosion Inhibitors in Chloride-Laden Environments. Ph.D thesis, Virginia Polytechnic Institute and State University, Blacksburg, Virginia: 140p.

Ziraba Y N, Baluch M H, Basunbul I A, Sharif A M, Azad A K. and Al-Sulaimani G J. 1994. Guidelines towards the design of reinforced concrete beams with external plates. ACI Structural Journal 91(6): 639-46.

Zoghmar A. 1998. Fiabilité des poutres en béton armé renforcées en flexion avec des lamelles de matériaux composites. Ph.D thesis, Department of civil engineering, Sherbrook University, Québec: 113p.

APPENDICES

APPENDICES

Appendix A

Table A.1: Experimental database of FRP strengthened RC beam failed by concrete crushing and FRP rupture failure modes.

Source	beam	h_c mm	b_c mm	d_s mm	d_{sc} mm	f_c MPa	E_c MPa	t_{FRP} mm	b_{FRP} mm	E_{FRP} MPa	$f_{FRP,ur}$ MPa
Toutanji et al	3L-1	158	108	132	26	49	33110	0.495	102	110000	660
2006	4L-1	158	108	132	26	49	33110	0.66	102	110000	660
	4L-2	158	108	132	26	49	33110	0.66	102	110000	660
	5L-1	158	108	132	26	49	33110	0.825	102	110000	660
	5L-2	158	108	132	26	49	33110	0.825	102	110000	660
	6L-1	158	108	132	26	49	33110	0.99	102	110000	660
	6L-2	158	108	132	26	49	33110	0.99	102	110000	660
Esfahani et al	B6-16D-1L10	200	150	164	25	23.8	23075	0.176	100	237000	2845
2007	B7-16D-1L15	200	150	164	25	23.8	23075	0.176	150	237000	2845
	B8-16D-2L15	200	150	164	25	23.8	23075	0.352	150	237000	2845
	B10-20D-1L10	200	150	162	25	24.1	23220	0.176	100	237000	2845
	B11-20D-1L15	200	150	162	25	24.1	23220	0.176	150	237000	2845
	B12-20D-2L15	200	150	162	25	24.1	23220	0.352	150	237000	2845
Gomes 2007	LC3R	80	450	70	10	56.3	36800	0.11	140	230	3400
	LC4R	80	450	70	10	56.3	36800	0.11	140	230	3400
	LC1S	80	450	70	10	56.3	36800	1.2	16	160000	3100
	LC2S	80	450	70	10	56.3	36800	1.2	16	160000	3100
Bian 2001	B2	150	115	130	20	30.3	26036	0.11	115	230	3400
	B3	150	115	130	20	30.3	26036	0.22	115	230	3400
	B4	150	115	130	20	30.3	26036	0.33	115	230	3400
	B5	150	115	130	20	30.3	26036	0.44	115	230	3400
Aram et al 2008	B1	150	250	130	20	39.2	29614	1.2	50	305000	1300
Ceroni 2010	A2	180	100	150	50	26.9	24523	07	100	230	3540
	A5	180	100	150	50	26.9	24523	07	100	230	3540
	B5	180	100	150	50	26.9	24523	07	100	230	3540
	B7	180	100	150	50	26.9	24523	07	100	230	3540
Zoghmar 1998	FL2	300	150	261	25	38.9	29501	1	125	137900	1462
	FL3	300	150	261	25	38.9	29501	1.5	125	137900	1462
Hashemi et al 2009	AH1	250	150	215	35	77	41506	0.045	150	230	3850
	AH4	250	150	215	35	77	41506	0.18	150	230	3850
	BH1	250	150	215	35	77	41506	0.045	150	230	3850
	BH4	250	150	215	35	77	41506	0.18	150	230	3850
Grace et al 2002	C-1	254	152	216	38	55.2	35142	0.13	152	217949	2615
	H-50-2	254	152	216	38	55.2	35142	1	152	22414	390
Toutanji et al	IS1	300	200	255	25	47.3	32531	0.142	152	200	1200
2006	IS2	300	200	255	25	47.3	32531	0.213	152	200	1200
	IS3	300	200	255	25	47.3	32531	0.355	152	200	1200
	IN-3L-A	158	108	130	25	46.9	32393	0.495	102	110000	770
	IN-3L-B	158	108	130	25	46.9	32393	0.495	102	110000	770
	IN-4L	158	108	130	25	53.8	34694	0.66	102	110000	770
	C3	150	200	120	25	49.2	33178	0.4	150	127000	1524
	C4	150	200	120	25	49.2	33178	0.4	150	127000	1524
	C5	150	200	120	25	49.2	33178	1.2	150	127000	1524
	C6	150	200	120	25	49.2	33178	1.2	150	127000	1524
	C7	150	200	120	25	49.2	33178	1.8	150	36000	1116
	C8	150	200	120	25	49.2	33178	1.8	150	36000	1116
	A3.1	300	140	275	25	30	25907	0.8	80	152000	1064
	A3.2	300	140	275	25	30	25907	0.8	80	152000	1520
	A3.3	300	140	275	25	30	25907	0.8	80	152000	1824

Table A.1 (continued): Experimental database of FRP strengthened RC beam failed by concrete crushing & FRP rupture failure modes.

Source	beam	E_s MPa	f_{ys} MPa	A_s mm	f_{ysc} mm	A_{sc} MPa	span m	B mm	$P_{u,exp}$ KN
Toutanji et al 2006	3L-1	200	427	142	427	56	1526	500	52.9
	4L-1	200	427	142	427	56	1526	500	55.7
	4L-2	200	427	142	427	56	1526	500	55
	5L-1	200	427	142	427	56	1526	500	62.7
	5L-2	200	427	142	427	56	1526	500	61.8
	6L-1	200	427	142	427	56	1526	500	63.6
	6L-2	200	427	142	427	56	1526	500	62.7
Esfahani et al 2007	B6-16D-1L10	200	406	402	365	157	1400	600	84.93
	B7-16D-1L15	200	406	402	365	157	1400	600	94.92
	B8-16D-2L15	200	406	402	365	157	1400	600	105.91
	B10-20D-1L10	200	350	628	365	157	1400	600	106
	B11-20D-1L15	200	350	628	365	157	1400	600	108.91
	B12-20D-2L15	200	350	628	365	157	1400	600	113.41
Gomes 2007	LC3R	225000	636	84.82	330.3	21.21	1600	550	39.1
	LC4R	225000	636	84.82	330.3	21.21	1600	550	31.3
	LC1S	225000	636	84.82	330.3	21.21	1600	550	34.1
	LC2S	225000	636	84.82	330.3	21.21	1600	550	37.7
Bian 2001	B2	183600	534	235.6	534	157.1	1350	500	72
	B3	183600	534	235.6	534	157.1	1350	500	86
	B4	183600	534	235.6	534	157.1	1350	500	82
	B5	183600	534	235.6	534	157.1	1350	500	79
Aram et al 2008	B1	200	485	150.8	485	150.8	2400	667	60
Ceroni 2010	A2	200	452	157.1	537	100.5	2000	880	37.4
	A5	200	452	157.1	537	100.5	2000	880	44.7*
	B5	200	441	226.2	537	100.5	1800	780	51.9*
	B7	200	441	226.2	537	100.5	1800	780	54.1*
Zoghmar 1998	FL2	200	400	606.8	400	100.5	2000	687.5	271.9
	FL3	200	400	606.8	400	100.5	2000	687.5	284.56
Hashemi et al 2009	AH1	200	413	402.1	420.6	157.1	2700	750	89.96
	AH4	200	413	402.1	420.6	157.1	2700	750	117.33
	BH1	200	413	760.3	420.6	157.1	2700	750	150
	BH4	200	413	760.3	420.6	157.1	2700	750	167
Grace et al 2002	C-1	200	415	402.1	415	147.7	2440	839	101.9
	H-50-2	200	415	402.1	415	147.7	2440	839	114.8
Toutanji et al 2006	IS1	200	447	258	447	0	3000	1000	80.4
	IS2	200	447	258	447	0	3000	1000	92
	IS3	200	447	258	447	0	3000	1000	110
	IN-3L-A	200	414	258	414	56	1524	560	73.21
	IN-3L-B	200	414	258	414	56	1524	560	75.71
	IN-4L	200	414	400	414	56	1524	560	95.35
	C3	210000	420	402	420	101	2100	750	74.93
	C4	210000	420	402	420	101	2100	750	77.33
	C5	210000	420	402	420	101	2100	750	103.2
	C6	210000	420	402	420	101	2100	750	101.33
	C7	210000	420	402	420	101	2100	750	87.2
	C8	210000	420	402	420	101	2100	750	86.67
	A3.1	200	435	400	435	400	4800	1800	74.78
	A3.2	200	435	400	435	400	4800	1800	98.89
	A3.3	200	435	400	435	400	4800	1800	98.22

*Anchorage end laminates. h_c is the total depth of the concrete section. b_c is the width of the concrete section. d_s is the depth of the tensile steel reinforcement. d_{sc} is the distance from the centre of top reinforcement to the top of the beam. f_c is the compressive strength of concrete. E_c is the modulus of concrete. b_{FRP} is the width of the FRP laminates. t_{FRP} is the thickness of the FRP laminate. E_{FRP} is the modulus of FRP composite. $f_{FRP,ur}$ is the strength of the FRP composite. E_s is the elastic modulus of steel. f_{ys} and f_{ysc} is the yield strength of tensile and compression reinforcement. A_s and A_{sc} is the area of tensile and compression reinforcement. B is the shear span. $P_{u,exp}$ is the ultimate load. (See Figure A.1).

Figure A.1: Geometrical and loading configuration of FRP strengthened RC beam.

Appendix A

Table A.2: Experimental database of FRP strip bonded to concrete prism.

Source	prism	b_c mm	h_c mm	f_c MPa	E_c MPa	f_{ct} MPa	t_{FRP} mm	b_{FRP} mm	L_{FRP} mm	E_{FRP} GPa	$f_{FRP,ur}$ MPa	$P_{u,exp}$ N
Chen & Teng	BN1	150	150	42.5	33500	3.5	1	25.4	180	29.2	472	11410
2001	BN2	150	150	42.5	33500	3.5	2	25.4	320	29.2	472	21400
	BN3	150	150	42.5	33500	3.5	0.33	25.4	160	75.7	1014	8500
	BN4	150	150	42.5	33500	3.5	0.66	25.4	320	75.7	1014	15100
	C1	228.6	152	36.1	28419	3.184	1.016	25.4	76.2	108	1655	8462
	C2	228.6	152	47.1	32462	3.637	1.016	25.4	76.2	108	1655	9931
	C3	228.6	152	47.1	32462	3.637	1.016	25.4	76.2	108	1655	10638
	C4	228.6	152	47.1	32462	3.637	1.016	25.4	76.2	108	1655	10638
	C5	228.6	152	43.6	31232	3.5	1.016	25.4	76.2	108	1655	10531
	C6	228.6	152	43.6	31232	3.5	1.016	25.4	76.2	108	1655	8956
	C7	228.6	152	43.6	31232	3.5	1.016	25.4	76.2	108	1655	9610
	C8	228.6	152	43.6	31232	3.5	1.016	25.4	76.2	108	1655	10518
	C9	228.6	152	43.6	31232	3.5	1.016	25.4	76.2	108	1655	11199
	C10	228.6	152	24	23172	2.596	1.016	25.4	76.2	108	1655	9869
	C11	228.6	152	28.9	25428	2.849	1.016	25.4	76.2	108	1655	9343
	C12	228.6	152	43.7	31268	3.504	1.016	25.4	76.2	108	1655	11204
	C13	228.6	152	36.4	28537	3.198	1.016	25.4	50.8	108	1655	8094
	C14	228.6	152	36.4	28537	3.198	1.016	25.4	101.6	108	1655	12811
	C15	228.6	152	36.4	28537	3.198	1.016	25.4	152.4	108	1655	11917
	C16	228.6	152	36.4	28537	3.198	1.016	25.4	203.2	108	1655	11570
	M1	100	100	40.8	30213	3.385	0.11	50	75	230	3500	5800
	M2	100	100	40.8	30213	3.385	0.11	50	150	230	3500	9200
	M3	100	100	43.3	31125	3.488	0.11	50	300	230	3500	11950
	M4	100	100	42.4	30800	3.451	05	50	75	280	3000	10000
	M5	100	100	42.4	30800	3.451	05	50	150	280	3000	7300
	M6	100	100	42.7	30908	33	0.22	50	65	230	3500	9550
	M7	100	100	42.7	30908	33	0.22	50	150	230	3500	16250
	M8	100	100	44.7	31624	3.543	0.11	50	700	230	3500	10000
	C100 50 A	200	200	45.2	35000	3.9	1	50	100	170	2497	17300
	C200 50 A	200	200	45.2	35000	4.1	1	50	200	170	2497	27500
	C300 50 A	200	200	45.2	35000	4.3	1	50	300	170	2497	35100
	C400 50 A	200	200	45.2	35000	4.3	1	50	400	170	2497	26900
	S100 40 A	200	200	45.2	35000	4.2	2.9	40	100	205	399	21100
	S200 40 A	200	200	45.2	35000	3.9	2.9	40	200	205	399	39500
	S400 40 A	200	200	45.2	35000	4.3	2.9	40	400	205	399	41100
	S50 60 A	200	200	45.2	35000	4.2	2.9	60	50	205	403	12700
	S100 60 A	200	200	45.2	35000	4.1	2.9	60	100	205	399	20000
	S150 60 A	200	200	45.2	35000	4.3	2.9	60	150	205	403	46300
	S200 60 B	200	200	45.2	35000	4.1	2.9	60	200	205	399	48800
	S400 60 A	200	200	45.2	35000	4.3	2.9	60	400	205	403	58400
	S400 60 B	200	200	45.2	35000	4.1	2.9	60	400	205	399	53000
	S100 80 C	200	200	45.2	35000	4.4	2.9	80	100	205	403	39600
	S150 80 A	200	200	45.2	35000	3.9	2.9	80	150	205	403	50900
	S200 80 A	200	200	45.2	35000	4.3	2.9	80	200	205	403	67300
	S300 80 C	200	200	45.2	35000	4.1	2.9	80	300	205	403	68000
	S500 80 C	200	200	45.2	35000	4.4	2.9	80	500	205	399	67300
	S600 80 B	200	200	45.2	35000	4.1	2.9	80	600	205	403	71400
	S800 80 A	200	200	45.2	35000	4.1	2.9	80	800	205	403	61600
	S1	60	60	19.8	21047	2.358	3	60	150	200	365	19530
	S2	60	60	35.5	28182	3.158	3	60	150	200	365	22680
	S3	60	60	47.6	32634	3.657	3	60	150	200	365	24930
	S4	60	60	56.3	35491	3.977	3	60	150	200	365	29970
	S5	60	60	35.6	28222	32	3	60	150	200	365	21780
	S6	60	60	35.6	28222	32	3	60	150	200	365	21420
	S7	60	60	35.6	28222	32	3	60	150	200	365	25470
Yao *et al* 2005	I-1	150	150	23	22684	2.542	05	25	75	256	4114	4750
	I-2	150	150	23	22684	2.542	05	25	85	256	4114	5690
	I-3	150	150	23	22684	2.542	05	25	95	256	4114	5760
	I-4	150	150	23	22684	2.542	05	25	95	256	4114	5760
	I-5	150	150	23	22684	2.542	05	25	95	256	4114	6170
	I-6	150	150	23	22684	2.542	05	25	115	256	4114	5960
	I-7	150	150	23	22684	2.542	05	25	145	256	4114	5950
	I-8	150	150	23	22684	2.542	05	25	190	256	4114	6680
	I-9	150	150	23	22684	2.542	05	25	190	256	4114	6350
	I-10	150	150	23	22684	2.542	05	25	95	256	4114	6170
	I-11	150	150	23	22684	2.542	05	25	75	256	4114	5720
	I-12	150	150	23	22684	2.542	05	25	85	256	4114	6000
	I-13	150	150	23	22684	2.542	05	25	95	256	4114	6140
	I-14	150	150	23	22684	2.542	05	25	115	256	4114	6190
	I-15	150	150	23	22684	2.542	05	25	145	256	4114	6270
	I-16	150	150	23	22684	2.542	05	25	190	256	4114	7030

	II-1	150	150	22.9	22635	26	05	25	95	256	4114	5200
	II-2	150	150	22.9	22635	26	05	25	95	256	4114	6750
	II-3	150	150	22.9	22635	26	05	25	95	256	4114	5510
	II-4	150	150	22.9	22635	26	05	25	190	256	4114	7020
	II-5	150	150	22.9	22635	26	05	25	190	256	4114	7070
	II-6	150	150	22.9	22635	26	05	25	190	256	4114	6980
	III-1	150	150	27.1	24623	2.759	05	25	100	256	4114	5940
	III-2	150	150	27.1	24623	2.759	05	50	100	256	4114	11660
	III-3	150	150	27.1	24623	2.759	05	75	100	256	4114	14630
	III-4	150	150	27.1	24623	2.759	05	100	100	256	4114	19070
	III-5	100	150	27.1	24623	2.759	05	85	100	256	4114	15080
	III-6	100	150	27.1	24623	2.759	05	100	100	256	4114	15750
	III-7	100	150	27.1	24623	2.759	1.27	25.3	100	22.5	351	4780
	III-8	100	150	27.1	24623	2.759	1.27	50.6	100	22.5	351	8020
	IV-1	150	150	18.9	20563	2.304	05	25	95	256	4114	5860
	IV-2	150	150	18.9	20563	2.304	05	25	95	256	4114	5900
	IV-3	150	150	19.8	21047	2.358	05	25	95	256	4114	5430
	IV-4	150	150	19.8	21047	2.358	05	25	95	256	4114	5760
	IV-5	150	150	18.9	20563	2.304	05	25	95	256	4114	5000
	IV-6	150	150	19.8	21047	2.358	05	25	95	256	4114	7080
	IV-7	150	150	18.9	20563	2.304	05	25	95	256	4114	5500
	IV-8	150	150	19.8	21047	2.358	05	25	95	256	4114	5930
	IV-9	150	150	18.9	20563	2.304	05	25	95	256	4114	5380
	IV-10	150	150	19.8	21047	2.358	05	25	95	256	4114	6600
	IV-11	150	150	18.9	20563	2.304	05	25	95	256	4114	5510
	IV-12	150	150	19.8	21047	2.358	05	25	95	256	4114	5670
	IV-13	150	150	18.9	20563	2.304	05	25	95	256	4114	6310
	IV-14	150	150	19.8	21047	2.358	05	25	95	256	4114	6190
	V-1	150	150	21.1	21727	2.435	05	15	95	256	4114	3810
	V-2	150	150	21.1	21727	2.435	05	15	95	256	4114	4410
	V-3	150	150	21.1	21727	2.435	05	25	95	256	4114	6260
	V-4	150	150	21.1	21727	2.435	05	50	95	256	4114	12220
	V-5	150	150	21.1	21727	2.435	05	75	95	256	4114	14290
	V-6	150	150	21.1	21727	2.435	05	100	95	256	4114	15580
	V-7	100	150	21.1	21727	2.435	05	80	95	256	4114	14270
	V-8	100	150	21.1	21727	2.435	05	80	95	256	4114	13780
	V-9	100	150	21.1	21727	2.435	05	90	95	256	4114	13560
	V-10	100	150	21.1	21727	2.435	05	90	95	256	4114	15660
	V-11	100	150	21.1	21727	2.435	05	100	95	256	4114	15570
	V-12	100	150	21.1	21727	2.435	05	100	95	256	4114	17430
	V-1	150	150	21.1	21727	2.435	05	15	95	256	4114	3810
	V-2	150	150	21.1	21727	2.435	05	15	95	256	4114	4410
	VI-1	150	150	21.9	22135	2.48	05	25	95	256	4114	6010
	VI-2	150	150	21.9	22135	2.48	05	25	95	256	4114	5850
	VI-3	150	150	21.9	22135	2.48	05	25	145	256	4114	5760
	VI-4	150	150	21.9	22135	2.48	05	25	145	256	4114	5730
	VI-5	150	150	21.9	22135	2.48	05	25	190	256	4114	5560
	VI-6	150	150	21.9	22135	2.48	05	25	190	256	4114	5580
	VI-7	150	150	21.9	22135	2.48	05	25	240	256	4114	5910
	VI-8	150	150	21.9	22135	2.48	05	25	240	256	4114	5050
	VII-1	150	150	24.9	23603	2.645	05	25	95	256	4114	6800
	VII-2	150	150	24.9	23603	2.645	05	25	95	256	4114	6620
	VII-3	150	150	24.9	23603	2.645	05	25	145	256	4114	7330
	VII-4	150	150	24.9	23603	2.645	05	25	145	256	4114	6490
	VII-5	150	150	24.9	23603	2.645	05	25	190	256	4114	7070
	VII-6	150	150	24.9	23603	2.645	05	25	190	256	4114	7440
	VII-7	150	150	24.9	23603	2.645	05	25	240	256	4114	7160
	VII-8	150	150	24.9	23603	2.645	05	25	240	256	4114	6240
Lu *et al* 2005	PG1-11	100	100	29.3	25615	2.9	09	50	130	97	2777	7780
	PG1-12	100	100	29.3	25615	2.9	09	50	130	97	2777	9190
	PG1-1W1	100	100	29.3	25615	2.9	09	75	130	97	2777	10110
	PG1-1W2	100	100	29.3	25615	2.9	09	75	130	97	2777	13950
	PG1-1L11	100	100	29.3	25615	2.9	09	50	100	97	2777	6870
	PG1-1L12	100	100	29.3	25615	2.9	09	50	100	97	2777	9200
	PG1-1L21	100	100	29.3	25615	2.9	09	50	70	97	2777	6460
	PG1-1L22	100	100	29.3	25615	2.9	09	50	70	97	2777	6660
	PG1-21	100	100	29.3	25615	2.9	0.338	50	130	97	2777	10490
	PG1-22	100	100	29.3	25615	2.9	0.338	50	130	97	2777	11430
	PC1-1C1	100	100	29.3	25615	2.9	0.111	50	130	235	3500	7970
	PC1-1C2	100	100	29.3	25615	2.9	0.111	50	130	235	3500	9190
	NJ2	150	150	16	18914	2	03	100	100	240	3550	11000
	NJ3	150	150	16	18914	2	03	100	150	240	3550	11250

Appendix A

NJ4	150	150	28.6	25307	2.87	03	100	100	240	3550	12500
NJ5	150	150	28.6	25307	2.87	03	100	150	240	3550	12250
NJ6	150	150	28.6	25307	2.87	03	100	150	240	3550	12750
1-11	100	100	28.5	25259	2.86	07	40	100	230	3481	8750
1-12	100	100	26.3	24269	2.74	07	40	100	230	3481	8850
1-21	100	100	28.5	25259	2.86	07	40	200	230	3481	9300
1-22	100	100	26.3	24269	2.74	07	40	200	230	3481	8500
1-31	100	100	28.5	25259	2.86	07	40	300	230	3481	9300
1-32	100	100	26.3	24269	2.74	07	40	300	230	3481	8300
1-41	100	100	28.5	25259	2.86	07	40	500	230	3481	8050
1-42	100	100	28.5	25259	2.86	07	40	500	230	3481	8050
1-51	100	100	26.1	24179	2.73	07	40	500	230	3481	8450
1-52	100	100	26.1	24179	2.73	07	40	500	230	3481	7300
2-11	100	100	24.7	23494	2.64	07	40	100	230	3481	8750
2-12	100	100	24.7	23494	2.64	07	40	100	230	3481	8850
2-13	100	100	25.8	24045	2.71	07	40	100	230	3481	7750
2-14	100	100	25.8	24045	2.71	07	40	100	230	3481	7650
2-15	100	100	24.1	23214	2.61	07	40	100	230	3481	9000
2-21	100	100	24.7	23494	2.64	0.334	40	100	230	3481	12000
2-22	100	100	24.7	23494	2.64	0.334	40	100	230	3481	10800
2-31	100	100	24.7	23494	2.64	0.501	40	100	230	3481	12650
2-32	100	100	24.7	23494	2.64	0.501	40	100	230	3481	14350
2-41	100	100	24.1	23214	2.61	05	40	100	373	2942	11550
2-42	100	100	24.1	23214	2.61	05	40	100	373	2942	11000
2-51	100	100	25.8	24045	2.71	07	40	100	230	3481	9850
2-52	100	100	25.8	24045	2.71	07	40	100	230	3481	9500
2-61	100	100	25.8	24045	2.71	07	40	100	230	3481	8800
2-62	100	100	25.8	24045	2.71	07	40	100	230	3481	9250
2-71	100	100	25.8	24045	2.71	07	40	100	230	3481	7650
2-72	100	100	25.8	24045	2.71	07	40	100	230	3481	6800
2-81	100	100	49.3	33223	3.87	07	40	100	230	3481	7750
2-82	100	100	49.3	33223	3.87	07	40	100	230	3481	8050
2-91	100	100	24.1	23214	2.61	07	40	100	230	3481	6750
2-92	100	100	24.1	23214	2.61	07	40	100	230	3481	6800
2-101	100	100	24.7	23494	2.64	0.111	40	100	230	3481	7700
2-102	100	100	25.8	24045	2.71	0.111	40	100	230	3481	6950
DLUT15-2G	150	150	22.4	22379	2.5	0.507	20	150	83	3271	5810
DLUT15-5G	150	150	22.4	22379	2.5	0.507	50	150	83	3271	10600
DLUT15-7G	150	150	22.4	22379	2.5	0.507	80	150	83	3271	18230
DLUT30-1G	150	150	35.3	28116	3.22	0.507	20	100	83	3271	4630
DLUT30-2G	150	150	35.3	28116	3.22	0.507	20	150	83	3271	5770
DLUT30-3G	150	150	35.3	28116	3.22	0.507	50	60	83	3271	9420
DLUT30-4G	150	150	35.3	28116	3.22	0.507	50	100	83	3271	11030
DLUT30-6G	150	150	35.3	28116	3.22	0.507	50	150	83	3271	11800
DLUT30-7G	150	150	35.3	28116	3.22	0.507	80	100	83	3271	14650
DLUT30-8G	150	150	35.3	28116	3.22	0.507	80	150	83	3271	16440
DLUT50-1G	150	150	43.3	31121	3.6	0.507	20	100	83	3271	5990
DLUT50-2G	150	150	43.3	31121	3.6	0.507	20	150	83	3271	5900
DLUT50-4G	150	150	43.3	31121	3.6	0.507	50	100	83	3271	9840
DLUT50-5G	150	150	43.3	31121	3.6	0.507	50	150	83	3271	12280
DLUT50-6G	150	150	43.3	31121	3.6	0.507	80	100	83	3271	14020
DLUT50-7G	150	150	43.3	31121	3.6	0.507	80	150	83	3271	16710
DLUT15-2C	150	150	22.4	22379	2.5	0.33	20	150	207	3890	5480
DLUT15-5C	150	150	22.4	22379	2.5	0.33	50	150	207	3890	10020
DLUT15-7C	150	150	22.4	22379	2.5	0.33	80	150	207	3890	19270
DLUT30-1C	150	150	35.3	28116	3.22	0.33	20	100	207	3890	5540
DLUT30-2C	150	150	35.3	28116	3.22	0.33	20	150	207	3890	4610
DLUT30-4C	150	150	35.3	28116	3.22	0.33	50	100	207	3890	11080
DLUT30-5C	150	150	35.3	28116	3.22	0.33	50	100	207	3890	16100
DLUT30-6C	150	150	35.3	28116	3.22	0.33	50	150	207	3890	21710
DLUT30-7C	150	150	35.3	28116	3.22	0.33	80	100	207	3890	22640
DLUT50-1C	150	150	43.3	31121	3.6	0.33	20	100	207	3890	5780
DLUT50-4C	150	150	43.3	31121	3.6	0.33	50	100	207	3890	12950
DLUT50-5C	150	150	43.3	31121	3.6	0.33	50	150	207	3890	16720
DLUT50-6C	150	150	43.3	31121	3.6	0.33	80	100	207	3890	16240
DLUT50-7C	150	150	43.3	31121	3.6	0.33	80	150	207	3890	22800
Ueda_A1	100	100	23.2	22781	2.55	0.11	50	75	230	3479	6250
Ueda_A2	100	100	40.8	30213	3.48	0.11	50	150	230	3479	9200
Ueda_A3	100	100	40.8	30213	3.48	0.11	50	300	230	3479	11950
Ueda_A4	100	100	43.3	31124	3.6	0.22	50	75	230	3479	10000
Ueda_A5	100	100	42.4	30800	3.56	0.11	50	150	230	3479	7300
Ueda_A6	100	100	42.4	30800	3.56	05	50	65	372	2940	9550

Specimen	h_c	b_c	f_c	E_c	f_{ct}	t_{FRP}	b_{FRP}	L_{FRP}	E_{FRP}	$f_{FRP,ur}$	$P_{u,exp}$
Ueda_A7	100	100	42.7	30910	3.57	0.22	50	150	230	3479	16250
Ueda_A8	100	100	42.7	30910	3.57	0.11	50	700	230	3479	11000
Ueda_A9	100	100	39.8	29842	3.43	0.11	50	150	230	3479	10000
Ueda_A10	100	100	23.8	23074	2.59	0.11	10	150	230	3479	2400
Ueda_A11	100	100	23.8	23074	2.59	0.11	20	150	230	3479	5350
Ueda_A12	100	100	23.8	23074	2.59	0.33	20	150	230	3479	9250
Ueda_A13	100	100	24.7	23509	2.64	0.55	20	150	230	3479	11750
Ueda_B1	500	500	24.7	23509	2.64	0.11	100	200	230	3479	20600
Ueda_B2	500	500	40.9	30251	3.49	0.33	100	200	230	3479	38000
Ueda_B3	500	500	45.9	32047	3.71	0.33	100	200	230	3479	34100
D-CFS-150-30a	100	100	45.9	32047	3.71	03	100	300	230	4200	12200
D-CFS-150-30b	100	100	57.6	35899	4.21	03	100	300	230	4200	11800
D-CFS-150-30c	100	100	57.6	35899	4.21	03	100	300	230	4200	12250
D-CFS-300-30a	100	100	57.6	35899	4.21	07	100	300	230	4200	18900
D-CFS-300-30b	100	100	57.6	35899	4.21	07	100	300	230	4200	16950
D-CFS-300-30c	100	100	57.6	35899	4.21	07	100	300	230	4200	16650
D-CFS-600-30a	100	100	57.6	35899	4.21	0.333	100	300	230	4200	25650
D-CFS-600-30b	100	100	57.6	35899	4.21	0.333	100	300	230	4200	25350
D-CFS-600-30c	100	100	57.6	35899	4.21	0.333	100	300	230	4200	27250
D-CFM-300-30a	100	100	57.6	35899	4.21	07	100	300	390	4400	19500
D-CFM-300-30b	100	100	57.6	35899	4.21	07	100	300	390	4400	19500
D-AR-280-30a	100	100	57.6	35899	4.21	1	100	300	23.9	4400	12750
D-AR-280-30b	100	100	57.6	35899	4.21	1	100	300	23.9	4400	12850
D-AR-280-30c	100	100	57.6	35899	4.21	1	100	300	23.9	4400	11900
S-CFS-400-25a	100	100	57.6	35899	4.21	0.222	40	250	230	4200	15400
S-CFS-400-25b	100	100	57.6	35899	4.21	0.222	40	250	230	4200	13900
S-CFS-400-25c	100	100	57.6	35899	4.21	0.222	40	250	230	4200	13000
S-CFM-300-25a	100	100	57.6	35899	4.21	07	40	250	390	4400	12000
S-CFM-300-25b	100	100	57.6	35899	4.21	07	40	250	390	4400	11900
S-CFM-900-25a	100	100	57.6	35899	4.21	0.5	40	250	390	4400	25900
S-CFM-900-25b	100	100	57.6	35899	4.21	0.5	40	250	390	4400	23400
S-CFM-900-25c	100	100	57.6	35899	4.21	0.5	40	250	390	4400	23700

h_c is the total depth of the concrete prism. b_c is the width of the concrete prism. f_c is the compressive strength of concrete. E_c is the modulus of concrete. f_{ct} is the tensile strength of the concrete. b_{FRP} is the width of the FRP laminates. t_{FRP} is the thickness of the FRP laminate. E_{FRP} is the modulus of FRP composite. $f_{FRP,ur}$ is the strength of the FRP composite. L_{FRP} is the length of the bonded laminate. $P_{u,exp}$ is the ultimate load. (See Figure A.2).
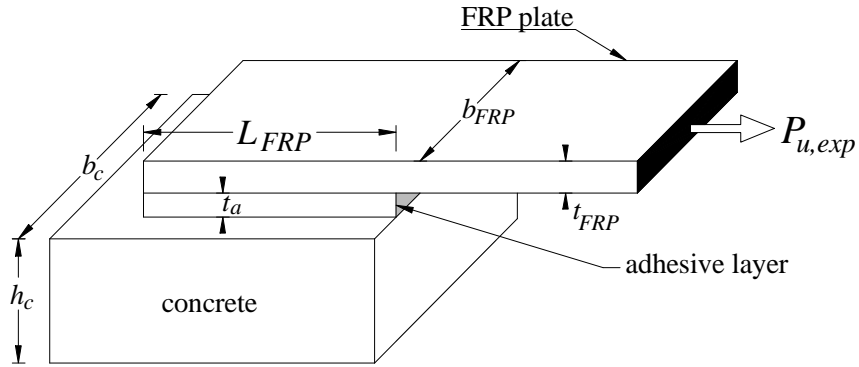
Figure A.2: Geometrical and loading configuration of FRP concrete bonded joint.

Table A.3: Experimental database of FRP strengthened RC beam failed by FRP intermediate crack debonding failure mode.

Source	beam	h_c mm	b_c mm	d_s mm	d_{sc} mm	f_c MPa	E_c MPa	f_{ct} MPa	n_{FRP}	$t_{FRP/l}$ mm	b_{FRP} mm	E_{FRP} MPa	$f_{FRP,ur}$ MPa
Aram &	2	150	250	130	20	39.2	29614	3	1	1.200	50	305	1300
Czaderski	3	150	250	130	20	39.2	29614	3	1	1.200	50	214	2000
2008	4	150	250	130	20	41.6	30507	3.42	1	1.200	50	155	2700
Esfahani *et al*	B11	200	150	162	25	24.1	23220	2.60	1	0.176	150	237	2845
2007	B12	200	150	162	25	24.1	23220	2.60	2	0.176	150	237	2845
	VIIR	400	200	380	20	39.9	32500	3.35	1	1.2	80	160	3000
Bogas &	1/D	200	300	180	20	35.2	28062	3.14	2	1.4	50	150	1740
Gomes	1/C	200	300	180	20	35.2	28062	3.14	1	1.4	100	150	1740
2007	1/C	200	300	180	20	35.2	28062	3.14	1	1.4	100	150	1740
	1/B	200	300	180	20	35.2	28062	3.14	1	1.4	100	150	1740
	1/A	200	300	180	20	35.2	28062	3.14	1	1.4	100	150	1740
	2/D	200	300	180	20	35.2	28062	3.14	1	1.4	100	150	1740
	2/C	200	300	180	20	35.2	28062	3.14	2	1.4	50	150	1740
	2/B	200	300	180	20	35.2	28062	3.14	2	1.4	50	150	1740
	2/A	200	300	180	20	35.2	28062	3.14	1	1.4	100	150	1740
	V2	180	120	160	20	36.7	28500	3.21	2	0.111	70	240	3700
	V4	180	120	160	20	36.7	28500	3.21	1	1.4	20	200	2200
Al Mahdi 2004	S1	260	140	240	46	47.7	32667	3.66	2	0.13	100	214	3900
	S2	260	140	240	46	47.7	32667	3.66	2	0.13	100	214	3900
	S3	260	140	240	46	47.7	32667	3.66	2	0.13	100	214	3900
Teng *et al* 2003	E4	455	205	400	55	35	28000	3.14	1	6	152	37	400
	A1	300	150	250	0	51.7	34000	3.81	1	05	150	230	3400
	A2	300	150	250	0	51.7	34000	3.81	2	05	150	230	3400
	A7	300	150	250	0	51.7	34000	3.81	2	05	75	230	3400
	C1	300	150	250	0	51.7	34000	3.81	1	05	150	230	3400
	B2	400	270	341	54	22.6	22500	2.52	2	05	250	230	3400
	4	127	76	111	0	44.7	31600	3.54	1	0.65	63.2	186	1450
	5	127	76	111	0	44.7	31600	3.54	1	0.65	63.2	186	1450
	6	127	76	111	0	44.7	31600	3.54	1	0.9	63.3	186	1450
	7	127	76	111	0	44.7	31600	3.54	1	0.9	63.3	186	1450
	8	127	76	111	0	44.7	31600	3.54	1	1.9	63	186	1450
	B3u	100	100	84	16	43.2	31100	3.48	1	0.82	67	111	1414
	B4u	100	100	84	16	43.2	31100	3.48	1	0.82	67	111	1414
	B5u	100	100	84	16	43.2	31100	3.48	1	0.82	67	111	1414
	B1u	230	145	205	25	37.6	29000	3	1	1.28	90	115	1284
	B3	150	200	120	30	49.2	25000	3.72	1	0.4	150	127	1532
	B4	150	200	120	30	49.2	25000	3.72	1	0.4	150	127	1532
	B5	150	200	120	30	49.2	25000	3.72	1	1.2	150	127	1532
	B6	150	200	120	30	49.2	25000	3.72	1	1.2	150	127	1532
	B7	150	200	120	30	49.2	25000	3.72	1	1.8	150	36	1074
	B8	150	200	120	30	49.2	25000	3.72	1	1.8	150	36	1074
Ceroni 2010	A2	180	100	150	50	26.88	24523	2.75	1	07	100	230	3450
Yao & Teng	CS-W50-B	255.3	150.6	222.8	30	31.6	26000	3.21	1	2.01	50	42	4114
2007	GS-B	252.2	151.1	217.7	30	31	28800	4.31	1	1.67	148	17	351
Maalej	A3	146	115	120	15	42.8	27000	3.41	1	05	107.8	235	3550
& Leong	A4	146	115	120	15	42.8	27000	3.41	1	05	107.8	235	3550
2005	A5	146	115	120	15	42.8	27000	3.41	2	0.33	107.8	235	3550
	A6	146	115	120	15	42.8	27000	3.41	2	0.33	107.8	235	3550
	B3	292	230	240	30	42.8	27000	3.41	2	0.33	215.6	235	3550
	B4	292	230	240	30	42.8	27000	3.41	2	0.33	215.6	235	3550
	B5	292	230	240	30	42.8	27000	3.41	4	0.66	215.6	235	3550
	B6	292	230	240	30	42.8	27000	3.41	4	0.66	215.6	235	3550
	C3	467.2	368	384	51	42.4	25000	3.24	3	0.495	368	235	3550
	C4	467.2	368	384	51	42.4	25000	3.24	3	0.495	368	235	3550
	C5	467.2	368	384	51	42.4	25000	3.24	6	0.99	368	235	3550
Zoghmar 1998	FL1	300	150	261	25	38.9	26800	3.31	1	0.5	125	138	1461.74
	F4L3	300	150	261	25	33.6	25600	3.07	3	1.5	125	138	1461.74
	F1L6/F2L6	300	150	261	25	33.6	25600	3.07	6	3	125	138	1461.75

Table A.3 (continued): Experimental database of FRP strengthened RC beam failed by FRP intermediate crack debonding failure mode.

Source	beam	E_s MPa	f_{ys} MPa	A_s mm	f_{ysc} mm	A_{sc} MPa	span m	B mm	$P_{u,exp}$ KN
Aram &	2	200000	485	151	485	151	2000	667	60
Czaderski	3	200000	485	151	485	151	2000	667	62.8
2008	4	200000	485	151	485	151	2000	667	58.4
Esfahani *et al*	B11	200000	350	628	365	157	1600	600	108.91
2007	B12	200000	350	628	365	157	1600	600	113.41
	VIIR	200000	475	603	475	101	4000	1500	165
Bogas &	1/D	200000	550	402	550	101	2000	1000	100.9
Gomes	1/C	200000	550	402	550	101	2000	1000	104
2007	1/C	200000	550	402	550	101	2000	1000	121
	1/B	200000	550	402	550	101	2000	1000	100.4
	1/A	200000	550	402	550	101	2000	1000	109
	2/D	200000	550	628	550	101	2000	1000	128
	2/C	200000	550	628	550	101	2000	1000	118.8
	2/B	200000	550	628	550	101	2000	1000	126
	2/A	200000	550	628	550	101	2000	1000	155
	V2	200000	533	101	555	57	1800	750	37.2
	V4	200000	533	101	555	57	1800	750	39.22
Al Mahdi 2004	S1	192000	504	339	504	226	2300	700	148
	S2	192000	504	339	504	226	2300	700	155
	S3	192000	504	226	504	226	2300	700	120.5
Teng *et al* 2003	E4	200000	0	0	456	253	4575	1983	65
	A1	207000	427	792	0	0	2130	1065	145.6
	A2	207000	427	792	0	0	2130	1065	169.8
	A7	207000	427	792	0	0	2130	1065	172.2
	C1	207000	427	792	0	0	2130	1065	154.4
	B2	201000	484	900	507	142	3650	1300	296
	4	200000	517	33	0	0	1220	458	29.6
	5	200000	517	33	0	0	1220	459	30.6
	6	200000	517	33	0	0	1220	460	28
	7	200000	517	33	0	0	1220	461	25.6
	8	200000	517	33	0	0	1220	462	37.4
	B3u	215000	350	85	350	57	900	340	34
	B4u	215000	350	85	350	57	900	400	34.5
	B5u	215000	350	85	350	57	900	400	34.6
	B1u	220000	556	226	556	101	4400	1525	60
	B3	210000	460	157	460	157	2100	750	55.2
	B4	210000	460	157	460	157	2100	751	52.6
	B5	210000	460	157	460	157	2100	752	69.8
	B6	210000	460	157	460	157	2100	753	69.6
	B7	210000	460	157	460	157	2100	754	59.2
	B8	210000	460	157	460	157	2100	755	61.6
Ceroni 2010	A2	200000	537	157	537	101	2000	880	37.4
Yao & Teng	CS-W50-B	199000	536	157	536	157	1500	500	71.3[a]
2007	GS-B	199000	536	157	537	157	1500	500	82[a]
Maalej	A3	180000	547	236	547	157	1500	500	77.5
& Leong	A4	180000	547	236	547	157	1500	500	75.5
2005	A5	180000	547	236	547	157	1500	500	87.4
	A6	180000	547	236	547	157	1500	500	85.8
	B3	183000	544	942	544	628	3000	1000	263.5
	B4	183000	544	942	544	628	3000	1000	260.3
	B5	183000	544	942	544	628	3000	1000	294.7
	B6	183000	544	942	544	628	3000	1000	284.3
	C3	181000	552	2413	552	1608	4800	1600	652.9
	C4	181000	552	2413	552	1608	4800	1600	669.3
	C5	181000	552	2413	552	1608	4800	1600	650.1
Zoghmar 1998	FL1	200000	400	607	400	101	2000	687.5	228.87
	F4L3	200000	400	607	400	101	2000	687.5	283.02
	F1L6/F2L6	200000	400	607	400	101	2000	687.5	300.85

h_c is the total depth of the concrete section. b_c is the width of the concrete section. d_s is the depth of the tensile steel reinforcement. d_{sc} is the distance from the centre of top reinforcement to the top of the beam. f_c is the compressive strength of concrete. E_c is the modulus of concrete. b_{FRP} is the width of the FRP laminates. n_{FRP} *is the number of FRP layer;* $t_{FRP/l}$ is the thickness of single layer; E_{FRP} is the modulus of FRP composite. $f_{FRP,ur}$ is the strength of the FRP composite. E_s is the elastic modulus of steel. f_{ys} and f_{ysc} is the yield strength of tensile and compression reinforcement. A_s and A_{sc} is the area of tensile and compression reinforcement. B is the shear span. $P_{u,exp}$ is the ultimate load (See Figure A.1). * denotes a three point loading test.

Table A.4: Experimental database of FRP strengthened RC beam failed by FRP end debonding based shear crack failure modes.

Source	beam	h_c mm	b_c mm	d_s mm	d_{sc} mm	f_c MPa	E_c MPa	f_{ct} MPa	t_{FRP} mm	b_{FRP} mm	E_{FRP} MPa	$f_{FRP,ur}$ MPa	E_a MPa	t_a mm
Ahmed *et al* 2001	AF.2	225	125	196	25	41	30287	34	0.334	75	240000	3500	7200	3
	AF.2-1	225	125	196	25	41	30287	34	0.334	75	240000	3500	7200	3
	AF3	225	125	193	32	46	32080	3.595	0.334	75	240000	3500	7200	3
	DF.4	225	125	193	32	46	32080	3.595	0.668	75	240000	3500	7200	3
Pham & El-Mahaidi 2004	E1	260	140	240	46	53.7	34662	3.884	0.78	100	213500	3900	3500	1
	E2	260	140	240	46	53.7	34662	3.884	0.78	100	213500	3900	3500	1
	E3	260	140	240	46	53.7	34662	3.884	0.78	100	213500	3900	3500	1
	E4	260	140	220	46	53.7	34662	3.884	0.78	100	213500	3900	3500	1
	E5	260	140	240	46	53.7	34662	3.884	1.17	100	213500	3900	3500	1
Ceroni 2010	A3	180	100	150	50	26.9	24523	2.748	0.334	100	230000	3450	na	na
	A8	180	100	150	50	26.9	24523	2.748	07	100	230000	3450	na	na
	B2	180	100	150	50	26.9	24523	2.748	07	100	230000	3450	na	na
	B3	180	100	150	50	26.9	24523	2.748	0.334	100	230000	3450	na	na
Ali *et al* 2005	SP-T6	370	200	330	20	35.3	34300	3.6	6	200	200000	365	na	na
	SP-T12	370	200	330	20	35.3	34300	3.6	12	200	200000	306	na	na

Table A.4 (continued): Experimental database of FRP strengthened RC beam failed by FRP end debonding based shear crack failure modes.

Source	beam	E_s MPa	f_{ys} MPa	ϕ_s mm	A_s mm^2	E_{sc} MPa	f_{ysc} MPa	A_{sc} mm^2	span mm	B mm	a mm	E_{sv} MPa	f_{ysv} MPa
Ahmed *et al* 2001	AF.2	185000	568	8	100.5	195000	553	56.55	1500	500	200	195000	553
	AF.2-1	185000	568	8	100.5	195000	553	56.55	1500	500	150	195000	553
	AF3	185000	568	8	100.5	195000	553	56.55	1500	500	100	195000	553
	DF.4	185000	568	8	150.8	195000	553	56.55	1500	500	50	195000	533
Pham & El-Mahaidi 2004	E1	192000	504	12	339.3	192000	504	226.2	2300	700	150	204000	334
	E2	192000	504	12	339.3	192000	504	226.2	2300	700	350	204000	334
	E3	192000	504	12	226.2	192000	504	226.2	2300	700	150	204000	334
	E4	192000	504	12	339.3	192000	504	226.2	2300	700	150	204000	334
	E5	192000	504	12	339.3	192000	504	226.2	2300	700	150	204000	334
Ceroni 2010	A3	200000	452	10	235.6	200000	537	100.5	2000	880	300	200000	452
	A8	200000	452	10	235.6	200000	537	100.5	2000	880	300	200000	452
	B2	200000	441	12	339.3	200000	537	100.5	1800	780	400	200000	452
	B3	200000	441	12	339.3	200000	537	100.5	1800	780	400	200000	452
Ali *et al* 2005	SP-T6	200000	433	20	1257	200000	474	157.1	4700	1250	50	200000	474
	SP-T12	200000	433	20	1257	200000	474	157.1	4550	1250	50	200000	474

Table A.4 (continued): Experimental database of FRP strengthened RC beam failed by FRP end debonding based shear crack failure modes.

Source	beam	A_{sv} mm^2	s_s mm	$V_{db,end,exp}= P_{u,exp}/2$ KN
Ahmed *et al* 2001	AF.2	56.55	71	41.5
	AF.2-1	56.55	71	42.85
	AF3	56.55	71	48
	DF.4	56.55	100	62.5
Pham & El-Mahaidi 2004	E1	157.1	125	72.625
	E2	157.1	125	44.3
	E3	157.1	125	65.55
	E4	157.1	125	70.1
	E5	157.1	125	63.2
Ceroni 2010	A3	100.5	150	20
	A8	100.5	150	13.9
	B2	100.5	150	24.6
	B3	100.5	150	33.4
Ali *et al* 2005	SP-T6	157.1	100	113
	SP-T12	157.1	100	113

h_c is the total depth of the concrete section. b_c is the width of the concrete section. d_s is the depth of the tensile steel reinforcement. d_{sc} is the distance from the centre of top reinforcement to the top of the beam. f_c is the compressive strength of concrete. E_c is the modulus of concrete. b_{FRP} and t_{FRP} are the width and thickness of the FRP laminates respectively; E_{FRP} and $f_{FRP,ur}$ are the modulus and strength of FRP composite respectively; E_a and t_a are the modulus and thickness of the adhesive layer respectively; E_s is the elastic modulus of steel. f_{ys} and f_{ysc} is the yield strength of tensile and compression reinforcement. A_s and A_{sc} is the area of tensile and compression reinforcement. B is the shear span. a is the distance from the plate end to the nearest support. $V_{db,end,exp}$ is the ultimate shearing force that cause end debonding. $P_{u,exp}$ is the ultimate load (See Figure A.1). na not available.

Table A.5: Experimental database of FRP strengthened RC beam failed by concrete cover separation failure modes.

Source	beam	h_c mm	b_c mm	d_s mm	d_{sc} mm	f_c MPa	E_c MPa	f_{ct} MPa	t_{FRP} mm	b_{FRP} mm	E_{FRP} MPa	$f_{FRP,ur}$ MPa
Maalej & Bian	3	150	115	125	25	30.3	26000	2.9	0.222	115	230000	3400
2001	4	150	115	125	25	30.3	26000	2.9	0.333	115	230000	3400
	5	150	115	125	25	30.3	26000	2.9	0.444	115	230000	3400
David *et al*	P2	300	150	257	0	40	29915	3.4	1.2	100	150000	2400
1999	P3	300	150	257	0	40	29915	3.4	1.2	100	150000	2400
	P4	300	150	257	0	40	29915	3.4	2.4	100	150000	2400
	P5	300	150	257	0	40	29915	3.4	2.4	100	150000	2400
Garden *et al*	1Au	100	100	84	16	47.3	39900	4.2	0.5	90	111000	1273
1997	1Bu	100	100	84	16	47.3	39900	4.2	0.7	65	111000	1273
	1B2u	100	100	84	16	47.3	39900	4.2	0.7	65	111000	1273
	1Cu	100	100	84	16	47.3	39900	4.2	1	45	111000	1273
	2Bu	100	100	84	16	47.3	39900	4.2	0.7	65	111000	1273
	2Cu	100	100	84	16	47.3	39900	4.2	1	45	111000	1273
Nguyen *et al*	A950	150	120	120	34	25.7	23970	2.7	1.2	80	181000	3140
2001	A1100	150	120	120	34	25.7	23970	2.7	1.2	80	181000	3140
	A1150	150	120	120	34	25.7	23970	2.7	1.2	80	181000	3140
	DF2	225	125	193	32	46	30000	3.6	0.334	75	240000	3500
2001	DF3	225	125	193	32	46	30000	3.6	0.501	75	240000	3500
	DF4	225	125	193	32	46	30000	3.6	0.668	75	240000	3500
Ahmed &	AF3	225	125	193	32	46	30000	3.6	0.334	75	240000	3500
Van-Gemert	CF2-1	225	125	193	32	46	30000	3.6	0.334	75	240000	3500
1999	CF3-1	225	125	193	32	46	30000	3.6	0.334	75	240000	3500
	CF4-1	225	125	193	32	46	30000	3.6	0.334	75	240000	3500
Beber *et al*	VR5	250	120	214	34	33.6	27418	3.1	0.44	120	230000	3400
1999	VR6	250	120	214	34	33.6	27418	3.1	0.44	120	230000	3400
	VR7	250	120	214	34	33.6	27418	3.1	0.77	120	230000	3400
	VR8	250	120	214	34	33.6	27418	3.1	0.77	120	230000	3400
	VR9	250	120	214	34	33.6	27418	3.1	1.1	120	230000	3400
	VR10	250	120	214	34	33.6	27418	3.1	1.1	120	230000	3400
Smith & Teng	B2	100	100	84	16	42.4	34000	3.5	1.2	80	49000	1078
2002[b]	B4	100	100	84	16	42.4	34000	3.5	1.6	60	49000	1078
	B6	100	100	84	16	42.4	34000	3.5	1.2	80	118500	987
	C	305	152	251	0	39.8	22754	3.3	4.76	152	11722	161
	D	305	152	251	0	39.8	22754	3.3	4.76	151	11722	161
	G	305	152	251	0	43	25512	3.5	4.19	152	10343	184
	I	305	152	251	0	39.8	22754	3.3	4.06	150	27580	319
	M	305	152	251	0	43	25512	3.5	1.27	152	117905	1489
	B1u,1.1	100	100	84	16	43.2	31088.7	3.7464	0.82	67	111000	1414
	B2u,1.0	100	100	84	16	43.2	31088.7	3.7464	0.82	67	111000	1414
	B1u,2.3	230	130	206	25	37.6	29003.8	3.4952	1.28	90	115000	1284
	2	250	150	205	45	35.4	28142.5	314	1	150	19720	259
	6	250	150	205	45	39.9	29877.7	3.6005	1	150	19720	259
	7	250	150	205	45	37.6	29003.8	3.4952	1	150	19720	259
	A3	300	150	250	0	51.7	34010	3.8	0.495	150	230000	3400
	A8	300	150	250	0	51.7	34010	3.8	0.99	75	230000	3400
	C2	300	150	250	0	51.7	34010	3.8	0.495	150	230000	3400
	B2	150	120	120	34	35.7	28254	3.2	1.2	80	181000	3140

Table A.5 (continued): Experimental database of FRP strengthened RC beam failed by concrete cover separation failure modes.

Source	beam	E_a MPa	t_a mm	E_s MPa	f_{ys} MPa	ϕ_s mm	A_s mm^2	E_{sc} MPa	f_{ysc} MPa	A_{sc} mm^2	span mm
Maalej & Bian	3	1470	0.636	183600	534	10	236	183600	534	157.1	1350
2001	4	1470	0.636	183600	534	10	236	183600	534	157.1	1350
	5	1470	0.636	183600	534	10	236	183600	534	157.1	1350
David *et al*	P2	8500	1	200000	500	14	308	0	0	0	2800
1999	P3	8500	1	200000	500	14	308	0	0	0	2800
	P4	8500	1	200000	500	14	308	0	0	0	2800
	P5	8500	1	200000	500	14	308	0	0	0	2800
Garden *et al*	1Au	11560	2	215000	350	6	85	215000	350	56.55	900
1997	1Bu	11560	2	215000	350	6	85	215000	350	56.55	900
	1B2u	11560	2	215000	350	6	85	215000	350	56.55	900
	1Cu	11560	2	215000	350	6	85	215000	350	56.55	900
	2Bu	11560	2	215000	350	6	85	215000	350	56.55	900
	2Cu	11560	2	215000	350	6	85	215000	350	56.55	900
Nguyen *et al*	A950	12800	1.5	200000	384	10	236	200000	400	56.55	1330
2001	A1100	12800	1.5	200000	384	10	236	200000	400	56.55	1330
	A1150	12800	1.5	200000	384	10	236	200000	400	56.55	1330
Ahmed et al	DF2	7200	na	185000	568	8	151	195000	553	56.55	1500
2001	DF3	7200	na	185000	568	8	151	195000	553	56.55	1500
	DF4	7200	na	185000	568	8	151	195000	553	56.55	1500
Ahmed &	AF3	7200	na	185000	568	8	101	195000	568	56	1500
Van-Gemert	CF2-1	7200	1	185000	568	8	129	195000	553	56.55	1500
1999	CF3-1	7200	1	185000	568	8	151	195000	553	56.55	1500
	CF4-1	7200	1	183000	586	10	207	195000	553	56.55	1500
Beber *et al*	VR5	8500	0.37	200000	565	10	157	200000	738	56.55	2350
1999	VR6	8500	0.37	200000	565	10	157	200000	738	56.55	2350
	VR7	8500	0.37	200000	565	10	157	200000	738	56.55	2350
	VR8	8500	0.37	200000	565	10	157	200000	738	56.55	2350
	VR9	8500	0.37	200000	565	10	157	200000	738	56.55	2350
	VR10	8500	0.37	200000	565	10	157	200000	738	56.55	2350
Smith & Teng	B2	11560	2	215000	350	6	85	215000	350	56.55	900
2002[b]	B4	11560	2	215000	350	6	85	215000	350	56.55	900
	B6	11560	2	215000	350	6	85	215000	350	56.55	900
	C	8500	2	200000	414	13	253	0	0	0	2438
	D	8500	2	200000	414	13	253	0	0	0	2438
	G	8500	2	200000	414	13	253	0	0	0	2438
	I	8500	2	200000	414	13	253	0	0	0	2438
	M	8500	2	200000	414	13	253	0	0	0	2438
	B1u,1.1	8600	2	215000	350	6	85	215000	350	57	900
	B2u,1.0	8600	2	215000	350	6	85	215000	350	57	900
	B1u,2.3	8600	2	220000	556	10	236	220000	556	101	2200
	2	3260	0.4	231000	537	10	157	231000	537	157	1500
	6	3260	0.4	231000	537	10	157	231000	537	157	1500
	7	3260	0.4	231000	537	10	157	231000	537	157	1500
	A3	2000	na	207000	427	16	792	0	0	0	2130
	A8	2000	na	207000	427	16	792	0	0	0	2130
	C2	2000	na	207000	427	16	792	0	0	0	2130
	B2	12800	1.5	200000	466	20	628	200000	400	57	1330

Table A.5 (continued): Experimental database of FRP strengthened RC beam failed by concrete cover separation failure modes.

Source	beam	B mm	a mm	E_{sv} MPa	f_{ysv} MPa	beam	A_{sv} mm^2	s_s mm	$P_{u,exp}/2$ KN
Maalej &	3	500	75	210900	365	MB3	56.55	60	43
Bian 2001	4	500	75	210900	365	MB4	56.55	60	41
	5	500	75	210900	365	MB5	56.55	60	39.5
David *et al*	P2	933	200	200000	500	P2	57	140	71.1
1999	P3	933	200	200000	500	P3	57	140	71
	P4	933	200	200000	500	P4	57	140	78
	P5	933	200	200000	500	P5	57	140	79.5
Garden *et al*	1Au	300	20	215000	350	1Au	14	51	19.8
1997	1Bu	300	20	215000	350	1Bu	14	51	18
	1B2u	300	20	215000	350	1B2u	14	51	18.2
	1Cu	300	20	215000	350	1Cu	14	51	15.95
	2Bu	340	20	215000	350	2Bu	14	51	17
	2Cu	340	20	215000	350	2Cu	14	51	17.75
Nguyen *et al*	A950	440	190	200000	400	A950	57	50	28.1
2001	A1100	440	115	200000	400	A1100	57	50	28.7
	A1150	440	90	200000	400	A1150	57	50	29.5
Ahmed et al	DF2	500	50	195000	553	DF2	57	100	120.6
2001	DF3	500	50	195000	553	DF3	57	100	120
	DF4	500	50	195000	553	DF4	57	100	125.6
Ahmed &	AF3	500	100	195000	553	AF3	56.55	71	48.3
Van-Gemert	CF2-1	500	100	195000	553	CF2-1	56.55	71	52.4
1999	CF3-1	500	100	195000	553	CF3-1	56.55	71	59.1
	CF4-1	500	100	195000	553	CF4-1	56.55	71	70.1
Beber *et al*	VR5	783	75	200000	738	VR5	56.55	110	51.1
1999	VR6	783	75	200000	738	VR6	56.55	110	50.3
	VR7	783	75	200000	738	VR7	56.55	110	62.1
	VR8	783	75	200000	738	VR8	56.55	110	62
	VR9	783	75	200000	738	VR9	56.55	110	64.8
	VR10	783	75	200000	738	VR10	56.55	110	68.5
Smith &	B2	300	20	215000	350	B2	14	50	17
Teng 2002[b]	B4	300	20	215000	350	B4	14	50	17.5
	B6	300	20	215000	350	B6	14	50	20.4
	C	914	203	200000	414	C	99	102	55.4
	D	914	203	200000	414	D	99	102	59.6
	G	914	0	200000	414	G	99	102	62.9
	I	914	203	200000	414	I	99	102	50.6
	M	914	0	200000	414	M	99	102	72.1
	B1u,1.1	300	20	215000	350	B1u,1.1	14	51	18.3
	B2u,1.0	300	20	215000	350	B2u,1.0	14	51	16
	B1u,2.3	844	20	215000	350	B1u,2.3	57	150	50.2
	2	500	350	231000	537	2	157	100	53
	6	500	200	231000	537	6	157	100	63.1
	7	500	350	231000	537	7	157	100	53.9
	A3	1065	0	207	427	A3	143	125	86.1
	A8	1065	0	207	427	A8	143	125	98.2
	C2	1065	0	207	427	C2	143	150	79.3
	B2	440	115	200000	400	B2	57	50	65.1

h_c is the total depth of the concrete section. b_c is the width of the concrete section. d_s is the depth of the tensile steel reinforcement. d_{sc} is the distance from the centre of top reinforcement to the top of the beam. f_c is the compressive strength of concrete. E_c is the modulus of concrete. b_{FRP} is the width of the FRP laminates. t_{FRP} is the thickness of FRP laminates; E_{FRP} is the modulus of FRP composite. $f_{FRP,ur}$ is the strength of the FRP composite. E_a and t_a are the modulus and thickness of the adhesive layer respectively; E_s is the elastic modulus of steel. f_{ys} and f_{ysc} is the yield strength of tensile and compression reinforcement. A_s and A_{sc} is the area of tensile and compression reinforcement. B is the shear span. a is the distance from the plate end to the nearest support. $P_{u,exp}$ is the ultimate load (See Figure A.1). na not available.

Table A.6: Experimental database of FRP strengthened RC beam for shear.

Source	beam	h_c	b_c	f_c	f_{ct}	E_{FRP}	$f_{FRP,ur}$			$n_{FRP,v}$	$t_{FRP,v/l}$	w_{FRP}	s_{FRP}	β	$V_{u,exp}$
		mm	mm	MPa	MPa	GPa	MPa				Mm	mm	mm		kN
Kim et al 2008	CP2-VW	250	250	34.7	3.19	158	3002	S	C	1	0.06	440	440	90	68
	CP2-1VS	250	250	34.7	3.19	158	3002	S	D	1	0.06	50	100	90	58
	CS2-VW	250	250	34.7	3.19	235	3525	S	C	1	0.06	440	440	90	65
	CS2-DW	250	250	34.7	3.19	235	3525	S	C	1	0.06	440	440	45	77
	CS3-VW	250	250	34.7	3.19	235	3525	S	C	1	0.06	660	660	90	45.5
	CS3-DW	250	250	34.7	3.19	235	3525	S	C	1	0.06	660	660	45	47.5
	CP2-VW	340	120	27.38	2.73	230	3800	U	D	1	0.09	80	150	90	38.25
	CP2-1VS	340	120	27.38	2.73	230	3800	U	D	1	0.09	80	200	90	18.295
Jayaprakash et al 2008	BT1-1I	340	120	16.73	1.96	230	3800	U	D	1	0.09	80	150	45	44.9
	BT1-2I	340	120	16.73	1.96	230	3800	U	D	1	0.09	80	150	45	13.3
	BT2-2I	340	120	16.73	1.96	230	3800	U	D	1	0.09	80	150	90	3.325
	BS2-2I	500	180	65.2	4.40	100.6	577	S	C	1	0.6	1	1	45	153.5
	BS2-2I	500	180	48.5	3.60	70.8	860	S	C	1	0.8	1	1	45	227
Taljsten & Elfgren 2000	S2	300	150	49.2	4.03	390	3000	U	D	2	0.167	25	190	90	10.83
	S4	300	150	49.2	4.03	166	2286	S	D	1	1.4	10	200	90	29.12
Barros & Dias 2003	A10_M	300	150	49.2	4.03	166	2286	S	D	1	1.4	10	300	45	28.3
	A10_VL	300	150	40.2	3.52	390	3000	U	D	2	0.167	25	95	90	31.52
	A10_IL	300	150	49.2	4.03	166	2286	S	D	1	1.4	10	100	90	59.305
	A12_M	300	150	49.2	4.03	166	2286	S	D	1	1.4	10	150	45	72.94
	A12_VL	150	150	56.2	4.40	390	3000	U	D	2	0.167	25	80	90	18.56
	A12_IL	150	150	56.2	4.40	166	2286	S	D	1	1.4	10	100	90	28.6
	B10_M	150	150	56.2	4.40	166	2286	S	D	1	1.4	10	150	45	23.21
	B10_VL	150	150	56.2	4.40	390	3000	U	D	2	0.167	25	40	90	33.65
	B10_IL	150	150	56.2	4.40	166	2286	S	D	1	1.4	10	50	90	31.75
	B12_M	150	150	56.2	4.40	166	2286	S	D	1	1.4	10	75	45	36.4
	B12_VL	405	150	35	3.21	228	3790	U	C	1	0.165	1	1	90	65
	B12_IL	405	150	35	3.21	228	3790	U	C	1	0.165	1	1	90	67.5
Khalifa & Nanni 2000	BT2	405	150	35	3.21	228	3790	U	D	1	0.165	50	125	90	72
	BT3	405	150	35	3.21	228	3790	S	D	1	0.165	50	125	90	31.5
	BT4	110	70	32	3.02	235	3300	S	D	1	0.155	30	60	90	12.3
	BT5	110	70	32	3.02	235	3300	S	D	1	0.155	45	60	90	14.3
	S4	600	140	44.1	3.28	230	3400	U	D	1	0.11	50	100	90	85.25
	T6NS-C45	250	100	33.4	2.59	240	3400	U	C	1	0.16	1	1	90	39.3
	T6S4-C90	300	100	33.4	2.59	240	3400	U	C	1	0.16	1	1	90	38.1
	SO3-2	305	150	35.5	2.73	228	3790	U	C	1	0.165	1	1	90	92.5
	SO3-3	305	150	35.5	2.73	228	3790	U	D	1	0.165	50	125	90	62.5
	SO3-4	305	150	35.5	2.73	228	3790	U	C	1	0.165	1	1	90	90
	SO3-5	300	150	27.5	2.17	234	3550	S	C	1	0.165	1	1	90	45.3
	SO4-2	300	150	31.4	2.45	234	3550	S	C	1	0.495	1	1	90	86
	SO4-3	300	150	32.8	2.55	230	3400	S	D	1	0.111	50	100	90	41.2
Triantafillou 1980	S1	110	70	32	3.02	235	3300	S	D	1	0.155	60	60	90	11.5
	S2	700	400	34.6	3.19	244	3990	W	D	1	0.11	40	100	90	174.7
	S3	300	150	43	3.68	73	2700	W	C	1	0.044	1	1	90	27.5
Kamiharako et al 1997	7	300	150	43	3.68	73	2700	W	D	1	0.044	100	200	90	26
Umezu 1997	As1	300	150	44.8	3.78	244	4200	W	D	1	0.111	100	200	90	52.3
	AS2	300	150	41.9	3.62	73	2700	W	C	1	0.044	1	1	90	63.5
	CS3	300	300	45.6	3.83	73	2700	W	C	1	0.044	1	1	90	45.6
	AB1	300	300	49.3	4.03	73	2700	W	C	1	0.088	1	1	90	96.6
	AB2	300	300	42.7	3.66	73	2700	W	C	1	0.144	1	1	90	126.6
	AB4	450	450	39.9	3.50	73	2700	W	C	1	0.144	1	2	91	163
	AB5	450	200	35.1	3.22	240	3400	U	D	1	0.11	100	400	90	41.2
	AB9	450	200	36.8	3.32	240	3400	U	D	1	0.11	50	400	90	33.4
Taerwe 1997	Bs2	450	200	35.8	3.26	240	3400	U	D	1	0.11	50	600	90	30
	BS4	450	200	43.8	3.26	280	3500	U	D	1	0.11	50	600	90	30
	Bs5	450	130	38	3.39	105	1400	U	D	1	0.43	40	200	90	32.5
	Bs6	450	130	38	3.39	105	1400	U	D	1	0.43	40	250	90	20
Diagana et al 2003	Pu1	450	130	38	3.39	105	1400	U	D	1	0.43	28.28	300	45	44.5
	Pu2	450	130	38	3.39	105	1400	U	D	1	0.43	28.28	350	45	40
	Pu3	450	130	38	3.39	105	1400	W	D	1	0.43	40	200	90	67.5
	Pu4	450	130	38	3.39	105	1400	W	D	1	0.43	40	250	90	45
	Pc1	450	130	38	3.39	105	1400	W	D	1	0.43	28.28	300	45	35.5
	Pc2	450	130	38	3.39	155	1400	W	D	1	0.43	28.28	350	45	22
	Pc3	200	125	36	3.27	34	390	U	C	1	1	1	1	90	18
	Pc4	250	150	40	3.51	50	2400	U	D	1	1	1	50	100	90	33
Norris et al 1997	E	190	64	46	3.85	11	200	U	C	1	1	1	1	90	15.6
Challal et al 1998	RS90	190	64	46	3.85	14	170	U	C	1	0.46	1	1	90	16.6
	RS90a	110	70	30	2.36	235	3300	S	D	1	0.155	30	60	90	11.25

Reference	ID														
Chajes	A	190	64	46	3.85	21	185	U	C	1	0.58	1	1	90	18.2
et al 1995	E	200	100	32.6	2.54	230	2645	W	C	1	0.097	1	1	90	34.5
	G	200	100	32.6	2.54	230	2645	S	C	1	0.097	1	1	90	20.5
Uji 1992*	3	200	100	35.4	2.73	230	2645	S	C	1	0.137	1	1.41	45	33
	5	200	100	35.4	2.73	230	2645	S	C	1	0.195	1	1	90	20.5
	6	300	200	53.2	3.81	230	3473	S	D	1	0.24	20	80	90	68.4
	7	300	200	45.5	3.36	230	3473	S	C	1	0.12	1	1	90	64.2
Satto et al*	S2	400	200	32.8	2.55	230	3473	W	D	1	0.11	20	84.62	90	35
1996	S4	400	200	32.9	2.56	230	3473	W	D	1	0.11	20	48.89	90	61
Araki et al*.															
1997	CF045	400	200	33.2	2.58	230	3473	W	D	1	0.11	20	28.57	90	106
	CF064	400	200	33.6	2.61	230	3473	W	C	1	0.22	1	1	90	206
	CF097	200	125	43.1	3.22	230	3473	W	D	1	0.111	50	250	90	18.75
	CF243	200	125	40.4	3.05	230	3473	W	D	1	0.111	50	100	90	29.5
Miyauchi *	1/5 Z-3	200	125	47.1	3.46	230	3473	W	D	1	0.111	50	100	90	34.55
et al 1997	1/2 Z-3	450	200	43.1	3.22	280	3500	U	D	1	0.11	100	400	90	41.2
	1/L Z-2	450	200	46.4	3.41	280	3500	U	C	1	0.11	1	1	90	115.4
Triantafillou	S1A	110	70	30	2.36	235	3300	S	D	1	0.155	30	60	45	14.05
1998	S1B	110	70	30	2.36	235	3300	S	D	1	0.155	45	60	90	15.85
	S145	110	70	30	2.36	235	3300	S	D	1	0.155	45	60	90	12.9
	S2A	110	70	30	2.36	235	3300	S	D	1	0.155	30	60	45	15.45
	S2B	110	70	30	2.36	235	3300	S	C	1	0.155	1	1	90	13.2
	S245	110	70	30	2.36	235	3300	S	C	1	0.155	1	1	90	10.55
	S3A	110	70	30	2.36	235	3300	S	C	1	0.155	1	1.4	45	12.15
	S3B	305	150	28.5	2.25	228	3500	U	D	1	0.165	50	125	90	40
	S345	305	150	28.5	2.25	228	3500	U	C	1	0.165	1	1	90	65
Khalifa	CO2	405	150	35	2.70	228	3790	U	C	1	0.165	1	1	90	65
et al 1998	CO3	405	150	35	2.70	228	3790	U	C	1	0.165	1	1	90	67.5
Deniaud &	2	305	150	27.3	2.16	228	3790	U	C	1	0.165	1	1	90	80.5
Cheng 2001	5	305	150	35.5	2.73	228	3790	U	D	1	0.165	50	125	90	54
Park et al	SW3-2	305	150	35.5	2.73	228	3790	U	D	1	0.165	75	125	90	56.5
2001	SW4-2	305	150	35.5	2.73	228	3790	U	C	1	0.165	1	1	90	67.5
Pellegrino	TR30C2	300	150	32.8	2.55	230	3400	S	D	1	0.111	50	100	90	47.37
& Modena															
2002	TR30D20	300	150	32.8	2.55	230	3400	S	D	1	0.111	50	100	90	58.27
Beber *	V9_A	300	150	32.8	2.55	230	3400	U	D	1	0.111	50	100	90	50.57
2003	V9_B	300	150	32.8	2.55	230	3400	U	D	1	0.111	50	100	90	49.07
	V21_A	300	150	32.8	2.55	230	3400	U	D	1	0.111	50	100	90	45.87
	V10_A	300	150	32.8	2.55	230	3400	U	D	1	0.111	50	100	90	41.51
	V10_B	300	150	32.8	2.55	230	3400	U	D	1	0.111	50	100	90	67.88
	V17_A	300	150	32.8	2.55	230	3400	U	D	1	0.111	50	100	90	36.01
	V11_A	300	150	32.8	2.55	230	3400	W	D	1	0.111	50	100	90	59.44
	V11_B	300	150	32.8	2.55	230	3400	W	D	1	0.111	50	100	90	70.37
	V17_B	300	150	32.8	2.55	230	3400	S	D	1	0.111	50	141.4	45	44.73
	V12_A	300	150	32.8	2.55	230	3400	S	D	1	0.111	50	141.4	45	34.73
	V18_A	300	150	32.8	2.55	230	3400	U	D	1	0.111	50	141.4	45	61.5
	V12_B	300	150	32.8	2.55	230	3400	U	D	1	0.111	50	141.4	45	58.21
	V14_B	300	150	32.8	2.55	230	3400	W	C	1	0.111	1	1	90	65.09
	V19_A	300	150	32.8	2.55	230	3400	W	C	1	0.111	1	1	90	68.83
	V19_B	300	150	32.8	2.55	230	3400	S	C	1	0.111	1	1	90	81.45
	V13_A	300	150	32.8	2.55	230	3400	S	C	1	0.111	1	1	90	55.51
	V13_B	300	150	32.8	2.55	230	3400	S	C	1	0.111	1	1.41	45	71.47
	V15_B	300	150	32.8	2.55	230	3400	S	C	1	0.111	1	1.41	45	63.64
	V16_B	450	130	38	2.90	105	1400	U	D	1	0.43	40	200	90	32.5
	V14_A	450	130	38	2.90	105	1400	U	D	1	0.43	40	250	90	20
	V15_A	450	130	38	2.90	105	1400	U	D	1	0.43	40	300	45	44.5
Täljsten	C3	300	300	49.1	3.57	230	3400	U	C	1	0.167	1	1	90	125.5
2003	C5	360	150	32.5	2.53	235	4200	U	C	1	0.22	1	1	90	63.5
Adhikary	C2	360	150	32.5	2.53	235	4200	U	C	1	0.22	1	1	90	76.5
et al 2004	C3	360	150	32.5	2.53	235	4200	U	D	1	0.22	40	120	90	69.5
Feng Xue Song	SB1	360	150	32.5	2.53	235	4200	U	D	1	0.22	40	120	90	53.5
et al. 2004*	SB1_4	360	150	32.5	2.53	235	4200	U	D	1	0.22	40	120	90	63.5
	SB1_5	360	150	32.5	2.53	235	4200	U	D	1	0.22	40	120	90	62.5
	SB1_6	360	150	32.5	2.53	235	4200	U	D	1	0.44	40	120	90	63.5
	SB1_7	360	150	32.5	2.53	235	4200	U	D	1	0.44	40	120	90	66.5
	SB1_8	360	150	32.5	2.53	235	4200	U	D	1	0.22	40	120	90	72
	SB1_9	360	150	32.5	2.53	235	4200	U	D	1	0.22	40	120	90	52
	SB1_10	360	150	32.5	2.53	235	4200	U	D	1	0.22	40	120	90	35
	SB2_2	360	150	32.5	2.53	235	4200	U	D	1	0.22	40	120	90	54
	SB2_3	500	180	67	4.55	234	4500	S	C	1	0.07	1	1.41	45	128
	SB3_2	500	180	71	4.75	234	4500	S	C	1	0.11	1	1.41	45	138
	SB3_3	500	180	46	3.39	234	4500	W	C	1	0.11	1	1.41	45	219
Carolin &	A145	500	180	67	4.55	234	4500	S	C	1	0.11	1	1.41	45	187
Täljsten	A245a	500	180	47	3.45	234	4500	S	C	1	0.11	1	1.41	45	132
2005	A245W	500	180	59	4.13	234	4500	S	C	1	0.11	1	1	90	137

Source	Specimen	h_c	b_c	f_c	f_{ct}	E_{FRP}	$f_{FRP,ur}$			$n_{FRP,v}$	$t_{FRP,v/l}$	w_{FRP}	s_{FRP}	β	$V_{FRPu,exp}$
	A245Ra	500	180	71	4.75	234	4500	S	C	1	0.17	1	1.41	45	215
	A245Rb	440	340	29.9	2.35	253	4840	W	D	1	0.111	50	150	90	81.3
	A290a	440	340	29.9	2.35	253	4840	W	D	1	0.111	75	150	90	122
	A345	440	340	29.9	2.35	253	4840	W	D	1	0.111	87.5	150	90	132
Miyajima *et al*	case2	440	340	29.9	2.35	253	4840	W	D	1	0.111	100	150	90	162
2005*	case3	220	95	25.5	2.02	231	3650	U	C	1	0.066	1	1	90	15.4
	case4	220	95	25.5	2.02	231	3650	U	C	1	0.132	1	1	90	13.8
	case5	220	95	25.5	2.02	231	3650	U	C	1	0.066	1	1	90	12.7
Bousselham	DBS01L	220	95	25.5	2.02	231	3650	U	C	1	0.132	1	1	90	17
& Chaallal	DBS02L	220	95	25.5	2.02	231	3650	U	C	1	0.066	1	1	90	23.2
2006*	DBS11L	220	95	25.5	2.02	231	3650	U	C	1	0.132	1	1	90	32.4
	DBS12L	220	95	25.5	2.02	231	3650	U	C	1	0.066	1	1	90	2.8
	SBS01L	220	95	25.5	2.02	231	3650	U	C	1	0.132	1	1	90	12.2
	SBS02L	300	150	49.2	3.58	390	3000	U	D	1	0.334	25	190	90	10.83
	SBS11L	150	150	56.2	3.97	390	3000	U	D	1	0.334	25	80	90	18.56
	SBS12L	150	150	56.2	3.97	390	3000	U	D	1	0.334	25	40	90	33.65
Dias & Barros	A10_M	250	250	34.7	3.19	158	3002	S	C	1	0.06	440	440	90	68
2008	B10_M	250	250	34.7	3.19	158	3002	S	D	1	0.06	50	100	90	58
	B12_M	250	250	34.7	3.19	235	3525	S	C	1	0.06	440	440	90	65

D: discrete configuration; C continuous configuration; S side bonded laminates; U jacket bonded laminates; W fully wrapped laminates. β is the inclination angle of FRP strips. h_c is the total depth of the concrete section. b_c is the width of the concrete section. f_c is the compressive strength of concrete. f_{ct} is the tensile strength of concrete. E_{FRP} is the modulus of FRP composite. $f_{FRP,ur}$ is the strength of the FRP composite; $n_{FRP,v}$ is the number of FRP layers for shear strengthening. $t_{FRP,v/l}$ is the thickness of a single FRP layer for shear strengthening; w_{FRP} is the width of the FRP strips. s_{FRP} is the spacing of FRP strips; $V_{FRPu,exp}$ is the FRP contribution to the shear strength (See Figure A.3). na not available. * reported in Sas (2008).
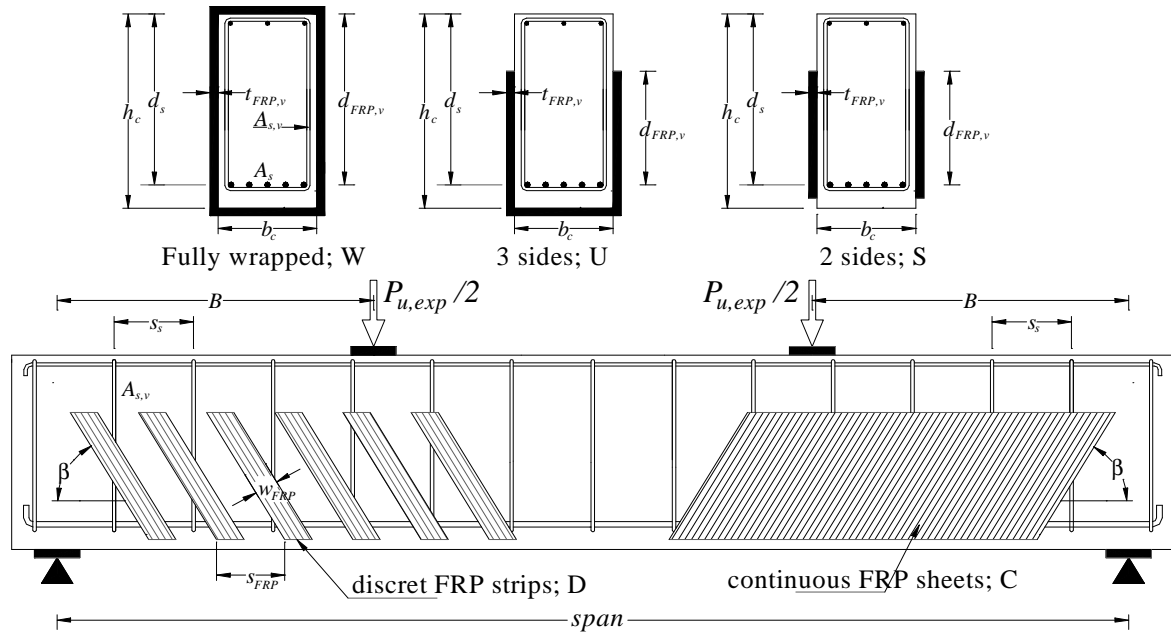
Figure A.3: Geometrical configuration of shear strengthening.

APPENDICES

Appendix B: Statistical distributions

B.1 Log-Normal distribution

The probability density function (PDF) of a Log-Normal random variable X is given as:

$$f_X(x) = \frac{1}{x\sigma_{\ln(X)}\sqrt{2\pi}}\exp\left[-\frac{1}{2}\left(\frac{x-\mu_{\ln(X)}}{\sigma_{\ln(X)}}\right)^2\right], \quad \text{with } 0 < x < \infty \qquad (B.1)$$

and the *CDF* is:

$$F_X(x) = \Phi\left(\frac{\ln(x)-\mu_{\ln(X)}}{\sigma_{\ln(X)}}\right), \qquad \text{with } 0 < x < \infty \qquad (B.2)$$

where Φ is the cumulative density function of the standard normal distribution. $\mu_{\ln(X)}$ and $\sigma_{\ln(X)}$ are the corresponding parameters of the Lon-Normal distribution:

- $$\sigma_{\ln(X)} = \sqrt{\ln\left[\left(\frac{\sigma_X}{\mu_X}\right)^2 + 1\right]}$$

- $$\mu_{\ln(X)} = \ln(\mu_X) - \frac{1}{2}\sigma_{\ln(X)}^2$$

An example of random variable with Log-Normal distribution is the yield stress of steel reinforcement (see Figure B.1); mean value μ_X=460MPa & standard deviation σ_X=46MPa
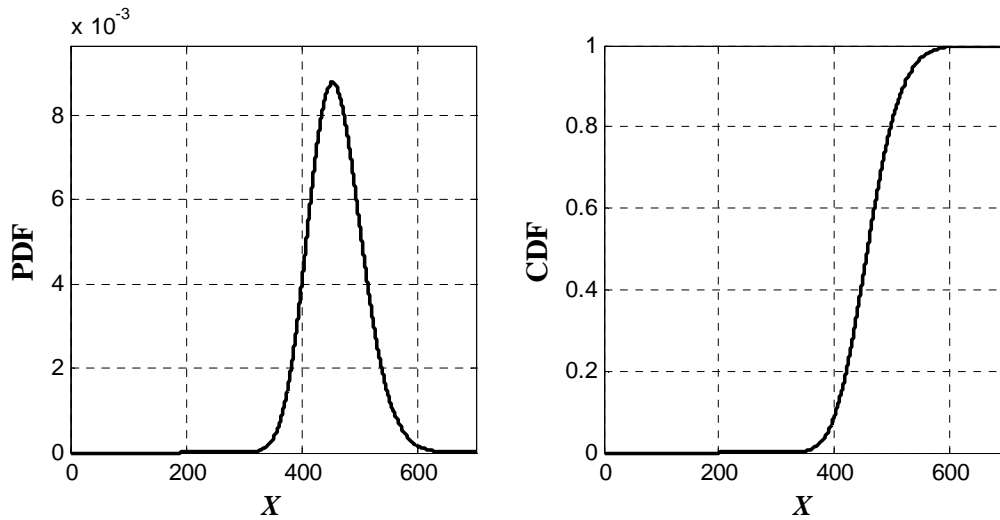
Figure B.1: Graphical representation of Lognormal Distribution

B.2 Weibull Distribution

The probability density function (PDF) of a Weibull random variable X is given as:

$$f_X(x) = \frac{\alpha x^{\alpha-1}}{\beta^\alpha} \exp\left[-\left(\frac{x}{\beta}\right)^\alpha\right], \qquad \text{with } x \geq 0, \alpha > 0, \beta > 0 \tag{B.3}$$

and the *CDF* is:

$$F_X(x) = 1 - \exp\left[-\left(\frac{x}{\beta}\right)^\alpha\right], \qquad \text{with } x \geq 0, \tag{B.4}$$

where α and β are the corresponding parameters of the Weibull distribution and can be obtained using numerical solving procedure of the following two equations:

$$\mu_X = \beta\, \Gamma\left(\frac{1}{\alpha}+1\right) \tag{B.5}$$

$$\sigma_X = \mu_X \sqrt{\frac{\Gamma\left(\frac{2}{\alpha}+1\right)}{\Gamma^2\left(\frac{2}{\alpha}+1\right)}-1} \tag{B.6}$$

where $\Gamma(.)$ is the gamma function. An example of random variable with Weibull distribution is the strength of the FRP composite laminates (see Figure B.2); mean value μ_X=620MPa & standard deviation σ_X=93MPa
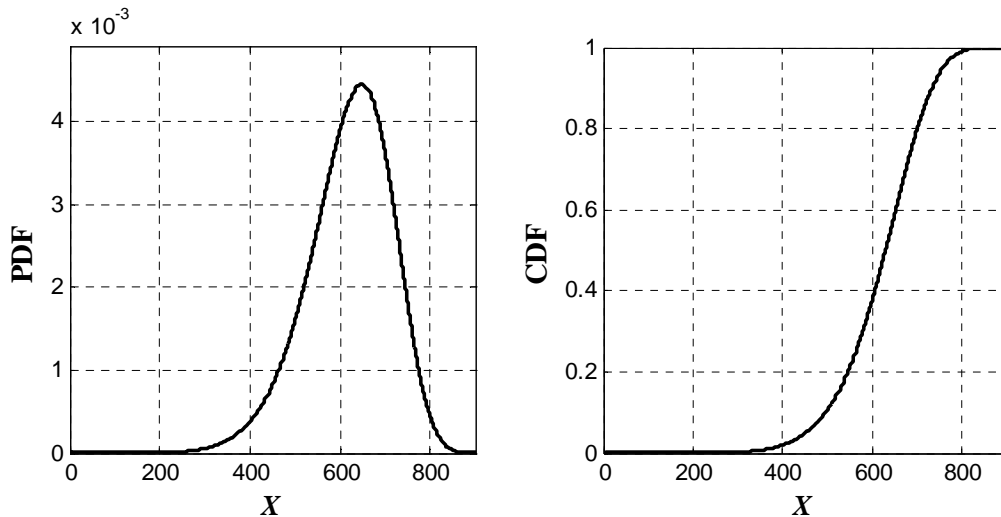
Figure B.2: Graphical representation of Weibull Distribution

B.3 Uniform Distribution

The probability density function (PDF) of a Uniform random variable X is given as:

$$f_X(x) = \begin{cases} 0 & \text{if } x < a \\ \dfrac{1}{b-a} & \text{if } x \in [a,b] \\ 0 & \text{if } a > b \end{cases} \quad \text{(B.7)}$$

and the *CDF* is:

$$F_X(x) = \begin{cases} 0 & \text{if } x < a \\ \dfrac{x-a}{b-a} & \text{if } x \in [a,b] \\ 1 & \text{if } a > b \end{cases} \quad \text{(B.8)}$$

where a and b are the corresponding parameters of the Uniform distribution:

- $a = \mu_X - \sqrt{3}\sigma_X$

- $b = \mu_X + \sqrt{3}\sigma_X$

An example of random variable with Uniform distribution is the threshold chlorides content required to initiate corrosion reactions in concrete (see Figure B.3); mean value μ_X=0.9kg/m^3 & standard deviation σ_X=0.171kg/m^3
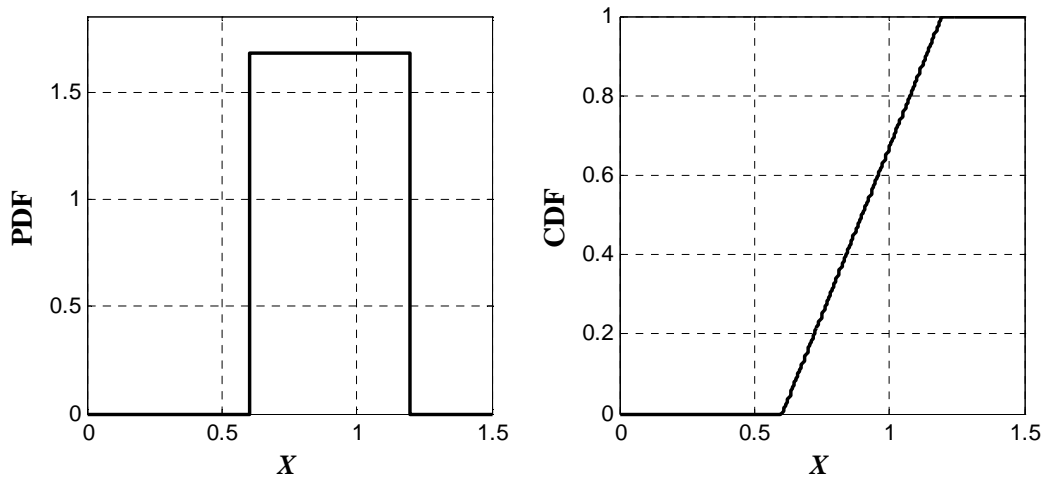
Figure B.3: Graphical representation of Uniform Distribution

B.4 Generalized extreme value (GEV) Distribution

The probability density function (PDF) of a Generalized Extreme Value (GEV) random variable X is given as:

$$f_X(x) = \frac{1}{s}\left[1 + k\left(\frac{x-m}{s}\right)\right]^{-\frac{1}{k}-1} \exp\left\{-\left[1 + k\left(\frac{x-m}{s}\right)\right]^{-\frac{1}{k}}\right\} \tag{B.9}$$

and the *CDF* is:

$$F_X(x) = \exp\left\{-\left[1 + k\left(\frac{x-m}{s}\right)\right]^{-\frac{1}{k}}\right\} \tag{B.10}$$

where m, k and s are the corresponding parameters of the GEV distribution and can be obtained using numerical solving procedure of the following equations

- $\mu_X = m - \dfrac{s}{k} - \dfrac{s}{k} g_1$

- $\sigma_X = \dfrac{s}{k} \sqrt{g_2 - g_1^2}$

- $\text{mod}(X) = m + \dfrac{s}{k}\left[(1+k)^{-k} - 1\right]$

where $g_i = \Gamma(1 - ik)$ as $i = 1, 2, \ldots$. $\Gamma(.)$ is the gamma function. $\text{mod}(X)$ is the mode value of the variable X (i.e., the most frequently occurring value in X). An example of random variable with GEV distribution is the coefficient of chlorides diffusion of concrete (see Figure B.4); mean value μ_X=54.65mm/year^3 & standard deviation σ_X=1975mm/year^3
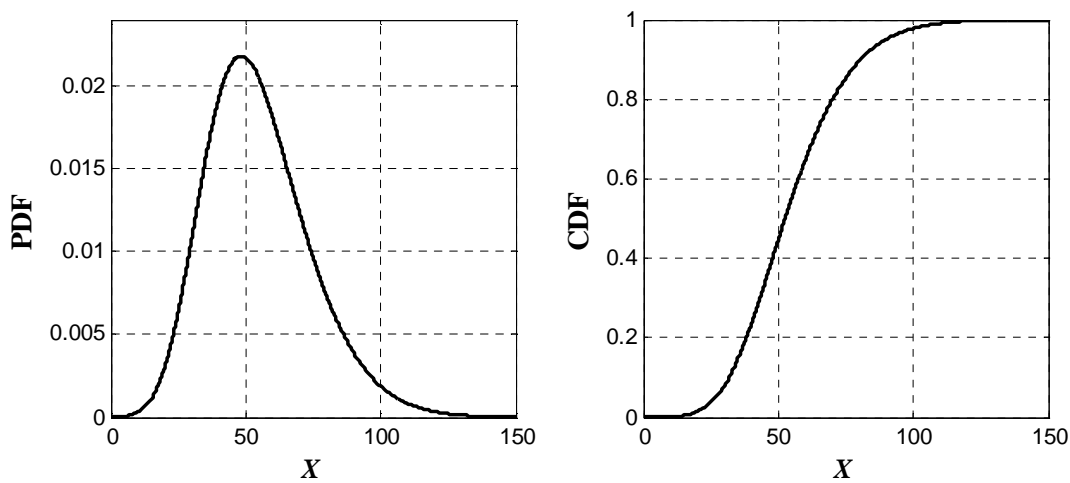
Figure B.4: Graphical representation of Uniform Distribution

B.5 Bi-model Distribution

The probability density function (PDF) of a Bi-model random variable X is given as:

$$f_X(x) = r\phi(x, \mu_{1X}, \sigma_{1X}) - (1-r)\phi(x, \mu_{1X}, \sigma_{1X})$$ (B.11)

and the *CDF* is:

$$F_X(x) = r\Phi(x, \mu_{1X}, \sigma_{1X}) - (1-r)\Phi(x, \mu_{1X}, \sigma_{1X})$$ (B.12)

where, μ_{1X} and μ_{2X} are the first and the second mean values, σ_{1X} and σ_{2X} are the first and second standard deviation. r is the mixture ratio. ϕ and Φ are the PDF and CDF of normal distribution (see § II.3.1.2).

An example of random variable with Bi-model distribution is corroded steel rebars embedded in concrete (see Figure B.5); r=0.9, μ_{1X}=405mm^2, μ_{1X}=477mm^2, σ_{1X}=25.5mm^2, σ_{1X}=9.9mm^2.
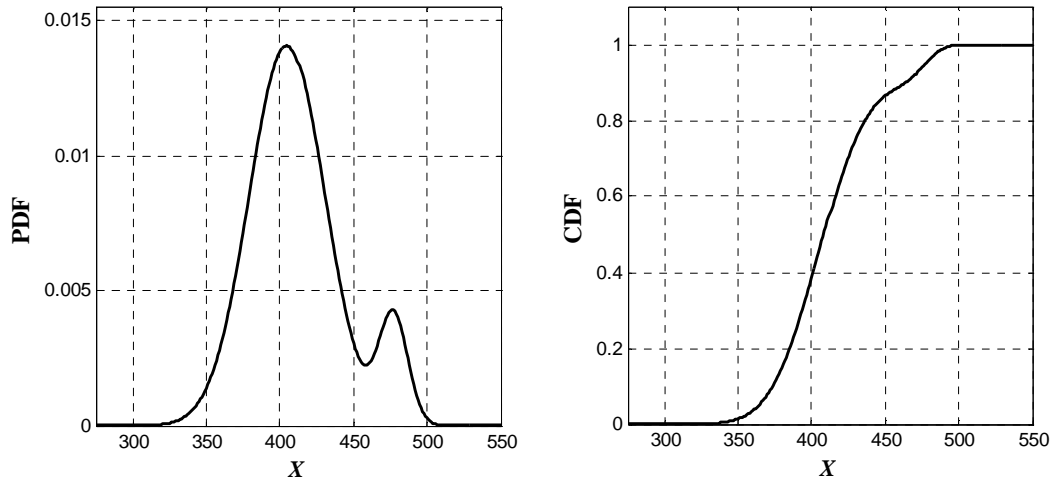
Figure B.5: Graphical representation of Bi-model Distribution

In the present study, non-linear fitting toolbox available in Matlab was used to calculate the five parameters (μ_{1X}, μ_{2X}, σ_{1X}, σ_{2X}, and r) of the Bi-model distribution for a given dataset of the variable.

B.6 Chi-square statistical test: "goodness-of-fit" test

Steps of Chi-square statistical test:

1. Divide the observed data range into equal intervals

2. Find the number of observations (n_i) within each interval which do not depend on the distribution type.

3. Assume different distribution types that will represent the random variable and find the theoretical distribution values (e_i) within each interval for the respective distributions. If a random variable, X, lies in an interval a to b such that $a<X\leq b$, then ei for a certain distribution type is given as: $e_i=P(a<X\leq b)*N$, where N is the total number of observation, and $P(a<X\leq b)=P(X\leq b)-P(X<a)$. The probability of X less than a or b, $P(X<a)$ and $P(X\leq b)$ is found using the CDF for the respective distribution.

4. Compute the summation; $\sum\limits_{i=1}^{m}\dfrac{(n_i-e_i)^2}{e_i}$, where, m is the total number of intervals.

5. Calculate the degree of freedom, f, for Chi-Square test which is given by $f=m\text{-}1\text{-}k$, where, k is the number of parameters required to describe a particular distribution.

6. The summation evaluated in step 4 is compared to the Chi-Square distribution for a certain significance level, α, which is always taken between 0.01-0.1. in the present study, an average value of α is considered equals to 0.05.

7. If $\sum\limits_{i=1}^{m}\dfrac{(n_i-e_i)^2}{e_i}<C_{\alpha,f}$, then the assumed distribution is fitting statistical data well enough. $C_{\alpha,f}$ can be obtained from Chi-square distribution tables or using Matlab software.

APPENDICES

Appendix C
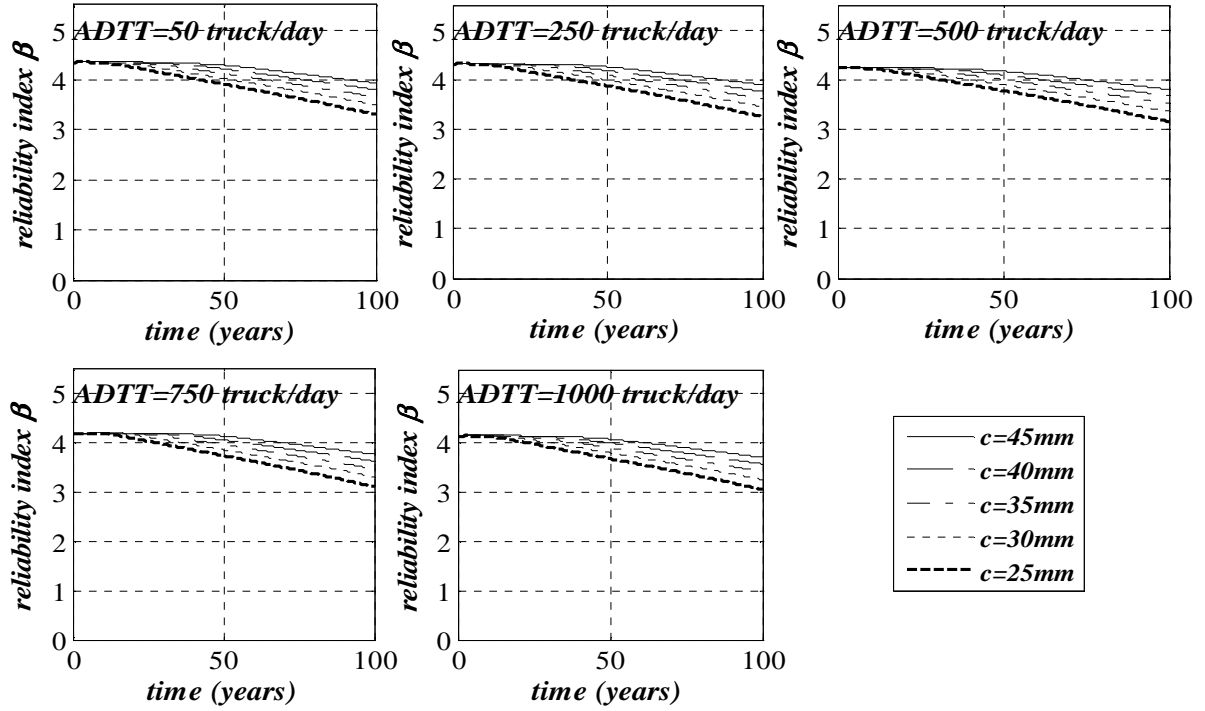
Figure C.1: Time-dependent flexural limit state reliability index of RC beam under uniform corrosion.
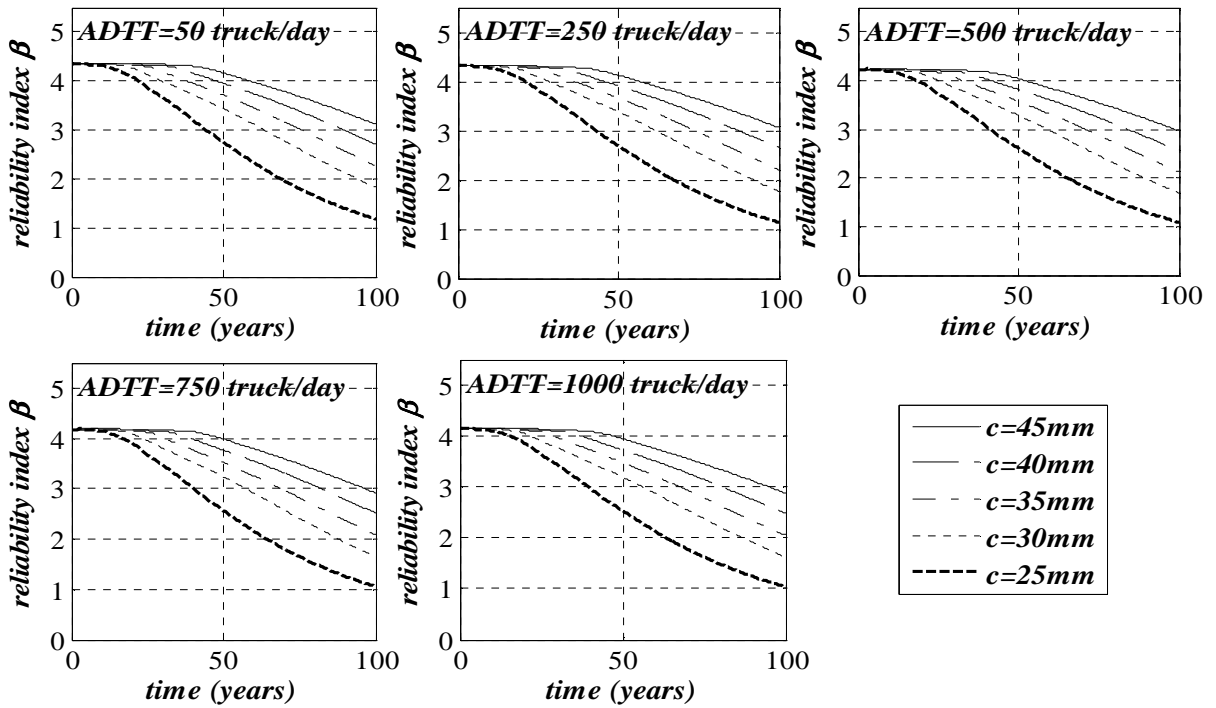
Figure C.2: Time-dependent flexural limit state reliability index of RC beam under pitting corrosion.
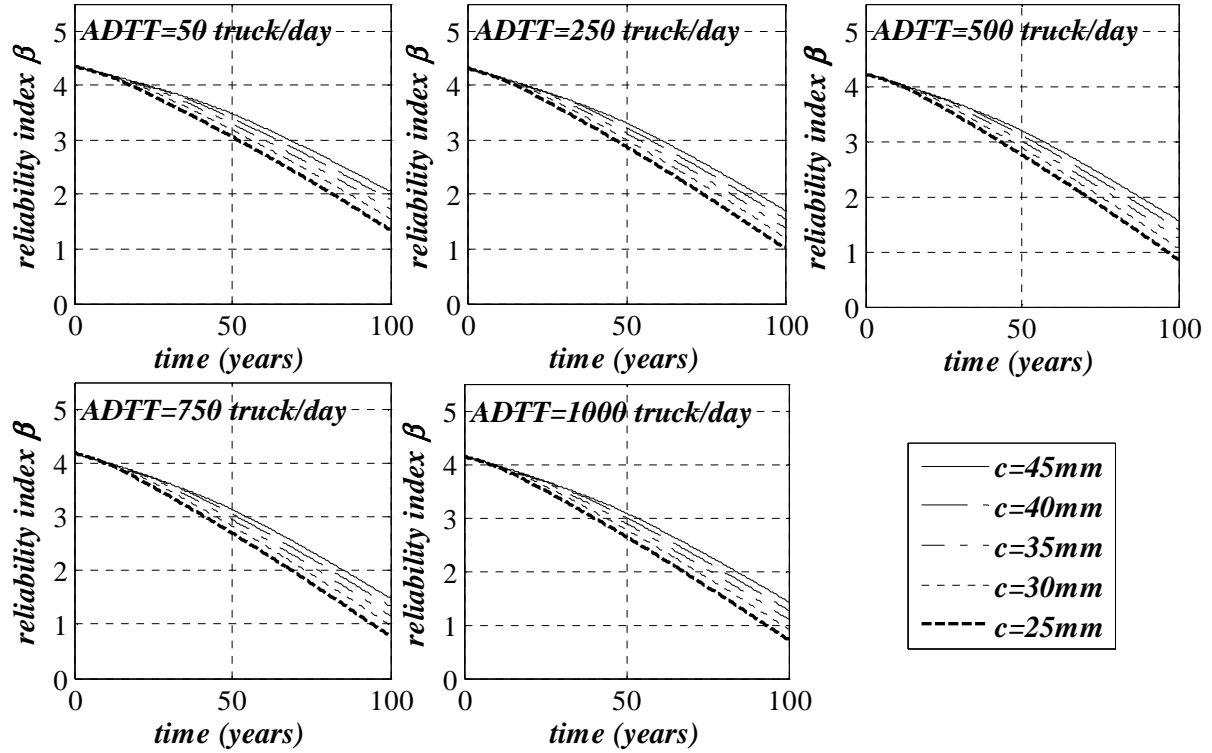
Figure C.3: Time-dependent flexural limit state reliability index of RC beam under uniform corrosion and growth of live load over time.
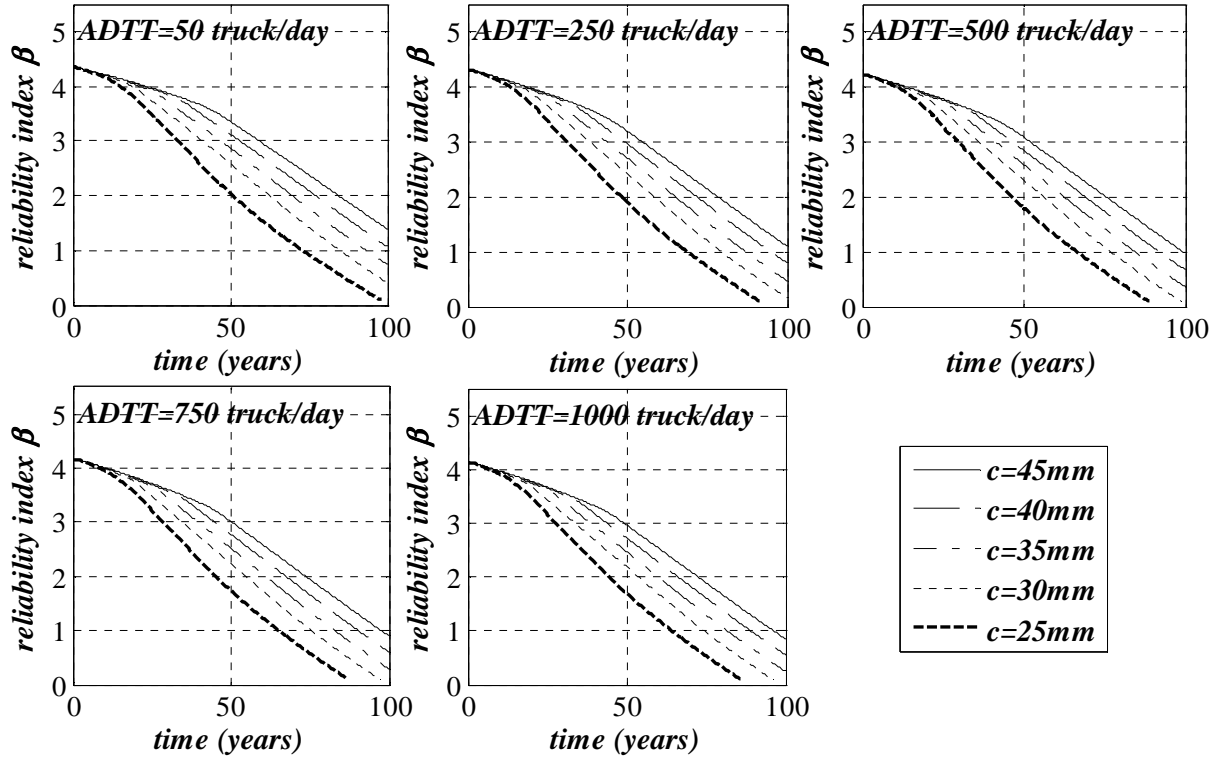
Figure C.4: Time-dependent flexural limit state reliability index of RC beam under pitting corrosion and growth of live load over time.
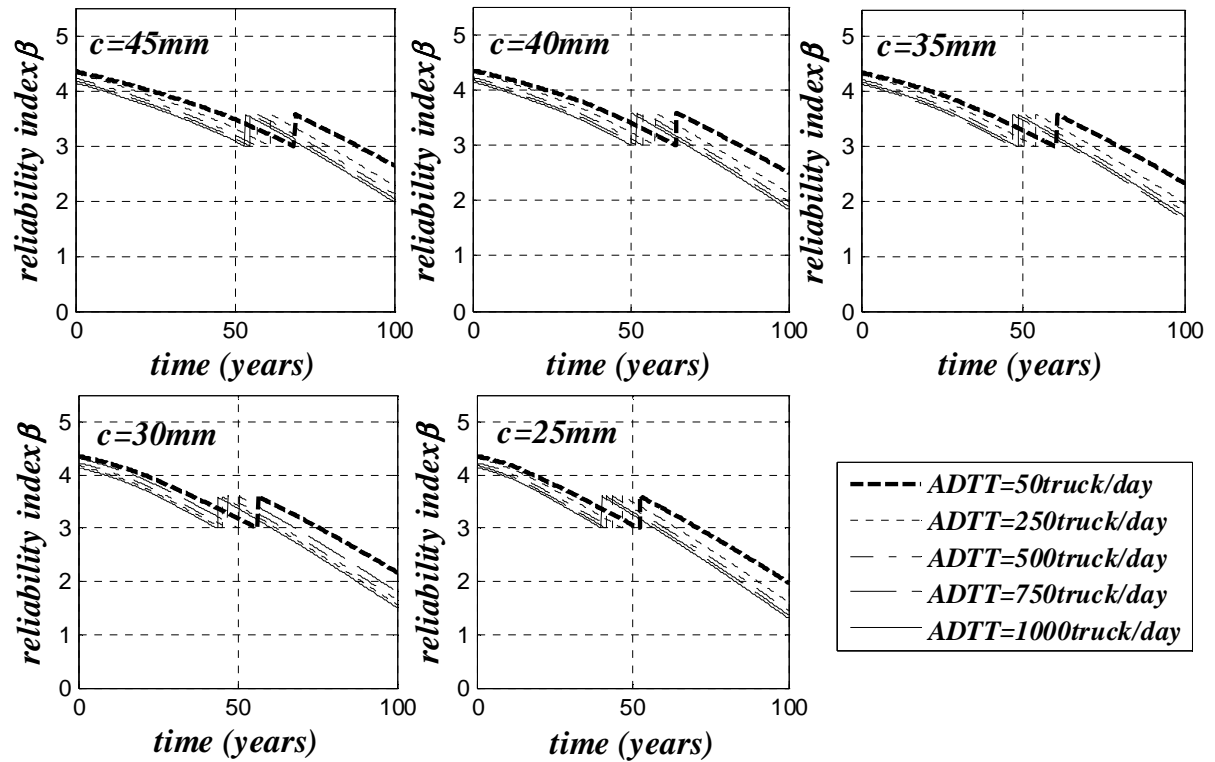
Figure C.5: Time-dependent flexural limit state reliability index of FRP strengthened RC, with non-anchorage laminates, beam under uniform corrosion and growth of live load over time.
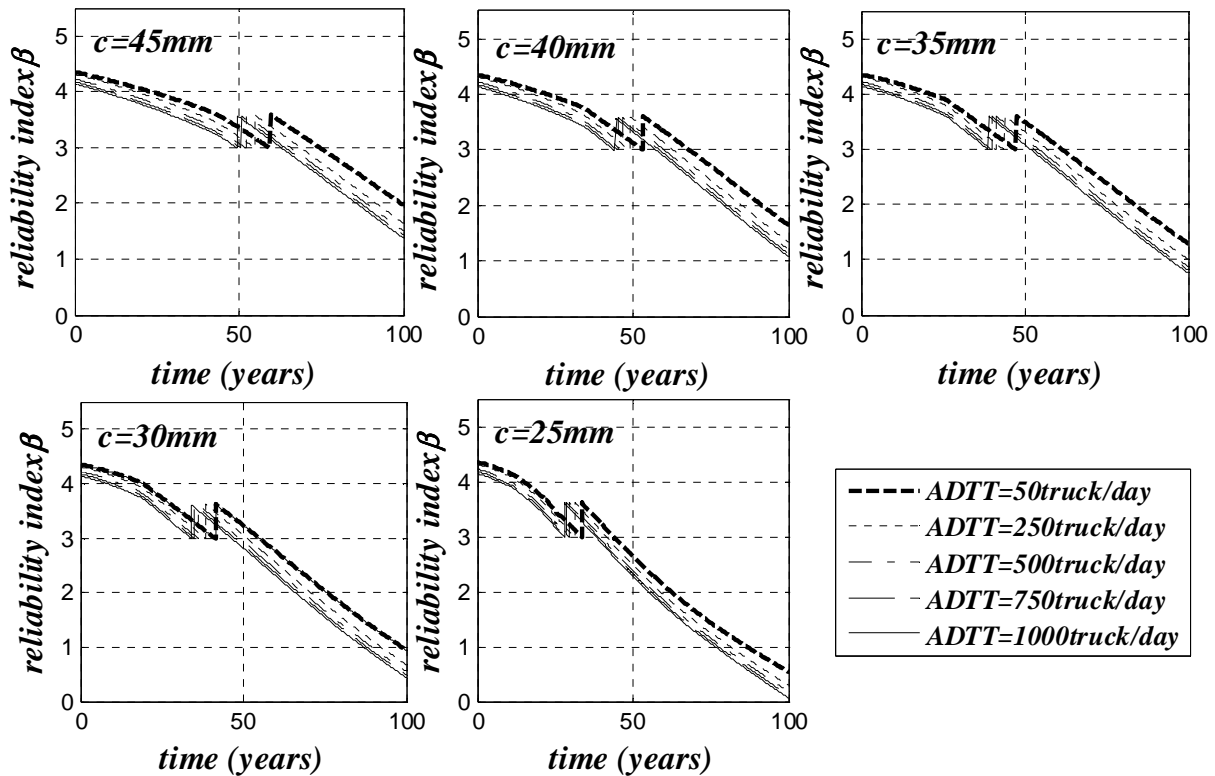
Figure C.6: Time-dependent flexural limit state reliability index of FRP strengthened RC, with non-anchorage laminates, beam under pitting corrosion and growth of live load over time.
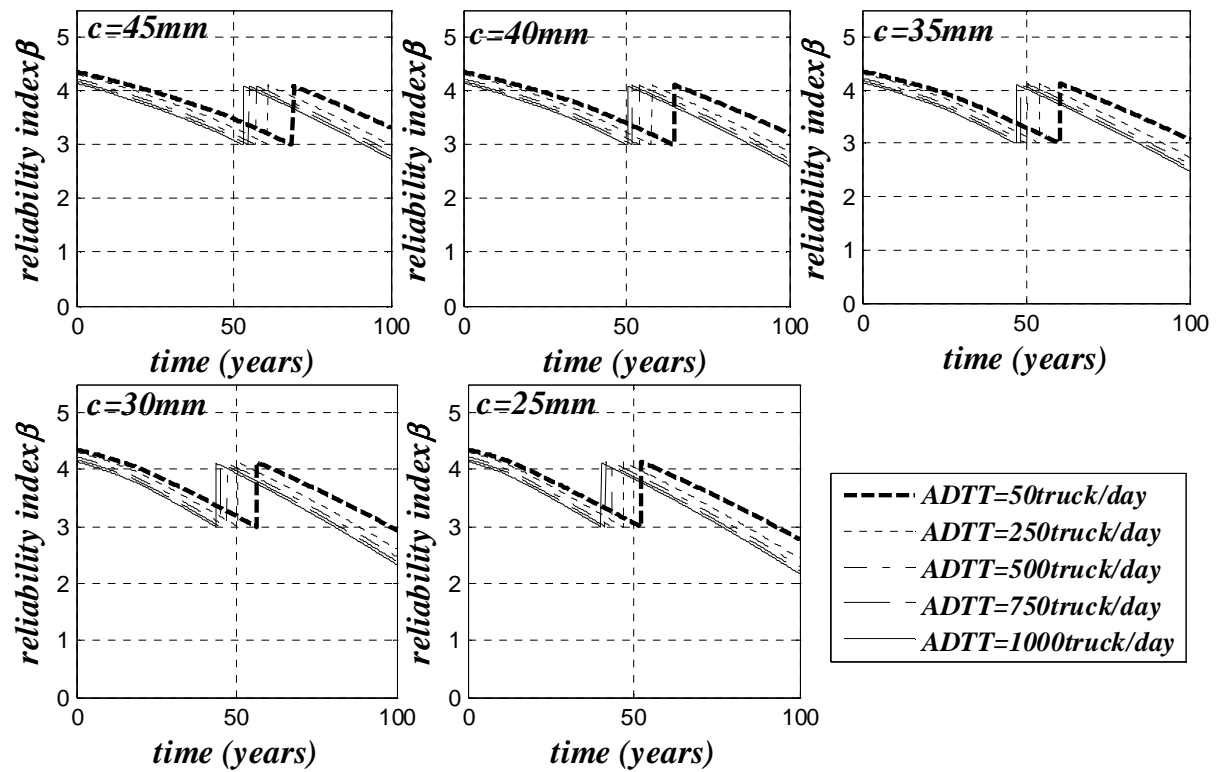
Figure C.7: Time-dependent flexural limit state reliability index of FRP strengthened RC, with anchorage laminates, beam under uniform corrosion and growth of live load over time.
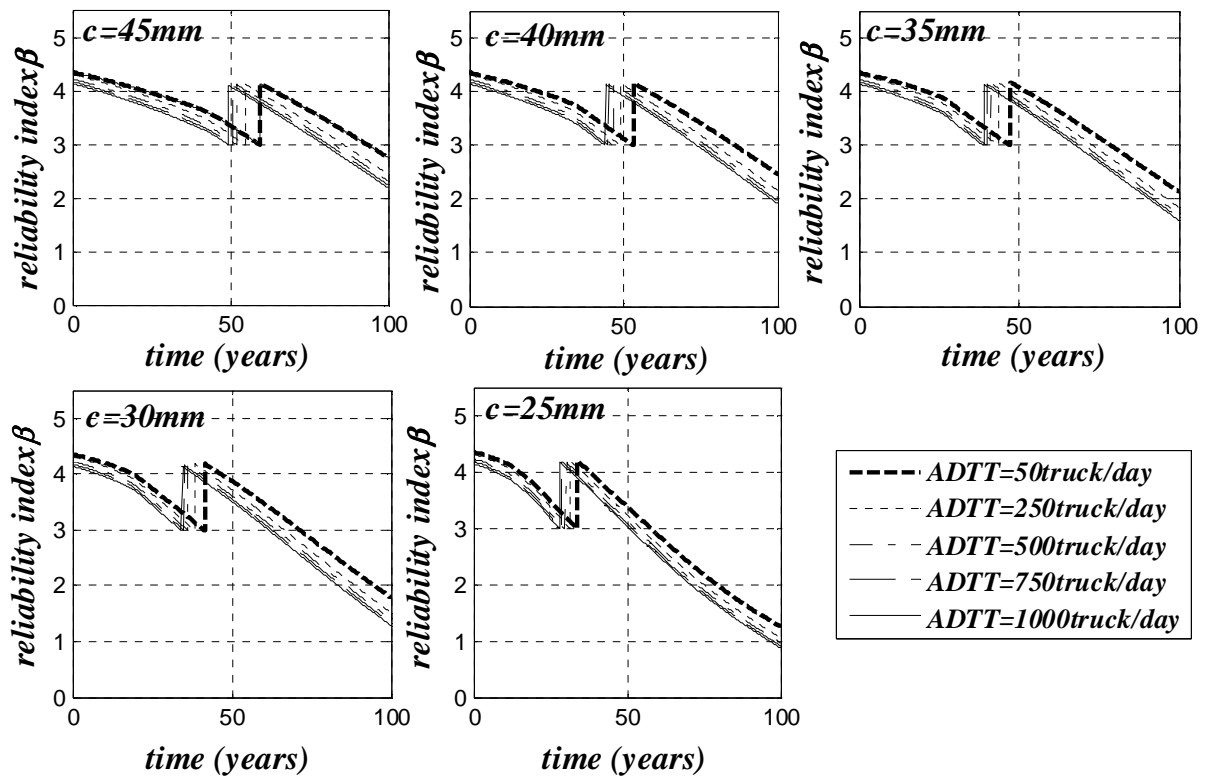
Figure C.8: Time-dependent flexural limit state reliability index of FRP strengthened RC, with anchorage laminates, beam under pitting corrosion and growth of live load over time.

Table C.1: Minimum & maximum values of relative importance factor of flexural limit state design variable; non-strengthened RC beam.

variable	Deterioration factor				
	Growth of live load	Uniform corrosion	Pitting corrosion	Growth of live load & uniform corrosion	Growth of live load & pitting corrosion
f_c	0.007:0.008	0.007:0.008	0.004:0.008	0.006:0.008	0.006:0.008
E_c	0.00	0.00	0.00	0.00	0.00
f_y	0.367:0.471	0.366:0.419	0.183:0.391	0.367:0.479	0.310:0.430
A_s	0.089:0.114	0.088:0.319	0.090:0.936	0.089:0.356	0.088:0.775
d_s	0.070:0.087	0.069:0.079	0.034:0.075	0.07:0.09	0.058:0.081
b_c	0.002	0.002	0.001:0.002	0.001:0.002	0.001:0.002
DL	-0.132:-0.108	-0.152:-0.134	-0.144:-0.076	-0.132:-0.111	-0.132:-0.089
LL	-0.390:-0.247	-0.337:-0.246	-0.319:0.127	-0.398:-0.247	-0.358:-0.247
λ_{flex}	0.776:0.878	0.768-0.879	0.250:0.879	0.685:0.878	0.423:0.878

Table C.2: Minimum & maximum values of relative importance factor of flexural limit state design variable; FRP strengthened RC beam with non-anchorage end laminates.

| variable		Deterioration factor				
		Growth of live load	Uniform corrosion	Pitting corrosion	Growth of live load & uniform corrosion	Growth of live load & pitting corrosion
f_c	B.S	0.007:0.008		0.006:0.008	0.006:0.008	0.006:0.008
	A.S	0.015-0.016		0.006:0.012	0.006:0.016	0.006:0.014
E_c	B.S	0.00		0.00	0.00	0.00
	A.S	0.00		0.00	0.00	0.00
f_y	B.S	0.383:0.442		0.334:0.395	0.334:0.437	0.334:0.418
	A.S	0.383:0.400		0.143:0.329	0.143:0.412	0.143:0.371
A_s	B.S	0.094:0.109		0.089:0.701	0.089:0.701	0.089:0.701
	A.S	0.094:0.098	Strengthening is not required	0.526:0.936	0.173:0.936	0.330:0.936
d_s	B.S	0.073:0.084		0.063:0.074	0.063:0.083	0.063:0.079
	A.S	0.084:0.089		0.039:0.078	0.039-0.099	0.039:0.085
b_c	B.S	0.002		0.002	0.002	0.002
	A.S	0.017:0.018		0.006:0.015	0.006-0.018	0.006:0.016
$f_{CFRP,u}$	B.S	0.00		0.00	0.00	0.00
	A.S	0.00		0.00	0.00	0.00
E_{CFRP}	B.S	0.00		0.00	0.00	0.00
	A.S	0.035:0.36		0.051:0.068	0.038:0.066	0.042:0.066
t_{CFRP}	B.S	0.00		0.00	0.00	0.00
	A.S	0.033:0.035		0.033:0.046	0.033:0.045	0.033:0.045
DL	B.S	-0.132:-0.119		-0.144:-0.131	-0.140:-0.122	-0.140:-0.122
	A.S	-0.120:-0.115		-0.151:-0.083	-0.140:-0.083	-0.140:-0.083
LL	B.S	-0.353:-0.299		-0.313:-0.231	-0.347:-0.231	-0.329:-0.231
	A.S	-0.410:-0.392		-0.319:-0.139	-0.427:-0.139	-0.390:-0.139
λ_{flex}	B.S	0.803:0.863		0.540:0.878	0.540:0.878	0.540:0.878
	A.S	0.799:0.817		0.262:0.713	0.262:0.809	0.262:0.769

B.S. denotes before strengthening; A.S. denotes after strengthening.

Table C.3: Minimum & maximum values of relative importance factor of flexural limit state design variable; FRP strengthened RC beam with anchorage end laminates.

variable		Deterioration factor				
		Growth of live load	Uniform corrosion	Pitting corrosion	Growth of live load & uniform corrosion	Growth of live load & pitting corrosion
f_c	B.S	0.007:0.008		0.006:0.008	0.006:0.008	0.006:0.008
	A.S	0.011		0.005:0.011	0.006:0.011	0.006:0.011
E_c	B.S	0.00		0.00	0.00	0.00
	A.S	0.00		0.00	0.00	0.00
f_y	B.S	0.383:0.442		0.334:0.395	0.334:0.437	0.334:0.418
	A.S	0.297:0.314		0.143:0.302	0.143:0.325	0.143:0.302
A_s	B.S	0.094:0.109		0.089:0.701	0.089:0.701	0.089:0.701
	A.S	0.073:0.077		0.402:0.936	0.135:0.936	0.265:0.936
d_s	B.S	0.073:0.084	Strengthening is not required	0.063:0.074	0.063:0.083	0.063:0.079
	A.S	0.071:0.076		0.039:0.072	0.039:0.082	0.039:0.077
b_c	B.S	0.002		0.002	0.002	0.002
	A.S	0.012:0.013		0.006:0.014	0.006:0.014	0.006:0.014
$f_{CFRP,u}$	B.S	0.00		0.00	0.00	0.00
	A.S	0.211-0.221		0.000:0.321	0.000:0.26	0.000:0.276
E_{CFRP}	B.S	0.00		0.00	0.00	0.00
	A.S	-0.047:-0.044		-0.043:0.066	-0.049:0.066	-0.047:0.066
t_{CFRP}	B.S	0.00		0.00	0.00	0.00
	A.S	0.042:0.044		0.033:0.064	0.033:0.056	0.033:0.065
DL	B.S	-0.132:-0.119		-0.140:-0.131	-0.140:-0.122	-0.140:-0.122
	A.S	-0.101:-0.098		-0.140:-0.083	-0.140:-0.083	-0.140:-0.083
LL	B.S	-0.353:-0.299		-0.313:-0.231	-0.347:-0.231	-0.329:-0.231
	A.S	-0.349:-0.329		-0.311:-0.139	-0.374:-0.139	-0.354:-0.139
λ_{flex}	B.S	0.803:0.863		0.540:0.878	0.540:0.878	0.540:0.878
	A.S	0.840:0.857		0.262:0.785	0.262:0.851	0.262:0.822

B.S. denotes before strengthening; A.S. denotes after strengthening.
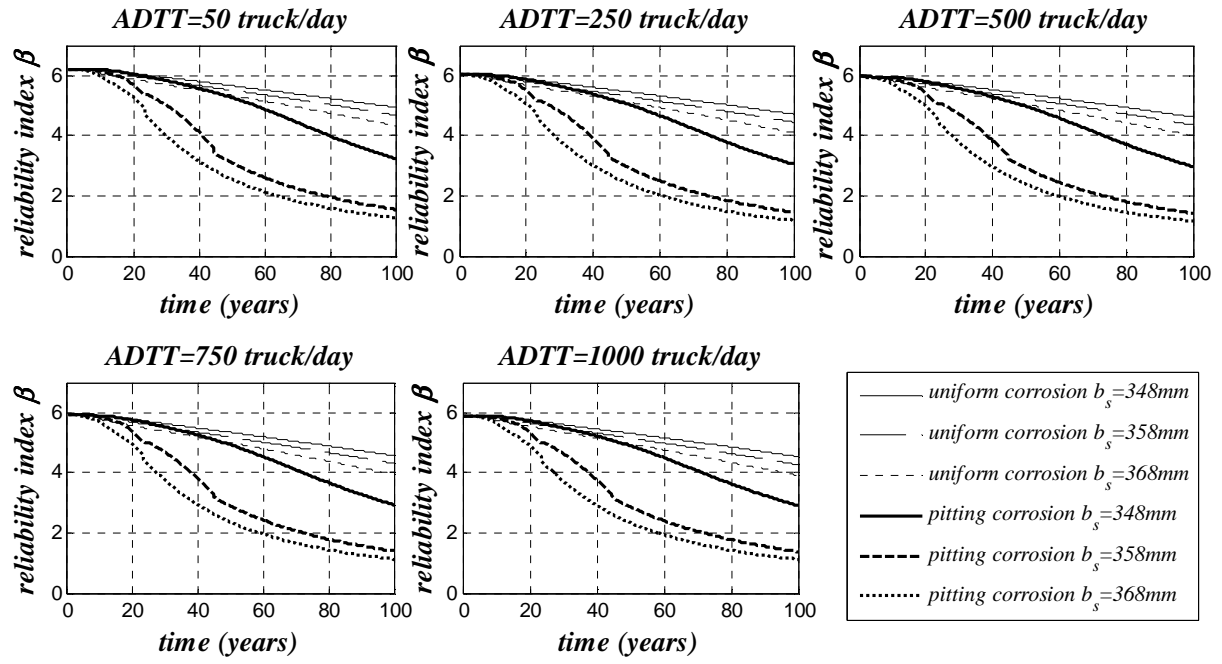
Figure C.9: Time-dependent shear limit state reliability index of RC beam under corrosion.
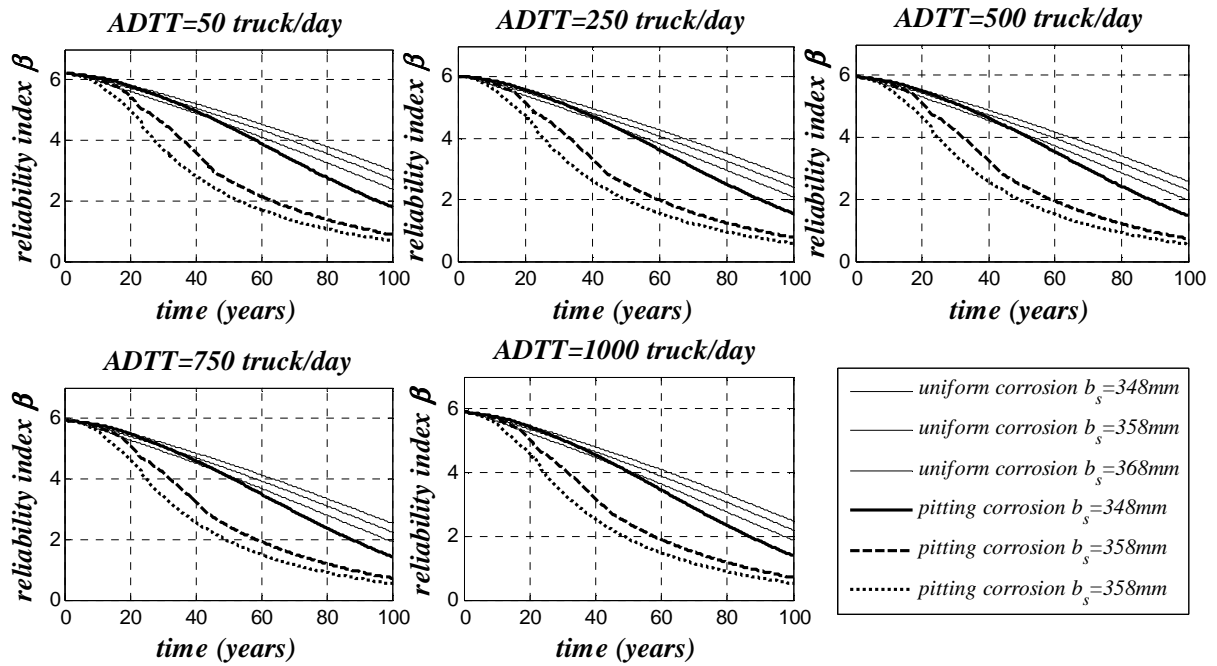
Figure C.10: Time-dependent shear limit state reliability index of RC beam under corrosion and growth of live load over time.

Table C.4: Maximum & minimum values of relative importance factor of shear limit state design variable; non-strengthened RC beam.

variable	Deterioration factor				
	Growth of live load	Uniform corrosion	Pitting corrosion	Growth of live load & uniform corrosion	Growth of live load & pitting corrosion
f_{yv}	0.000:0.041	0.000:0.001	0.000:0.001	0.000:0.001	0.000:0.001
A_{sv}	0.041:0.062	0.043:0.488	0.041:0.972	0.044:0.499	0.041:0.971
f_c	0.121:0.179	0.121:0.307	0.121:0.294	0.121:0.293	0.109:0.275
b_c	0.013:0.019	0.013:0.031	0.013:0.030	0.013:0.033	0.013:0.029
d_s	0.052:0.077	0.052:0.073	0.020:0.067	0.052:0.086	0.024:0.073
s_v	-0.244:-0.164	-0.177:-0.098	-0.177:0.062	-0.205:-0.144	-0.190:0.020
LL	-0.417:-0.312	-0.450:-0.312	-0.420:-0.112	-0.470:-0.312	-0.435:-0.131
DL	-0.098:-0.091	-0.131:-0.097	-0.121:-0.044	-0.114:-0.097	-0.114:-0.036
$\lambda_{sh,RC}$	0.848:0.916	0.677:0.916	0.136:0.916	0.653:0.916	0.163:0.916

Table C.5: Minimum & maximum values of relative importance factor of shear limit state design variable; FRP strengthened RC beam.

variable	Deterioration factor				
	Growth of live load	Uniform corrosion	Pitting corrosion	Growth of live load & uniform corrosion	Growth of live load & pitting corrosion
f_{yv}			0.000	0.000	0.000
A_{sv}			0.099:0.138	0.229:0.494	0.188:0.507
E_{FRP}			0.014:0.029	-0.021:0.030	-0.041:0.030
$f_{FRP,u}$	Strengthening is not required	Strengthening is not required	-0.065:-0.032	-0.069:0.054	-0.069:0.113
t_{FRP}			-0.017:-0.008	-0.018:0.012	-0.017:0.024
f_c			0.073:0.078	0.073:0.078	0.070:0.079
b_c			0.007:0.008	0.007:0.010	0.007:0.011
d_s			0.017:0.020	0.011:0.013	0.013:0.020
s_v			-0.069:-0.049	-0.034:0.059	-0.059:0.052
LL			-0.107:-0.094	-0.068:-0.065	-0.107:-0.075
DL			-0.027:-0.026	-0.026:-0.025	-0.027:-0.024
$\lambda_{sh,RC}$			0.174:0.198	0.045:0.150	0.0539:0.184
$\lambda_{sh,FRP}$			0.961:0.965	0.858:0.953	0.840:0.953

APPENDICES

Appendix D: Abaqus input files

D.1 Abaqus input file example of dataset required for live load model (see § III.1.2.3.1).

```
*HEADING
case=810
*PREPRINT, ECHO=NO, MODEL=NO, HISTORY=NO
**--------------------Deck nodes------------
*NODE
1,    00000.0, 0.0,  0000.0
51,   10000.0, 0.0,  0000.0
2041, 00000.0, 0.0, -8000.0
2091, 10000.0, 0.0, -8000.0
*NGEN, NSET=lower_line
1,51,1
*NGEN,  NSET=upper_line
2041,2091,1
*NFILL, NSET=surf
lower_line,upper_line,40,51
*NSET, NSET=mid
740
*NSET, NSET=beam_weight
154,204,1
715,765,1
1327,1377,1
1888,1938,1
*NSET, NSET=support
154
*NSET, NSET=load_max
515,536,974,995,1556,1577,1097,1118
*NSET, NSET=load_min
557,1016,1535,1076
**----------------------------- slab ---------------------
*ELEMENT, TYPE=S4R, ELSET=slab
1, 1,2,53,52
*ELGEN,  ELSET=slab
1,50,1,1,40,51,50
*SHELL SECTION, ELSET=slab, MATERIAL=concrete,  CONTROLS=CONT
250.0
*REBAR LAYER
L_main_slab_rft,113.097, 150.0, -104.0, steel, 90.0, 1
U_main_slab_rft,113.097, 150.0,  104.0, steel, 90.0, 1
L_sec_slab_rft, 78.5398, 150.0, -104.0, steel, 0.00, 1
U_sec_slab_rft, 78.5398, 150.0,  104.0, steel, 0.00, 1
**----------------------------- beams ---------------------
*ELEMENT, TYPE=B21, ELSET=beam
10001, 154,155
10051, 715,716
10101, 1327,1328
10151, 1888,1889
*ELGEN,  ELSET=beam
10001,50,1,1
10051,50,1,1
10101,50,1,1
10151,50,1,1
```

```
*BEAM SECTION, SECTION=RECT, ELSET=beam, MATERIAL=concrete
400,950
,
15
*REBAR, ELEMENT=BEAM,  MATERIAL=steel, NAME=st_beam_lower1
beam,490.625,22.5,-425
*REBAR, ELEMENT=BEAM,  MATERIAL=steel, NAME=st_beam_lower2
beam,490.625,-22.5,-425
*REBAR, ELEMENT=BEAM,  MATERIAL=steel, NAME=st_beam_lower3
beam,490.625,72.5,-425
*REBAR, ELEMENT=BEAM,  MATERIAL=steel, NAME=st_beam_lower4
beam,490.625,-72.5,-425
*REBAR, ELEMENT=BEAM,  MATERIAL=steel, NAME=st_beam_lower5
beam,490.625,122.5,-425
*REBAR, ELEMENT=BEAM,  MATERIAL=steel, NAME=st_beam_lower6
beam,490.625,-122.5,-425
*REBAR, ELEMENT=BEAM,  MATERIAL=steel, NAME=st_beam_lower7
beam,490.625,172.5,-425
*REBAR, ELEMENT=BEAM,  MATERIAL=steel, NAME=st_beam_lower8
beam,490.625,-172.5,-425
*REBAR, ELEMENT=BEAM,  MATERIAL=steel, NAME=st_beam_upper1
beam,314,0.0000,425
*REBAR, ELEMENT=BEAM,  MATERIAL=steel, NAME=st_beam_upper2
beam,314,152.5,425
*REBAR, ELEMENT=BEAM,  MATERIAL=steel, NAME=st_beam_upper3
beam,314,-152.5,425
*ELSET, ELSET=all, GENERATE
1,2000,1
*ELSET, ELSET=b1, GENERATE
10051,10100,1
**----------------------------- concrete beams--------------
*section controls, name=CONT, element deletion=no, max degradation=0.95
*MATERIAL,  NAME=concrete
*ELASTIC
32642,0.2
*CONCRETE DAMAGED PLASTICITY
35.0,0.10,1.16,0.6667
*CONCRETE COMPRESSION HARDENING
15.560,0.0000000000
19.081,0.0000975027
22.283,0.0001451778
25.155,0.0002030103
27.685,0.0002713451
29.862,0.0003505427
31.673,0.0004409804
33.107,0.0005430531
34.148,0.0006571746
34.784,0.0007837783
35.000,0.0009233188
32.338,0.0015051882
23.872,0.0022656265
*CONCRETE TENSION STIFFENING, TYPE=DISPLACEMENT
3.209966 , 0.000000
0.000000 , 0.209752
**----------------------------- steel --------------
*MATERIAL,  NAME=steel
*ELASTIC
201300.0,0.3
*PLASTIC
414.0,0.0
**--------------------------------- CONCRETE BEAMS -------------------
```

```
*STEP, NAME=ST1, INC=10000
appling dead and live loads
*STATIC
0.25, 1.0, 0.000000001 , 1.0
*CONTROLS, PARAMETERS=FIELD
0.01,,,
,,
*BOUNDARY
154,    1
154,    2
154,    3
715,    1
715,    2
715,    3
1327,   1
1327,   2
1327,   3
1888,   1
1888,   2
1888,   3
204,    2
204,    3
765,    2
765,    3
1377,   2
1377,   3
1938,   2
1938,   3
*CLOAD
beam_weight,2,-1152
load_max,2,-288889
load_min,2,-72222.2
*DLOAD
all, P, -0.0060
all, P, -0.00162
*NODE PRINT, FREQUENCY=1, NSET=support, SUMMARY=NO, TOTALS=yes, GLOBAL=NO
RF2
*NODE PRINT, FREQUENCY=1, NSET=mid,      SUMMARY=NO, TOTALS=NO,  GLOBAL=NO
U2
*EL PRINT, FREQUENCY=1, ELSET=b1,    POSITION= NODES
SM1
*END STEP
```

D.2 Abaqus input file example of dataset required for serviceability limit state (see §
III.2.2.2).

```
*HEADING
case=108
*PREPRINT, ECHO=NO, MODEL=NO, HISTORY=NO
**--------------------Deck nodes------------
*NODE
1,      0.0,      0.0,      0.0
2,      200.0,    0.0,      0.0
10,     600.0,    0.0,      0.0
58,     10200.0, 0.0,       0.0
66,     10600.0, 0.0,       0.0
67,     10800.0, 0.0,       0.0
2681,  0.0,      0.0,      -8000.0
2682,  200.0,    0.0,      -8000.0
2690,  600.0,    0.0,      -8000.0
2738,  10200.0, 0.0,       -8000.0
2746,  10600.0, 0.0,       -8000.0
2747,  10800.0, 0.0,       -8000.0
*NGEN, NSET=lower_line
2,     10, 1
10,    58, 1
58,    66, 1
1,     67, 66
*NGEN,  NSET=upper_line
2682, 2690, 1
2690, 2738, 1
2738, 2746, 1
2681, 2747, 66
*NFILL, NSET=surf
lower_line,upper_line,40,67
*NGEN, NSET=line_a
203,   211,  1
211,   259,  1
259,   267,  1
202,   268,  66
*NCOPY, CHANGE NUMBER=2799, OLD SET=line_a, NEW SET=line_a1, SHIFT
0.0,-880.0,0.0
0.0,      0.0,    0.0, 200.0,   0.0,    0.0, 0.0
*NGEN, NSET=line_b
940,   948,  1
948,   996,  1
996,   1004, 1
939,   1005, 66
*NCOPY, CHANGE NUMBER=3062, OLD SET=line_b, NEW SET=line_b1, SHIFT
0.0,-880.0,0.0
0.0,      0.0,    0.0, 200.0,   0.0,    0.0, 0.0
*NGEN, NSET=line_c
1744,   1752,  1
1752,   1800,  1
1800,   1808,  1
1743,   1809,  66
*NCOPY, CHANGE NUMBER=3258, OLD SET=line_c, NEW SET=line_c1, SHIFT
0.0,-880.0,0.0
0.0,      0.0,    0.0, 200.0,   0.0,    0.0, 0.0
*NGEN, NSET=line_d
2481,   2489,  1
2489,   2537,  1
2537,   2545,  1
2480,   2546,  66
```

```
*NCOPY, CHANGE NUMBER=3521, OLD SET=line_d, NEW SET=line_d1, SHIFT
0.0,-880.0,0.0
0.0,      0.0,    0.0, 200.0,   0.0,    0.0, 0.0
*NSET, NSET=line0
line_a1,line_b1,line_c1,line_d1
*NCOPY, CHANGE NUMBER=67,   OLD SET=line0, NEW SET=line1, SHIFT
0.0, 40.0,0.0
0.0, 0.0,    0.0, 200.0,   0.0,    0.0, 0.0
*NCOPY, CHANGE NUMBER=67,   OLD SET=line1, NEW SET=line2, SHIFT
0.0, 40.0,0.0
0.0, 0.0,    0.0, 200.0,   0.0,    0.0, 0.0
*NCOPY, CHANGE NUMBER=67,   OLD SET=line2, NEW SET=line3, SHIFT
0.0, 187.5,0.0
0.0, 0.0,    0.0, 200.0,   0.0,    0.0, 0.0
*NCOPY, CHANGE NUMBER=67,   OLD SET=line3, NEW SET=line4, SHIFT
0.0, 187.5,0.0
0.0, 0.0,    0.0, 200.0,   0.0,    0.0, 0.0
*NCOPY, CHANGE NUMBER=67,   OLD SET=line4, NEW SET=line5, SHIFT
0.0, 187.5,0.0
0.0, 0.0,    0.0, 200.0,   0.0,    0.0, 0.0
*NCOPY, CHANGE NUMBER=67,   OLD SET=line5, NEW SET=line6, SHIFT
0.0, 187.5,0.0
0.0, 0.0,    0.0, 200.0,   0.0,    0.0, 0.0
*NSET, NSET=roller_support
3006,4006,5006,6006
*NSET, NSET=hinge_support
3062,4062,5062,6062
*NSET, NSET=mid
4101
*NSET, NSET=beam_load, GENERATE
203,    211,  4
211,    259,  1
259,    267,  4
202,    268,  66
940,    948,  4
948,    996,  1
996,    1004,  4
939,    1005,  66
1744,   1752,  4
1752,   1800,  1
1800,   1808,  4
1743,   1809,  66
2481,   2489,  4
2489,   2537,  1
2537,   2545,  4
2480,   2546,  66
*NSET, NSET=beam_surf
line0,line1,line2,line3,line4,line5,line6
*NSET, NSET=load_max1
147,168,750,771
*NSET, NSET=load_min1
189,792
*NSET, NSET=load_max2
1709,1730,1642,1663,2312,2333,2245,2266
*NSET, NSET=load_min2
2291,2224,1688,1621
**------------------------------ slab ---------------------
*ELEMENT, TYPE=S4R, ELSET=slab
1, 1,2,69,68
*ELGEN,  ELSET=slab
1,66,1,1,40,67,66
```

```
*SHELL SECTION, ELSET=slab, MATERIAL=concrete,  CONTROLS=CONT
250.0
*REBAR LAYER
L_main_slab_rft,113.097, 150.0, -104.0, slab_st, 90.0, 1
U_main_slab_rft,113.097, 150.0,  104.0, slab_st, 90.0, 1
L_sec_slab_rft, 78.5398, 150.0, -104.0, slab_st, 0.00, 1
U_sec_slab_rft, 78.5398, 150.0,  104.0, slab_st, 0.00, 1
*MATERIAL,  NAME=slab_st
*density
7.85E-9
*DAMPING, STRUCTURAL=0.25
*ELASTIC
201300.0,0.3
*PLASTIC
460.0,0
**----------------------------- beams ----------------------
*ELEMENT, TYPE=S4R, ELSET=beam
3001, 3068, 3069, 3136, 3135
3331, 3403, 3404, 203,  202
4331, 4403, 4404, 940,  939
5331, 5403, 5404, 1744, 1743
6331, 6403, 6404, 2481, 2480
*ELGEN,  ELSET=beam
3001, 66,1,1,5,67,66,4,1000,1000
3331, 66,1,1
4331, 66,1,1
5331, 66,1,1
6331, 66,1,1
*SHELL SECTION, ELSET=beam, MATERIAL=concrete, CONTROLS=CONT
400.0
**----------------------------- concrete material ----------
*section controls, name=CONT, element deletion=no, max degradation=0.95
*MATERIAL,  NAME=concrete
*density
2.4E-9
*DAMPING, STRUCTURAL=0.25
*ELASTIC
30154.096471,0.2
*CONCRETE DAMAGED PLASTICITY
30.0,0.10,1.16,0.6667
*CONCRETE COMPRESSION HARDENING
10.261083,0.000000
15.952964,0.000196
19.965033,0.000381
22.580786,0.000613
24.023322,0.000884
24.470617,0.001188
24.111739,0.001500
23.097466,0.001834
21.509659,0.002187
20.367263,0.002397
*CONCRETE TENSION STIFFENING, TYPE=DISPLACEMENT
2.528628,0.000000
1.291717,0.021170
0.755081,0.042341
0.525968,0.063511
0.403687,0.084681
0.311343,0.105852
0.228623,0.127022
0.154443,0.148192
0.091201,0.169363
```

```
0.091201,0.190533
0.000000,1.058516
**------------------------------ support_steel --------
*ELEMENT, TYPE=S4R, ELSET=support
3397,3003,3004,3071,3070
3403,3059,3060,3127,3126
*ELGEN,  ELSET=support
3397, 6, 1, 1, 4, 1000, 1000
3403, 6, 1, 1, 4, 1000, 1000
*SHELL SECTION, ELSET=support, MATERIAL=support_steel
400.0
*MATERIAL,  NAME=support_steel
*density
7.85E-9
*DAMPING, STRUCTURAL=0.25
*ELASTIC
2013000000.0,0.3
**------------------------------ MAIN_steel --------
*ELEMENT, TYPE=T3D2, ELSET=BARS1
3409,3135,3136
*ELGEN,  ELSET=BARS1
3409,66,1,1,4,1000,1000
*SOLID SECTION, ELSET=BARS1, MATERIAL=lower_steel
2887.993287
*MATERIAL,  NAME=lower_steel
*density
7.85E-9
*DAMPING, STRUCTURAL=0.25
*ELASTIC
201300.0,0.3
*PLASTIC
450.748815,0.0
**--------------------------------- upper steel -------------------
*ELEMENT, TYPE=T3D2, ELSET=BARS2
3475, 202,  203
4475, 939,  940
5475, 1743, 1744
6475, 2480, 2481
*ELGEN,  ELSET=BARS2
3475,66,1,1
4475,66,1,1
5475,66,1,1
6475,66,1,1
*SOLID SECTION, ELSET=BARS2, MATERIAL=upper_steel
942.5
*MATERIAL,  NAME=upper_steel
*density
7.85E-9
*DAMPING, STRUCTURAL=0.25
*ELASTIC
201300.0,0.3
*PLASTIC
460.0,0.0
**--------------------------------- side bar steel -------------------
*ELEMENT, TYPE=T3D2, ELSET=BARS4
3541,3269,3270
*ELGEN,  ELSET=BARS4
3541,66,1,1,4,1000,1000
*SOLID SECTION, ELSET=BARS4, MATERIAL=side_steel
226.2
*MATERIAL,  NAME=side_steel
```

```
*density
7.85E-9
*DAMPING, STRUCTURAL=0.25
*ELASTIC
201300.0,0.3
*PLASTIC
460.0,0.0
**--------------------------- CFRP -----------------------
*ELEMENT, TYPE=T3D2, ELSET=CFRP
3607,3077,3078
*ELGEN,  ELSET=CFRP
3607,48,1,1,4,1000,1000
*SOLID SECTION, ELSET=CFRP, MATERIAL=CFRP_PLATE
762.0
*MATERIAL, NAME=CFRP_PLATE
*density
1.8E-9
*DAMPING, STRUCTURAL=0.25
*ELASTIC
51700.000000,0.3
**-------------------------------- stirrups steel ----------------
*ELEMENT, TYPE=T3D2, ELSET=BARS5
3655, 3135, 3202
3656, 3136, 3203
3658, 3144, 3211
3706, 3192, 3259
3709, 3201, 3268
3875, 3403, 202
4875, 4403, 939
5875, 5403, 1743
6875, 6403, 2480
*ELGEN,  ELSET=BARS5
3655, 4,  67, 55, 4, 1000, 1000
3656, 2,  4,  1,  4, 67,   55,  4, 1000, 1000
3658, 48, 1,  1,  4, 67,   55,  4, 1000, 1000
3706, 3,  4,  1,  4, 67,   55,  4, 1000, 1000
3709, 4,  67, 55, 4, 1000, 1000
3875, 2,  1,  1
4875, 2,  1,  1
5875, 2,  1,  1
6875, 2,  1,  1
3876, 3,  4,  1
4876, 3,  4,  1
5876, 3,  4,  1
6876, 3,  4,  1
3878, 49, 1,  1
4878, 49, 1,  1
5878, 49, 1,  1
6878, 49, 1,  1
3926, 3,  4,  1
4926, 3,  4,  1
5926, 3,  4,  1
6926, 3,  4,  1
3928, 2,  1,  1
4928, 2,  1,  1
5928, 2,  1,  1
6928, 2,  1,  1
*SOLID SECTION, ELSET=BARS5, MATERIAL=stirrups_steel
226.2
*MATERIAL,  NAME=stirrups_steel
*density
```

```
7.85E-9
*DAMPING, STRUCTURAL=0.25
*ELASTIC
201300.0,0.3
*PLASTIC
460.0,0.0
**------------------------------ step --------------
*BOUNDARY
roller_support,2
roller_support,3
hinge_support ,1
hinge_support ,2
hinge_support ,3
surf,    3
surf,    5
beam_surf,      3
beam_surf,      4
beam_surf,      5
*AMPLITUDE,NAME=P1, value=relative, smooth=0.01, DEFINITION=SMOOTH STEP
0.0,0.0,   1.5,1.0
*STEP, NAME=ST1
*Dynamic, Explicit, FIXED TIME INCREMENTATION
, 1.5
*FIXED MASS SCALING, DT=0.75E-5, TYPE=BELOW MIN, FACTOR=1
*DLOAD, AMPLITUDE=P1
slab, P,-0.0100583
*CLOAD, AMPLITUDE=P1
beam_load,2,-1495.29
load_max1,2,-226970
load_min1,2,-56742.5
load_max2,2,-113485
load_min2,2,-28371.2
*FILE OUTPUT, NUMBER INTERVAL=50, TIME MARKS=NO
*EL FILE,   ELSET=beam
S
LE
*NODE FILE, NSET=mid
U
**************************************************
*OUTPUT,FIELD,VARIABLE=PRESELECT, NUMBER INTERVAL=50
*ELEMENT OUTPUT,   ELSET=beam,POSITION=NODES
LE,S
*ELEMENT OUTPUT,   ELSET=CFRP, POSITION=NODES
LE,S
*NODE  OUTPUT,     NSET=mid
U
**************************************************
*OUTPUT,HISTORY,VARIABLE=PRESELECT,TIME INTERVAL=0.05
*ELEMENT OUTPUT,   ELSET=beam
LE,S11
*ELEMENT OUTPUT,   ELSET=CFRP
LE,S
*NODE  OUTPUT,     NSET=mid
U2
*END STEP
```

D.3 Abaqus input file example of dataset required for flexural limit state (see § III.2.2.3).

```
*HEADING
case=155
*PREPRINT, ECHO=NO, MODEL=NO, HISTORY=NO
**--------------------Deck nodes------------
*NODE
1,        0.0000, 0.0000, 0.0000
865,      5400.0, 0.0000, 0.0000
6921,     0.0000, 40.000, 0.0000
7785,     5400.0, 40.000, 0.0000
117641,   0.0000, 840.00, 0.0000
118505,   5400.0, 840.00, 0.0000
118506,   0.0000, -1.000, 0.0000
119370,   5400.0, -1.000, 0.0000
119371,   0.0000, -20.00, 0.0000
120235,   5400.0, -20.00, 0.0000
130001,   5099.9, 0.0000, 0.0000
136921,   5100.0, 40.000, 0.0000
136922,   5099.9, -1.000, 0.0000
*NGEN
1,      865,     1
6921,   7785,    1
117641, 118505,  1
118506, 119370,  1
119371, 120235,  1
130001, 136921,  865
*NGEN,    NSET=raw_1
1, 865,         1
*NGEN,    NSET=raw_2
6921, 7785,     1
*NGEN,    NSET=raw_3
117641, 118505, 1
*NFILL
raw_1, raw_2, 8,    865
raw_2, raw_3, 128,  865
*NSET, NSET=support
119435
*NSET, NSET=side, GENERATE
865, 119370,  865
*NSET, NSET=mid
865
**--------------------------- CONCRETE (ELEMENTS AND MATERIALS)
--
*ELEMENT, TYPE=CPS4R, ELSET=beam
1   , 1,      9,      6929, 6921
24  , 185,    193,    7113, 7105
649 , 41521, 41529, 48449, 48441
8001, 857,    865,    7785, 7777
1837, 105,    113,    3573, 3569
1838, 105,    3569,   7029, 7025
1839, 7025,   7029,   10489, 13945
1840, 10489, 10493, 13953, 13945
1849, 3569,   3573,   7033, 7029
1861, 177,    185,    3641, 3637
```

```
1862, 3641,   185,    7105,   7101
1863, 7101,   7105,   14025,  10561
1864, 10557,  10561,  14025,  14017
1873, 113,    117,    3577,   3573
1913, 27801,  27805,  31265,  31261
1937, 34713,  34717,  38177,  38173
1941, 34725,  34729,  38189,  38185
2241, 38173,  38177,  41641,  41633
2245, 34717,  34721,  41641,  38177
2249, 121,    125,    1855,   1853
2253, 121,    1853,   3583,   3581
2257, 3581,   3583,   5313,   7041
2261, 5313,   5315,   7045,   7041
2265, 1853,   1855,   3585,   3583
2277, 125,    127,    1857,   1855
2329, 22613,  22615,  24345,  24343
2351, 24343,  24345,  26075,  26073
2780, 26075,  26077,  27809,  27805
2781, 24347,  24349,  27809,  26077
2798, 165,    169,    1897,   1895
2799, 1897,   169,    3629,   3627
2806, 20889,  20891,  22621,  22619
2822, 129,    131,    996,    995
2828, 129,    995,    1860,   1859
2834, 1859,   1860,   2725,   3589
2835, 2725,   2726,   3591,   3589
2860, 20026,  20027,  20893,  20891
2861, 19162,  19163,  20893,  20027
2894, 159,    161,    1025,   1024
2895, 1025,   161,    1891,   1890
2906, 995,    996,    1861,   1860
2930, 19161,  19162,  20027,  20026
2932, 19164,  19165,  20030,  20029
2944, 131,    132,    997,    996
8944, 803,    804,    1669,   1668
9168, 7723,   7724,   8589,   8588
8958, 817,    818,    1683,   1682
8957, 816,    130001, 130866,1681
9153, 6871,   136056, 7737,   7736
*ELGEN, ELSET=beam
1   , 13,  8,      1, 6, 6920, 108
24  , 74,  8,      1, 6, 6920, 108
649 , 108, 8,      1, 11,6920, 108
8001, 6,    6920,  1
8944, 13,  1,      1, 8, 865,  28
9168, 28,  1,      1, 14,865,  28
8958, 14,  1,      1, 8, 865,  28
8957, 7,    865, 28
*SOLID SECTION, ELSET=beam, MATERIAL=MAT11, CONTROLS=CONTT
400.0
*section controls, name=CONTT, element deletion=no, max
degradation=0.95
*ELGEN, ELSET=beam_fine_mesh1
1837, 3,    13840, 4
1838, 3,    13840, 4
1839, 3,    13840, 4
```

```
1840, 3,    13840, 4
1849, 2,    3460, 1, 2,   68,   2,    3, 13840, 4
1861, 3,    13840, 4
1862, 3,    13840, 4
1863, 3,    13840, 4
1864, 3,    13840, 4
1873, 2,    4,     1, 10, 3460, 2, 2, 56, 20
1913, 12,   4,     1, 2,   3460, 12
1937, 4,    16,    1
1941, 4,    16,    1
1847, 5,    16,    98
1848, 5,    16,    98
2241, 4,    16,    1
2245, 4,    16,    1
2249, 4,    6920,  1
2253, 4,    6920,  1
2257, 4,    6920,  1
2261, 4,    6920,  1
2265, 2,    1730,  1, 3,   6920, 2, 2, 42,  6
2277, 2,    2,     1, 13, 1730, 2, 2, 36,  26
2329, 22,   2,     1
2351, 2,    2,     1, 6,    8, 2
2260, 6,    8,     103
2264, 6,    8,     103
2780, 6,    8,     2
2781, 6,    8,     2
2790, 4,    -6920, 2
2791, 4,    -6920, 2
2798, 4,    6920,  2
2799, 4,    6920,  2
2806, 16,   2,     1
2822, 6,    3460,  1
2828, 6,    3460,  1
2834, 6,    3460,  2
2835, 6,    3460,  2
2844, 8,    4,     2
2845, 8,    4,     2
2860, 8,    4,     2
2861, 8,    4,     2
2874, 6,    -3460, 2
2875, 6,    -3460, 2
2894, 6,    3460,  2
2895, 6,    3460,  2
2906, 2,    865,   1, 6, 3460, 2, 2, 29,12
2930, 2,    27,    1
2932, 2,    1,     1, 6, 4, 2
*SOLID SECTION, ELSET=beam_fine_mesh1, MATERIAL=MAT11,
CONTROLS=CONTT2
400.0
*section controls, name=CONTT2, element deletion=no, max
degradation=0.95
*ELGEN, ELSET=beam_fine_mesh11
2944, 28, 1,      1, 22, 865,  28
*SOLID SECTION, ELSET=beam_fine_mesh11, MATERIAL=MAT11,
CONTROLS=CONTT22
400.0
```

```
*section controls, name=CONTT22, element deletion=no, max
degradation=0.95
*ELCOPY, ELEMENT SHIFT=6000,OLD SET=beam_fine_mesh1,SHIFT
NODES=672,NEW SET=beam_fine_mesh2
*SOLID SECTION, ELSET=beam_fine_mesh2, MATERIAL=MAT11,
CONTROLS=CONTT3
400.0
*section controls, name=CONTT3, element deletion=no, max
degradation=0.95
*MATERIAL,  NAME=MAT11
*density
2.4E-9
*DAMPING, STRUCTURAL=0.25
*ELASTIC
36791.514252,0.2
*CONCRETE DAMAGED PLASTICITY
30.0,0.10,1.16,0.6667
*CONCRETE COMPRESSION HARDENING
20.288690,0.000000
28.112545,0.000119
34.712167,0.000219
39.852058,0.000359
43.232181,0.000546
44.464221,0.000791
42.805422,0.001137
37.206024,0.001589
26.441020,0.002181
22.232111,0.002381
*CONCRETE TENSION STIFFENING, TYPE=DISPLACEMENT
1.506106,0.000000
0.769375,0.046781
0.449742,0.093561
0.313278,0.140342
0.240445,0.187122
0.185443,0.233903
0.136173,0.280683
0.091990,0.327464
0.054321,0.374244
0.054321,0.421025
0.000000,2.339027
*ELSET, ELSET=beam1, GENERATE
1750, 1836, 1
*ELSET, ELSET=raw_dist_load, GENERATE
1729, 1836, 1
*ELSET, ELSET=cover, GENERATE
2837, 2882, 45
2944, 3167, 1
**-------------------------------- support steel --------------
-----
*ELEMENT, TYPE=CPS4R, ELSET=support
3801, 119419, 119427, 57, 49
*ELGEN,  ELSET=support
3801, 4, 8, 1
*SOLID SECTION, ELSET=support, MATERIAL=support_steel
400.0
*MATERIAL,  NAME=support_steel
```

```
*density
7.85E-9
*DAMPING, STRUCTURAL=0.25
*ELASTIC
201300000000.0,0.3
**--------------------------------- lower steel ----------------
---
*ELEMENT, TYPE=T2D2, ELSET=BARS1
4001, 6921, 6929
4014, 7025, 7029
4019, 7045, 7047
4022, 7051, 7052
4050, 7079, 7081
4053, 7085, 7089
4058, 7105, 7113
4132, 7697, 7701
4137, 7717, 7719
4140, 7723, 7724
4168, 7751, 7753
4173, 7757, 7761
4178, 7777, 7785
*ELGEN,  ELSET=BARS1
4001, 13, 8, 1
4014, 5,  4, 1
4019, 3,  2, 1
4022, 28, 1, 1
4050, 3,  2, 1
4053, 5,  4, 1
4058, 74, 8, 1
4132, 5,  4, 1
4137, 3,  2, 1
4140, 28, 1, 1
4168, 3,  2, 1
4173, 5,  4, 1
*SOLID SECTION, ELSET=BARS1, MATERIAL=lower_steel
4325.757234
*MATERIAL,  NAME=lower_steel
*density
7.85E-9
*DAMPING, STRUCTURAL=0.25
*ELASTIC
201300.0,0.3
*PLASTIC
303.691603,0.0
*ELSET, ELSET=mid_BARS1
4178
**--------------------------------- upper steel ----------------
---
*ELEMENT, TYPE=T2D2, ELSET=BARS2
4501, 110721, 110729
*ELGEN,  ELSET=BARS2
4501, 108, 8, 1
*SOLID SECTION, ELSET=BARS2, MATERIAL=upper_steel
942.477000
*MATERIAL,  NAME=upper_steel
*density
```

```
7.85E-9
*DAMPING, STRUCTURAL=0.25
*ELASTIC
201300.0,0.3
*PLASTIC
414.0,0.0
**---------------------------------- side bar steel -------------
------
*ELEMENT, TYPE=T2D2, ELSET=BARS4
4801,62281,62289
*ELGEN,  ELSET=BARS4
4801, 108, 8, 1
*SOLID SECTION, ELSET=BARS4, MATERIAL=side_steel
226.194000
*MATERIAL,  NAME=side_steel
*density
7.85E-9
*DAMPING, STRUCTURAL=0.25
*ELASTIC
201300.0,0.3
*PLASTIC
414.0,0.0
**---------------------------------- stirrups steel -------------
----
*ELEMENT, TYPE=T2D2, ELSET=BARS3
5001, 6921,  13841
5061, 7049,  8779
5071, 24349, 27809
5076, 41649, 48569
5111, 7113,  14033
5396, 7785,  14705
5411, 7721,  9451
5431, 25021, 28481
5446, 42321, 49241
*ELGEN, ELSET=BARS3
5001, 15, 6920, 1, 4,  32, 15
5061, 10, 1730, 1, 2,  32, 25
5071, 5,  3460, 1, 2,  32, 25
5076, 10, 6920, 1, 2,  32, 25
5111, 15, 6920, 1, 19, 32, 15
5396, 15, 6920, 1
5411, 10, 1730, 1, 2,  32, 25
5431, 5,  3460, 1, 2,  32, 25
5446, 10, 6920, 1, 2,  32, 25
*SOLID SECTION, ELSET=BARS3, MATERIAL=stirrups_steel
226.1940
*MATERIAL,  NAME=stirrups_steel
*density
7.85E-9
*DAMPING, STRUCTURAL=0.25
*ELASTIC
201300.0,0.3
*PLASTIC
414.0,0.0
**---------------------------CFRP-------------------------------
---
```

```
*ELEMENT, TYPE=T2D2, ELSET=CFRP
5501,118650,118651
5515,118664, 118666
5518,118670, 118674
5521,118682, 118690
5597,119290, 119294
5600,119302, 119304
5603,119308, 119309
5616,119321, 136922
5617,136922, 119322
5618,119322, 119323
5632,119336, 119338
5635,119342, 119346
5638,119354, 119362
*ELGEN,  ELSET=CFRP
5501, 14,1, 1
5515, 3, 2, 1
5518, 3, 4, 1
5521, 76,8, 1
5597, 3, 4, 1
5600, 3, 2, 1
5603, 13,1, 1
5618, 14,1, 1
5632, 3, 2, 1
5635, 3, 4, 1
5638, 2, 8, 1
*SOLID SECTION, ELSET=CFRP, MATERIAL=CFRP_PLATE
762.2
*MATERIAL, NAME=CFRP_PLATE
*density
1.8E-9
*DAMPING, STRUCTURAL=0.25
*ELASTIC
51700.0,0.3
**---------------------------COH--------------------------------
---
*ELEMENT, TYPE=COH2D4, ELSET=COH
6001, 118650, 118651, 146,    145
6015, 118664, 118666, 161,    159
6018, 118670, 118674, 169,    165
6021, 118682, 118690, 185,    177
6097, 119290, 119294, 789,    785
6100, 119302, 119304, 799,    797
6103, 119308, 119309, 804,    803
6116, 119321, 136922, 130001, 816
6117, 136922, 119322, 817,    130001
6118, 119322, 119323, 818,    817
6132, 119336, 119338, 833,    831
6135, 119342, 119346, 841,    837
6138, 119354, 119362, 857,    849
*ELGEN,  ELSET=COH
6001,14,  1, 1
6015, 3,  2, 1
6018, 3,  4, 1
6021, 76, 8, 1
6097, 3,  4, 1
```

```
6100, 3,  2, 1
6103, 13, 1, 1
6118, 14, 1, 1
6132, 3,  2, 1
6135, 3,  4, 1
6138, 2,  8, 1
*COHESIVE SECTION, ELSET=COH, MATERIAL=EPOXY,RESPONSE=TRACTION
SEPARATION, THICKNESS=SPECIFIED
1.0,300.0
*MATERIAL, NAME=EPOXY
*density
1.8E-9
*DAMPING, STRUCTURAL=0.25
*ELASTIC, TYPE=TRACTION
2500.0,508.4602,508.4602
*DAMAGE INITIATION, CRITERION=QUADS
1.506106,1.5,1.5
*damage evolution, type=energy, softening=exponential, mixed mode
behavior=bk, power=1.45
0.09,0.9,0.9
*section controls, name=CONT1, element deletion=yes, max
degradation=0.95
**------------------------------------------------------------------
---
*BOUNDARY
side,    1
support, 2
*AMPLITUDE,NAME=P1, value=relative, smooth=0.01, DEFINITION=SMOOTH
STEP
0.0,0.0,   1.5,1.0
*STEP, NAME=ST1
*Dynamic, Explicit, FIXED TIME INCREMENTATION
, 1.5
*FIXED MASS SCALING, DT=1.0E-6, TYPE=BELOW MIN, FACTOR=1
*DLOAD, AMPLITUDE=P1
raw_dist_load,P3,0.0705762
1785,P3,6.5979
1786,P3,6.5979
*FILE OUTPUT, NUMBER INTERVAL=50, TIME MARKS=NO
*EL FILE,   ELSET=beam1
S,LE
*EL FILE,   ELSET=cover
S,LE
*EL FILE,   ELSET=mid_BARS1
LE
*EL FILE,   ELSET=CFRP
S,LE
*EL FILE,   ELSET=COH
LE,S
*NODE FILE, NSET=mid
U
**************************************************
*OUTPUT,FIELD,VARIABLE=PRESELECT, NUMBER INTERVAL=50
*ELEMENT OUTPUT,   ELSET=beam1,POSITION=NODES
LE,S
*ELEMENT OUTPUT,   ELSET=cover,POSITION=NODES
```

```
LE,S
*ELEMENT OUTPUT,    ELSET=mid_BARS1,POSITION=NODES
LE,S
*ELEMENT OUTPUT,    ELSET=CFRP,POSITION=NODES
LE
*ELEMENT OUTPUT,    ELSET=COH,POSITION=NODES
LE,SDEG,S
*NODE  OUTPUT,     NSET=mid
U
*************************************************
*OUTPUT,HISTORY,VARIABLE=PRESELECT,TIME INTERVAL=0.001
*ELEMENT OUTPUT,    ELSET=beam1
LE,S11
*ELEMENT OUTPUT,    ELSET=cover
LE,S
*ELEMENT OUTPUT,    ELSET=mid_BARS1
LE,S
*ELEMENT OUTPUT,    ELSET=CFRP
LE,S
*ELEMENT OUTPUT,    ELSET=COH
LE,SDEG,S
*NODE  OUTPUT,     NSET=mid
U2
*END STEP
```